High Resolution Simulation of Laminar and Transitional Flows in a Mixing Vessel

Matthew J. Rice

Dissertation submitted to
Virginia Polytechnic Institute and State University
in partial fulfillment of the requirements for the degree
of
Doctor of Philosophy
in
Mechanical Engineering

Clinton L. Dancey, Chair
Saad A. Ragab
Danesh K. Tafti
Brian L. Vick
Pavlos P. Vlachos
Mark A. Stremler

School of Engineering
Department of Mechanical Engineering

April 2011
Blacksburg, Virginia, USA

Keywords:Mixing Vessel, Rushton Turbine, Laminar Flow, Transitional Flow, Direct Numerical Simulation (DNS), Turbulence Transport Equation, Force Interaction, Analytical Solution

Abstract

The present work seeks to fully investigate, describe and characterize the distinct flow regimes existing within a mixing vessel at various rotational speeds. This investigation is computational in nature and simulates the flow within a baffled tank containing a Rushton turbine of the standard configuration. For a Re based on impeller diameter and blade rotational speed ($Re \equiv \rho N D^2/\mu$) the following flow regimes were identified and investigated in detail: *Reverse/reciprocating flows* at very low Re ($\lessapprox 10$);*stalled flows* at low Re ($Re \approx 10$); *laminar pumping flow* for higher Re and *transitional pumping flow* ($10^2 \lesssim Re \lesssim 10^4$).

For the three Re numbers 1, 10 and 28, it was found that for the higher Re number (28), the flow exhibited the familiar outward pumping action associated with radial impellers under turbulent flow conditions. However, as the Re number decreases, the net radial flow during one impeller revolution was reduced and for the lowest Re number a *reciprocating* motion with negligible net pumping was observed. In order to elucidate the physical mechanism responsible for the observed flow pattern at low Re, the forces acting on a fluid element in the radial direction were analyzed. Based on this analysis, a simplified quasi-analytic model of the flow was developed that gives a satisfactory qualitative, as well as quantitative representation of the flow at very low Re.

Investigation of the transitional flow regime ($Re \approx 3(10^3)$) includes a compilation and characterization of ensemble and turbulent quantities such as the Reynolds stress components, dissipation length η and time scales τ, as well a detailed investigation of the near-impeller flow and trailing vortex. Calculation and compilation of all terms in the turbulent kinetic energy transport equation was performed (including generation and the illusive turbulent pressure work). Specifically, the most important transport mechanism was turbulent convection/diffusion from the impeller disk-plane/trailing vortex region. Mean flow transport of turbulent kinetic energy was primarily towards the impeller disk-plane and radially outward from the trailing vortex region. The turbulent pressure work was found to partially counteract turbulent convection. Turbulent dissipation followed by turbulent viscous work were found to be the least important mechanism responsible for turbulent transport with both terms being maximized within the vortex region and at the disk-plane down-stream from the vortices.

Original Contribution

The following work provides a detailed and thorough analysis of the flow physics present within a Rushton turbine stirred vessel, producing the following original contributions:

1. Detailed numerical investigation of laminar flow and the associated pumping breakdown within a stirred vessel:

   (a) Determination of physical mechanism responsible for the change in flow pattern from pumping to stall at very low Re (generally applicable to all radial flow impellers)

   (b) Explicit investigation of the near impeller forces on the fluid particle

   (c) Development of an accurate quasi-analytical equation of motion in the radial direction which incorporates all relevant physical processes for flow at very low Re

2. Detailed high resolution (DNS) numerical investigation of transitional flow within a mixing vessel with explicit resolution down to length scales of $\approx 10\eta$:

   (a) Use of experimentally corrected LES simulation results to formulate proper high resolution (DNS) simulation geometry

   (b) Explicit investigation of the near impeller mean flow forces on the fluid particle

   (c) Highly detailed investigation of near-impeller flow dynamics including inception and propagation of the impeller trailing vortex

   (d) Investigation and visualization of impeller trailing vortex in the vortex relative frame

   (e) Direct calculation and subsequent investigation of most turbulent quantities of interest within the entire mixing vessel

   (f) Formulation and utilization of a Reynolds stress parameter to quantify turbulence anisotropy

   (g) Direct calculation and investigation of all terms in the steady-state TKE transport equation including generation and pressure-work

Acknowledgments

I would like to dedicate this Dissertation to my Father who passed away in July of 2009. He would have wanted to see this day.

I would also like to express my appreciation to those who have helped make this work possible over the last five years (too long!):

- My adviser Dr. Clinton Dancey for his patience, as well as Dr. George Papadakis at King's College for direction when the coding became tedious.
- My family back in Portland and Phoenix, especially my Grandparents Fred and Betty, Uncle Paul, Mother Phyllis and Aunt Kathy.
- The 'Gang' at King's College, Sergio, Mardit, Simon, Shogi and Stathis, for their humor, tasty lunches, tipsy dinners, good conversation and honest friendship.
- The other 'Gang' of Hancock 111: Ozan, John and Soonkie for their fun and easy conversation.
- Dr. Ivana Milanovic, for showing what was possible
- Tao, for just being there.

Typeset in glorious LaTeX

Contents

List of Tables

List of Figures

Chapter 1

Introduction

1.1 Motivation

Agitators and mixing devices are commonly used in various industries such as the chemical, petro-chemical and food/pharmaceutical processes industries. As a result, a large number of studies on various mixer configurations have been performed for the purpose of minimizing process wastage, duration and enhancement of product quality. Traditionally, experiment-based design methods using scaling laws or bulk control volume analysis have been used in designing industrial mixers. Even though this method of design is economic given the high cost of alternative methods, such as computationally based design procedures, (as used in the aero-space industry), substantial product wastage and resulting productivity losses still persist: For the overall U.S. chemical process industry, losses are estimated to be on the order of $\$1 - 2$-B's per year [1]. However, with the increased sophistication of computational fluid dynamics codes and reduced cost of computing power, computational methods are becoming a more practical method for analyzing the complex flows present in mixing vessels. Benefits of the computational approach include the extensive and detailed information yielded by (proper) computational simulations. In the case of direct numerical simulations (DNS), the full (time accurate) velocity, pressure and hence turbulent kinetic energy and dissipation field can be calculated everywhere within the vessel (including the near impeller region). In addition, extraction of the detailed force interaction on the fluid can be performed, further increasing the information available via computational methods. Thus, the potential utility of computational methods in investigating fundamental flow physics in a mixing vessel is greater than experimental methods. Costs associated with such high resolution (direct) simulation of the flow is the extensive computational power (speed), memory and file storage requirements associated with the requirement of resolving the flow down to (on the order of) the dissipation length and time scales. These costs can be lowered by progressively more complex modeling assumptions, (thus alleviating the explicit requirement for resolving the small scale dissipative motions), as in the case of RANS and LES models for turbulent flow. However, with the application of further modeling assumptions detailed information is necessarily lost, thus reducing the explanatory power and/or accuracy of the resulting computational solution.

Impeller configurations used in industry range from axial flow impellers to shrouded-

impellers to high shear (high power consumption) radial impellers such as the Rushton turbine (used primarily for high shear applications such as liquid-gas dispersion agitators). It is the latter which has received extensive experimental (and moderate numerical) investigation, and which will now be analyzed in detail via numerical methods herein.

1.2 Scope of the Work

The following provides the key objectives to be pursued by this work, where it must be noted that the methods used are computational in nature and apply to a Rushton turbine agitated tank for a single phase fluid. This research is sub-divided into two general areas of investigation: Low Re laminar flow and medium Re transitional flow in an agitated tank. With respect to the low Re flow the following investigation will be performed:

1. Identify the distinct flow regimes present at low ($Re = 28$) and very low ($Re = 1$) Reynolds numbers for flow within a mixer: Reciprocating and pumping flow.
2. Identify via a force analysis, the physical mechanism responsible for these alternate flow regimes (i.e. reciprocating vs. pumping flow).
3. Verify the previous observations by formulating a pseudo-analytical solution which qualitatively predicts the flow, thus demonstrating the completeness of the previous analysis of the physics governing the flow at low vs. very low Re.

In the case of medium (transitional) flow $Re = 3000$, the following will be investigated:

1. With respect to mean-flow properties:
   (a) Identify the origin and propagation of the macro-instabilities (trailing vortices) and elucidate details of the near impeller flow.
   (b) Identify the fundamental force interactions responsible for the overall and detailed flow pattern near the impeller, including the causal mechanism responsible for the origin of macro-instabilities such as the trailing vortices.
2. Extraction of turbulent quantities such as Reynolds stresses, turbulence intensities and thus, with respect to turbulent properties:
   (a) Identify and examine the extent to which turbulence is isotropic within the vessel.
   (b) Calculate and investigate the local turbulent dissipation based on calculation of all relevant spacial velocity gradients.
   (c) Calculate and investigate the spacial distribution of Kolmogorov length and time scales based on calculated dissipation.
   (d) Completely identify and examining the separate mechanisms responsible for distribution of turbulence within the vessel: The decomposition of the turbulent transport equation to quantify convection, diffusion/work (including the experimentally illusive pressure work/diffusion term), generation and dissipation.

3. Based on the above, formulate general mixing strategies for dilute mixtures with $\mathcal{SCH} \equiv \frac{\nu}{D} \sim 1$ based of the observations gleaned from the previous

1.3 Thesis Outline

The remainder of this thesis is subdivided into the following six chapters: Chapter 2 provides the relevant theoretical analysis of the physical phenomena (i.e. single phase turbulent flow for a Newtonian fluid) and hence, the scientific foundation for the thesis. The resulting mathematical relationships derived is that chapter are reduced to numerically amenable form and the relevant flow solution (computational) methods and procedures are presented in chapter 3. The remaining chapters present results on the high resolution simulation of flow within a mixing vessel for laminar and transitional flow. Specifically, chapter 4 presents an analysis of the flow and the governing physical mechanisms in a mixing vessel at low and very low Re numbers (Re = 28, 10 and 1). This is followed by two additional chapters which sub-divide the investigation and analysis of transitional flow in a mixing vessel at a $Re = 3000$. Specifically, chapter 5 presents the procedure used to formulate the simulation geometry, technique of statistical analysis and the resulting mean-flow analysis along with experimental validation. Chapter 6 extends the analysis for transitional flow in a mixing vessel to turbulent quantities including calculation of the Reynolds stresses, turbulent kinetic energy and dissipation, dissipation scales and the resulting turbulent processes extracted via the decomposition of the turbulent kinetic energy transport equation. Comparison of turbulent quantities with experimental data is performed where possible for purposes of simulation validation. Recommendations with respect to mixing strategies are also given herein. Chapter 7 gives a brief conclusion and overview of the research presented in this work including the main findings, followed by a recommendation for future research.

Finally, it should be noted that each results chapter, (4 through 6), are formatted, as near as possible, in the standard stand-alone paper format and include a distinct introductory, results and conclusion section with associated literature review.

References

[1] G. Tatterson. *Scale-up and design of industrial mixing processes.* McGraw-Hill, 1994.

Chapter 2

Fundamental Processes

2.1 Outline

Given that fluid flow and flow *turbulence* are central to this work, an effort will be made, where possible, to justify the numerical treatment in terms of basic flow physics. To this end, the current chapter will be arranged as follows:

1. Formulation of the fluid equations of motion and mass conservation via fundamental concepts (e.g. $\vec{F} = m\vec{a}$), as well at the characterization of the conversion of mechanical to internal energy via viscous dissipation: §2.2

2. Demonstration of the instability of fluid motion (under certain conditions) for a simple engineering case (flat plate flow) and hence, establish the existence of the flow phenomena known as *turbulence*: §2.3

3. Demonstration of the *suitability* or *physicality* of characterizing these flow instabilities via Fourier analysis: §2.3

4. Combine the previous with the ideas of Kolmogorov to fully characterize, (in a statistical sense), turbulent motion under restricted, but useful conditions: §2.4

5. Provide an illustration of the methods used in turbulence modeling (e.g. mixing length ℓ, $k\epsilon$, LES turbulence models) : §2.6.1, §2.6.2 and §2.6.3

6. Describe the model-less turbulence formulation known as the **D**irect **N**umerical **S**imulations **DNS** methodology:§2.7

7. Apply the previous concepts to formulate important parameters used to characterize flows in mixing vessels via dimensional analysis: §2.9

8. Describe rudimentary vortex dynamics including an illustration of the concept of the *vortex relative frame* as well as various vortex detection methods: §**??**

2.2 Fluid Dynamics

The general purpose of any numerical investigation of a flow process is to determine flow properties such as velocity $\vec{V}$ and pressure P satisfying conservation of momentum and mass (i.e. the fluid equation of motion ($\vec{F} = m\vec{a}$) and the continuity equation ($\dot{m} = 0$) as applied to an open system). In addition, the conversion of fluid mechanical energy into internal energy via viscous dissipation (i.e. the source of losses) is of fundamental interest.

2.2.1 Fluid Equation of Motion

For an intensive property ϕ, corresponding to the extensive property Φ, we have the general transport or conservation equation

$$\frac{D\Phi}{Dt} = NSD,$$

$$NSD \equiv \textit{Net Source and Diffusion} \tag{2.1}$$

where the term NSD represents the net source and diffusion of the extensive property Φ for a system of *fixed mass* in space. For the case of mass M and linear momentum component L_i we have the following values of NSD as given in Table 2.1.[1]

Table 2.1: Fundamental conservation relationships in mechanics

Φ	ϕ	NSD	Conservation law
M	1	0	Mass Conservation
L_i	V_i	$[_{surface}F_i +_{body} F_i]$	Newton's Second Law
M_i	y_i	$[_{surface}Diffusion]$	Fick's Law of Species Diffusion

In the case of an Eulerian frame (fixed or moving), the conservation laws for mass M and linear momentum $\vec{L}$ (for a constant density), reduce to the incompressible fluid continuity

[1] It should be noted that for a Lagrangian or particle following frame of reference, $\phi(t)$, while for an Eulerian frame (where the position of observation is located arbitrarily in space) $\phi(t, \vec{r})$ (where $\vec{r}$ is a position vector). Thus the material derivative $D()/Dt$ given in (2.1) reduces to

$$\frac{d\Phi}{dt} = NSD|_{\textit{fixed mass/closed system}} : \text{Lagrangian Frame} \tag{2.2}$$

$$\frac{\partial(\rho\phi)}{\partial t} + \nabla(\vec{\rho\phi}) \cdot \frac{\partial \vec{r}}{\partial t} = \frac{\partial(\rho\phi)}{\partial t} + \nabla(\vec{\rho\phi}) \cdot \vec{V} = NSD|_{\textit{Per unit Volume on fixed mass system}} : \text{Eulerian Frame/CV} \tag{2.3}$$

Specifically, in the Eulerian expression for conservation of $\Phi(t, \vec{r})$, the first term represents the temporal change in Φ (within the infinitesimal control volume CV), while the second term represents the net convection of Φ through the (infinitesimal) control volume. Note, it should be pointed out that the term NSD is the net source for the *fixed mass system* (which is moving through a region in space designated as the (open) control volume). Hence, for example, if the intensive property of interest ϕ is energy per unit mass e, quantities with origin in the NSD term, such as pressure or viscous work, are based on the product of local control volume (which coincides with the fixed mass system) stresses and the fixed mass system velocity (i.e. absolute velocity).

and fluid equations of motion[2]

$$\begin{aligned} \vec{\nabla} \cdot \vec{V} &= 0 \\ \rho \frac{\partial \phi}{\partial t} + \rho \vec{\nabla} \cdot (\vec{V}\phi) &= \vec{\nabla} \cdot (\Gamma \vec{\nabla} \phi) + NS_i, \\ \phi &= V_i, i = 1, 2, 3 \end{aligned} \tag{2.6}$$

where Γ is the gradient transport diffusive coefficient (i.e. the absolute viscosity μ for a Newtonian fluid). Hence, in the i^{th}-direction we define the net source *less gradient transport diffusion* NS_i as

$$\begin{aligned} NS_i &\equiv NSD_i - \vec{\nabla} \cdot (\Gamma \vec{\nabla} \phi), \\ \phi &= V_i, i = 1, 2, 3 \end{aligned} \tag{2.7}$$

The source term NS_i represents surface and body forces (per unit mass) *excluding* net diffusive momentum transfer (e.g. pressure force per-unit volume $-\partial P/\partial x_i$).

2.2.2 Momentum and Energy Transfer

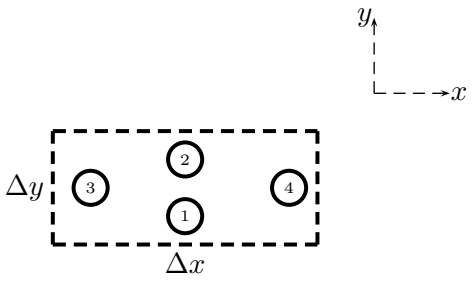

Figure 2.1: Control volume analysis for dissipation determination

Noting the previous treatment of the fluid equation of motion, (2.6) and (2.7), one can view the viscous diffusion terms as momentum sinks which effectively convert mechanical energy into internal energy (heat) via a molecular (frictional) process. In terms of energy alone, one can view the process as one of *dissipation of mechanical energy* (*ke*, *pe* and pressure work per unit mass) via shear and irreversible fluid deformation work. The concept of dissipation can be made exact by investigation of the power consumption due to friction within a differential control volume.

[2] In the case of an Eulerian frame (fixed or moving), the conservation laws for mass M and linear momentum $\vec{L}$ reduce to the continuity and equations of motion

$$\begin{aligned} \frac{\partial \rho}{\partial t} + \vec{\nabla} \cdot (\vec{V}\rho) &= 0 \\ \frac{\partial (\rho \phi)}{\partial t} + \nabla \vec{(\rho \phi)} \cdot \vec{V} &= (_{surface} F_i + _{body}\, F_i)_{per\ unit\ vol.}, \\ \phi &= V_i, i = 1, 2, 3 \end{aligned} \tag{2.4}$$

where V_i refers to the $\hat{x}$, $\hat{y}$ or $\hat{z}$ components of velocity. Thus, this present work will be entirely composed of investigating the phenomena associated with conservation of mass and momentum applied to a particular physical process. The convective term can be rewritten in the case of divergence free (i.e. incompressible $\rho = const. \Longrightarrow \nabla \cdot \vec{V} = 0$) flow as

$$\nabla \vec{(\rho \phi)} \cdot \vec{V} = \rho((\vec{\nabla} \phi \cdot \vec{V} + \phi(\vec{\nabla} \cdot \vec{V})) - \phi(\vec{\nabla} \cdot \vec{V})) = \rho(\vec{\nabla} \cdot (\phi \vec{V})) \tag{2.5}$$

Specifically, referring to Figure 2.1 we utilize a control volume bound by surfaces ①, ②, ③ and ④. To determine the shear induced power consumption for the system bound by the control volume, the net shear power must be summed over all surfaces. For a divergence free flow (incompressible) the relevant shear and normal stress components in the x-direction are

$$\tau_{yx} = \mu \left[\frac{\partial U_x}{\partial y} + \frac{\partial U_y}{\partial x} \right] \tag{2.8}$$

$$\tau_{xx} = 2\mu \left[\frac{\partial U_x}{\partial x} \right] \tag{2.9}$$

(where the second term in the tangential stress expression τ_{yx} is the *effective* induced shear stress due to internal fluid element deformation via U_y gradients in the x-direction). Recalling that power is the product of force and velocity, the net x-direction shear work done on the CV per unit volume is

$$[(U_x\tau_{yx})\Big|_2 - (U_x\tau_{yx})\Big|_1)\Delta x + ((U_x\tau_{xx})\Big|_4 - (U_x\tau_{xx})\Big|_3)\Delta y]\frac{1}{\Delta V} \tag{2.10}$$

Or, in the limit as $\Delta V \to 0$

$$\left[\frac{\partial (U_x\tau_{yx})}{\partial y} + \frac{\partial (U_x\tau_{xx})}{\partial x} \right] =$$

$$\left[\frac{\partial (U_x\tau_{yx})}{\partial y} + \frac{\partial (U_x\tau_{xx})}{\partial x} \right] = \frac{\partial}{\partial y}[U_x\mu[\frac{\partial U_x}{\partial y} + \frac{\partial U_y}{\partial x}]] + \frac{\partial}{\partial x}[(U_x 2\mu \frac{\partial U_x}{\partial x}] =$$

$$\mu[\frac{\partial U_x}{\partial y}[\frac{\partial U_x}{\partial y} + \frac{\partial U_y}{\partial x}] + U_x[\frac{\partial^2 U_x}{\partial y^2} + \frac{\partial^2 U_y}{\partial y \partial x}] + 2[(\frac{\partial U_x}{\partial x})^2 + U_x \frac{\partial^2 U_x}{\partial x^2}]] \tag{2.11}$$

yielding

$$\mu[(\frac{\partial U_x}{\partial y})^2 + \frac{\partial U_x}{\partial y}\frac{\partial U_y}{\partial x} + U_x[\frac{\partial^2 U_x}{\partial y^2} + \frac{\partial^2 U_x}{\partial x^2}] + 2(\frac{\partial U_x}{\partial x})^2] \tag{2.12}$$

Now, let direction x correspond to an index direction i, the above reduces to

$$\mu[U_i(\frac{\partial^2 U_i}{\partial x_j^2}) + (\frac{\partial U_i}{\partial x_j})^2 + \frac{\partial U_i}{\partial x_j}\frac{\partial U_j}{\partial x_i}] \text{ (sum over } j) =$$

$$\mu[\frac{\partial}{\partial x_j}(U_i\frac{\partial U_i}{\partial x_j}) + \frac{\partial}{\partial x_j}(U_i\frac{\partial U_j}{\partial x_i})] \text{ (sum over } j) \tag{2.13}$$

where continuity has been utilized at the last step. Summing the viscous power over all directions (sum over i) as applied to (2.13) gives the final expression for the viscous power consumptions where the Einstein summation notation applies for all indices

$$\boxed{\mu \frac{\partial}{\partial x_j}[(\frac{\partial U_i}{\partial x_j} + \frac{\partial U_j}{\partial x_i})U_i]} \tag{2.14}$$

Note that (2.14) gives an expression for the shear induced viscous power consumption and thus is composed of two parts: The conversion of viscous work into fluid kinetic energy and heat via irreversible viscous deformation. Carrying out the differentiation in (2.14) and applying continuity we have

$$\boxed{\overbrace{\mu(\frac{\partial U_i}{\partial x_j} + \frac{\partial U_j}{\partial x_i})\frac{\partial U_i}{\partial x_j}}^{\textit{Visc. Diss. via Deformation}} + \overbrace{\mu(\frac{\partial^2 U_i}{\partial x_j \partial x_j})U_i}^{\textit{Kinetic E. Increase Via Shear Work}}} \tag{2.15}$$

Thus, the viscous dissipation per unit volume, for a general incompressible flow field, can be written as[3]

$$\boxed{\text{Visc. Diss. per Unit Vol.} = \mu(\frac{\partial U_i}{\partial x_j} + \frac{\partial U_j}{\partial x_i})\frac{\partial U_i}{\partial x_j}} \tag{2.17}$$

To determine the total instantaneous power consumption due to frictional losses one must integrate the local dissipation (2.17) (or if one can assume isotropic flow, (2.16)) over a given system volume giving

$$\text{Total/Integrated Dissipation} = \int_{Vol} \mu(\frac{\partial U_i}{\partial x_j} + \frac{\partial U_j}{\partial x_i})\frac{\partial U_i}{\partial x_j} dVol \tag{2.18}$$

2.3 Solutions to the Fluid Equation of Motion: Stability

Due to the non-linearity of the convection terms, the solution to the fluid equations of motion (2.6) may not be unique. An example of this fact is the laminar flow solution for the flat plate which should, theoretically, describe the motion for all Re. Yet, experimental evidence indicates that such solutions break-down as the fluid particle moves along the plate over an extended distance. This break-down in the initial *laminar* flow pattern into a complex, unsteady flow exhibiting significant bulk flow mixing, is referred to as the *transition to turbulence*. Thus, we can state that laminar flow solutions for the fluid equation of motion can become unstable as confirmed by observations of natural processes.

We begin the description of laminar flow instabilities, as a precursor to turbulence, by investigating one of the simplest, but most useful flows in fluid engineering: Flow over a flat plate.

[3]The fact will be utilized later that under conditions of isotropic flow where $U_i = U_j$ (applicable to isotropic turbulence where $u_i' = u_j'$), viscous dissipation reduces to the following via continuity

$$\boxed{\text{Visc. Diss. per Unit Vol. Isotropic Flow} = \mu \frac{\partial U_i}{\partial x_j}\frac{\partial U_i}{\partial x_j}} \tag{2.16}$$

2.3.1 A Characterization of Turbulence

The instability known as turbulence can be described (following the treatment originated by Reynolds [8]), in terms of small local perturbations from the local, (assumed steady), average flow pattern. Specifically, we express a local (instantaneous) turbulent generic fluid property $\phi(t,\vec{r})$ in terms of an averaged $\overline{\phi}(\vec{r})$ and perturbation or fluctuating property component $\phi'(t,\vec{r})$

$$\phi(t,\vec{r}) = \overline{\phi}(\vec{r}) + \phi'(t,\vec{r}) \tag{2.19}$$

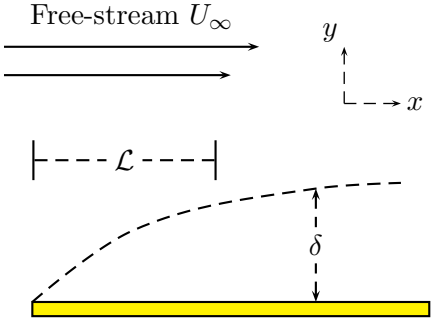

Figure 2.2: Flat plate diagram

where in the case of velocity $\phi = V_i$ for $i = 1,2,3$ or $\vec{V} = \vec{\overline{U}} + \vec{u'}$. Next, we substitute the the above definition (2.19) into the $2-D$ fluid motion and continuity equations (2.6), Making boundary layer assumptions for the flat plate while noting that the diffusive process is that of molecular momentum diffusion (i.e. $\Gamma \equiv \mu$) we get, assuming incompressible flow ($\rho =$ constant)

$$\frac{\partial \hat{u}'}{\partial \hat{x}} + \frac{\partial \hat{v}'}{\partial \hat{y}} = 0 \tag{2.20}$$

$$\dot{\hat{u}}' + \overline{\hat{U}}\frac{\partial \hat{u}'}{\partial \hat{x}} + \hat{v}'\frac{\partial \overline{\hat{U}}}{\partial \hat{y}} = -\frac{1}{L\rho U_\infty^2}\frac{\partial p'}{\partial \hat{x}} + Re^{-1}[\frac{\partial^2 \overline{\hat{U}}}{\partial \hat{y}^2} + \frac{\partial^2 \hat{u}'}{\partial \hat{x}^2} + \frac{\partial^2 \hat{u}'}{\partial \hat{y}^2}] \tag{2.21}$$

$$\dot{\hat{v}}' + \overline{\hat{U}}\frac{\partial \hat{v}'}{\partial \hat{x}} = -\frac{1}{L\rho U_\infty^2}\frac{\partial p'}{\partial \hat{y}} + Re^{-1}[\frac{\partial^2 \hat{v}'}{\partial \hat{x}^2} + \frac{\partial^2 \hat{v}'}{\partial \hat{y}^2}] \tag{2.22}$$

where position and velocity have been non-dimensionalized via plate length L and the free-stream velocity U_∞ yielding $\hat{()}$ quantities. Eliminating the pressure term via subtracting $(\partial/\partial x(2.22))$ from $(\partial/\partial y(2.21))$ and utilizing the continuity equation for the perturbation velocities (2.20) yields

$$\frac{\partial}{\partial t}[\frac{\partial \hat{u}'}{\partial \hat{y}} - \frac{\partial \hat{v}'}{\partial \hat{x}}] + \frac{\partial \overline{U}}{\partial \hat{y}}[\frac{\partial \hat{u}'}{\partial \hat{x}} + \frac{\partial \hat{v}'}{\partial \hat{y}}] + \overline{U}[\frac{\partial^2 \hat{u}'}{\partial \hat{x}\partial \hat{y}} - \frac{\partial^2 \hat{v}'}{\partial \hat{x}^2}] + \hat{v}'\frac{\partial^2 \overline{U}}{\partial \hat{y}^2} = Re^{-1}[\frac{\partial^3}{\partial \hat{y}^3}(\hat{\overline{U}} + \hat{u}') + \frac{\partial^3 \hat{u}'}{\partial \hat{y}\partial \hat{x}^2} - \frac{\partial^3 \hat{v}'}{\partial \hat{x}\partial \hat{y}^2} - \frac{\partial^3 \hat{v}'}{\partial \hat{x}^3}] \tag{2.23}$$

Or

$$\frac{\partial}{\partial t}[\frac{\partial \hat{u}'}{\partial \hat{y}} - \frac{\partial \hat{v}'}{\partial \hat{x}}] + \overline{U}[\frac{\partial^2 \hat{u}'}{\partial \hat{x}\partial \hat{y}} - \frac{\partial^2 \hat{v}'}{\partial \hat{x}^2}] + \hat{v}'\frac{\partial^2 \overline{U}}{\partial \hat{y}^2} =$$

$$Re^{-1}[\frac{\partial^3}{\partial \hat{y}^3}(\hat{\overline{U}} + \hat{u}') + \frac{\partial^3 \hat{u}'}{\partial \hat{y}\partial \hat{x}^2} - \frac{\partial^3 \hat{v}'}{\partial \hat{x}\partial \hat{y}^2} - \frac{\partial^3 \hat{v}'}{\partial \hat{x}^3}] \tag{2.24}$$

Thus, (2.24) *is an equivalent equation of motion for the perturbation velocities* u' and v'.

Noting that experimental observation indicates transition to turbulence occurs at some distance L_{trans} along the plate, this implies a direct dependence of growth or decay of some perturbation on normalized plate position $\hat{x}$ and time t. In addition, one assumes these perturbations are harmonic and thus amenable to Fourier analysis (see Appendix E). Given the previous, one can hypothesize a normalized perturbation stream function of the form $\Psi(\hat{x},\hat{y},t) \equiv \psi(\hat{y})e^{i\kappa\hat{x}-i\beta t}$. The perturbation x and y normalized velocity components $\hat{u}'$ and $\hat{v}'$ (which automatically satisfy continuity by definition of the stream function Ψ) are given by $\frac{d\psi(\hat{y})}{d\hat{y}}e^{i\kappa\hat{x}-i\beta t}$ and $-i\kappa\psi(\hat{y})e^{i\kappa\hat{x}-i\beta t}$ respectively. It should be clear that the resulting perturbation velocities are simply waves with complex wave number κ and complex wave speed β/κ. Most importantly, it should be noted that the perturbation magnitude increases with time if $\mathbf{Im}(\beta) > \mathbf{0}$. Substitution of the above perturbation velocity functional forms into the *perturbation equation of motion* (2.24) yields

$$[-i\beta\frac{d^2\psi}{d\hat{y}^2} - i\beta(i\kappa)^2\psi] + \overline{U}[i\kappa\frac{d^2\psi}{d\hat{y}^2} + (i\kappa)^3\psi] + [(i\kappa)\psi\frac{\partial^2\overline{U}}{\partial\hat{y}^2}] = Re^{-1}[\kappa^4\psi - 2\kappa^2\frac{d^2\psi}{d\hat{y}^2} + \frac{d^4\psi}{d\hat{y}^4}] \quad (2.25)$$

Introducing the complex wave speed $c \equiv \beta/\kappa$ yields a final reduced form for (2.25)

$$\boxed{[\overline{U} - c][\tfrac{d^2\psi}{d\hat{y}^2}] - \kappa^2\psi] + [\psi\tfrac{\partial^2\overline{U}}{\partial\hat{y}^2}] = \tfrac{1}{i\kappa Re}[\kappa^4\psi - 2\kappa^2\tfrac{d^2\psi}{d\hat{y}^2} + \tfrac{d^4\psi}{d\hat{y}^4}]} \quad (2.26)$$

For boundary conditions (2.26) is subject to vanishing velocity perturbation at the wall ($\hat{y} = 0$) and far away from the plate surface ($\hat{y} \to \infty$).[4] Equation (2.26), known as the Orr-Sommerfeld equation, was derived in total by Orr [5] and Summerfield and partially for the inviscid case ($Re \to \infty$) by Rayleigh [7]. It specifies an Eigen-value problem with Eigen-function $\psi(\hat{y})$ and Eigenvalue c for a given wave number κ. A solution to (2.26) was found by Tollmien [12] and Schlichting where the resulting periodic motions are henceforth referred to as Tollmien-Schlichting waves. Regions of damped $\mathbf{Im}(\beta) < \mathbf{0}$, stable $\mathbf{Im}(\beta) = \mathbf{0}$ and amplified flow perturbation $\mathbf{Im}(\beta) > \mathbf{0}$ are mapped as a function of wave number κ and the Re in Figure 2.3 indicating that the inception of wave growth occurs at a Re of approximately 500 while the broadest (in wave number) and highest (in amplification) growth occurs for $Re \approx 10^4$. Noting that transition to turbulence occurs at $Re^{trans}_{flatplate} \approx 5(10^5) > 10^4$ it was conjectured that turbulent flow perturbations have their inception prior (i.e. upstream) of the location corresponding to Re^{trans}, but that significant growth in these flow perturbations as they travel downstream would eventually disrupt the overall (laminar) flow pattern, thus causing a transition to turbulent flow. This conjecture as to the origins and composition of turbulence (harmonic waves which grow and disrupt the bulk flow pattern) remained unsubstantiated experimentally and largely dismissed for some time. However, experimental

[4] Which corresponds to

$$\hat{u}'|_{\hat{y}=0,\infty} = 0, \Rightarrow \frac{\psi}{d\hat{y}}|_{\hat{y}=0,\infty} = 0$$
$$\hat{v}'|_{\hat{y}=0,\infty} = 0, \Rightarrow \psi|_{\hat{y}=0,\infty} = 0 \quad (2.27)$$

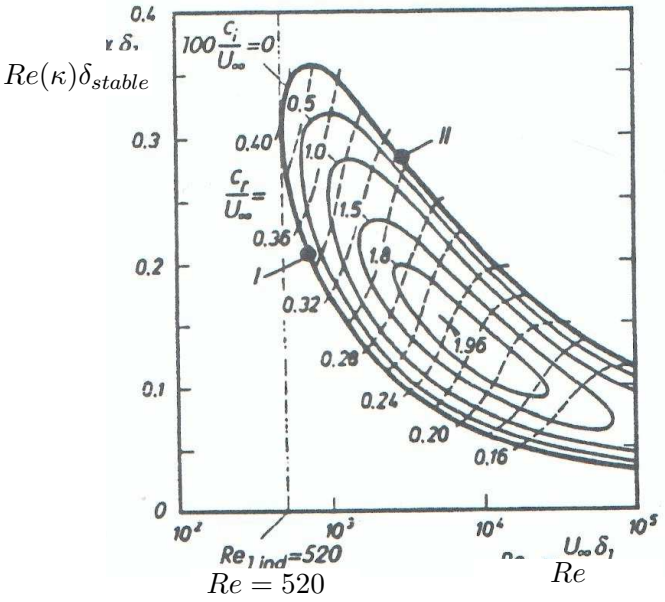

(a) $\frac{c_i*100}{U_\infty} \equiv \frac{\mathbf{Im}(\beta)*100}{U_\infty}$ as a function of Re and normalized wave number $Re(\kappa)/\delta_{stable}$

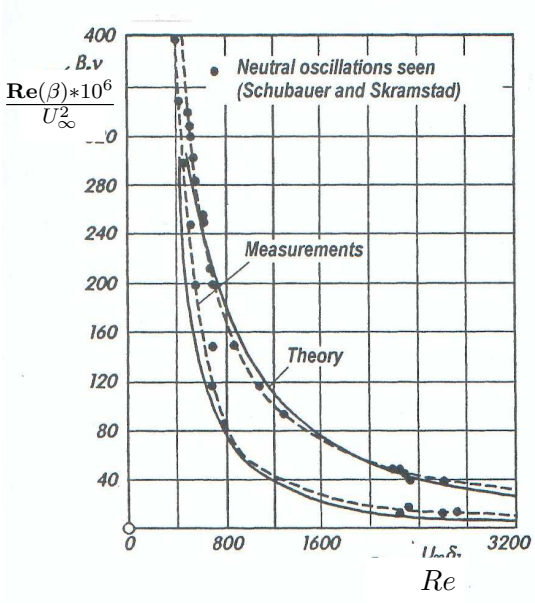

(b) Indifference region for $\frac{\mathbf{Re}(\beta)*10^6}{U_\infty^2}$ as a function of Re

Figure 2.3: (a) Theoretical Normalized Amplificaiton Factor, (b) Theoretical Indifference Curve with Superimposed Experimtal Data of Schubauer and Skramstad as a Function of $Re \equiv \frac{U_\infty \delta_{stable}}{\nu}$ [10] via [9]

confirmation eventually came in the form of hot wire and acoustic measurements of flow over a flat plate. Schubauer and Skramstad's [10] original experiments dealt with precise measurements of BL transition on a flat plate for negligible free-stream turbulence. However, the focus soon centered on the appearance of acoustical waves appearing upstream of the transition location. The inception of these waves in terms of the Re and their composition in terms of wave number (or frequency $Re(\beta/\kappa)/(2\pi)$) were exactly confined to those which should be amplified according to the Orr-Sommerfeld equation (2.26). Specifically, Schubauer and Skramstad determined the indifference wave number (κ such that $\beta = 0$ (i.e. corresponding to detection of perturbation growth free flow)) and plotted these results against those of Schliting via the Orr-Sommerfeld equation. These results are given in Figure 2.3(b) and show a remarkable agreement between theory and experiment. Additionally, it was also determined that the growth of these waves was responsible for the eventual break-down in the laminar flow pattern. Specifically, the perturbation wave motion increased in amplitude, until the wave motion dominated the laminar flow solution, resulting in transition to turbulence.

2.3.2 Treatment of Isotropic Homogeneous Turbulence

Given that the wave nature of induced turbulent disturbances has been established in §2.3.1, the special case of isotropic turbulence should be defined. Specifically, as shall be seen in the following section §2.4, turbulent flows can be considered *statistically invariant* for small scales.

This leads naturally to the further assumption that turbulence is *directionally invariant at all scales*. This imposed constraint reduces turbulence to an 'isotropic' form where turbulent statistics are unchanged with coordinate rotations and hence directionally independent. In addition to isotropy, turbulence can be spatially constrained by requiring that the turbulent kinetic energy is spatially invariant as well. Specifically if $\nabla(u_i'u_i') = 2\nabla k = 0$ then the turbulent is deemed to be 'Homogeneous'.

2.4 Kolmogorov and the Energy Cascade

After experimental confirmation of the wave nature of turbulent instabilities, further progress in the understanding of turbulence is made via the ideas of Kolmogorov. Specifically, if the instantaneous flow kinetic energy and dissipation can be expressed as a mean plus fluctuating component (as in the case of a generic turbulent quantity ϕ) the transfer of turbulent kinetic energy per unit mass $(u_i'u_i')/2$ from large scale motions to smaller, dissipative scales, can be visualized in Figure 2.4, henceforth referred to as the *energy cascade*.[6] If the largest scale of motion is given by $\mathcal{U}$ and $\mathcal{L}$ (which are associated with the geometric velocity and length scales), large scale turbulent motion (i.e. tumbling eddies with length and velocity scale $\lesssim \mathcal{L}$ and $\lesssim \mathcal{U}$) decompose (due to instability) into smaller intermediate eddies. This decomposition/breakup process proceeds until an eddy length/size and velocity scale (η and u_η) are reached, for which viscous dissipation is dominant. The result is a conversion of eddy kinetic energy into internal energy (heat) due to the action of molecular viscosity (friction or viscous dissipation).

2.4.1 The Kolmogorov Hypothesis

The Kolmogorov hypothesis can be stated as follows:

- For sufficiently small scales ($\ell < l_{IE}$ as illustrated in Figure 2.4) turbulence scales are locally isotropic and independent of large scale (l_0) turbulent processes.

This implies:

- For sufficiently small scales of turbulence, all fundamental statistical information is obtained via the averaged local dissipation and molecular viscosity (i.e. $\overline{\epsilon'}$ and ν).

The first statement implies the (direct) *independence of all small scale local turbulence statistics on macro-scopic variables* (i.e. Turbulent Parameters $\neq f(\mathcal{L},\mathcal{U})$) thus establishing the *universal applicability* of the Hypothesis. The second statement makes explicit that since small scale dissipative turbulent velocity u_η and length ℓ_η parameters are locally independent of macro-quantities, the only remaining independent variables of physical significance are the local (molecular) viscosity μ and turbulent energy dissipation (of turbulent kinetic energy $\rho\overline{k'}$) per unit volume $\rho\overline{\epsilon'}$, where $\overline{\epsilon'}$ is the average turbulent dissipation per unit mass.

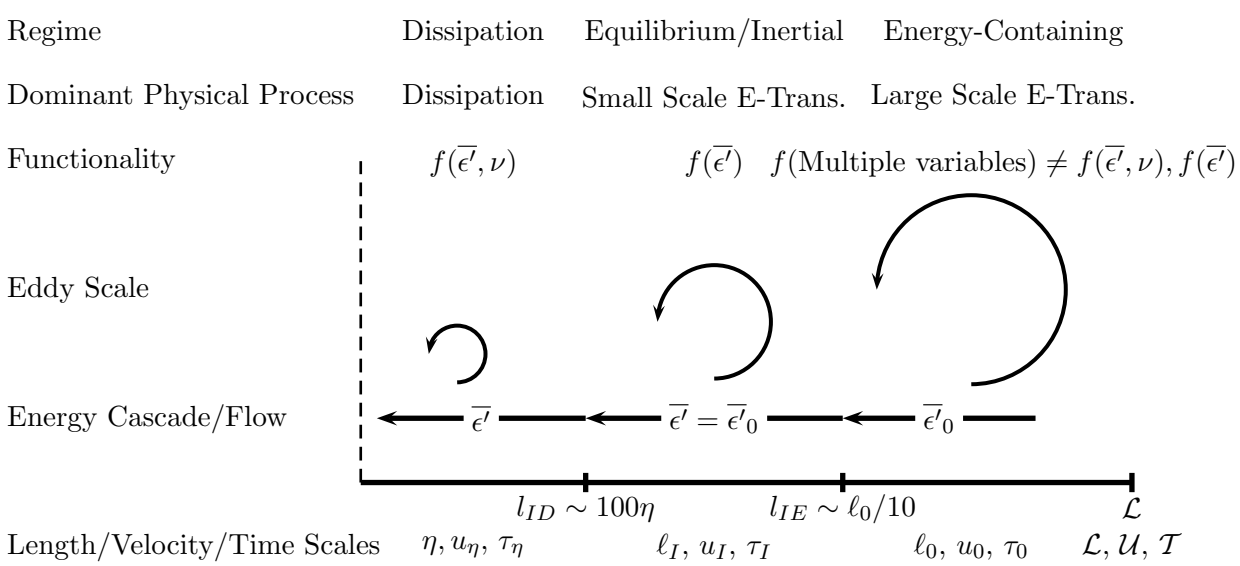

Figure 2.4: Energy cascade, associated scales and statistics functionality $f()$ (courtesy of Pope [6]).

In other words, for sufficiently small scales, turbulence descriptors are at most $f(\nu, \overline{\epsilon'})$.[5] Another implication of the Kolmogorov Hypothesis is that viscous dissipation via viscous power conversion of turbulent kinetic energy to internal energy or heat, is of direct importance only for the small, dissipative scales of turbulent motion in the dissipation region (see Figure 2.4), where turbulent quantities are a function of fluid kinematic viscosity as well as the local dissipation (i.e. $f(\overline{\epsilon'}, \nu)$). Thus, for larger scales $l_{ID} \lesssim \ell_I \lesssim l_{IE}$ (average) turbulent processes are $f(\overline{\epsilon'})$. Hence, the above implies three distinct spacial regions or scales of turbulence: A large scale energetic region $I_{IE} \lesssim \ell_0 \lesssim \mathcal{L}$ where local turbulent scales $\ell = \ell_0$ are directly related to macro-scopic scales. A dissipative region with scale $\ell \sim \eta \lesssim l_{ID}$ where turbulence is not a function of large scale motion, and turbulent kinetic energy is dissipated via molecular friction. An intermediate or equilibrium region with scale $\ell = \ell_I$ such that $l_{ID} \lesssim \ell_I \lesssim l_{IE}$ where dissipation of turbulent kinetic energy into internal energy is negligible and large scale turbulent motions $\sim l_{IE}$ are progressively broken down into smaller motions $\sim l_{ID}$.

Finally, it should be stated that the phrase *for sufficiently small scales* implies that turbulent processes occur an scales much smaller than the macro-scopic or geometric scales. Indeed, for $Re \to 0$ large (macro) scale motion length $\mathcal{L}$ and velocity $\mathcal{V}$ scales become similar to the large-scale turbulent velocity u_0 and length ℓ_0 scales. Hence, the Kolmogorov Hypothesis describes motions only in the case of sufficiently high Re numbers.

2.4.2 Implication of the Kolmogorov Hypothesis

Given the fundamental importance of local (average) dissipation $\overline{\epsilon'}$ and (kinematic) viscosity ν in describing the smallest scales of turbulence, the following combinations can be formed

[5] It should be noted that via the Buckingham Pi Theorem time, length (and consequently velocity) scales can be formed via the two physical quantities ν and $\overline{\epsilon'}$ (having units of m^2/s and m^2/s^3).

$(\nu^3/\overline{\epsilon'})^{1/4}$, $(\nu\overline{\epsilon'})^{1/4}$ and $(\nu/\overline{\epsilon'})^{1/2}$ having dimensions of length, velocity and time respectively.[6] In reference to Figure 2.4, the dissipation length, velocity and time scales are thus given by the Kolmogorov scales

$$\boxed{\begin{aligned}\eta &\equiv (\nu^3/\overline{\epsilon'})^{1/4}\\ u_\eta &\equiv (\nu\overline{\epsilon'})^{1/4}\\ \tau_\eta &\equiv (\nu/\overline{\epsilon'})^{1/2}\end{aligned}} \tag{2.29}$$

Given the importance of these scales to the fundamental physical process of viscous dissipation, it is desirable to know how these scales vary with macro-scopic flow parameters such as $\mathcal{L}$ and $\mathcal{U}$. [7]

$$\boxed{\begin{aligned}\eta(Re) &\sim \mathcal{L}Re^{-3/4}\\ u_\eta(Re) &\sim \mathcal{U}Re^{-1/4}\\ \tau_\eta(Re) &\sim \mathcal{T}Re^{-1/2}\end{aligned}} \tag{2.31}$$

2.4.3 The Kolmogorov Spectra

The Kolmogorov Hypothesis, while effective in terms of providing a qualitative description of turbulent processes, has not, as yet provided quantitative results. This deficiency can be addressed by applying the Hypothesis directly to the turbulent kinetic energy (per unit mass) spectra $\hat{E}$ where[8]

[6] These scales also accurately characterize the laminar shear power associated with viscous dissipation. Note that ϵ = shear power per unit mass = velocity × (net shear force per unit mass). Thus, substitution of the length and velocity scales $\ell \equiv (\frac{\nu^3}{\overline{\epsilon'}})^{1/4}$ and $u \equiv (\nu\overline{\epsilon'})^{1/4}$ yields the following value for the shear power or dissipation

$$\overline{\epsilon'} \sim u(\nu\frac{u}{\ell^2}) = (\nu\overline{\epsilon'})^{1/4}[\nu\frac{((\nu\overline{\epsilon'})^{1/4})}{((\frac{\nu^3}{\overline{\epsilon'}})^{1/4})^2}] = \overline{\epsilon'} \tag{2.28}$$

[7] Noting that the large scale energy transfer (i.e. dissipation via eddy-breakup $\overline{\epsilon'}_0$ *which is not due to molecular or viscous dissipation*) out of the large scale motion must ultimately be dissipated via viscosity at the Kolmogorov scales (i.e via $\overline{\epsilon'}$). Hence one can apply a dissipation balance between the large energy containing scales ℓ_0 and dissipation scales η giving $\overline{\epsilon'}_0 = \overline{\epsilon'}$ where $\overline{\epsilon'}_0$ = kinetic energy per unit mass/second $\sim u_0^2/(\ell_0/u_0)$. Noting that the macro-scopic scales $\mathcal{L}$ and $\mathcal{U}$ are on the order of and scale with the large energy containing scales of turbulent motion (i.e. $\mathcal{L} \gtrsim \ell_0$ and $\mathcal{U} \gtrsim u_0$) we have the following relationship between the macro-scopic Re and the Kolmogorov length scale η

$$\eta \equiv (\nu^3/\overline{\epsilon'})^{1/4} = (\nu^3/\overline{\epsilon'}_0)^{1/4} = (\nu^3/(u_0^3/\ell_0))^{1/4} = \ell_0(\nu^3/(u_0\ell_0)^3)^{1/4} = \ell_0(\nu/(u_0\ell_0))^{3/4} \tag{2.30}$$

Or since $\ell_0 \sim \mathcal{L}$ and $u_0 \sim U$ we have $\eta \sim \mathcal{L}Re^{-3/4}$ where Re is based on macro-scopic quantities. The remaining scaling laws are found via a similar procedure.

[8] $\hat{E}$ is the Fourier Transform of turbulent kinetic energy per unit mass with units ℓ^3/t^2. We can apply the Kolmogorov Hypothesis to yield a *universal function for $\hat{E}$ applicable throughout the inertial and dissipation range of scales*. Specifically, given that, according to the Kolmogorov Hypothesis, all small scale turbulence statistics are (i.e. in the inertial or dissipative range) at most a function of $\overline{\epsilon'}$ and ν, then $\hat{E} = g(\|\vec{\kappa}\|, \overline{\epsilon'}, \nu)$ or equivalently $\hat{E}(\|\vec{\kappa}\|, \eta, \overline{\epsilon'})$ where $\vec{\kappa} = 2\pi/\vec{\ell}$ where $\vec{\ell}$ is the multi-dimensional eddy scale ($3-D$ turbulence is assumed). Applying the Buckingham Pi theorem the two dimensionless groups derived from $\hat{E}$, $\|\vec{\kappa}\|$, $\overline{\epsilon'}$ and ν are $\hat{E}/((\overline{\epsilon'})^{2/3}\|\vec{\kappa}\|^{-5/3})$ and $\eta\|\vec{\kappa}\|$. Thus, equivalently we can express the spectrum via the function $\hat{E}(\|\vec{\kappa}\|, \eta, \overline{\epsilon'}) = \frac{(\overline{\epsilon'})^{2/3}}{\|\vec{\kappa}\|^{5/3}}\varphi(\eta\|\vec{\kappa}\|)$. In addition, we have the average or expectation values of turbulent kinetic energy and dissipation via the inverse Fourier Transform.

$$\overline{k'} = \int_{\|\vec{\kappa}\|=0}^{\infty} \hat{E}(\|\vec{\kappa}\|) d\|\vec{\kappa}\| \tag{2.34}$$

$$\overline{\epsilon'} = 2\nu \int_{\|\vec{\kappa}\|=0}^{\infty} \|\vec{\kappa}\|^2 \hat{E}(\|\vec{\kappa}\|) d\|\vec{\kappa}\| \tag{2.35}$$

where $\|\vec{\kappa}\|$ is a multi-dimensional wave number, $\kappa_i \equiv 2\pi/\ell_i$ and $\hat{E}$ can be expressed via the following

$$\boxed{\hat{E}(\|\vec{\kappa}\|, \eta, \overline{\epsilon'}) = \frac{(\overline{\epsilon'})^{2/3}}{\|\vec{\kappa}\|^{5/3}} \varphi(\eta\|\kappa\|)} \tag{2.36}$$

where $\varphi(\eta\|\vec{\kappa}\|)$ is a dimensionless function which must be specified. The required functional form for $\varphi(\eta\|\vec{\kappa}\|)$ can be ascertained by investigation into the phenomena know as the *final decay of turbulence*.[9] This yields

$$\boxed{\hat{u}(\|\vec{\kappa}\|, t) = Ae^{(-\nu\|\vec{\kappa}\|^2 t)}} \tag{2.38}$$

where $\hat{u}(\|\vec{\kappa}\|, t)$ is the Fourier transform of the velocity perturbation $u'(\vec{r}, t)$. Thus, the time and wave number evolution of turbulent motion is that of an exponential decay with increasing time and wave number magnitude $\|\vec{\kappa}\| = \sqrt{(2\pi/\ell_i)(2\pi/\ell_i)}$. Likewise, the decay of turbulent kinetic energy should proceed according to $\hat{u}(\|\vec{\kappa}\|, t)^2$ or $e^{(-2\nu\|\vec{\kappa}\|t)}$. This provides the motivation for supposing that the energy spectrum function $\hat{E}(\|\vec{\kappa}\|, \eta, \overline{\epsilon'})$ approximates exponential decay in the dissipation range. On the other hand, there exist small scales of turbulence ℓ that are larger than the dissipative scale η (see Figure 2.4), thus turbulent quantities in this regime are not a function of local molecular or kinematic viscosity (in the inertial/equilibrium sub-range, $\hat{E} \neq f(\nu)$ and thus $\hat{E} \neq f(\eta)$ according to the Kolmogorov Hypothesis). With the above observations one imposes the following constraint on the functionality of $\varphi(\eta\|\vec{\kappa}\|)$ in (2.36)

$$\overline{k'} = \int\int_{wavespace} \int \hat{E}(\|\vec{\kappa}\|, \eta, \overline{\epsilon'}) e^{(-i\vec{\kappa}\cdot 0)} d\vec{\kappa} = \int\int_{wavespace} \int \hat{E}(\|\vec{\kappa}\|, \eta, \overline{\epsilon'}) d\vec{\kappa} \tag{2.32}$$

$$\overline{\epsilon'} = \nu \overline{\frac{\partial u_i}{\partial x_j} \frac{\partial u_i}{\partial x_j}} = 2\nu \int\int_{wavespace} \int \|\vec{\kappa}\|^2 \hat{E}(\|\vec{\kappa}\|, \eta, \overline{\epsilon'}) e^{(-i\vec{\kappa}\cdot 0)} d\vec{\kappa} =$$

$$\nu \int\int_{wavespace} \int \|\vec{\kappa}\|^2 \hat{E}(\|\vec{\kappa}\|, \eta, \overline{\epsilon'}) d\vec{\kappa} \tag{2.33}$$

[9]Specifically, starting with the fluid equation of motion (2.6) for a zero mean, turbulent isotropic flow $u(\vec{\kappa}, \vec{r}, t) = \hat{u}(\vec{\kappa}, t) e^{-i\vec{\kappa}\cdot\vec{r}}$, we note that in the dissipation range, turbulent fluid convection becomes negligible compared to viscous dissipation. Thus, the fluid equation of motion specifies a balance between the temporal reduction in turbulent motion (i.e. kinetic energy) and viscous damping. Specifically, we have

$$\frac{d}{dt} u(\vec{\kappa}, \vec{r}, t) = \nu \frac{\partial^2}{\partial r_i \partial r_i} u(\vec{\kappa}, \vec{r}, t) \Longrightarrow (\frac{d}{dt} \hat{u}(\vec{\kappa}, t) + \nu\|\vec{\kappa}\|^2 \hat{u}(\vec{\kappa}, t)) e^{-i\vec{\kappa}\cdot\vec{r}} = 0 \Longrightarrow \hat{u}(\|\vec{\kappa}\|, t) = e^{-\nu\|\vec{\kappa}\|^2 t} \tag{2.37}$$

$$\boxed{\varphi(\eta\|\vec{\kappa}\|) \sim \begin{cases} 1 & \text{Equilibrium/Inertial sub-range} \\ e^{(-\beta\nu\|\vec{\kappa}\|^{\alpha})}, & \text{Dissipation sub-range} \end{cases}} \tag{2.39}$$

where β and α are some constants ~ 1. Curve fits of the form

$$\varphi(\eta\|\vec{\kappa}\|) = C[\frac{\|\vec{\kappa}\|\mathcal{L}}{[(\|\vec{\kappa}\|\mathcal{L})^2 + C_L]^{1/2}}]^{5/3+p_0} e^{-\beta[[(\|\vec{\kappa}\|\eta)^4 + c_\eta^4]^{1/4} - c_\eta]} \tag{2.40}$$

where C, c_η, c_L and p_0 are constants which have been successfully obtained by various researchers via the following procedure. Given that the expectation value for turbulent dissipation is

$$\overline{\epsilon'} = 2\nu \int_{\|\vec{\kappa}\|=0}^{\infty} \|\vec{\kappa}\|^2 \hat{E}(\|\vec{\kappa}\|, \eta, \overline{\epsilon'}) d\|\vec{\kappa}\| \tag{2.41}$$

if $\hat{E}(\|\vec{\kappa}\|, \eta, \overline{\epsilon'})$ is known $\overline{\epsilon'}$ can be calculated. Specifically, for the integrated dissipation we have, via substituting (2.36) and (2.40) into (2.41)

$$\overline{\epsilon'} = 2\nu \int_{\|\vec{\kappa}\|=0}^{\infty} \|\vec{\kappa}\|^2 \frac{(\overline{\epsilon'})^{2/3}}{\|\vec{\kappa}\|^{5/3}} C[\frac{\|\vec{\kappa}\|\mathcal{L}}{[(\|\vec{\kappa}\|\mathcal{L})^2 + C_L]^{1/2}}]^{5/3+p_0} e^{-\beta[[(\|\vec{\kappa}\|\eta)^4 + c_\eta^4]^{1/4} - c_\eta]} d\|\vec{\kappa}\| \tag{2.42}$$

This can be re-written with either $\|\vec{\kappa}\|\mathcal{L}$ or $\|\vec{\kappa}\|\eta$ as the variable of integration. Choosing the latter (2.42) becomes

$$\overline{\epsilon'} = 2C\frac{\nu}{\eta^{4/3}}(\overline{\epsilon'})^{2/3} \int_{\|\vec{\kappa}\|\eta=0}^{\infty} (\|\vec{\kappa}\|\eta)^{1/3} [\frac{\|\vec{\kappa}\|\eta\frac{\mathcal{L}}{\eta}}{[(\|\vec{\kappa}\|\eta\frac{\mathcal{L}}{\eta})^2 + C_L]^{1/2}}]^{5/3+p_0} e^{-\beta[[(\|\vec{\kappa}\|\eta)^4 + c_\eta^4]^{1/4} - c_\eta]} d(\|\vec{\kappa}\|\eta) \tag{2.43}$$

Finally, the non-dimensional dissipation gives the following constraint on (2.43).[10]

$$1 = 2C \int_{\|\vec{\kappa}\|\eta=0}^{\infty} (\|\vec{\kappa}\|\eta)^{1/3} [\frac{\|\vec{\kappa}\|\eta\frac{\mathcal{L}}{\eta}}{[(\|\vec{\kappa}\|\frac{\mathcal{L}}{\eta})^2 + C_L]^{1/2}}]^{5/3+p_0} e^{-\beta[(\|\vec{\kappa}\|\eta)^4 + c_\eta^4]^{1/4} - c_\eta} d(\|\vec{\kappa}\|\eta) = \frac{1}{\overline{\epsilon'}} \int_{\|\vec{\kappa}\|\eta=0}^{\infty} D(\|\vec{\kappa}\|\eta) d(\|\vec{\kappa}\|\eta) \tag{2.45}$$

where $D()$ is the dissipation spectrum function. Equations (2.45) and (2.44)) provide a system of equations with six unknowns p_0, β, C, C_L, C_η and the ratio $\mathcal{L}/\eta$. Assumed values for three of these constants is given in the literature: $p_0 = 2.0$, $\beta = 5.2$ and $C = 1.5$. The

[10] A similar constraint is found for the turbulent kinetic energy

$$1 = \int_{\|\vec{\kappa}\|\mathcal{L}=0}^{\infty} \frac{1}{(\|\vec{\kappa}\|\mathcal{L})^{5/3}} C[\frac{\mathcal{L}}{[(\|\vec{\kappa}\|\mathcal{L})^2 + C_L]^{1/2}}]^{5/3+p_0} e^{-\beta[[((\|\vec{\kappa}\|\mathcal{L})\frac{\eta}{\mathcal{L}})^4 + c_\eta^4]^{1/4} - c_\eta]} d(\|\vec{\kappa}\|\mathcal{L}) \tag{2.44}$$

where $\overline{k'} \sim \overline{\epsilon'}(\text{time}) \sim (\text{length}^2)/(\text{time}^3) \Rightarrow \overline{k'} \sim \overline{\epsilon'}\mathcal{L}$ (as noted from Figure 2.4 the length scale for the energy containing region is $\sim \mathcal{L}$ (while for the dissipation region the corresponding length scale is $\sim \eta$)). Thus, the chosen variable of integration is $\|\kappa\|\mathcal{L}$.

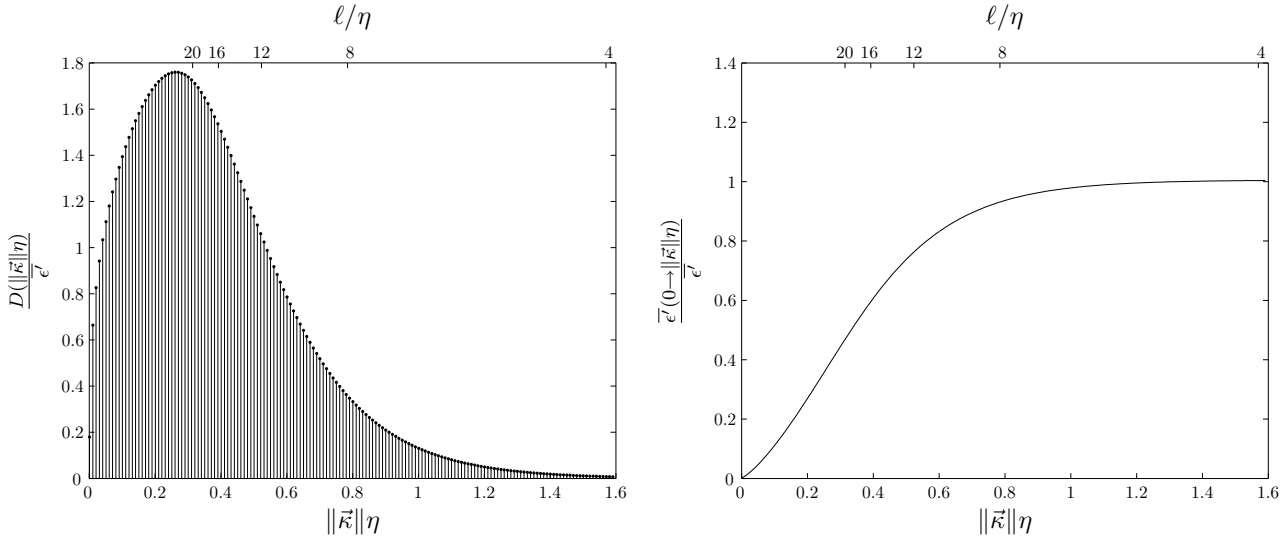

Figure 2.5: Normalized dissipation spectra $\frac{D(\|\vec{\kappa}\|\eta)}{\overline{\epsilon'}}$ and integrated dissipation $\frac{\overline{\epsilon'}(0\rightarrow\|\vec{\kappa}\|\eta)}{\overline{\epsilon'}}$ ($Re_\lambda = 700$).

Table 2.2: Integrated Dissipation $\frac{\overline{\epsilon'}(0\rightarrow\|\vec{\kappa}\|\eta)}{\overline{\epsilon'}}$ vs. Cut-off Normalized Eddy Scale ℓ/η.

$\frac{\overline{\epsilon'}(0\rightarrow\|\vec{\kappa}\|\eta)}{\overline{\epsilon'}}$	$\|\vec{\kappa}\|\eta$	ℓ/η
0.25	0.191	32.9
0.5	0.331	18.9
0.75	0.511	12.3
0.80	0.561	11.2
0.85	0.631	9.9
0.90	0.711	8.8
0.95	0.851	7.4

remaining parameters are found via the constraints (2.44) and (2.45) for a given Re number. Specifically, for a Taylor length scale based Reynolds Number $Re_\lambda = 700$ ($Re_\mathcal{L} = 7.3(10^4)$), it was found that $C_\eta = 0.405$ and $C_L = 6.45$.[11] Figure 2.5 shows the normalized dissipation spectra $D(\|\vec{\kappa}\|\eta)/\overline{\epsilon'}$ and the integrated normalized dissipation $\frac{\overline{\epsilon'}(0\rightarrow\|\vec{\kappa}\|\eta)}{\overline{\epsilon'}}$ as a function of the non-dimensionalized wave number $\kappa\eta$ as well as the non-dimensionalized (eddy) length scale ℓ/η (again, recall that $\|\vec{\kappa}\| \equiv 2\pi/\ell$). From Figure 2.5 (b) it can be seen that almost all of the turbulent dissipation can be attributed to eddies of normalized wave number magnitude $\|\vec{\kappa}\|\eta < 1.0$ (corresponding to a normalized eddy length scale of $\ell/\eta \approx 6.0$. Thus, in order to capture the overwhelming bulk of the dissipation, resolution down to the Kolmogorov scale is not required. Table 2.2 gives precise values for integrated dissipation as a function of eddy wave number $\kappa\eta$ or normalized length scale ℓ/η. Specifically, to resolve %50 or %90 of the

[11] These estimates are based on the approximate relationship between the macro-scopic and Taylor length scale based Reynolds number $Re_\lambda \approx \sqrt{2Re}$.[6]

turbulent dissipation, the contribution from the largest turbulent eddy scale down to ℓ/η of 18.9 and 8.8 must be resolved respectively.

2.5 Turbulent Transport

Having established the nature of turbulent fluctuations in §2.3.1 the starting point for the rigorous formulation of quantitative models of turbulent flows for use in applications of engineering interest is the following: substituting of the mean and perturbation velocities into the property transport equations (2.6) (i.e. for steady flow in the mean $\vec{V}(\vec{r},t) \equiv \vec{\overline{U}}(\vec{r}) + \vec{u}'(\vec{r},t)$ and $\phi \equiv \overline{\phi}(\vec{r}) + \phi'(\vec{r},t)$) where we have assumed a gradient diffusion transport mechanism as well as no additional sources gives

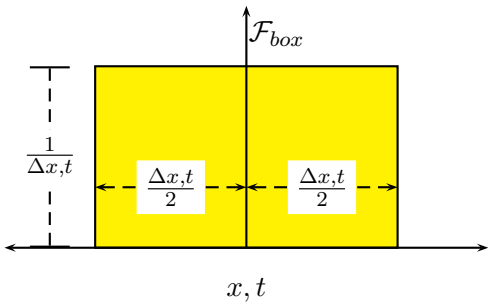

Figure 2.6: Characterization box function $\mathcal{F}_{box}$

$$\rho\vec{\nabla}\cdot[((\vec{\overline{U}}(\vec{r}) + \vec{u}'(\vec{r},t))\overline{\phi}(\vec{r}) + \phi'(\vec{r},t))] = \vec{\nabla}\cdot[(\Gamma\vec{\nabla}(\overline{\phi}(\vec{r}) + \phi'(\vec{r},t)))] \tag{2.46}$$

To proceed one must note the following: Given the difficulty in directly solving the fluid equations of motion for turbulent flow one can attempt to *smooth* the fluid equations of motion by either temporal or spacial integration over some small scale Δt or Δx. Taking the former approach (i.e. temporal smoothing of the fluid equations of motion) we apply the $\backslash\!\backslash() /\!/_t$ operator described in §D.2 to the product of the box function $\mathcal{F}_{box}(t,\Delta t)$ as illustrated in Figure 2.6 and the fluid equation of motion (2.46) (i.e. $\backslash\!\backslash\mathcal{F}_{box}(t,\Delta t)(2.46)/\!/_t$). Specifically, we take Δt to be some time scale large enough to smooth out the energy containing turbulent fluctuations (i.e. $\mathcal{T} \gg \Delta t \gg \tau_0$ where τ_0 is the period of turbulent fluctuation associated with the energy containing eddies in reference to Figure 2.4). Thus, performing the given operation $\backslash\!\backslash(\mathcal{F}_{box}(t,\Delta t)(2.46)/\!/_t$ one obtains[12]

$$\rho\vec{\nabla}\cdot((\vec{\overline{U}}(\vec{r})\overline{\phi}(\vec{r}) + \overline{\vec{u}'(\vec{r},t)\phi'(\vec{r},t)}) = \vec{\nabla}\cdot(\Gamma\vec{\nabla}\overline{\phi}(\vec{r})) \Longrightarrow$$

$$\rho\vec{\nabla}\cdot((\vec{\overline{U}}(\vec{r})\overline{\phi}(\vec{r})) = \vec{\nabla}\cdot(\Gamma\vec{\nabla}\overline{\phi}(\vec{r}) - \rho\overline{\vec{u}'(\vec{r},t)\phi'(\vec{r},t)}) \tag{2.47}$$

Thus, we see that the inclusion of flow turbulence introduces the term $(\rho\overline{\vec{u}'(\vec{r},t)\phi'(\vec{r},t)})$ associated with turbulent mixing or diffusion of ϕ. It is natural to ask to what extent this term actually contributes to mixing or diffusion of the property ϕ. To answer this one proposes a simple situation involving uniform (velocity) turbulence in a duct with an initial property jump in ϕ. Hence, Figure 2.7 gives an example of a mixing-layer within a duct of uniform

[12]Note that $\backslash\!\backslash(\mathcal{F}_{box}(t,\Delta t)\text{constant}/\!/_t$ = constant and for a large enough filter width Δt $\backslash\!\backslash(\mathcal{F}_{box}(t,\Delta t)\phi'(\vec{r},t))/\!/_t \approx 0$ (see discussion in §D.2).

velocity turbulence intensity and length scale (which, given a characteristic mean-flow velocity and length scale, specifies $\overline{k'}$ and $\overline{\epsilon'}$). Specifically, at the duct inlet there is a (upper) half-height application of a ϕ source, after which diffusion (turbulent and molecular) will have a dispersing effect on the property ϕ down-stream, resulting in the development of a mixing layer.

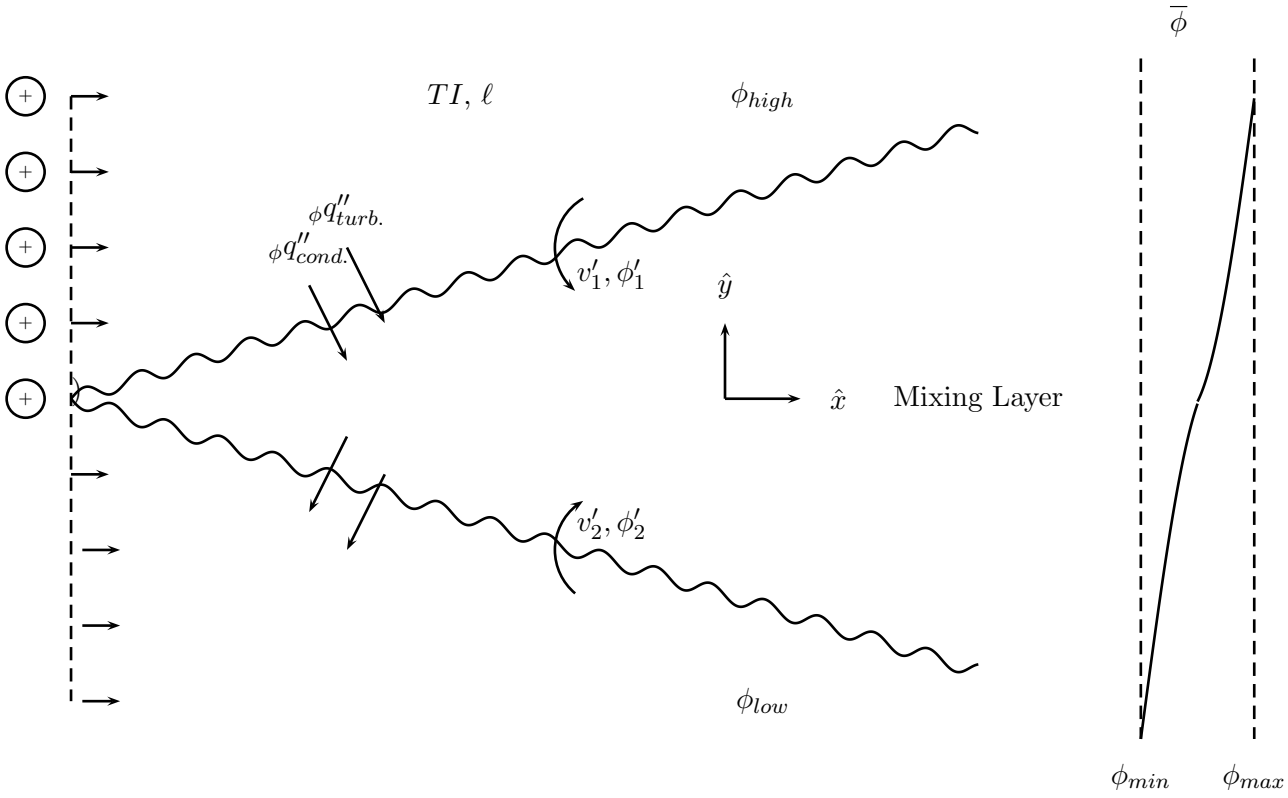

Figure 2.7: Illustration of channel diffusion and turbulent transport process

For a positive ϕ mean gradient ($\partial\overline{\phi}/\partial y > 0$), flow turbulence carries ϕ perturbations ϕ' into the mixing layer with value $\phi' > 0$, or $\overline{v'_1\phi'_1} < 0$ at the top of the mixing layer for location 1. Likewise, the flow turbulence also carries ϕ perturbations in the mixing layer of value $\phi' < 0$, or $\overline{v'_1\phi'_1} < 0$ at the bottom of the mixing layer for location 2. It should be noted that in this case the molecular diffusive flux of ϕ in the y-direction is downward, or ${}_\phi\overrightarrow{\overline{q}''_{diff.}} \cdot \hat{y} < 0$ where $\hat{y}$ is a unit vector. In addition, the turbulent diffusive flux in the y-direction ${}_\phi\overline{q}''_{turb.} \sim \overline{\phi' v'} < 0$, thus we see that turbulent transport augments molecular diffusion. Conversely, for the case of a negative mean property gradient for ϕ ($\partial\overline{\phi}/\partial y < 0$), the sign of the ϕ property perturbation is reversed in the above analysis leading to a turbulent flux ${}_\phi\overline{q}''_{turb.} \sim \overline{\phi' v'} > 0$, again augmenting the molecular diffusion in the y-direction ${}_\phi\overrightarrow{\overline{q}''_{diff.}} \cdot \hat{y} > 0$. These results are summarized in Table 2.3.

We can draw two general conclusions from this analysis: First, turbulent fluctuations enhance molecular diffusion. But most importantly, the driving mechanism for turbulent *and diffusive molecular flux is the mean property gradient.* Specifically, a positive mean flow gradient in ϕ results in a diffusive *and* turbulent flux in the opposing direction, and visa

Table 2.3: Process Summary in Reference to Figure 2.7

station	$\frac{\partial\overline{\phi}}{\partial y}$	${}_{\phi}\overline{q}''_{cond.}$	$\phi_{\prime}$	v'	${}_{\phi}\overline{q}''_{turb.} \sim \overline{\phi' v'}$
1	$-$	$+$	$-$	$-$	$+$
1	$+$	$-$	$+$	$-$	$-$
2	$-$	$+$	$+$	$+$	$+$
2	$+$	$-$	$-$	$+$	$-$

versa. This also leads to two further results: A vanishing $\overline{\phi}$ gradient eliminates turbulent transport while the local turbulence intensity $\overline{\phi'^2}$ can be increased by increasing the mean property gradient. It is this observation which provides the motivation for:

- Turbulence models based on mean flow gradient transport such as LES Smagorinski (§2.6.3) and zero-equation mixing length models (§2.6.1) utilizing an effective diffusion coefficient $\gamma_{eff} = \gamma + \gamma_{turb}$.
- Two-equation models utilizing a turbulence generation source based on the mean property gradient such as $k\epsilon$ (§2.6.2) and $k\omega$ models.
- The interpretation of the mean-flow gradient contribution to turbulent convection/energy exchange as a source in the exact turbulence transport equations for turbulent kinetic energy and turbulent species concentration rms fluctuation based on $RANS$ as given in (2.49) and (2.83).

These observations have been verified via fundamental experiments utilizing, for example, a heated channel where the property ϕ is internal energy and hence related to temperature T as carried out by Ma and Warhaft [3]. They found that the location within the mixing layer which maximized the cross-flow gradient of $\overline{T}$ coincided with maximum turbulent heat flux $\overline{u'T'}$. While the location of minimum turbulent heat flux corresponded to a region of vanishing mean temperature gradient $\nabla\overline{T}$.

Having established the nature of the turbulent diffusive term $\rho\overline{\vec{u}'(\vec{r},t)\phi'(\vec{r},t)}$ we can look into the specific nature of turbulent transport. Given that the three momentum conservation equations correspond to $\phi \equiv V_i, i = 1,2,3$ applied to (2.47), where the molecular diffusion coefficient Γ corresponds to molecular viscosity μ, the terms $\Gamma\vec{\nabla}\overline{\phi}(\vec{r})$ now correspond to surface shear stresses, the additional term $\rho\overline{\vec{u}'(\vec{r},t)\phi'(\vec{r},t)}$ resulting from turbulent velocity fluctuations represents an additional *apparent* stress due to turbulent *convective mixing* of momentum. These turbulent convection induced stresses correspond to the elements in the Reynolds Stress Tensor $\mathcal{RST}$ as defined by (2.48).

$$\mathcal{RST} \equiv \begin{bmatrix} \overline{u'_1u'_1} & \overline{u'_2u'_1} & \overline{u'_3u'_1} \\ \overline{u'_1u'_2} & \overline{u'_2u'_2} & \overline{u'_3u'_2} \\ \overline{u'_1u'_3} & \overline{u'_2u'_3} & \overline{u'_3u'_3} \end{bmatrix} \tag{2.48}$$

where the Reynolds Stress Tensor is (necessarily) symmetric (with six independent elements), where the trace is related to turbulent kinetic energy per unit mass via $\mathrm{Tr}(\mathcal{RST}) = 2k$.

While the previous description of the *apparent turbulent* stress or Reynolds stress, is of descriptive interest, of equal interest is the transport processes for turbulent kinetic energy itself. Specifically, summing the perturbation velocity moments of the Navier-Stokes equations and Reynolds averaging the result, or in terms of the box filter functions $\backslash\backslash(\mathcal{F}_{box}(t,\Delta t)u_i'(N-S)_i \,/\!/_t \,)$ yields an exact transport equation for the mean turbulent kinetic energy $\overline{k'} \equiv \overline{(u_r')^2 + (u_\theta')^2 + (u_z')^2}/2 = \overline{(u_x')^2 + (u_y')^2 + (u_z')^2}/2 = \overline{u_i'u_i'}/2$:

$$\overbrace{\dot{\overline{k'}}}^{\textit{Temporal Variation in } \overline{k'}} + \overbrace{\overline{U}_i \frac{\partial \overline{k'}}{\partial x_i}}^{\textit{Conv. } \overline{k'} \textit{ Via Mean Flow}} + \overbrace{\tilde{u}_i \frac{\partial \overline{k'}}{\partial x_i}}^{\textit{Conv. } \overline{k'} \textit{ Via Periodic Flow}} + \overbrace{\overline{u_i' \frac{\partial k'}{\partial x_i}}}^{\textit{Conv. } \overline{k'} \textit{ Via Turbulence}} =$$
$$- \overbrace{\overline{u_i' \frac{\partial}{\partial x_i}(\frac{P'}{\rho})}}^{\textit{Pressure Work/Diff. of } \overline{k'}} - \overbrace{\overline{u_i'u_j'} \frac{\partial \overline{U}_i}{\partial x_j}}^{\textit{Prod. of } \overline{k'} \textit{ Via Mean Flow}} - \overbrace{\overline{u_i'u_j'} \frac{\partial \tilde{u}_i}{\partial x_j}}^{\textit{Prod. of } \overline{k'} \textit{ Via Periodic Flow}} +$$
$$\overbrace{\nu \frac{\partial}{\partial x_i}(\overline{u_j'(\frac{\partial u_i'}{\partial x_j} + \frac{\partial u_j'}{\partial x_i})})}^{\textit{Viscous Work/Diff. of } \overline{k'} \textit{ Via Turb. Motion}} - \overbrace{\overline{\epsilon'}}^{\textit{Viscous Dissipation of } \overline{k'}} \tag{2.49}$$

where $\overline{\epsilon'}$, the local averaged viscous dissipation per unit mass due to turbulent motion is $\nu\overline{\partial u_i'/\partial x_j(\partial u_i'/\partial x_j + \partial u_j'/\partial x_i)}$ via (2.17).[13] *In addition, note we have further decomposed the velocity, taking into account the possibility of periodic (in addition to turbulent) motion.* Hence, (2.49) is based on the velocity decomposition $\vec{V} = \vec{\overline{U}} + \vec{\tilde{u}} + \vec{u}'$ where $\vec{\tilde{u}}$ is the periodic motion (due for example, to periodic boundary conditions). In the case of negligible periodic motion and steady turbulence (2.49) reduces (via the application of continuity) to

[13] The transport equation (2.49) can be developed via the following: For turbulent flow composed of a mean, periodic and turbulent velocity component $\vec{\overline{U}}$, $\vec{\tilde{u}}$ and $\vec{u}'$ the transport equation for $\overline{k'}$ can be found by Reynold's averaging the perturbation velocity moment of the N-S equations. Specifically, for a time interval Δt where $\tau_0 << \Delta t << T_{periodic}, \mathcal{T}$ we perform the following

$$\backslash\backslash(\mathcal{F}_{box}(t,\Delta t)u_i'(N-S)_i \,/\!/_t = \frac{1}{\Delta t}\int_{\tau=t-\Delta t/2}^{t+\Delta t/2} u_i'(N-S)_i d\tau \tag{2.50}$$

where Einstein summation notation is here applied. Time averaging the product of the perturbed velocity and the temporal momentum derivative we have

$$\frac{1}{\Delta t}\int_{\tau=t-\Delta t/2}^{t+\Delta t/2} u_i' \frac{\partial}{\partial t}(\overline{U}_i + \tilde{u}_i + u_i')d\tau = \frac{1}{2\Delta t}\frac{\partial}{\partial t}\int_{\tau=t}^{t+\Delta T}((u_i'u_i'))d\tau = \frac{1}{2}\frac{\partial}{\partial t}(\overline{(u_i'u_i')}) = \frac{\partial}{\partial t}(\overline{k'}) \tag{2.51}$$

Next, time averaging the product of the perturbed velocity and the $N-S$ convective transport term yields

$$\overbrace{\frac{\partial(\overline{U}_i\overline{k'})}{\partial x_i}}^{\text{Conv. } \overline{k'} \text{ Via Mean Flow}} + \overbrace{\frac{\partial(\overline{u_i'k'})}{\partial x_i}}^{\text{Conv. } \overline{k'} \text{ Via Turbulence}} =$$

$$- \overbrace{\frac{\partial}{\partial x_i}(\frac{\overline{u_i'P'}}{\rho})}^{\text{Pressure Work/Diff. of } \overline{k'}} - \overbrace{\overline{u_i'u_j'}\frac{\partial\overline{U}_i}{\partial x_j}}^{\text{Prod. of } \overline{k'} \text{ Via Mean Flow}} + \overbrace{\nu\frac{\partial}{\partial x_i}(\overline{u_j'(\frac{\partial u_i'}{\partial x_j} + \frac{\partial u_j'}{\partial x_i})})}^{\text{Viscous Work/Diff. of } \overline{k'} \text{ Via Turb. Motion}} - \overbrace{\overline{\epsilon'}}^{\text{Viscous Dissipation of } \overline{k'}} \quad (2.55)$$

2.6 Turbulence Modeling

All attempts to account for the effects of turbulent motion require the neglecting or modeling of the various terms in the $\mathcal{RST}$ (2.48), with or without, the utilization of a turbulence trans-

$$\frac{1}{\Delta t}\int_{\tau=t-\Delta t/2}^{t+\Delta t/2} u_i'\nabla\cdot(\vec{V}u_i')d\tau = \frac{1}{\Delta t}\int_{\tau=t-\Delta t/2}^{t+\Delta t/2} u_i'\frac{\partial}{\partial x_j}[(\overline{U}_j+\tilde{u}_j+u_j')(\overline{U}_i+\tilde{u}_i+u_i')]d\tau =$$
$$\frac{1}{\Delta t}\int_{\tau=t-\Delta t/2}^{t+\Delta t/2} u_i'\frac{\partial}{\partial x_j}((\overline{U}_ju_i'+\tilde{u}_ju_i')+u_j'(\overline{U}_i+\tilde{u}_i+u_i'))d\tau =$$
$$\frac{1}{\Delta t}\int_{\tau=t-\Delta t/2}^{t+\Delta t/2}[(\frac{1}{2}\overline{U}_j\frac{\partial(u_i'u_i')}{\partial x_j}+(u_i'u_i')\frac{\partial\overline{U}_j}{\partial x_j})+$$
$$(\frac{1}{2}\tilde{u}_j\frac{\partial(u_i'u_i')}{\partial x_j}+(u_i'u_i')\frac{\partial\tilde{u}_j}{\partial x_j})+(\overline{U}_i+\tilde{u}_i)\frac{\partial u_j'}{\partial x_j}+\frac{1}{2}\frac{\partial}{\partial x_j}(u_j'(u_i'u_i'))-(u_i'u_i')\frac{\partial u_j'}{\partial x_j}]d\tau$$
$$= \frac{1}{\Delta t}\int_{\tau=t-\Delta t/2}^{t+\Delta t/2}[(\frac{1}{2}\overline{U}_j\frac{\partial(u_i'u_i')}{\partial x_j})+(\frac{1}{2}\tilde{u}_j\frac{\partial(u_i'u_i')}{\partial x_j})+\frac{1}{2}\frac{\partial}{\partial x_j}(u_j'(u_i'u_i'))+(u_i'u_i')\frac{\partial\overline{U}_j}{\partial x_j}+(u_i'u_i')\frac{\partial\tilde{u}_j}{\partial x_j}]d\tau =$$
$$\frac{1}{\Delta t}\int_{\tau=t-\Delta t/2}^{t+\Delta t/2}[(\overline{U}_j\frac{\partial k'}{\partial x_j})+(\tilde{u}_j\frac{\partial k'}{\partial x_j})+\frac{\partial}{\partial x_j}(u_j'k')+(u_i'u_i')\frac{\partial\overline{U}_j}{\partial x_j}+(u_i'u_i')\frac{\partial\tilde{u}_j}{\partial x_j}]d\tau \quad (2.52)$$

where the continuity equation and properties of the RANS operator have been utilized ($\overline{\partial U_i/\partial x_i} = \partial(\overline{U}_i+\tilde{U}_i)/\partial x_i = 0 \rightarrow \overline{\partial u_i'/\partial x_i} = 0$). The average of the pressure moment terms is relatively straight forward.

$$-\frac{1}{\rho\Delta t}\int_{\tau=t-\Delta t/2}^{t+\Delta t/2} u_i'\frac{\partial}{\partial x_i}(\overline{P}+\tilde{P}+p')d\tau = -\frac{1}{\rho\Delta t}\int_{\tau=t-\Delta t/2}^{t+\Delta t/2} u_i'\frac{\partial}{\partial x_i}(p')d\tau = -\frac{1}{\rho\Delta t}\int_{\tau=t-\Delta t/2}^{t+\Delta t/2}\frac{\partial}{\partial x_i}(u_i'p')d\tau \quad (2.53)$$

Finally, a time average of the moment of the viscous term yields

$$\frac{\nu}{\Delta t}\int_{\tau=t-\Delta t/2}^{t+\Delta t/2} u_i'\nabla\cdot\nabla(V_i)d\tau = \frac{\nu}{\Delta t}\int_{\tau=t-\Delta t/2}^{t+\Delta t/2}[u_i'\frac{\partial}{\partial x_j}\frac{\partial}{\partial x_j}(\overline{U}_i+\tilde{u}_i+u_i')]d\tau =$$
$$\frac{\nu}{\Delta t}\int_{\tau=t-\Delta t/2}^{t+\Delta t/2}[u_i'\frac{\partial}{\partial x_j}\frac{\partial}{\partial x_j}(u_i')]d\tau =$$
$$\frac{\nu}{\Delta t}\int_{\tau=t-\Delta t/2}^{t+\Delta t/2}[(\frac{\partial}{\partial x_j}(u_i'\frac{\partial u_i'}{\partial x_j})-(\frac{\partial(u_i')}{\partial x_j})^2)+(\frac{\partial u_j'}{\partial x_i}\frac{\partial u_i'}{\partial x_j})-(\frac{\partial u_j'}{\partial x_i}\frac{\partial u_i'}{\partial x_j})]d\tau =$$
$$\frac{\nu}{\Delta t}\int_{\tau=t-\Delta t/2}^{t+\Delta t/2}[\frac{\partial}{\partial x_j}(u_i'(\frac{\partial u_i'}{\partial x_j}+\frac{\partial u_j'}{\partial x_i}))-$$
$$\frac{\partial u_i'}{\partial x_j}(\frac{\partial u_i'}{\partial x_j}+\frac{\partial u_j'}{\partial x_i})]d\tau \quad (2.54)$$

where the commutative property of the partial derivative has been used along with continuity and the averaging property of the RANS operator.

Finally, as the indical notation uses the Einstein summation where turbulent kinetic energy is $\overline{u_i'u_i'} = 2\overline{k'}$. Hence, we arrive at (2.49).

port equation (i.e. of $\overline{k'}$ or $\overline{\epsilon'}$). Given that turbulent eddies can, in principle, be characterized via a length ℓ and velocity scale u (or equivalently, an angular speed or frequency ω and a length scale ℓ), these models can be grouped together as follows:

- Mixing length models: Only the evolution of eddy size or length scale ℓ is directly modeled.
- Two-equation models: The evolution of eddy velocity and size via eddy kinetic energy $\overline{k'}$ and dissipation $\overline{\epsilon'}$ are modeled.
- Large Eddy Simulations (LES): Energy transfer from bulk flow to large scale energy containing eddies is directly resolved while viscous power consumption by smaller eddies (dissipation $\overline{\epsilon'}$) is modeled.

The above generally refers to modeling in ascending order of accuracy and realism in predicting turbulent flow processes.

2.6.1 Mixing Length Models

Mixing length models, which are typically used in the context of boundary-layer flow adjacent to walls provide an opportunity to apply, qualitatively, the hypothesis of Kolmogorov. In the case of flat plate boundary-layer flow it can be surmised that since the boundary-layer thickness δ is much smaller than the distance along the plate (i.e. $\delta \ll x \sim \mathcal{L}$) the partial derivatives $\partial/\partial x \ll \partial/\partial y$ (via $\partial/\partial x \sim 1/\mathcal{L}$ and $\partial/\partial y \sim 1/\delta$). Thus, if the y-direction is normal to the plate surface, see Figure 2.2, the effect of the stress term $u_1' u_1'$ can be neglected. For scales smaller than that of the energetic region $\ell < \ell_{IE}$ in the near wall region (see Figure 2.4), bulk flow convective momentum transfer is relatively unimportant compared to turbulent convective momentum transfer. Thus, the x-momentum equation ((2.47) for $\phi = V_1$) becomes

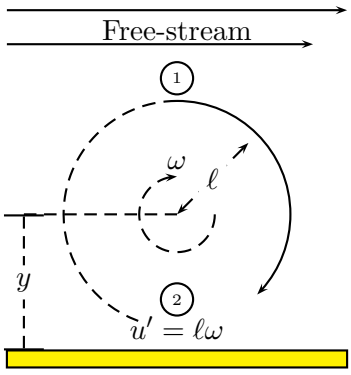

Figure 2.8: Characterization of turbulent eddy

$$\frac{\partial}{\partial y}(\nu \frac{\partial \overline{U}_1}{\partial y} - \overline{u_1' u_2'}) = 0 \tag{2.56}$$

Inside this region, where bulk momentum transfer is negligible, one can model the turbulent transport of momentum as follows: From Figure 2.8 we can view the turbulent transport process as removing fluid from a region of high bulk momentum $u_1 + u_1'$ at location 1 to a region of low momentum u_1 at 2 over some eddy (or mixing) length ℓ. Viewed in this way one can postulate a relationship between the bulk flow velocity derivative, the large energy containing velocity and perturbation length scale $\frac{\partial U_1}{\partial y} \sim \frac{U_1}{\mathcal{L}} \sim \frac{u_1'}{\ell}$ where the later quantity is the turbulent frequency ω. Since the eddy is essentially

symmetric we have $\overline{u_1'} \sim -\overline{u_2'}$ (via the fact that from continuity $\overline{u_1'}/\ell + \overline{u_2'}/\ell \sim 0$) and thus

$$\overline{u_1' u_2'} \sim -\overline{u_1'^2} \sim -\ell^2 (\frac{\partial \overline{U_1}}{\partial y}) \| \frac{\partial \overline{U_1}}{\partial y} \| \Longrightarrow \overline{u_1' u_2'} = -\epsilon_D \frac{\partial \overline{U_1}}{\partial y}, \epsilon_D \equiv \ell^2 \| \frac{\partial \overline{U_1}}{\partial y} \| \tag{2.57}$$

where ϵ_D is referred to as the eddy-diffusivity. In terms of the previous and the Kolmogorov Hypothesis, (2.56) reduces to a two part function. Specifically, in the dissipation sub-range (where turbulent transport is negligible) and the inertial/equilibrium sub-range (where viscous diffusion is negligible) we have

$$\begin{cases} \frac{\partial}{\partial y}(\epsilon_D \frac{\partial \overline{U_1}}{\partial y}) = 0, & \text{Inertial/Equilibrium sub-range (inner-layer)} \\ \frac{\partial}{\partial y}(\nu \frac{\partial \overline{U_1}}{\partial y}) = 0, & \text{Dissipation sub-range (viscous sub-layer)} \end{cases} \tag{2.58}$$

Integrating (2.58) within the dissipation region (i.e. viscous sub-layer), we have $\rho\nu \partial \overline{U_1}/\partial y = constant = \overline{\tau_{wall}}$ or $\overline{U_1} = y\frac{\overline{\tau_{wall}}}{\mu} + C$ where C is a constant and $\overline{\tau_{wall}}$ is the average wall shear-stress at a distance $x \sim \mathcal{L}$ along the plate. This result can be recast in a more *universally* applicable form by noting that $\sqrt{\frac{\overline{\tau_{wall}}}{\rho}} \sim \frac{m}{s} \sim V$ and $\nu \sim \frac{m^2}{s}$, hence, the previous can be rewritten in non-dimensional form $U^+ = y^+ + C_1$ where $U^+ \equiv \frac{\overline{U_1}}{U^*}$ ($U^* \equiv \sqrt{\overline{\tau_{wall}}/\rho}$ friction velocity) and $y^+ = y\frac{\sqrt{\tau_{wall}/\rho}}{\nu}$. Thus, the average plate parallel velocity profile is linear in y^+ (or y) within the dissipation region or viscous sub-layer. To proceed further we note that the characterization of turbulent transport near the wall (but outside the viscous sub-layer) is dependent on the mixing-length ℓ as discussed previously. A plausible functional form for the mixing-length is given by the Prandlt mixing-length model: $\ell(y) = \overline{\kappa} y$ where $\overline{\kappa}$ is some constant with units of length ~ 1. Substituting this functional form for the mixing length ℓ into (2.57) we have $\epsilon_D = (\kappa y)^2 |\partial \overline{U_1}/\partial y|$. From (2.58) we then have $(y^+)(\partial U^+/\partial y^+) = C_2$ or $U^+(y^+) = C_2 ln(y^+) + C_3$. Thus, the velocity profile within the dissipation region (viscous sub-layer) and the energy containing region (inner-layer) is the two-part function

$$U^+(y^+) = \begin{cases} C_2 ln(y^+) + C_3, & \text{Inertial sub-range/ inner-layer} \\ y^+ + C_1, & \text{Dissipation sub-range/viscous sub-layer} \end{cases} \tag{2.59}$$

Figure 2.9 shows verification of these results for a turbulent (pipe) boundary layer and indicates that up to a critical value of normalized wall distance $y^+ \sim 10$, normalized average x-velocity U^+ is a linear function (where C_1 in (2.59) ≈ 0). After an intermediate buffer region where turbulent convective and viscous diffusion are both important, the velocity profile conforms to a *log* function. This result is of practical significance insofar that it indicates the near wall velocity profile is linear in wall distance (unlike laminar boundary-layer flow).[14] Curve fits according to (2.59) via Prandlt are super-imposed on the data and indicate the appropriateness of the treatment. In addition, the use of a simplified power-law profile (2.60) in the inertial/equilibrium sub-range is also demonstrated.

[14]Note that this result will prove important in determining computational first-cell off the wall distance for turbulent (e.g. LES and DNS) flow simulations to be performed later.

$$U^+ = 8.74(y^+)^{1/7} \tag{2.60}$$

It should be noted that while the use of a mixing-length model facilitates our understanding of turbulent processes for wall bounded flows, such an approach in dependent of *tuned* coefficients (e.g. C_2, C_3 and κ) which do not apply for all geometries or free-stream conditions (e.g. turbulent free-streams).

2.6.2 Two-Equation Models

Motivation

As shown in the previous section §2.6.1, mixing length models do not explicitly treat the evolution of turbulent velocity fluctuations u' (or equivalently, turbulent kinetic energy per unit mass $k' \equiv (u_i' u_i')/2$). In addition, the turbulent length scale ℓ is treated in relation to some geometric distance. This results in theoretical and analytical ambiguities as to the characterization of turbulence far from a surface, (i.e. in the energy containing regions or free-stream), as well as choice of length scale in the case of complex geometries. A solution to these difficulties can be found by returning to the fundamental turbulence descriptors $\overline{k'}$ and $\overline{\epsilon'}$ (or $\omega \equiv \overline{\epsilon'}/\overline{k'}$) and viewing them as conserved flow quantities whose evolution can be modeled according to conservation equations. Thus, in terms of (2.3) we set $\phi = \overline{k'}, \overline{\epsilon'}$ whereupon the task is to determine the net source NS and diffusive coefficient Γ for each quantity.

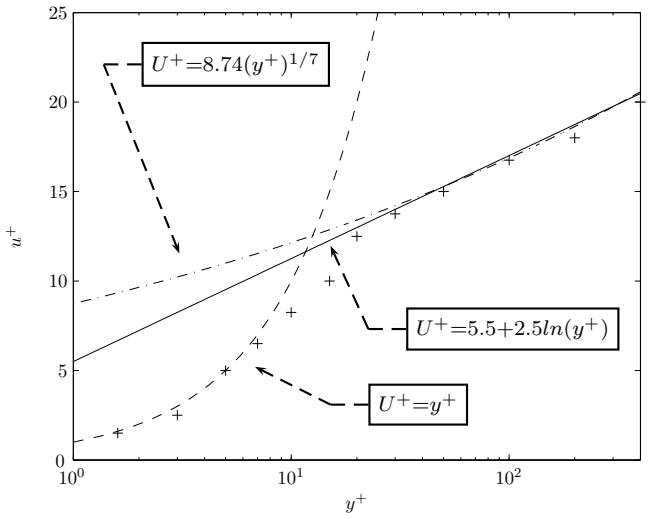

Figure 2.9: Data U^+ vs. y^+ (+):Illustration of law of the wall $U^+ = f(y^+)$ with associated curve fits.[4]

Conservation Equation for $\overline{k'}$

Given that turbulent processes can be viewed as a mixing process with an associated eddy diffusive (i.e. ϵ_D), we can assume (neglecting molecular diffusion processes) $\Gamma \sim \epsilon_D$ or referring to (2.57), we have, noting the approximation $\partial \overline{U}_1/\partial y \sim \overline{u'}_1/\overline{\ell} \sim (\overline{k'})^{1/2}/\overline{\ell}$ as well as the definition of $\overline{k'}$

$$\Gamma \sim \epsilon_D = \ell^2 \| \frac{\partial \overline{U_1}}{\partial y} \| \sim \ell(\overline{k'})^{1/2} \Longrightarrow \Gamma = C_1 \ell(\overline{k'})^{1/2} \tag{2.61}$$

To quantify the net source of $\overline{k'}$, recall that from inspection of the energy cascade, mean-flow kinetic energy is removed from the bulk flow and converted into turbulent velocity fluctu-

ations. In the discussion regarding the mixing-length model, this conversion of bulk flow kinetic energy into turbulent kinetic energy (which is ultimately dissipated by molecular viscosity in the dissipation region) induced a *turbulent or apparent* shear stress due to turbulent mixing of high and low momentum fluid $\overline{\tau^{turb.}}$. This average shear stress can be characterized in terms of the eddy-diffusivity and bulk or mean-flow velocity gradient via (2.57). Noting that the *apparent or turbulent* shear power is completely analogous to the shear power as discussed in §2.2.2, the turbulent shear power (i.e. conversion of bulk flow energy into turbulent kinetic energy (per unit time per unit mass)) is

$$\frac{1}{\rho}\text{Turbulent shear power} \sim \frac{1}{\rho}\frac{\partial(\overline{\tau^{turb.}}\overline{U_1})}{\partial y} \tag{2.62}$$

Or assuming variations in mean-flow are larger than variation in average turbulent shear stress we have

$$\frac{k^{gen.}}{time} = \frac{1}{\rho}\text{Turbulent shear power} = C_2\epsilon_D(\frac{\partial\overline{U_1}}{\partial y})^2 \tag{2.63}$$

where we have utilized the fact that $\tau^{turb.}/\rho = \epsilon_D\partial\overline{U_1}/\partial y$ and $k^{gen.}$ is the generation of averaged turbulent kinetic energy per unit mass. The destruction of averaged turbulent kinetic energy arises from the kinetic energy transport from large scale motions $\ell = \ell_0$ to small scales $\ell = \eta$ resulting in viscous dissipation in the dissipation region or $\overline{\epsilon'}$. To quantify this destruction of $\overline{k'}$, (i.e. the flow of turbulent kinetic energy per unit volume per unit time $\overline{\epsilon'}$ into the dissipation region (see Figure 2.4)), one can view the turbulent eddy as a quantity of high or low speed fluid moving through a quiescent medium (relative to the main or bulk flow frame of reference). Thus, an effective turbulent eddy drag coefficient C_D can be specified: $C_D = F_{Drag}/(area \times (KE_{flow}/Vol)) \sim F_{Drag}/\ell^2\rho\overline{k'}$ or $F_{Drag} = C_D\ell^2\rho\overline{k'}$. Thus, noting that the dissipation or destruction of turbulent kinetic energy *per unit mass* $\overline{k'}$ is given by $F_{Drag} \times velocity \times (\ell^3\rho) \sim F_{Drag}\frac{(\overline{k'})^{1/2}}{\ell^3\rho}$ we have

$$\overline{\epsilon'} = \frac{C_D\ell^2\rho(\overline{k'})(\overline{k'})^{1/2}}{\rho\ell^3} = C_D\frac{(\overline{k'})^{3/2}}{\ell} \tag{2.64}$$

where we have observed that the average eddy area and volume scales in the equilibrium range are given by ℓ^2 and ℓ^3 respectively. Now, it is important to note that (2.64), (2.61) and (2.63) specify three equations with four unknowns: The three modeling constants C_1, C_2 and C_D, and an unknown eddy length scale ℓ. Given that we desire the closure of the two equation model in terms of $\overline{k'}$ and $\overline{\epsilon'}$ we can specify ℓ and ϵ_D by setting a value for one of the model coefficients and solving for ℓ. Specifically, solving (2.64) for ℓ gives $\ell = C_D(\overline{k'})^{3/2}/\overline{\epsilon'}$. Setting $C_D = 1$ we have $\ell = (\overline{k'})^{3/2}/\overline{\epsilon'}$ and substituting the result into the expression (2.61) for the eddy diffusivity ϵ_D we get

$$\epsilon_D = C_1\overline{k'}^{1/2}\ell = C_1\frac{\overline{k'}^2}{\overline{\epsilon'}} \tag{2.65}$$

Thus, a final transport equation can be assembled via (2.65), (2.63), (2.61), (2.7) and (2.6)

for $\phi = \overline{k'}$.

$$\frac{D\overline{k'}}{Dt} = \overbrace{C_1 \frac{\partial}{\partial y}(\epsilon_D \frac{\partial \overline{k'}}{\partial y})}^{Turb.\ Diffusion\ of\ \overline{k'}} + \overbrace{C_2 \epsilon_D (\frac{\partial \overline{U}_1}{\partial y})^2}^{Turb.\ Generation\ of\ \overline{k'}} + \overbrace{(-\overline{\epsilon'})}^{Turb.\ Destruction/Diss.\ of\ \overline{k'}}, \tag{2.66}$$

$$\epsilon_D = C_1 \frac{\overline{k'}^2}{\overline{\epsilon'}} \tag{2.67}$$

Conservation Equation for $\overline{\epsilon'}$

To formulate the conservation equation for the averaged dissipation $\overline{\epsilon'}$, we again apply (2.6) and (2.7) in the case of $\phi = \overline{\epsilon'}$. If τ is some time scale associated with the turbulence, it should be noted that the units of the dissipation conservation equation are dissipation per unit time $\overline{\epsilon'}/\tau$. If we form τ via $\overline{k'}/\overline{\epsilon'}$ then $\overline{\epsilon'}/\tau = (\overline{\epsilon'})^2/\overline{k'}$. Thus, since the destruction of $\overline{\epsilon'}$ is equal to the destruction of turbulent kinetic energy per unit mass per unit time per unit time we have

$$\frac{\epsilon^{dest.}}{time} = \frac{\epsilon^{dest}}{\tau} \sim \frac{\overline{\epsilon'}}{\frac{\overline{k'}}{\overline{\epsilon'}}} \Longrightarrow \frac{\epsilon^{dest.}}{time} = C_3 \frac{(\overline{\epsilon'})^2}{\overline{k'}} \tag{2.68}$$

where C_3 is some constant. The generation of $\overline{\epsilon'}$ can be found by referring to Figure 2.4 and noting that in the equilibrium range the in-flow of energy via turbulence generation is equal to the out-flow of energy via dissipation $\overline{\epsilon'}_0 = \overline{\epsilon'}$ or $(k^{gen.}/sec)/sec = \overline{\epsilon'}/sec$. Thus, referring to (2.63)

$$\frac{\epsilon^{Gen.}}{time} \sim \frac{k^{Gen.}}{time} \frac{\overline{\epsilon'}}{\overline{k'}} \sim \epsilon_D (\frac{\partial \overline{U_1}}{\partial y})^2 \frac{\overline{\epsilon'}}{\overline{k'}} \Longrightarrow \frac{\epsilon^{Gen.}}{time} = C_4 \epsilon_D (\frac{\partial \overline{U_1}}{\partial y})^2 \frac{\overline{\epsilon'}}{\overline{k'}} \tag{2.69}$$

where C_4 is some constant. The turbulent diffusion of dissipation $\overline{\epsilon'}$ is completely analogous to the turbulent transport of any property ϕ, thus the diffusion gradient transport diffusivity Γ/ρ is proportional to the eddy diffusivity or $\Gamma/\rho = C_5 \epsilon_D$ (neglecting viscous diffusion). Combining the previous results gives the conservation equation for dissipation in terms of $\overline{k'}$ and $\overline{\epsilon'}$ where C_5, C_4 and C_3 are modeling constants

$$\frac{D\overline{\epsilon'}}{Dt} = \overbrace{C_5 \frac{\partial}{\partial y}(\epsilon_D \frac{\partial \overline{\epsilon'}}{\partial y})}^{Turb.\ Diffusion\ of\ \overline{\epsilon'}} + \overbrace{C_4 \epsilon_D (\frac{\partial \overline{U_1}}{\partial y})^2 \frac{\overline{\epsilon'}}{\overline{k'}}}^{Turb.\ Generation\ of\ \overline{\epsilon'}} + \overbrace{-C_3 \frac{(\overline{\epsilon'})^2}{\overline{k'}}}^{Turb.\ Destruction/Diss.\ of\ \overline{\epsilon'}}, \tag{2.70}$$

$$\epsilon_D = C_1 \frac{(\overline{k'})^2}{\overline{\epsilon'}} \tag{2.71}$$

Generalization of the Two-Equation Model

The previous derivations were performed, for simplicity, assuming boundary layer flow with free-stream parallel to the plate. For the general case of $3 - D$ isotropic turbulence the

following $\overline{k'}$ and $\overline{\epsilon'}$ transport equations are given as proposed by Jones and Launder [2]

$$\frac{D\overline{k'}}{Dt} = \overbrace{\hat{C}_1\vec{\nabla}\cdot(\epsilon_D\nabla\overline{k'})}^{\textit{Turb. Diffusion of } \overline{k'}} + \overbrace{\hat{C}_2\epsilon_D\nabla^2\vec{\overline{U}}}^{\textit{Turb. Generation of } \overline{k'}} + \overbrace{(-\overline{\epsilon'})}^{\textit{Turb. Destruction/Diss. of } \overline{k'}}, \tag{2.72}$$

$$\frac{D\overline{\epsilon'}}{Dt} = \overbrace{\hat{C}_5\vec{\nabla}\cdot(\epsilon_D\nabla\overline{\epsilon'})}^{\textit{Turb. Diffusion of } \overline{\epsilon'}} + \overbrace{\hat{C}_4\epsilon_D\nabla^2\vec{\overline{U}}\frac{\overline{\epsilon'}}{\overline{k'}}}^{\textit{Turb. Generation of } \overline{\epsilon'}} + \overbrace{-C_3\frac{(\overline{\epsilon'})^2}{\overline{k'}}}^{\textit{Turb. Destruction/Diss. of } \overline{\epsilon'}}, \tag{2.73}$$

$$\epsilon_D = C_1(\overline{k'})^{1/2}\ell = C_1\frac{(\overline{k'})^2}{\overline{\epsilon'}} \tag{2.74}$$

Finally, it should be stated that the previously described $k\epsilon$ model in no way attempts to directly resolve turbulent processes on *any scale*. Hence, only the bulk flow averaged quantities are directly resolved and turbulent processes in the energy, equilibrium and dissipation regions are modeled where the flow resolved scales are $\ell \gtrsim \ell_0$ (see Figure 2.4).

2.6.3 Large Eddy Simulations (LES)

The modeling assumptions underpinning the Two-equation $k\epsilon$ turbulence model specifies an assumed behavior for the flow turbulence which is only affected by geometric conditions and flow turbulence indirectly (via the mean flow solution as well as boundary conditions for the $\overline{k'}$ and $\overline{\epsilon'}$ transport equations). Specifically, the tuned coefficients values imply an applicability to a certain class of flows from which the coefficients were calculated. Thus, Two-equation models are limited in their applicability given that the large scale turbulent motions are determined by flow *and* geometric conditions. A reasonable solution to this deficiency is to resolve the large scale (energy containing) turbulent motion and directly model turbulent processes in the inertial and dissipative region which, according to the Kolmogorov hypothesis, are approximately isotropic and universal in structure. Large Eddy Simulations (pioneered by Smagorinsky [11]), as in the case of the RANS approach, seeks a solution to an averaged fluid equation of motion. Where RANS results from the *temporal smoothing* of the fluid equations of motion using a temporal filter width larger than the period of the energy containing eddies, LES instead *spatially smooths* the governing equations of motion while retaining the direct influence of the (large $\ell_0 \gtrsim \ell_{IE}$) energy containing turbulent motions. Thus, we apply a spacial averaging operation $\backslash\backslash(\mathcal{F}_{box}(\vec{r},\Delta\|\vec{r}\|)(N-S)_i\,/\!/_{\vec{r}}$ to the momentum transport equations. Specifically, we take $\Delta\|r\|$ to be some length scale large enough to smooth out turbulent fluctuations *smaller in scale than the large energy containing eddies* (i.e. $\mathcal{L} \gg \Delta\|r\| \gtrsim \ell_{IE}$ where ℓ_{IE} is the turbulent length scale associated with the eddies at the upper end of the equilibrium region (see Figure 2.4)). This yields for steady mean flow, (where prime values denote property perturbations in space *not time*)

$$\rho\vec{\nabla}\cdot((\vec{\overline{U}}(\vec{r})\overline{\phi}(\vec{r})+\overline{\vec{u}'(\vec{r},t)\phi'(\vec{r},t)}+\overline{\vec{U}(\vec{r},t)\phi'(\vec{r},t)}+\overline{\vec{u}'(\vec{r},t)\phi(\vec{r},t)})=\vec{\nabla}\cdot(\Gamma\vec{\nabla}\overline{\phi}(\vec{r}))\Longrightarrow$$

$$\rho\vec{\nabla}\cdot((\vec{\overline{U}}(\vec{r})\overline{\phi}(\vec{r}))=\vec{\nabla}\cdot(\Gamma\vec{\nabla}\overline{\phi}(\vec{r})-\rho(\overline{\vec{u}'(\vec{r},t)\phi'(\vec{r},t)}+\overline{\vec{U}(\vec{r},t)\phi'(\vec{r},t)}+\overline{\vec{u}'(\vec{r},t)\phi(\vec{r},t)})) \quad (2.75)$$

Modeling only the first mean turbulent stress term $\rho(\overline{\vec{u}'(\vec{r},t)\phi'(\vec{r},t)}$ (and neglecting the others) via a eddy viscosity concept (completely analogous to the RANS mixing length approach), while noting that the relevant *resolved* eddy length scale ℓ is the filter width $\Delta\|r\|$, gives

$$\vec{\nabla}\cdot((\vec{\overline{U}}(\vec{r})\overline{\phi}(\vec{r}))=\vec{\nabla}\cdot((\frac{\Gamma}{\rho}+\epsilon_D)\vec{\nabla}\overline{\phi}(\vec{r}))$$
$$\epsilon_D=(C_s\Delta\|r\|)^2\|\vec{S}\| \quad (2.76)$$

where C_s is the Smagorinsky constant and $\|\vec{S}\|$ is defined as the strain-rate tensor magnitude based on the large-scale motions

$$\|\vec{S}\|\equiv\sqrt{2\overline{S}_{ij}\overline{S}_{ij}},\qquad \overline{S}_{ij}\equiv\frac{1}{2}(\frac{\partial\overline{U}_i}{\partial x_j}+\frac{\partial\overline{U}_j}{\partial x_i}) \quad (2.77)$$

A natural choice for the filter width $\Delta\|r\|$ is a representative length scale of the computation cell, or

$$\Delta\|r\|=2^3\sqrt{\Delta x\Delta y\Delta z}=2^3\sqrt{\Delta Vol}, \quad (2.78)$$

This is due to the fact that since ϕ in this case is V_i, the modeled term represents the transport of turbulent kinetic energy of which the most energetic will have length scale equal to the computational cell size. Thus, we see a repeat of the familiar (mean-flow) gradient based transport mechanism for turbulent momentum diffusion. Finally, note that in the context of the LES model, (which assumes isotropic turbulence), the turbulent dissipation (per unit mass) is calculated via (2.16)

$$\overline{\epsilon'}=\epsilon_D(\frac{\partial\overline{U}_i}{\partial x_j}\frac{\partial\overline{U}_i}{\partial x_j}) \quad (2.79)$$

2.7 Direct Numerical Simulation of Turbulence: DNS

In contrast to LES or any other modeling of turbulent flow, Direct Numerical Simulation (DNS) involves solving the N-S equations down to and within the viscous sub-range, hence resolving all (significant) scales of turbulent motion. Specifically, from the previous discussion in §2.4.2 recall that most of the (integrated) dissipation is associated with turbulent motion of length scale ℓ above approximately 10η. Thus, neglecting discretization error (which will be discussed later) the unsteady (numerical) solution to the Navier-Stokes equations should replicate qualitatively and quantitatively behavior in terms of turbulence as exhibited by

the physical flow if the computational cell size is sufficiently small. Indeed, provided the computational cell size is $\approx 10\eta$ approximately 90% of the dissipation should be resolved via the unsteady solution to the Navier-Stokes equations.

2.8 Species Transport: Concentration Transport Equation

After completing our treatment of turbulent momentum transport, we note that an almost identical transport process exists for dilute mixture component species. Specifically, if the extensive quantity of a system of fixed mass $M_{mixture}$ is a constituent component mass M_i then as given in Table 2.2, the transport process for the intensive property y_i, scalar component i mass fraction subject to Fick's law of species (molecular) diffusion. Specifically, assuming equal component molecular weights and a dilute mixture (i.e. $\rho_{mixture} \approx$ constant) then the scalar transport equation for the species i concentration $C \equiv$ moles i-component/moles mixture is given by

$$\frac{\partial(C)}{\partial t} + \nabla\vec{(C)} \cdot \vec{U} = NSD|_{control\ volume} = \frac{D_i}{\rho_{mixture}} \frac{\partial^2}{\partial x_i \partial x_i} C = \frac{D_i}{\rho_{mixture}} \vec{\nabla} \cdot (\vec{\nabla} C) \qquad (2.80)$$

Using the Reynolds concept of a mean, periodic and perturbation concentration component we have $C \equiv \overline{C} + \tilde{C} + C'$. Thus, Reynolds averaging (2.80), in other words, applying the filtering operation $\backslash\backslash(\mathcal{F}_{box}(t, \Delta t)(2.80))\ /\!/_t$ yields

$$\frac{1}{2}[\dot{\overline{C}} + \vec{\nabla}(\overline{C}) \cdot \vec{\overline{U}}] = -\frac{D_i}{\rho_{mixture}} \vec{\nabla} \cdot [\frac{\overline{\vec{u}' C'}}{D_i/\rho_{mixture}} + (\vec{\nabla}\overline{C})] \qquad (2.81)$$

Thus, as in the case of momentum, the inclusion of a turbulent concentration perturbation produces an *apparent* diffusive flux which exceeds the laminar diffusion. Now, as in the case of $\overline{k'}$ for turbulent momentum transport, a suitable scalar quantity can be devised representing the turbulent concentration fluctuation squared: $\hat{C} \equiv C'^2$. In addition, as in the case of $\overline{k'}$, a transport equation for $\hat{C}$ can be derived by applying the RANS operator to the concentration perturbation weighted species transport equation or $\backslash\backslash \mathcal{F}_{box}(t, \Delta t)\hat{C}(2.80)\ /\!/_t$ yielding

$$\frac{1}{2}[\overbrace{\dot{\overline{\hat{C}}}}^{Temporal\ Variation\ in\ \hat{C}} + \overbrace{\overline{U}_i \frac{\partial \overline{\hat{C}}}{\partial x_i}}^{Conv.\ c\ Via\ Mean\ Flow} + \overbrace{\tilde{U}_i \frac{\partial \overline{\hat{C}}}{\partial x_i}}^{Conv.\ \hat{C}\ Via\ Phase\ Res.\ Flow} + \overbrace{\overline{u'_i \frac{\partial \hat{C}}{\partial x_i}}}^{Conv.\ \hat{C}\ Via\ Turbulence}] =$$

$$\overbrace{-\overline{C' u'_i} \frac{\partial \overline{C}}{\partial x_i}}^{Prod.\ of\ \hat{C}\ Via\ Mean\ Flow} - \overbrace{\overline{C' u'_i} \frac{\partial \tilde{C}}{\partial x_i}}^{Prod.\ of\ \hat{C}\ Via\ Periodic\ Flow} + \frac{D_i}{\rho_{mixture}} (\overbrace{\frac{\overline{\nabla^2 \hat{C}}}{2}}^{Diff.\ of\ \hat{C}\ Via\ Turb.\ Motion} - \overbrace{\overline{\frac{\partial C'}{\partial x_i} \frac{\partial C'}{\partial x_i}}}^{Turbulent\ Dissipation\ of\ \hat{C}}) \qquad (2.82)$$

Thus, we have a familiar transport equation involving mean, periodic and perturbation convection with mean and periodic concentration turbulence generation followed by diffusion and dissipation of $\hat{C}$. In the case of negligible periodic motion we have the reduced turbulent transport for $\hat{C}$

$$\frac{1}{2}[\overbrace{\dot{\overline{\hat{C}}}}^{\text{Temporal Variation in } \hat{C}} + \overbrace{\overline{U}_i\frac{\partial\overline{\hat{C}}}{\partial x_i}}^{\text{Conv. c Via Mean Flow}} + \overbrace{\overline{u_i'\frac{\partial\hat{C}}{\partial x_i}}}^{\text{Conv. } \hat{C} \text{ Via Turbulence}}] =$$
$$\overbrace{-\overline{C'u_i'}\frac{\partial\overline{C}}{\partial x_i}}^{\text{Prod. of } \hat{C} \text{ Via Mean Flow}} + \frac{D_i}{\rho_{mixture}}(\overbrace{\frac{\overline{\nabla^2\hat{C}}}{2}}^{\text{Diff. of } \hat{C} \text{ Via Turb. Motion}} - \overbrace{\overline{\frac{\partial C'}{\partial x_i}\frac{\partial C'}{\partial x_i}}}^{\text{Turbulent Dissipation of } \hat{C}}) \tag{2.83}$$

2.8.1 Characterization of Mixing Times

Finally, it should be pointed out that globally, one can define a mixing effectiveness in terms the instantaneous (vessel) average deviation of concentration C from the final steady-state concentration $C_{s.s.}$. Specifically, one can define the time required for any given volume within the vessel to achieve a species concentration C value within %5 of the steady-state value $C_{s.s.}$. Or defining the local indicator function

$$\boxed{\alpha = \begin{cases} 1, & 0.95 \leq \frac{C}{C_{s.s.}} \leq 1.05 \\ 0, & 0.95 > \frac{C}{C_{s.s.}}, 1.05 < \frac{C}{C_{s.s.}} \end{cases}} \tag{2.84}$$

the vessel volume averaged value of α can the ascertained via

$$\overline{\alpha} = \frac{1}{Vol.}\int_{Vol.} \alpha dV \tag{2.85}$$

Thus, one can define a mixing time τ_{mix} required for $\overline{\alpha} > 0.95$ (mixing criterion other than 95% can be chosen).

2.9 Mixing Vessels: Dimensional Analysis

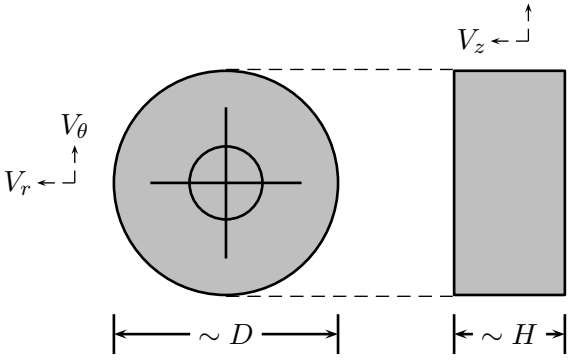

Figure 2.10: Control Volume for Mixing Vessel Dimensional Analysis

In order to extract suitable mixing vessel dimensionless quantities and determine their functionality, it is necessary to define the physical domain and range of motion. Specifically, the domain characterizing a idealized mixing process via an impeller illustrated in Figure 2.10 is a cylindrical impeller region of diameter $\sim D$, height $\sim H$, rotational speed N, with velocity ranges $\Delta V_r \sim V_r$ and $\Delta V_\theta \sim V_\theta \sim ND$.

The Re is defined as

$$Re \equiv \frac{ND^2}{\nu} \tag{2.86}$$

where N is the impeller speed in revolutions per second, D is the impeller diameter and ν is the kinematic viscosity of the fluid.

2.9.1 Flow Number $\mathcal{F}$

The volume flow rate ($\pi HD\overline{V}_r$) (or volume efflux from the impeller region) based on an average radial velocity $\overline{V}_r$ can be non-dimensionalized via the product of the blade tip velocity and impeller diameter squared or something proportional to it (e.g. ND^3). Thus, the ratio of $\overline{V}_r$ to V_{tip} is proportional to the the dimensionless quantity defined here as the Flow Number $\mathcal{F}$

$$\mathcal{F} \equiv \frac{\pi HD\overline{V}_r}{ND^3} \sim \frac{\overline{V}_r}{V_{tip}} \tag{2.87}$$

The utility of the Flow Number can be seen by noting that if $\mathcal{F} \neq f(Re)$ for a given flow geometry, (i.e. $D, H =$ constant), then as the scaling factor for the non- dimensionalized fluid equations of motion, $\overline{V}_r \sim V_{tip} \propto ND$. Hence, a Re invariant flow number $\mathcal{F}$ implies the suitability of scaling circumferential *and* radial velocities V_r and V_θ by the blade tip speed V_{tip}. In addition to the previous, $\mathcal{F}$ represents a measure of the impeller pumping effectiveness (i.e. to maximize $\mathcal{F}$ is to maximize volume or mass-pumped per impeller revolution).

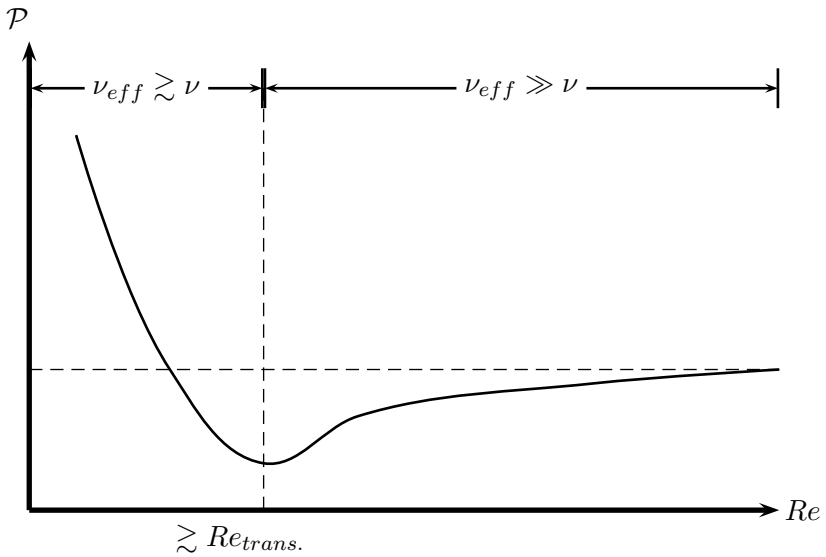

Figure 2.11: Power Number $\mathcal{P}$ vs. Re via dimensional analysis

2.9.2 Power Number $\mathcal{P}$

Behavior of the non-dimensional impeller power $\mathcal{P}$, or the Power Number defined as

$$\mathcal{P} \equiv \frac{\tau\omega}{\rho N^3 D^5} \tag{2.88}$$

where τ and ω are the impeller torque and angular velocity, can be ascertained by examining the (relative, impeller fixed) fluid equation of motion in the θ direction. Noting that the velocity field in the near impeller region relative to a rotating coordinate system attached to the impeller is approximately steady, the steady-flow Navier-Stokes equation in the θ-direction expressed in terms of the relative velocity in a rotating coordinate system about the z-axis (neglecting gravitational forces) gives

$$V_r^{rel}\frac{\partial V_\theta^{rel}}{\partial r}+\frac{V_\theta^{rel}}{r}\frac{\partial V_\theta^{rel}}{\partial \theta}+V_z^{rel}\frac{\partial V_\theta^{rel}}{\partial z}-V_r^{rel}\|\vec{\omega}\|-\frac{\partial V_\theta^{rel}}{\partial \theta}\|\vec{\omega}\|+\frac{V_r^{rel}}{r}(V_\theta^{rel}-\|\vec{\omega}\|r)$$
$$=-\frac{1}{\rho r}\frac{\partial P}{\partial \theta}+\nu[\frac{\partial^2 V_\theta^{rel}}{\partial z^2}+(\frac{1}{r}\frac{\partial}{\partial r}[r\frac{\partial V_\theta^{rel}}{\partial r}])+\frac{1}{r^2}\frac{\partial^2 V_\theta^{rel}}{\partial \theta^2}+\frac{2}{r^2}\frac{\partial V_\theta^{rel}}{\partial \theta}-\frac{V_\theta^{rel}}{r^2}+\frac{\|\vec{\omega}\|}{r}] \quad (2.89)$$

where $\vec{V}\equiv\vec{V}^{rel}-\vec{r}\times\vec{\omega}$ and $\vec{\omega}$ is the frame rotational vector (which is in the axial direction $\vec{z}$). Assuming a turbulent flow field with perturbation velocity and pressure components in the relative frame $\vec{V}^{rel\prime}$ and $P^{rel\prime}$, we apply the averaging operator with the box filter $\backslash\backslash\mathcal{F}_{box}(t,\Delta t)(2.89)\,/\!/_t$ and invoking the eddy viscosity concept gives

$$\overline{V}_r\frac{\partial V_\theta^{rel}}{\partial r}+\frac{\overline{V}_\theta^{rel}}{r}\frac{\partial \overline{V}_\theta^{rel}}{\partial \theta}+\overline{V}_z^{rel}\frac{\partial \overline{V}_\theta^{rel}}{\partial z}-\overline{V}_r^{rel}\|\omega\|+\frac{\overline{V}_r^{rel}}{r}(\overline{V}_\theta^{rel}-\|\omega\|r)=$$
$$-\frac{1}{\rho r}\frac{\partial \overline{P}}{\partial \theta}+(\nu+\epsilon_D)[\frac{\partial^2 \overline{V}_\theta}{\partial z^2}+(\frac{1}{r}\frac{\partial}{\partial r}[r\frac{\partial \overline{V}_\theta^{rel}}{\partial r}])+\frac{1}{r^2}\frac{\partial^2 \overline{V}_\theta^{rel}}{\partial \theta^2}+\frac{2}{r^2}\frac{\partial \overline{V}_\theta^{rel}}{\partial \theta}-\frac{\overline{V}_\theta^{rel}}{r^2}+\frac{\|\omega\|}{r}] \quad (2.90)$$

Noting the scaling laws given in §2.9 we see that $\Delta\theta\sim V_\theta/\Delta t\sim V_r/(D/N)$, then average pressure force induced torque $\tau\sim$ Mean net pressure stress $\times$length $\times$area or $\tau\sim-(\Delta\overline{P}/\Delta\theta)D^3$ then evidently $\mathcal{P}$ is

$$\mathcal{P}=(\tau\omega)/(\rho N^3D^5)\sim-\frac{ND^3\frac{\Delta\overline{P}}{\Delta\theta}}{\rho N^3D^5}=-\frac{\frac{\Delta\overline{P}}{\Delta\theta}}{\rho N^2D^2} \quad (2.91)$$

where we have also noted that $\omega\propto N$. In addition since $\Delta z\sim H_{BL}\sim D$ and if we assume that $\overline{V}_r,\overline{V}_Z\propto\overline{V}_\theta\sim ND$ then substitution of the previous (2.91) into the mean fluid equation of motion in the θ-direction (2.90) and applying the scaling laws given previously yields

$$\mathcal{P}\sim\text{non-dimensionalized}[F_{inertial}-F_{viscous}]\sim 1+(\frac{\nu_{eff}}{\nu})\frac{1}{Re} \quad (2.92)$$

where the effective viscosity $\nu_{eff}\equiv(\nu+\epsilon_D)$. This is an interesting result given that (2.92) specifies a trade-off between the laminar effects at higher Re (i.e. the tending towards negligible viscous effects as Re increases) and the effects of transition to turbulent flow (i.e. $\nu_{eff}\gg\nu$). Specifically, (2.92) indicates that as the Re increases up to the transitional value $Re_{trans.}$ the power number tends towards a constant ~ 1. However, when transition occurs ($Re\approx Re_{trans.}$) the effective fluid viscosity increases till $\nu_{eff.}\gg\nu$, thus increasing viscous losses via turbulent dissipation. To see this we note that for dimensional reasons at large scales and for high Re we have $\nu_{eff}\approx\epsilon_D\sim\ell u\sim\mathcal{LU}$ and consequently $\nu_{eff}/\nu\sim Re$. Thus,

for low Re (before transition where $\nu_{eff} \approx \nu$) the power curve is downward sloping (tending towards ~ 1). For transitional flow when ν_{eff} increases quickly along with viscous power consumption, the power curve may become upward sloping. And finally, for fully turbulent flow the power curve tends towards a constant value > 1 and becomes invariant to Re (i.e. . $(\frac{\nu_{eff}}{\nu}) \propto \frac{1}{Re} \rightarrow (\frac{Re}{1})\frac{1}{Re} = 1$). The previous Power Number dependence on the Re is illustrated in Figure 2.11. Of course it should be noted that the exact shape of the $\mathcal{P}$ vs. Re curve depends on the rapidity of the increase in effective viscosity as well as the final value for the total dissipation. Specifically, Figure 2.12 gives $\mathcal{P}$ vs. Re for baffle-less and baffled tank configurations from the data of Rushton et al [1]. Clearly, the power consumption for the former is less than in the baffled configuration. Evidently the use of baffles increases turbulent power dissipation significantly. Note that transition for the Rushton turbine type impeller occurs for a $Re \approx 10^2$ (the $\mathcal{P}$ curve slope vanishes for a Power number greater than 1). In addition, fully turbulent flow is achieved after the Power number becomes invariant with respect to Reynolds number or $Re \approx 10^4$. All these observations are consistent with the theoretical arguments put forth previously with respect to the Power number dependency on the the Reynolds Number.

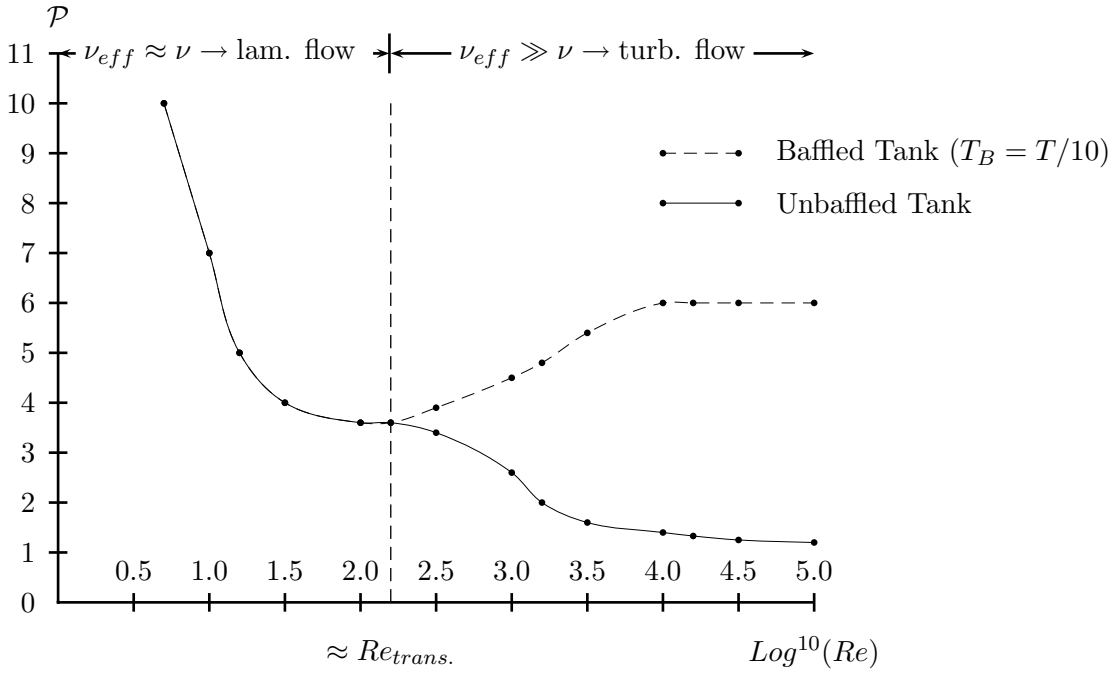

Figure 2.12: Power Number $\mathcal{P}$ vs. Re: Data (Rushton et al)

References

[1] J. Rushton E. Costich and H. Everett. Power characteristics of mixing impellers: Part ii. *Chemical Engineering Progress:46*, pages 467–476, 1950.

[2] W. Jones and B. Launder. The prediction of laminarization with a two-equation model of turbulence. *Int. Journal of Heat and Mass Transfer:15*, pages 301–314, 1972.

[3] B. Ma and Z. Warhaft. Some aspects of the thermal mixing layer in grid turbulence. *Journal of Fluid Mechanics*, 1986.

[4] R.C. Martinelli. *Trans. ASME 69*, pages 947–959, 1947.

[5] W. Orr. The stability or instability of steady motions of a perfect liquid and of a viscous liquid: Part i, ii. *Proc. Royal Irish Academy:27*, pages 9–38, 69–138, 1907.

[6] S. Pope. *Turbulent Flows*. Cambridge University Press, 2000.

[7] J. Rayleigh. On the stability or instability of certain fluid motions. *Proc. London Mathematical Soceity:II*, pages 57–70, 1880.

[8] O. Reynolds. On the dynamic theory of incompressible viscous fluids and the determination of the criterion. *Phil. Trans. Royal Society:186*, pages 123–164, 1895.

[9] H. Schlichting. *Boundary-Layer Theory*. McGraw Hill, 1968.

[10] G. Schubauer and H. Skramstad. Laminar boundary-layer oscillations and transition on a flat plate. *NACA Report 909*, pages 327–357, 1948.

[11] J. Smagorinsky. General circulation experiments with the primitive equations. *Monthly Weather Review*, pages 99–164, 1963.

[12] W. Tollmien. *NACA TM 609*.

Chapter 3

Numerical Methodology

3.1 Review of the Problem

As stated previously in §2.2, the continuity and momentum conservation equations reduce to (for the case of an incompressible fluid)

$$\begin{aligned} \vec{\nabla} \cdot \vec{V} &= 0 \\ \rho \frac{\partial(\phi)}{\partial t} + \rho \vec{\nabla} \cdot (\vec{V}\phi) &= \vec{\nabla} \cdot (\Gamma \vec{\nabla}\phi) + NS_i, \\ \phi &\equiv V_i, i = 1, 2, 3 \end{aligned} \tag{3.1}$$

where the body forces have been neglected and normal pressure forces have been absorbed into the source term NS. Note also that for simplicity, the individual Cartesian velocity components V_i have been replaced by the generic scalar ϕ. Thus, the Navier-Stokes or fluid equations of motion reduce to passive scalar transport equations exhibiting gradient based diffusion. In addition, the diffusive coefficient Γ may take on the value of either molecular μ or *effective* viscosity μ_{eff} (e.g. for laminar or turbulent flow respectively).

We begin our discussion of the implementation of the numerical solution algorithm for the above equations by decomposing the flow domain into a number of finite control volumes ΔV. The momentum transport equations, which are given in differential form above can by transformed into integral equations by simple spatial integration over ΔV. This yields

$$\begin{aligned} \int_{\Delta V} (\vec{\nabla} \cdot \vec{V}) dV &= 0 \\ \int_{\Delta V} (\rho \frac{\partial(\phi)}{\partial t} + \rho \vec{\nabla} \cdot (\vec{V}\phi)) dV &= \int_{\Delta V} (\Gamma \vec{\nabla} \cdot (\vec{\nabla}\phi) + NS_i) dV \\ \phi &\equiv V_i, i = 1, 2, 3 \end{aligned} \tag{3.2}$$

where ΔV and dV are finite and differential volumes is space respectively, while $d\vec{S}$ is a differential surface normal vector residing on an element of the surface ΔS bounding ΔV.

The convective and diffusive terms can be evaluated via the divergence theorem

$$\int_{\Delta V} \vec{\nabla} \cdot \vec{\phi} dV = \int_{\Delta S} \vec{\phi} \cdot \vec{dS} \tag{3.3}$$

where again $\vec{dS}$ is the surface normal. Thus, the final *exact* expression for a scalar transport process is

$$\begin{aligned} \int_{\Delta S} \vec{V} \cdot d\vec{S} = 0 \\ \rho(\frac{\partial}{\partial t} \int_{\Delta V} \phi dV + \int_{\Delta S} \phi \vec{V} \cdot \vec{dS}) = \int_{\Delta S} \Gamma(\vec{\nabla}\phi) \cdot \vec{dS} + \int_{\Delta V} NS_i dV \\ \phi \equiv V_i, i = 1, 2, 3 \end{aligned} \tag{3.4}$$

Introducing the notation for the volume (or cell) averaged value for an intensive property

$$\mathbf{\Phi} \equiv \frac{1}{\Delta V} \int_{\Delta V} \phi dV \tag{3.5}$$

(3.4) can be rewritten

$$\begin{aligned} \int_{\Delta S} \vec{V} \cdot \vec{dS} = 0 \\ \rho \Delta V \frac{\partial}{\partial t} \mathbf{\Phi} + \int_{\Delta S} \phi \rho \vec{V} \cdot \vec{dS} = \int_{\Delta S} \Gamma(\vec{\nabla}\phi) \cdot \vec{dS} + \mathbf{NS}_i \Delta V \\ \phi \equiv V_i, i = 1, 2, 3 \end{aligned} \tag{3.6}$$

Finally, the temporal term in the volume integrated momentum equation can be evaluated by time integration over the interval $t \rightarrow t + \Delta t$, yielding, for a non-deformable control volume

$$\begin{aligned} \rho(\mathbf{\Phi}^{t+\Delta t} - \mathbf{\Phi}^t) \Delta V + \rho \int_t^{t+\Delta t} [\int_{\Delta S} \phi \vec{V} \cdot \vec{dS}] dt = \\ \int_t^{t+\Delta t} [\int_{\Delta S} \Gamma(\vec{\nabla}\phi) \cdot \vec{dS}] dt + \Delta V \int_t^{t+\Delta t} \mathbf{NS}_i dt \end{aligned} \tag{3.7}$$

where we have dropped the explicit reference to the value of ϕ.

At this point the purely mathematical treatment ends and the above expressions must be solved via finite discretization in space and time.

3.2 Numerical Evaluation

Time integration of (3.7) can be carried out, in the approximate, by introduction of the temporal integration parameter θ defined as follows:

$$\theta \equiv [\frac{\int_t^{t+\Delta t} \mathbf{\Phi} dt}{\Delta t} - \mathbf{\Phi}^t]/[\mathbf{\Phi}^{t+\Delta t} - \mathbf{\Phi}^t] \tag{3.8}$$

or

$$\theta = 1 \Rightarrow \frac{1}{\Delta t}\int_t^{t+\Delta t} \mathbf{\Phi} dt = \mathbf{\Phi}^{t+\Delta t}$$

$$\theta = 0 \Rightarrow \frac{1}{\Delta t}\int_t^{t+\Delta t} \mathbf{\Phi} dt = \mathbf{\Phi}^{t} \tag{3.9}$$

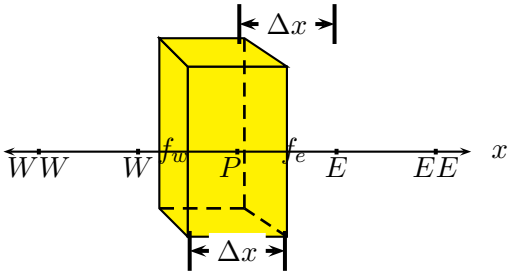

Figure 3.1: Cell location and terminology

Hence, the transport equation for $\mathbf{\Phi}$ is treated explicitly if $\theta = 0$ and implicitly for $\theta = 1$. Needless to say, a mixed evaluation can take place by choosing an intermediate value for θ. Using this definition along with the assumption that the control volume control surfaces are represented by a finite number of planar control faces, (3.7) can be evaluated as

$$\rho(\mathbf{\Phi}^{t+\Delta t} - \mathbf{\Phi}^t)\frac{\Delta V}{\Delta t} + \theta \sum_{faces} (\rho\phi\vec{V} \cdot \vec{\Delta A})_f^{t+\Delta t} + (1-\theta) \sum_{faces} (\rho\phi\vec{V} \cdot \vec{\Delta A})_f^{t} =$$

$$\theta \sum_{faces} ((\Gamma\vec{\nabla}\phi) \cdot \vec{\Delta A})_f^{t+\Delta t} + (1-\theta) \sum_{faces} ((\Gamma\vec{\nabla}\phi) \cdot \vec{\Delta A})_f^{t} + (\theta \mathbf{NS}_i{}^{t+\Delta t} + (1-\theta)\mathbf{NS}_i{}^t)\Delta V \tag{3.10}$$

where $\vec{\Delta A}$ is the surface normal vector. Gathering terms yields

$$\rho\mathbf{\Phi}^{t+\Delta t}\frac{\Delta V}{\Delta t} + \theta[\sum_{faces} ((\rho\phi\vec{V} - \Gamma\vec{\nabla}\phi) \cdot \vec{\Delta A})_f]^{t+\Delta t} =$$

$$\rho\mathbf{\Phi}^{t}\frac{\Delta V}{\Delta t} - (1-\theta)[\sum_{faces} ((\rho\phi\vec{V} - \Gamma\vec{\nabla}\phi) \cdot \vec{\Delta A})_f]^{t} + [\theta\mathbf{NS}^{t+\Delta t} + (1-\theta)\mathbf{NS}^t]\Delta V \tag{3.11}$$

where the term $\sum_{faces}((\rho\phi\vec{V} - \Gamma\vec{\nabla}\phi) \cdot \vec{\Delta A})_f$ represent convection less diffusion. To proceed further, it is now necessary to evaluate the face fluxes $(\rho\phi\vec{V} \cdot \vec{\Delta A})_f$ and surface gradients $\vec{\nabla}\phi \cdot \vec{\Delta A}$ of ϕ. For the purpose of illustration, a simplified case is evaluated first: We assume that all transport processes (i.e. flow and diffusion) is 1-D, where cell volumes are evenly spaced

with cell width Δx and have unit height and depth as shown in Figure 3.1. Specifically, using a second order accurate central difference interpolation, the value of the flux and gradient terms at face e and w is given in Table 3.1 where $\Delta A_f \equiv |\vec{\Delta A}_f|$ and $\dot{m}_f \equiv (\rho\vec{V} \cdot \vec{\Delta A})_f$.

Table 3.1: Discretized Convective and Diffusive Terms

Term	East face	West face
$\rho\phi\vec{V} \cdot \vec{\Delta A}$	$\dot{m}_e(\mathbf{\Phi}_E(1 - WF_e) + \mathbf{\Phi}_P WF_e))$	$-\dot{m}_w(\mathbf{\Phi}_P WF_w + \mathbf{\Phi}_W(1 - WF_w))$
$\Gamma\vec{\nabla}\phi \cdot \vec{\Delta A}$	$\Gamma_e \Delta A_e \frac{\mathbf{\Phi}_E - \mathbf{\Phi}_P}{\Delta x}$	$\Gamma_w \Delta A_w \frac{\mathbf{\Phi}_P - \mathbf{\Phi}_W}{\Delta x}$

Note that Table 3.1 assumes the possibility of irregularly spaced $1 - D$ grids where [1]

$$WF_{e,w} \equiv \frac{1 - \overline{e, wP}}{\overline{\overline{e, wP} + \overline{e, w(E, W)}}} \tag{3.12}$$

Thus, the difference in the convection and diffusion terms in the above expression for a second order central difference scheme is

$$\begin{aligned} \sum_f Conv - \sum_f Diff = \\ \dot{m}_e(WF_e\mathbf{\Phi}_P + (1 - WF_e)\mathbf{\Phi}_E) + \dot{m}_w(WF_w\mathbf{\Phi}_P + (1 - WF_w)\mathbf{\Phi}_W) - \\ (\frac{\Gamma_e \Delta A_e}{\Delta x}(\mathbf{\Phi}_E - \mathbf{\Phi}_P) - \frac{\Gamma_w \Delta A_w}{\Delta x}(\mathbf{\Phi}_P - \mathbf{\Phi}_W)) \end{aligned} \tag{3.13}$$

where $\dot{m}$ is positive from West to East. Or

$$\begin{aligned} \sum_f Conv - \sum_f Diff = \\ \mathbf{\Phi}_P \sum_{f=P\to nb} (\dot{m}_f WF_f - \frac{\Gamma_f \Delta A_f}{\Delta x})_f - \sum_{f=P\to nb} (-\dot{m}_f(1 - WF_f) - \frac{\Gamma_f \Delta A_f}{\Delta x})_f \mathbf{\Phi}_{nb} \end{aligned} \tag{3.14}$$

where the summation index f is over all faces of the control volume and $\mathbf{\Phi}_{nb}$ is the neighbor cell centered property. Equation (3.11) can thus be rewritten in a form

$$\begin{aligned} \theta(A_P^{t+\Delta t}\mathbf{\Phi}_P^{t+\Delta t} - \sum_{f=P\to nb} a_f^{t+\Delta t}\mathbf{\Phi}_{nb}^{t+\Delta t}) = \\ (1 - \theta)(\sum_{f=P\to nb} a_f^t \mathbf{\Phi}_{nb}^t - A_P^t \mathbf{\Phi}_P^t) + \theta \mathbf{NS}_{i,P}^{t+\Delta t} \Delta V_P^{t+\Delta t} + (1 - \theta)\mathbf{NS}_{i,P}^t \Delta V_P^t \end{aligned} \tag{3.15}$$

where the neighboring face and present cell coefficients a_f and A_P are given in Table 3.2. Or

[1] This expression for the weight factor can be found by introducing a *first order* polynomial $\phi_f = a + bx$ expression for the property face value of Φ.

introducing a redefined source term $\hat{\mathbf{NS}}$ as given in Table (3.2)

$$\boxed{\theta A_P^{t+\Delta t,n-1}\mathbf{\Phi}_P^{t+\Delta t,n} = \theta\sum_{f=P\rightarrow nb} a_f^{t+\Delta t,n-1}\mathbf{\Phi}_{nb}^{t+\Delta t,n} + \hat{\mathbf{NS}}_{i,P}^{t+\Delta t,n-1}} \tag{3.16}$$

where we are taking into account the fact that the above equation will be solved iteratively yielding a solution $\mathbf{\Phi}^{t+\Delta t,n}$ based on coefficients (A_P and a_f) calculated via properties at iteration $n-1$. The central, neighbor node coefficients (A_p and a_f) and source term $\hat{\mathbf{NS}}$ again are given in Table 3.2. In addition, note the introduction of a present cell source S_P. The motivation for this is that introduction of S_P eases implementation of boundary conditions and certain source terms by allowing the *implicit* treatment of such additional terms via the function $G(\mathbf{\Phi}_P, \mathbf{\Phi}_{nb}) = 0$. Specifically, at a boundary, the condition placed on the flow can be expressed as $G_1 * (\mathbf{\Phi}_P) + G_2(\mathbf{\Phi}_{nb}) = 0$ where G_1 and $G_2()$ are the present cell coefficient and a function based on neighboring cell values respectively (see §3.3.4 for application of this approach to no-slip wall boundaries). Thus, the value added to S_P would be G_1 while the value added to the net source $\hat{\mathbf{NS}}$ would be $G_2(\mathbf{\Phi}_{nb})$.

Finally, it should be noted that the preceding discussion only applies to the case of orthogonal grids using 2^{nd} order central differences. For non-orthogonal grids, interpolation of the diffusive flux at a face must be corrected (see §3.3.2).

Table 3.2: Coefficient definitions and values corresponding to expression (3.16)

Term	Definition
$a_f^{t+\Delta t}$	$-(\dot{m}(1-WF_f) + \frac{\Gamma\Delta A_f}{\Delta x})_f^{t+\Delta t}$
$S_P^{t+\Delta t}$	$-(\frac{\rho\Delta V_P^{t+\Delta t}}{\theta\Delta t} + \sum_{f=P\rightarrow nb}\dot{m}_f^{t+\Delta t})$
$A_P^{t+\Delta t}$	$\sum_{f=P\rightarrow nb} a_f^{t+\Delta t} - S_P^{t+\Delta t}$
$\hat{\mathbf{NS}}_P^{t+\Delta t}$	$(1-\theta)[(-A_P^t + (1/(1-\theta) + 1/\theta)\rho\frac{\Delta V_P}{\Delta t})\mathbf{\Phi}_P^t + \sum_{f=P\rightarrow nb} a_f^t\mathbf{\Phi}_{nb}^t] + \theta\mathbf{NS}_P^{t+\Delta t}\Delta V_P^{t+\Delta t} + (1-\theta)\mathbf{NS}_P^t\Delta V_P^t$

3.3 Application to the Fluid Equation of Motion

As stated previously, the above development for a generic scalar is directly applicable to the Navier-Stokes equation where ϕ takes on the value of each Cartesian component of velocity V_i, $i = 1$, 2 and 3. In addition, a pressure force (per unit volume) term is added $-\partial P/\partial x_i$. Thus, for the case of constant density with spatially varying diffusivity $\Gamma(\vec{r})$ or an *effective* viscosity μ_{eff}

$$\rho\frac{\partial V_i}{\partial t} + \rho\nabla\cdot(\vec{V}V_i) = -\frac{\partial P}{\partial x_i} + \vec{\nabla}\cdot(\mu_{eff}\nabla\vec{V}_i) \tag{3.17}$$

In terms of the set of scalar transport equations to be solved (3.1), the source term NS is given by

$$NS_i = -\frac{\partial P}{\partial x_i} + {}^{non\text{-}pressure}_{analytical}NS_i \tag{3.18}$$

where ${}^{non-press}_{analytical}NS_i$ represents surface or fictitious forces such as, for example, gravitational, surface tension or, for the application of a rotating reference frame, centrifugal forces (none of which are modeled in this work). The result is the discretized equation

$$\boxed{\theta A_{i,P}^{t+\Delta t,n-1}\mathbf{V}_{i,P}^{t+\Delta t,n} = \theta\sum_{f=P\rightarrow nb} a_{i,f}^{t+\Delta t,n-1}\mathbf{V}_{i,nb}^{t+\Delta t,n} + \mathbf{SU}_{i,P}^{t+\Delta t,n-1}} \tag{3.19}$$

where one is now making explicit the values of the nodal and face coefficients $A_{i,P}$ and $a_{i,f}$ associated with the discretized equation calculated for each Cartesian component of velocity V_i. In addition, the source term is given by **SU**

$$\begin{aligned}\mathbf{SU}_{i,P}^{t+\Delta t,n-1} \equiv \theta[-\frac{\partial P}{\partial x_i}\Big|_P^{t+\Delta t,n-1} + NS_{i,P}^{t+\Delta t}]\Delta V_P^{t+\Delta t} + (1-\theta)[(-\frac{\partial P}{\partial x_i}\Big|_P^{t} + \\ NS_{i,P}^{t})\Delta V_P^{t} + \sum_{f=P\rightarrow nb} a_{i,f}^{t}\mathbf{V}_{i,nb}^{t} - (A_{i,P}^{t} - (\frac{1}{1-\theta}+\frac{1}{\theta})\rho\frac{\Delta V_P{}^{t}}{\Delta t})\mathbf{V}_{i,P}^{t}]\end{aligned} \tag{3.20}$$

$$NS \equiv {}^{non\text{-}pressure}_{analytical}\, NS + {}_{numerical}\, NS + {}_{Dis.\ Scheme}\, NS \tag{3.21}$$

The terms NS^t and $NS^{t+\Delta t}$ given in (3.21) represent the sum of the additional source terms evaluated at times t and $t+\Delta t$. These source terms are the contribution associated with additional non-pressure force sources in the momentum transport equation ${}^{non\text{-}pressure}_{analytical}NS$, as well as additional sources required for different discretization schemes ${}_{Dis.\ Scheme}S$ and the sources used to correct for the use of non-orthogonal grids ${}_{numerical}NS$. The latter will be discussed in §3.3.2.

3.3.1 Treatment of the Pressure Term

The effect of pressure, diffusion, convection and the source terms on the calculated values of $V_{i,P}$ can be made clear by re-arrangement of expression (3.19).

$$\mathbf{V}_{i,P}^{t+\Delta t} = \frac{\sum_{f=P\rightarrow nb} a_{i,f}^{t+\Delta t}\mathbf{V}_{i,nb}^{t+\Delta t}}{A_P^{t+\Delta t}} - \frac{\Delta V_P^{t+\Delta t}}{A_P^{t+\Delta t}}\frac{\partial P}{\partial x_i}\Big|_P^{t+\Delta t} + \frac{\tilde{\mathbf{SU}}_{i,P}^{t+\Delta t}}{\theta A_P^{t+\Delta t}} \tag{3.22}$$

$$\tilde{\mathbf{SU}}_{i,P}^{t+\Delta t} \equiv \mathbf{SU}_{i,P}^{t+\Delta t} + \frac{\partial P}{\partial x_i}\Big|_P^{t+\Delta t}\Delta V_P^{t+\Delta t} \tag{3.23}$$

where we have simply extracted the time implicit pressure term from the source **SU**. Thus, the effect of pressure on the local nodal velocity is given by the second term on the right-hand side of (3.22). Now according to Figure 3.1, a cell centered central difference evaluation of a first derivative of any property (for example, pressure), is given by

$$\left.\frac{\partial P}{\partial x_i}\right|_P \approx \frac{P_E - P_W}{2\Delta x} \tag{3.24}$$

Hence, a central difference scheme for pressure has, in the case of uniform grids, a stencil length of twice the cell width. Thus, pressure variations of a purely numerical nature, with wavelength $2\Delta x$ could occur during the solution iteration process. Possible approaches to eliminating these spurious variations include: Staggering the computational nodes such that pressure and velocities are solved at nodal locations with a relative displacement of Δx. This has the effect of allowing a (velocity) cell centered calculation of the pressure gradient via

$$\left.\frac{\partial P}{\partial x_i}\right|_P \approx \frac{P_e - P_w}{\Delta x} \tag{3.25}$$

where P_e and P_w are the face values of pressure as mapped from the staggered (pressure) grid nodal values. Clearly (3.25) has a stencil length of Δx, thus eliminating the possibility of numerical oscillations in the pressure field. Another approach is to solve pressure and velocity at co-located (i.e. coincident) nodal locations while incorporating the equivalent effect of staggering the grids. Specifically, if the effect of the central difference pressure term on velocity is subtracted out and a pressure term is added which has a stencil width of Δx, then spurious pressure oscillations would be eliminated. In terms of Figure 3.1 this approach is represented via (3.26) for the calculation of i-th velocity component at face e.

$$\left.\overbrace{(\frac{\partial \mathbf{P}}{\partial x_i}\frac{V_P}{A_P})}^{+\ pres.\ interp.\ of\ stencil\ \Delta x}\right|_e \approx \frac{\mathbf{P}_E - \mathbf{P}_P}{\Delta x}\left.(\frac{V_{i,P}}{A_{i,P}})\right|_e,$$

$$\left.\mathbf{V}_i\right|_e = (\mathbf{V}_{i,P} + \left.\overbrace{(\frac{\partial \mathbf{P}}{\partial x_i}\frac{V_{i,P}}{A_{i,P}})}^{-\ pres.\ interp.\ of\ stencil\ 2\Delta x}\right)\Big|_e - \left.\overbrace{(\frac{\partial \mathbf{P}}{\partial x_i}\frac{V_{i,P}}{A_{i,P}})}^{+\ pres.\ interp.\ of\ stencil\ \Delta x}\right|_e \tag{3.26}$$

Once the velocity correction is known $\dot{m}_f$ can be corrected. The result thus renders the velocity field calculation (via the discretized equation) implicitly dependent on a pressure field interpolation of stencil width Δx. This procedure is referred to as the Rhie and Chow velocity correction method.

3.3.2 Correction for Grid Non-orthogonality

From (3.4) we can see that the diffusive term implies, for a finite number of planar faces

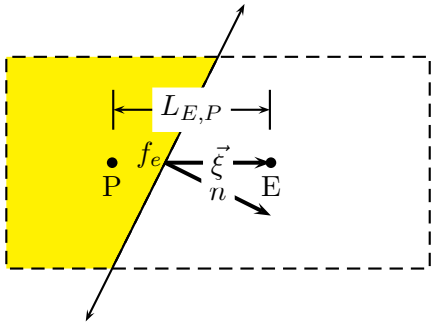

Figure 3.2: Cell location and terminology: Non-orthogonal grid

$$\int_{\Delta S} \Gamma(\vec{\nabla}\phi)\cdot d\vec{S} \cong \sum_{f=P\rightarrow nb} \Gamma_f(\vec{\nabla}\phi)_f \cdot \Delta\vec{A}_f = \sum_{f=P\rightarrow nb} \Gamma_f(\frac{\partial\phi}{\partial n})\hat{n}\cdot\Delta\vec{A}_f = \sum_{f=P\rightarrow nb} \Gamma_f \frac{\partial\phi}{\partial n}\Delta A_f \tag{3.27}$$

where, with reference to Figure 3.2, $\vec{\xi} \equiv \xi\hat{\xi}$ and $\vec{n} \equiv n\hat{n}$ where $\hat{n}$ and $\hat{\xi}$ are unit vectors. However, the previous calculation for the diffusive term (see (3.14)) instead assumed orthogonal grid lines (i.e. $\vec{\xi}\times\vec{n} = 0$) with the resulting diffusion at face f given by $\Gamma(\mathbf{\Phi}_P - \mathbf{\Phi}_E)/(L_{E,P})A_{f_e}$ which corresponds instead to the gradient $\partial\phi/\partial\xi$. Given the desire to express the correct property gradient, a suitable correction term for the normal diffusive flux at the face is given by

$$\textit{Normal diffusion correction due to non-orthogonal. grids} = (\frac{\partial\phi}{\partial\hat{n}} - \frac{\partial\phi}{\partial\hat{\xi}})\Big|_f \Gamma_f\Delta A_f = \Gamma_f\Delta A_f(\vec{\nabla}\phi\cdot\hat{n} - \vec{\nabla}\phi\cdot\hat{\xi}))_f = \Gamma_f\Delta A_f(\vec{\nabla}\phi\cdot(\hat{n}-\hat{\xi}))_f \tag{3.28}$$

Thus, yielding a source term for the local grid non-orthogonal correction of

$$\boxed{{}_{non-orth}\mathbf{SU}_{i,P}^{t+\Delta t,n} = \textstyle\sum_{f=P\rightarrow nb}\Gamma_f\Delta A_f(\vec{\nabla}\mathbf{V}_i^{t+\Delta t,n-1}\cdot(\hat{n}-\hat{\xi}))_f} \tag{3.29}$$

Note that this correction is calculated explicitly using the velocity field from the previous iteration $(n-1)$ thus allowing the term to be incorporated into the source term (as opposed to the nodal or face coefficients A_P and a_f).

3.3.3 Alternative Discretization Schemes

The previous treatment of *convective momentum transfer* utilized a *second order accurate* central difference interpolation based on the two neighboring cell property values to the face.

4^{th}-order Discretization

A higher order interpolation can be determined via recourse of a 4^{rth}-*order polynomial* of the form

$$\phi = a + bx + cx^2 + dx^3 \tag{3.30}$$

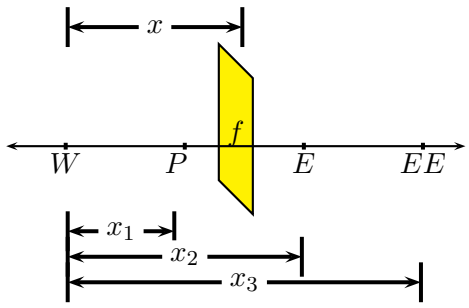

Figure 3.3: Coordinate system: 3^{rd} and 4^{rth}-order schemes

Using a $1-D$ coordinate systems as displayed in Figure 3.3 one can see that $a = \phi_W$, thus (3.30) can be reformulated as

$$\phi - \phi_W = bx + cx^2 + dx^3 \tag{3.31}$$

Applying the conditions for the value of ϕ at the (known) remaining three nodal points gives the system of equations $[A][C] = [Z]$

$$\begin{bmatrix} x_1 & x_1^2 & x_1^3 \\ x_2 & x_2^2 & x_2^3 \\ x_3 & x_3^2 & x_3^3 \end{bmatrix} \begin{bmatrix} b \\ c \\ d \end{bmatrix} = \begin{bmatrix} \phi_P - \phi_W \\ \phi_E - \phi_W \\ \phi_{EE} - \phi_W \end{bmatrix} \tag{3.32}$$

Inverting the matrix $[A]$ we have

$$[A]^{-1} = \frac{\begin{bmatrix} (x_1x_2)^2(x_3-x_2) & -(x_1x_3)^2(x_3-x_1) & (x_1x_2)^2(x_2-x_1) \\ -(x_2x_3)(x_3-x_2)(x_3+x_2) & (x_1x_3)(x_3-x_1)(x_3+x_1) & -(x_1x_2)(x_2-x_1)(x_2+x_1) \\ (x_2x_3)(x_3-x_2) & -(x_1x_3)(x_3-x_1) & (x_1x_2)(x_2-x_1) \end{bmatrix}}{x_1x_2x_3[x_2x_3(x_3-x_2) - x_1x_3(x_3-x_1) + x_1x_2(x_2-x_1)]} \tag{3.33}$$

Solving for the coefficient vector $[C]$ and substituting into (3.31) gives

$$\phi_f = \frac{\begin{bmatrix} \phi_W + \\ \phi_W[-(x_2x_3)^2(x_3-x_2) + (x_1x_3)^2(x_3-x_1) - (x_1x_2)^2(x_2-x_1)]x + \\ \phi_W[(x_2x_3)(x_3-x_2)(x_3+x_2) - (x_1x_3)(x_3-x_1)(x_3+x_1) + (x_1x_2)(x_2-x_1)(x_2+x_1)]x^2 + \\ \phi_W[-(x_2x_3)(x_3-x_2) + (x_1x_3)(x_3-x_1) - (x_1x_2)(x_2-x_1)]x^3 + \\ \phi_P[[(x_2x_3)^2(x_3-x_2)]x - [(x_2x_3)(x_3-x_2)(x_3+x_2)]x^2 + [(x_2x_3)(x_3-x_2)]x^3] + \\ \phi_E[-[(x_1x_3)^2(x_3-x_1)]x + [(x_1x_3)(x_3-x_1)(x_3+x_1)]x^2 - [(x_1x_3)(x_3-x_1)]x^3] + \\ \phi_{EE}[[(x_1x_2)^2(x_2-x_1)]x - [(x_1x_2)(x_2-x_1)(x_2+x_1)]x^2 + [(x_1x_2)(x_2-x_1)]x^3] \end{bmatrix}}{x_1x_2x_3[x_2x_3(x_3-x_2) - x_1x_3(x_3-x_1) + x_1x_2(x_2-x_1)]} \tag{3.34}$$

Using a deferred correction approach the source terms is modified by the 4^{rth}-order scheme according to (3.35)

$$S_{scheme} = \sum_{f=P\rightarrow nb} (\dot{m}(1-WF))_f \phi_{nb}^{n-1} + \sum_{f=P\rightarrow nb} (\dot{m}(WF))_f \phi_P^{n-1} - \sum_{f=P\rightarrow nb} (\dot{m})_f \phi_f^{n-1} \tag{3.35}$$

where the last term represents the direct contribution of the 4^{rth}-order property interpolation at the face.

3^{rd}-order Up-winded Discretization

A 3^{rd}-order accurate upwinded interpolation for face property values, (originally termed the QUICK scheme as formulated by Leonard [1]), can be developed via recourse of a *third order polynomial* of the form

$$\phi = a + bx + cx^2 \tag{3.36}$$

If, referring to Figure 3.3, we assume U is positive from the W to E direction, the interpolation can be upwind biased via the use of ϕ_W, ϕ_P as upstream properties, and ϕ_E as the downstream property For the $1-D$ coordinate systems displayed previously, one can see that $a = \phi_W$, thus (3.36) can be reformulated as

$$\phi - \phi_W = bx + cx^2 \tag{3.37}$$

As in the 4^{th}-order case we apply the conditions for the value of ϕ at the (known) remaining two nodal points giving the system of equations $[A][C] = [Z]$

$$\begin{bmatrix} x_1 & x_1^2 \\ x_2 & x_2^2 \end{bmatrix} \begin{bmatrix} b \\ c \end{bmatrix} = \begin{bmatrix} \phi_P - \phi_W \\ \phi_E - \phi_W \end{bmatrix} \tag{3.38}$$

Inverting the matrix $[A]$ we have

$$[A]^{-1} = \frac{\begin{bmatrix} x_2^2 & -x_1^2 \\ -x_2 & x_1 \end{bmatrix}}{x_1x_2^2 - x_1^2x_2} \tag{3.39}$$

Thus the coefficient vector is

$$\begin{bmatrix} b \\ c \end{bmatrix} = \frac{\begin{bmatrix} x_2^2 & -x_1^2 \\ -x_2 & x_1 \end{bmatrix}}{x_1x_2^2 - x_1^2x_2} \begin{bmatrix} \phi_P - \phi_W \\ \phi_E - \phi_W \end{bmatrix} = \frac{\begin{bmatrix} \phi_W(-x_2^2 + x_1^2) + \phi_P(x_2^2) + \phi_E(-x_1^2) \\ \phi_W(x_2 + x_1) + \phi_P(-x_2) + \phi_E(x_1) \end{bmatrix}}{x_1x_2^2 - x_1^2x_2} \tag{3.40}$$

yielding via (3.36)

$$\phi_f = \frac{\phi_W[(-x_2^2 + x_1^2)x + (x_2 - x_1)x^2 + (x_1x_2^2 - x_1^2x_2)] + \phi_P[x_2^2x - x_2x^2] + \phi_E[-x_1^2x + x_1x^2]}{x_1x_2^2 - x_1^2x_2} \tag{3.41}$$

Or if $g_1 \equiv \frac{-x_1^2x + x_1x^2}{x_1x_2^2 - x_1^2x_2}$ and $g_2 \equiv \frac{-(-x_2^2 + x_1^2)x - (x_2 - x_1)x^2 - (x_1x_2^2 - x_1^2x_2)}{x_1x_2^2 - x_1^2x_2}$ then

$$\phi_f = [(-g_2)\phi_W + (1 - g_1 + g_2)\phi_P + (g_1)\phi_E] \tag{3.42}$$

As in the case of the 4^{th}-order discretization scheme, using a deferred correction approach

the source terms is modified by the Quick-scheme according to (3.43)

$$S_{scheme} = \sum_{f=P\rightarrow nb} (\dot{m}(1-WF))_f \phi_{nb}^{n-1} + \sum_{f=P\rightarrow nb} (\dot{m}(WF))_f \phi_P^{n-1} - \sum_{f=P\rightarrow nb} (\dot{m})_f \phi_f^{n-1} \quad (3.43)$$

where the last term represents the direct contribution of the Quick-scheme property interpolation at the face again assuming U is positive from the W to E direction. Note that for flow in the opposite direction the previous derivation can be repeated, producing a slightly modified expression.

3.3.4 Implementation of Boundary Conditions

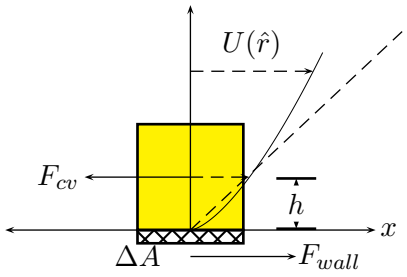

Figure 3.4: Near wall flow and computational control volume

For the purpose of illustration, the imposition of a moving or stationary wall boundary condition will be described. In terms of the fluid equation of motion the imposition of an arbitrary localized nodal force can be viewed as a momentum source (or sink) applied at a control volume adjacent to the wall. Specifically, the shear stress applied at a control volume surface can be expressed as

$$\tau_{wall} \approx \hat{\tau}({}_{rel.\ \parallel\ wall}V) \quad (3.44)$$

where ${}_{rel.\ \parallel\ wall}V$ is the (relative) parallel wall velocity at the first off the wall fluid cell and $\hat{\tau}$ takes on the values

$$\hat{\tau} = \frac{\mu}{D_{\perp dist.\ P\rightarrow wall\ cell}} = \frac{\mu}{h} \} laminar\ flow\ constant\ \mu \quad (3.45)$$

where h is the wall normal distance to node center P. Thus, if the relative fluid velocity off the wall is ${}_{1st\ cell\ off\ wall}\vec{V} - {}_{wall}\vec{V}$ and we define $\hat{\Delta A}_f$ as a vector planar to the wall face with magnitude $\|\vec{\Delta A}\|$ then the total applied nodal force is $\hat{\tau}({}_{1st\ cell\ off\ wall}\vec{V} - {}_{wall}\vec{V}) \cdot \hat{\Delta A}_f$ and the resulting source term in the discretized equation, assuming node P is the first cell of the wall, is simply

$$\begin{aligned} {}_{analytic:wallbc}SU_{i,P} &= \hat{\tau}[{}_{relative}\vec{V}_P - V_{P,i}\hat{e}_i] \cdot \hat{\Delta A}(\frac{\hat{\Delta A}}{\|\vec{\Delta A}\|} \cdot \hat{e}_i) \\ {}_{analytic:wallbc}SP_{i,P} &= \hat{\tau}\frac{(\hat{\Delta A} \cdot \hat{e}_i)^2}{\|\vec{\Delta A}\|} \end{aligned} \quad (3.46)$$

where we have utilized Newton's 3^{rd} Law in applying the wall force component at the cell center. Note also that as previously stated, it is desirable to maintain an implicit treatment of $\mathbf{\Phi}_P$ in the formulations of the discretized equations. Thus, (3.46) is based on the form $\hat{S} = -{}_{bc}S_P\mathbf{\Phi}_P$ and $A_P =_{bc} S_P$ where ${}_{bc}S_P$ is the present cell P contribution to the boundary condition source.

3.4 Solution to the Discretized Equation

To repeat a general statement of the problem: We are interested in finding the solution to the following set of equations

$$\theta A_{i,P}^{t+\Delta t}\mathbf{V}_{i,P}^{t+\Delta t} = \theta \sum_{f=P\rightarrow nb} a_{i,f}^{t+\Delta t}\mathbf{V}_{i,nb}^{t+\Delta t} + \mathbf{SU}_{i,P}^{t+\Delta t}$$
$$\sum_{f=P\rightarrow nb} \dot{m}_f = 0 \tag{3.47}$$

One thus seeks a solution to the discretized Navier-Stokes equation which are constrained to satisfy continuity. However, given that pressure $\mathbf{P}$ and $\mathbf{\Phi}$ (i.e. $\mathbf{V}_i$) are unknown, (3.47) represents a coupled set of equations in velocity and thus can be solved iteratively.

Specifically, we can determine the solution to the above set of equations according to a *guessed* and subsequent *correction* of $\mathbf{\Phi}$. Thus, if $\mathbf{\Phi}^*$ is the guessed property and $\mathbf{\Phi}'$ is the correction, then $\mathbf{\Phi} = \mathbf{\Phi}^* + \mathbf{\Phi}'$. Or applied to pressure as well as velocity, $\mathbf{V}_i = \mathbf{V}_i^* + \mathbf{V}_i'$ and $\mathbf{P} = \mathbf{P}^* + \mathbf{P}'$. Introducing the Discretized Momentum Operator $\ominus()$ (where, for example, $\ominus(\mathbf{V}_i)$ yields the first expression in (3.47)) we note that

$$\ominus(\mathbf{V}_i') = \ominus(\mathbf{V}_i) - \ominus(\mathbf{V}_i^*) \longrightarrow \theta A_{i,P}\mathbf{V}_{i,P}' = \theta \sum_{f=P\rightarrow nb} a_{i,f}\mathbf{V}_{i,nb}' + (\mathbf{SU}_{i,P} - \mathbf{SU}_{i,P}^*) \tag{3.48}$$

Noting that upon convergence $\Phi^* \rightarrow \Phi$ then $\mathbf{SU}_P^* \rightarrow \mathbf{SU}_P$, while ignoring all the source term components except those corresponding to the pressure gradient $\partial\mathbf{P}/\partial x_i$, the result is an i-th velocity (V_i) correction equation

$$\boxed{\mathbf{V}_{i,P}'^{,t+\Delta t} \approx \frac{\sum_{f=P\rightarrow nb} a_{i,f}^{t+\Delta t}\mathbf{V}_{i,nb}'^{,t+\Delta t}}{A_{i,P}^{t+\Delta t}} - \frac{\Delta V_P^{t+\Delta t}}{A_P^{t+\Delta t}} \frac{\partial P'}{\partial x_i}\Big|_P^{t+\Delta t}} \tag{3.49}$$

Thus, if the pressure correction field (i.e. P') in known, the local velocity correction can be calculated, however, we will return to this shortly. To determine the pressure correction field, the flow field constraint due to continuity can be applied yielding

$$\sum_{f=P\rightarrow nb} \dot{m}_f = \sum_f \rho(\vec{\mathbf{V}})_f \cdot \Delta\vec{A} = \sum_i [\sum_f \rho(\mathbf{V}_i^* + \mathbf{V}_i')_f \Delta A_{f,i}] = 0 \tag{3.50}$$

where $\Delta A_{f,i}$ is the projection of $\Delta\vec{A}$ in the $\hat{e}_i$ direction. To satisfy (3.50) while correcting velocity via (3.49) we institute the following two part correction process.

3.4.1 PISO Algorithm: First Corrector Step

Noting that upon convergence $\sum_{f=P\rightarrow nb} a_{i,f}V_{i,nb}' = 0$ one can initially neglect this term in the velocity correction equation (3.49). The result is a simplified version of the expression for pressure correction equation (3.51).

Table 3.3: Definitions and values corresponding to first Piso pressure corrector step (3.52)

Term	α_e	α_w	α_P	β_P
	$\frac{(\rho dA)_e}{(\Delta x)_{P\to E}}$	$\frac{(\rho dA)_w}{(\Delta x)_{P\to W}}$	$\sum_f \alpha_f$	$\sum_f \dot{m}^*_f = \sum_f (\rho \vec{\Delta A} \cdot \vec{\mathbf{V}}^*)\Big\vert_f$

$$\sum_i \sum_f \rho(\mathbf{V}^*_i + V'_i)_f \Delta A_{i,f} = \sum_i [\sum_f \rho \mathbf{V}^*_{f,i} (\rho \Delta A_{f,i})_f - \sum_f (\frac{\partial \mathbf{P}'}{\partial x_i})_f (\rho d_{i,P} \Delta A_{f,i})_f] =$$
$$\sum_f \dot{m}^*_f + \sum_f (\frac{\partial \mathbf{P}'}{\partial x_i})_f (\rho d_{i,P} \Delta A_{f,i})_f = 0 \quad (3.51)$$

where $d_{i,P} \equiv \Delta V / A_{i,P}$. If a stencil width of Δx is used for the evaluation of the facial pressure correction gradient then we have the following discretized equation for $\mathbf{P}'$

$$\boxed{\alpha_P \mathbf{P}'_P = \textstyle\sum_{f=P\to nb} \alpha_f \mathbf{P}'_{nb} + \beta_P} \quad (3.52)$$

where in the context of Figure 3.1 $\alpha_{P,nb}$ and β_P are given in Table (3.3). A solution to (3.52) is thus found after which pressure is corrected along with facial mass fluxes via (3.49) or

$$\boxed{\dot{m}'_{f=P\to nb} \approx \vec{\Delta A}_f \cdot \vec{\mathbf{V}}'_f \rho_f, \mathbf{V}'_{i,P}\Big\vert_f \approx (\tfrac{\Delta V_P}{A_{i,P}} \partial \mathbf{P}' / \partial x_i)\Big\vert_f} \quad (3.53)$$

3.4.2 PISO Algorithm: Further PISO Corrector Steps

The previously described process could be continued repeatedly resulting in a partial convergence towards a flow solution which satisfies momentum and mass conservation. However, the actual attainment of convergence is not guaranteed given the terms neglected in the velocity correction expression. Indeed any attainment of convergence will be accidental resulting in, at best, a partially converged solution. To overcome this, additional corrector steps are taken which incorporate these neglected terms. If for a general property we define via recursion $\mathbf{\Phi}^{***} \equiv \mathbf{\Phi}^{**} + \mathbf{\Phi}''$ where $\mathbf{\Phi}^{**}$ is defined as the (first) corrected property ($\mathbf{\Phi}^{**} \equiv \mathbf{\Phi}^{*} + \mathbf{\Phi}'$) we can express an improved approximation for the velocity correction based on (3.49)

$$\mathbf{V}''_{i,P} \approx \frac{\sum_{f=P\to nb} a_{i,f} \mathbf{V}'_{i,nb}}{A_p} + \frac{\Delta V_P}{A_p} \partial \mathbf{P}'' / \partial x_i \quad (3.54)$$

where the sum is treated explicitly in velocity correction. As in the previous §3.4.1 the requirements of mass conservation are applied yielding a similar discretized (second) pressure correction equation (3.55).

$$\sum_f \dot{m}^{***} = \sum_i \sum_f \rho(\mathbf{V}^{**}_i + \mathbf{V}''_i) \Delta A_{i,f} = \sum_f \dot{m}^{**}_f + \sum_i \sum_f \frac{\partial \mathbf{P}''}{\partial x_i}_f (\rho d_p \Delta A_i)_f = 0 \quad (3.55)$$

Table 3.4: Definitions and values corresponding to second PISO pressure corrector step (3.52)

Term	α_e	α_w	α_P	β_P
	$\frac{(\rho dA)_e}{(\Delta x)_{P\to E}}$	$\frac{(\rho dA)_w}{(\Delta x)_{P\to W}}$	$\sum_f \alpha_f$	$\sum_f \dot{m}_f^{**} + \frac{1}{A_P}\sum_f \rho\vec{\Delta A}\cdot\sum_{f=P\to nb} a_{nb}\vec{\mathbf{V}}'_{nb}$

Again, if a stencil width of Δx is used for the evaluation of the facial (second) pressure correction gradient then we have the following discretized equation for P''

$$\boxed{\alpha_P \mathbf{P}''_P = \sum_{f=P\to nb} \alpha_f \mathbf{P}''_{nb} + \beta_P} \tag{3.56}$$

As before, in the context of Figure 3.1 $\alpha_{P,nb}$ and β_P are given in Table (3.4) where terms $()'$ and $()^*$ become $()''$ and $()^{**}$.
A solution to (3.56) is thus found after which pressure is corrected a second time and facial mass fluxes and velocities are again corrected via (3.57)

$$\boxed{\dot{m}''_{f=P\to nb} \approx \vec{\Delta A}_f \cdot \vec{\mathbf{V}}''_f \rho_f, \mathbf{V}''_{i,P}\Big|_f \approx \frac{\sum_{f=P\to nb} a_{i,f}\mathbf{V}'_{i,nb}}{A_p}\Big|_f + \left(\frac{\Delta V_P}{A_{i,P}}\partial\mathbf{P}''/\partial x_i\right)\Big|_f} \tag{3.57}$$

This process can be repeated until both the mass residual $\sum_f \dot{m}_f$ and velocity correction $\vec{V}''$ falls to some negligible value. However, from inspection of the source term in the subsequent pressure correction equation in Table 3.4, it is apparent that this is equivalent to the minimization of β_P. Thus, in practice convergence is achieved when β_P falls to some negligible value.

3.5 Review and Application to a Solver

3.5.1 Discretized Equation

In order to render the previous results applicable to a general (pre-existing) CFD solver, slight notational modifications were made. Specifically, we introduce the θ *based* coefficients for the new time step $t + \Delta t$

$$\begin{aligned} {}^{\theta}A_P^{t+\Delta t} &\equiv \theta A_P^{t+\Delta t}, \\ {}^{\theta}a_f^{t+\Delta t} &\equiv \theta a_f^{t+\Delta t} \\ {}^{\theta}d_{i,P}^{t+\Delta t} \equiv \frac{\theta}{{}^{\theta}A_{i,P}^{t+\Delta t}} = \frac{\theta}{\theta A_{i,P}^{t+\Delta t}} &= \frac{1}{A_{i,P}^{t+\Delta t}} = d_{i,P}^{t+\Delta t} \end{aligned} \tag{3.58}$$

The result is a slight modification of the discretized equation (3.19) yielding

$$\boxed{{}^{\theta}A_{i,P}^{t+\Delta t,n-1}\mathbf{V}_{i,P}^{t+\Delta t,n} = \sum_{f=P\rightarrow nb} {}^{\theta}a_{i,f}^{t+\Delta t,n-1}\mathbf{V}_{i,nb}^{t+\Delta t,n} + \mathbf{SU}_{i,P}^{t+\Delta t,n}} \tag{3.59}$$

where

$$\begin{aligned}\mathbf{SU}_{i,P}^{t+\Delta t,n-1} \equiv \theta[-\frac{\partial P}{\partial x_i}\Big|_P^{t+\Delta t,n-1} + \mathbf{NS}_{i,P}^{t+\Delta t,n-1}]\Delta V_P^{t+\Delta t} + \\ (1-\theta)[(-\frac{\partial P}{\partial x_i}\Big|_P^{t} + \mathbf{NS}_{i,P}^{t})\Delta V_P^{t} + \\ \sum_{f=P\rightarrow nb} a_{i,f}^t\mathbf{V}_{i,nb}^t - (A_{i,P}^t - (\frac{1}{1-\theta}+\frac{1}{\theta})\rho\frac{\Delta V_P^t}{\Delta t})\mathbf{V}_{i,P}^t]\end{aligned} \tag{3.60}$$

If we define $\overline{\mathbf{NS}}_i^t$ as those terms in the source evaluated for time level t then

$$\boxed{\overline{\mathbf{NS}}_i^t \equiv (1-\theta)[(-\frac{\partial P}{\partial x_i}\Big|_P^{t} + \mathbf{NS}_{i,P}^t)\Delta V + \sum_{f=P\rightarrow nb} a_{i,f}^t\mathbf{V}_{i,nb}^t - (A_{i,P}^t - (\frac{1}{1-\theta}+\frac{1}{\theta})\rho\frac{\Delta V_P^t}{\Delta t})\mathbf{V}_{i,P}^t]} \tag{3.61}$$

giving the simplified expression for the discretized momentum equation source

$$\boxed{\mathbf{SU}_{i,P}^{t+\Delta t,n} \equiv \theta[-\frac{\partial P}{\partial x_i}\Big|_P^{t+\Delta t,n-1} + \mathbf{NS}_{i,P}^{t+\Delta t,n}]\Delta V_P^{t+\Delta t} + \overline{\mathbf{NS}}_i^t} \tag{3.62}$$

3.5.2 Treatment of Pressure Term

From §3.3.1 making the substitution for $A_{i,P}^{t+\Delta t}$ in the expression for Rhie and Chow pressure corrected velocity (3.63).

$$\begin{aligned}\overbrace{(\theta\frac{\partial \mathbf{P}}{\partial x_i}\frac{V_P^{t+\Delta t}}{\theta A_P^{t+\Delta t}})}^{+\ pres.\ interp.\ of\ stencil\ \Delta x}\Bigg|_e &= \overbrace{(\theta\frac{\partial \mathbf{P}}{\partial x_i}\frac{V_P^{t+\Delta t}}{\theta A_P^{t+\Delta t}})}^{+\ pres.\ interp.\ of\ stencil\ \Delta x}\Bigg|_e = \overbrace{\frac{\partial \mathbf{P}}{\partial x_i}d_{i,P}^{t+\Delta t}}^{+\ pres.\ interp.\ of\ stencil\ \Delta x}\Bigg|_e \approx \frac{\mathbf{P}_E - \mathbf{P}_P}{\Delta x}d_{i,P}^{t+\Delta t}\Bigg|_e, \\ \mathbf{V}_i\Big|_e &= (\mathbf{V}_{i,P} + \overbrace{(\frac{\partial \mathbf{P}}{\partial x_i}d_{i,P}^{t+\Delta t})}^{-\ pres.\ interp.\ of\ stencil\ 2\Delta x}\Bigg|_e - \overbrace{(\frac{\partial \mathbf{P}}{\partial x_i}d_{i,P}^{t+\Delta t})}^{+\ pres.\ interp.\ of\ stencil\ \Delta x}\Bigg|_e\end{aligned} \tag{3.63}$$

Thus, introduction of the θ time-stepping scheme has no effect of the Rhei & Chow pressure treatment provided d is calculated via A_P.

3.5.3 PISO Corrector Steps

In terms of the velocity correction we have from §3.4.2 and §3.4.1

Table 3.5: Definitions and values corresponding to first and second Piso pressure corrector step (3.52)

Step/term	α_e	α_w	α_P	β_P
First	$\frac{(\rho dA)_e}{(\Delta x)_{P\to E}}$	$\frac{(\rho dA)_w}{(\Delta x)_{P\to W}}$	$\sum_f \alpha_f$	$\sum_f \dot{m}_f^*$
Second	$\frac{(\rho dA)_e}{(\Delta x)_{P\to E}}$	$\frac{(\rho dA)_w}{(\Delta x)_{P\to W}}$	$\sum_f \alpha_f$	$\sum_f \dot{m}_f^{**} + \frac{1}{{}^\theta A_{i,P}} \sum_f \rho \vec{\Delta A} \cdot \sum_{f=P\to nb} {}^\theta a_{i,nb} \vec{\mathbf{V}}'_{i,nb}$

$$\boxed{\mathbf{V}'_{i,P} \approx \frac{{}^\theta \sum_{f=P\to nb} a_{i,f} \mathbf{V}'^{,t+\Delta t}_{i,nb}}{{}^\theta A_{i,P}} + \theta \frac{\Delta V_P}{{}^\theta A_{i,P}} \frac{\partial \mathbf{P}'^{,t+\Delta t}}{\partial x_i}\Big|_P = \frac{\sum_{f=P\to nb} {}^\theta a_{i,f} \mathbf{V}'^{,t+\Delta t}_{i,nb}}{{}^\theta A_{i,P}} + d_{i,P}^{t+\Delta t} \frac{\partial \mathbf{P}'^{,t+\Delta t}}{\partial x_i}\Big|_P} \tag{3.64}$$

yielding a first velocity or mass flux correction

$$\boxed{\dot{m}'_{f=P\to nb} \approx \vec{\Delta A}_f \cdot \vec{\mathbf{V}}'_f \rho_f, \quad \mathbf{V}'_{i,P}\Big|_f \approx (d_{i,P}^{t+\Delta t} \partial \mathbf{P}'^{,t+\Delta t}/\partial x_i)\Big|_f} \tag{3.65}$$

The resulting coefficients for the pressure correction equation are given in Table 3.5
Note the form is identical to that given in §3.4 except for the substitution of ${}^\theta A_P$a nd ${}^\theta a_{nb}$ in the place of A_P and a_{nb}. The second velocity correction is given by (3.66)

$$\boxed{\dot{m}''_{f=P\to nb} \approx \vec{\Delta A}_f \cdot \vec{\mathbf{V}}''_f \rho_f, \quad \mathbf{V}''_{i,P} \approx \frac{\sum_{f=P\to nb} {}^\theta a_{i,nb} \mathbf{V}'_{i,nb}}{{}^\theta A_{i,P}} + d_{i,P}^{t+\Delta t} \partial \mathbf{P}''/\partial x_i} \tag{3.66}$$

giving via continuity

$$\sum_f \dot{m}^{***} = \sum_i \sum_f \rho(\mathbf{V}_i^{**} + \mathbf{V}_i'')\Delta A_{i,f} = \sum_f \dot{m}_f^{**} + \sum_i \sum_f \frac{\partial \mathbf{P}''}{\partial x_i}_f (\rho d_p \Delta A_i)_f = 0 \tag{3.67}$$

the discretized second pressure correction equation

$$\boxed{\alpha_P \mathbf{P}''_P = \textstyle\sum_{f=P\to nb} \alpha_{nb} \mathbf{P}''_{nb} + \beta_P} \tag{3.68}$$

where the coefficients are again given in Table 3.5.

A diagram of the implementation of the θ time-stepping scheme in a general flow solver is shown in Figure 3.5 where we have used the formulation of the source term via (3.62).

3.6 Modification due to Sliding Deformable Mesh

The previous discussion §3.1 involving volume integration of the differential momentum (Navier-Stokes) and continuity equation (3.6) resulted in a temporal, convective and (in the case of momentum) integration of surface stresses over a CV. Simulation of rotating

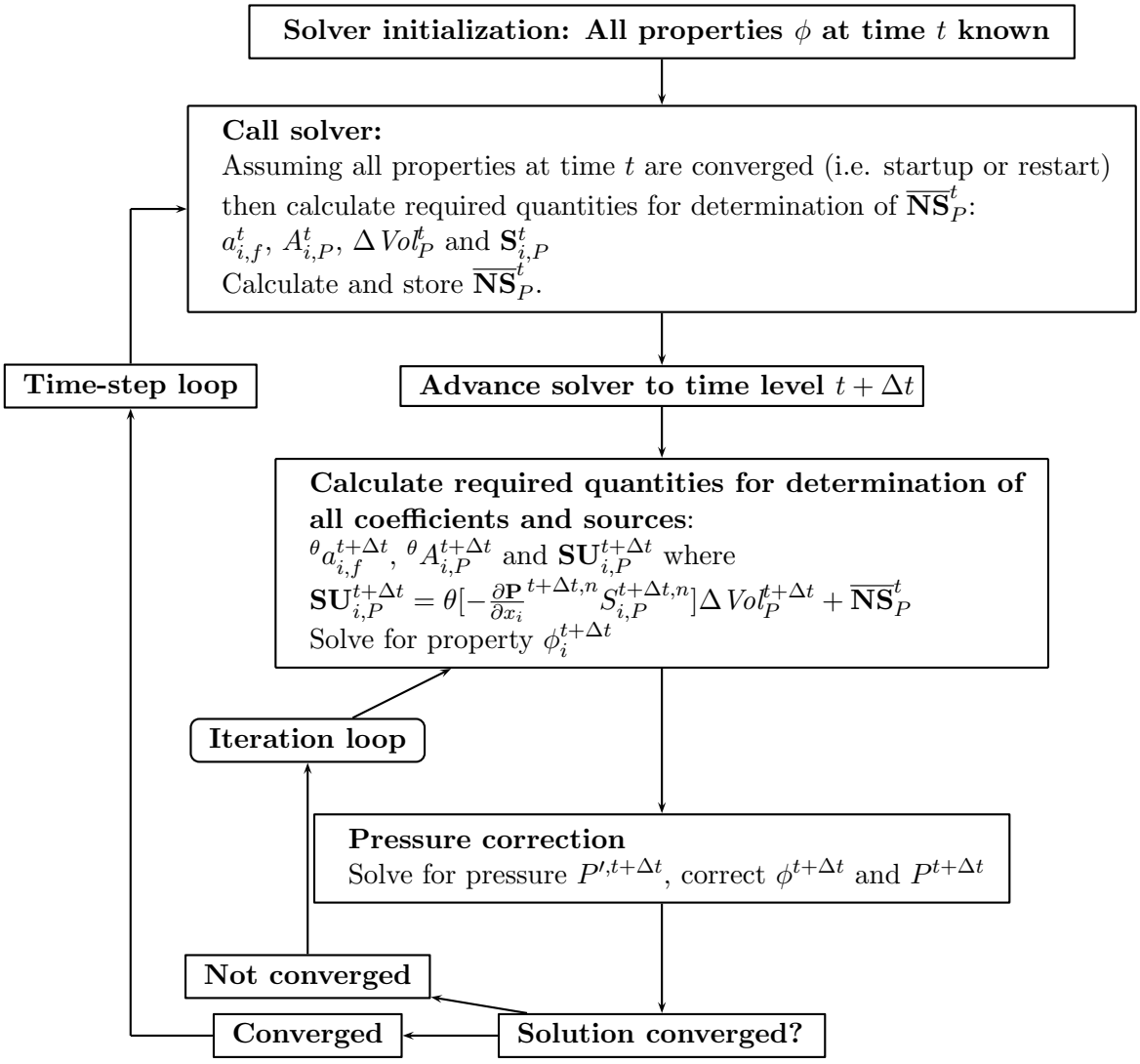

Figure 3.5: General implementation of the θ time-stepping scheme

machinery can be performed using a number of different strategies: Explicit boundary methods which either solve the fluid equations of motion (and continuity) or the stream-function given a combination of inflow, turbulent wall, symmetric jet, symmetry boundary condition such as Placek et al [3]; Pseudo-steady (fixed grid) inner-outer methods (solution to the rotating/stationary equations of motion); Sliding mesh (deformable and non-deformable interface) first performed by Tabor et al [4]; And finally, Chimera (overlapping) grids which utilize overlapping deformable grids (utilizing inter-grid property projection) as demonstrated by Takeda et al [5].

Given that a sliding deformable mesh is used to simulate the moving impeller in this study, (first developed by Luo et al [2]), with stationary outer tank geometry, the way in which the terms in the discretized equation are transformed in the case of a moving control volume must be explored. First, the surface stresses (not present in the continuity equation) coincide from the moving CV and the system of fixed mass as $\Delta t \to 0$. Thus, whether the CV is moving

or stationary, evaluation of the system surface stress are equal to the stresses evaluated on the CV surface (moving or otherwise). In addition, should a body force be present in the momentum conservation equation (e.g. due to buoyancy, etc), the mass enveloped by the CV will correspond to the mass on the system again as $\Delta t \rightarrow 0$. Thus, no changes to the **RHS** of the volume integrated N-S equation (second equation from top in 3.2) are required. With respect to the **LHS** of the N-S or continuity equation, the volume integrated temporal term is over a CV, which occupies the same spacial location for a moving or stationary frame as $\Delta t \rightarrow 0$. Thus, the temporal term is unaffected by CV motion. However, the remaining (convective) term is a surface integral involving a total surface momentum flux (the product of a differential mass flux $\rho\vec{V} \cdot d\vec{A}$ and specific momentum $\phi = V_i$). Given a moving CV this surface flux must be modified via the CV velocity $\vec{U}_{cv}$ yielding a modified surface integral representing the convective term

$$\int_{\Delta S} \phi[\rho(\vec{V} - \vec{U}_{cv})] \cdot d\vec{S} \tag{3.69}$$

In terms of coefficients of the discretized equation, the result of this is simply a modification of the total mass-flux at the CV faces according to

$$\dot{m}_f \equiv (\rho\vec{V} \cdot \delta\vec{A})_f \longrightarrow (\rho(\vec{V} - \vec{U}_{cv}) \cdot \Delta\vec{A})_f \tag{3.70}$$

Finally, the boundary conditions within the moving frame must be modified for wall surfaces and a wall velocity imposed equal to the local CV velocity at the wall face. The remaining quantities in the system of equations remaining unchanged.[2]

In terms of operation, the sliding deformable mesh methodology utilized a stationary and moving mesh whose interface is deformed up to some limit whereupon connectivity is broken between the meshes, the deformation is relaxed and connectivity is re-established. Figure 3.6 illustrates this process over one cycle (3-time steps).

3.7 Implementation of a Parallel Computational Capability

Given the prohibition in terms of grid size and simulation time (or problem extent) imposed by the reliance on a single processor solver, extension of the newly implemented (θ-scheme) solver to multiple processors was undertaken. To demonstrate the concepts involved, a geographical surface over which a discretized equation is to be solved, subject to boundary conditions, is shown in Figure 3.7. Specifically, an assumed 2-D flow domain with global fluid cells numbering from 1 to NC is placed in a single process domain as shown on the left. This is in contrast to the case on the right (of Figure 3.7) which shows the fluid domain sub-divided in half between two processors 0 and 1. In this case the number of fluid cells in each process domain are numbered from 1 to $NC_{local}^{proc.\#}$ with a physical interface (line)

[2] See §2.2.1 for a more general theoretical treatment.

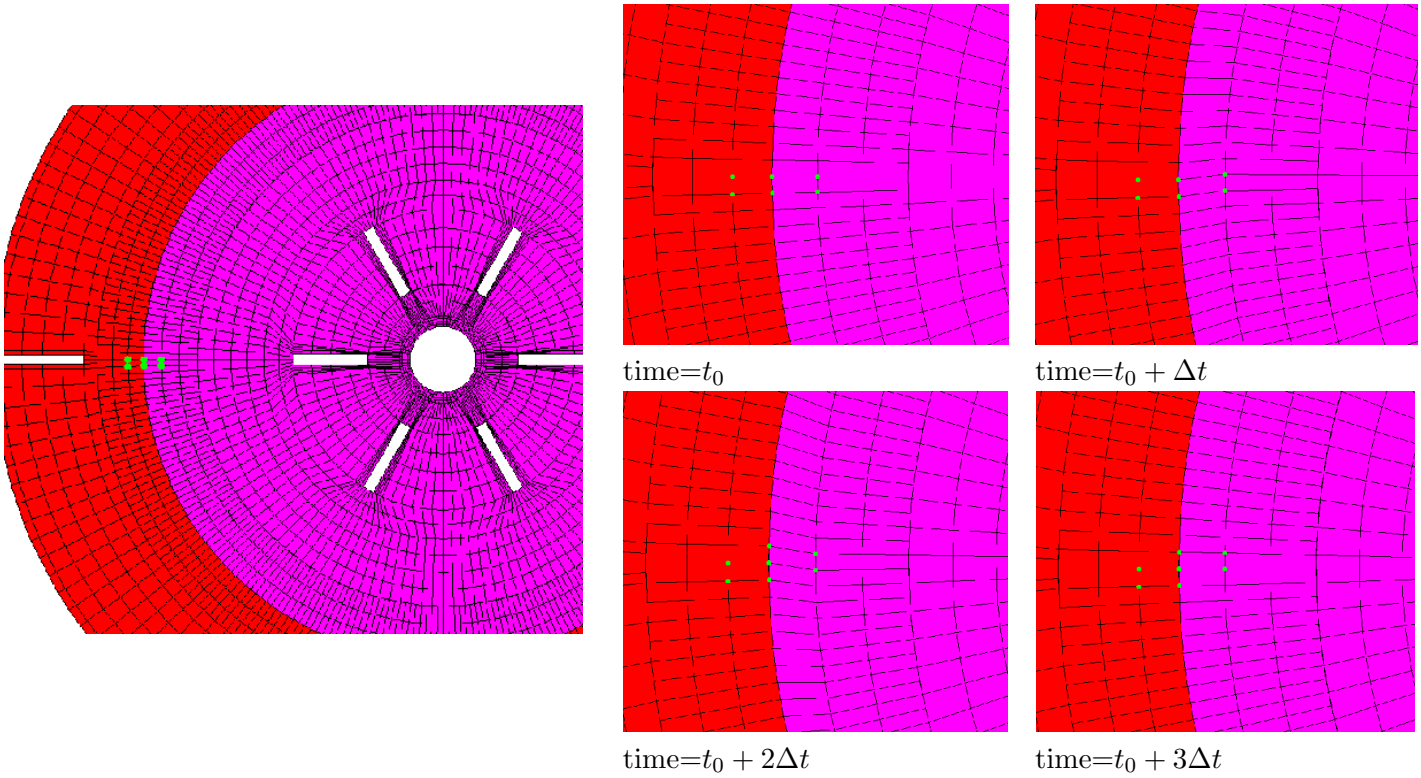

Figure 3.6: Illustration of sliding mesh operation over cycle of 3-time steps. Vertices at two interface grid cells highlighted to enhance clarity of mesh movement.

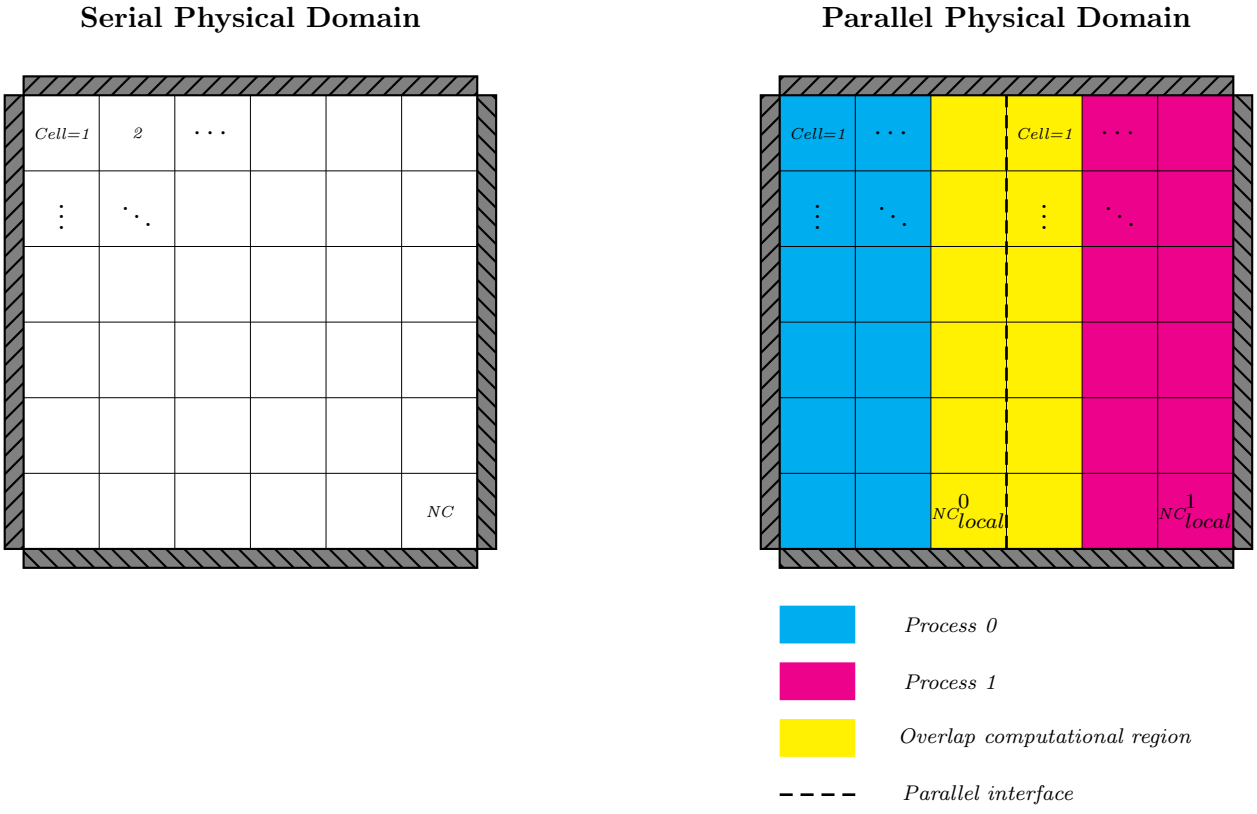

Figure 3.7: Comparison of serial and parallel physical domain

separating the domains. This interface separating the physical domains will, henceforth, be referred to as a *parallel interface*. Note from Figure 3.7, there exists an overlap region which includes cells immediately neighboring the parallel interface.[3]

Thus, the strategy is to treat each process domain as a separate (physical) fluid region containing *live* (fluid) cells, to which, are attached a layer of storage or *inert* (fluid) cells affixed at the parallel interface. These inert cells act as storage locations for flow properties and geometric parameters used to solve the discretized equation over the *local* process region. If communication is established between the live cells of one process and the corresponding inert cells of a neighboring process (sharing a parallel interface), then the discretized equation can be solved iteratively over the entire physical domain. To be more precise, NC^i_{local} is the number of *live* (i.e. to be locally solved) fluid cells residing in process i and NC^i_{total} is the total number of cells (locally) which includes live (NC^i_{local}), boundary (NC^i_{bc}) and parallel interface inert cells ($NC^i_{parallel\,inert}$). In terms of Figure 3.7 we see that process 1 has a total number of cells (live, inert and boundary) of $NC^1_{total} = NC^1_{local} + NC^1_{parallel\,inert} + NC^1_{bc}$ where all inert cells have cell number great than $NC^{proc.\#}_{local}$.[4] The same is true for process 0. Thus, the discretized equation (3.19) applies for live cells $1 \rightarrow NC^{proc.\#}_{local}$ for each process where, if cell P lies adjacent to a parallel interface, the contribution from the neighboring (inert) cell is known via a previous time-step or iteration.

Note that the motivation for attaching *inert* cells to a local domain as opposed to the application of a parallel boundary condition on a face, is that a pre-existing CFD algorithm would require minimal modification since required quantities for cells near an inter-process (parallel) interface such as cell volumes, weight-factors, face normals, etc can be calculated and stored in a natural and economical way. Thus, this discussion suggests, in general, the implementation of a parallel solution algorithm as shown in Algorithm 1

Finally, Figure 3.8 makes no reference as to how a global solution for $\mathbf{\Phi}$ is produced. The method used for producing a global solution via (parallel) local iterations will be discussed in §3.9.2.

3.8 Solution to the Algebraic System

3.8.1 Under-relaxation

A solution to the discretized momentum equation (3.59) for iteration n is found via iterative methods. Specifically, the system given by (3.59) which expresses an algebraic equation for each unknown $\mathbf{\Phi}_P$ can be solved to yield a solution based on coefficients calculated by properties at iteration $n-1$. However, to prevent *numerical overshoot* of the solution $\mathbf{\Phi}_P$

[3]Note that this assumes a required overlap region of a *single* layer of cells. For 1^{st} order up-wind and 2^{nd} order central differences this is adequate. However, use of higher order spatial discretization schemes will required additional layers of cells. Specifically, for the 4^{rth} order central difference scheme a set of parallel storage cells two cells thick is required.

[4]Given the indexing system utilized, we could define a new quantity representing the number of finite volume cells (*live or inert*) in the process domain: $NC_{domain} = NC_{local} + NC_{parallel\,inert}$. Thus, calculations involving geometric parameters and setting of coefficients could be sub-divided into two distinct groups:$1 \rightarrow NC_{local}, NC_{local}+1 \rightarrow NC_{domain}$.

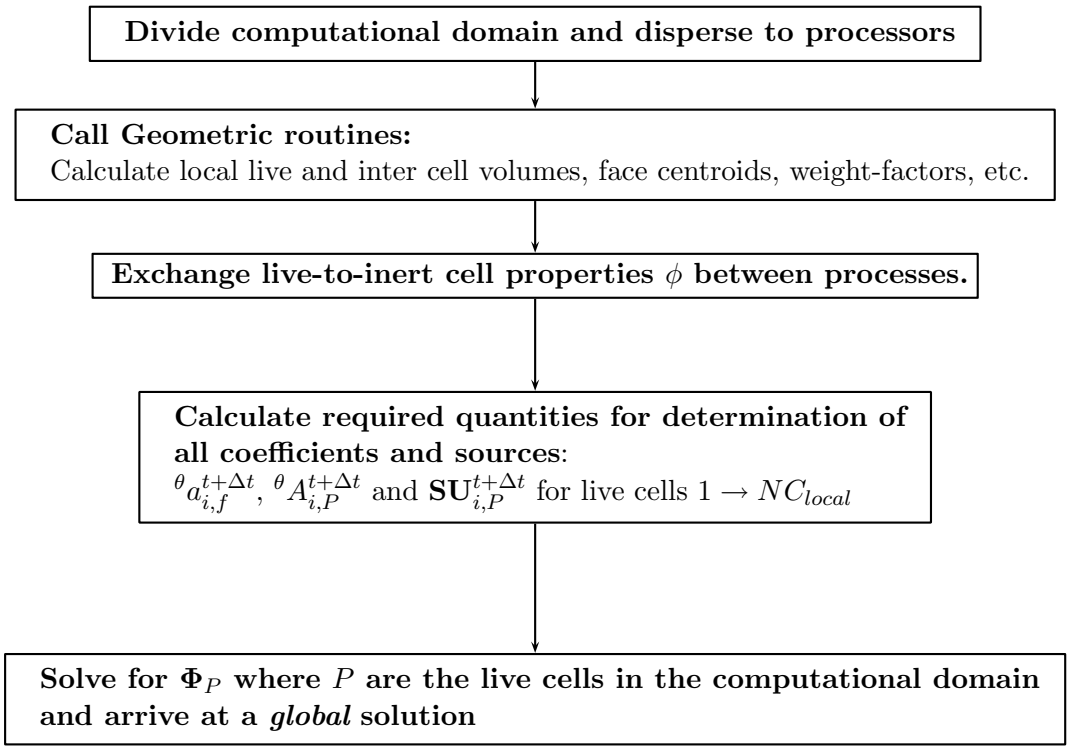

Figure 3.8: General implementation of the parallel solver

a weighting or *relaxation* factor is introduced. Specifically, if a solution is found to the discretized equation yielding a solution $\mathbf{\Phi}_P^{new}$, then a new *relaxed* value for $\mathbf{\Phi}_P^n$ is given by

$$\mathbf{\Phi}_P^n \equiv \mathbf{\Phi}_P^{n-1} + \sigma_{\mathbf{\Phi}}(\phi_P^{new} - \mathbf{\Phi}_P^{n-1}) \Longrightarrow \mathbf{\Phi}_P^{new} = \frac{\mathbf{\Phi}_P^n - \mathbf{\Phi}_P^{n-1}}{\sigma_{\mathbf{\Phi}}} + \mathbf{\Phi}_P^{n-1} \tag{3.71}$$

where $\sigma_{\mathbf{\Phi}}$ is the relaxation factor for property $\mathbf{\Phi}$. The expression for $\mathbf{\Phi}_P^{new}$ (which is just the solution satisfying the discretized equation for the n-th iteration (3.59)) is simply

$$\mathbf{V}_{i,P}^{t+\Delta t,new} = \frac{\sum_{f=P\rightarrow nb} {}^{\theta}a_{i,f}^{t+\Delta t,n-1}\mathbf{V}_{i,nb}^{t+\Delta t,n} + \mathbf{SU}_{i,P}^{t+\Delta t,n}}{{}^{\theta}A_{i,P}^{t+\Delta t,n-1}} \tag{3.72}$$

Substituting for $\mathbf{V}_{i,P}^{t+\Delta t,new}$ in (3.71) in the case of $\mathbf{\Phi} = \mathbf{V}_{i,P}^{t+\Delta t,n}$ yields

$$\frac{\sum_{f=P\rightarrow nb}{}^{\theta}a_{i,nb}^{t+\Delta t,n-1}\mathbf{V}_{i,nb}^{t+\Delta t,n}+\mathbf{SU}_{i,P}^{t+\Delta t,n}}{{}^{\theta}A_{i,P}^{t+\Delta t,n-1}}=\frac{\mathbf{V}_{i,P}^{t+\Delta t,n}-\mathbf{V}_{i,P}^{t+\Delta t,n-1}}{\sigma_{\mathbf{V}_i}}+\mathbf{V}_{i,P}^{t+\Delta t,n-1}\Longrightarrow$$

$$\sum_{f=P\rightarrow nb}{}^{\theta}a_{i,f}^{t+\Delta t,n-1}\mathbf{V}_{i,nb}^{t+\Delta t,n}+\mathbf{SU}_{i,P}^{t+\Delta t,n}=\frac{{}^{\theta}A_{i,P}^{t+\Delta t,n-1}}{\sigma_{\mathbf{V}_i}}(\mathbf{V}_{i,P}^{t+\Delta t,n}-\mathbf{V}_{i,P}^{t+\Delta t,n-1})+$$

$$\mathbf{V}_{i,P}^{t+\Delta t,n-1}\frac{\sigma_{\mathbf{V}_i}{}^{\theta}A_{i,P}^{t+\Delta t,n-1}}{\sigma_{\mathbf{V}_i}}=\frac{{}^{\theta}A_{i,P}^{t+\Delta t,n-1}}{\sigma_{\mathbf{V}_i}}(\mathbf{V}_{i,P}^{t+\Delta t,n}-(1-\sigma_{\mathbf{V}_i})\mathbf{V}_{i,P}^{t+\Delta t,n-1})$$

(3.73)

or the discretized equation for the *relaxed* property $\mathbf{V}_{i,P}^{t+\Delta t,n}$

$$\boxed{{}^{\theta^*}A_{i,P}^{t+\Delta t,n-1}\mathbf{V}_{i,P}^{t+\Delta t,n}=\sum_{f=P\rightarrow nb}{}^{\theta}a_{i,f}^{t+\Delta t,n-1}\mathbf{V}_{i,nb}^{t+\Delta t,n}+{}^{*}\mathbf{SU}_{i,P}^{t+\Delta t,n}}\tag{3.74}$$

where

$${}^{\theta^*}A_{i,P}^{t+\Delta t,n-1}\equiv\frac{{}^{\theta}A_{i,P}^{t+\Delta t,n-1}}{\sigma_{\mathbf{V}_i}}$$

$${}^{*}\mathbf{SU}_{i,P}^{t+\Delta t,n}\equiv\mathbf{SU}_{i,P}^{t+\Delta t,n}+{}^{\theta*}A_{i,P}^{t+\Delta t,n-1}(1-\sigma_{\mathbf{V}_i})\mathbf{V}_{i,P}^{t+\Delta t,n-1}\tag{3.75}$$

It should be noted that in the limit as $\mathbf{V}_{i,P}^{t+\Delta t,n-1}\Rightarrow\mathbf{V}_{i,P}^{t+\Delta t,n}$ then (3.74) reduces to (3.59) as expected. Similarly, for the pressure correction equation, the relaxation can be affected by replacing ${}^{\theta}d$ with ${}^{\theta*}d\equiv{}^{\theta}d/\sigma_P$.[5]

3.9 The Solver

3.9.1 The System of Equations

For momentum, the algebraic systems as specified by (3.74) in its final form can be expressed via the matrix equation

[5]In preparation for the next section §3.9 it should be pointed out that the *relaxation procedure* as specified by (3.75) has the effect of increasing the magnitude of A_P relative to a_{nb}. This strengthening of the present cell coefficient thus serves to increase the *diagonal-dominance* of the system of equations (see (3.76)).

$$\begin{bmatrix} A_{1,1} & A_{1,2} & \vdots & \vdots & \vdots & \vdots & \vdots & A_{1,NC} \\ A_{2,1} & A_{2,2} & \ddots & \ddots & \vdots & \vdots & \vdots & \vdots \\ \vdots & A_{1,2} & \ddots & \ddots & \ddots & \vdots & \vdots & \vdots \\ \vdots & \ddots & \ddots & \ddots & \ddots & \ddots & \vdots & \vdots \\ \vdots & \vdots & \ddots & \ddots & \ddots & \ddots & \ddots & \vdots \\ \vdots & \vdots & \vdots & \ddots & \ddots & \ddots & \ddots & \vdots \\ \vdots & \vdots & \vdots & \vdots & \ddots & \ddots & \ddots & A_{NC-1,NC} \\ A_{NC,1} & \vdots & \vdots & \vdots & \vdots & \vdots & \vdots & A_{NC,NC} \end{bmatrix} \begin{bmatrix} \mathbf{\Phi}_1 \\ \mathbf{\Phi}_2 \\ \vdots \\ \vdots \\ \vdots \\ \vdots \\ \mathbf{\Phi}_{NC-1} \\ \mathbf{\Phi}_{NC} \end{bmatrix} = \begin{bmatrix} {}^*\mathbf{SU}_1 \\ {}^*\mathbf{SU}_2 \\ \vdots \\ \vdots \\ \vdots \\ \vdots \\ {}^*\mathbf{SU}_{NC-1} \\ {}^*\mathbf{SU}_{NC} \end{bmatrix} \tag{3.76}$$

where the first array is the coefficient matrix whose elements $A(,)$ are calculated via A_P or a_{nb}. Upon inspection of (3.74) is should be apparent that most of these elements are zero, thus the $[A]$ is termed a *sparse matrix* whose elements are, due to the discretization and relaxation, *diagonally dominant*. Furthermore, the matrix $[A]$, for the case of structured grids would be (for a central difference scheme) tri-diagonal in structure thus allowing for use of special (non-iterative) matrix inversion algorithms for tri-diagonal systems (e.g. Thompson Algorithm or Gaussian elimination). These non-iterative methods all rely on various matrix operations such as row reduction and substitution resulting in a system whose matrix elements are composed of an upper matrix and diagonal (all other elements identically equation to zero). Such systems can thus be solved.

The flow solver used in this work is, however, an unstructured non-orthogonal code and thus $[A]$, while being sparse, is not, in general tri-diagonal or banded. Hence, other non-direct (i.e. iterative) methods for solving the system $[A]\vec{\mathbf{\Phi}} = \mathbf{S}\vec{\mathbf{U}}$ must be used.

3.9.2 Parallel Conjugate Gradient Solver

Given the desire to solve the *global solution vector* $\vec{\mathbf{\Phi}}$ *via iterative processes conducted on local process domains*, the conjugate-gradient method must be modified or *parallelized* to take into account solution/solver information for inert cells along an inter-process boundary. Specifically, §B.3.1 gives a general treatment of the serial solver used. Shown as Algorithm 1 is a *parallelized version* of the serial Conjugate Gradient Solver as given in Algorithm 5 §B.3.1 (where the nomenclature used in described in detail).

3.10 Calculation of Turbulent Transport Terms

The material presented previously dealt with determining the solution to the cell averaged mass and momentum conservation relationships, i.e. the volume averaged continuity and Navier-Stokes equations. Additional conservation relationships can be treated in a similar fashion including the determination of the individual terms in the turbulent kinetic energy equation (i.e. conservation of turbulent kinetic energy) restated here from §2.5

Algorithm 1 Preconditioned Conjugate Gradient Algorithm: Local and Parallel Operations

$m = 0$	
$\vec{\mathbf{\Phi}}^m = \vec{\mathbf{\Phi}}^0$	**Local**:Guess initial solution for system (e.g. $\vec{\mathbf{\Phi}} = [\vec{0}]$)
$\vec{\mathbf{R}}^m = -[\mathbf{A}]\vec{\mathbf{\Phi}}^m + \mathbf{S}\vec{\mathbf{U}}$	**Local**: Calculate residual of system.
Parallel Exchange $\vec{\mathbf{R}}^m$	**Parallel**: Exchange of residual vector
$\hat{\mathbf{R}}^m_{local} = \sum_{i=1}^{NC_{local}} \mathbf{R}_i$	**Local**: Sum residuals
Parallel Sum $\hat{\mathbf{R}}^m_{local} \rightarrow \hat{\mathbf{R}}^m_{global}$	**Parallel**: Sum local residuals
If $\frac{\hat{\mathbf{R}}^m_{global}}{\text{normalization constant}} <$ User Def. Tolerance	**Local**: Return Check global residual tolerance.
$[\mathbf{M}]\vec{\mathbf{Z}}^m = \vec{\mathbf{R}}^m$, $\vec{\mathbf{\Pi}}^m = \vec{\mathbf{Z}}^m$	**Local**: Solve for initial search vector via the Steepest Descent Criterion.
Parallel Exchange $\vec{\mathbf{\Pi}}^m$	**Parallel**: Exchange of auxiliary vector
Begin iteration loop:	
$m = m + 1$	**Local**:
$\epsilon^m_{local} = \vec{\mathbf{R}}^m \cdot \vec{\mathbf{Z}}^m$	**Local**:
$\eta^m_{local} = \vec{\mathbf{\Pi}}^m \cdot ([\mathbf{A}]\vec{\mathbf{\Pi}}^m)$	**Local**:
Parallel Sum $\epsilon^m_{local}, \eta^m_{local} \rightarrow \epsilon^m_{global}, \eta^m_{global}$	**Parallel**: Sum local dot-products
$\alpha^m_{global} = \frac{\epsilon^m_{global}}{\eta^m_{global}}$	**Local**: Calculate global scaling factor using Greatest Descent (see (B.21)).
$\vec{\mathbf{R}}^{m+1} = \vec{\mathbf{R}}^m - \alpha^m_{global}([\mathbf{A}])(\vec{\mathbf{\Pi}}^m)$	**Local**: Update residual vector $\vec{\mathbf{R}}$
Parallel Exchange $\vec{\mathbf{R}}^{m+1}$	**Parallel**: Exchange of residual vector
$\vec{\mathbf{\Phi}}^{m+1} = \vec{\mathbf{\Phi}}^m + \alpha^m \vec{\mathbf{\Phi}}^m$	**Local**: Update solution vector $\vec{\mathbf{\Phi}}$
$\hat{\mathbf{R}}^{m+1}_{local} = \sum_{i=1}^{NC_{local}} \mathbf{R}_i$	**Local**: Sum residuals
Parallel Sum $\hat{\mathbf{R}}^{m+1}_{local} \rightarrow \hat{\mathbf{R}}^{m+1}_{global}$	**Parallel**: Sum local residuals
If $\frac{\hat{\mathbf{R}}^{m+1}_{global}}{\text{normalization constant}} <$ User Def. Tolerance Then	**Local**: Check global residual tolerance
Parallel Exchange $\vec{\mathbf{\Phi}}^{m+1}$	**Parallel**: Exchange of property vector
Return	Exit solver
Endif	
$\vec{\mathbf{Z}}^{m+1} = [\mathbf{M}]^{-1}\vec{\mathbf{R}}^{m+1}$	**Local**: Solve for new auxiliary vector $\vec{\mathbf{Z}}$.
$\epsilon^{m+1} = \vec{\mathbf{R}}^{m+1} \cdot \vec{\mathbf{Z}}^{m+1}$	**Local**:
Parallel Sum $\epsilon^{m+1}_{local} \rightarrow \epsilon^m_{global}$	**Parallel**: Sum local dot-products
$\beta^{m+1} = \frac{\epsilon^{m+1}}{\epsilon^m}$	**Local**: Calc. scaling factor according to conj. requirement (see (B.24)).
$\vec{\mathbf{\Pi}}^{m+1} = \vec{\mathbf{Z}}^{m+1} + \beta^m(\vec{\mathbf{\Pi}}^m)$	**Local**: Update modified search vector $\vec{\mathbf{\Pi}}$
Parallel Exchange $\vec{\mathbf{\Pi}}^{m+1}$	**Parallel**: Exchange of auxiliary vector
Continue Loop	

$$\overbrace{\frac{\partial(\overline{U}_i\overline{k'})}{\partial x_i}}^{\text{Conv. } \overline{k'} \text{ Via Mean Flow}} + \overbrace{\frac{\partial(\overline{u'_i k'})}{\partial x_i}}^{\text{Conv. } \overline{k'} \text{ Via Turbulence}} = - \overbrace{\frac{\partial}{\partial x_i}(\frac{\overline{u'_i P'}}{\rho})}^{\text{Pressure Work/Diff. of } \overline{k'} \text{ via Turb. Motion}}$$
$$- \overbrace{(\overline{u'_i u'_j})\frac{\partial \overline{U}_i}{\partial x_j}}^{\text{Prod. of } \overline{k'} \text{ Via Mean Flow}} + \overbrace{\nu\frac{\partial}{\partial x_i}(\overline{u'_j(\frac{\partial u'_i}{\partial x_j} + \frac{\partial u'_j}{\partial x_i})})}^{\text{Viscous Work/Diff. of } \overline{k'} \text{ Via Turb. Motion}} - \overbrace{\overline{\epsilon'}}^{\text{Viscous Dissipation of } \overline{k'}} \quad (3.77)$$

Pursuant to determining the individual terms in the turbulent transport equation we restate the previous (which utilized Einstein-notation) in terms of the Del-operator $\vec{\nabla}$ giving

$$\overbrace{\vec{\nabla}\cdot(\overline{\vec{U}}\overline{k'})}^{Conv.\ \overline{k'}\ Via\ Mean\ Flow} + \overbrace{\vec{\nabla}\cdot(\overline{\vec{u'}k'})}^{Conv.\ \overline{k'}\ Via\ Turbulence} = - \overbrace{\frac{1}{\rho}\vec{\nabla}\cdot(\overline{\vec{u'}P'})}^{Pressure\ Work/Diff.\ of\ \overline{k'}\ via\ Turb.\ Motion} -$$
$$\overbrace{[\vec{\nabla}\cdot(\overline{\vec{u'}u'_i}\overline{U_i}) - \overline{U_i}\vec{\nabla}\cdot(\overline{\vec{u'}u'_i})]}^{Prod.\ of\ \overline{k'}\ Via\ Mean\ Flow} + \overbrace{\nu\vec{\nabla}\cdot\vec{\Psi}}^{Viscous\ Work/Diff.\ of\ \overline{k'}\ Via\ Turb.\ Motion} - \overbrace{\overline{\epsilon'}}^{Viscous\ Dissipation\ of\ \overline{k'}} \tag{3.78}$$

where we have introduced the vector $\vec{\Psi}$ defined as follows

$$\boxed{\vec{\Psi} \equiv \begin{bmatrix} \sum_{j=1}^{3} \overline{u'_j(\frac{\partial u'_1}{\partial x_j} + \frac{\partial u'_j}{\partial x_1})} \\ \sum_{j=1}^{3} \overline{u'_j(\frac{\partial u'_2}{\partial x_j} + \frac{\partial u'_j}{\partial x_2})} \\ \sum_{j=1}^{3} \overline{u'_j(\frac{\partial u'_3}{\partial x_j} + \frac{\partial u'_j}{\partial x_3})} \end{bmatrix}} \tag{3.79}$$

Averaging (3.78) over the cell volume (i.e. $1/\Delta Vol.\int_{\Delta V}[(3.78)]dVol.$) and applying the divergence theorem (3.3) yields

$$\frac{1}{\Delta V}[\overbrace{\int_{\Delta S}(\overline{\vec{U}}\overline{k'})\cdot d\vec{S}}^{Conv.\ \overline{k'}\ Via\ Mean\ Flow} + \overbrace{\int_{\Delta S}(\overline{\vec{u'}k'})\cdot d\vec{S}}^{Conv.\ \overline{k'}\ Via\ Turbulence} = \frac{1}{\Delta V}[- \overbrace{\frac{1}{\rho}\int_{\Delta S}(\overline{\vec{u'}P'})\cdot d\vec{S}}^{Pressure\ Work/Diff.\ of\ \overline{k'}\ via\ Turb.\ Motion} -$$
$$\overbrace{[\int_{\Delta S}(\overline{\vec{u'}u'_i}\overline{U_i})\cdot d\vec{S} - \overline{U_i}\int_{\Delta S}(\overline{\vec{u'}u'_i})\cdot d\vec{S}]}^{Prod.\ of\ \overline{k'}\ Via\ Mean\ Flow} + \overbrace{\nu\int_{\Delta S}\vec{\Psi}\cdot d\vec{S}}^{Visc.\ Work/Diff.\ of\ \overline{k'}\ Via\ Turb.\ Motion}] - \overbrace{\overline{\epsilon'}}^{Visc.\ Diss.\ of\ \overline{k'}} \tag{3.80}$$

where the double index on the production terms imply summation over i (Einstein-notation). Finally, it should be noted that care must be taken given that a sliding deformable mesh is used for the simulation. Specifically, integrals of the form $\int_{\Delta S}\rho\vec{u}\phi\cdot d\vec{S}$ represent a volume flux of the intensive property ϕ. In the context of the sliding mesh (i.e. moving control volume ΔV), the flux represents *relative or moving frame flux*. Thus for clarity, vector quantities with origin on the convective $(D()/Dt)$ or LHS-side of the transport equation must be calculated in a frame relative sense and are denoted by an $*$ yielding a revised volume averaged turbulent kinetic energy transport equation

$$\frac{1}{\Delta V}[\overbrace{\int_{\Delta S}(\overline{\vec{U}^*}\overline{k'})\cdot d\vec{S}}^{Conv.\ \overline{k'}\ Via\ Mean\ Flow} + \overbrace{\int_{\Delta S}(\overline{u'^*k'})\cdot d\vec{S}}^{Conv.\ \overline{k'}\ Via\ Turbulence}] = \frac{1}{\Delta V}[- \overbrace{\frac{1}{\rho}\int_{\Delta S}(\overline{\vec{u'}P'})\cdot d\vec{S}}^{Pressure\ Work/Diff.\ of\ \overline{k'}\ via\ Turb.\ Motion} -$$
$$\overbrace{[\int_{\Delta S}(\overline{u'^*u'_i}\overline{U_i})\cdot d\vec{S} - \overline{U_i}\int_{\Delta S}(\overline{u'^*u'_i})\cdot d\vec{S}]}^{Prod.\ of\ \overline{k'}\ Via\ Mean\ Flow} + \overbrace{\nu\int_{\Delta S}\vec{\Psi}\cdot d\vec{S}}^{Visc.\ Work/Diff.\ of\ \overline{k'}\ Via\ Turb.\ Motion}] - \overbrace{\overline{\epsilon'}}^{Visc.\ Diss.\ of\ \overline{k'}} \tag{3.81}$$

Hence, as indicated in (3.81) only the turbulent, mean-flow convective and generation terms are to be evaluated in terms of a relative flux.[6]

Finally, it is of interest to determine the form of the transport equation in the restricted case of constant, or approximately constant, relative motion in a given direction. Specifically, in the case of steady control volume motion $\overline{\vec{u'^*}} = \overline{\vec{u'}} - \vec{V}_{CV}$ we have, for any generic perturbation property ϕ' (with vanishing averaged value), the following

$$\overline{\vec{u'^*}\phi'} = \overline{(\vec{u'} - \vec{V}_{CV})\phi'} = \overline{\vec{u'}\phi'} - \overline{\vec{V}_{CV}\phi'} = \overline{\vec{u'}\phi'} \tag{3.86}$$

Thus, (3.81) reduces in the case of constant mesh motion to

[6]The previous can be demonstrated by noting that any transport equation (differential or bulk flow) can be re-cast via the Reynold's Transport Equation for the extensive property β as

$$\frac{D\beta}{Dt}|_{system} = \frac{\partial}{\partial t}\int_{Vol}(\rho b)dVol|_{CV} + \int_{Sur}(\rho b)\vec{V}^* \cdot d\vec{S}|_{CV} \tag{3.82}$$

where the control volume and system (of fixed mass) occupy (in an instantaneous sense) the same space. Hence, the LHS of (3.82) can be calculated with respect to the system of fixed mass moving through the control volume while the RHS includes a control volume surface flux of the property β, or $\int_{Sur}(\rho b)\vec{V}^* \cdot d\vec{S}|_{CV}$ where $\vec{V}^*$ is the system (or fluid) velocity relative to the control volume (moving or otherwise). Thus, any resulting terms with origin in the convective property flux integral $\int_{Sur}(\rho b)\vec{V}^* \cdot d\vec{S}|_{CV}$ must be calculated using the frame relative flux. Therefore, with respect to the turbulent kinetic energy transport equation (3.80), the surface pressure and viscous force induced power terms are calculated in the system frame (absolute velocities used) while the turbulent, mean-flow convective and generation terms (all of which originate with Dk/Dt or LHS of the perturbation velocity weighted Navier-Stokes equations (see §2.5)) are calculated via the control volume relative flux (velocity). To illustrate the previous development let us apply (3.82) to the conservation of energy or $\phi = e$ for a finite control volume.

$$\dot{Q} - \dot{W} = \frac{D\beta}{Dt}|_{system} = \frac{\partial}{\partial t}\int_{Vol}(\rho e)dVol|_{CV} + \int_{Sur}(\rho e)\vec{V}^* \cdot d\vec{S}|_{CV} \tag{3.83}$$

where the work interactions include pressure, viscous, electric or shaft work on the fixed mass system. Noting that pressure power on the fixed mass system is $\int_{Sur}(\rho(Pv))\vec{V} \cdot d\vec{S}|_{CV}$ we can can rewrite the absolute velocity at a face $\vec{V}$ via the transformation $\vec{V} = \vec{V}^* + \vec{w}$ where $\vec{w}$ and (again) $\vec{V}^*$ are the face velocity and flow relative velocity at the face. Substitution of this transformation into the fixed mass pressure power gives

$$\overbrace{\int_{Sur}(\rho(Pv))\vec{V} \cdot d\vec{S}|_{CV}}^{\textit{Pressure power on fixed mass system}} = \overbrace{\int_{Sur}(\rho(Pv))\vec{V}^* \cdot d\vec{S}|_{CV}}^{\textit{Relative pressure power on control volume}} + \overbrace{\int_{Sur}(\rho(Pv))\vec{w} \cdot d\vec{S}|_{CV}}^{\textit{Pressure power due to CV deformation (boundary work)}} \tag{3.84}$$

Substitution of the transformed expression for pressure (or flow) power (3.84) into the energy conservation equation (3.83) yields

$$\dot{Q} - \tilde{\dot{W}} = \frac{\partial}{\partial t}\int_{Vol}(\rho e)dVol|_{CV} + \int_{Sur}(\rho(Pv + u + ke + pe))\vec{V}^* \cdot d\vec{S}|_{CV} = \frac{\partial}{\partial t}\int_{Vol}(\rho e)dVol|_{CV} + \int_{Sur}(\rho(h + ke + pe))\vec{V}^* \cdot d\vec{S}|_{CV} \tag{3.85}$$

where $\tilde{\dot{W}}$ now *includes electric, shaft and control volume boundary power, but explicitly excludes relative pressure flow power.*

$$\frac{1}{\Delta V}[\overbrace{\int_{\Delta S}(\overrightarrow{\overline{U}^{*}}\overline{k'})\cdot\vec{dS}}^{Conv.\ \overline{k'}\ Via\ Mean\ Flow} + \overbrace{\int_{\Delta S}(\overrightarrow{\overline{u'^{*}k'}})\cdot\vec{dS}}^{Conv.\ \overline{k'}\ Via\ Turbulence}] = \frac{1}{\Delta V}[-\overbrace{\frac{1}{\rho}\int_{\Delta S}(\overrightarrow{\overline{u'P'}})\cdot\vec{dS}}^{Pressure\ Work/Diff.\ of\ \overline{k'}\ via\ Turb.\ Motion} - \overbrace{[\int_{\Delta S}(\overrightarrow{\overline{u'u_i'}}\overline{U_i})\cdot\vec{dS} - \overline{U_i}\int_{\Delta S}(\overrightarrow{\overline{u'u_i'}})\cdot\vec{dS}]}^{Prod.\ of\ \overline{k'}\ Via\ Mean\ Flow} + \overbrace{\nu\int_{\Delta S}\vec{\Psi}\cdot\vec{dS}}^{Visc.\ Work/Diff.\ of\ \overline{k'}\ Via\ Turb.\ Motion}] - \overbrace{\overline{\epsilon'}}^{Visc.\ Diss.\ of\ \overline{k'}} \tag{3.87}$$

where only the averaged convective terms (turbulent and mean-flow induced) require calculations based on mesh relative motion convective flux.

References

[1] B. Leonard. A stable and accurate convective modelling proceedure based on quadratic upstream interpolation. *Computer Methods in Applied Mechanics and Engineering*, 1979.

[2] J. Luo, A. Gosman, R. Issa, J. Middleton, and M. Fitzgerald. Full flow computation of mixing in baffled stirred vessels. *IChemE*, 1993.

[3] J. Placek, L. Tavlarodes, G. Smith, and I. Fort. Turbulent flow in a stirred tanks, ii: A two-scale model of turbulence. *A.I.Ch.E.*, 1986.

[4] G. Tabor, A. Gosman, and R. Issa. Numerical simulation of the flow in a mixing vessel stirred by a Rushton turbine. *IChemE Symposium Series 140*, 1996.

[5] H. Takeda, K. Narasaki, H. Kitajima, and S. Sudoh. Numerical simulation of mixing flows in agitated vessels with impellers and baffles. *Computers $ Fluids*, 1993.

Chapter 4

Laminar Hydro-dynamics in Mixing Vessels

4.1 Introduction

Many mixing applications involve fluids of varying viscosity, stirred under laminar flow conditions, where knowledge of the local and overall flow pattern as well as shear stress distribution is of paramount importance. For example in the processing of biological agents, knowledge of the local shear stress and global transport of material is important in ensuring mixing while minimizing shear induced damage to cells. While most studies to date have concentrated on turbulent flow in mixing vessels, there are many industrial applications involving highly viscous fluids or requiring very slow mixing rates. These applications necessarily operate in the laminar flow regime where mixing is often inefficient due to the presence of segregated regions above and below the impeller. Thus, extreme care must be taken in the design of these systems. Very few studies exist to date for laminar mixing at very low Re numbers and while it has been observed that mixing times increase with decrease in Re number, there has been little detailed investigation into the associated 'breakdown' in bulk flow pumping (i.e. $\mathcal{F} \to 0$) as $Re \to 0$.

Lamberto et al [9] gathered PIV data and performed CFD calculations in an unbaffled vessel stirred by a Rushton impeller at Re numbers between 8 to 69, i.e. conditions similar to the ones examined in this study. Since there are no baffles, the flow is steady (in the impeller frame) and the simulations can be carried out in a rotating frame of reference. There was good qualitative agreement between the PIV measurements and the predicted flow patterns. Quantitative comparisons were presented for the probability density function (pdf) for all three velocity components using data in the vertical plane for the axial and radial velocities or the horizontal plane for the tangential velocity. An excellent agreement was found between the measured and predicted pdf's. The Authors also presented the variation of the flow number $\mathcal{F}$ with Re and reported small values (less that 0.2) for the lowest Re number examined. However, the breakdown in the pumping capacity was not investigated further. Hall [7] performed LDA ensemble and phase averaged measurements of a Rushton turbine

for Re as low as 1. Hall reports an abrupt change in ensemble averaged flow discharge angle as well as localized flow reversal near the impeller blade for $Re \lesssim 10$.

There are several studies that primarily focus on the characterization of the chaotic nature of mixing processes in laminar flows as opposed to the detailed investigation of the flow field. For example, Alvarez et al [1] studied the chaotic nature of the flow in mixing vessels for Re in the region 20 to 80 and found that the passing of the impeller blades triggers the onset of chaos by introducing small perturbations to the underlying regular flow that is observed when impellers are substituted with disks. Zalc et al [19] investigated experimentally and computationally the overall mixing characteristics for a three impeller mixer in an unbaffled tank for Re ranging from 20 to 200. Again the flow was computed on a rotating frame of reference. The predictions were validated against PIV data and excellent agreement was found for the variation of the axial and radial velocity components along the height of the vessel. Both experimental and computational results revealed the extensive flow compartmentalization associated with diffusion-based laminar mixing, however, there was little investigation of the local flow field near the impeller blades and a breakdown of pumping was not reported. Likewise, Ranada [15] employed CFD to investigate turbulent and laminar flows in a baffled tank at Re as low as 5, and while observing a breakdown in net pumping did not report any localized flow reversal near the impeller. In addition, these results compared favorably to the experimental observations of Dyster [5] who also reported an overall breakdown in net pumping at very low impeller speeds for a Rushton turbine. Other studies that have investigated the laminar and chaotic mixing process for both single and multiple impellers include [20], [2], [11], [17] and [10].

In contrast to Newtonian fluids, reverse flow and flow stall near the impeller has been reported in the case of Non-Newtonian fluids. Bartels [3] reports negative ensemble averaged radial flow (i.e. $\mathcal{F} \lesssim 0$) at low impeller speeds for a Rushton impeller. In addition, Nouri et al [12] and Green et al [6] report an abrupt change in the flow discharge angle (and thus flow pattern) for a pitch and axial flow impeller at a critical Re.

Hence, a detailed numerical analysis of the flow field in the near impeller region using phase-resolved data in baffled vessels for low Re numbers is still lacking. In particular, the physical mechanisms that lead to pumping breakdown have not been investigated thus far. The aim of the present study is to fill this gap via a computational and theoretical investigation (with experimental validation). The remainder of this chapter is organized as follows: First, §4.2 provides details for the geometry and operating conditions as well as details on the techniques used. Then §4.3 presents computational results (with experimental validation) followed by an analysis of the forces acting on a fluid element in the radial direction. Based on these results, a simplified analytic model of the flow is developed and validated in §4.4. Finally, the important conclusions are presented in §4.5.

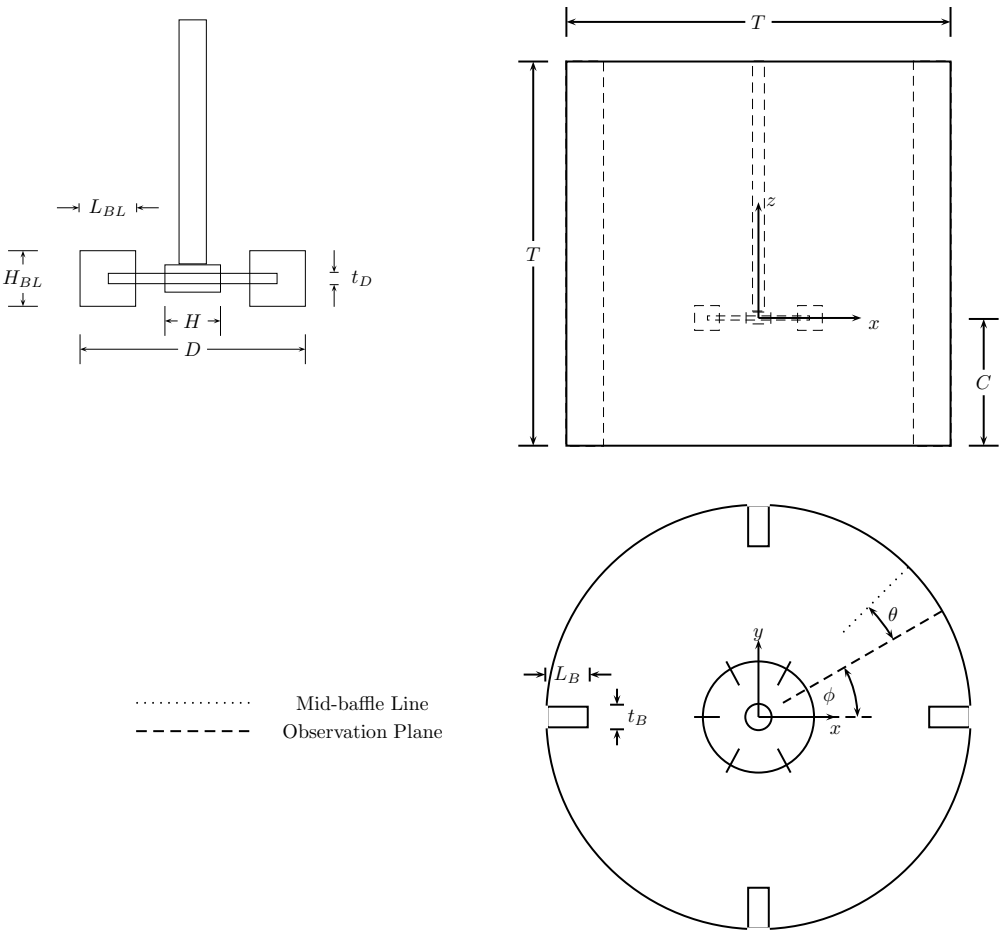

Figure 4.1: Experimental geometry and dimensions.

4.2 Geometry, Op. Cond. and Methods

The stirred vessel consists of a cylindrical baffled tank of diameter $T = 0.0805m$ and a standard six-blade Rushton impeller of diameter $D = T/3$ positioned at the center of the tank with clearance from the bottom $C = T/3$. The blade height, width and thickness are $H_{BL} = 0.2D$, $L_{BL} = 0.25D$ and $t_{BL} = 0.01T$ respectively. The tank contains four equally spaced baffles of width and thickness $L_B = T/10$ and $t_B = 0.01T$ respectively. The working fluid used in the simulations (and experiments used for simulation validations) is Silicon oil $Si1000$, with a viscosity 1000 times larger than that of water. Flow fields corresponding to three Re, namely 1, 10, and 28 were investigated, where again, the Re is defined as

$$Re \equiv \frac{ND^2}{\nu} \tag{4.1}$$

where N is the impeller speed in revolutions per second, D is the impeller diameter and ν is the kinematic viscosity of the fluid.[1]

[1] Or in terms of impeller tip speed V_{tip}

$$Re \equiv \frac{ND^2}{\nu} = \frac{DV_{tip}}{\pi\nu} \rightarrow V_{tip} = Re\frac{\pi\nu}{D} \tag{4.2}$$

The experimentally based phase-resolved velocity field used for simulation validation was measured by Hall using the Laser Doppler Anemometry (LDA) technique [7]. The numerical simulations were performed with an *in-house* code employing an unstructured mesh of approximately $500,000$ cells. In order to maximize the computational solution accuracy for comparison with experimental results a sliding and deforming mesh was employed in order to account for rotation of the impeller relative to the baffles (see [18]). The 2^{nd}-order central differencing scheme was used for the evaluation of convection and diffusion terms and the first order Euler implicit scheme for time marching. For all Re examined, each revolution required 216 time steps, corresponding to an angle of approximately 1.6° per time step. Solution files were created every 5° of impeller rotation. Finally, a separate *in-house* post-processor was written in order to calculate each term of the Navier-Stokes equations i.e. the material derivative of momentum as well as the pressure and viscous terms at the centroid of each cell.

The lowest Re examined posed the greatest difficulty both from the experimental as well as the computational point of view. As will be demonstrated in the following section, for that Re, the maximum radial velocity very close to the blade tip is around 10% of the tip velocity, $0.116m/s$ for the fluid examined. Therefore, typical radial velocities measured are on the order of $5 \times 10^{-3} - 10^{-2}m/s$ or even less. In order to obtain a statistically large sample of data to resolve the variation of radial velocity with impeller angle, long measurement times are necessary. Also small convective velocities make the inertia terms in the momentum equations (i.e. both temporal and convective terms) negligible with respect to the viscous and pressure forces, which therefore balance each other. From the computational point of view, this has two implications: First the equations become more elliptic in character and therefore the elements of the coefficient matrix are no longer zero (or close to zero) for the downstream nodes since the transportive property is lost. Linear systems with such matrices require more internal iterations for their solution. The second implication is that the contribution of the temporal derivative term in the diagonal coefficients of the system matrix, which is known to promote the stability of the iterative method, is now greatly reduced. To put it differently, the instantaneous structure of the flow depends solely upon the boundary configuration and boundary conditions and the history of motion enters the problem only insofar as to determine the current boundary configuration as the terms $\frac{\partial u_i}{\partial t}$ are negligible. Thus, for the simulations reported herein, in order to reduce the normalized residuals to a tolerance less than 10^{-3}, about 50 and 200 iterations are needed per time step for $Re = 28$ and 1 respectively.

4.3 Results and Discussion

Phase-resolved CFD based velocity measurements were carried out. In order to provide motivation for what is to follow, the pumping capacity of the impeller at different operating conditions can be assessed via the calculated flow number $\mathcal{F}$ based on ensemble-averaged data of Hall [7]. Again, recall the flow number $\mathcal{F}$ is defined as

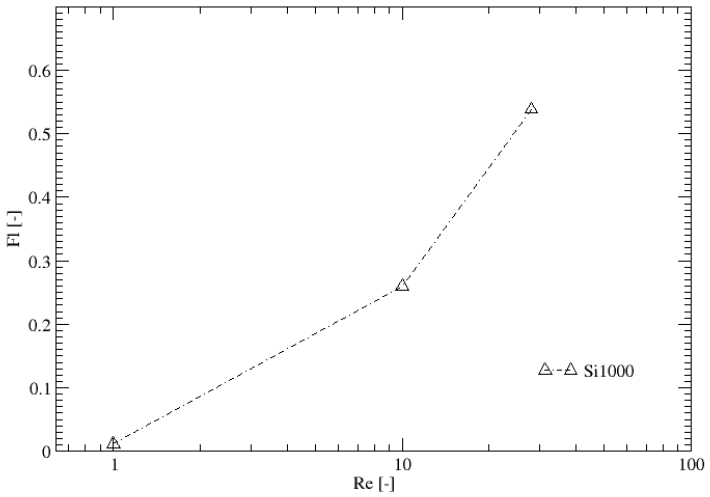

Figure 4.2: Variation of flow number $\mathcal{F}$ near the blade tip against Re number (Courtesy Hall [7]).

$$\mathcal{F} \equiv \frac{Q(r)}{ND^3} \tag{4.3}$$

where $Q(r)$ is the volumetric flow rate of fluid passing through an area surrounding the impeller with a height equal to that of the impeller blade. The radius r where Q is evaluated was equal to 0.186T i.e at a distance $1.55mm$ from the blade tip. The variation of flow number $\mathcal{F}$ against the Re is shown in Figure 4.2. It can be seen that $\mathcal{F}$ reduces steadily with decreasing Re, attaining values close to zero at very low Re numbers, thus indicating a breakdown in pumping capacity. Measurements for other fluids (both Newtonian and non-Newtonian) are reported by Hall [7] and confirm the same trend. This behavior has also been observed by Lamberto et al [9] who reported similar values for the $\mathcal{F}$.

The measured ensemble-averaged velocity field [7], from which $\mathcal{F}$ was calculated, is shown in Figure 4.3. Note the change in the velocity scale vector at the top of Figure 4.3(c) for $Re = 1$. It can be seen that not only the magnitude of velocity is reduced (as expected), but the flow pattern has changed as well. For $Re = 28$ and 10, the familiar pattern of two ring (recirculation zone) loops are evident above and below the impeller, while for the lowest Re downward motion near to the tip is discernible resulting in a negative flow discharge angle relative to the horizontal plane of the impeller. The variation of this angle near the bottom corner of the impeller tip (r/T=0.224 and z/T=0.298) with respect to Re is shown in Figure 4.4. The measured values of flow angle show significant scatter for Re smaller than 1 for reasons reported in the previous section. Nevertheless, there is a noticeably clear trend. Measurements for other fluids reported by Hall [7] also confirmed the same trend.

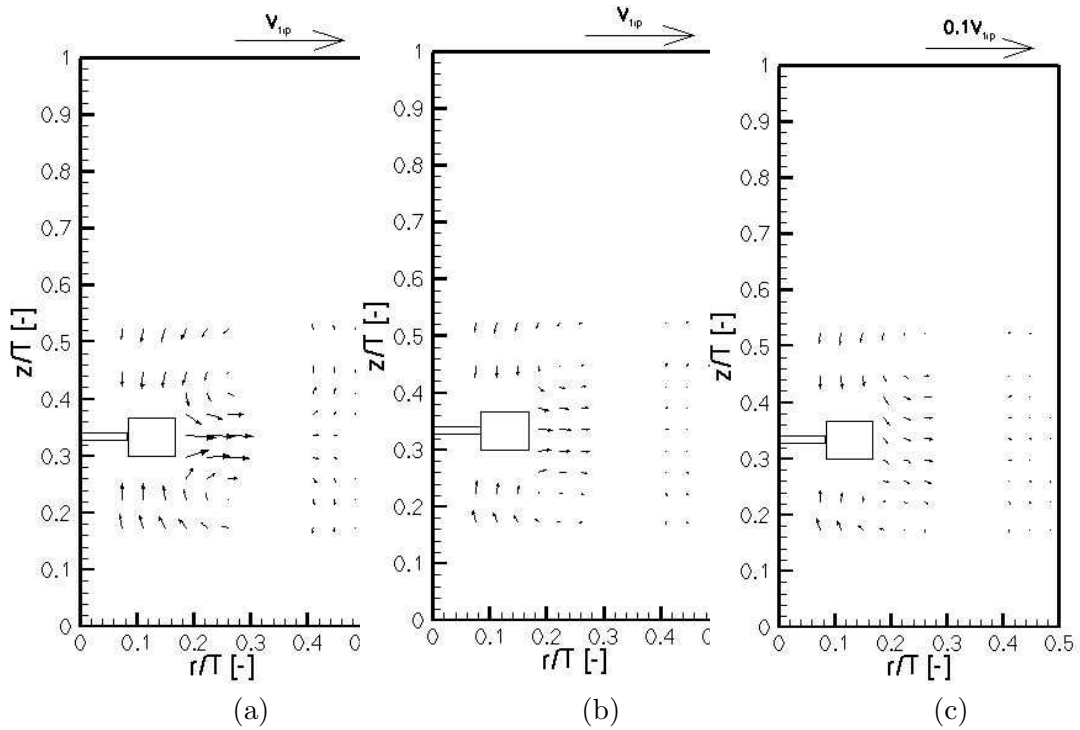

Figure 4.3: Ensemble average velocity field for (a) Re=28, (b) Re=10 and (c) Re=1 (Hall [7]).

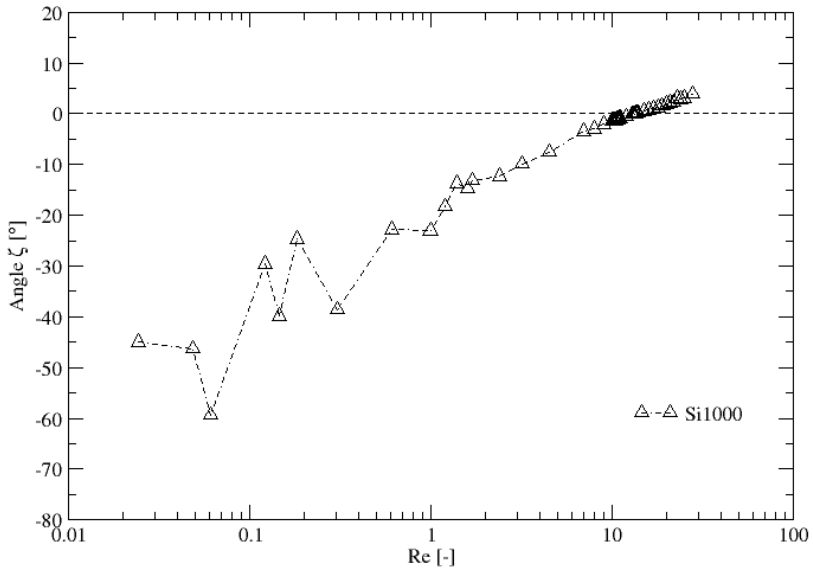

Figure 4.4: Variation of the flow discharge angle near the bottom corner of the impeller tip against *Re* number (Hall [7]).

4.3.1 Computational Results

All the aforementioned observations indicate that, for low Re, significant changes take place in the flow pattern close to the impeller tip. In order to study these changes in more detail, detailed CFD simulations were carried out.

Figure 4.5 shows comparison between experimental (Hall [7]) and CFD based predictions of the variation of the normalized radial velocity V_r/V_{tip} near the upper tip of the blade ($z/T = 1/30$) at three radial locations as a function of phase angle ϕ. This angle is zero when the blade is located exactly midway between two baffles. Hence, in terms of the nomenclature given in Figure 4.1, the observation plane corresponds to $\theta = 0$. In the inset of each figure, there is a radial velocity vector plot for a single impeller revolution. Note that the direction of rotation is clockwise. There is generally good agreement between experiments and predictions, especially for $Re = 28$ and 10. However, for $Re = 1$ there is a slight shift of a few degrees in the local maximum and minimum values. For the two higher Re, both the CFD and experimental results of Hall indicate positive radial velocities for all phase angles ϕ, therefore the ensemble-averaged velocity is positive. It can be seen that for the three Re examined, the maximum radial velocity occurs near the pressure side of the blade at $\phi \approx -5°$, which is the approximate location of the minimum radial pressure gradient as will be shown in the next section. Conversely, the minimum radial velocity occurs near the suction side of the blade at $\phi \approx 5 - 10°$. As the fluid moves away from the blade in the radial direction, the variation of the radial velocity profile with blade angle, under the influence of viscosity, becomes less pronounced. Note the effect of Re on the magnitude of radial velocity: the higher the Re, the higher the magnitude of radial velocity attained. Thus, the ensemble-averaged radial velocity is reduced with a decrease in Re ($< V_r/V_{tip} >= 0.145$ and 0.08 for $Re = 28$ and 10 respectively). This trend continues for the lowest Re resulting in almost complete cessation (breakdown) of pumping (the resulting average normalized radial velocity is very small, $< V_r/V_{tip} >= 0.007$).

Figure 4.6 shows radial velocity with contour plots of pressure superimposed near the impeller upper tip, for $Re = 1$. It is evident that the flow behavior is characterized by the following: Positive radial flow near the pressure-side (PS) of the blade, which vanishes at the blade tip, followed by localized reverse flow at the suction-side (SS) of the impeller blade. It is this transition from pumping, to stall and finally reverse flow at very low Re, which has hitherto remained unreported in the literature. Note also that the almost symmetric pressure contour magnitude on either side of the blade revealing the absence of a wake behind the blades. The next section provides a more thorough explanation of the observed phenomenon.

4.3.2 Evaluation of Forces

In order to thoroughly explain the change in flow pattern from uniformly positive to localized reverse pumping, the forces acting upon the fluid elements in the radial direction will be investigated in this section. Specifically, the inertial force experienced by a fluid element per unit volume, that is the material derivative of velocity multiplied by density ρa, is balanced

by two surface forces due to pressure and viscosity. Figure 4.7 displays the variation of the material derivative and the two surface forces (viscous and pressure) with the radial location r at $\phi = 0°$. All quantities are normalized by $\rho\omega^2 D/2$, that is the radial inertial force per unit volume at the impeller tip. Note that the maximum (absolute) value of the acceleration is approximately 0.8 and not exactly 1.0 because the first radial location considered is slightly displaced from the tip. It can be seen that the maximum values for all quantities are attained near the impeller tip and then rapidly decline. For a more detailed investigation of the force variation against ϕ, attention is focused on a point close to the upper blade tip $z/T = 1/30$, at a radius $0.186T$, the same radial location used for the calculation of the flow number $\mathcal{F}$ in the previous sections.

Referring to Figure 4.8(a) it can be observed that the fluid acceleration is primarily negative (fluid deceleration) for a large interval of blade angle ϕ, indicating a radially inward acceleration due to the rotation of the fluid in the mixing vessel. One should also note that this inward acceleration is maximized at an angle $\phi \approx 0°$ which corresponds to the blade tip passing. The important qualitative difference to notice for the three Re is the increase in the relative magnitude of pressure and viscous forces compared to the inertial force with decreasing Re. $Re = 10$ represents a transitional case whereby pressure, viscous and inertial forces are comparable. However, for $Re = 1$ a very interesting behavior is observed: Essentially a balance exists between the pressure and viscous forces with very small values for the inertial force. In other words, the fluid behavior can be described as conforming to that of slug or creeping flow. Since inertia is very small compared to the pressure and viscous forces, the fluid particles react instantaneously to the pressure field. This is evident from Figure 4.6 but can be seen more clearly in Figure 4.9 where the variation of the pressure field induced by the passing of an impeller blade at low speed ($Re = 1$) is plotted along with the radial velocity. Clearly the two quantities are almost perfectly in phase. Note that for purposes of illustration, the normalized pressure force has been rescaled (divided by 20) in order to fit in the same graph as normalized velocity.

It must be noted at this point that negative radial velocities close to the impeller disk have been reported in the past for non-Newtonian fluids, and more specifically viscoelastic materials. However, the mechanism responsible for this is different compared to the one identified here for laminar Newtonian fluid flow. Viscoelastic materials exhibit a very interesting behavior due to the presence of elastic forces in addition to the classical Newtonian inertial, pressure and viscous forces. The elastic forces act in the direction opposite to the inertial forces and cause a decrease in pumping capacity. For low rotational speeds and a highly elastic material this can result in an inward flow at the impeller and breakdown of the pumping action as reported by Bartels [3].

Having established the basic fluid dynamic phenomena taking place and confirming the presence of creeping flow, the Navier-Stokes equations (fluid equations of motion) become linear in velocity allowing the development of a simplified analytical model for the flow, which is presented in the next section.

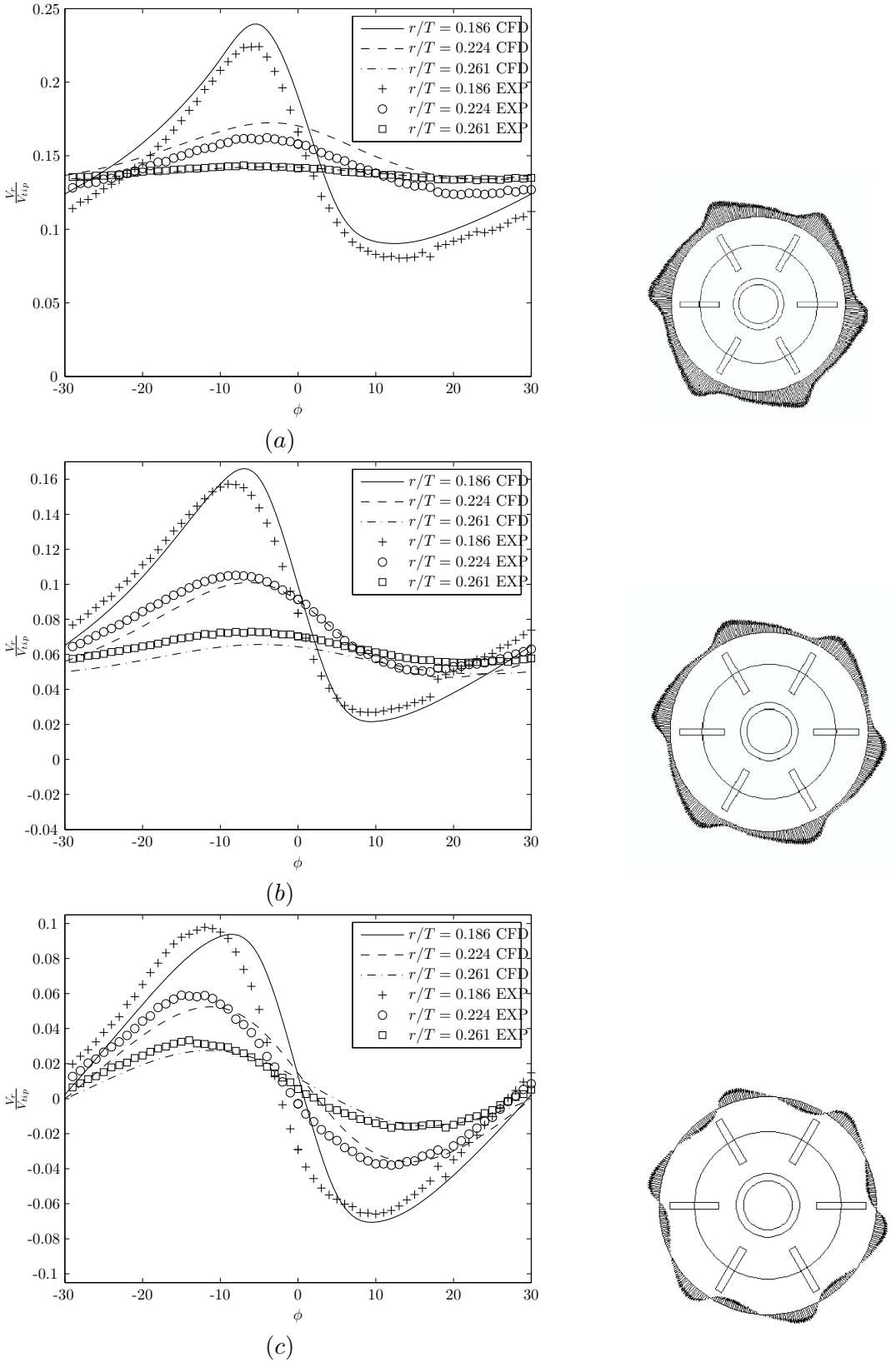

Figure 4.5: CFD and experimental (Hall [7]) radial velocity components at various normalized distances r/t for (a) $Re = 28$, (b) $Re = 10$ and (c) $Re = 1$ (near upper blade tip at $\frac{z}{T} = \frac{1}{30}$)

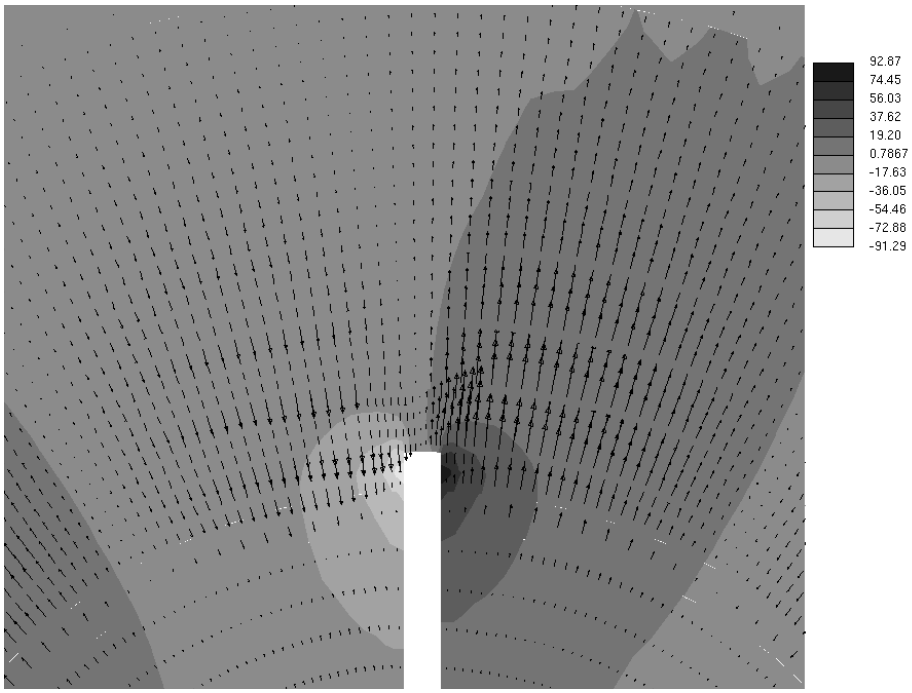

Figure 4.6: Radial velocity and pressure contours (units in Pa) for $Re = 1$ (in plane $z/T = 1/30$). The rotation of the blade is clockwise.

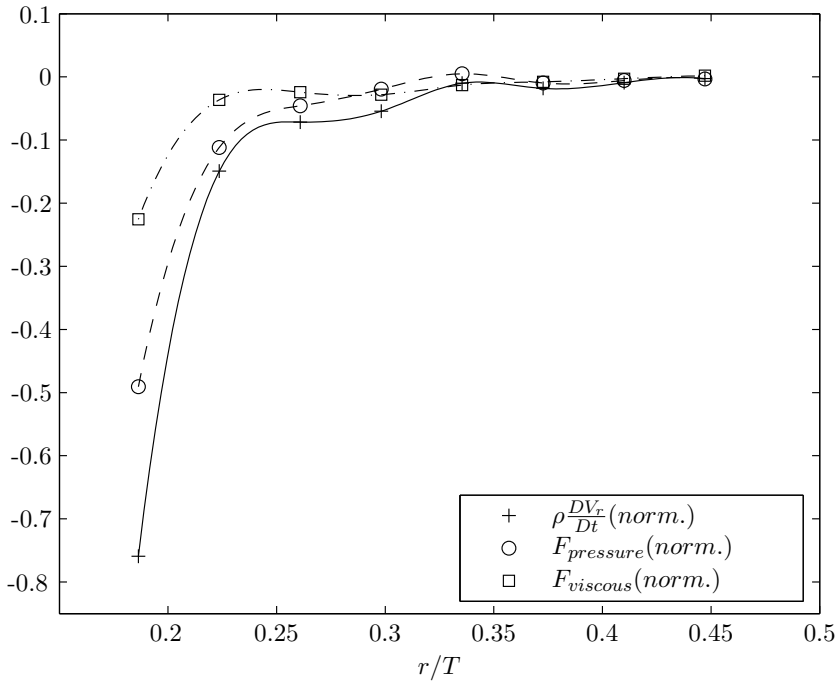

Figure 4.7: Variation of normalized acceleration, pressure and viscous forces in the radial direction for $\phi = 0°$, $z/T = 1/30$ (upper blade tip) and $Re = 28$.

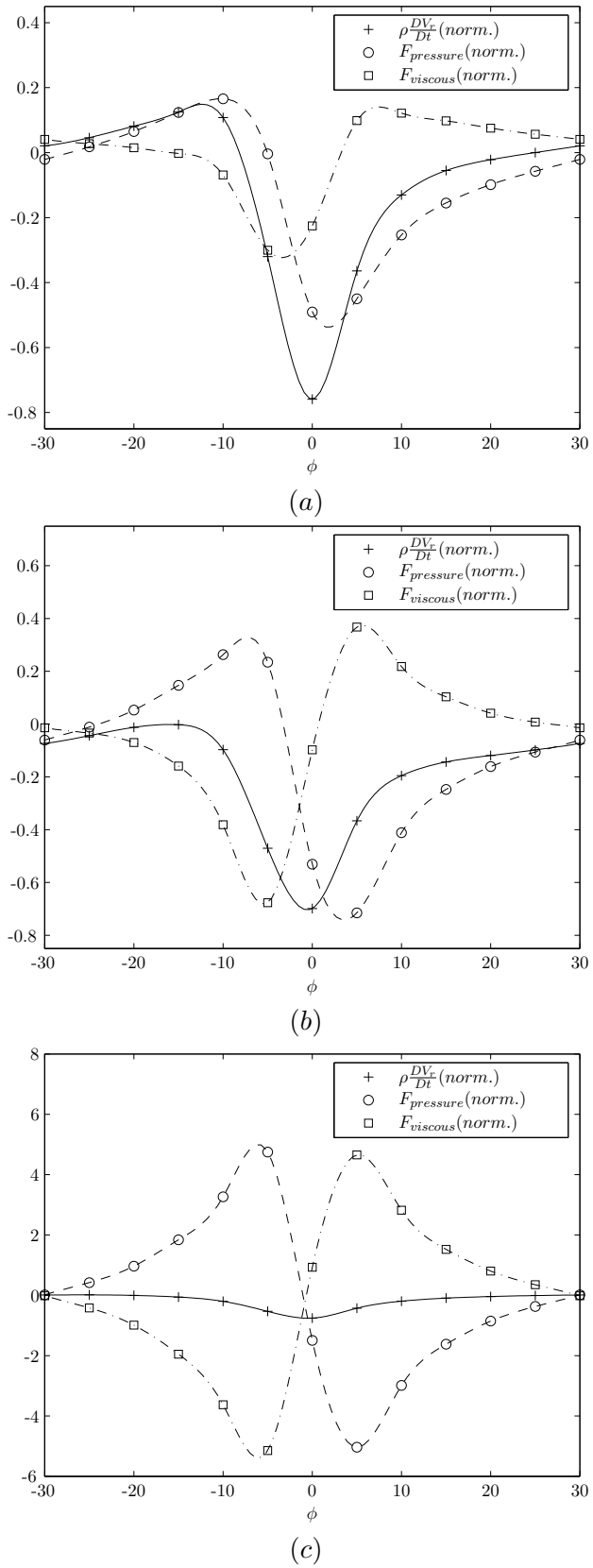

Figure 4.8: Radial force components at near upper tip location (normalized distance $r/T = 0.186$ and $z/T = 1/30$) for (a) $Re = 28$, (b) $Re = 10$ and (c) $Re = 1$.

4.4 Analytical Model of the Flow

Analytical models of the flow field produced by radial impellers in stirred vessels have been developed by Desouza and Pike [4] and Kolar et al [8] among others. However, these models refer to steady, fully turbulent and axially symmetric flows without pressure gradients. Here an analytical model is presented, tailored to creeping flows in stirred vessels.

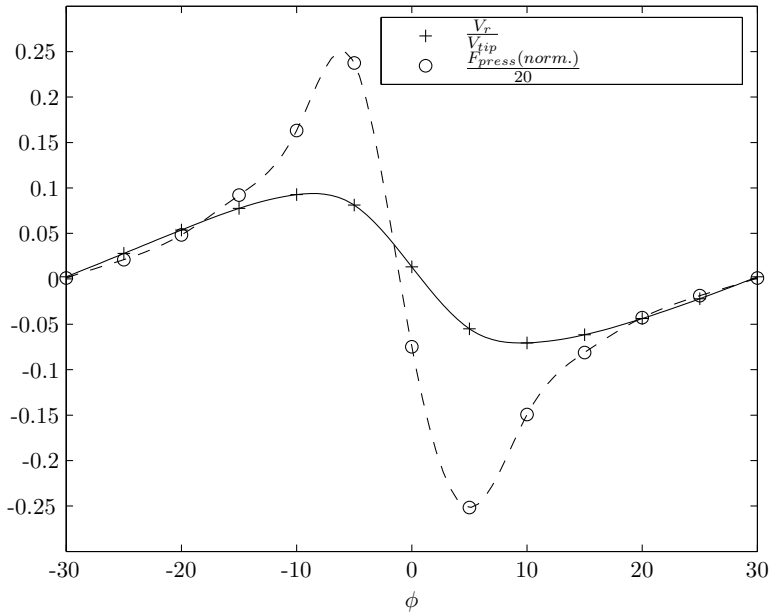

Figure 4.9: Variation of radial velocity and pressure force along the radial direction for $Re = 1$ near upper blade tip ($r/T = 0.186$ and $z/T = 1/30$).

Ignoring the material derivative and keeping only the pressure and viscous terms, the momentum equation (fluid equation of motion) in the radial direction can be written as:

$$\frac{\partial P}{\partial r} = \mu\{\frac{\partial}{\partial r}(\frac{1}{r}\frac{\partial(rv_r)}{\partial r}) + \frac{1}{r^2}\frac{\partial^2 v_r}{\partial \theta^2} - \frac{2}{r^2}\frac{\partial v_\theta}{\partial \theta} + \frac{\partial^2 v_r}{\partial z^2}\} \tag{4.4}$$

Note in this expression the variable θ has been used for the azimuthal angle in order to avoid confusion with the phase angle ϕ (and is not related to the observation plane angle). The continuity equation in polar coordinates, neglecting the contribution due to axial flow, can be written as

$$\frac{\partial}{\partial r}(rv_r) + \frac{\partial v_\theta}{\partial \theta} = 0 \tag{4.5}$$

The previous formulation of the continuity equation requires negligible (or uniform) axial flow in the axial direction. Indeed, Figure 4.10 (upper right corner) indicates the presence of a horizontal plane of symmetry at the impeller disk with negligible axial velocity.
Utilizing the continuity equation (4.5), the derivative of the circumferential velocity v_θ can be eliminated from the momentum equation (4.4):

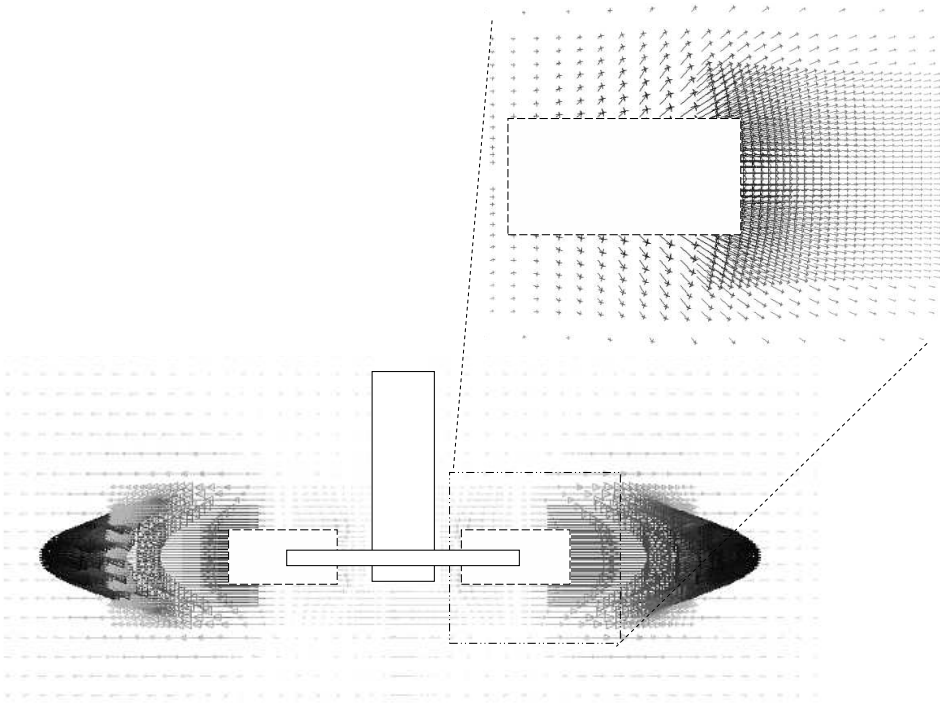

Figure 4.10: Radial (lower left) and absolute velocity (upper right) for Re=1 at $\phi = -10°$ including approximate impeller blade locations.

$$\frac{\partial}{\partial r}(\frac{1}{r}\frac{\partial(rv_r)}{\partial r}) + \frac{1}{r^2}\frac{\partial^2 v_r}{\partial \theta^2} + \frac{2}{r^2}\frac{\partial(v_r r)}{\partial r} + \frac{\partial^2 v_r}{\partial z^2} = \frac{1}{\mu}\frac{\partial P}{\partial r} \tag{4.6}$$

Expanding the first and third term on the left hand side, the following equation is obtained:

$$\frac{\partial^2 v_r}{\partial r^2} + \frac{1}{r^2}\frac{\partial^2 v_r}{\partial \theta^2} + \frac{v_r}{r^2} + \frac{3}{r}\frac{\partial v_r}{\partial r} + \frac{\partial^2 v_r}{\partial z^2} = \frac{1}{\mu}\frac{\partial P}{\partial r} \tag{4.7}$$

This is a second order partial differential equation for the radial velocity that can be solved if the radial pressure gradient is known. The boundary condition at the walls is no slip/penetration hence, from the above, the radial velocity inside the vessel is determined by the pressure gradient.

Analytic solutions for two dimensional creeping flows in polar coordinates can be found in simplified cases, where the unknown velocities and pressure depend on only two coordinate variables (r, θ) or (r, z) (see for example [13] and [14]). However in the present case, the radial velocity depends on all three coordinates. An order of magnitude analysis also shows that it is not possible to ignore the viscous term in the axial direction, $\frac{\partial^2 v_r}{\partial z^2}$, because the characteristic length scale in z is of the order of the blade height H, which is 5 times smaller than the impeller diameter as already mentioned, therefore this term is expected to be important. In order to derive a simplified analytic model, an approximation related to the variation of the

radial velocity in the axial direction is made: it is assumed that the velocity distribution in the z direction is parabolic i.e.

$$\boxed{v_r(r,\theta,z,t) = v_r^{ms}(r,\theta,t)\left[1-\left(\frac{z}{h}\right)^2\right]} \tag{4.8}$$

where v_r^{ms} is the radial velocity at the impeller midsection (disk-plane at $z = 0$) and h is a characteristic length of the order of the height (H) of the impeller blade. The analytic solution for a laminar, two dimensional, plane jet injected in a quiescent environment is given by Schlichting [16] but it is quite complicated and difficult to use in the present context. On the other hand, the parabolic variation is simple and has a constant second order derivative. Furthermore, in referring to Figure 4.10 it can be seen that the radial flow component is indeed approximately parabolic at least near the impeller tip thus confirming the suitability of our choice. Substituting this expression (4.8) into (4.7) yields:

$$\left(\frac{\partial^2 v_r^{ms}}{\partial r^2}+\frac{1}{r^2}\frac{\partial^2 v_r^{ms}}{\partial \theta^2}+\frac{v_r^{ms}}{r^2}+\frac{3}{r}\frac{\partial v_r^{ms}}{\partial r}\right)\left[1-\left(\frac{z}{h}\right)^2\right]-\frac{2}{h^2}v_r^{ms}=\frac{1}{\mu}\frac{\partial P}{\partial r} \tag{4.9}$$

Therefore, the variation of the radial velocity at the midsection of the impeller v_r^{ms} is governed by the following partial differential equation, obtained by setting $z = 0$:

$$\frac{\partial^2 v_r^{ms}}{\partial r^2}+\frac{1}{r^2}\frac{\partial^2 v_r^{ms}}{\partial \theta^2}+\frac{v_r^{ms}}{r^2}+\frac{3}{r}\frac{\partial v_r^{ms}}{\partial r}-\frac{2}{h^2}v_r^{ms}=\frac{1}{\mu}\frac{\partial P}{\partial r}^{ms} \tag{4.10}$$

where P^{ms} is the pressure at the midsection of the impeller (i.e. the disk). The method of separation of variables will now be used for the solution of this equation. This is a standard approach for equations in the creeping flow regime ([13] and [14]). Inspection of the CFD results, reveals a periodic variation of the pressure gradient and therefore, the following variation is assumed with the angle θ and time t:

$$\boxed{-\frac{\partial P}{\partial r}^{ms}(r,\theta,t) = N(r)sin(\alpha(\theta-\omega t))} \tag{4.11}$$

where $N(r)$ is the amplitude of the variation of pressure gradient, ω is the angular velocity of the impeller and α is the number of blades. The angle θ increases in the direction of impeller rotation and at time $t = 0$ a blade tip is located at $\theta = 0$. Since the radial velocity varies in phase with the pressure gradient, we assume:

$$\boxed{v_r^{ms}(r,\theta,t) = f(r)sin(\alpha(\theta-\omega t))} \tag{4.12}$$

Apart from simplicity, this approximation of the radial velocity has the additional advantage of automatically satisfying the no slip boundary condition at the (assumed thin) impeller blades. It should be noted that (4.11) and thus (4.12) are applicable for any finite number of blades where a sinusoidal radial pressure force exists due to the passing of the impeller blade pressure and suction sides. Substituting the two previous expressions into (4.10) and

canceling out the factor $sin(\alpha(\theta - \omega t))$ gives:

$$\frac{\partial^2 f(r)}{\partial r^2} - \frac{\alpha^2}{r^2} f(r) + \frac{1}{r^2} f(r) + \frac{3}{r} \frac{\partial f(r)}{\partial r} - \frac{2}{h^2} f(r) = -\frac{N(r)}{\mu} \tag{4.13}$$

Noting that $f(r)$ is a function of r alone, the radial momentum equation reduces to the following second order ordinary differential equation

$$\boxed{f_r'' + \tfrac{3}{r} f_r' - f_r(\tfrac{2}{h^2} + \tfrac{\alpha^2 - 1}{r^2}) = -\tfrac{N(r)}{\mu}} \tag{4.14}$$

The two boundary conditions for the solution of this equation are the no penetration (i.e. $f = 0$) at the impeller disk and tank wall. For a constant value of h, analytical solutions for this equation can be found for simple polynomial expressions of N(r). For the case examined, there is no simple expression for N(r) and its values are determined from the CFD results. Specifically, pressure forces were sampled at the blade angle for which the maximum value appears ($\theta = \phi = -5°$) and a cubic spline was interpolated to the CFD derived pressure force data. The resulting (interpolated) function $N(r)$ was used to solve numerically for the radial velocity amplitude $f(r)$.

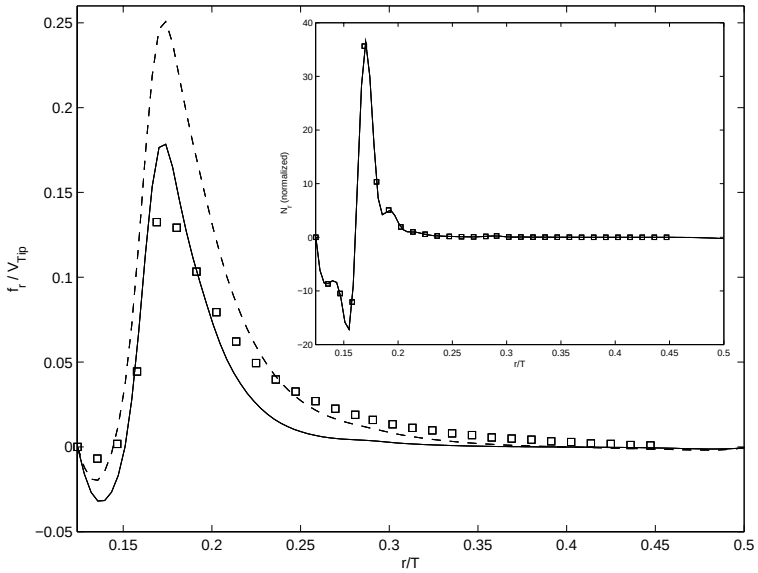

Figure 4.11: Variation of amplitude $f(r)/V_{tip}$ in the radial direction and comparison with computational results (□ □ □ □) for $Re = 1$ (– – – – $h = H_{BL}$; ——— $h = H_{BL}/2$). At the inset the variation of normalized $N(r)$ is shown.

Figure 4.11 displays the solution $f(r)$ for the amplitude of radial velocity v_r^{ms}. Given the somewhat arbitrary choice for the constant axial jet height h, $f(r)$ was solved both for h equal to the blade half-height ($H_{BL}/2$) as well as the full blade height (H_{BL}). As expected, a thicker

jet (i.e. higher h) decreases the viscous retarding force on the fluid yielding a higher predicted radial velocity magnitude. Discrete values for the computationally predicted velocity profile are superimposed, indicating qualitatively correct behavior. More specifically, not only is the general shape of the radial flow profile well predicted by the simplified model, but the analytically predicted peak velocity near the blade tip is within 30% of the computational value if $h = H_{BL}/2$. The sharper decay in $f(r)$ compared to the CFD derived radial velocity is most likely due to the assumption of a constant value for the jet height, h. Indeed, as the fluid stream travels towards the tank wall, the jet height h must increase due to diffusion and entrainment from the surrounding area. Hence the improved data fit for $f(r)$ towards the outer tank wall if $h = H_{BL}$ as shown in Figure 4.11.

The inset Figure 4.11 also gives the interpolated maximum radial pressure force function is displayed along with the sensor points obtained from the CFD results. Note that Figures 4.11 and 4.8(c) refer to different axial locations (i.e. the disk and blade upper tip respectively). Finally, a three-dimensional surface plot of equation 4.12 for the radial velocity at the midsection of the impeller (disk-plane) along with the associated location of the impeller is shown in Figure 4.12.

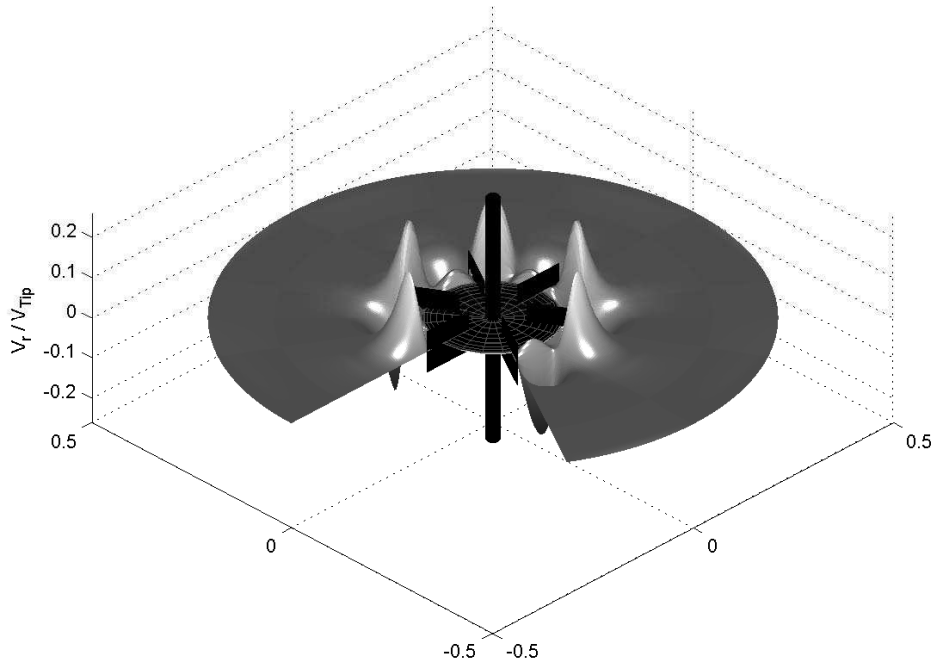

Figure 4.12: Three dimensional view of the solution of the analytical model for $Re = 1$ ($h = H_{BL}/2$).

4.5 Concluding Remarks

Novel computational and theoretical results, (with experimental validation), for the flow in a vessel stirred by a Rushton turbine at low Re were examined (for $Re = 1$, 10 and 28). It was

found that as the Re is reduced, the net pumping capacity of the impeller is reduced as well. In fact, for the lowest Re examined pumping all but ceased due to fluid reciprocation in the radial direction. Numerical simulations (CFD) successfully captured this behavior. A force decomposition using CFD derived measurements established the progressive strengthening of the pressure and viscous terms compared to inertial forces with reduction in Re. In fact, for the lowest Re the flow is characterized by a balance between pressure and viscous forces where changes in fluid momentum can be neglected. A simplified analytical model of the flow was developed that gives quantitatively very reasonable results. Finally, note that although we have dealt with Newtonian fluids at very low Re, the current work can be extended to non-Newtonian fluids as well with the aim to understand and predict the onset of localized flow stall and the corresponding breakdown in pumping.

References

[1] M.M. Alvarez, J.M. Zalc, T. Shinbrot, P.E. Arratia, and F.J. Muzzio. Mechanisms of mixing and creation of structure in laminar stirred tanks. *AIChE Journal*, 48(10):2135–2148, 2002.

[2] M.M. Alvarez-Hernández, T. Shinbrot, J. Zalc, and F.J. Muzzio. Practical chaotic mixing. *Chemical Engineering Science*, 57:3749–3753, 2002.

[3] P. Bartels. *An Experimental Study on Turbulent Mixing of Visco-Elastic Fluids*. Technische Universiteit Delft, 1988.

[4] A. Desouza and R. Pike. Fluid dynamics and flow patterns in stirred tanks with a turbine impeller. *Canadian Journal of Chemical Engineering 50*, pages 15–23, 1972.

[5] D. Dyster and E.K. Jaworski. An LDA study of the radial discharge velocities generated by a Rushton turbine. *IChemE*, 71:11–23, 1993.

[6] H. Green, C. Carpenter, and L. Casto. Mixing characteristics of an axial impeller with newtonian and non-newtonian fluids. *Fourth European Conference on Mixing*, 57:109–126, 1982.

[7] J. Hall. *Study of viscous and visco-elastic flows with reference to laminar stirred vessels*. PhD thesis, Department of Mechanical Engineering, King's College London, 2005.

[8] V. Kolar, P. Filip, and A. Curev. Hydrodynamics of a radially discharging impeller stream in agitated vessels. *Chemical Engineering Communications 27*, pages 313–326, 1984.

[9] D.J. Lamberto, M.M. Alvarez, and F.J. Muzzio. Experimental and computational investigation of the laminar flow structure in a stirred vessel. *Chemical Engineering Science*, 54:919–942, 1999.

[10] D.J. Lamberto, F.J. Muzzio, P.D. Swanson, and A.L. Tonkovich. Using time-dependent RPM to enhance mixing in stirred vessels. *Chemical Engineering Science*, 51(5):733–741, 1996.

[11] B. Letellier, C. Xuereb, P. Swaels, P. Hobbes, and J. Bertrand. Scale-up in laminar and transient regimes of a multi-stage stirrer, a CFD approach. *Chemical Engineering Science*, 57:4617–4632, 2002.

[12] J. Nouri and J. Whitelaw. Flow characteristics of stirred reactors with newtonian and non-newtonian fluids. *AIChE*, 36:627–629, 1990.

[13] T. Papanastasiou, G. Georgiou, and A. Alexandrou. *Viscous Fluid Flow*. CRC Press, 2000.

[14] C. Pozrikidis. *Introduction to Theoretical and Computational Fluid Dynamics*. Oxford University Press, 1997.

[15] V.V. Ranade. An efficient computational model for simulating flow in stirred vessels: A case of Rushton turbine. *Chemical Engineering Science*, 52(24):4473–4484, 1997.

[16] H. Schlichting. *Boundary-Layer Theory*. McGraw Hill, 1968.

[17] P.A. Tanguy, F. Thibault, E.B. Fuente, T. Espinosa-Solares, and A. Tecante. Mixing performance induced by coaxial flat blade-helical ribbon impellers rotating at different speeds. *Chemical Engineering Science*, 52:1733–1741, 1997.

[18] S.L. Yeoh, G. Papadakis, and M. Yianneskis. Numerical simulation of turbulent flow characteristics in a stirred vessel using the LES and RANS approaches with the sliding/deforming mesh methodology. *Chemical Engineering Research and Design, Trans IChemE, Part A*, 82(7):834–848, 2004.

[19] J.M. Zalc, M.M. Alvarez, F.J. Muzzio, and B.E. Arik. Extensive validation of computed laminar flow in a stirred tank with three Rushton turbines. *AIChE Journal*, 47(10):2144–2154, 2001.

[20] J.M. Zalc, E.S. Szalai, M.M. Alvarez, and F.J. Muzzio. Using CFD to understand chaotic mixing in laminar stirred tanks. *AIChe Journal*, 48(10):2124–2134, 2002.

Chapter 5

Transitional Hydro-dynamics: Mean Motion

5.1 Introduction

In contrast to laminar flow mixers, where molecular diffusion and large scale convection are the primary mixing mechanisms, turbulent flows result in enhanced mixing due to local small scale property fluctuations (i.e. larger energy containing and small scale dissipative turbulent fluctuations which serve to enhance property transport). Applications of turbulent (and transitional) mixing include petro-chemical, pharmaceutical and many other industrial mixing processes. In the case of reacting flows, the rate of rejected (waste) product formation is often related to the mismatch between desired and actual constituent component mixing. Hence, insofar as momentum transfer mechanisms are similar to those of species transport, knowledge of flow perturbations and hence local dissipation and turbulence intensity is important. Specifically, regions of high dissipation, (via property gradients), both mean-flow and turbulent fluctuation induced, correspond to regions of high mixing rates via diffusion. In addition, regions of high turbulence intensity can correspond to high turbulent species as well as momentum flux (i.e. enhanced effective diffusion). Therefore, a thorough understanding of the flow physics, including flow turbulence, is important for improving mixer performance and formulating optimal mixing strategies.

The Literature

Due to the large number of studies (numerical and experimental) investigating flow in mixing vessels, the following introduction will be confined to selective works primarily using Rushton turbines while excluding laminar flow (previously covered in Chapter 4). Specifically, experimental studies will be reviewed first, followed by numerical studies. In addition, studies specific to measurement and prediction of turbulent energy dissipation are covered in §5.2.1 while previous investigations of the blade trailing vortex will be reviewed in §5.4.2.

General flow visualization experiments for mixing vessels were performed by Hockey et

al [30] who used flow visualization techniques (laser sheet and tracers) to visualize the upper and lower recirculation loops above and below the impeller jet. Specifically, for low $Re \approx 300$ the flow appeared laminar while for much higher values ($\approx 25(10^3)$) the flow appeared highly erratic, indicative of turbulence.

Early experimental studies on mixing in stirred tanks primarily centered on estimation of mixing times and power consumption. With respect to the former, a dimensionless mixing time $\tilde{t}_{mix}$ can be formed via

$$\tilde{t}_{mix} \equiv N t_{mix} \tag{5.1}$$

where N is the impeller speed in rev/sec. and t_{mix} is the mixing time (or time required for the tank volume integrated mean concentration to achieve, for example, 95% of the steady-state value). In the earliest work of Kramers et al [37], it was found that in the range of fully turbulent flow, $\tilde{t}$ is constant for a fixed geometry and fluid (mixture component) properties. Further investigation of the functional dependence of mixing time on geometric and dilutant/carrier properties was performed by a number of researchers of which the works of Shiue et al [69], Raghav Rao et al [56], Mahmoudi [47] and Distelhoff [18] were applicable to Rushton turbines. For the previous, dimensionless mixing times for 95% mixing were found to range from $35-50$ while for 99% mixing the dimensionless time was ≈ 60 [18] (i.e. $35-50$ or ≈ 60 impeller revolutions for 95% or 99% mixing respectively). An additional study into the effect of the blade trailing vortices (examined in §5.4.2) on mixing rates was made by Asserelli et al [2] using an iodide-iodate reaction mechanism to gauge a mixing effectiveness.

Studies measuring power consumption of the standard configuration Rushton turbine (discussed in §2.9.2) were performed by Rushton [64], [13], and for various impeller thicknesses by Rutherford [65] and Chapple et al [10]. All these studies found the power number to asymptotically approach ~ 5 as $Re \to \infty$ (or $Re \gtrsim 10^4$). In addition, as the blade t_{BL} and disk thickness t_d increase, the pumping capacity/flow number $\mathcal{F}$ and thus the power number $\mathcal{P}$ decline.

Previous experimental works investigating, in detail, the turbulent flow field within Rushton turbine mixers have included LDA, PIV or hot-wire anemometry studies of the impeller/flow discharge region by van't Riet et al [63], Wu et al [74], Stoots et al [70], Yianneskis et al [76], Hall [29], Mujumdar [52], Ducci et al [21], [22] [20], Micheletti et al [51], [50], Sharp et al [68] and Dyster [24], to name a few. Studies relevant to the measurement of turbulent dissipation will be discussed in detail in §5.2.1.

A number of studies investigating the near impeller macro-instabilities (impeller trailing vortices and axial vortices originating at the impeller and terminating at the top/bottom of the tank) have been performed by researchers such as Yianneskis et al [77], Derksen et al [16], Escudie et al [26], Schafer et al [66], Stoots et al [70] and Van't Riet et al [63] and will

be reviewed in detail in §5.4.2. Suffice to say, one of the earliest studies was performed by Gunkel et al [28] who used LDA to extract phase averaged and perturbation velocities near the impeller for turbulent flow, the former of which were used to identify trailing vortices in the vicinity of the impeller. Axial vortices (macro-instabilities) associated with the meandering large-scale vortices terminating at the top and bottom of the tank, have been identified and associated with enhanced mixing. Doulgerakis et al [19] used PIV based measurements of a Rushton turbine mixing tank and found that these macro-instabilities originate near the lower (and presumably upper) tips of the impeller and direct fluid from below (and above) onto the impeller region. They hypothesized that these axial macro-instabilities, which feed material into the impeller region, could be used to enhance species transport and mixing. Experimental verification of the hypothesis of macro-instability enhanced mixing was attempted by Ducci et all [23] who found a statistically significant reduction in mixing time due to direct injection of a tracer into the axial vortex/macro-instability compared with non-macro-instability injection.

Detailed studies of flow turbulence in the impeller stream include that of Ducci [21], [22], Dyster et al [24], Sharp et al [68] and Micheletti [50] [51]. Ducci performed a series of LDA phase resolved measurements of the (fully turbulent) velocity field for $Re = 32(10^3)$. In Ducci et al [21] phase averaged dissipation and calculated Kolmogorov and Taylor length scales in the near impeller region were examined. Micheletti et al [51], [50] measured ensemble averaged turbulence intensity, Reynolds stress and normalized mean velocities in the near-impeller and jet region for Re down to $4(10^3)$. Dyster et al [24] correlated radial perturbation rms velocity (i.e. components of $\overline{k'}$) as a function of Re from $Re = 5$ to $5(10^4)$. He found that the flow in the near impeller region transitions to turbulent for $Re \approx 5(10)^2$. Sharp et al [68] performed 3-D velocimetry measurements on Rushton turbine stirred tank, identifying the blade trailing vortices and directly measuring turbulent kinetic energy. The most detailed and direct experimental measurements of flow turbulence to date was performed by Ducci [22], who gathered phase resolved small scale flow perturbation data which were used to decompose the TKE transport equation and calculate individual terms: Convection, Diffusion and Generation. However, it should also be noted that these results examine only the impeller discharge region (jet) and not flow near the baffles or outer tank walls nor the inner-impeller (i.e. very near blade and disk) region. In addition, measurements of the flow pressure field could not be obtained (due to the invasive nature of the required measurement technique). Thus, the pressure diffusion term, for example in the TKE transport equation, was not determined.

Finally, Yoon et al [78] performed PIV measurements of flow in two different sized Rushton turbine mixing vessels at various Reynolds numbers. It was found that normalized ensemble averaged quantities (i.e. mean flow velocities scaled by blade tip velocity) became Reynolds number invariant at $Re \sim 15,000$. Quantities associated with the trailing vortex (vorticity, vortex size, etc.) however, did not achieve independence until a much higher Reynolds number $\sim 50,000$. In addition, it was also found that these flow parameters associated with the vortex were highly sensitive to small variations in impeller geometry, while ensemble averaged

quantities were not.

Numerical simulations of rotating machinery, in particular, mixing vessels, can be sub-divided into two broad classifications: Steady and unsteady. For steady simulations the rotation of the impeller relative to the outer tank wall is not modeled, but instead the (steady) fluid equations of motion are solved in the impeller relative and/or the baffle (stationary) frame (for example Luo et al [46], Ciofalo et al [11], Brucato et al [9] and Sun et al [71]). Of the previous, the most useful steady-state methodology includes the multiple reference frame (MRF) approach whereby the flow domain is sub-divided into two regions: The stationary region in which the steady, fixed frame, fluid equations of motion are solved, and a rotating region where the fluid equations of motion are solved steady in the blade relative frame. The interface between domains represents a computational boundary between domains (whereupon impeller frame flow properties are circumstantially averaged and subsequently imposed as boundary conditions on the fixed frame domain). Luo et al [46] implemented this approach, thus simulating turbulent flow in a Rushton turbine. The methodology well predicted radial and axial mean velocities compared to the experimental data of Yianneskis et al [76]. Unsteady simulations on the other hand, can accommodate relative motion between impeller and tanks baffles (via an explicit rotation of an impeller attached mesh relative to a baffle attached mesh along some interface). Researchers such as Luo et al [45], Murthy et al [53], Khopkar et al [36] and Ng et al [54] have utilized such a technique. In addition, if relative motion of the mesh is not utilized, unsteady simulations can be performed by imposing the appropriate time dependent sources associated with the instantaneous blade surface locations and solving the resulting unsteady fluid equations of motion (see the works of Eggels [25], Derksen et al [17], Revstedt et al [60] [59] and Lu et al [44]).[1]

In addition to the above, cruder simulation methods can also be used such as that of Placek et al [55] who perform an elaborate simulation of flow in a stirred tank via explicit boundary method. Specifically, one quarter of the tank geometry was simulated utilizing symmetry (no penetration) at tank top and disk plane, specified velocity down-stream of the impeller, turbulent wall (outer tank wall) and symmetric jet (associated with flow at the impeller shaft) boundary conditions. The pressure dependence in the equation of motion was eliminated by reduction of the flow field variables to the local stream function and vorticity. The effects of turbulence was incorporated via an eddy viscosity concept and a $k\epsilon$ turbulence model. The mean-flow velocity was in qualitative agreement with experimental results, however, quantitatively errors were on the order of 50%. The maximum turbulent kinetic energy and dissipation were found to be within the impeller stream near the impeller. Similarly, Yoon et al [79] attempted to simulated mixing in a baffle-less tank using source terms to model the effect of the impeller motion (based on experimentally derived measurements). Results were generally poor with significant qualitative deviation between simulated and experimental radial velocity within the impeller jet.

[1]Pseudo-unsteady techniques such as Ranade's snapshot approach [57] whereby the unsteady contribution in the Navier-Stokes equation due to the motion of the blades is approximated, yield mixed results in reproducing flow within the tank, and will not be discussed further.

Comparison of steady and unsteady calculations were performed by Tabor et al [72] who compared the MRF and sliding mesh methodology solutions for a Rushton turbine stirred tank with the experimental data of Wu et al [74]. Mean velocities were well predicted using both methods. Additional sliding mesh studies include the turbulent flow Rushton turbine simulations of Ng et al [54] who implemented the approach of Luo et al [45] using a standard $k\epsilon$ turbulence model. Comparison of the simulated turbulent dissipation $\overline{\epsilon'}$ with LDA and PIV based estimates of dissipation were inconclusive due to measurement discrepancies between the two experimental methods. However, turbulent kinetic energy was, in general, under-predicted in the simulation.

General turbulence model assessment (or applicability to mixing flow) studies have also been performed by Jones et al [35] and Jaworski et al [31] using a rotating frame simulation of turbulent flow in a Rushton turbine and pitch-blade baffle-less tank respectively. Both studies found that RANS formulations, in general, poorly predict radial mean velocities near the impeller as well as turbulent kinetic energy. In addition, Jenne et al [32] performed a comparison of various two-equation turbulence models for steady-flow mixing simulations (on a quarter geometry) and, from the basis of their results, formulated an tuned $k\epsilon$ model based on matching the mean-flow velocity distribution within the impeller exit-stream. The result was a (ad hoc) tuned $k\epsilon$ model which accurately predicted the mean-flow in the jet and bulk-flow region (including the local dissipation maxima associated with the vortex cores very near the impeller trailing edge).

Additional computational studies investigated macro-instabilities within the tank associated with the blade trailing vortices and will be discussed in detail in §5.4.2.

Given the somewhat poor performance of RANS based turbulent flow simulations, further progress in mixing vessel simulation was made with the application of LES methodologies. Specifically, Eggels [25] performed an LES (Smagorinsky) based lattice-Boltzmann simulation using a static grid with time dependent forcing functions/boundary conditions applied to approximate the motion of the impeller. Mean radial and axial velocities compared well against data for a slightly different impeller geometry. Revstedt et al [59], [60] used a single static mesh to simulate a Rushton stirred tank. LES turbulence modeling was also used with source based fluid forcing via the impeller. Mean axial velocity was well predicted, but not radial velocity. Radial perturbation rms values were not well predicted, however the resulting turbulence spectra exhibited the familiar $-5/3$-slope associated with the equilibrium region. In addition, Verzicco at al [73] performed LES simulations for the purpose of validating their own (purported) DNS simulation.

In addition, to the above, Bakker et al [3] performed an LES simulation of a Rushton impeller in a baffled tank using a sliding deformable mesh. Although the presence of the trailing vortices were evident, no comparison was made between the simulated flow and experimental measurements.

Finally, Yeoh [75] implemented the sliding deformable mesh methodology and conducted a simulation of high Re (turbulent) flow in a Rushton stirred vessel using LES turbulence

modeling. Phase averaged flow velocities compared well with experimental results of Lee [41]. Turbulent RMS velocity components were qualitatively well predicted as well.

Direct Numerical Simulations of transitional (turbulent in the near-impeller region) mixer flows were attempted by Bartels et al [6], Verzicco et al [73] and Eggels [25]. Verzicco at al [73] performed DNS on an eight-bladed disk-less impeller for $Re = 2.7(10^3)$. Post-processing was modest and included comparisons with experiments for turbulent velocity fluctuations and mean velocities at various locations within the tank. These comparisons were satisfactory, however, the simulation was performed assuming flow symmetry at 180° blade angle (i.e. half-domain). In addition, with the exception of a favorable comparison of integrated dissipation with comparable LES results, no treatment of dissipation was presented and no justification for the assumption that the simulation could be termed DNS (e.g. in the sense of significantly resolving dissipation). Bartels et al [6] performed high resolution simulations of a Rushton turbine baffled tank using fixed (outer) and rotating (inner) reference-frames for Re ranging from 0.1 to $7(10)^3$. Although they well predicted integrated dissipation in the mixer, post-processing was rudimentary and included only a qualitative treatment of the mean-flow and TKE field. No detailed investigation of turbulence generation, transport or dissipation was made. In addition, the simulations failed to re-produce the development of the reverse-flow regime investigated by Hall [29] and Rice et al [61] (and subsequently reported by Barailler et al [5] for a stator-rotor mixer) at very low Re. Finally, Eggels [25] utilized the Lattice-Boltzmann technique to perform DNS on a Rushton turbine and although mean and perturbation velocities were well predicted, minimal post-processing or investigation of the flow physics was performed.

Thus, the literature presents deficiencies in the form of: Detailed investigation of the near-impeller and outer-tank region in the case of turbulent flow (experimental or computational via direct simulation). Comprehensive treatment of the TKE transport equation along with elucidation of the relevant transport mechanisms (in the inner-impeller and outer tank region), in particular investigation of the pressure diffusion/work mechanism. In addition, as will be shown in §5.4, a detailed investigation of the impeller trailing vortex flow dynamics (i.e. inception/formation and near impeller flow dynamics) is also lacking.

Numerical methods such as direct simulation (DNS) represents a substantial advantage in the investigation of turbulent or transitional flow in a mixer given the availability of the pressure field throughout the tank as well as the complete flow field in the near-impeller region. With respect to the latter, the use of Direct Numerical Simulation potentially allows for the detailed investigation of near impeller dynamics such as turbulent diffusion (viscous and pressure induced), dissipation and generation within the trailing vortex, as well as flow dynamics (e.g. separations) very near the impeller blades and disk. With respect to the former, direct simulation allows for the study of pressure-flow interactions such as turbulent pressure work.

Organization

It is the intent of this present study to redress the deficiencies described previously by performing high resolution calculations on a Rushton Turbine for the near-impeller turbulent flow regime (i.e. transition flow) at a $Re = 3(10)^3$. In addition, a thorough investigation of the blade vortex and near blade fluid dynamics shall be performed. Turbulent and mean-flow properties are to be obtained including the local turbulent dissipation and turbulent pressure diffusion/work.

This chapter will thus be organized as follows:

1. §5.2 gives an outline of the simulation strategy which includes the grid generation methodology as well as choice of appropriate spatial and temporal discretization.

2. §5.2.6 describes the post-processing procedure for the resulting high-resolution simulations of a transitional mixing vessel.

3. §5.2.7 begins the preliminary analysis of the high-resolution simulation results via bulk-flow properties used to gauge simulation convergence to an approximate steady-state solution.

4. §5.3 begins the detailed analysis of the simulated flow field. Specifically:

   §5.3.1 examines the instantaneous flow solution.

   §5.3.2 - §5.4 examines the mean-flow and pressure field including a detailed investigation of near impeller flow dynamics, force interactions and trailing vortices.

5. §5.5 investigates the contribution of the periodic motion to the overall flow field.

6. Finally, §5.6 gives concluding remarks.

Turbulent results will subsequently be presented in Chapter 6.

5.1.1 The Geometry

The geometry to be simulated under transitional conditions at a $Re = 3(10^3)$ is similar to that investigated previously in Chapter 4 under laminar flow conditions. With respect to Figure 4.1, the only changes from the previous geometry is the blade and impeller thickness (t_{BL} and t_d), and tank diameter T which now take on the values $1mm$ and $80.5mm$ respectively.

5.2 Simulation Strategy

Given the importance of simulation geometry (or mesh) in successfully performing Direct Numerical Simulations (DNS), a clear description of the methodology used for formulating the simulation grid requirements is important. The following illustrates the procedure:

- Review the methods used for experimental determination of turbulent dissipation and associated dissipative scales η and τ_η:§5.2.1
- Determine the approximate computational requirements in terms of cell counts (via an average cell size Δx) and the maximum value of the time-step Δt based on a control volume analysis of an approximate mixing vessel geometry (a toroid): §5.2.2
- Given the possibility of performing DNS on a mixing vessel based on the previous analysis, the distribution of turbulent scales, (spatial η and temporal τ_η), must be known in detail if an appropriate computational cell size distribution is to be calculated with the goal of resolving most of the turbulent dissipation ($\lesssim 80\%$). This distribution can be (approximately) found by performing an LES simulation of the flow, and extracting modeled dissipation ϵ_{LES} and thus η_{LES} from their definition: §5.2.3
- The LES modeling of the flow suggested previously may produce a correct distribution of turbulent scales within a fully turbulent vessel, but provide inaccurate absolute values. To minimize the possibility of this, experimentally measured fully turbulent values of turbulent dissipation length scales η, which for mixing vessels are limited in their availability, can be used to rescale the estimated dissipation length scales η_{LES} calculated from the LES simulation results. The end product is a corrected dissipation length $\eta_{LES}^{Corr.}$ and time scale $\tau_{\eta_{LES}}^{Corr.}$ field which is now assumed to be approximately correct. Once these length scales are known, DNS grid suitability can be verified by recourse to the corrected LES derived length $\eta_{LES}^{Corr.}$ and time scale $\tau_{\eta_{LES}}^{Corr.}$ distributions as calculated above.: §5.2.3

Finally, a short discussion of the envisioned post-processing procedure is discussed primarily from the point of maximizing statistical information while minimizing simulation time and storage requirements.

5.2.1 Estimation of Turbulent Length Scale η

In performing high resolution simulations of turbulent flow it is of critical importance to know the approximate turbulent length scale η distribution throughout the tank (or at least in the (turbulent) impeller exit stream). Experimental determination of η is of course predicated on determination of the local turbulent dissipation $\overline{\epsilon'}$. Methods for the determination of $\overline{\epsilon'}$ include direct calculation according to measurement of the turbulent velocity gradients (2.17) as well as dimensional methods based on $\overline{k'}$, $\sqrt{\overline{u'^2}}$ and a length scale ℓ. In the latter case, the local turbulent dissipation per unit mass can be formed on dimensional grounds by noting that

$$\overline{\epsilon'} \sim \frac{\overline{\sqrt{u'^2}}^2}{t}, \frac{\overline{\sqrt{u'^2}}^3}{\ell} \tag{5.2}$$

where u' is a perturbation velocity component. If the flow turbulence is isotropic, a single perturbation velocity (or something proportional to it) can be chosen (e.g. $\sqrt{\overline{k'}}$). Further-

more, if one assumes a constant turbulent length scale ℓ proportional to some macro-scopic scale such at the impeller diameter D, the general form for the expression of local turbulent dissipation based on dimensional methods becomes

$$\overline{\epsilon'} = A\frac{\overline{k'}^{3/2}}{D}, A\frac{\overline{\sqrt{u'^2}}^3}{D} \tag{5.3}$$

The constant of proportionality (determined via an energy balance over some volume (e.g. the overall tank volume or the discharge stream/impeller jet region)), based on one's choice of definition, has been measured by a number researchers yielding the following:

$$\overline{\epsilon'} = \begin{cases} 6.6\frac{\overline{\sqrt{u_r'^2}}^3}{D}, & \text{Laufhutte \& Mersmann [39]} \\ 4.4\frac{\overline{k'}^{3/2}}{D}, & \text{Costes \& Couderc [12]} \\ \frac{\overline{k'}^{3/2}}{D/10}, & \text{Kresta \& Wood [38]} \\ 4.4\frac{\overline{\sqrt{u_r'^2}}^3}{D/2}, & \text{Rao \& Brodkey [58]} \end{cases} \tag{5.4}$$

Returning to the dimensional approach (5.3), Wu et al [74] also measured the local, large scale, turbulent time scales τ_0 via the measured auto-correlation function. The local large scale turbulent length scale can be formed via the mean and perturbation radial velocities $\tau_0\sqrt{\overline{U_r}^2 + \sqrt{\overline{u_r'^2}}^2}$ giving the expression for local dissipation

$$\overline{\epsilon'} = 0.85\frac{\sqrt{\overline{u_r'^2}}^{3/2}}{\tau_0\sqrt{\overline{U_r}^2 + \sqrt{\overline{u_r'^2}}^2}} \tag{5.5}$$

where the constant A was found by equating the integrated calculated dissipation (via (5.5)) to the measured rate of reduction turbulent kinetic energy within an annulus around the impeller via an energy balance. An additional estimate of the dissipation can be made via the estimated local Taylor length scale resulting in (5.6)

$$\overline{\epsilon'} = 15\nu\frac{(u')^2}{\lambda^2} \tag{5.6}$$

as was performed by Komasawa et al [58] and Wu et al [74]. Lee et al [42] calculated the correlation function based on LDA measurements, and hence the micro (Taylor) length scale λ. The local dissipation was then estimated based on LDA measurements as

$$\overline{\epsilon'} = \frac{\overline{k'}^{3/2}}{\sqrt{3}\tau_0\overline{U_r}} \tag{5.7}$$

For the previous (5.7), local turbulence length scale is apparently estimated as $\ell \sim \sqrt{3}\tau_0\overline{U_r}$ where τ_0 is the integral time-scale calculated via the correlation function.

Applying an indirect approach, Escudie et al [27] have estimated $\overline{\epsilon'}$ based on the residual

of the TKE transport equation using measurements down to the Taylor length scale λ.

In contrast to previous dimensional methods of estimating local dissipation, direct measurement of turbulent dissipation require sufficient spatial resolution down to $\sim \eta$. Sharp et al [67] performed PIV measurement on a turbulent flow Rushton turbine down to a resolution of 7η in the impeller stream (or $3.5\eta_{av}$ where η_{av} is the average turbulent length scale in the tank as estimated based on total tank dissipation (impeller power derived)). Note that in the previous, the turbulent dissipation scales η in the exit stream was determined by measuring the impeller power input (torque based) and assuming $\overline{\epsilon'}_{jet} \sim 20\overline{\epsilon'}_{av}$. Finally, Sharp applied an LES Smagorinsky model to the measured mean-flow field in a turbulent stirred vessel and determined that the sub-grid turbulent dissipation was approximately 30% larger than the turbulent dissipation measured by PIV data, indicating that the PIV measurements captured $\approx 70\%$ of the dissipation. Baldi et al [4] carried out 2-D PIV measures of the local turbulent dissipation rates in a vessel stirred by a Rushton Turbine via measurements of most of the terms in (2.17) (based on the assumption of statistically isotropic turbulence). Local dissipation rates were then compared with that provided by the various dimensionally based estimates (5.4). Dimensional methods for estimated dissipation were found to underestimate the maximum and over estimate the minimum dissipation levels within the tank. Michelet et al [49] measure turbulent dissipation within a Rushton stirred reactor directly using LDA. Total dissipation within the impeller exist stream (jet) was calculated based on measurements of most of the terms in (2.17). However, comparison of jet-to-total tank dissipation (based on impeller power) indicated a significant underestimation of dissipation within the impeller stream. Finally, Ducci et al [21] performed LDA measurements with resolution down to approximately 1.5η evaluating most of the spatial gradients in the perturbation velocity field, and calculated turbulent dissipation $\overline{\epsilon'}$ directly via (2.17) for a Rushton turbine of $Re = 2(10^4) - 4(10^4)$. Extensive comparison with dissipation estimated via 2-D PIV measurements and dimensional methods were conducted. It was found that the direct LDA based calculation of dissipation was within $10 - 40\%$ of these other techniques. It is these measurement in conjunction with LES simulation dissipation calculations which will be used to estimate the turbulent dissipation length η and time τ_η scales throughout the tank.

5.2.2 Requirements: Approx. Analysis

To estimate the number of computational cells required for the high resolution simulation geometry we formulate the expression for the number of cells required to fill a toroidal region of normalized height $\Delta\hat{z} \equiv \Delta z/\mathcal{L}$, inner and outer normalized radius $\hat{r}_i \equiv r_i/\mathcal{L}$ and $\hat{r}_o \equiv r_o/\mathcal{L}$ where $\mathcal{L}$ is some geometric length scale. The cell size Δx is assumed to be proportional to the Kolomogorov length scale, or $\Delta x = \alpha\eta$. To determine the appropriate values for η we note that if the turbulent length scale is known experimentally for a given Re number, then using the scaling laws given by (2.31), an estimate for the length scale as a function of the Re can be calculated via

$$\frac{\frac{\eta}{\mathcal{L}}}{(\frac{\eta}{\mathcal{L}})|_{exp}} = (\frac{Re}{Re|_{exp}})^{-3/4} \Longrightarrow \eta = \mathcal{L}((\frac{\eta}{\mathcal{L}})|_{exp})(\frac{Re}{Re|_{exp}})^{-3/4} \tag{5.8}$$

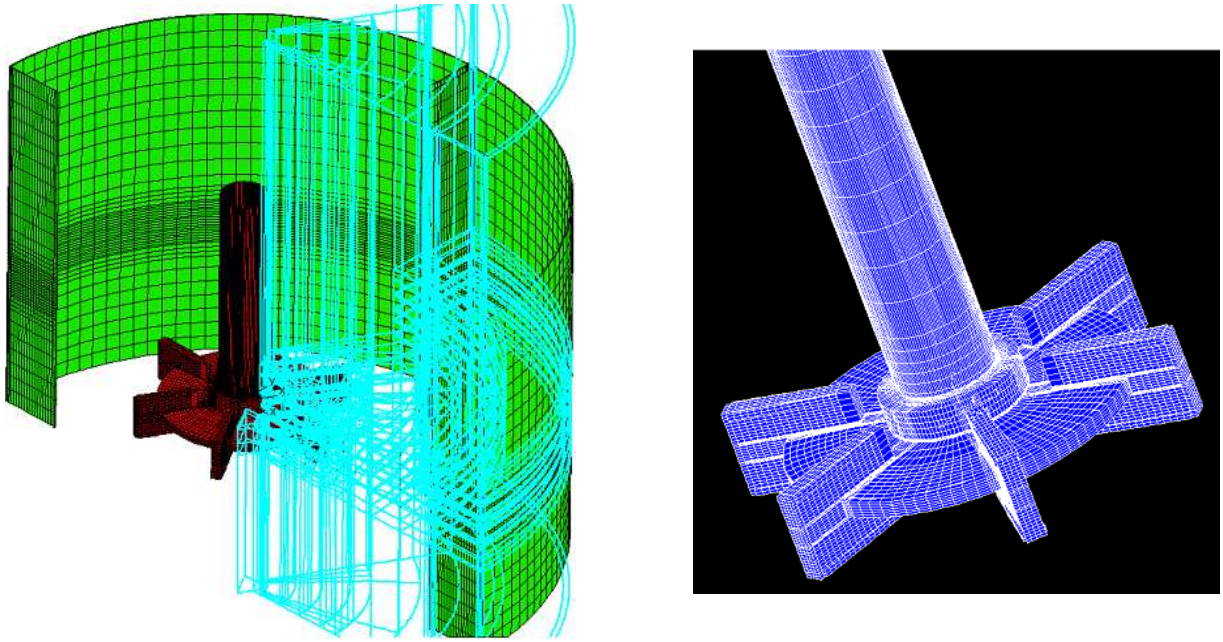

Figure 5.1: Block structure with LES (Coarse) surface grid and impeller surface geometry

Hence, recalling that $\Delta x = \alpha\eta$ the number of uniformly distributed cells to fill a Toroidal region is thus given by

$$N_{\text{Cells Toroid}} = \frac{\text{Vol. Toroid}}{\Delta\text{Vol. Cell}} = \frac{\mathcal{L}^3\pi[\Delta\hat{z}(\hat{r}_o^2 - \hat{r}_i^2)]}{[\Delta x]^3} = \frac{\mathcal{L}^3\pi[\Delta\hat{z}(\hat{r}_o^2 - \hat{r}_i^2)]}{[\alpha(\mathcal{L}(\frac{\eta}{\mathcal{L}})|_{Exp.})(\frac{Re}{Re|_{Exp.}})^{-3/4}]^3} \tag{5.9}$$

where the scaling length $\mathcal{L}$ refers to the macro-scopic length scale (e.g. tank diameter T). For a 3^{rd}-order spatial discretization scheme with a target resolution of 80% of the turbulent dissipation (with an associated 15% aliasing error (see §C.4)) we have $\alpha \equiv \Delta x/\eta = 2.45$ where α has been set taking into account the dissipation resolution requirements as well as discretization error for a 3^{rd} order upwind differencing.[2] Near the impeller the average length scale for the fully turbulent experiment is $\eta|^{L=0.294m}_{Re=32(10)^3} = 0.035mm$ as provided by Ducci et al [21]. Thus, for the current study $\mathcal{L} = T = 0.0805(\text{m})$, $Re = 3(10^3)$, $\Delta\hat{z} = 0.1$, $\hat{r}_i = 0.2$ and $\hat{r}_o = 0.32$ utilizing (5.9) gives $N_{\text{Cells Toroid}} \approx 3.75(10^6)$. Thus, to populate the near

[2]This is found by conducting a spectral analysis of the *resolved wave number* $\|\kappa\|$ *as a function of the true input wave number*. Specifically, if one seeks a discretized 3^{rd}-order 1-D finite-difference representation of a wave with wavelength ℓ and wave number $\|\kappa\| = 2\pi/\ell$, one finds that the required (discretization) nodal displacement $\Delta x \leq 0.218\ell$ to maintain wave number aliasing errors to less than 15%. Thus, if the relevant wave length we wish to resolve (with aliasing error less than 15%) is $\ell = 11.2\eta$ (see Figure 5.3) then the required maximum nodal displacement is $\Delta x = 0.218\ell = 0.218(11.2\eta) = 2.45\eta$.

impeller region, (which is assumed to exhibit fully turbulent flow), requires approximately 4 million uniformly distributed cells. Incidentally, from the scaling laws and experimental measurements the estimated average Kolomogorov length scale (for the current study) is $\eta|_{Re=3(10)^3}^{L=0.0805m} = 0.056mm$ via (5.8).

Determination of the minimum required simulation time-step Δt and the number of time-steps per revolution are made via two possible methods: A CFL number and a turbulence/Kolmogorov time-scale τ_η based method. The first method imposes an upper limit on the CFL number within the toroidal domain. Specifically, the maximum velocity within the domain is $\propto V_{tip}$ or $V \equiv \beta V_{tip}$, thus the CFL number can be defined as

$$CFL \equiv \frac{V\Delta t}{\Delta x} = \frac{\beta V_{tip}\Delta t}{\Delta x} = \frac{\beta V_{tip}\Delta t}{\alpha\eta} \Longrightarrow \Delta t = CFL\frac{\alpha\eta}{\beta V_{tip}} = CFL(\frac{\alpha\eta}{\beta\frac{(Re)\pi\nu}{D}}) \tag{5.10}$$

where (4.1) has been used to express tip velocity as a function of Re. For $\alpha = 2.45$, $\beta = 0.7$ $Re = 3(10^3)$, $CFL = 0.5$, $\eta = 0.056mm$, $D = \mathcal{L}/3$ and $\mathcal{L} = T = 0.0805m$ we have $\Delta t = 2.787(10^{-4})sec.$ Again, from the definition of the Re, (4.1) in terms of tip velocity, we have $N|_{Re=3(10^3)} = 4.1(rev/sec.) \approx 240rpm$ and via (5.10)

$$\left.\frac{steps}{rev.}\right|_{cfl\ based} = (N\Delta t)^{-1} = 859(tmst/rev.) \sim 1,000(tmst/rev.) \tag{5.11}$$

If instead we take the characteristic turbulent dissipation time-scale τ_η and set the required simulation time step as some small fraction of the (dissipative) eddy circulation time τ_η, say $\tau_\eta/10$ we have via (2.31) $N\tau_\eta \propto Re^{-0.5} \Longrightarrow \tau_\eta \sim 1/(N\sqrt{Re})$

$$\left.\frac{steps}{rev.}\right|_{\tau_\eta\ based} = (N\Delta t)^{-1} \approx \frac{10(N)Re^{0.5}}{N} = 10Re^{0.5} = 547(steps/rev.) \sim 1,000(tmst/rev.) \tag{5.12}$$

where incidentally $\tau_\eta|_{Re=3(10)^3} \sim 4.4(10^{-3})sec.$

Thus, the previous results indicates a requirement for, on the order of 3.5 million cells and $1,000$ time-steps per impeller revolution to resolve turbulence within the turbulent (near impeller) exit stream.

5.2.3 LES Geometry and Simulations

The previous analysis provides an approximate estimate for the average dissipation scale within the near impeller region. However, to formulate a more precise estimate for the distribution of dissipation length scales throughout the tank, an LES simulation of the mixing vessel was performed. The resulting calculated dissipation scales η_{LES} (based on $\epsilon = \epsilon_{LES} = \epsilon_{SGS} + \epsilon_{RS}$) was then corrected at a precise location within the tank yielding an experimentally

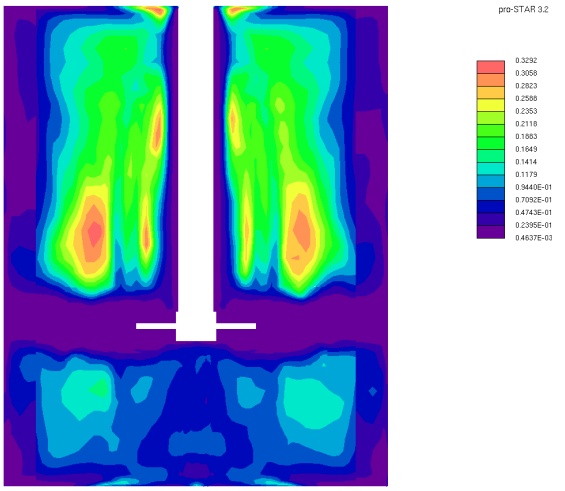

(*a*) τ(s) in $y-z$ plane for $x=0$

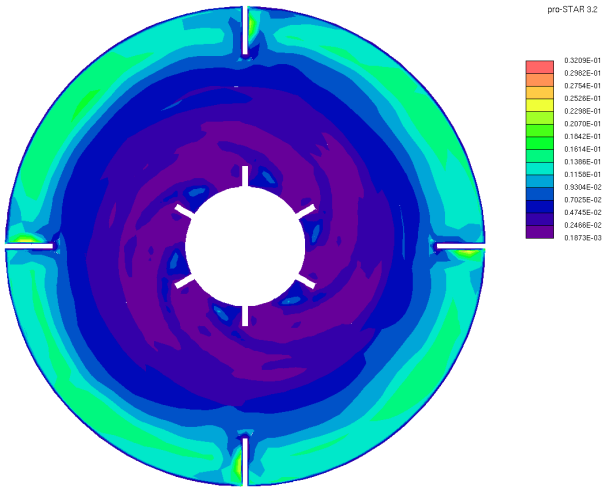

(*b*) τ(s) in Disk-plane ($z=0$)

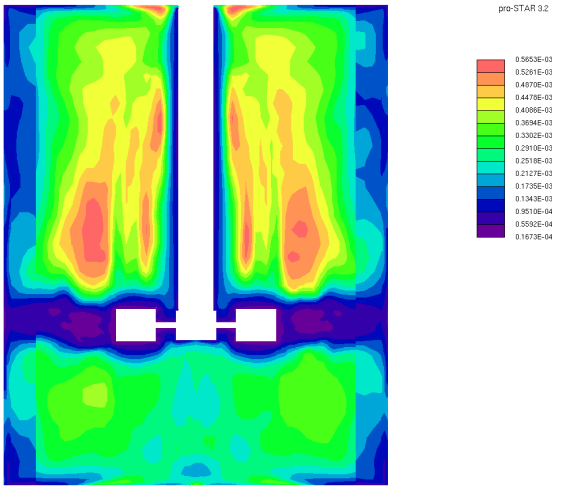

(*c*) η(m) in $x-z$ plane for $y=0$

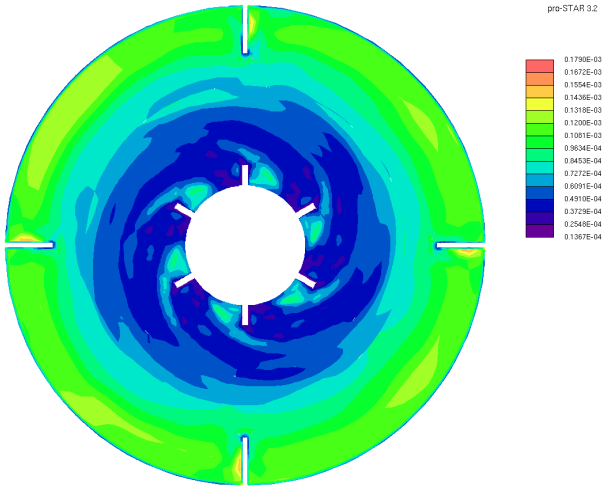

(*d*) η(m) in Disk-plane ($z=0$)

Figure 5.2: LES derived Kologorov length η and time τ_η scales

corrected length scale $\eta_{LES}^{Corr.}$.[3]

However, given that pseudo-experimentally derived dissipation length scales will be used to formulate the transitional DNS mesh, it is prudent and necessary to validate first the (coarse) LES geometry from which the DNS grid/geometry will be based both for the transitional $Re = 3(10^3)$ and fully turbulent $Re = 32(10^3)$ flow: The rationale being that the LES simulated flow field should qualitatively represent the flow while the calculated overall power consumption should be on the order of the estimated experimental values.

[3]It should be stated that the LES model used is the static Smagorinsky model which assumes turbulent flow throughout the flow domain, isotropic turbulence and explicit resolution of down to turbulence scales at the upper end of the equilibrium range. In addition, a grid sensitivity study was not performed. Thus none of these modeling assumptions can be assumed to be satisfied. Hence, the requirement to rescale LES calculated dissipation time τ_η and length scale η.

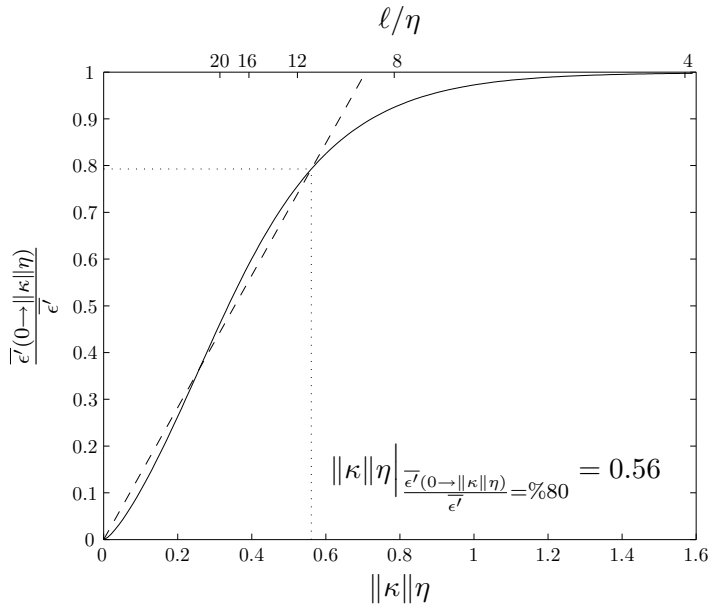

Figure 5.3: Fractional integrated dissipation $\frac{\overline{\epsilon'}(0\rightarrow\|\kappa\|\eta)}{\overline{\epsilon'}}$ for $Re_\lambda = 100$ ($Re \approx 3000$).

The LES (and subsequent DNS) Rushton turbine geometries were created via a commercial multi-block unstructured pre-processor utilizing hexahedral cells. The block structure was formulated in such a way as to provide the maximum control of cell refinement near the impeller and baffles in general, and near all surfaces (stationary and moving) specifically. In addition, the block structure accommodates moderate variation in impeller and tank geometry (if required). The block structure and tank/impeller surfaces are shown in Figure 5.1 along with the (coarse) LES impeller surface. Of particular importance is the resolution of the boundary-layer on the impeller disk and blades surfaces as well as the tank outer/upper/lower walls and baffles. For turbulent flat plate boundary layers, the laminar sublayer (where the mean velocity profile varies linearly with wall distance) extends throughout the region $y^+ \lessapprox 5 - 10$. Thus, to resolve the boundary-layer and correct surface shear stress it is important that the first cell off the wall has a $y^+ \lessapprox 5-10$. Recalling the definition of $U^+ \equiv \overline{U}/U^*$ we have from the seventh power-law turbulent velocity profile $U^+ = 8.74(y^+)^{1/7}$ evaluated at the boundary layer thickness δ corresponding to free-stream velocity U_∞ the following expression for the normalized wall shear-stress

$$\frac{\tau_w}{\rho\overline{U}_\infty^2} = 0.0225\frac{1}{(\frac{\delta\overline{U}_\infty}{\nu})^{1/4}} \tag{5.13}$$

where (5.13) is a function of the turbulent boundary-layer thickness. To proceed further we note the boundary layer momentum integral derived for an appropriate CV gives

$$\frac{\tau_w}{\rho\overline{U}_\infty^2} = \frac{d\delta}{dx}\int_{\eta=0}^{1}\overline{U}(\hat{\eta})(\overline{U}_\infty - U(\hat{\eta}))d\hat{\eta} \tag{5.14}$$

where $\hat{\eta}$ is the scaled normal displacement from the wall y/δ. Utilizing (5.13), (5.14) and assuming a seventh power profile for the mean turbulent flow velocity within the boundary-

layer ($\frac{\overline{U}}{\overline{U}_\infty} = \hat{\eta}^{1/7}$) yields

$$\frac{\delta}{x} = 0.37 {Re_x}^{-1/5} \tag{5.15}$$

where $Re_x \equiv \frac{\overline{U}_\infty x}{\nu}$. Thus, one can combine (5.15) and (5.13) along with the definition of the y^+ ($y\sqrt{(\tau_{wall}/\rho)}/\nu$) to specify $y = f(y^+, Re_x, \overline{U}_\infty)$. To utilize the previous in formulating the required minimum target first cell off the wall distance y one specifies $\overline{U}_\infty$ as some fraction β of the impeller tip speed, or

$$\overline{U}_\infty \equiv \beta V_{tip} = 2\pi\beta N r_{imp} = \frac{\beta\pi\nu}{D}\frac{D^2 N}{\nu} = \frac{\pi\beta\nu}{D} Re \tag{5.16}$$

By choosing a value of $\beta = 0.5$, setting a target first cell y^+ value equal to 2 ($\lesssim 10$) and utilizing (5.16), (5.15), (5.14) a first cell off the wall distance can be calculated. Specifically, the minimum simulation boundary-layer thickness will be associated with the highest Re flows, in this case $Re = 32(10^3)$, while we choose a representative length scale (plate displacement x) equal to $R/2$ where R is the impeller radius. Next, we note that near the impeller, the characteristic velocity is $\lessapprox V_{tip}$ while far away from the impeller, fluid speed decreases. Thus, for all surfaces on the impeller we set $\beta = 0.5$ (corresponding to half the tip speed) while along the tank walls and baffles we set $\beta = 0.125$. The resulting calculated target y distance based on the $Re = 32(10^3)$ operating condition was used as the approximate upper-bound on first cell normal distance from the wall for the LES simulations of both high and low Re ($32(10^3)$ and $3(10^3)$.[4] This can be justified since $\delta \propto Re^{-1/5}$, a reduction in Re from the high to low Re number operating condition results in an increase in boundary-layer thickness on the order of 60%. In addition, a decrease in Re by an order of magnitude increases the first cell off the wall y^+ value from 2 to 15 $\sim$ 10: just outside the viscous sub-layer. Thus, the grid formulated for $Re = 32(10^3)$ is still approximately acceptable for simulating a lower $Re = 3(10^3)$ using LES.[5]

5.2.4 LES Results and DNS Geometry

As previously stated, the determination of an approximate distribution of the turbulent dissipation time τ_η and length scales η throughout the vessel is of critical importance. It is this scale distribution which is used to formulate an approximate DNS mesh cell size distribution as well as the corresponding simulation time-step Δt. Again, the following procedure for the determination of a DNS cell size distribution will be utilized:

[4] A representative calculation for $Re = 32(10^3)$, $x = r/2 = 6.7(10^{-3})$m with $K = 2$, $\nu = 10^{-6}$ gives $U_\infty = 1.87$m/s. The associated turbulent boundary-layer thickness via (2.60) is $\delta = 3.75(10^{-4})$. The calculated non-dimensional local wall shear stress $\tau_{wall}/(\rho U_\infty^2)$ is $4.27(10^{-3})$ (or $\tau_{wall} = 14.9 N/m^2$) via (5.13). Finally, setting the target $y^+ = 2$ and utilizing the definition of $y^+ = yu*/\nu = y(\sqrt{\tau_{wall}/\rho})/\nu$ gives $y_{target} = y^+\nu/(\sqrt{\tau_{wall}/\rho}) = 2(10^{-6}/\sqrt{14.9/10^3} = 1.64(10^{-5}) = 0.0164mm$.

[5] From (5.13) $\tau_{wall}^{turb.} \propto \overline{U}_\infty^{7/4}\delta^{-1/4}$ while noting from (5.15) $\delta \propto Re^{-1/5}$ or $\delta \propto \overline{U}_\infty^{-1/5}$. Thus, $\tau_{wall}^{turb.} \propto \overline{U}_\infty^{7/4}\delta(\overline{U}_\infty^{-1/5})^{-1/4} = \overline{U}_\infty^{36/20} = \overline{U}_\infty^{9/5}$. And given that $\overline{U}^* \propto \tau_{wall}^{-1/2}$ we have $\overline{U}^* \propto \overline{U}_\infty^{9/10} \approx \overline{U}$ for the turbulent boundary-layer.

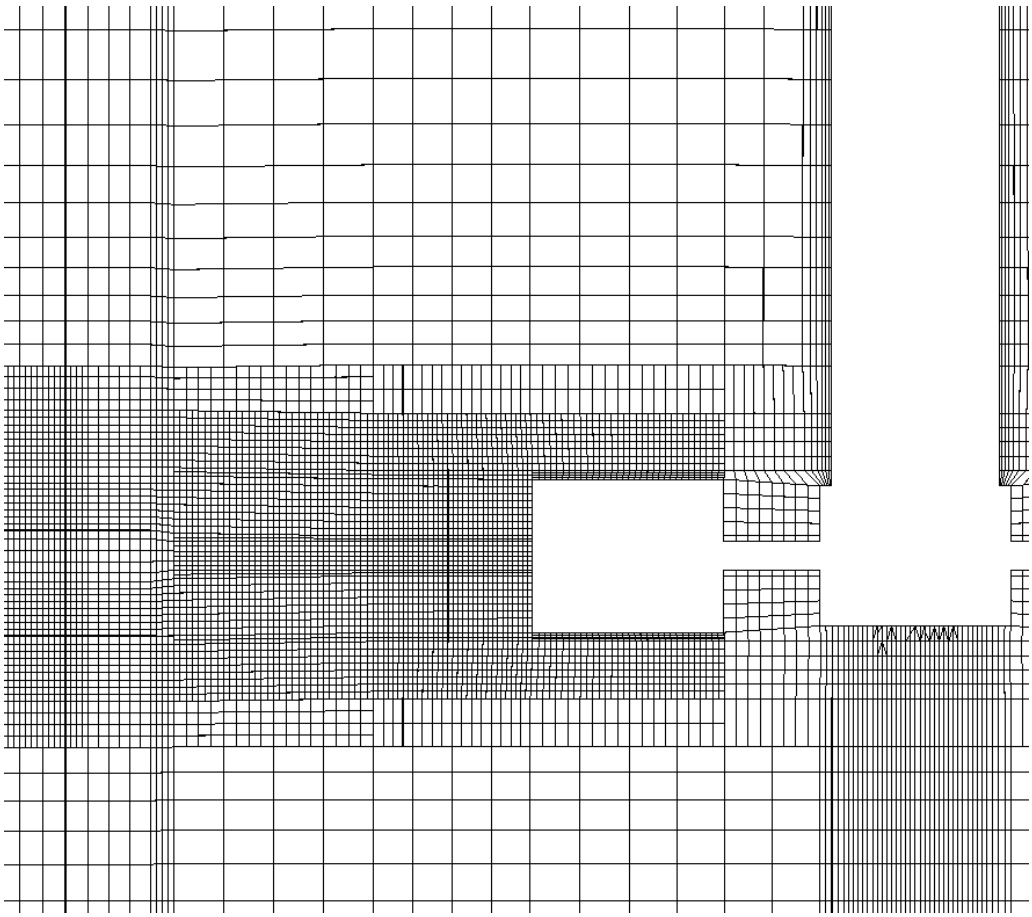

(a) $x-z$-plane $y=0$

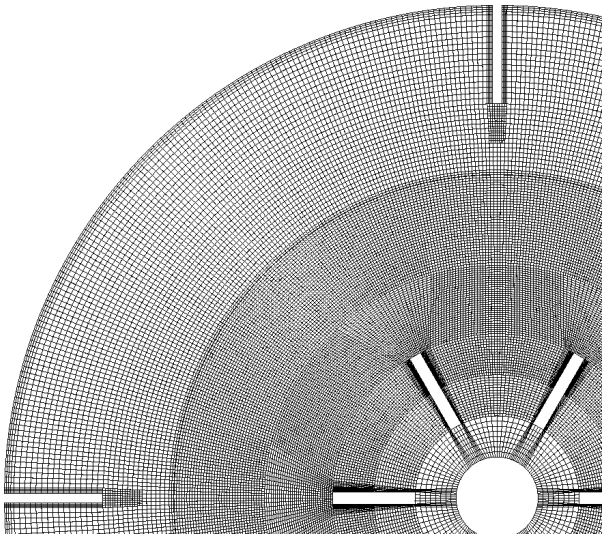

(b) $x-y$-plane $z=-H_{BL}/4$

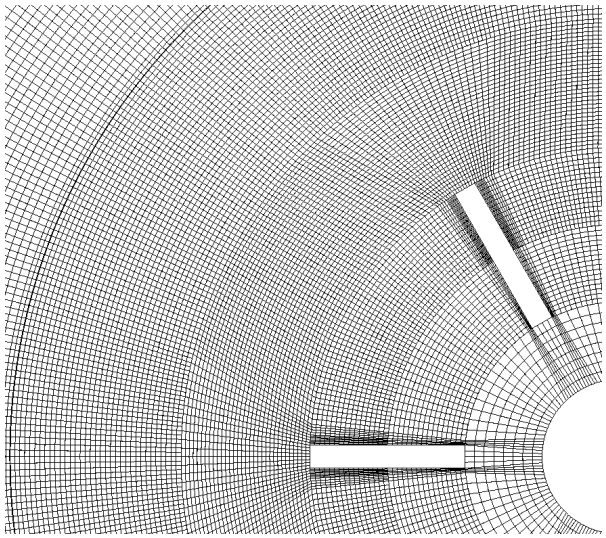

(c) $x-y$-plane $z=-H_{BL}/4$ Magnified

Figure 5.4: High resolution geometry mesh at various planes

1. Perform LES simulations at $Re = 32(10^3)$ and $Re = 3(10^3)$ to obtain an estimate of the dissipation scale distribution throughout the vessel (i.e the Kolmogorov scales η and τ_η via their definition (2.79) and (2.29) where $\overline{\epsilon'}$ is calculated via (2.79)). These simulations utilized the LES Smagorinski turbulence model formulation with first cell off the wall Van Driest damping.

2. Utilize experimentally derived $Re = 32(10^3)$ data on point-position values of η in the near-impeller region (see Ducci et al [21]) and scaling laws for η to re-scale the LES derived distribution of η and τ_η corresponding to $Re = 3(10^3)$ via (5.8). This yields a semi-experimental estimate of the turbulence scales distribution near the impeller and jet.

3. Set a target of approximately $\approx 80\%$ for resolved dissipation and estimate required grid length scales.

4. Perform cell coarse grid refinement to produce an equivalent DNS geometry according to the following procedure:

   If cell has a non-uniform aspect ratio, refine to rendering cell approximately symmetric and then proceed with additional re-sizing uniformly on all cell dimensions as required (*assumes turbulence is approximately isotropic*). Near wall cells necessarily having an aspect ratio $\not\sim 1$ and were approximately refined in all computational directions in accordance with the required reduction in maximum cell length scale Δx.

The above procedure will now be described in detail.

Given that we are interested in ultimately obtaining the turbulent length and time scale (η and τ_η) variations in space for a $Re = 3(10^3)$, it is important to validate the geometry and modeling used to obtain these estimates. Specifically, two LES simulations were performed at $Re = 32(10^3)$ and $Re = 3(10^3)$. These simulations were performed until the calculated power number based on dissipation essentially stabilized. For $Re = 32(10^3)$ and $Re = 3(10^3)$ the power number at simulation termination was ≈ 2.5. The corresponding experimental measured power consumption is ≈ 4 and ≈ 3 for $Re = 32(10^3)$ and $Re = 3(10^3)$ respectively via the measurements of Rutherford et al [65] and Rushton [13]. Assuming the LES derived simulation dissipation (and thus η_{LES}) field approximately yields the true turbulent scale distribution, at least near the impeller, experimentally derived data can be used to *correct the distribution to obtain a more accurate prediction of the scales* or $\eta_{LES}^{Corr.}$ and $\tau_{\eta_{LES}}^{Corr.}$. To this end, Item 2 specifies the correction of these scales predicted by the LES simulation. Experiments performed by Ducci et al [21] for $Re = 32(10^3)$ yield a minimum Kolmogorov length scale of 0.024mm ($\eta/T = 0.082(10^{-3})$) at the disk-plane for $r/T = 0.22$ (note that $R/T = 0.166$). Using the Kolmogorov scaling laws (5.8) yields an estimated, re-scaled Kolmogorov length scale η of $0.038(10^{-4}) \approx 0.04(10^{-3})m$ for $Re = 3(10^3)$, $r/T = 0.22$ at the disk-plane.[6] A plot

[6] Given that the experimental value of $\eta = 0.024(10^{-3})m$ corresponds to a $Re = 32k$ with $\mathcal{L} \sim T = 0.294m$, while the desired scale is associated with a $Re = 3k$ and $\mathcal{L} \sim T = 0.0805m$ we get $\eta_{Re=3k}^{estimate} 0.024(10^{-3}) \frac{0.0805}{0.294} [\frac{32(10^3)}{3(10^3)}]^{3/4} = 0.038(10^{-3})m \approx 0.04(10^{-3})m$.

of the resulting rescaled Kolmogorov scales are given in Figure 5.2. As can be seen, the minimum time and length scales are associated with the turbulent near-impeller region while the maximum length and time scales are centered about the upper and lower re-circulation zones far from the impeller. In anticipation of Item 4 it will be noted that these rescaled turbulence lengths could be utilized to determine a suitable grid cell size distribution by recalling that for perfect numerical resolution, $\Delta x = 11\eta$ corresponds to $\approx 80\%$ resolution of turbulent dissipation $\overline{\epsilon'}$. If a 3^{rd}-order upwinded spatial discretization scheme is used $\Delta x = 2.8\eta$ and refinement of the coarse (LES) grid yields the high resolution grid as shown in Figure 5.4. Note that the mesh length scale Δx are smallest within the impeller jet or impeller stream, and largest in the bulk flow recirculation zone above and below the impeller jet. In addition, the inter-process domains (utilized by the parallel Navier-Stokes solver described in Chapter 3) are distributed amongst processors as indicated by the displaced and approximately equi-cell domains shown in Figure 5.5.

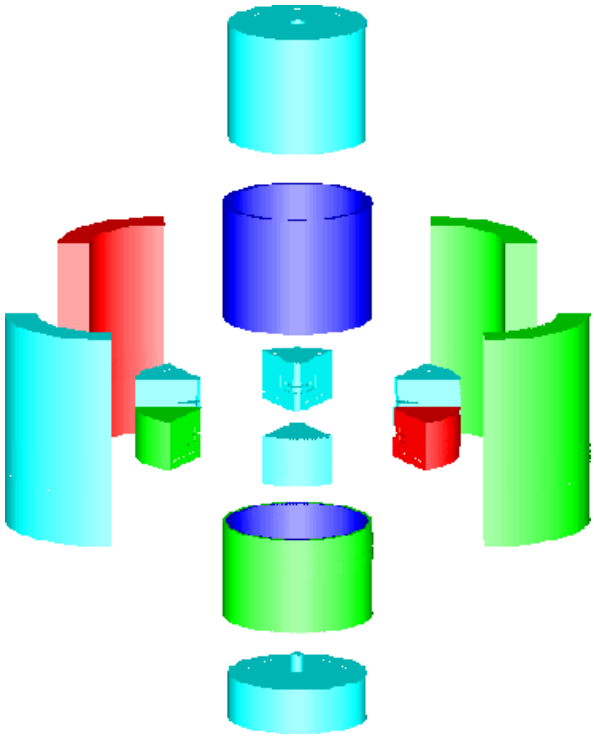

Figure 5.5: DNS computational domain decomposition grouped by process domain (*not* according to color).

5.2.5 Planned DNS Simulation

From the experimentally corrected LES derived mesh, using a newly parallelized flow solver, a high resolution (DNS) flow simulation will be performed. From the procedure given in the previous section, the resolved dissipation is expected to be $\lesssim 80\%$ of the total turbulent dissipation. The resulting DNS geometry contained $\approx 3.7(10^6)$ cells and a simulation time-step $\Delta t \approx 1.5(10^{-4})(sec.)$ corresponding to $\approx 1,700 tmst/rev$. The discretization schemes to be used are 2^{nd}-order Euler-Implicit in time, 3^{rd}-order Quadratic Upwind (QUICK) for the

convective and 2^{nd}-order Central Differences for the diffusive fluxes.

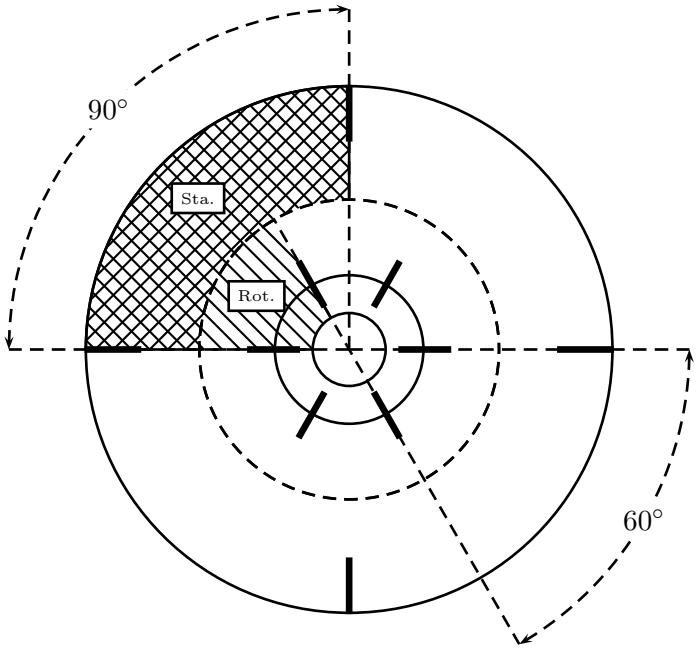

Figure 5.6: Illustration of statistical sample regions: Impeller position associated with $\theta = 0°$, $\phi = 45°$.

5.2.6 Post-processing Procedure

Given the computationally intensive nature of the DNS calculations in terms of solution storage space and running time, it is advantageous, not to say critical that the most statistical information be gathered per impeller revolution. In terms of the spatial region in which we require statistical information, within the rotating mesh (i.e. in the impeller region), we desire statistics about the flow within a 60° wedge spanning two adjacent impeller blades. Likewise, within the stationary mesh (i.e. in the outer tank and baffle region), we desire statistics for the flow over a 90° region spanning two adjacent baffles. These regions are specified in Figure 5.6 and are denoted via 'Rot 'and 'Sta 'corresponding to the rotating and stationary regions respectively.

The flow solution to be sampled in terms of impeller blade angles ϕ are $-30°$, $-20°$, $-10°$, $0°$, $10°$ and $20°$ for an observation plane angle $\theta = 45°$ (see Figure 4.1). Note that the number of blade passes per baffle is 6 per revolution, thus if all vector quantities are expressed in cylindrical coordinates, for any given blade angle ϕ there exist $4(6) = 24$ samples of the rotating and stationary sample domains per impeller revolution. To illustrate this we proceed through a 60° rotation of the impeller using 30° steps as shown in Figures 5.7. Specifically, Figure 5.7(a) shows a geometry with a relative impeller angle $\phi = 0°$ where the circled region pairs (⑥ &⓪) and (⑧ & ③) also correspond to a impeller angle $\phi = 0°$ (for $\theta = 45°$). Likewise, for the impeller rotation of 30° as shown in Figure 5.7(b)the circled region pairs (①

&⑦) and (⑨ & ④) correspond to a configuration with impeller angle $\phi = 0°$. Finally, for the impeller rotation 60° the circled region pairs are (⑤ &⑥) and (⑧ & ②) correspond to the same configuration. Hence, through 60° of impeller rotation there are 2 snap-shots each containing 2 statistical region pairs with an impeller configuration of $\phi = 0°$. Thus, for a full impeller revolution there are a total of $2(2)6 = 24$ snap-shot-regions from which to sample statistics. If all vector quantities are expressed in cylindrical form, the resulting statistical pairs can be aggregated and projected onto one representative region pair (stationary and rotational) for visualization. In terms of Figure 5.7 all statistical information, expressed in cylindrical coordinates derived from the region pairs in (a), (b) and (c) can be collapsed (for example) onto the region pair ⑥ & ⓪ in (a). Thus, if $\approx 1,000$ samples are required to extract approximately converged statistics, then a simulation time corresponding to 40 impeller revolutions would be necessary. Note that the previous treatment is suitable for extraction of phase resolved data, *but if variations in flow properties with impeller angle ϕ is negligible, then all solution snap-shots can be utilized to calculate rotation and stationary region mean properties.*

5.2.7 Bulk Quantities Validation

Desired quantities to be extracted from the simulation results specifically include:

- Mean and perturbation velocity and pressure fields
- Calculated Reynolds stress components to fully describe the local rate of turbulent convection/diffusion momentum flux
- Calculated dissipation and TKE field within the tank, including TKE transport terms such as Convection, Diffusion, Dissipation and Generation

In terms of required statistics, LES simulations of mixing vessels require ~ 100 samples to achieve converged Reynolds stress components (see Yeoh [75]). On the other hand, gradients of turbulent stresses, measured experimentally, achieve statistical convergence after approximately $1,000 - 10,000$ samples [20]. With respect to the achievement of a statistically fully-developed flow, high Re LES simulations of mixing vessels require at least 40 revolutions from start-up (see Yeoh [75] and Verzicco et al [73]). Thus, for the present study it is assumed that at least 1000 samples are required for approximate statistical convergence of all terms in the $\overline{k'}$ transport equation, while $\gtrapprox$ 40 impeller revolutions are required to achieve (statistically) fully-developed flow, after which statistics can be collected.

To determine the reliability of the simulation (in a bulk sense), integrated dissipation (i.e. power consumption) is used to compare the simulation Power Number $\mathcal{P}$ to experimentally derived measurements. Specifically, data for $\mathcal{P}$ as a function of Re are provided by Rushton [13] for a generic turbine, while the variation of $\mathcal{P}$ are provided by Rutherford et al [65] for various geometric parameters. The estimated value for $\mathcal{P}$ at $Re = 3(10)^3$ for the turbine used in this study is ≈ 3.0. This estimate is based on the experiments of Chapple et al [10] who measured the power number (via impeller torque) over a range $Re = 200 - 10^5$ for an turbine

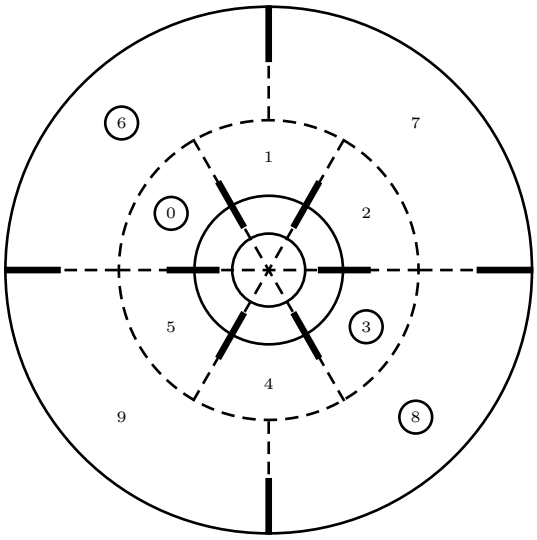

(a) Impeller Angle=0°

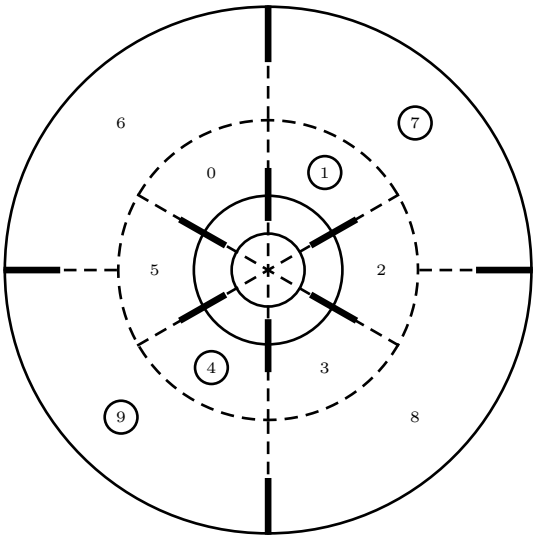

(b) Impeller Angle=30°

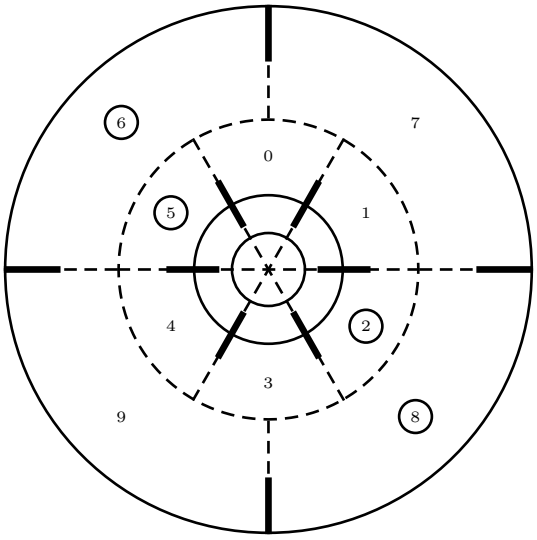

(c) Impeller Angle=60°

Figure 5.7: Illustraction of impeller symmetry.

disk/blade thickness-to-disk ratio t/D of 0.034 and 0.011 resulting in a power number of 3.7 and 4.7 respectively for a $Re = 3(10^3)$. This yields a variation in $\Delta\mathcal{P}/\Delta(t/D) = 43.5$. The turbine geometry used in this study is of slightly thicker disk and blade thickness $t/D = 0.037$ resulting in an estimated or adjusted power number for the current configuration $\mathcal{P} = 3.55 \approx 3.5$.[7] Thus, validation of the high resolution simulation results was performed via calculation of bulk parameters such as the power $\mathcal{P}$ and flow $\mathcal{F}$ numbers. With respect to the former,

[7]From Chapple et al we have $\mathcal{P}|_{Re=3k,t/D=0.034} = 3.7$. In addition, $\partial\mathcal{P}/\partial(t/D) = -43.5$ where $t/D = 0.037$ for the present geometry studies. Thus $\mathcal{P}|_{Re=3k,t/D=0.037} = 3.7 - 43.5(0.037 - 0.034) = 3.55$.

total dissipation ϵ was calculated via a finite volume summation based on (2.18).

$$\text{Total/Integrated Dissipation} = \sum_{Vol} \Delta\epsilon =$$
$$\sum_{Vol} \Delta(\text{visc. dis. power }) = \sum_{Vol} \mu(\frac{\partial U_i}{\partial x_j} + \frac{\partial U_j}{\partial x_i})\frac{\partial U_i}{\partial x_j}\Delta Vol \tag{5.17}$$

During the simulation (5.17) was calculated at each time-step and is plotted in Figure 5.8 from 25 to 90 revolutions. As can be seen via the trend-line, $\mathcal{P} \approx 3.0$ with a slight increase over the interval. Again, the results derived from Chapple et al [10] give an experimentally based estimate for the $\mathcal{P} = 3.55 \approx 3.5$.

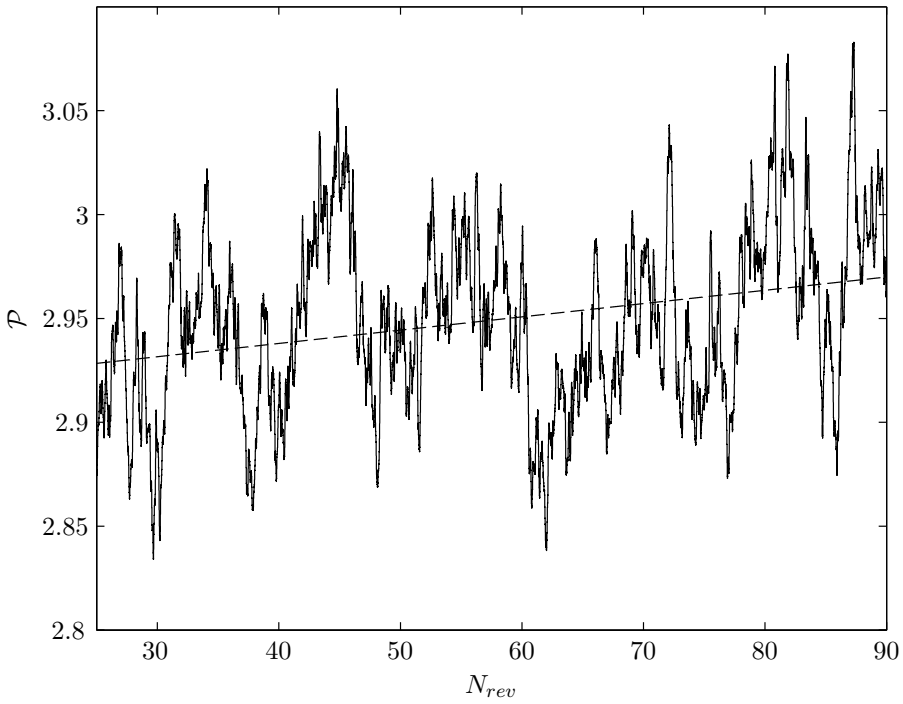

Figure 5.8: Simulation Power Number $\mathcal{P}$ as a function of impeller revolutions N_{rev} including trend-line.

The flow number $\mathcal{F}$ was also calculated and compared with available approximations in the literature. From the definition given by (2.87) the volume flow rate $\dot{Q} = \pi H_{BL} D \overline{V}_r$ can be determined via surface integration over a band centered at the impeller disk down-stream from the impeller blade

$$\dot{Q} = r \int_{z=z_{lower}}^{z_{upper}} \int_{\theta=-\pi}^{\pi} \hat{r} \cdot \vec{\overline{V}} dz d\theta \tag{5.18}$$

Following the suggestions of Hall [29] setting $z_{upper} = -z_{lower} = H_{BL}/2$ and $r = 1.12R$ yields a flow number of 0.73. Measured flow numbers (which are dependent on impeller geometry (e.g. t/D)) range from 0.75 for fully turbulent flow ($Re \to \infty$, i.e. fully turbulent flow ([76] Yianneskis et al)) to 0.9 (Hall [29]) for $Re = 42(10^2)$.

Additional simulation checks include y^+ values for the first cell off the wall which was found to be $\approx 0.5 \rightarrow 1.5$ on the outer tank wall and baffle surfaces, and $\approx 0.1 \rightarrow 4$ on the impeller surface. The flow domain average CFL number was ≈ 0.1 while the maximum values ≈ 1.0 are confined to mesh refinement regions on the impeller upper/lower tip.

5.3 Simulation Results

The following examines high resolution simulation results for transitional flow $Re = 3(10^3)$ in a Rushton turbine and is organized as follows:

- §5.3.1 examines the instantaneous flow solution at 90 revolutions via visual inspection. The flow is found to exhibit turbulence (flow populated with unsteady eddies of various scales) within the impeller stream and near the outer-tank wall. In addition, via visualization of the swirl parameter, the impeller trailing vortices are found to be present.

- The mean-flow is calculated and presented in §5.3.2. Specifically, the section serves to illustrate the double and triple-looped recirculation pattern as well as establish the existence of the blade trailing vortices within the impeller stream.

- For the purpose of validation §5.3.3 gives a comparison of mean axial, radial and circumferential experimental and simulated flow velocities within the impeller-stream. Good quantitative agreement is found between the experimental results of Micheletti [50] for an identical geometry and the simulation mean-flow results.

- Section §5.3.4 investigates the normalized pressure and viscous force interactions with specific reference to the blade vortex dynamics (i.e. position and structure). In accordance with the definition of the Re as the ratio of inertial to viscous forces, the mean-flow is found to be pressure driven with negligible viscous forces except within the boundary-layer of the impeller surface. With respect to pressure forces, a detailed investigation of the blade trailing vortex is also performed, whereupon the vortex core is identified and tracked based on a mean-flow pressure force convergence method.

- In §5.4 the impeller trailing vortex is examined in further detail by calculation of the flow velocity in the vortex relative frame as well as visualization using stream-lines in the impeller frame of reference. The mechanism responsible for the vortex formation is explicitly identified: The inception of the vortex on the blade suction-side (SS) due to upper and lower blade tip pressure driven separation, followed by (SS) trailing edge separation and subsequent detachment of the vortex from the blade.

- The impeller/tank relative periodic motion (e.g. $\tilde{V}$ and $\tilde{k}$) is calculated and found to be negligible compared to the mean-motion (e.g. $\overline{V}$ and $\overline{k}$).

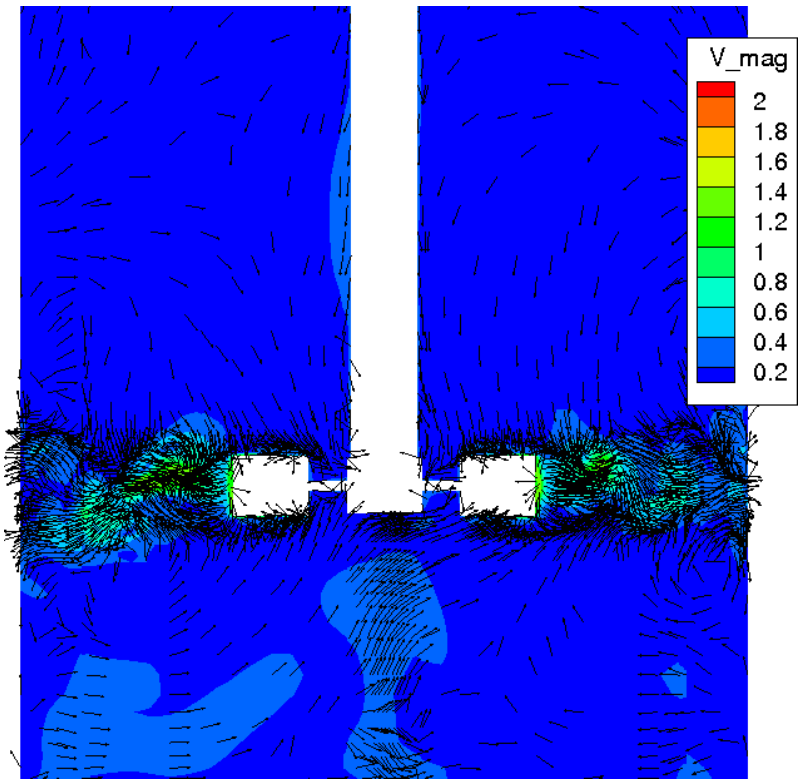

(a) $x-z$-plane at $y=0$ (shaft center).

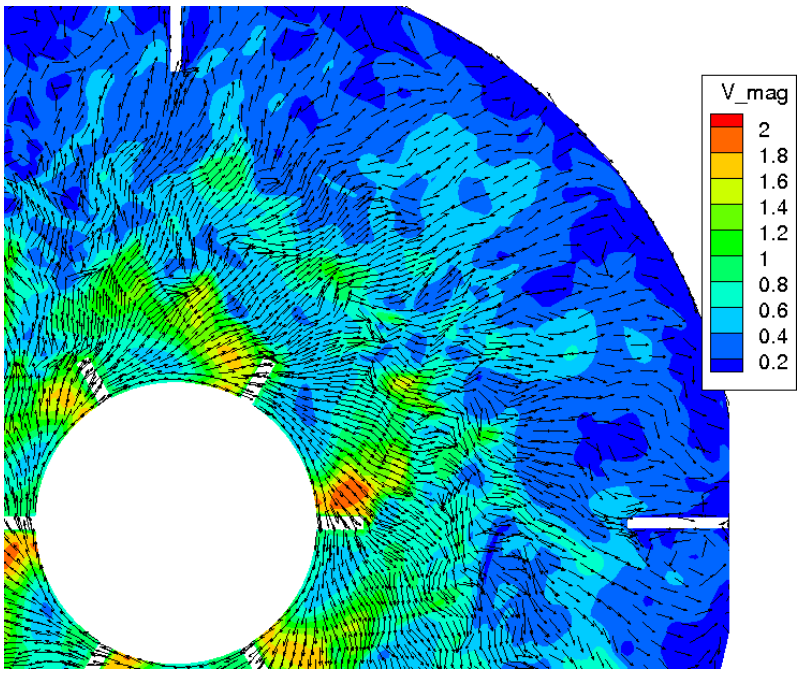

(b) $y-x$-plane at $z=0$ (disk-plane). Blade rotation is clockwise.

Figure 5.9: Instantaneous flow unit-vectors and normalized velocity magnitude contours $\|\vec{V}\|/V_{tip}$ at various planes. Vectors are thinned.

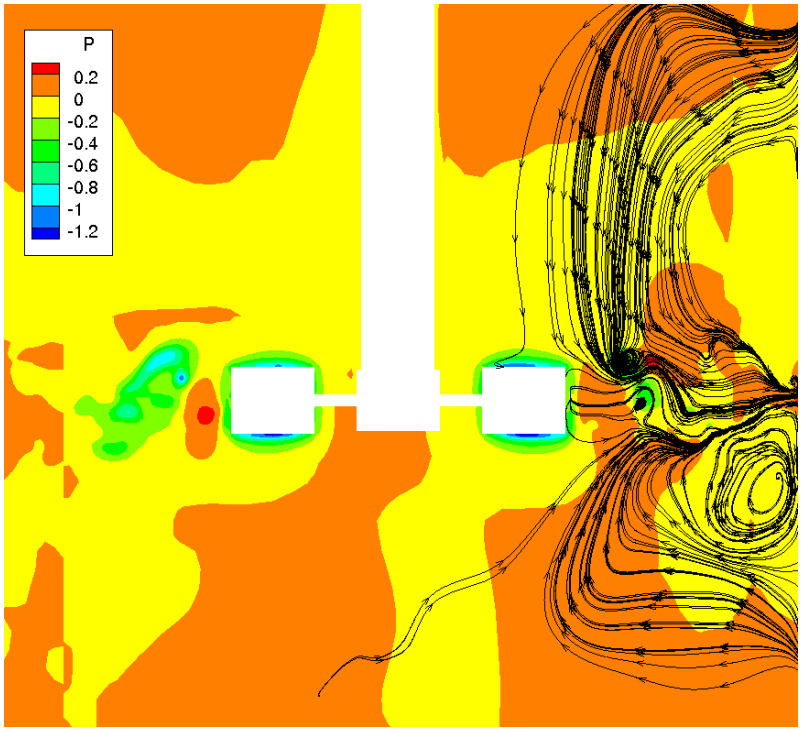

(a) $x-z$-plane at $y=0$ (shaft center)

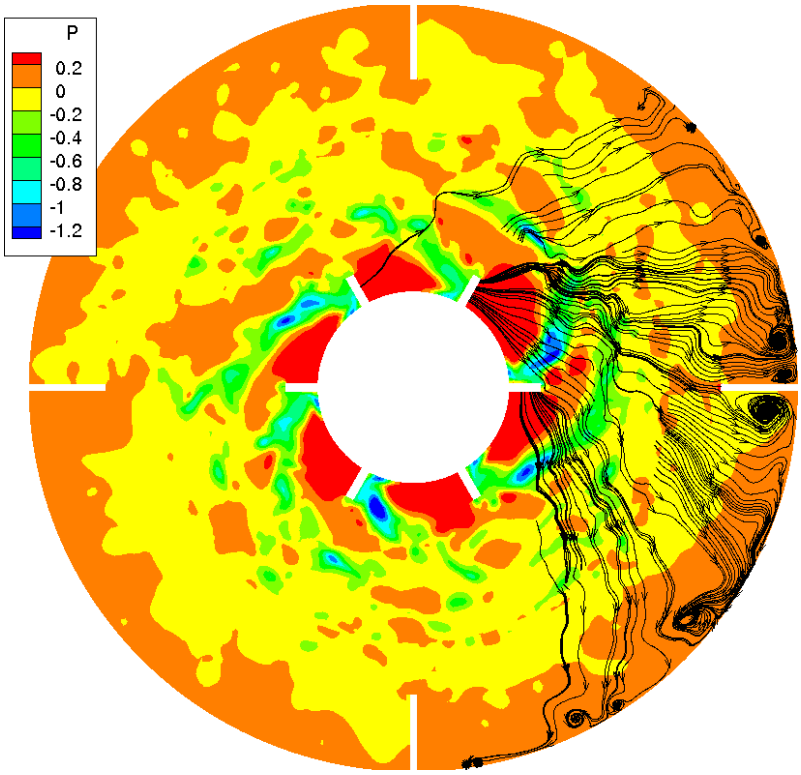

(b) $y-x$-plane at $z=0$ (disk center). Blade rotation is clockwise.

Figure 5.10: Instantaneous flow streamlines and normalized pressure contours $P/P_{dynamic}$ (based on V_{tip}).

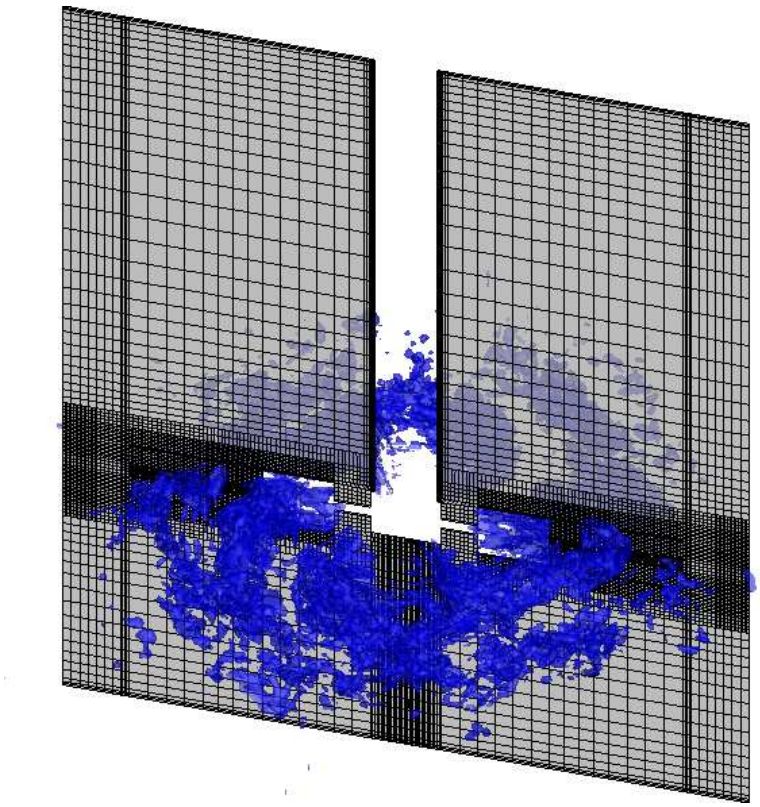

(a) $x - z$-plane at $y = 0$ (shaft center)

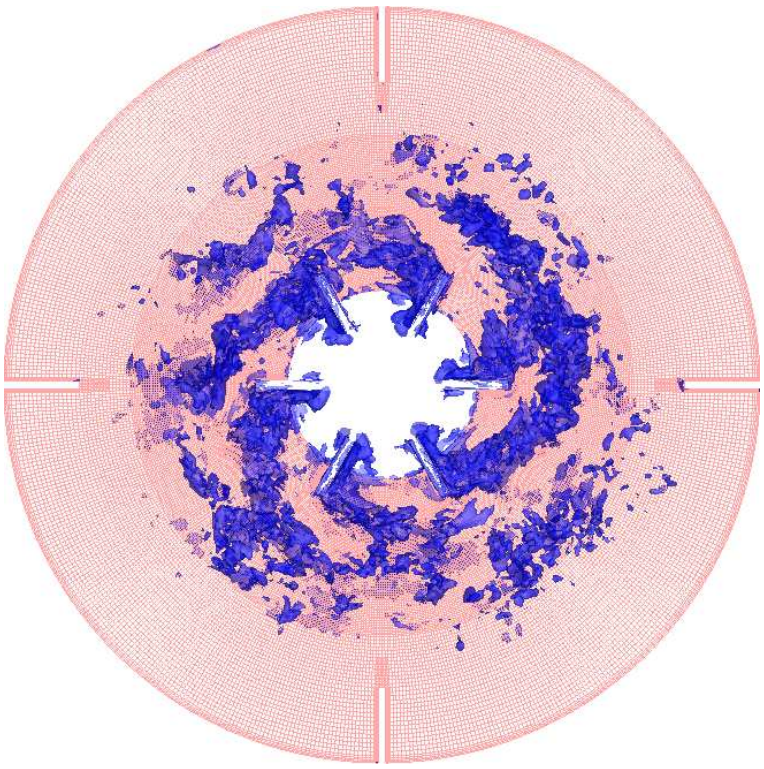

(b) $y - x$-plane at $z = 0$ (disk center). Blade rotation is clockwise.

Figure 5.11: Iso-surfaces of instantaneous swirl parameter at various locations.

Finally, it should be pointed out that all flow properties ($\vec{V}$ and P) in the presentation to follow have been normalized according to tip velocity V_{tip} and dynamic pressure so as to maximize the generality and utility of the presentation. Specifically, we define any normalized velocity as V/V_{tip} while the normalized pressure is defined as $P/P_{dynamic} = P/(\rho {V_{tip}}^2/2)$. In addition, forces (per unit mass), kinetic energy (per unit mass) and dissipation (per unit mass) are normalized via V_{tip}^2/R, $V_{tip}^2/2$ and $(V_{tip}/D)^2/(\mu/\rho)$ respectively.

5.3.1 Instantaneous Flow

The flow solution state at 90-revolutions is extracted and visualized in Figure 5.9, 5.10 and 5.11. Specifically, Figure 5.9 shows $x-z$ ($y=0$) and disk-plane ($z=0$) flow unit vectors and normalized velocity magnitude, indicating maximum flow $\|\vec{V}\|/V_{tip} \sim 1.0$ near the impeller and within the impeller exit stream (jet). In addition, although the Figure shows thinned velocity vectors, turbulence in apparent in Figure 5.9 (b) via the swirling, disorganized motions of various scales in the impeller stream. The turbulent motions present within the flow are further illustrated in Figure 5.10 (a) which visualizes the eddies present via stream-lines and local pressure mimina (associated with the local turbulence vortex cores) in the impeller exit stream. Turbulent structures are also evident near the outer tank wall associated with the impeller jet flow deceleration as shown in Figure 5.10 (b). It should be noted that at the location $y=0$, the outer edge of image in Figure 5.9 (a) and 5.10 (a) corresponds not with the outer tank wall, but to the inner baffle edge. Finally, the organized motion associated with the trailing vortex is illustrated in Figure 5.11 which gives instantaneous swirl parameter (see §5.4.1 for treatment of vortex dynamics and the swirl parameter vortex detection method). Specifically, Figure 5.11 (a) indicates the presence of a turbulent wake associated with the impeller motion, while Figure 5.11 (b) indicates that the origin of the wake is the suction side (SS) of the blade whereupon the wake structure (vortex) detaches from the blade and is convected outward (presumably due to the bulk motion of the fluid). Note that the specific structure of the wake is difficult to discern based on examination of the instantaneous flow alone. This deficiency will be addressed in §5.4 where the mean-flow will be used to not only establish the presence of a coherent vortex structure *in the mean*, but to investigate and analyze the wake/vortex structure itself as well as the physical mechanism responsible for formation.

5.3.2 Mean-Flow Field

The mean-flow was calculated via a cell specific averaging of the flow field over 40 revolutions starting at the 50^{th} revolution (corresponding to a total simulation time of $\approx 13sec$). This yields an initial averaging based on 36 samples per revolution, or 1440 samples. Next, two global regions were specified as statistical regions to sample corresponding to the Rotor-to-sliding-mesh and Stator-to-sliding-mesh regions (see Figure 5.6) as discussed previously in §5.2.6. Vector quantities such as velocity were then transformed into polar coordinates yielding, over the four Stator and six Rotor-to-sliding-mesh regions, $4 * 1440 = 5760$ and $6 * 1440 = 8640$ samples for the Stator and Rotor statistical regions respectively.

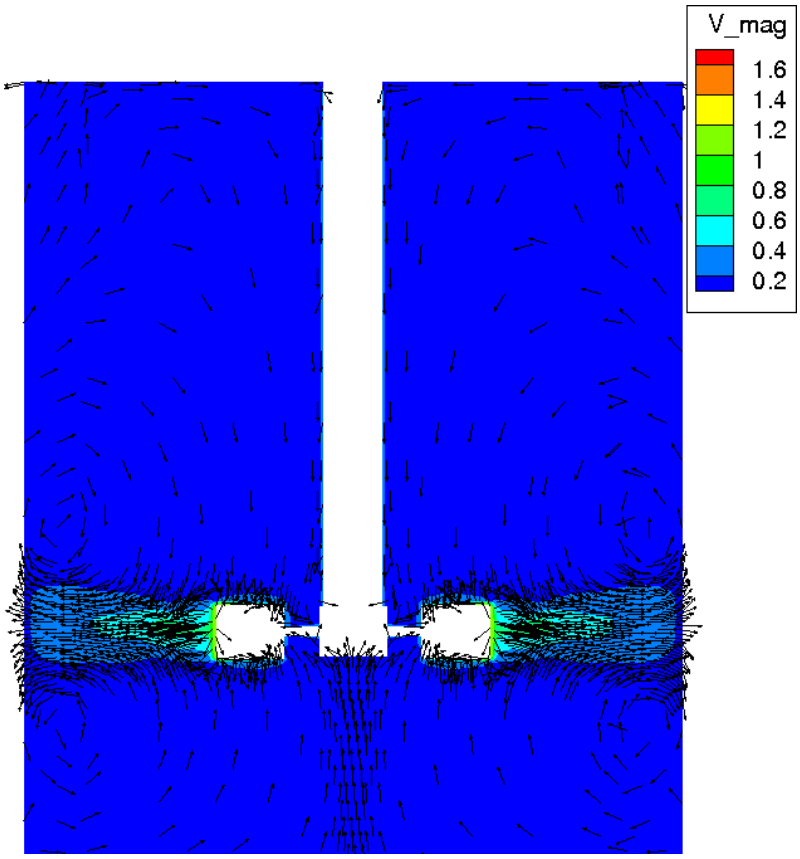

(a) $x-z$-plane at $y=0$ (shaft center)

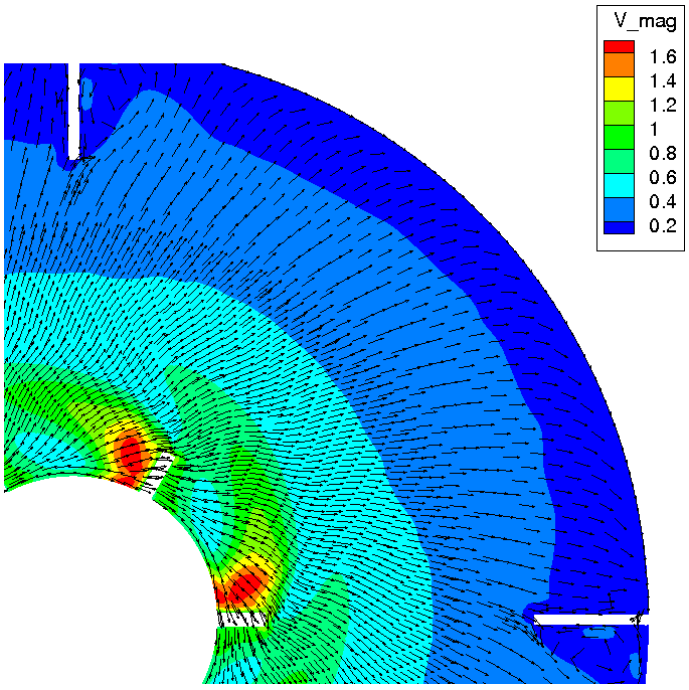

(b) $y-x$-plane at $z=0$ (disk-plane). Blade rotation is clockwise.

Figure 5.12: Mapped mean flow unit-vectors (unit length) and normalized velocity magnitude $\|\vec{\overline{V}}\|/V_{tip}$ at various locations. Vectors are thinned.

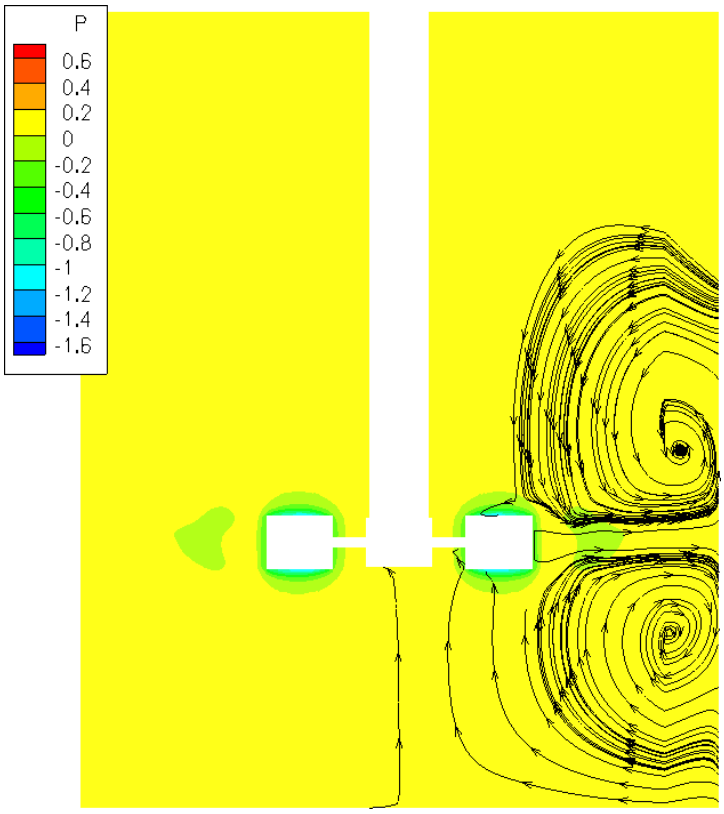

(a) $x-z$-plane at $y=0$ (shaft center)

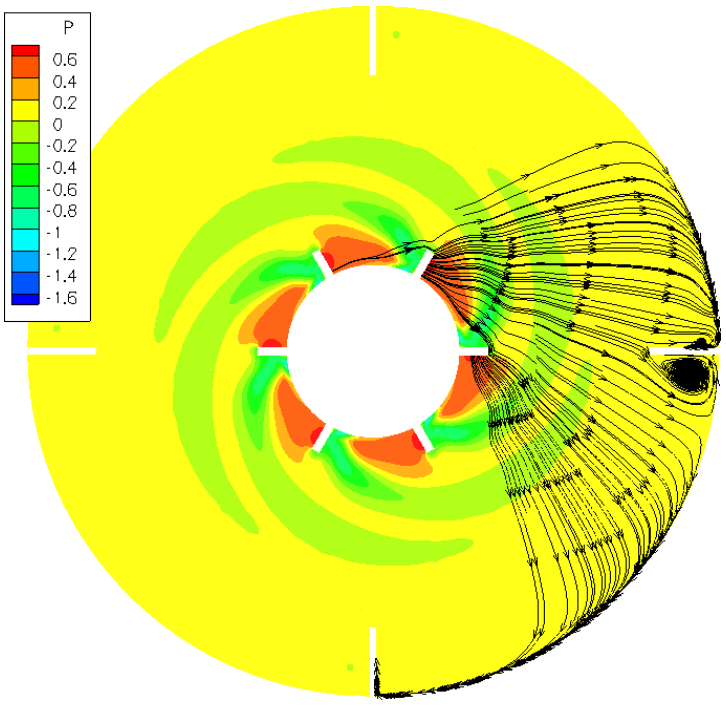

(b) $y-x$-plane at $z=0$ (disk-plane). Blade rotation is clockwise.

Figure 5.13: Mapped mean flow streamlines and normalized pressure $P/P_{dynamic}$ (based on V_{tip}).

The resulting statistical region mean-flow solution, now in polar coordinates, is mapped onto the flow field and converted to Cartesian coordinates. The result is a repeating flow solution within the entire region based on the mapped or *patterned average* on a subset of the geometry (i.e. Rotor/Stator statistical regions): A *rotor-fixed* mean-flow field for $r < R_{sl}$ and a *baffle-fixed* mean-flow field for $r > R_{sl}$ where R_{sl} is the radial location of the sliding mesh interface. It should be noted that this method of averaging results in the presence of a flow and pressure discontinuity at the sliding meshes between averaged regions. This is due to the fact that, as stated previously, the rotor-attached statistical region is at rest relative to the impeller while the stator-attached statistical region is at rest with respect to the outer tank region (i.e. the baffles).[8]

Mean-flow properties such as $\|\overline{\vec{V}}\|/V_{tip}$, $\overline{P}/P_{dynamic}$ and the swirl parameter are illustrated in Figure 5.12, 5.13 and 5.14. Specifically, Figure 5.12 gives (thinned) velocity unit-vectors and normalized velocity at the $x-z$-plane for $y = 0$ (a) and disk-plane ($z = 0$) (b). Figure 5.12 (a) illustrates the presence of the upper and lower bulk-flow recirculation zones above and below the disk-plane ($z = 0$) towards the outer tank wall associated with the impeller jet. Like in the instantaneous flow plots, the maximum flow $\|\vec{V}\|/V_{tip} \sim 1.0$ near the impeller and within the impeller exit stream (jet). Figure 5.12 (b) indicates outward flow from the impeller as well as the apparent presence of a high velocity region on the suction-side (SS) of the impeller, possibly associated with a mean-flow recirculation zone and/or wake behind the impeller. To more clearly illustrate the detailed flow pattern, Figure 5.13 shows normalized mean pressure and flow stream-lines (i.e. impeller/tank or rotating/stationary frame stream-lines based on absolute velocity). Both Figure 5.13 (a) and (b) indicated outward pumping via the impeller with max or min pressure on the pressure or suction-side of the blade respectively. Of additional interest are the upper and lower recirculation zones due to the impeller jet in Figure 5.13 (a) impinging on the outer tank wall, as well as the separation (in the mean) on the suction-side (SS) of the baffle Figure 5.13 (b). Again, it should be noted that at the location $y = 0$, the outer edge of image in Figure 5.13 (a) corresponds not with the outer tank wall, but to the inner baffle edge. In addition, the pressure contours indicate a region of low pressure originating at the blade (SS) and subsequently convected outward with the flow. Hence, this indicates the presence of a vortex induced wake generated at the suction-side (SS) of the impeller blade. To identify these trailing vortices the swirl-parameter was calculated based on the mean-flow. Figure 5.14 illustrates the coherent vortical structures in the form of two (one above and one below the disk-plane) vortices originating at the blade suction-side (SS), which subsequently detach and are then convected, via the bulk mean-flow, outward and down-stream relative to the impeller blade. In addition, the iso-surface of λ_2 (discussed in §5.4.1) is plotted Figure 5.15 indicating the presence of two, well defined, vortices with origin at the blade suction-side. This establishes the presence of upper and lower vortex which will be investigated in more detail in §5.3.4, §5.4.3 and §5.4. Finally, unlike the instantaneous flow snap-shot, shown in Figure 5.9, the mean-flow field appears smooth (gradual spatial changes

[8]Both vector quantities are however calculated via the flow solver and presented in the absolute frame unless otherwise specified.

in properties such as velocity and pressure) with an associated lack of turbulent structures. This suggests sufficient convergence of the statistical averaging process and hence, a sufficient number of sample flow states (at least with respect to the calculation of the mean motion).

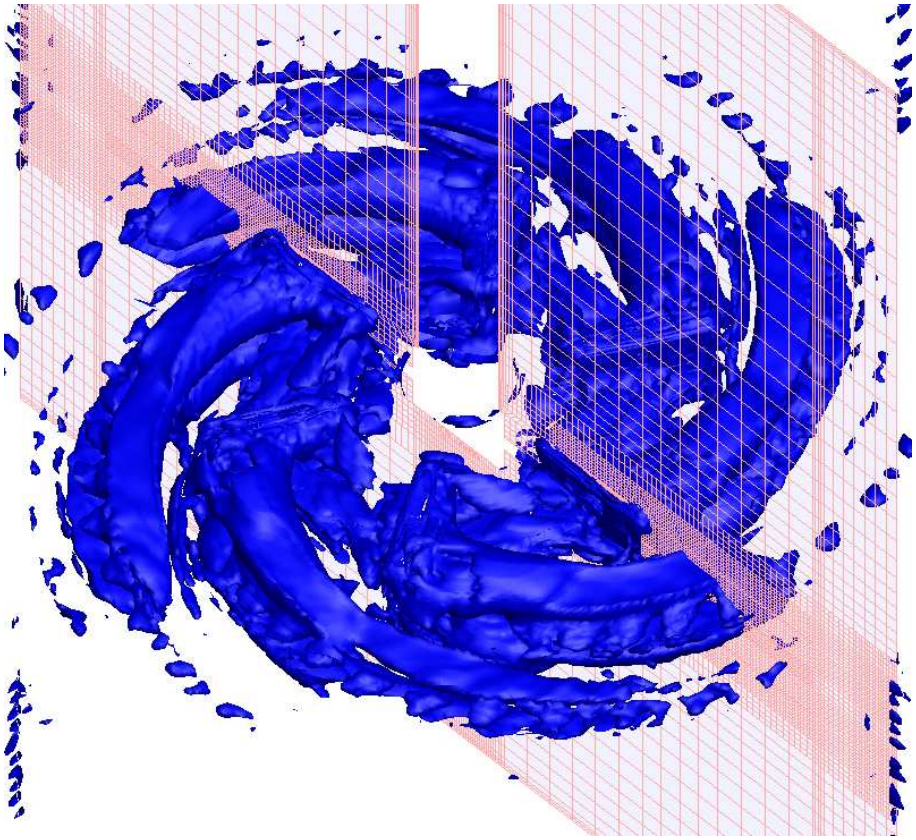

Figure 5.14: Iso-surfaces of swirl parameter for the mapped mean flow (note dual blade trailing (suction-side) vortices visible). Blade rotation is clockwise.

5.3.3 Mean-Flow Validation

Before proceeding further, the calculated mean-flow field must be validated against existing experimental data. Measurements of radial, circumferential and axial mean velocities ($\overline{V_r}$, $\overline{V_\theta}$, $\overline{V_z}$ measured in the rest frame) for an identical geometry studied herein were performed by Micheletti [50] for an observation plane half-way between baffles ($\theta = 0$). Specifically, the curve fit for turbulent and transitional flow normalized radial mean velocity at the disk ($z = 0$) is given as

$$(\frac{\overline{V}_r}{V_{tip}})_{disk} = 0.67(\frac{r}{R})^{-0.93} \tag{5.19}$$

Figure 5.16 (a) compares the circumferential average of simulation normalized mean-flow radial velocity $\overline{V}_r/V_{tip}$ to the correlation (5.19) as a function of normalized radial distance r/R and indicated good quantitative agreement. Specifically, from near the impeller tip ($r/R = 1$) to the near baffle region (the outer tank location corresponds to $r/R = 3$) divergence from the experimental results are approximately 10%. Additionally, Figure 5.16 (b) compares

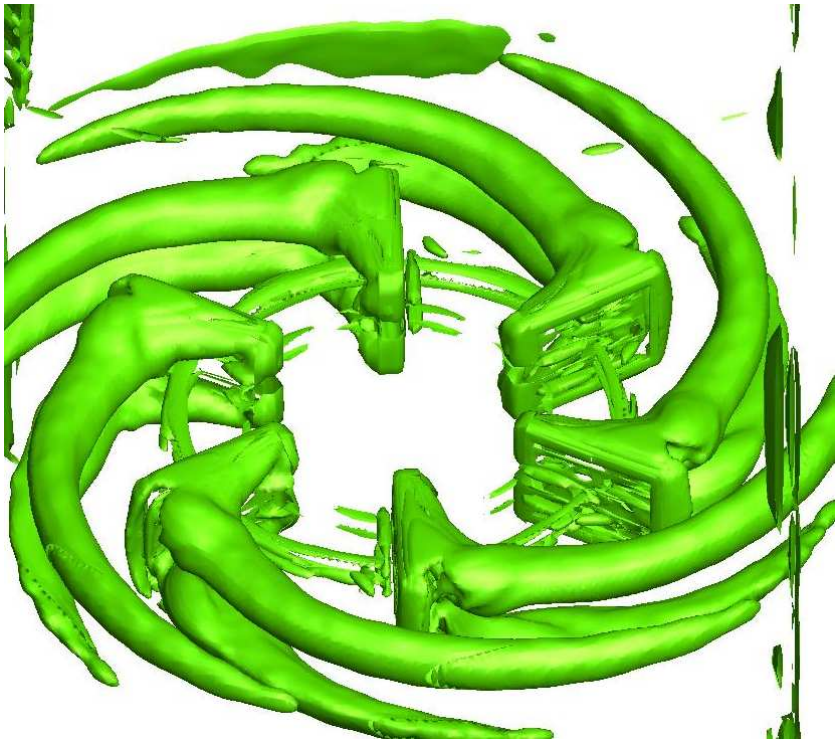

Figure 5.15: Iso-surfaces of $\lambda_2 = -600$ for the mapped mean flow (note dual blade trailing (suction-side) vortices visible). Blade rotation is clockwise.

simulation normalized mean-flow circumferential velocity $\overline{V}_\theta/V_{tip}$ with the experimental data of Micheletti for transitional flow with $Re = 4250$. Again, computational and experimental results are in good quantitative agreement, with a divergence of approximately 20% from experimental data. Further comparison with experimental data are given in Figure 5.17 which illustrate radial $\overline{V}_r/V_{tip}$, circumferential $\overline{V}_\theta/V_{tip}$ and axial $\overline{V}_z/V_{tip}$ normalized simulated and experimentally measured mean velocity in the $x-y$-plane at lower blade tip $z/(H_{BL}/2) = -1$ as a function of normalized radial position r/R. Again, divergence between the simulated and experimental data are approximately 20%, indicating a good correlation with experimental data. Sources of error in the aforementioned comparisons arise from the probability that current simulation has not achieved a statistically steady-state solution (as indicated in Figure 5.8 by the slight upward trend in power number from 50 to 90 revolutions). In addition, given that the calculated simulation circumferential averages are with respect to an impeller or baffle attached frame, (for $r < R_{sl}$ and $r > R_{sl}$ respectively), for radial locations near the outer tank wall the simulation data need not correspond with flow velocities mid-way between the baffles as measured experimentally by Mitcheletti. In addition, the previous experimental data of Mitcheletti were measured at a flow Reynolds number $Re = 4,250$ with the exception of disk-plane radial profile which is based on curve-fits to transitional and fully turbulent flow ($Re = 4,250 - 42,500$).

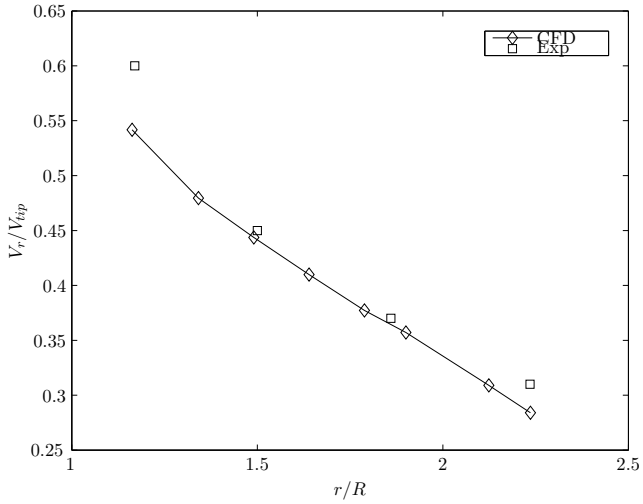

(a) $\overline{V}_r/V_{tip}$

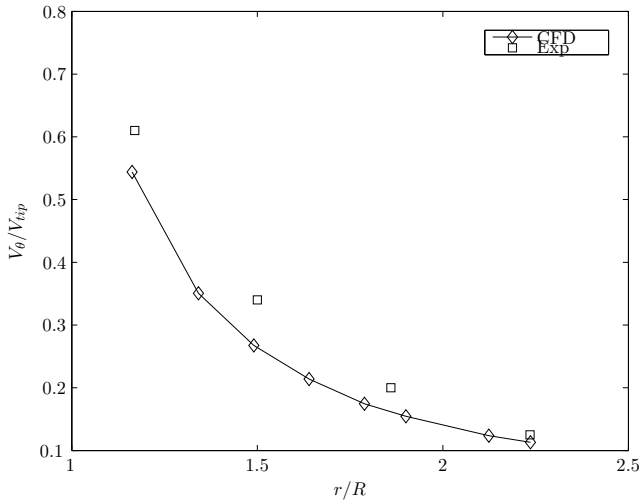

(b) $\overline{V}_\theta/V_{tip}$

Figure 5.16: Experimental and computational $\overline{V}_r/V_{tip}$ and $\overline{V}_\theta/V_{tip}$ at disk $(x-y)$-plane $z=0$. Source Micheletti [50].

5.3.4 Mean-Flow Force Decomposition

To glean an understanding of the fundamental fluid dynamical processes within the mixing vessel, this section presents a detailed investigation of the near impeller fluid dynamics based on a mean-flow derived force decomposition. This not only allows for a highly detailed examination of the fundamental causal mechanisms governing the flow, but also allows for the application of a pressure force, convergence-based, detection method for identifying the spatial location of the trailing vortex core.

Given that an examination of the swirl parameter implies the presence of a vortex with inception at the blade suction-side (SS) which is then convected outwards, an inspection of the pressure force is warranted. To this end, Figure 5.18 (b) shows a contour and unit vector

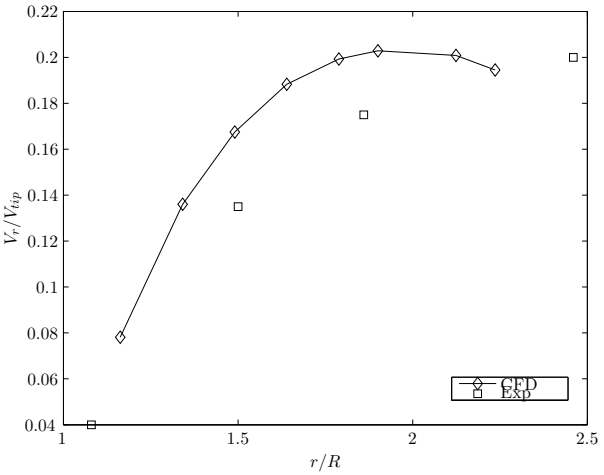

(a) $\overline{V}_r/V_{tip}$

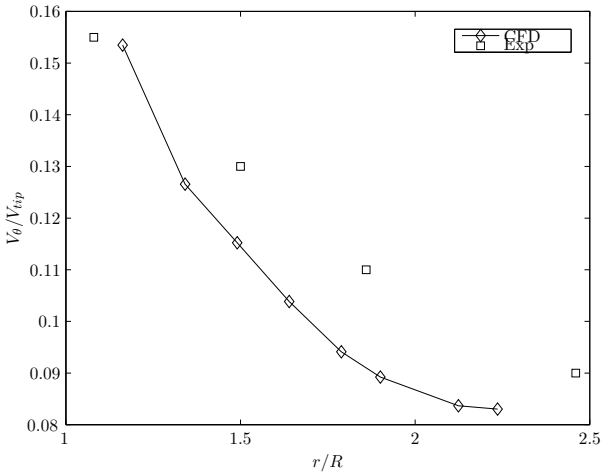

(b) $\overline{V}_\theta/V_{tip}$

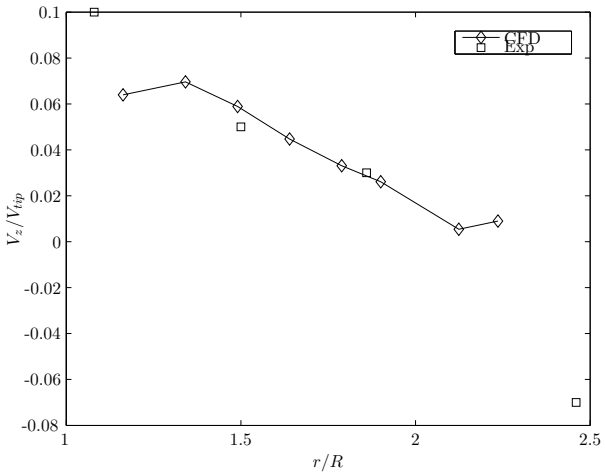

(c) $\overline{V}_z/V_{tip}$

Figure 5.17: Experimental and computational $\overline{V}_r/V_{tip}$, $\overline{V}_\theta/V_{tip}$ and $\overline{V}_z/V_{tip}$ at lower blade tip ($x-y$-plane) for $z/(H_{BL}/2) = -1$. Source Micheletti [50].

plot of normalized pressure force (on a per unit volume basis $-\vec{\nabla}\overline{P}$) within the $x-y$-plane at axial location of one half of the blade half-height below the disk center $z/(H_{BL}/2) = -0.5$. Specifically, Figure 5.18 (b) indicates that on the blade suction-side the convergence of the pressure force is towards a core line as signified by the dashed line $- - -$. A projection of this core line onto a contour plot of pressure with pressure force unit-vectors as shown in Figure 5.18 (c) indicates the presence of a local pressure minimum at the vortex core along the core line. Hence, an inward pressure force exists within the vortex counteracting the outward acceleration of the fluid particle due to centrifugal motion about the core.

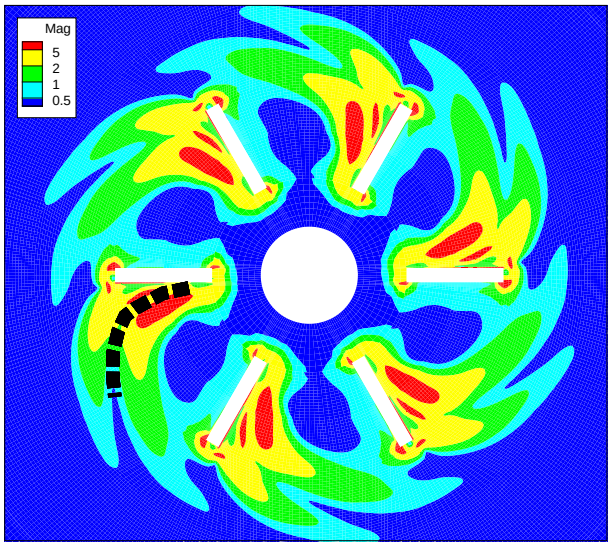

(a) Contour of normalized in-plane pressure force.

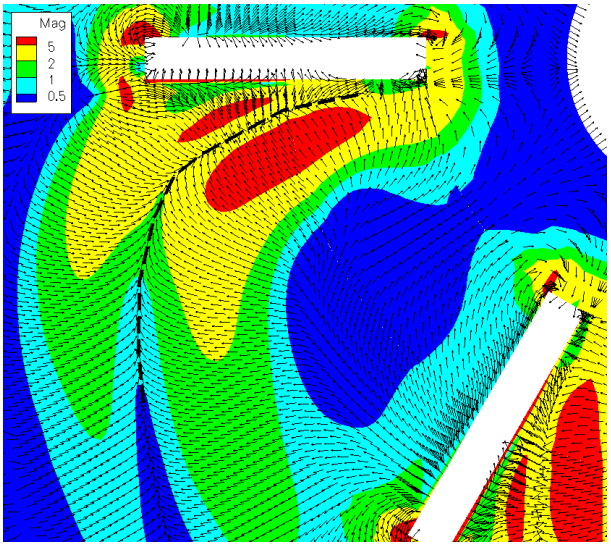

(b) Near-blade contour and unit vector plot.

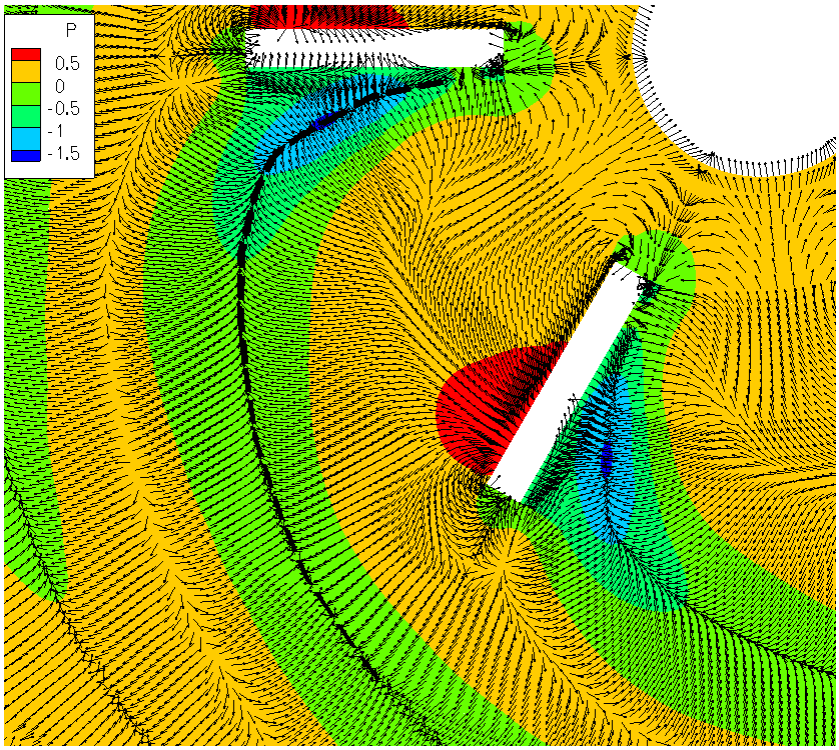

(c) Contour of normalized pressure with pressure force unit vectors overlaid.

Figure 5.18: $\vec{F}_{press}^{norm}$ tangent to $x-y$-plane at $z/(H_{BL}/2) = -0.5D$ (quarter-depth of blade) normalized by tip acceleration $\|V_{tip}^2\|/R$ ((a) and (b)) and pressure contours with unit pressure force vectors overlaid (c). Note, approximate vortex core is visible via $---$. Blade rotation is clockwise.

In addition, the core originates near the blade leading edge on the blade suction-side (SS), and then detaches at a location approximately mid-cord along the blade surface. The core then moves outward under the influence of the bulk-flow, the pressure force declining as the core moves away from the impeller (as indicated by the pressure force magnitude contours shown in Figure 5.18 (b)). In addition, this core trajectory is in good qualitative agreement with the results of Van't Riet et al [62], Stoots et al [70], Yianneskis et al [76], Sharp et al [68] and Lee et al [42]. Direct comparison of the pressure force based vs. the λ_2 vortex detection scheme (presented in §5.4.1) indicates satisfactory agreement between the two methods. Specifically, Figure 5.19 gives the contour plot of λ_2 and indicates an approximate 15% variation in location of the core position based on radial distance from the impeller trailing edge.

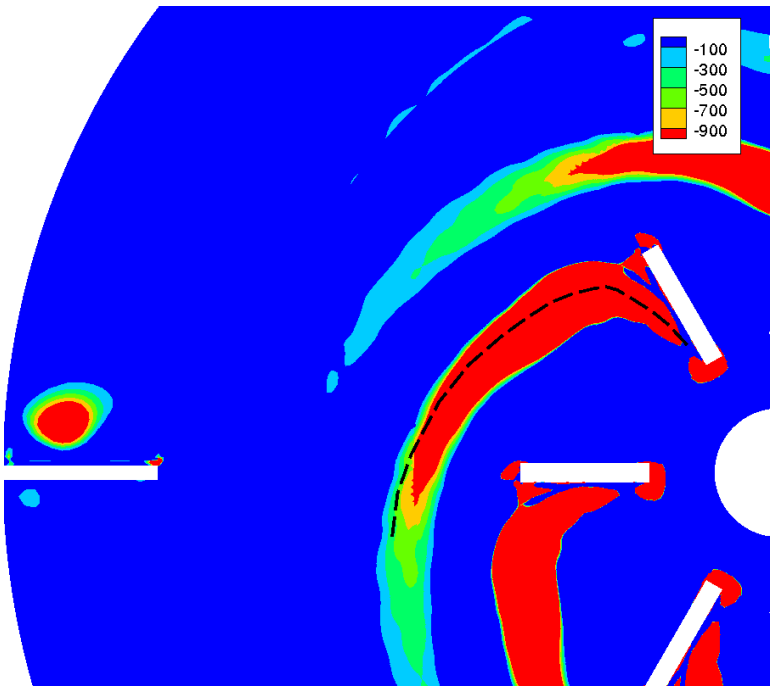

Figure 5.19: Contours of λ_2 in $y-x$-plane at $z/(H_{BL}/2) = -0.5$ (half-depth of blade) with pressure-force based core-line indicated by $- - - - -$.

With respect to successive vortices and their inter-section, it should be noted that the inter-vortex boundary can be observed as a line of diverging pressure force approximately half-blade cord length $L_{BL}/2$ radially down-stream from the vortex core location. In other words, this line of diverging pressure force can be interpreted as the local spatial location separating successive trailing vortices: Flow radially inward of this pressure force divergence line is accelerated towards the vortex with core indicated by $- - - - -$, while flow radially outward is accelerated towards the vortex core originating one blade-pass upstream.

Additional points of interest include the pressure force exerted from the pressure-side (PS) and towards the suction-side (SS) of the blade, again due to the pressure gradient as shown in Figure 5.18 (c). This results in an acceleration of the fluid particle radially outward and away from the blade near the pressure-side (PS) tip (resulting in the pumping

action of the impeller) and a corresponding acceleration of the flow towards the blade and inwards on the suction-side (SS). Given the high Reynolds number of the flow at the suction-side tip, fluid particle inertia is high enough to prevent local suction-side (SS) flow stall. Recall that this is in contrast to the case of very low flow $Re \sim 1$ investigated in §4.3.2 where the suction-side inward pressure force results in flow stall or back-flow. Returning to Figure 5.18 (b) it should also be noted that the normalized pressure force magnitude is ≈ 1 near/at the blade tip, indicating a correct choice of force normalization based on tip inertia (or in terms of acceleration V_{tip}^2/R). With respect to the relative strength of the pressure

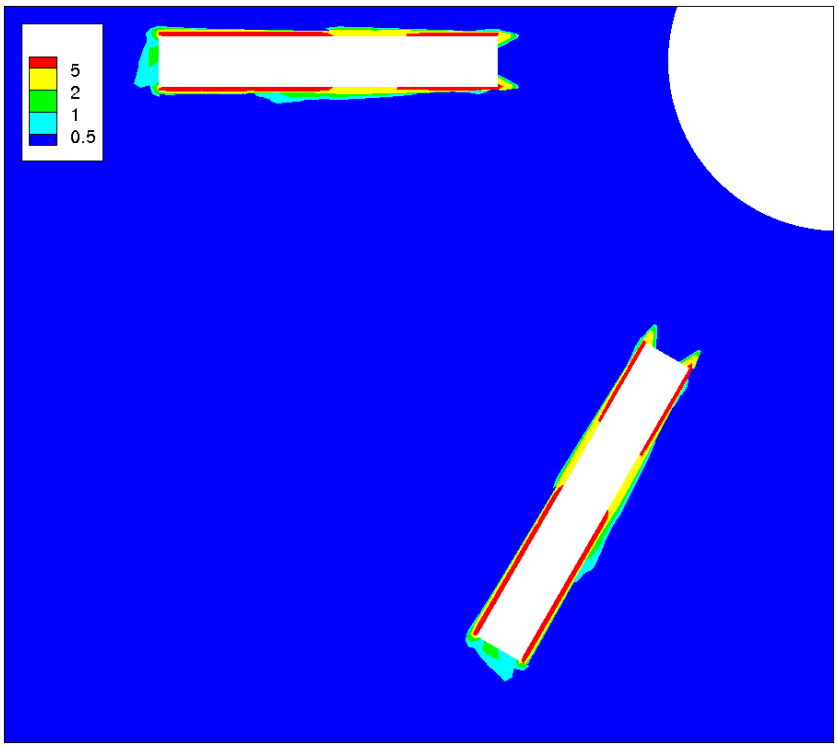

Figure 5.20: $\|\vec{F}_{visc}^{norm}\|$ tangent to $y-x$-plane at $z/(H_{BL}/2) = -0.5$ (half-depth of blade) normalized by tip acceleration $\|V_{tip}^2\|/R$.

vs. viscous forces, it should first be noted that the normalized pressure force magnitude is ~ 1 as indicated in Figure 5.18 (a) and (b). This can be compared to the normalized viscous force as shown in Figure 5.20 again in the $x-y$-plane at one half of the blade half-height below the disk center $z/(H_{BL}/2) = -0.5$. Specifically, the normalized viscous force magnitude is negligible everywhere except very near the blade (within the blade mean-flow boundary-layer).[9] Given that the inertial force is the sum of the pressure and viscous forces, this implies that the inertial force is much greater than the viscous force except very near the blade. This observation is buttressed by the fact that the flow is of high Reynolds number, or based on the definition, $F_{inertial} \sim F_{press} \gg F_{visc}$. For the purpose of completeness, Figure 5.21 shows normalized radial pressure and viscous force as a function of blade angle ϕ at a location very near the lower blade tip $z/(H_{BL}/2) = -1$ and $r/R = 1.116$. Again, the Figure

[9]Note the discrete increase in viscous force exactly half the blade cord-length along the surface. This is due to an increase in local refinement as indicated in Figure 5.4 (c).

indicates that the flow is pressure driven with negligible viscous forces at almost all blade angles (corresponding to high Re flow). This is in contrast to Figure 4.8 (b) where viscous and pressure forces are comparable leading to stalled flow for $Re = 10$ and Figure 4.8 (c) where inertial forces are negligible resulting in local reverse flow at very low Reynolds number $Re = 1$.

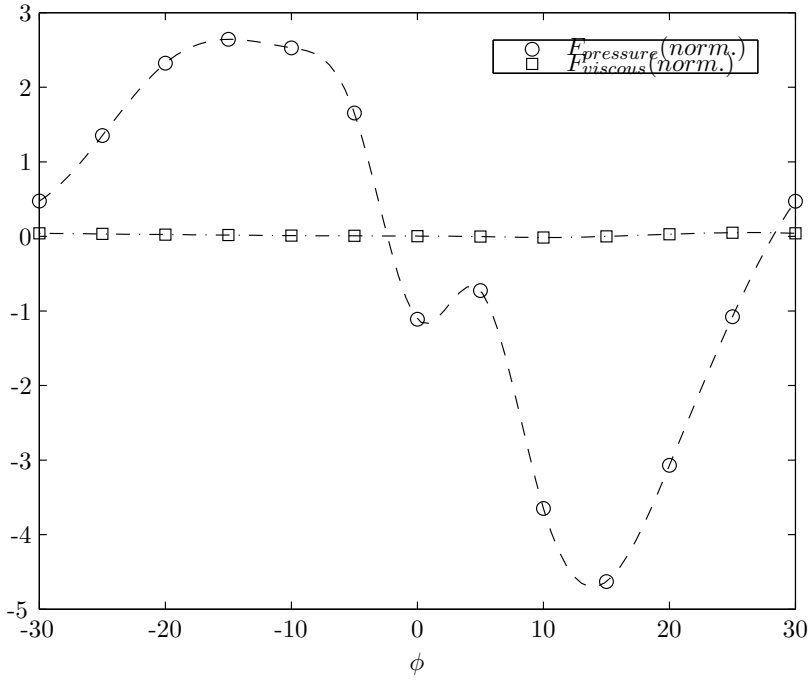

Figure 5.21: Normalized radial pressure and viscous force at lower blade tip $z/(H_{BL}/2) = -1$ and $r/R = 1.116$ as a function of blade angle ϕ.

Finally, the normalized pressure force and pressure field can be examined near the blade to further examine flow acceleration. Specifically, Figure 5.22 (a) gives in-plane pressure force unit-vectors and pressure contours in the $x-z$-plane at a location 2.5 blade thicknesses down-stream from the blade suction-side ($y = 3t_{BL}$ where t_{BL} is blade thickness) indicating the presence of a vortex core at approximately mid-blade location above and below the disk-plane ($z = 0$). Likewise, Figure 5.22 (b) gives in-plane pressure force unit-vectors and pressure contours in the $y-z$-plane at a location just outward of the impeller disk $x/R = 0.82$. The presence of two pressure minimums located at the vortex core is evident just down-stream from the blade suction-side (SS) surface. In addition, the pressure differential between the pressure and suction-side of the blade results in an acceleration of fluid particles from the pressure to suction-side at the blade. It will be shown in the following section §5.4 that this results in fluid flow, in the impeller relative frame, from the pressure to suction-side of the upper and lower blade tip producing a swirling motion. This swirling fluid convects outward radially and eventually detaches from the impeller blade (due to the blade trailing edge separation) resulting in a vortex induced wake which propagates outwards towards the outer tank wall.

5.4 Blade Trailing Vortex

5.4.1 Dynamics and Detection Methods

The structure of an idealized vortex can be approximated as a solid-body rotation. Applying the Navier-Stokes equation yields the expression for the pressure gradient

$$\rho \frac{V_\theta^2}{r} = \frac{\partial P}{\partial r} \tag{5.20}$$

This implies the existence of a local pressure minimum at the vortex center and a suitable method for detecting vortex centers (i.e. the point of local pressure minimum). Alternatively, a velocity based method for vortex center detection can be performed by noting that in the case of an ideal $3-D$ vortex (helix), the flow at the core convects in the direction of the vorticity vector. Hence, one can define a parameter termed the *helicity* as the product of the unit-vectors $\hat{\omega} \cdot \hat{\vec{V}}$ (where $\hat{\omega}$ is the vorticity unit-vector) which is necessarily maximized along the vortex core (assuming the flow is $3-D$). However, a deficiency of the helical method is the fact that non-vortical structures need not have zero vorticity. Hence, the method does not exclusively identify regions exhibiting vortical rotation.

A more subtle method has been formulated by Jeong et al [33] who noted that under the conditions of steady, high Reynolds number flow (negligible viscous forces), the gradient of the Navier-Stokes equation yields

$$\Omega_{ik}\Omega_{kj} + S_{ik}S_{kj} \approx -\frac{1}{\rho}\frac{\partial^2 P}{\partial x_i \partial x_j} \tag{5.21}$$

where $\mathbf{S}$ and $\mathbf{\Omega}$ are the symmetric (strain) and anti-symmetric (rotation or spin) components of the velocity gradient tensor. In a $2-D$ plane containing the unit-vectors $\hat{x}_1$ and $\hat{x}_2$ with normal perpendicular to the vortex core line, the existence of a local pressure minimum requires two negative Eigen-values for the symmetric tensor $\mathbf{S}^2 + \mathbf{\Omega}^2$. Hence, a vortex can be detected by ranking Eigen-values $\lambda_1 \geq \lambda_2 \geq \lambda_3$ for the tensor $\mathbf{S}^2 + \mathbf{\Omega}^2$ and plotting values of λ_2: Large positive values $-\lambda_2$ implying a strong local minimum in pressure and the presence of a vortex.

An alternative velocity based method which is suitable for identifying vortical structures formulated by Berdahl et al [7] is to compare two time-scales: The first is associated with the orbital time for a particle circling a vortex core τ_{orbit} and the second is a convective time-scale associated with the time taken for a given fluid particle to convect along the vortex core a unit distance $\tau_{convection}$. Within the vortex, the vortex strength is high when $\tau_{orbit} \ll \tau_{convection}$ and visa versa. In addition, a necessary characteristic of the method it that $\tau_{convection} = 0$ in the absence of any vortical motion. To implement this method we first note that a convective time can be formed via the quantity $\ell_{conv}/(\hat{\omega} \cdot \vec{V})$ where ℓ_{conv} is some length-scale associated with fluid convection at the core. Determination of the orbital time-scale is more subtle. We note that flow within a $3-D$ ideal vortex (a helix) can be accelerated or decelerated linearly along the direction of the core-line only. Hence, if we define velocity gradient tensor $[\mathbf{A}]$

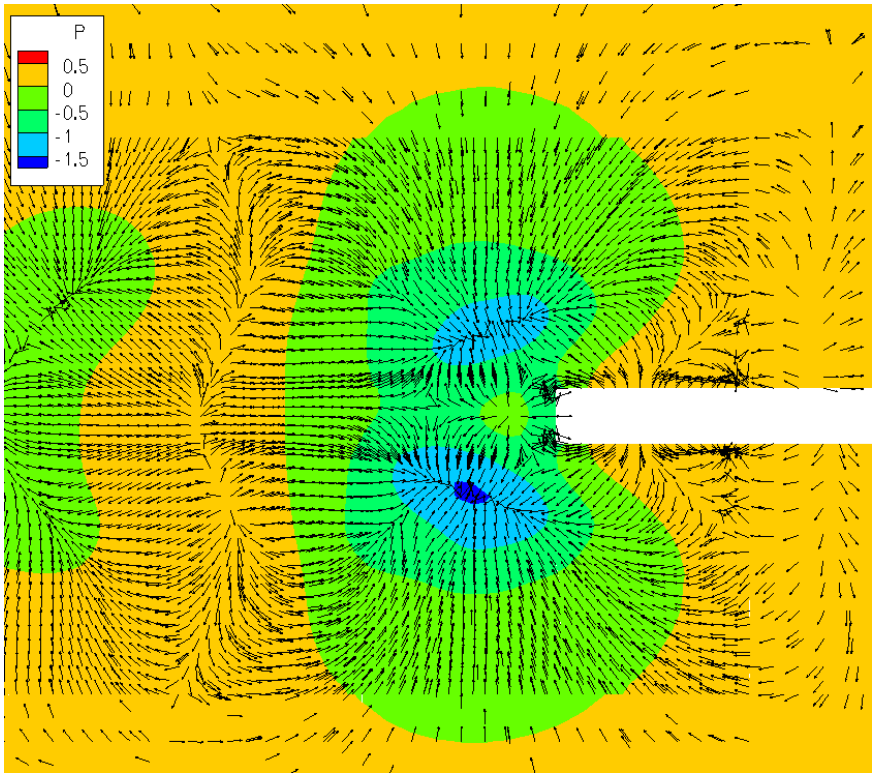

(a) $x-z$-plane at $y = 3t$ ($2.5t$ downstream (SS) from blade surface). Blade motion into page.

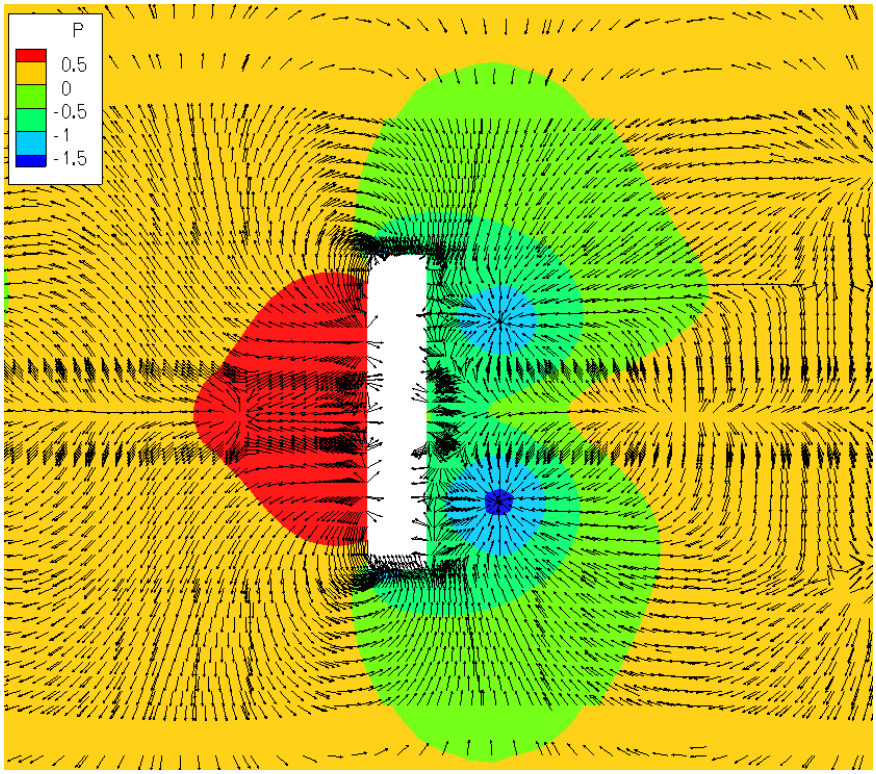

(b) $y-z$-plane a distance $x/R = 0.82$ from impeller center. Blade motion right to left.

Figure 5.22: In plane $\|\vec{F}^{norm}_{pres}\|$ unit-vectors and pressure normalized by tip acceleration $\|V^2_{tip}\|/R$ contours at distance $y = 3t_b$ from blade center (a) and $x/R = r/R = 0.82$ from impeller center (note vortex centers above and below disk indicated by converging pressure force vectors).

$$[\mathbf{A}] \equiv \begin{bmatrix} \frac{\partial V_x}{\partial x} & \frac{\partial V_x}{\partial y} & \frac{\partial V_x}{\partial z} \\ \frac{\partial V_y}{\partial x} & \frac{\partial V_y}{\partial y} & \frac{\partial V_y}{\partial z} \\ \frac{\partial V_z}{\partial x} & \frac{\partial V_z}{\partial y} & \frac{\partial V_z}{\partial z} \end{bmatrix} \tag{5.22}$$

there exist within a helix ($3-D$ vortex) two imaginary (complex conjugate) and one real Eigenvalue (corresponding to linear acceleration along the core-line) for the Tensor $[\mathbf{A}]$. Specifically, the imaginary (complex conjugate) Eigenvalues are related to an orbital velocity, length and time-scale via $\|\lambda_{im}\|/(2\pi) \sim V_{orbit}/(2\pi\ell_{orbit}) \sim 1/\tau_{orbit}$, or $\tau_{orbit} \sim 2\pi/\|\lambda_{im}\|$. Defining the swirl parameter as the ratio of the convective-to-orbital time and setting the convective length scale $\ell_{conv} = 1$ we have

$$\frac{\tau_{convection}}{\tau_{orbit}} \sim \frac{\ell_{conv}/\hat{\omega}\cdot\vec{V}}{2\pi/\|\lambda_{im}\|} \sim \frac{\|\lambda_{im}\|}{2\pi(\hat{\omega}\cdot\vec{V})} \Rightarrow \mathbf{S}p \equiv \frac{\|\lambda_{im}\|}{2\pi(\hat{\omega}\cdot\vec{V})} \tag{5.23}$$

In practice, the vortex can be visualized by displaying iso-surfaces of larger and larger values of the swirl parameter until the vortex structure becomes visible. It should also be noted that since the value of ℓ_{conv} has been set to unity, the actual value of the swirl parameter is only approximately representative of the strength of the helical vortex and thus is suitable only for visualization purposes.

Finally, it should be pointed out that the Helical and Swirl Parameter detection methods are not frame (Galilean) invariant: Both methods involve a vorticity dotted with a velocity, the later of which is frame dependent. On the other hand, the λ_2 detection method (which seeks a local pressure minimum via the determination of a velocity gradient tensor Eigenvalue) is invariant.[10]

5.4.2 Augmentation Due to Bulk Motion

Once a vortex has been detected using one of the various methods explained in §5.4.1, examination and visualization of the vortical structure can be performed. To this end, it is critical to understand how the vortex structure and motion can be augmented due to convection via the bulk flow. Figure 5.23 (a) illustrates an idealize vortex (solid-body rotation) in quiescent bulk flow where the actual center or core is denoted by a + while the *apparent center* is indicated by an O. The maximum vortex velocity magnitude existing at the outer edge is $\|V\|_{vortedge}$. Now, augmentation of the vortex due to bulk fluid motion (convection of the vortex) can be visualized by applying a free-stream flow of increasing strength as shown in Figure 5.23 (b)-(e) and noting the displacement of the *apparent* vortex center O from the true vortex center +. Specifically, as the bulk-flow velocity magnitude $\|U\|_{fs}$ is increased from $0.25\|V\|_{vortedge}$ to $1.0\|V\|_{vortedge}$, the vortex structure is distorted while the apparent center is displaced and ultimately vanishes. In other words, as $\|U\|_{fs} \longrightarrow \|V\|_{vortedge}$ the vortex (which is being convected due to the bulk motion in the absolute frame) is no longer discernible. Hence, this illustrates the fact that true vortex core need not be associated with location of vanishing velocity in the absolute frame (i.e. the apparent vortex center).

[10] For further discussion see Jiang at al [34], Jeong et al [33] and Berdahl et al [7].

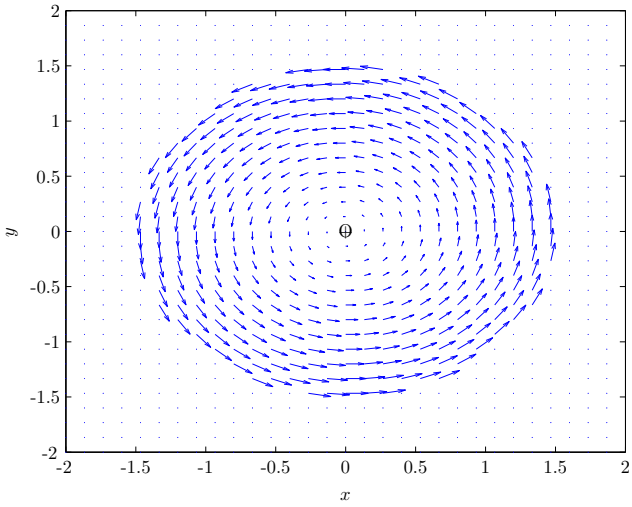

(a) $\|U\|_{fs}/\|V\|_{vortedge} = 0.0$

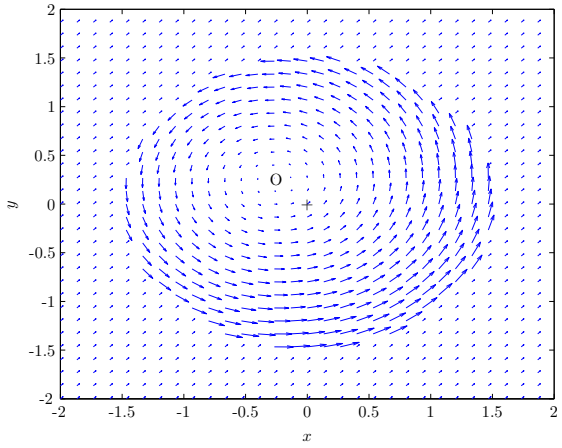

(b) $\|U\|_{fs}/\|V\|_{vortedge} = 0.25$

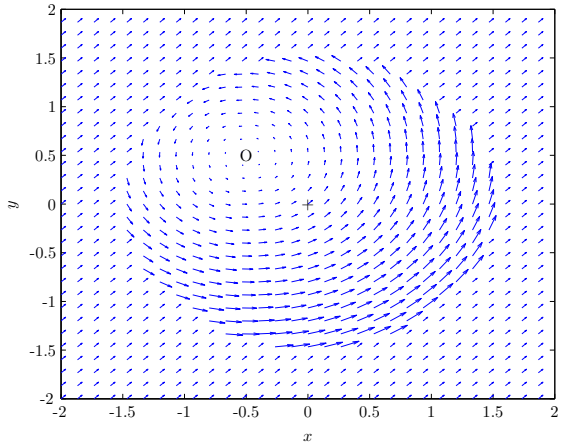

(c) $\|U\|_{fs}/\|V\|_{vortedge} = 0.5$

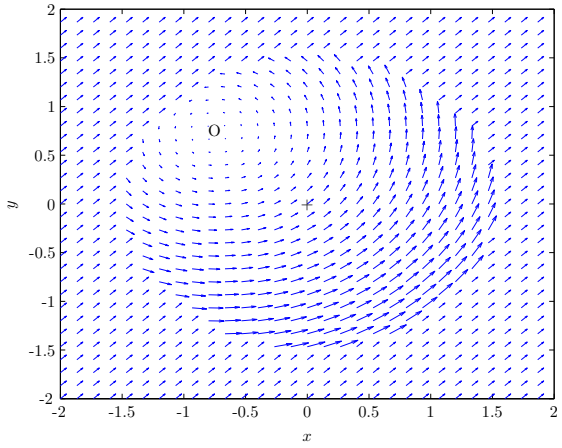

(d) $\|U\|_{fs}/\|V\|_{vortedge} = 0.75$

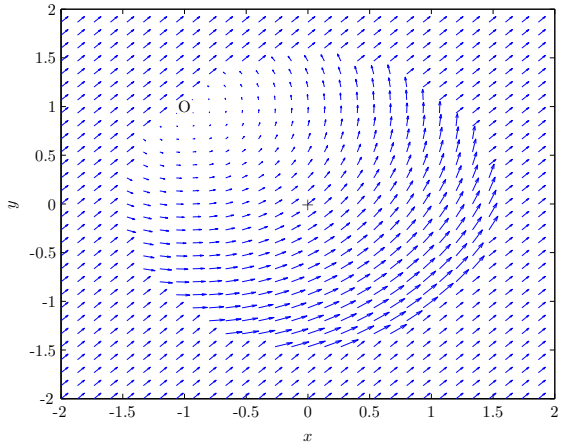

(e) $\|U\|_{fs}/\|V\|_{vortedge} = 1.0$

Figure 5.23: Solid body rotation of outer edge velocity magnitude $\|V\|_{vortedge}$ with superimposed free-stream velocity of magnitude $\|U\|_{fs}$ varying in strength.

This implies that in the presence of a non-zero bulk or free-stream flow an alternative method for identification of the vortex (core) must be found (e.g. a minimum pressure point based or a λ_2 method) after which a vortex stationary frame can be defined and vortex core relative velocities calculated.[11]

Literature

Given that an analysis of vortices on a micro and macro-scale is integral to this study, it is important to investigate some aspect of vortex dynamics as well as vortex detection methods. Fundamental investigation of vortices in the context of convection-diffusion mass transfer (mixing) has been carried out by Meunier et al [48] who investigate characteristics of the analytical solution to the concentration transport equation for a blob stretched into a thin spiral. They found that the local concentration gradients decline quickest at the leading edge of the spiral where the spiral thickness was minimized. In addition, from a comparison of experimental results on diffusion via vortical elongation and subsequent diffusion and scalar analysis performed on pure diffusion of an initial blob of dilutant, the Authors report that the presence of a vortex effectively reduces mixing time an order of magnitude or more. The fluid deformation associated with the presence of vortical structures was investigated in detail by Bouremel et al [8] who used a λ_2 technique for detecting and decomposing local strain rates due to a translating vortex. They found that compression and expansion (normal strains) existed at the leading and trailing edge of the vortex as it travels through and displaces fluid in the free-steam. This behavior was observed both for an isolated vortex ring in quiescent field (via PIV) and the trailing edge vortices exhibited in a Rushton turbine mixing tank (via LDA).

As will be shown in §6.10.4, the blade trailing vortices are associated with turbulence generation as well as inducing mean-flow strains within the flow-field responsible for, amongst other things, strain induced dispersion of gas in liquid. In other words, these vortices primarily serve to enhance mixing via local straining of the flow as well as conversion of mean-flow kinetic energy $\overline{k}$ into turbulent (i.e. turbulent kinetic energy $\overline{k'}$) and ultimately dissipative motion.

With respect to mixing and mixing enhancement via the instabilities present due to the trailing vortices, Asserelli et al [2] use an iodide-iodate reaction mechanism to gauge mixing effectiveness for a process utilizing a Rushton turbine. Specifically, this reaction mechanism allows for desirable and undesirable product production, the concentration of the undesirable products being a function of the rate of local component mixing (i.e. rapid mixing minimizes undesirable product formation). Under high Reynolds number flow ($Re \approx 80(10^3)$) Asserelli found that injection of the reactants into the impeller stream near the upper tip blade edge significantly reduced the steady-state concentration of the undesirable products by nearly an order of magnitude compared with reactant injection near the top surface of the tank. This is indicative of the enhanced mixing associated with the trailing vortices.

[11] I should be noted that pressure based vortex detection techniques are least accurate for viscous dominated or unsteady flows (as implied by the derivation of the λ_2 detection technique).

Detailed studies of the fluid dynamical behavior of the blade trailing vortices have been performed. Gunkel et al [28] examined the trailing vortices using LDA to extract phase averaged and perturbation velocities near the impeller. For a range of Re numbers of $14(10^3)-3(10^4)$ the Authors claim to identify not two, but four trailing vortices: Two originating at the blade suction-side (SS) and two at the blade pressure-side (PS). However, no detailed visualization of either set of vortices were given. Confirmation of the existence of vortices within a Rushton agitated tank under turbulent conditions ($Re = 5(10^4)$) was sought by Yianneskis et al [77] who established that variations in axial velocity, above/below the disk, as a function of impeller location, was due to the presence of trailing vortices. However, unlike Gunkel et al, the existence of pressure-side vortices could not be verified.

Escudie et al [26] performed phased-resolved PIV based measurements on a turbulent mixer down-stream from the impeller and used a λ_2 based vortex detection method. Specifically, they confirmed the presence of the trailing vortex via inspection of the phase-averaged velocities as well as a λ_2 based detection method, and found that the vortex core propagates with the phase resolved flow (at the core). In addition, they found that the vortex strength (or circulation) Γ defined as

$$\Gamma \equiv \int_{A_{\text{core norm}}} (\vec{\nabla} \times \vec{V}) \cdot \hat{n} dA_{\text{core norm}} \tag{5.24}$$

where the unit vector $\hat{n}$ it tangent to the vortex core-line and the area of integration $A_{\text{core norm}}$ is in the plane normal to $\hat{n}$, decreased downstream (presumably due to energy transfer from the organized (vortex) motion to the smaller (turbulent) scales). In addition, the Authors compared the λ_2 based detection method with a vorticity (threshold) based method and concluded that the latter was highly dependent on threshold level and thus not suitable for vortex identification. The null axial velocity technique for vortex detection was also compared with both the λ_2 and (planar maximum) vorticity tracking scheme and found to be unsuitable far from the blade ($r/R > 1.6$) where the mean axial velocity $\not\approx 0$. Sharp et al [68] performed 3-D PIV phase-averaged measurements on a Rushton stirred vessel and utilized a λ_2 as well as vorticity-based vortex detection scheme. The trailing vortices were clearly identified (and the location of peak TKE was found to be near the disk-plane between the trailing vortex pairs). Finally, Schafer et al [66] made ensemble and phase averaged measurement of velocity for a Rushton turbine under turbulent conditions ($Re = 5(10^4)$). They, like the previous studies, observed the dual trailing vortices.

Stoots et al [70] examine LDA measurements derived phase averaged blade relative velocities (flow in blade relative frame) for turbulent flow ($Re = 3(10^4)$). They found that in the blade frame the vortices begin to lose their coherence within 20° of impeller rotation down-stream from blade suction-side. The maximum/minimum radial velocities on the pressure/suction-side of the blades is evident and the upper and lower blade suction-side tip separations also are visible. Finally, the region of maximum (phase-averaged) flow deformation (related to turbulence generation) occurs on the blade suction-side and is associated with the presence of the blade trailing vortex.

Derksen et al [16] performed phase averaged LDA measurements down-stream for the

impeller for a Rushton turbine at a $Re = 29(10^3)$, identified and tracked the vortex core via a λ_2 technique and found the familiar radial and subsequent circumferential progression of the vortex down-stream of the blade SS. In addition, Derksen found that axial velocity based vortex core detection methods are inaccurate due to the requirement of a vanishing axial mean-flow velocity component at the vortex core. However, this need not be the case very near the impeller blade trailing edge where the exit stream mean-flow axial velocity is negligible. It should also be noted that the Authors determined resolution to be relatively poor near the blade, thus tracking of the vortex and its visualization near the impeller trailing edge is suspect.

Van't Riet et al [63] measured impeller exit stream velocities (via hot wire anemometry), calculated mean-flow and corresponding perturbation values and found that the periodic motion due to impeller wake/vortex produced pseudo-turbulence. The Authors found that the resulting power spectrum did not exhibit the classic $-5/3$ power law in the inertial range close to the impeller (i.e. in the wake/vortex effected region). This is in contrast to locations near the tank wall where the $-5/3$ power spectrum was identified. The Authors concluded that the measured perturbation velocities near the blade included pseudo-turbulence associated with the periodic motion which is not, strictly speaking turbulence, but periodic flow perturbations from the passing blades. Likewise, correspondence of the power spectrum to the classic $-5/3$ power law farther away from the impeller indicates the periodic motion due to the impeller induced vortex (termed pseudo-turbulence) decays to turbulence upon vortex breakup down-stream from the impeller.

Tabor et al [72] performed a sliding deformable mesh simulation for turbulent flow in a Rushton turbine mixer. The Authors examined vorticity and noted the double looped flow structure above and below the impeller disk associated with the trailing vortices. The Authors also note a region of high vorticity adjacent to the blade and disk on the suction-side which they attribute to boundary-layer effects.

Brucato et al [9] perform a comparison of explicit boundary condition, multiple reference frame and sliding deformable mesh simulations of a Rushton turbine under turbulent flow conditions ($k\epsilon$ turbulence modeling). They found the sliding deformable mesh methodology provided a highly accurate representation of the mean-flow compared to the alternative methods. The trailing vortex was also resolved via inspection of the turbulence intensity (however, actual levels of turbulence were significantly under-predicted).

Khopkar et al [36] performed an inner/outer region, turbulent simulations (via $k\epsilon$) on a Rushton Turbine at a Reynolds number $Re = 45(10^3)$ and observed the presence of two trailing vortices emanating from the suction-side (SS) blade surface. However, no further investigation of the vortex details (e.g. core path, dissipation, local pressure field, or causal mechanism via near-blade flow dynamics) was conducted.

Jenne et al [32] performed a number of steady turbulent $k\epsilon$-based simulations for the purpose of assessing performance of various two equation turbulence models in predicting mixing vessel mean-flow quantities (e.g. mean-flow profiles). The standard $k\epsilon$ model of Launder and Spalding [40] failed to predict the presence of trailing vortices (via inspection

of spatial distribution of dissipation down-stream from the blade suction-side). The Authors proceeded to formulate an optimized model based on the best match for the mean-flow velocity distribution in the impeller stream. In contrast to the standard model, the tuned $k\epsilon$ model predicted the local dissipation maxima (at the vortex core) associated with the presence of trailing vortices as previously shown by Wu et al [74]. However, no direct investigation of the vortices is presented nor is direct evidence for the presence of the vortices given (near blade flow field, pressure distribution, etc).

A more detailed approach was undertaken by Lu et al [43] also using computational methods. The Authors use a pressure minimum based vortex tracking method to assess the effect of blade size on vortex size and propagation down-stream for a $Re = 9,200$.
Specifically, they report that the smaller impeller blade produces a smaller vortex which tends to be displaced towards the impeller center-line relative to the larger vortices produced by larger bladed impellers. Sketches of the presumed vortex structure are given for the range of blade sizes indicating that the vortex originates at the suction-side blade leading edge near the disk. The core line then proceeds upwards (i.e. in the axial direction) towards the SS upper tip, turns towards the radial direction at an axial location $\approx H_{BL}/4$, after which detaches from the blade to be convected outward and down-stream from the blade SS. In addition, turbulent kinetic energy increases with distance along the vortex core, indicating the break-up of the vortex into small scale turbulent motions. As in all the previous studies mentioned, no explanation or investigation of the physical mechanism responsible for vortex generation or detachment from the blade are given. In addition, no detailed investigation of the actual flow field near the impeller is given to justify or validate the vortex core tracking method.

Delafosse et al [14] present an even more detailed treatment of the vortices and assess the ability of LES (Smagorinski based) vs. RANS (standard $k\epsilon$) sliding mesh simulations to resolve the trailing vortices for a Rushton turbine operating at $Re = 56(10^3)$. A (phase averaged flow) vorticity based vortex tracking method was then used to identify the path of the vortex core which was then compared with the experimental results of Yianeskis et al [77] and Escudie et al [26]. LES simulation (as opposed to $k\epsilon$) based core trajectories were qualitatively in better agreement with experiments. In addition, for the LES results, turbulent kinetic energy is maximized down-stream from the blade in the vicinity of the vortex core (indicating the vortex break-up in the wake).

Derksen et al [15] utilized a Lattice-Bolzmann unsteady parallel computational technique to simulate Rushton turbine induced turbulent flow in baffled tank using LES (standard Smagorinski). From phase resolved data, the vortices were identified and the core trajectories corresponded qualitatively to the experimental results of Yianneskes et al [76] and Derksen et al [16].

Given the enhance mixing associated with the turbulent motion and fluid stretching present in the impeller trailing vortices, the transport (or injection) of reactants/dilutants into the vortex region is advantageous for enhancing mixing. To this end, the macro-instabilities associated with the intermittent meandering large-scale vortices originating at the impeller

and terminating at the top and bottom of the tank have been studied. Specifically Doulgerakis et al [19] using PIV based measurements of a Rushton turbine mixing tank found that these macro-instabilities originate near the lower (and presumably upper) edge of the impeller and direct fluid from below (and above) onto the impeller region. The implication is that these macro-instabilities could be utilized as a transport mechanism for the transfer of reactants into the impeller region, subsequently entrained in to the trailing vortices, followed by dispersion throughout the tank after which turbulent (small scale) diffusion becomes dominant resulting in effective mixing. Experimental verification of the hypothesis of macro-instability enhanced mixing was attempted by Ducci et all [23] who measured dilute passive scalar mixing times with, and without, injection of the scalar into surface vortices associated with the macro-instabilities. They claimed a statistically significant reduction in mixing time due to direct injection into the macro-instability of $\approx 20\%$ compared with non-macro-instability injection, thus indicating that the macro-instabilities represent a potential species transport mechanism into the near impeller region.

Finally, it should be noted that in none of the studies above is the vortex investigated/analyzed explicitly in the *vortex core frame of reference*.

Investigation of the Vortex

Given the previous visualization of the blade trailing vortices via direct methods such as the swirl parameter (§5.3.2) or indirect methods such as pressure force convergence core detection (§5.3.4), have indicated the existence of a trailing vortex and associated wake, velocity based visual methods will now be utilized for investigative purposes.

Recalling the discussion on augmentation of the vortex flow field in the presence of non-zero bulk fluid motion (see §5.4.2), for visualization purposes it is thus necessary to visualize the flow in the vortex core frame of reference as opposed to the absolute frame (as discussed by Adrian et al [1]). Figure 5.24 (a) gives in-plane velocity unit-vectors and pressure contours in the $x-z$-plane at a location 2.5 blade thicknesses down-stream from the blade suction-side ($y = 3t_{BL}$) and indicates a pressure minimum presumably associated with the vortex cores. Subtracting off the velocity at the pressure minimums for the flow above and below the disk yields a vortex relative flow field as shown in Figure 5.24 (b). The resulting vortex relative velocity field clearly indicates the presence of swirling flow about the local pressure minimum. Similarly, Figure 5.25 (a) gives in-plane absolute velocity unit-vectors and pressure contours in the $y-z$-plane a distance $x/R = 0.82$ (a small distance radially outward from the impeller disk). The vortex is clearly not evident. Again, subtracting off the velocity corresponding to the suction-side pressure minimums for the flow above and below the disk yields a vortex relative flow field as shown in Figure 5.25 (b). The swirling flow associated with the trailing vortices are clearly evident in the resulting vortex frame. Hence, via visual inspection of the flow field in the appropriate (vortex relative) frame, the existence of two well defined suction-side vortices has been verified. The question now arises as to how far down-stream a coherent pair of trailing vortices propagate. Figure 5.26 shows approximate (a) scaled and (b) unit-vector (right most vortex based) relative velocities and pressure contours in the $x-z$

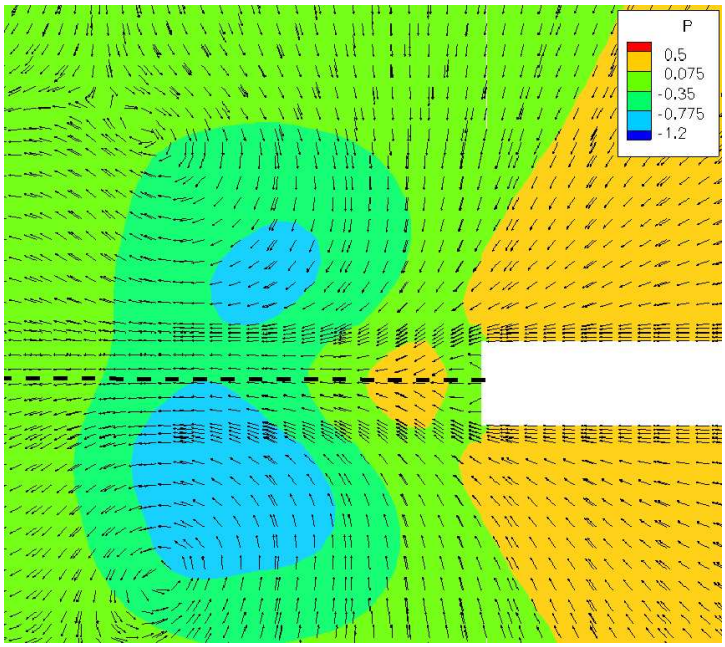

(a) Absolute velocity

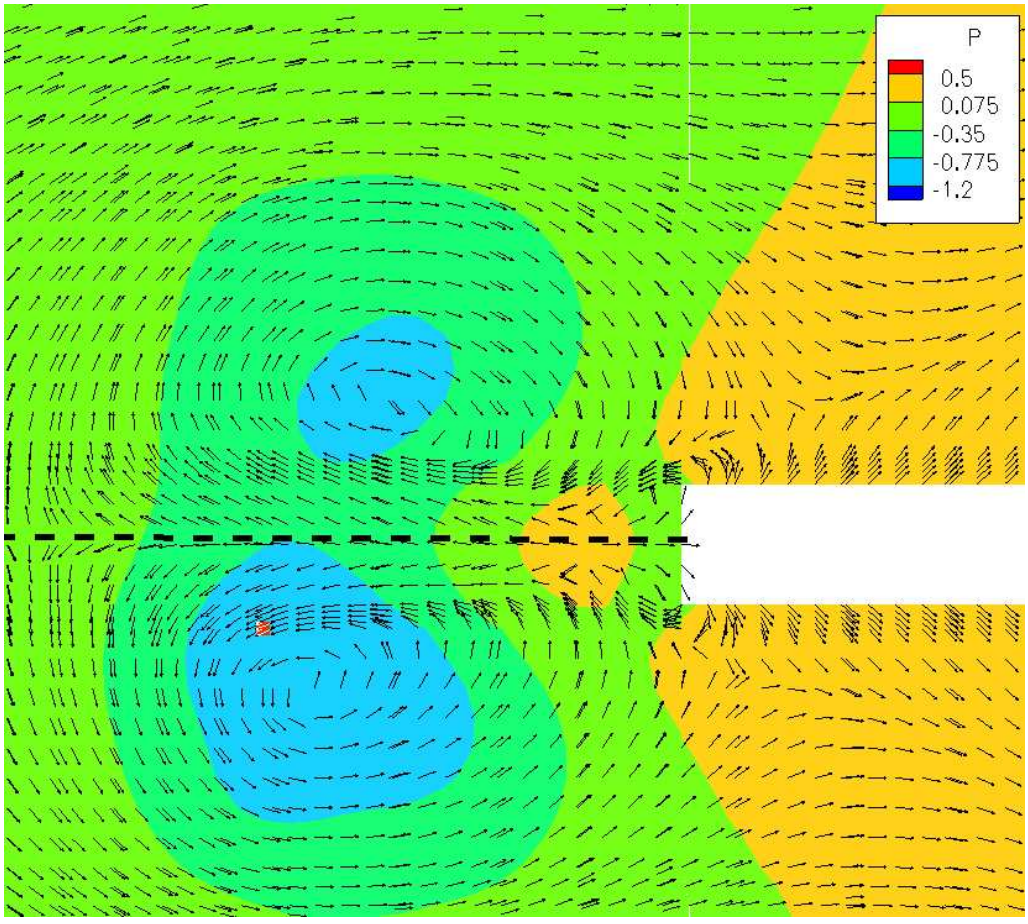

(b) Vortex relative velocity

Figure 5.24: Absolute (a) and vortex relative frame (b) velocity unit-vectors and normalized pressure contours in $x-z$-plane at $y = 3t_{BL}$ ($2.5t_{BL}$ downstream (suction-side) from blade surface). Blade motion into page. Disk plane signified by dashed line $- - -$.

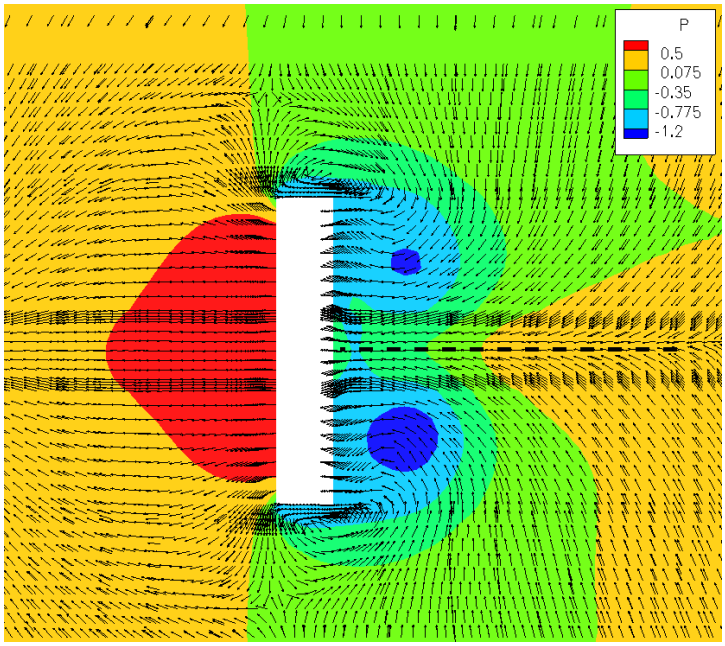

(a) Absolute velocity

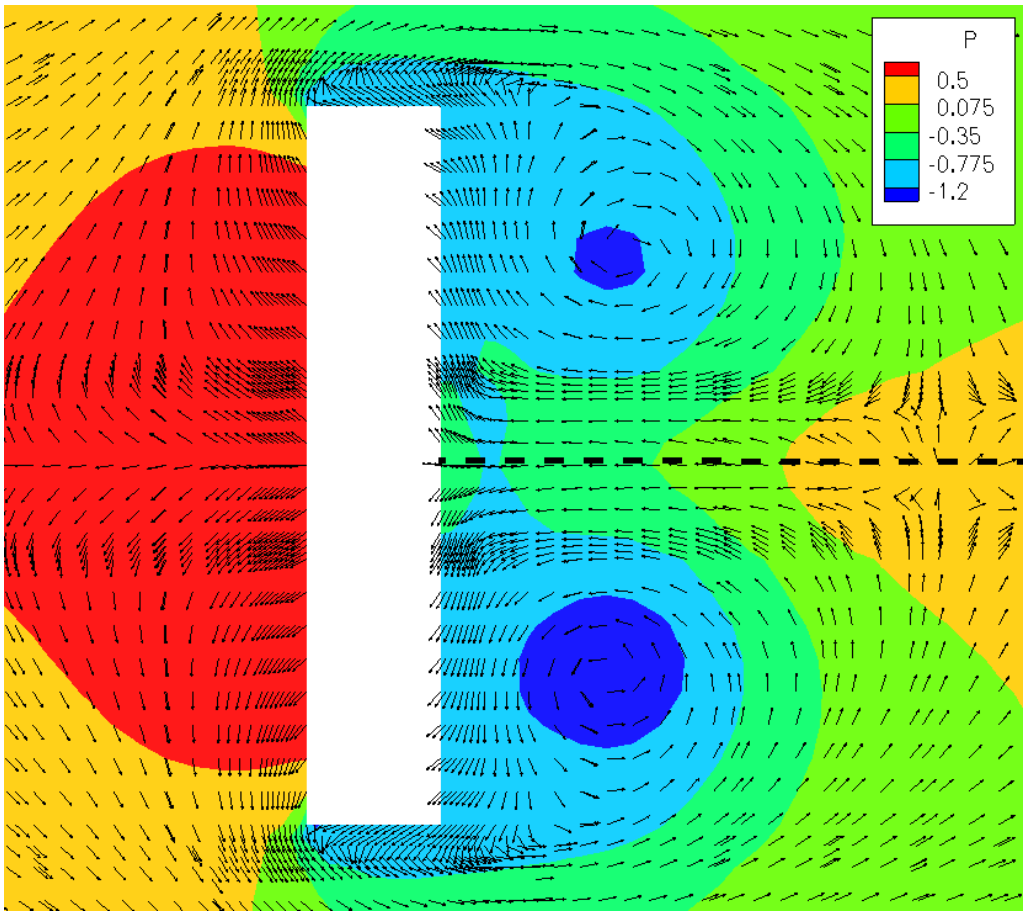

(b) Vortex relative velocity

Figure 5.25: Absolute (a) and vortex relative frame (b) velocity unit-vectors and normalized pressure contours at $y-z$-plane a distance $x/R = 0.82$ from impeller center. Blade motion right to left. Disk plane signified by dashed line $- - -$.

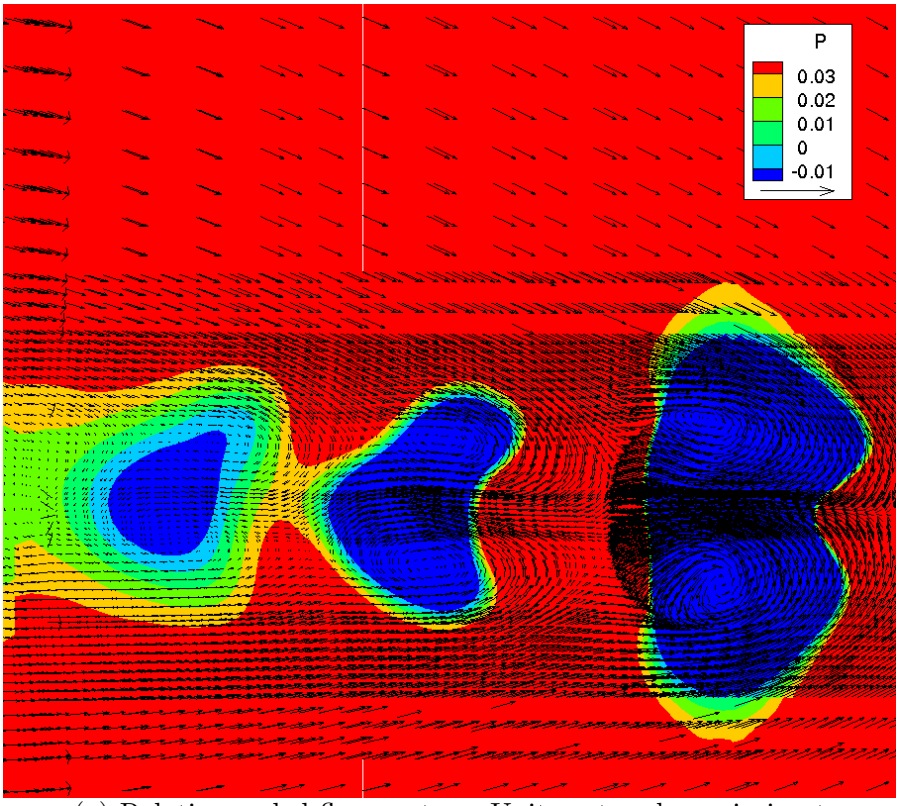

(a) Relative scaled flow vectors. Unit-vector shown in inset

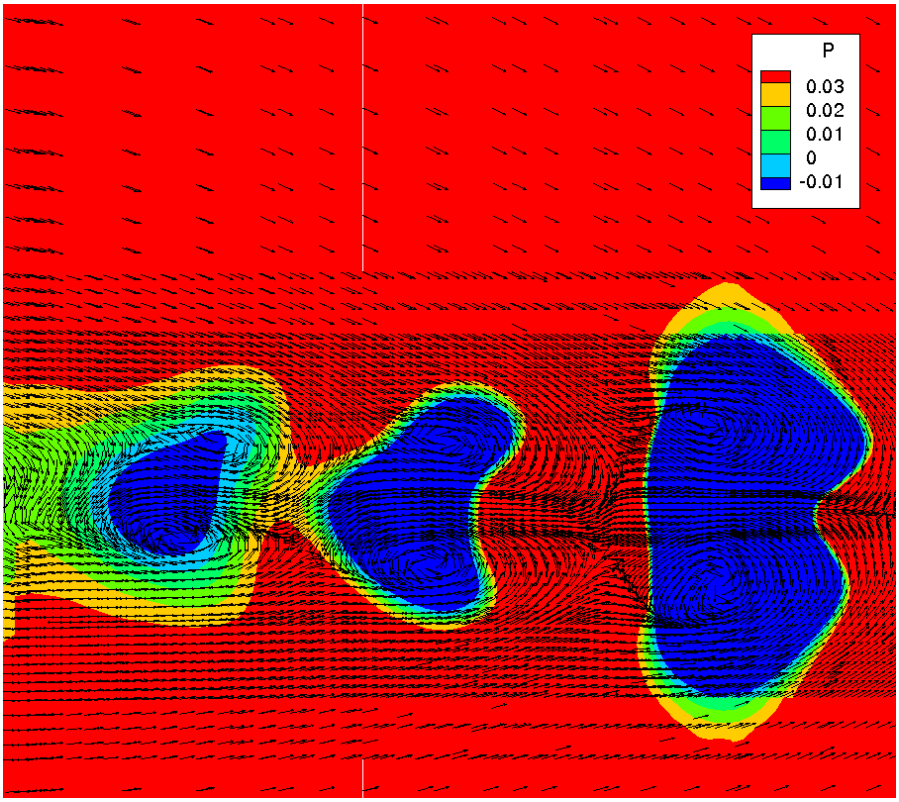

(b) Relative flow vectors normalized

Figure 5.26: Vortex relative frame velocity scaled vectors (a) normalized velocity, (b) unit-vectors and scaled pressure contours in $x-z$-plane at $y = R$.

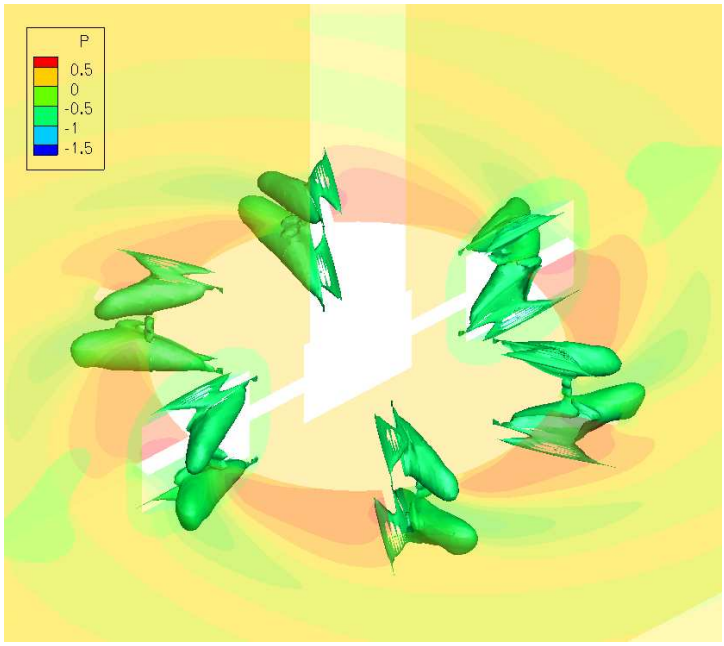

(a) Normalized pressure iso-surface

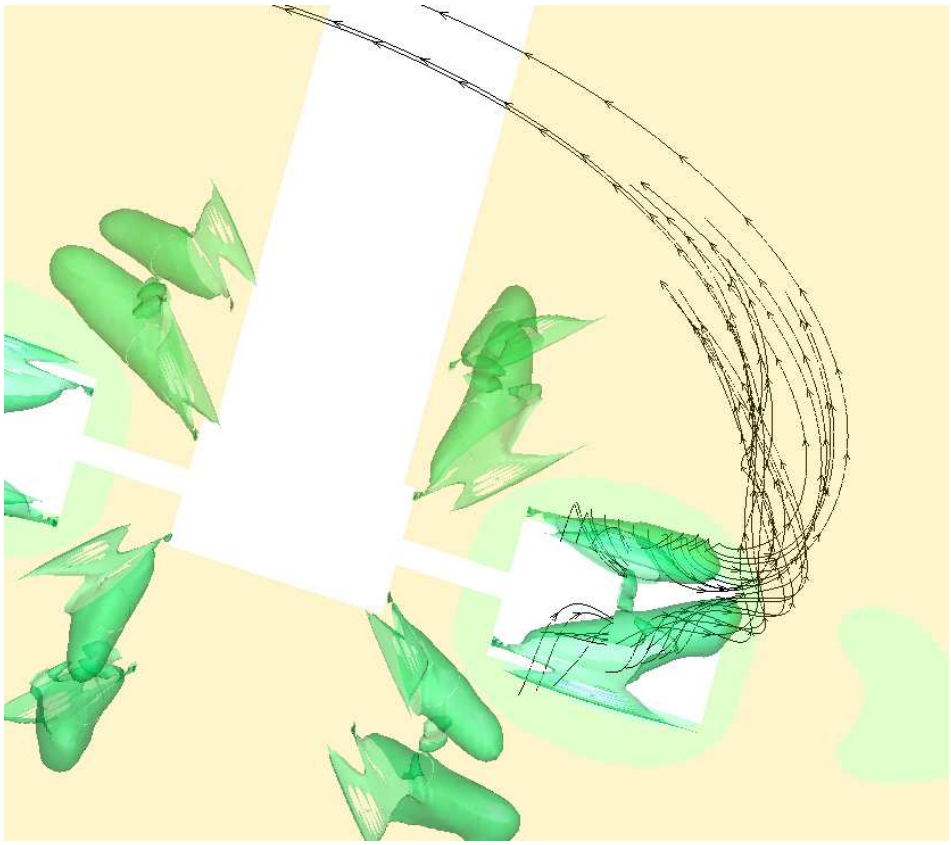

(b) Normalized pressure iso-surfaces and blade relative velocity stream-lines

Figure 5.27: Normalized pressure iso-surfaces (a) with blade relative stream-lines (b) (for $P_{norm} = -0.9$). Blade motion is clockwise.

plane at a distance $y = R$. From Figure 5.26 (b) it is apparent that there exists three pairs of vortices and their associated pressure minimums.

The right most vortex pair is due to the trailing vortex just down-stream (suction-side) from a given blade. The intermediate vortex pair is associated with the trailing vortex shed from a preceding blade 60° up-stream, while the left most pair is associated with a preceding blade at total of 120° upstream. Thus, it is apparent that the underlying trailing vortex structure remains in-tact at least 120° of blade rotation down-stream from the blade of origin. Note, this is a minimum distance given that the sliding mesh interface exists just to the left of both images and, due to the fact that the vortices have their origin at the impeller, it is not possible to resolve these vortex flow structures in the tank-fixed or baffle frame $r > R_{sl}$. However, it is assumed that viscous effects (perturbation and mean-flow induced) serve to eventually dissipate the vortical motion as the vortices are convected down-stream from the impeller. This is indicated by Figure 5.26 (a) where we see a significant reduction in vortex strength from right to left.

The presence of the vortex can be further illustrated by Figure 5.27 (a) which gives iso-surface of normalized pressure (-0.9) and indicates a pressure minimum, cone-like structure associated with the upper and lower vortex cores. Figure 5.27 (b) superimposes stream-lines based on the velocity in the impeller relative frame. The movement of flow from the pressure to the suction-side, (due to the pressure differential), is evident, resulting in the instigation of swirling flow on the blade suction-side. Further, as indicated by the relative velocity stream-lines, the swirling flow (vortex) is convected outwards and down-stream relative to the blade. This motion follows the trajectory of the pressure minimum and verifies the analysis made using the pressure force convergence method in §5.3.4. These observations are reinforced by Figures 5.28 and 5.29 which give scaled blade relative velocity and pressures in both the $x-y$ and $y-z$-planes. Specifically, Figure 5.28 (b) gives scaled impeller frame unit flow vectors a slight distance radially outward from the impeller disk surface $r/R = 0.75$. As can be seen, the flow moves under the influence of the pressure force up and over or down and around the upper or lower blade tip respectively, resulting in the formation of two suction-side trailing vortices. In addition to the trailing vortices, separations form on the upper and lower blade tip surfaces as well as the upper suction-side (SS) surface, however these separations are small compared with the overall size and strength of the trailing vortex as can be seen from Figure 5.28 (a) which gives impeller frame flow vectors. It should also be noted that a small vortex/separation forms near the inter-section between the blade (SS) surface and disk.

While the flow separation on the blade upper/lower tip/suction-side surface, (driven by the pressure-side to suction-side pressure differential induced force), explains the origin of the blade trailing vortex, it remains to be seen what additional mechanism is responsible for the detachment of the vortex from the blade suction-side surface. To this end Figure 5.29 gives scaled impeller frame flow vectors and pressure in the $x-y$ plane as various axial locations below the disk-plane ($z = 0$). Figure 5.29 (a) ($z = 0$) indicates that flow is moving (relative to the blade) from the pressure to suction side as dictated by the pressure force (see Figure 5.18 (b) or (c)), and detaches from the blade at the impeller blade trailing edge due to flow

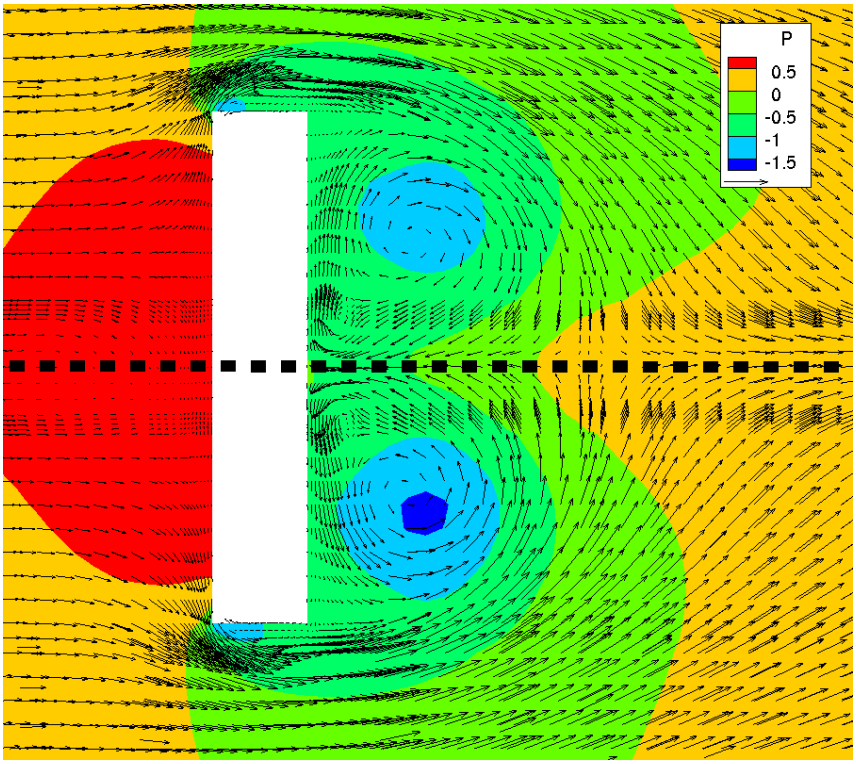

(a) Blade relative flow vectors

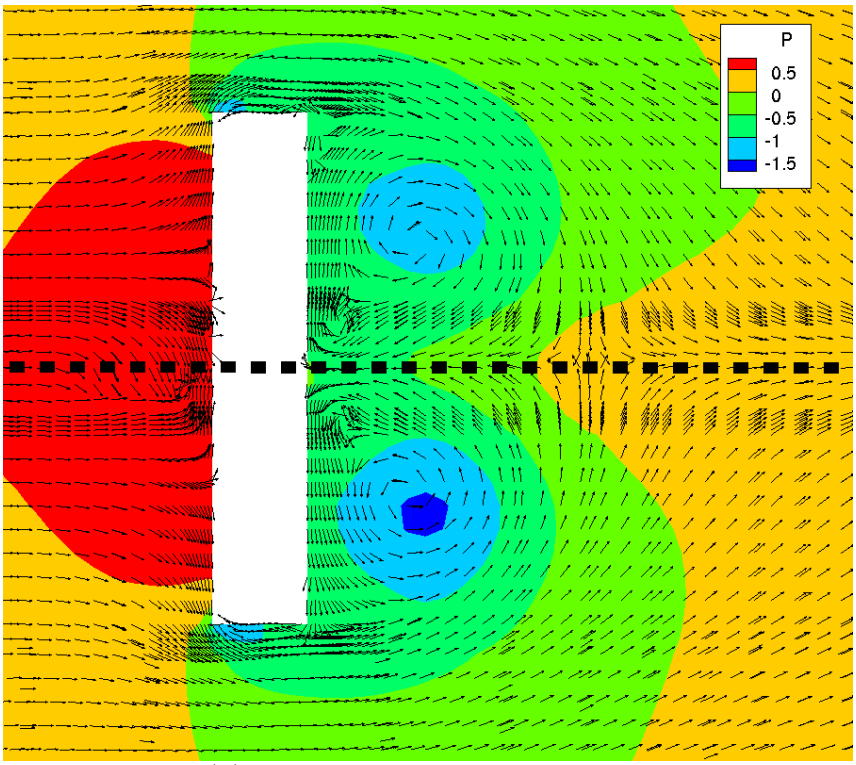

(b) Blade relative flow unit-vectors

Figure 5.28: Impeller relative velocity vectors (a) and unit-vectors (b) and normalized pressure contours in $y-z$-plane at $x/R = 0.75$. Blade motion from right to left. Disk plane signified by dashed line $- - -$.

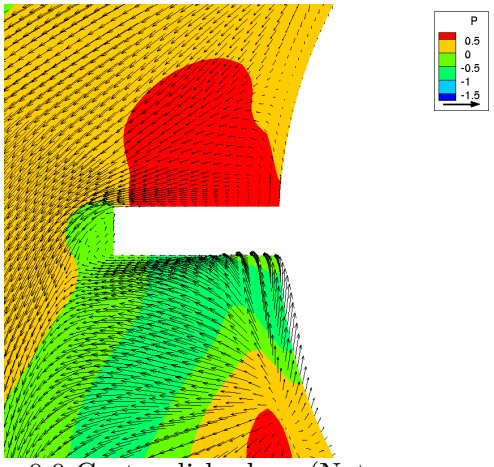

(a) $z/(H_{BL}/2) = 0.0$ Center disk-plane (Note presence of disk on rhs)

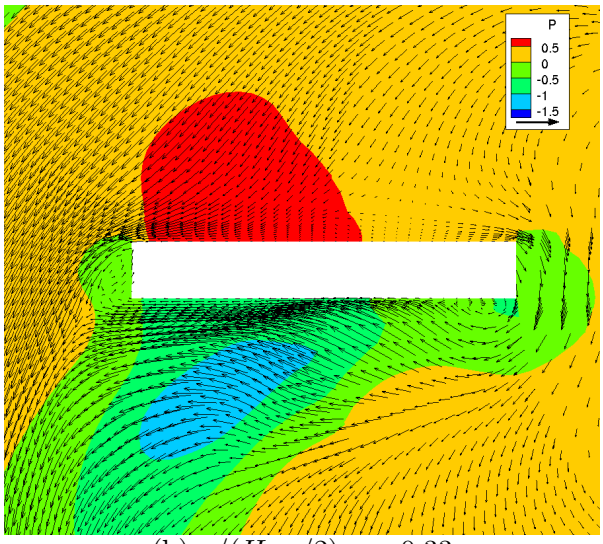

(b) $z/(H_{BL}/2) = -0.33$

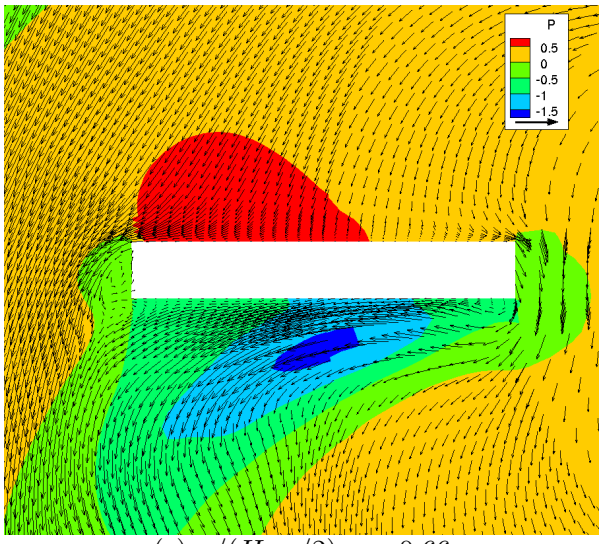

(c) $z/(H_{BL}/2) = -0.66$

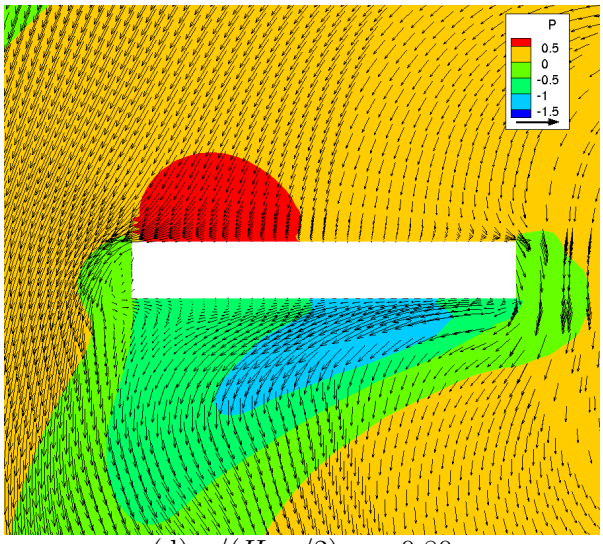

(d) $z/(H_{BL}/2) = -0.80$

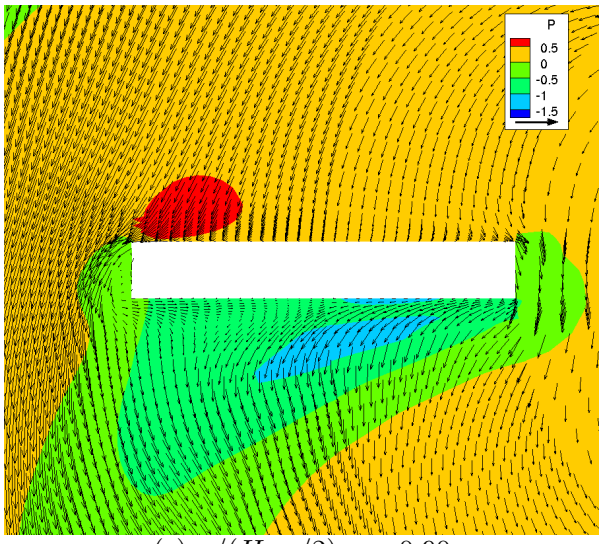

(e) $z/(H_{BL}/2) = -0.90$

Figure 5.29: Impeller relative normalized velocity vectors and pressure contours at impeller blade in the $x-y$-plane for various distances below the disk center. Blade motion is upward. Note, $H_{BL}/2$ is blade half-height and reference (unit) vector provided in inset.

separation. This separation is, however, confined to the trailing edge only and does not result in reverse flow on the blade SS. However, the same cannot be said as we move downward from the disk plane to the lower tip surface (at $z/(H_{BL}/2) = -1.0$). Specifically, at $z/(H_{BL}/2) = -0.66$ a separation at the blade SS trailing edge is evident as flow moves around the impeller trailing edge under the influence of the pressure force. Moving further down to $z/(H_{BL}/2) = 0.9$ significant separation is evident and nearly half of the blade SS surface is separated. This indicates that the vortex formed on the SS migrates outward and detaches from the impeller surface under the influence of reverse flow originating at the blade SS upper and lower trailing edge. Again, as indicated in Figure 5.18 this separation on the SS trailing edge is due to the presence of the SS/PS pressure difference induced force. It should also be noted that minimum SS scaled pressure appears to occur at $z/(H_{BL}/2) = -0.66 \approx -0.5$. Given that the pressure minimum is associated with the trailing vortex core, this indicates that near the blade, the vortex core is located approximately half way between the disk and the upper/lower blade surfaces. Hence, justifying the use of the mid-half-blade depth at the pressure force convergence vortex core detection plane discussed in §5.3.4.

5.4.3 Dissipation and Kinetic Energy

To conclude the examination of the mean-flow field, we turn our attention to the mean-dissipation $\overline{\epsilon}$ and kinetic energy $\overline{k}$.

Integrated quantities such as the (mean-flow based) flow number $\overline{\mathcal{F}}$ and instantaneous power $\mathcal{P}$ number were used previously to establish the validity of the simulation. With respect to the latter, power consumption is due to mean, periodic and turbulent dissipation, arising due the mean, periodic and perturbation flow gradients respectively. Specifically, the instantaneous power number $\mathcal{P}$ can be decomposed as follows

$$\mathcal{P} \equiv \overline{\mathcal{P}} + \tilde{\mathcal{P}} + \mathcal{P}' \tag{5.25}$$

where the periodic flow contribution to dissipation will be shown to be negligible, $\tilde{\mathcal{P}} \approx 0$ (see §5.5), and the mean-flow contribution $\overline{P}$ is given by

$$\overline{\mathcal{P}} = \frac{\int_{Vol} \mu(\frac{\partial \overline{U}_i}{\partial x_j} + \frac{\partial \overline{U}_j}{\partial x_i})\frac{\partial \overline{U}_i}{\partial x_j} dVol}{\rho N^3 D^5} \tag{5.26}$$

Calculation of the mean-flow power number via the mean-flow velocities yields $\overline{\mathcal{P}} = 1.78$. Compared to the simulation instantaneous power number $\mathcal{P} \approx 2.95$ we find that approximately 40% of the simulation dissipation is due to turbulent fluctuations. Note that this provides a means of making an estimate for the simulation resolved dissipation compared to the physical system. Specifically, we can estimate that at least 66% of the (global) turbulent dissipation was resolved. This is in comparison with the expected resolution with upper and lower bounds of 80% and 60% respectively assuming a steady-state (statistical) convergence of the simulation. Thus, the estimate of 66% resolution is deemed plausible.[12] Figure 5.30

[12] If we assume the simulation has achieved a statistical steady-state, which Figure 5.8 indicates is clearly

provides a more detailed treatment of mean-flow dissipation. Specifically, Figure 5.30 (a) gives the iso-surface of normalized mean-flow dissipation per unit mass $\bar{\epsilon}$ and indicates two general regions of high mean-flow dissipation: The first being all wetted stationary surfaces adjacent to high velocity flow such as the baffle suction-sides surfaces (where there exists a recirculation zone in the mean (see Figure 5.13 (b))), indicating significant dissipation due to boundary-layer effects. The second is the impeller region which exhibits significant dissipation due to the velocity boundary-layer over the disk, blade edge separations and the resulting trailing-edge vortex. This can be more clearly seen by reference to Figure 5.30 (b) and (c) which give normalized mean-flow dissipation $\bar{\epsilon}$ in the $x-y$-plane at $z=0$ (disk-plane), as well as at the half depth between disk and lower blade edge $z/(H_{BL}/2) = -0.5$. Specifically, regions of high dissipation are at the baffle edges, blade surfaces, (and especially) the suction-side (SS) as well as a region down-stream of the (SS). This latter region (blade suction-side) of high dissipation strengthens as one moves below, or above the disk and results from the influence of the strong swirling flow associated with the blade trailing vortex.

The numerical values given should be noted insofar that the velocity and spatial scales used in the normalization are the tip velocity V_{tip} and impeller diameter D.[13] For example, given that the trailing vortex has a length scale of approximately half the blade half-height and velocity scale on the order of the tip velocity, we expect the *normalized* mean-flow dissipation within the vortex region to take on a value of approximately $((1/(0.1D/2))/D)^2 = 400$. Referring to Figure 5.30 (c) we can see that this is indeed the case since normalized mean-flow dissipation on the blade (SS) takes on the value of $\approx 300 \sim 400$. In addition, the high values of normalized dissipation associated with the blade boundary-layers is due to the fact that the viscous length scales at the blade surface are very small. Indeed, the maximum dissipation due to the boundary-layer at the impeller blade is $\approx 10^6$ indicating a viscous length scale on the order of $D/300 = T/1000 = t_{BL}/10$ or approximately one tenth of the blade/disk thickness.

Figure 5.31 gives normalized mean-flow kinetic energy $\overline{k}$ per unit mass of which high values are primarily associated with the impeller stream and trailing vortex. Specifically, Figure 5.31 (b) gives contours of mean-flow kinetic energy $\overline{k}$ at the disk-plane ($z=0$) and indicates a maximum just down-stream of the blade (SS) at the disk.

---

not the case, then based on the mean-flow power number $\overline{\mathcal{P}}$, the estimated turbulent contribution to the experimental power number (neglecting the contribution due to periodic motion) is $3.55 - 1.78 = 1.77$. Thus, given the instantaneous power number for the simulation is ≈ 2.95, the fraction of resolved to experimental turbulent dissipation is estimated to be $(2.95 - 1.78)/(3.55 - 1.78) = 0.66$, or 66%. Again, it should be noted that this is clearly a lower bound estimate given the lack of steady-state convergence for the simulation. This fraction should be compared with the maximum target resolution of $\sim 80\%$ (which assumes perfect resolution of the target cut-off eddy with length-scale ℓ). If we take into account the fact that our grid formulation assumed a 15% aliasing error in the cut-off eddy frequency (see §C.4) which, for a given velocity scale, implies an over-estimate in eddy length scale of 18% or conversely, an under-estimate of eddy velocity of 15% for a given length-scale, this yields an expected resolution fraction of $0.8 * (0.85)^2 = 0.58 \approx 0.6$ (noting that dissipation scales as $(V/\ell)^2$). This estimate compares relatively well with our estimated (minimum) resolution fraction of 0.66 or 66%. Finally, total integrated mean-flow-dissipation was found to be 0.00158 Watts.

[13]The normalization was performed via the following: The quantity $S_{ij}S_{ij}/(\mu/\rho)$ represents dissipation (power) per unit mass and has units $(V/\ell)^2\nu \sim V^2/t$ hence, an appropriate normalization is of the form $(V_{tip}/D)^2\nu$.

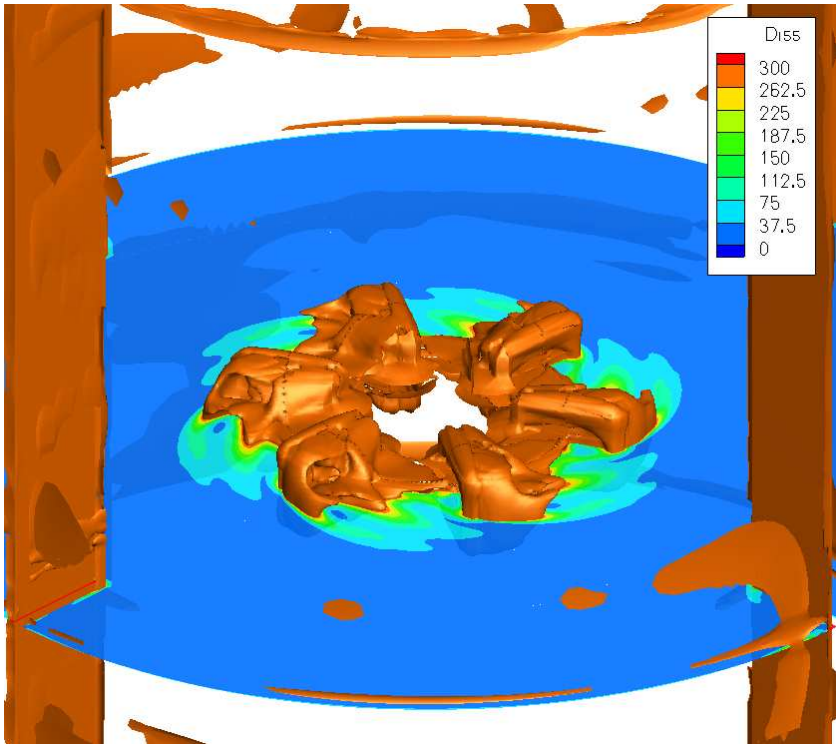

(a) Iso-surface of normalize dissipation of $\overline{\epsilon}/\epsilon_{V_{tip},D} = 300$.

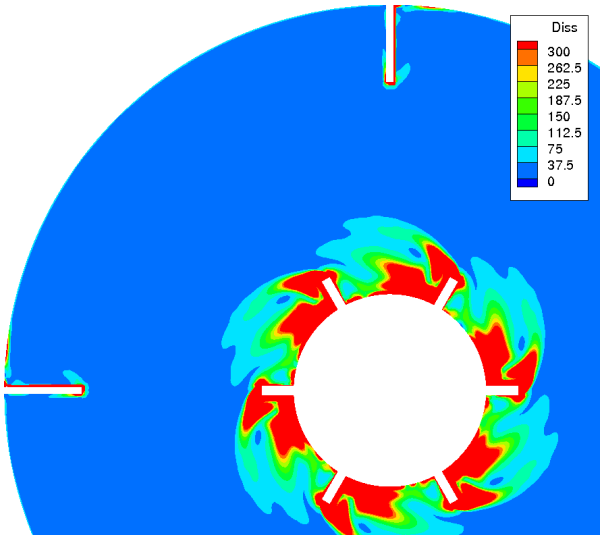

(b) $\overline{\epsilon}/\epsilon_{V_{tip},D}$ at disk-plane ($z = 0$)

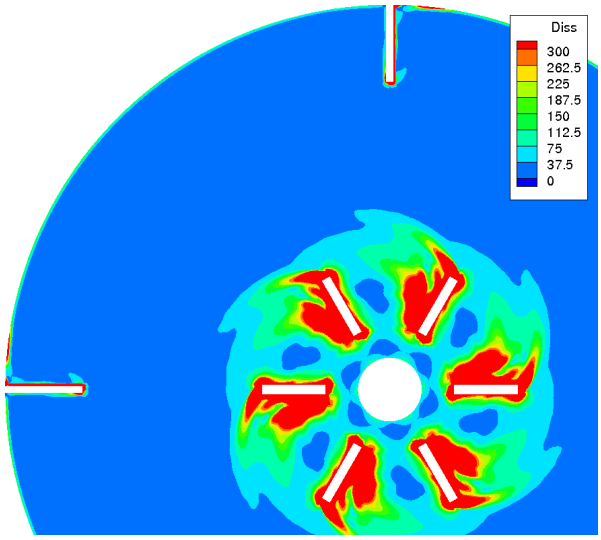

(c) $\overline{\epsilon}/\epsilon_{V_{tip},D}$ in $x-y$-plane at $(z/(H_{BL}/2) = -0.5)$

Figure 5.30: Normalized mean-flow dissipation $\overline{\epsilon}/\epsilon_{V_{tip},D}$ iso-surface (a) and contours. Blade rotation is clockwise.

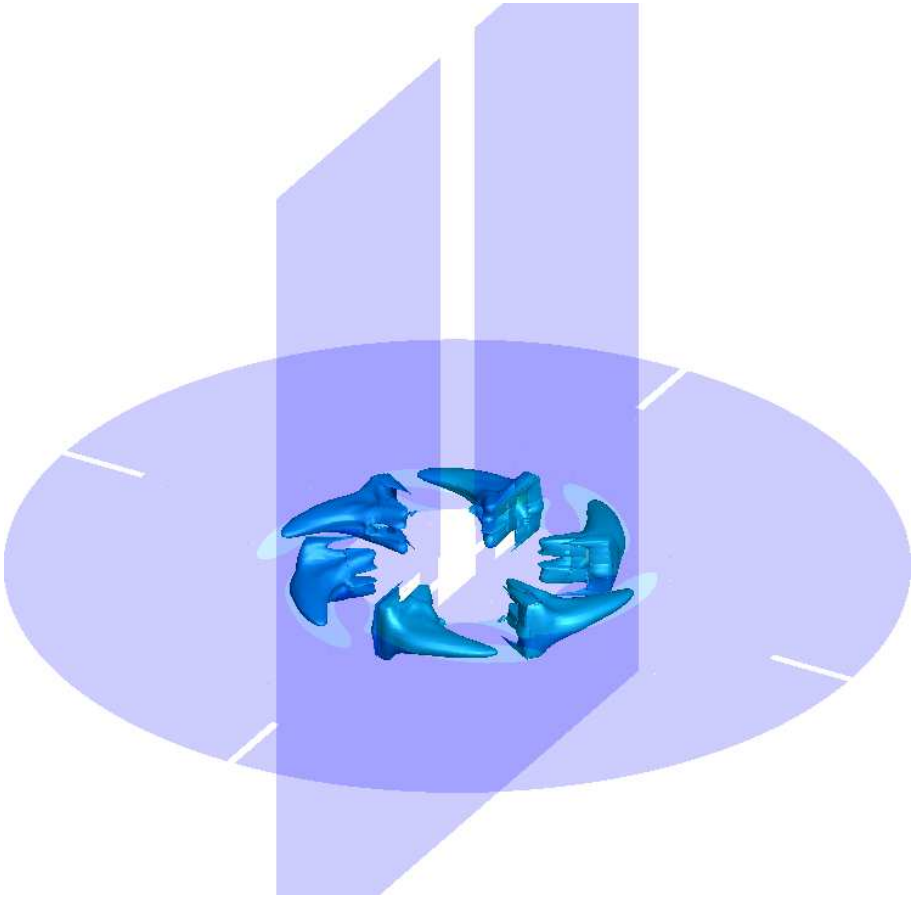

(a) Iso-surface of normalize $\overline{k}/k_{V_{tip}}$ of 0.75.

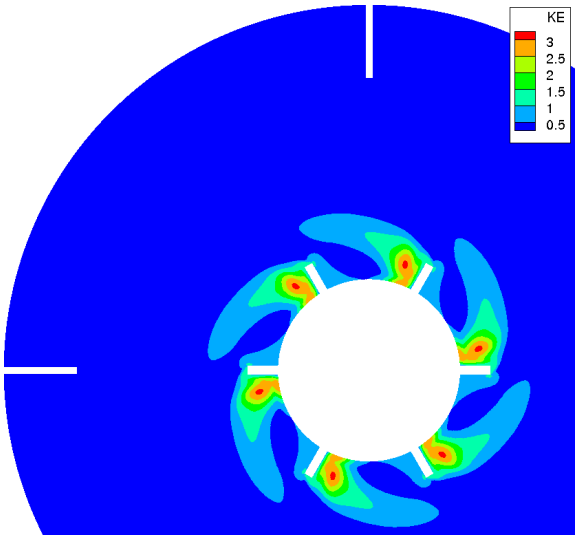

(b) $\overline{k}/k_{V_{tip}}$ at disk-plane ($z = 0$)

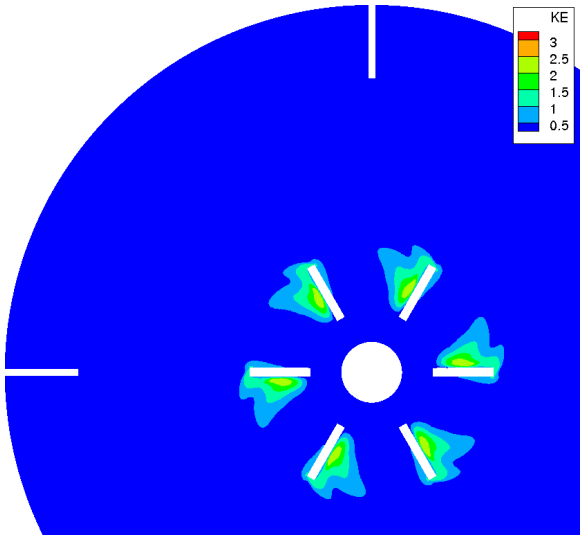

(c) $\overline{k}/k_{V_{tip}}$ in $x - y$-plane at $(z/(H_{BL}/2) = -0.5)$

Figure 5.31: Normalized mean-flow Kinetic Energy $\overline{k}/k_{V_{tip}}$ iso-surface (a) and contours. Blade rotation is clockwise.

This local maximum is associated with compression of the impeller stream via the presence of the upper and lower trailing vortices as well as flow acceleration towards the local pressure minimum associated with the vortex core. Hence, the blade pressure-side, which lacks a vortex pair, has a normalized mean-flow kinetic energy approximately equal to the tip velocity (i.e. a normalized flow kinetic energy $\overline{k}$ is ≈ 1). The same observations apply below the disk at the mid-half depth position ($z/(H_{BL}/2) = -0.5$) in the $x-y$-plane, where normalized mean-flow kinetic energy ranges from 1 near the blade (PS) to 2 on the (SS). Finally, for both planes as well as from the iso-surface shown in Figure 5.31 (a) we see that the mean-flow kinetic energy rapidly declines as the fluid moves away from the blade region into the outer tank which contains relatively slow moving fluid.

Finally, Figure 5.32 shows normalized mean-flow kinetic energy $\overline{k}$ and dissipation $\overline{\epsilon}$ just down-stream from the suction-side impeller surface ($y-z$-plane at distance $x = 1.5t_{BL}$ from SS surface). Specifically, Figure 5.32 (a) shows mean-flow dissipation $\overline{\epsilon}$ is locally minimized at the vortex center and increases towards the outer edge. On the other hand, mean-flow kinetic energy $\overline{k}$ is maximized between the vortices corresponding to the maximum radial velocity associated with the impeller exist stream/jet. Conversely, the minimum mean-flow kinetic energy occurs at the upper and lower vortex outer edges (opposite the central jet) where the vortex relative velocity is in opposition to and counteracts the bulk flow velocity due to the presence of the jet.

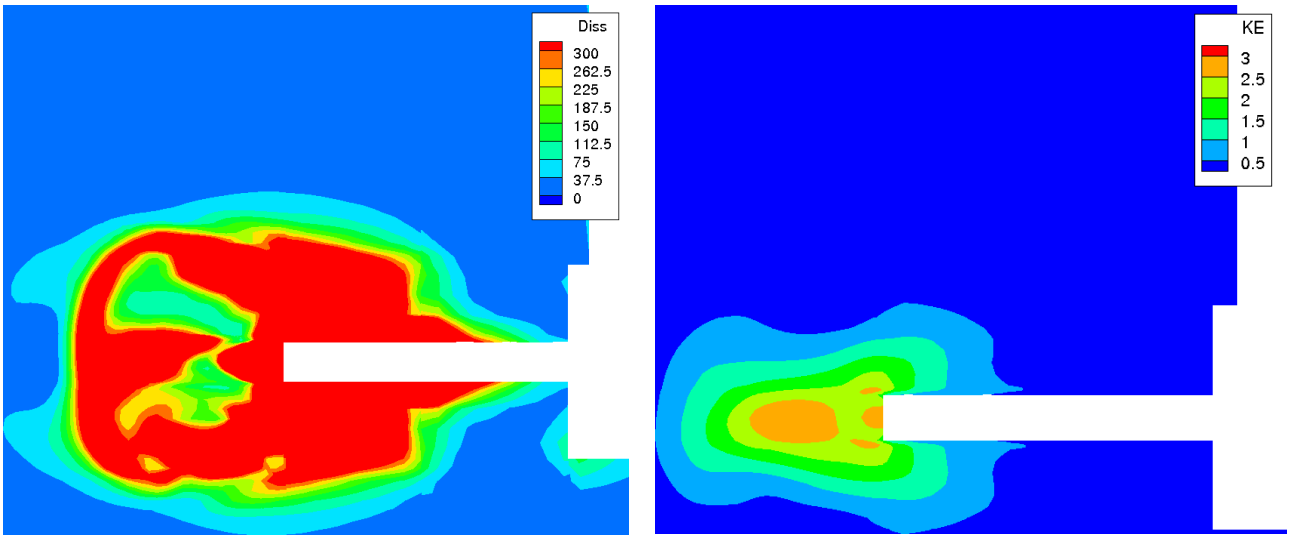

(a) $\overline{\epsilon}/\epsilon_{V_{tip},D}$ (b) $\overline{k}/k_{V_{tip}}$

Figure 5.32: Normalized mean-flow Kinetic Energy $\overline{k}/k_{V_{tip}}$ and Dissipation $\overline{\epsilon}/\epsilon_{V_{tip},D}$ in the $x-z$ plane a distance $2t_b$ downstream from blade SS.

5.5 The Periodic Motion

Given the complexity of calculating and then extracting the periodic contribution to the instantaneous flow, a preliminary estimate for the periodic motion was calculated to ascertain its significance compared to the mean and turbulent flow. Specifically, given the discussion in §5.2.6 the instantaneous flow solution less mean-flow were averaged over every 6^{th} and 4^{th} of an impeller revolution to arrive at a stator and impeller frame averaged periodic flow respectively. Given the low number of samples, 240 and 160 for the stator and impeller relative frames, cylindrical symmetry was utilized to double the number of samples for a given impeller angle. The result is Figure 5.33 which gives normalized periodic velocity vectors $\tilde{\vec{V}}/V_{tip}$ and periodic pressure $\tilde{P}/P^{dyn}_{V_{tip}}$ for an impeller angle $\phi = 30°$ (corresponding to observation plane $\theta = 0°$). Although lack of convergence of the periodic flow is evident, the partially converged periodic motion can be used to ascertain the importance of the periodic flow contribution to the instantaneous velocity and pressure field. Specifically, from inspection Figure 5.33 indicates periodic flow magnitudes on the order of $\sim 0.05V_{tip}$ while variations in periodic pressure are on the order of $0.01P^{dyn}_{V_{tip}}$. No apparent flow structures are evident. Comparing the disk plane periodic flow given in Figure 5.33 (b) with the mean-flow shown in Figure 5.12 (b) indicates that the mean-flow with velocity magnitude $\sim V_{tip}$ typically exceeds the periodic flow by over an order of magnitude. Likewise, from Figure 5.13 variations of mean-flow pressure are $\sim P^{dyn}_{V_{tip}}$ which is approximately two orders of magnitude higher than the periodic pressure variations as indicated in Figure 5.33. Furthermore, comparison of the mean $\overline{k}$ and periodic flow normalized kinetic energy $\tilde{k}$ shown in Figure 5.31 and 5.34 respectively, indicates a normalized mean-flow kinetic energy ~ 1 while the periodic motion exhibits normalized kinetic energy ~ 0.001. This indicates that the contribution of the periodic velocity and pressure variations to the instantaneous velocity and pressure field variations are, compared with the mean-flow, negligible. In addition, given that the periodic motion is negligible, viscous dissipation due to such motions is also negligible compared to the mean flow dissipation. Note, it has yet to be determined if the periodic variation in flow properties $\tilde{\vec{V}}$ and $\tilde{P}$ can be neglected compared with turbulent property perturbations $\vec{V}'$ and P', however, as will be shown in §6.5, averaged perturbation kinetic energy fluctuations $\overline{k'}$ exceed that of the periodic motion $\tilde{k}$ by several orders of magnitude.

Hence, the contribution of the periodic motion, (in both the impeller and baffle/tank frame), to the flow is found to be negligible, thus allowing for direct calculation of the flow perturbation properties from the mean and instantaneous flow solution. This analysis of the turbulent motion will be conducted in Chapter 6.

5.6 Concluding Remarks

A high resolution (direct numerical) simulation of transitional flow for a Rushton stirred mixing vessel at a $Re = 3(10^3)$ was performed and mean-flow properties were investigated and analyzed. In preparation for this investigation, a combination of experimental, bulk control volume and LES derived estimates for turbulent length and time scales were formulated.

These turbulent scale estimates were used to create a suitable high resolution geometry from which the unsteady, time accurate flow solutions are calculated via a parallel flow solver. The resulting flow simulation results are estimated to resolve $60 - 80\%$ of the turbulent dissipation based on comparison with the estimated experimentally derived power number. The instantaneous flow solution exhibited flow structures indicative of turbulence over a range of scales as well as the presence of trailing vortices within the impeller stream.

Mean-flow properties (in the impeller or baffle fixed frame) were calculated. The mean-flow field indicates the presence of two, well defined, trailing vortices as well as the familiar dual looped bulk-flow recirculation zones above and below the impeller stream. Comparison with experimentally derived mean-flow axial, radial and circumferential velocities indicated good quantitative agreement between experimental and simulation results.

The fundamental force interactions were also investigated. It was found that the flow, except very near the impeller and tank wall surfaces, is pressure driven with an associated balance between pressure and inertial forces. This is in contrast to the case of low and very low Re flows investigated in Chapter 4 where the interaction between pressure and viscous forces were important. From the calculated pressure force a pressure force convergence based vortex core tracking procedure was used to visualize the trajectory of the trailing vortex. This trajectory is in qualitative agreement with experimental measurements of the vortex core location relative to the blade. The concept of a vortex relative frame was then utilized to distinctly visualize the trailing vortices. The vortices were found to originate due to the movement of fluid from the blade pressure-side, over the blade tip and toward the disk via the blade suction-side (SS) under the influence of the pressure force. The resulting recirculation zone, (visible in the vortex relative and impeller frames) detaches from the blade suction-side (SS) due to a separation on the blade trailing edge near the blade upper/lower trailing edge. The resulting impeller frame mean-flow vortices are convected outward and remain coherent for at least two full blade passes 120° down-stream.

Finally, for the impeller and baffle-fixed frame, an estimate of the periodic flow field was calculated, indicating that for a sliding mesh formulation, the periodic velocity and pressure variation are negligible compared to the impeller/baffle frame mean-flow. Hence, the present impeller/baffle frame mean-flow solution can be utilized directly in the calculation of perturbation or turbulent properties as presented Chapter 6.

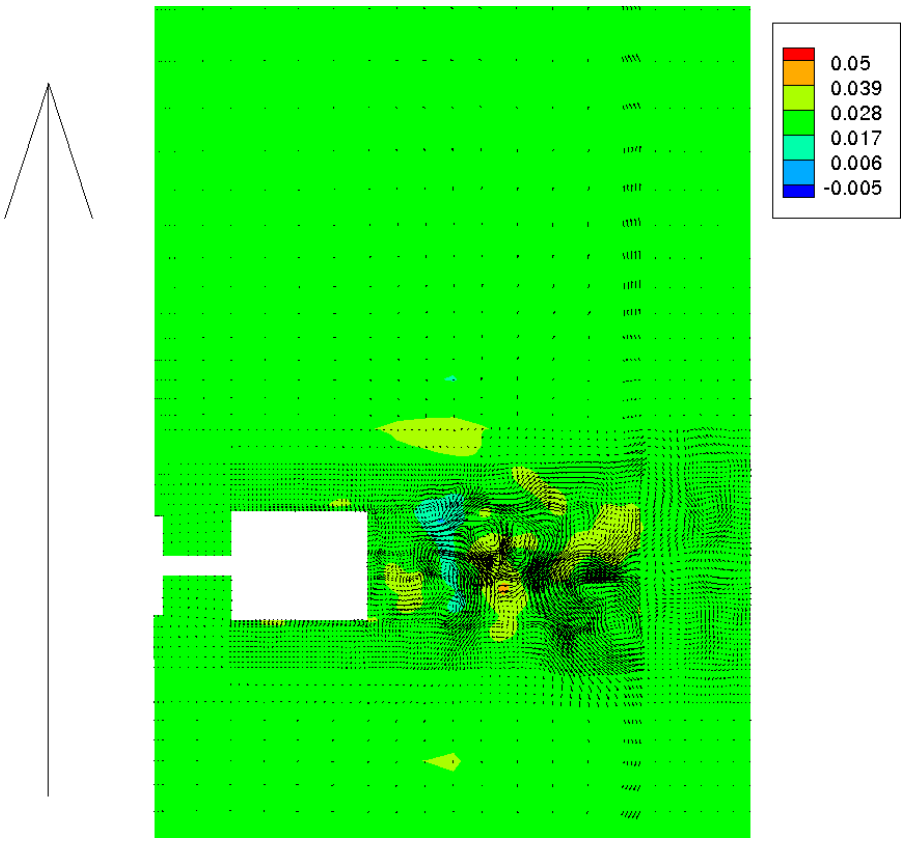

(a) $x-z$-plane $y=0$.

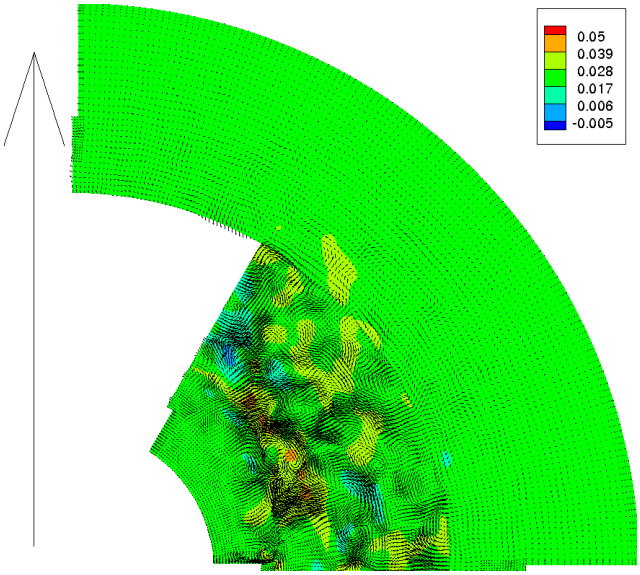

(b) Disk-plane ($z=0$)

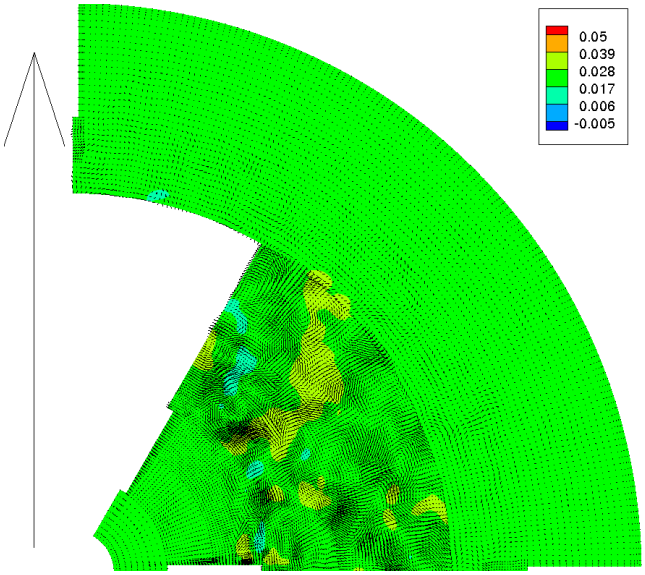

(c) $x-y$-plane at $(z/(H_{BL}/2)=-0.5)$

Figure 5.33: Normalized periodic flow velocity vectors $\tilde{\vec{V}}/V_{tip}$ and pressure contours $\tilde{P}/P^{dyn}_{V_{tip}}$. Unit vector shown left. Blade rotation is clockwise (b) and (c).

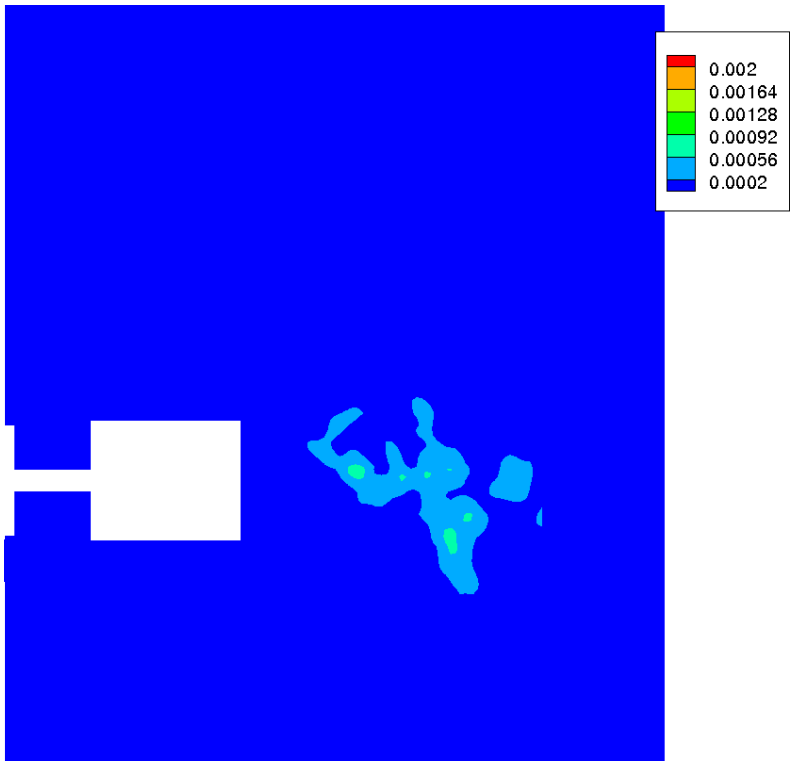

(a) $\tilde{k}/k_{V_{tip}}$ $x-z$-plane $y=0$.

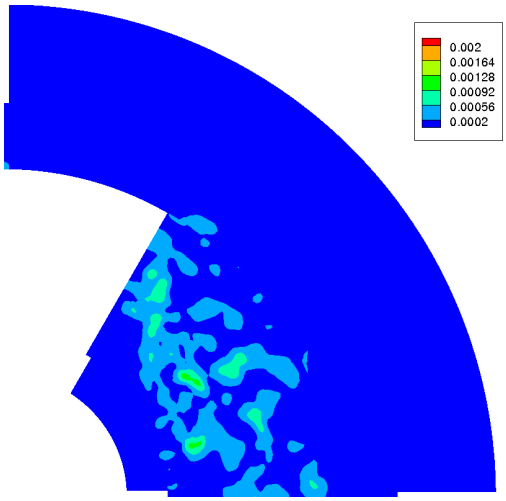

(b) $\tilde{k}/k_{V_{tip}}$ at disk-plane $(z=0)$

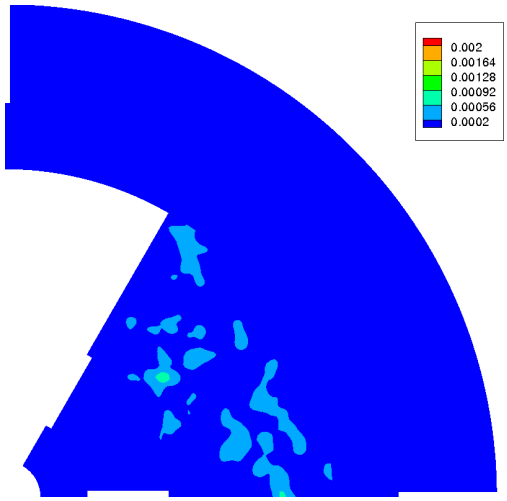

(c) $\tilde{k}/k_{V_{tip}}$ in $x-y$-plane at $(z/(H_{BL}/2)=-0.5)$

Figure 5.34: Normalized periodic flow Kinetic Energy $\tilde{k}/k_{V_{tip}}$ contours. Blade rotation is clockwise.

References

[1] R. Adrian, K. Christensen, and Z. Liu. Analysis and interpretation of instantaneous turbulent velocity fields. *Experiments in Fluids*, 2000.

[2] M. Assirelli, W. Bujalski, A. Eaglesham, and A. Nienow. Intensifying micro-mixing in a semi-batch reactor using a Rushton turbine. *Chemical Engineering Science*, 2004.

[3] A. Bakker and L. Oshinowo. Modelling of turbulence in stirred vessels using large eddy simulation. *Trans. IChemE*, 82:1169–1178, 2004.

[4] S. Baldi, A. Ducci, and M. Yianneskis. Determination of dissipation rate in stirred vessels through direct measurements of fluctuating velocity gradients. *Chemical Engineering Technology*, 2004.

[5] F. Barailler, M. Heniche, and P. Tanguy. CFD analysis of a rotor-stator mixer with viscous fluids. *Chemical Engineering Science 61*, pages 2888–94, 2006.

[6] C. Bartels, M. Breuer, and K. Wechsler F. Durst. Computational fluid dynamics applications on parallel-vector computers: Computations of stirred vessel flows. *Computers and Fluids 31*, pages 66–97, 2002.

[7] C. Berdahl and D. Thompson. Eduction of swirling structure using the velocity gradient tensor. *AIAA Journal*, 1993.

[8] Y. Bouremel, M. Yianneskis, and A. Ducci. On the utilization of vorticity and strain dynamics for improved analysis of stirred processes. *Fluid Mixing* 13, 2009.

[9] A. Brucato, M. Ciofalo, F. Grisafi, and M. Giorgio. Numerical prediction of flow fields in baffled stirred vessels: A comparison of alternative modelling approaches. *Chemical Engineering Science*, 1998.

[10] D. Chapple, S.M. Kresta, Wall, and A. Afacan. The effect of impeller and tank geometry on the power number for a pitched blade turbine. *Trans IChemE 80*, 2002.

[11] M. Ciofalo, A. Brucato, F. Grisafi, and N. Torraca. Turbulent flow in closed and free-surface unbaffled tanks by radial impellers. *Chemical Engineering Science*, 1996.

[12] J. Costes and J. Couderc. Study by LDA of the turbulent flow induced by a Rushton turbine in a stirred tank. *Chemical Engineering Science*, 1988.

[13] J. Rushton E. Costich and H. Everett. Power characteristics of mixing impellers: Part ii. *Chemical Engineering Progress:46*, pages 467–476, 1950.

[14] A. Delafosse, J. Morchain, P. Guiraud, and A. Line. Trailing vortex generated by a Rushton turbine: Assessment of RANS and LES. 13^{th} *European Conference on Mixing*, 2009.

[15] J. Derksen and A. Van den Akker. Large eddy simulations on the flow driven by a Rushton turbine. *AIChE*, 1999.

[16] J. Derksen, H. Doelman, and H. Van den Akker. Three-dimension LDA measurements in the impeller region of a turbulently stirred tank. *Experiments in Fluids 27*, 1999.

[17] J. Derksen and H. van den Akker. Large eddy simulation of stirred tank flow by means of a lattice-Boltzmann scheme. *Int. J. Heat and Fluid Flow*, 1998.

[18] M. Distelhoff, A. Marquis, J. Nouri, and J. Whitelaw. Scalar mixing measurements in batch operated stirred tanks. *Canadian Journal of Chemical Engineering*, 1997.

[19] Z. Doulgerakis, M. Yianneskis, and A. Ducci. On the interaction of trailing and macro-instability vortices in a stirred vessel-enhanced energy levels and improved mixing potential. *Fluid Mixing* 13, 2009.

[20] A. Ducci. *Direct measurement of the viscous dissipation rate of turbulent kinetic energy in a stirred vessel with two-point LDA*. PhD thesis, Department of Mechanical Engineering, King's College London, 2004.

[21] A. Ducci and M. Yianneskis. Direct determination of energy dissipation in stirred vessels with two-point LDA. *AIChe Journal 51*, pages 2133–2149, 2005.

[22] A. Ducci and M. Yianneskis. Turbulent kinetic energy transport processes in the impeller stream of a stirred vessel. *Chemical Engineering Science 61*, pages 2780–90, 2006.

[23] A. Ducci and M. Yianneskis. Vortex tracking and mixing enhancement in stirred processes. *AIChe Journal*, 2007.

[24] D. Dyster and E.K. Jaworski. An LDA study of the radial discharge velocities generated by a Rushton turbine. *IChemE*, 71:11–23, 1993.

[25] J. Eggels. Direct and large-eddy simulation of turbulent fluid flow using the lattice-bolzmann scheme. *Int. J. Heat and Fluid Flow*, 1996.

[26] R. Escudie, D. Bouyer, and A. Line. Characterization of trailing vortices generated by a Rushton turbine. *AIChE 50*, 2004.

[27] R. Escudie and A. Line. Experimental analysis of hydrodynamics in a radially agitated tank. *AIChE Journal 49*, pages 585–603, 2003.

[28] A. Gunkel and M. Weber. Flow phenomena in stirred tanks part i: The impeller stream. *AIChE*, 1975.

[29] J. Hall. *Study of viscous and visco-elastic flows with reference to laminar stirred vessels.* PhD thesis, Department of Mechanical Engineering, King's College London, 2005.

[30] R. Hockey, J. Nouri, and F. Pinho. *Flow Visualization V.* mcGraw-Hill, 1990.

[31] Z. Jaworski and B. Zakrzewska. Modelling of the turbulent wall jet generated by a pitched blade turbine impeller. the effect of turbulence model. *Trans. IChemE:Chemical Engineering Research and Design 80*, 2002.

[32] M. Jenne and M. Reuss. A critical assessment of the use of $k - \epsilon$ turbulence models for simulation of the turbulent liquid flow induced by a Rushton-turbine in baffled stirred-tank reactors. *Chemical Engineering Science 54*, 1999.

[33] J. Jeong and F. Hussain. On the identification of a vortex. *Journal of Fluid Mechanics*, 1995.

[34] M. Jiang, R. Machiraju, and D. Thompson. Detection and visualization of vortices. *Visualization Handbook*, 2004.

[35] R. Jones, A. Harvey, and S. Acharya. Two-equation turbulence modeling for impeller stirred tanks. *Trans. ASME: Journal of Fluids Engineering*, 2001.

[36] A. Khopkar, J. Aubin, C. Rubio-Atoche, C. Xuereb, N. La Sauze, J. Bertrand, and V. Ranade. Flow generated by radial flow impellers: PIV measurements and CFD simulations. *International Journal of Chemical Reactor Engineering 2*, 2004.

[37] H. Kramers, G. Baara, and W. Knoll. A comparative study on the rate of mixing in stirred tanks. *Chemical Engineering Science*, 1953.

[38] S. Kresta and P. Wood. Flow field produced by a pitched blade turbine. *Chemical Engineering Science 48*, pages 1761–1774, 1993.

[39] H. Laufhutte and A. Mersmann. Dissipation of power in stirred vessels. *Proc.* 5^{th} *Conf. on Mixing*, pages 331–339, 1985.

[40] B. Launder and D. Spalding. *Mathematical Models of Turbulence.* New York:Academic Press, 1972.

[41] K. Lee. *An experimental investigation of the trailing vortex structure and mixing characteristics of mixing vessels.* PhD thesis, King's College London, 1995.

[42] K. Lee and M. Yianneskis. Turbulence properties of the impeller stream of a Rushton turbine. *AIChE Journal 44*, pages 13–24, 1998.

[43] W. Lu, H. Wu, N. Chuang, and Y. Lin. Effect of the blade size on the vortex structure and gas dispersion in gas-liquid stirred vessels with a single Rushton turbine impeller. *Proceedings of the National Science Council R.O.C.*, 2000.

[44] Z. Lu, Y. Liao, D. Qian, J. McLaughlin, J. Derksen, and K. Kontomaris. Large eddy simulations of a stirred tank using the lattice Boltzmann method on a non-uniform grid. *Journal of Computational Physics*, 2002.

[45] J. Luo, A. Gosman, R. Issa, J. Middleton, and M. Fitzgerald. Full flow computation of mixing in baffled stirred vessels. *IChemE*, 1993.

[46] J. Luo, R. Issa, and A. Gosman. Prediction of impeller induced flows in mixing vessels using multiple frames of reference. *IChemE Symposium Series*, 1994.

[47] S. Mahmoudi. *Velocity and mixing characteristics of stirred vessels with two Rushton impellers*. PhD thesis, King's College London, 1994.

[48] P. Meunier and E. Villermaux. How vortices mix. *Journal Fluid Mechanics*, 2003.

[49] S. Michelet. *Turbulent dissipation within a agitation reactor by a Rushton turbine*. PhD thesis, National Polytechnic Institute of Lorraine, 1998.

[50] M. Micheletti. *Study of fluid velocity and mixing characteristics in stirred solid-liquid suspensions*. PhD thesis, Department of Mechanical Engineering, King's College London, 2004.

[51] M. Micheletti, S. Baldi, S. Yeoh, A. Ducci, G. Papadakis, K. Lee, and M. Yianneskis. On spatial and temporal variations and estimates of energy dissipation in stirred reactors. *Chemical Engineering Research and Design 82*, pages 1188–98, 2004.

[52] A. Mujumdar, B. Huang, D. Wold, M. Weer, and W. Douglas. Turbulence parameters in a stirred tank. *Canadian Journal of Chemical Engineering 48*, 1997.

[53] J. Murthy, S. Mathur, and C. Choudhury. CFD simulation of flow in stirred tank reactor using a sliding mesh technique. *IChemE Symposium Series 136*, 1994.

[54] K. Ng, J. Fentiman, K. Lee, and M. Yianneskis. Assessment of sliding mesh CFD predictions and LDA measurements of the flow in a tank stirred by a Rushton turbine. *IChemE*, 1998.

[55] J. Placek, L. Tavlarodes, G. Smith, and I. Fort. Turbulent flow in a stirred tanks, ii: A two-scale model of turbulence. *A.I.Ch.E.*, 1986.

[56] K. Raghav Rao and J. Joshi. Liquid phase mixing in mechanically agitated vessels. *Chemical Engineering Communications*, 1988.

[57] V.V. Ranade and Y.T. Krishnan. Cfd rredictions of flow near impeller blades in baffled stirred vessels:assesment of computational approach. *Chemical Engineering Comm.*, 189:895–922, 2002.

[58] M. Rao and R. Brodkey. Continuous flow stirred tank turbulence parameters in the impeller stream. *Chemical Engineering Science 27*, pages 137–156, 1972.

[59] J. Revstedt, L. Fuchs, T. Kovacs, and C. Tragardh. Influence of impeller types on the flow structure in a stirred reactor. *AIChE Journal 46*, 2000.

[60] J. Revstedt, L. Fuchs, and C. Tragardh. Large eddy simulations of turbulent flow in a stirred reactor. *Chemical Engineering Science*, 1998.

[61] M. Rice, J. Hall, G. Papadakis, and M. Yianneskis. Investigation of laminar flow in a stirred vessel at low reynolds number. *Chemical Engineering Science 61*, pages 2762–70, 2006.

[62] K. Van't Riet and J. Smith. The trailing vortex system produced by Rushton turbine agitators. *Chemical Engineering Science*, 1975.

[63] K. Van't Riet and J. Smith. Real and pseudo-turbulence in the discharge stream from a Rushton turbine. *Chemical Engineering Science*, 1976.

[64] J. Rushton, E. Costich, and H. Everett. Power characteristics of mixing impellers: Part i. *Chemical Engineering Progress:46*, pages 467–476, 1950.

[65] K. Rutherford, S. Mahmoudi, K. Lee, and M. Yianneskis. The influence of Rushton impeller bland and disk thickness on mixing characteristics in a stirred vessel. *IChemE:74*, pages 369–378, 1996.

[66] M. Schafer, M. Hofken, and F. Durst. Detailed ldv measurements for visualization of the flow field within a stirred-tank reactor equipped with a Rushton turbine. *IChemE*, 1997.

[67] K. Sharp and R. Adrian. PIV study of small-scale flow structure around a Rushton turbine. *AIChE Journal 47*, pages 766–778, 2001.

[68] K. Sharp, D. Hill, D. Troolin, G. Walters, and W. Lai. Volumetric three-component velocimetry measurements of the turbulent flow around a rushton turbine. *Experiments in Fluids*, 48:167–183, 2010.

[69] M. Shiue and C. Wong. Studies on homogenization efficiency of various agitators in liquid blending. *Canadian Journal of Chemical Engineering 62*, 1984.

[70] C. Stoots and R. Calabrese. Mean velocity field relative to a Rushton turbine. *AIChE*, 1995.

[71] H. Sun, W. Wang, and Z. Mao. Numerical simulation of the whole three-dimensional flow in a stirred tank with anisotropic algebraic stress model. *Chinese Journal of Chemical Engineering*, 2002.

[72] G. Tabor, A. Gosman, and R. Issa. Numerical simulation of the flow in a mixing vessel stirred by a Rushton turbine. *IChemE Symposium Series 140*, 1996.

[73] R. Verzicco, M. Fatica, G. Iaccarino, and P. Orlandi. Flow in an impeller-stirred tank using an immersed-boundary method. *AIChE Journal 50*, pages 1109–18, 2004.

[74] H. Wu and J. Patterson. Laser-doppler measurements of turbulent flow parameters in a stirred mixer. *Chemical Engineering Science 44*, pages 2207–, 1989.

[75] S. Yeoh. *Large eddy simulation of turbulent flow and mixing in a stirred vessel.* PhD thesis, Department of Mechanical Engineering, King's College London, 2004.

[76] M. Yianneskis, Z. Popiolek, and J. Whitelaw. An experimental study of the steady and unsteady flow characteristics of stirred reactors. *Journal of Fluid Mechanics 175*, pages 537–555, 1987.

[77] M. Yianneskis and J. Whitelaw. On the structure of the trailing vortices around Rushton turbine blades. *Trans. IChemE*, 1993.

[78] H. Yoon, D. Hill, S. Balachandar, R. Adrian, and M. Ha. Reynolds number scaling of flow in a rushton turbine stirred tank. part i-mean flow. *Chemical Engineering Science*, 60:3169–3183, 2005.

[79] H.S. Yoon, K.V. Sharp, D.F. Hill, R.J. Adrian, S. Balachandar, M.Y. Ha, and K. Kar. Integrated experimental and computational approach to simulation of flow in a stirred tank. *Chemical Engineering Science*, 56:6635–6649, 2001.

Chapter 6

Transitional Hydro-dynamics: Turbulent Motion

6.1 The Turbulent Motion

The current Chapter extends the numerical analysis of transitional hydro-dynamics in a stirred vessel at a $Re = 3000$ from the mean flow, discussed in Chapter 5, to flow turbulence.

6.2 Chapter Organization

Given the in-depth introduction, literature review and justification of the numerical method presented in Chapter 5, Chapter 6 will be restricted to an analysis of the turbulent motion. Specifically, the present Chapter will be organized as follows:

1. A supplemental review of the literature pertinent to turbulence measurements as a compliment to §5.1, §5.2.1, and §5.4.2 is given in §6.3.
2. An examination of the instantaneous turbulent motion $\vec{u}'$ in §6.4
3. A detailed analysis of the averaged turbulent/perturbation quantities such as:
   RMS perturbation velocities $\overline{\|\vec{u'}\|}$ in §6.5
   Flow turbulent kinetic energy $\overline{k'}$ in §6.6
   Flow turbulent dissipation $\overline{\epsilon'}$ in §6.7
   Flow turbulence length η and time-scales τ_η in §6.7.1
   Turbulent (Reynolds) stresses $\overline{u_i' u_j'}$ in §6.8
4. An examination of the instantaneous flow energy spectra in §6.9
5. The decomposition of the $\overline{k'}$ transport equation in §6.10
6. A discussion of implications for mixing in §6.11
7. And finally, concluding remarks are given §6.12.

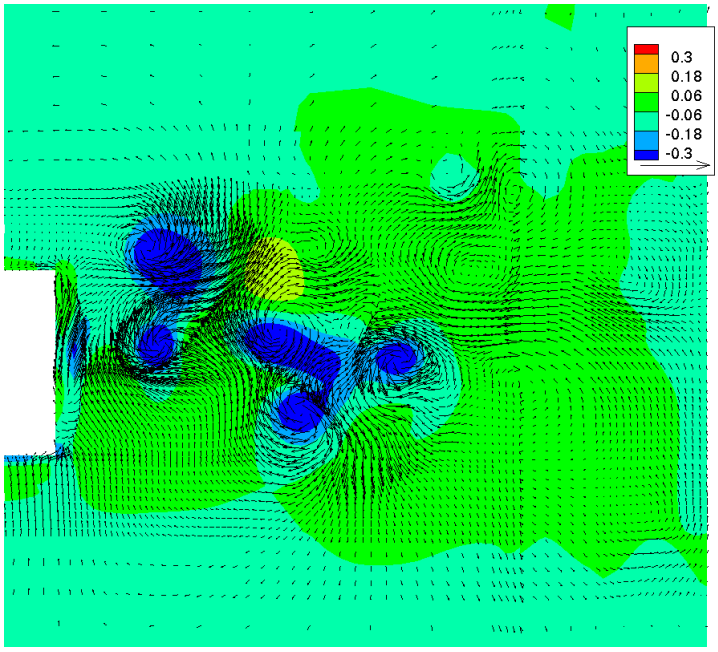

(a) $z-x$-plane ($y=0$)

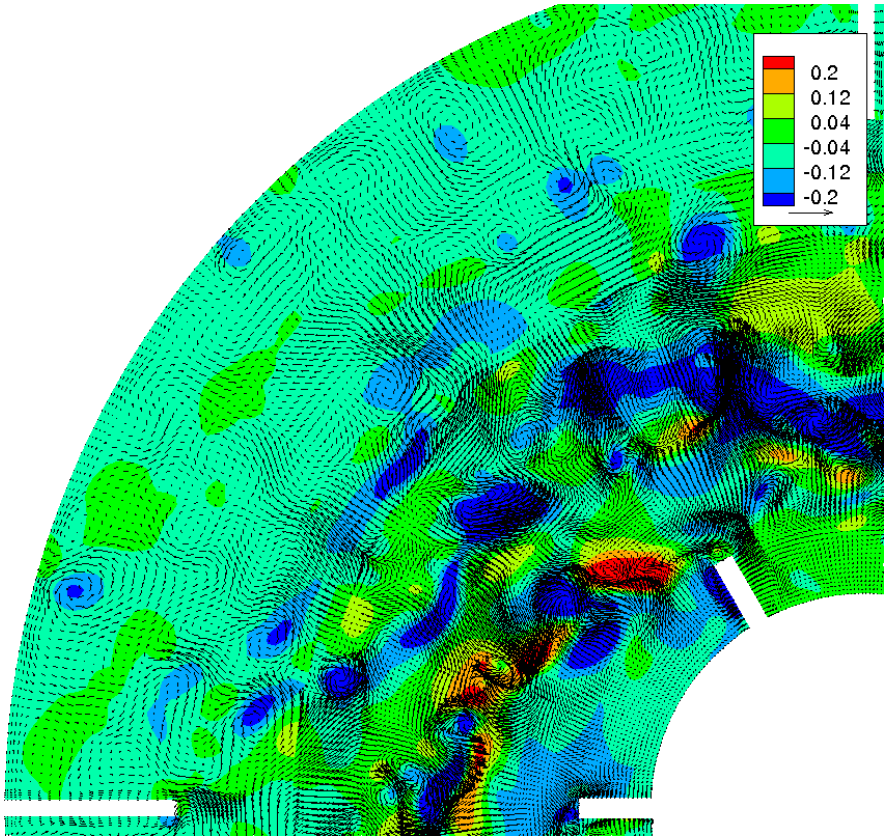

(b) $x-y$-plane ($z=0$). Blade rotation is clockwise

Figure 6.1: Normalized instantaneous perturbation-flow velocity vectors $\vec{u}'/V_{tip}$ and pressure contours $P'/P^{dyn}_{V_{tip}}$ for $N_{rev}=90$. Unit-vector shown in inset

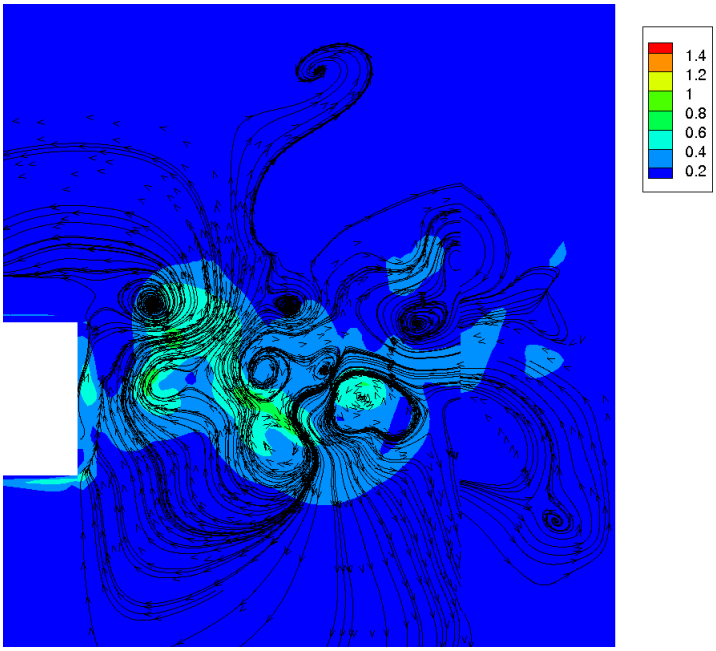

(a) $x-z$-plane ($y=0$)

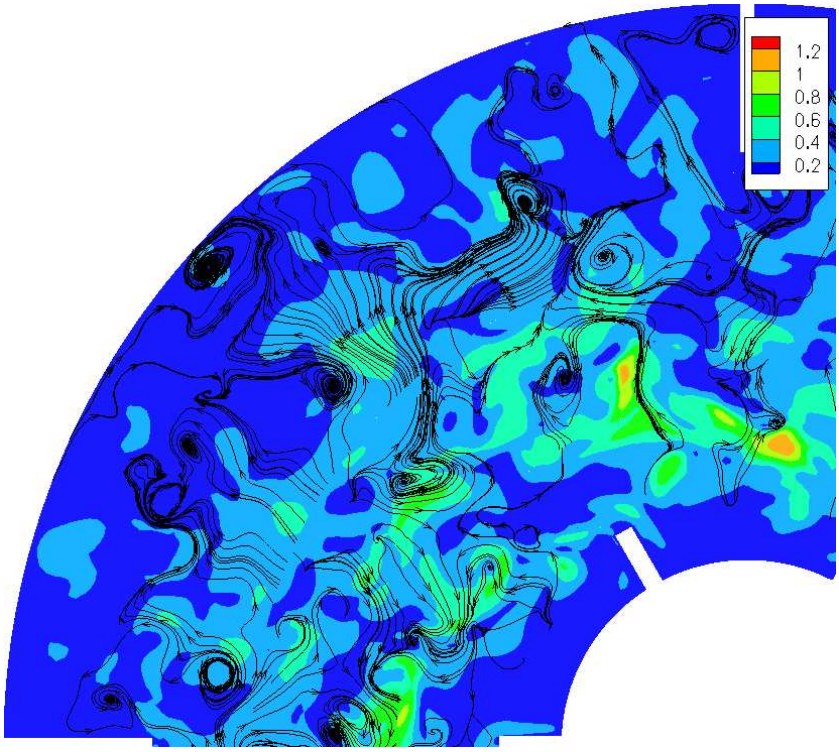

(b) $x-y$-plane ($z=0$). Blade rotation is clockwise

Figure 6.2: Normalized instantaneous perturbation-flow velocity magnitude $\|\vec{u}'\|/V_{tip}$ and stream-lines for $N_{rev}=90$.

As in Chapter 5, it should be pointed out that all flow properties ($\vec{V}$ and P) in the presentation to follow have been normalized according to tip velocity and dynamic pressure so as to maximize the generality and utility of the presentation. Specifically, we define any normalized velocity as V/V_{tip} while the normalized pressure is defined as $P/P_{dynamic} = P/(\rho {V_{tip}}^2/2)$. In addition, forces (per unit mass), kinetic energy (per unit mass) and dissipation (per unit mass) are normalized via V_{tip}^2/R, $V_{tip}^2/2$ and $\nu(V_{tip}/D)^2$ respectively unless otherwise stated.

6.3 Supplemental Literature

In addition to the general literature review given in §5.1, the specific review of dissipation measurements in §5.2.1 and treatment of the vortices in §5.4.2, a brief supplemental review of any additional flow studies directly related to turbulence measurements discussed in the present Chapter is presented herein.

As mentioned previously in §5.1 experimental works investigating, in detail, the high Re turbulent flow field within Rushton turbine mixers have included LDA, PIV or hot-wire anemometry studies of the impeller/flow discharge region by van't Riet et al [17], Wu et al [22], Stoots et al [21], Yianneskis et al [23], Hall [10], Mujumdar [15], Ducci et al [5], [6] [4], Micheletti et al [14], [13] and Hall [10], to name a few. Studies relevant to the measurement of turbulent dissipation were discussed in §5.2.1 with the most relevant study being that of Ducci [5].

A number of studies have been performed on Rushton turbines with implications regarding turbulence associated with the trailing vortices. Yianneskis et al [24] established the presence of trailing vortices emanating from the blade suction-side using variations in phase averaged axial velocity variations. The Authors calculated turbulent kinetic energy with and without the phase induced velocity variation (i.e. periodic motion) included and found that inclusion of the phase induced velocity perturbation (periodic motion) increased calculated turbulence intensity by as much as 400% locally. In addition, the Authors found that phase averaged turbulent kinetic energy peaked at the axial and angular location corresponding to that of the vortex cores. Derksen et al [3] performed LDA measurements and found that the turbulence within the vortex was anisotropic with maximum anisotropy near the blade SS. Hence, $k\epsilon$ and LES based turbulence models (which assume isotropic turbulence) may be less accurate in modeling the flow near the vortex core. Escudie et al [8], using PIV based measurements determined that turbulent kinetic energy was maximized locally at the cores. Schafer et al [19], measuring fully turbulent flow in a Rushton stirred tank ($Re = 50(10^3)$) identified regions of high turbulent kinetic energy associated with the trailing vortices. Specifically, turbulence intensity was found to range from 16% to 0.4% (based on tip velocity) within the impeller exit stream (jet) vs. the outer tank region respectively. Also, like Escudie et al, Schafer et al found that turbulent kinetic energy was maximized locally within the vortex core. In addition, most of the turbulent dissipation resides within the impeller swept region (18%) and exit stream (60%). Lee and Yianneskis [12] performed detailed LDA based measurements of flow turbulence within a Rushton turbine stirred tank at a high Re number. They found the

trailing vortices to be associated with elevated turbulence levels with maximum turbulence intensity (based on tip velocity) of $\approx 20\%$. The anisotropy of turbulence was also measured within the impeller exit stream and found to be less than 15%. Finally, Hall [10] measured via LDA turbulence within a Rushton stirred tank for Re ranging from $4250 - 1$ indicating increasing levels of turbulence with increased Re. The region of maximum turbulence was found to be located in the disk-plane.

Extraction of the (1-D single-point) turbulent energy spectra has been performed by Gunkel et al [9] on a Rushton stirred tank. They found that near the impeller tip, the energy spectrum was dominated by contributions associated with the frequency of the passing blades and their first harmonic (a side-effect of the tank fixed-frame measurement technique). Further from the blade however, the $-5/3$-power energy spectrum as a function of frequency was evident along with exponential decay associated with the dissipation region. Similar (LDA based) measurement were found by Lee et al [12] who employed a band-stop filtering technique to eliminate spurious contributions to the energy spectrum due to the periodic motion of the passing blades. The result, as in the case of Gunkel et al, is a well defined $-5/3$-power energy spectrum for radial locations far from the impeller $r/R \gtrapprox 1.8$. The measurements of Van't Reit et al [17] also yield a well defined $-5/3$-power energy spectrum only for locations away from the impeller blade tips (but within the impeller discharge stream). Again, this can be attributed (as indeed the Authors do) to the periodic motion of the passing blades. With respect to computational experiments, Alcamo et al [1] performed an LES-Smagorinsky (impeller fixed frame) simulation on a baffle-less Rushton stirred tank and calculated the energy spectrum as a function of frequency. The Authors identified both the energy and inertial range, but the dissipation region was not resolved.

As mentioned previously in §5.2.1, Ducci et al [5] performed LDA measurements with resolution down to approximately 1.5η, evaluating most of the spatial gradients in the perturbation velocity field, and calculated turbulent dissipation $\overline{\epsilon'}$ directly via (2.17) for a Rushton turbine of $Re = 2(10^4) - 4(10^4)$. Extensive comparison with dissipation estimated via 2-D PIV measurements and dimensional methods were conducted. It was found that the direct LDA based calculation of dissipation was within $10 - 40\%$ of these other techniques.

6.4 Instantaneous Motion

Extraction of the mean $\overline{\vec{U}}$ from the instantaneous flow solution $\vec{U}$ yields the instantaneous perturbation (turbulent) flow properties $\vec{u}'$ and P' at 90 revolutions as shown in Figure 6.1. Specifically, Figure 6.1 (a) gives normalized turbulent velocity vectors $\vec{u}'/V_{tip}$ and pressures $P'/P^{dyn}_{V_{tip}}$ within the impeller exit stream, ($x-z$-plane $y = 0$ with the impeller trailing edge tip to the left), thus illustrating the turbulent vortical structures emanating from the impeller as indicated by the presence of numerous local perturbation pressure minimums and associated swirling eddies. The flow structure length scales appear to vary over an order of magnitude with the largest (energetic) structures of length $\ell \lesssim H_{BL}/2$.

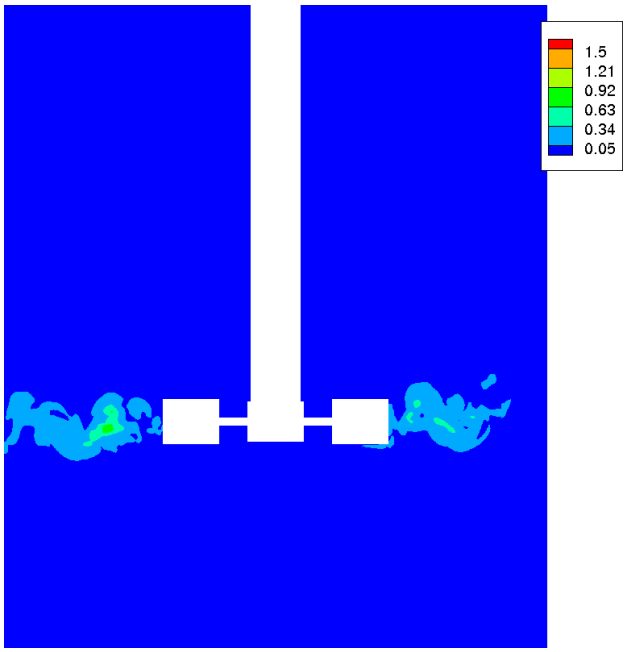

(a) $x-z$-plane ($y=0$)

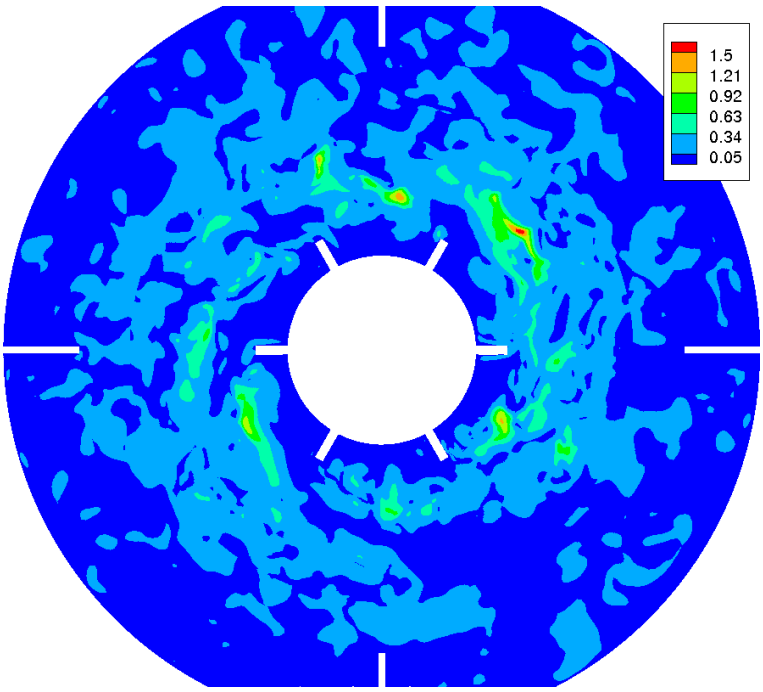

(b) $x-y$-plane ($z=0$). Blade rotation is clockwise

Figure 6.3: Normalized instantaneous perturbation-flow kinetic energy $k'/k_{V_{tip}}$ contours for $N_{rev}=90$.

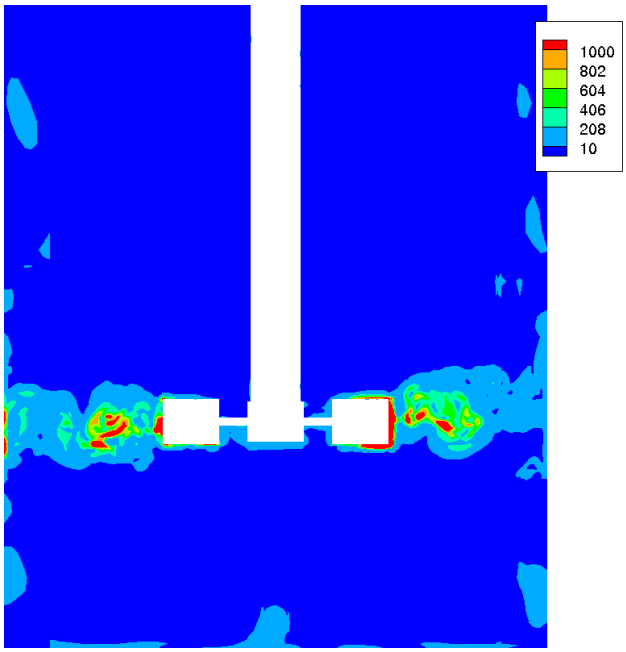

(a) $x-z$-plane ($y=0$)

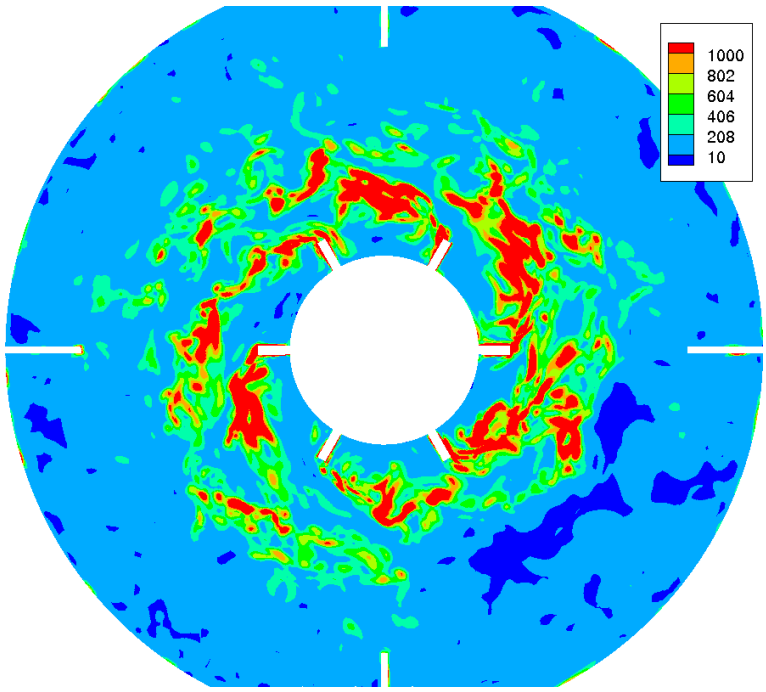

(b) $x-y$-plane ($z=0$). Blade rotation is clockwise

Figure 6.4: Normalized instantaneous perturbation-flow dissipation $\epsilon'/\epsilon_{V_{tip},D}$ contours for $N_{rev}=90$.

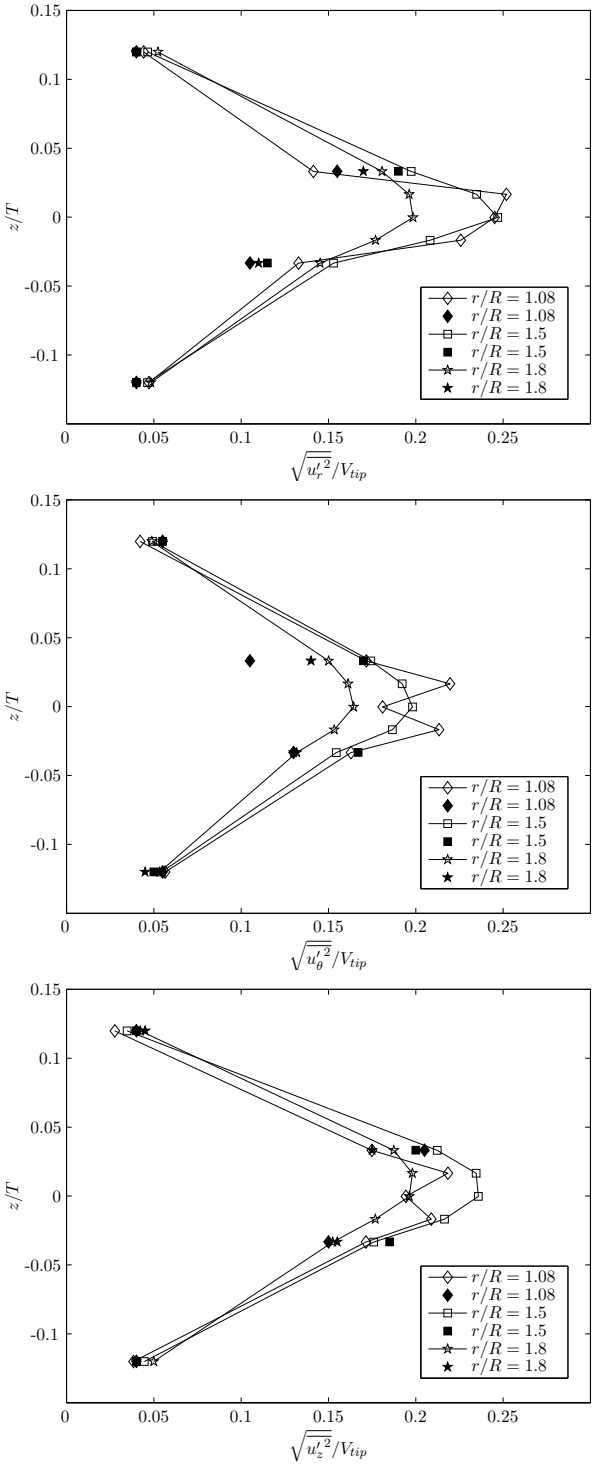

Figure 6.5: Simulation normalized circumferentially averaged turbulent RMS velocities $\sqrt{\overline{u_i'^2}}$ and experimental values of Mecheletti (solid) [13]. Disk-plane at $z/T = 0$.

Figure 6.1 (b) gives instantaneous normalized perturbation velocity and pressure in the $x-y$-plane at $z = 0$ (i.e. disk-plane) and likewise indicates a region heavily populated with turbulent flow structures of varying scales $10t_b \gtrsim \ell \gtrsim t_b/2$. Note, the inset provides a (scaled) flow velocity unit vector and indicates turbulent velocity scales are on the order of $\lesssim V_{tip}$ while the corresponding turbulent pressure fluctuation ranges on the order of $\lesssim P^{dyn}_{V_{tip}}$. In terms of the general flow structure, the blade suction-side (SS) and trailing edge (flow separation) represents a source of flow turbulence as indicated by the trailing turbulent wake emanating from each blade trailing edge. These turbulent structures are further illustrated via Figure 6.2 which gives normalized perturbation (in-plane) flow stream-lines and normalized perturbation flow velocity magnitude. Specifically, Figure 6.2 (a) and (b) indicate the presence of turbulent structures of varying size $H_{BL} > \ell > H_{BL}/10$ concentrated in the impeller exit stream. These structures are highly energetic, having velocities on the scale of $\lesssim V_{tip}$ as indicated by the normalize velocity magnitude contours. Regions of high instantaneous turbulence are illustrated in Figure 6.3 which gives normalized instantaneous turbulent kinetic energy $k'/k_{V_{tip}}$. As indicated by the previous discussion of the perturbation velocity magnitude, turbulent kinetic energy of the *local structures* is $\lesssim k_{V_{tip}}$ in the impeller exit stream and decays as the turbulent vortices are convected via the mean flow towards the outer tank wall. High levels of turbulence appear to be associated with the impeller jet downstream from the impeller suction-side (SS) and is indicative of the conversion of the mean flow kinetic energy within the jet and vortex region to turbulence motions (the conversion of organized to turbulent motion (i.e. turbulence generation) which will be investigated in §6.10.4).

With respect to turbulent dissipation, Figure 6.4 gives instantaneous normalized dissipation (based on V_{tip} and D or $\epsilon'/(\nu V_{tip}^2/D^2)$) $\epsilon'/\epsilon_{V_{tip},D}$ in the disk $z = 0$ (b) and $x - z$-plane $y = 0$ (a). Several regions of high instantaneous turbulent dissipation occur within the tank: The blade pressure (PS) and suction-side (SS) boundary layers, blade upper/lower tip and blade trailing edge edge induced separations as well as the trailing vortex region (associated with high turbulent kinetic energy) and baffle tips.

6.5 Averaged Quantities

Although instantaneous values of turbulent properties provides qualitative information on the structure of the local turbulent motions, statistical information on turbulent properties also provides useful information. Figure 6.5 gives normalized RMS radial $\sqrt{\overline{u_r'^2}}$, circumferential $\sqrt{\overline{u_\theta'^2}}$ and axial $\sqrt{\overline{u_z'^2}}$ circumferential averaged perturbation velocities at various axial and radial locations along with experimental results of Micheletti [13] for an identical geometry at a $Re = 4250$ (recall, the current simulation operating point corresponds to $Re = 3000$). Both experimental and simulation turbulence exhibit maximum turbulence near the impeller disk-plane (jet) $z/T = 0$ (i.e. the impeller exit stream/jet bound by the upper and lower impeller tip axial limits $z/T = \pm 0.033$). Conversely, RMS turbulence is minimized away from the impeller exit stream in the tank bulk-flow region. Variations between experimental and simulation perturbation RMS values are typically $\lesssim 20\%$ with a maximum deviation of $\approx 50\%$ corresponding to the circumferential component of turbulence near the impeller upper tip trailing edge. With respect to isotropy, the magnitude of the normalized RMS radial and axial perturbations are both ≈ 0.24 while circumferentially averaged normalized RMS averaged turbulence is marginally lower at ≈ 0.2 (at the disk-plane for $r/R = 1.5$). This observation applies to both the present simulation and the experimental data of Micheletti [13]. Hence, the (circumferentially averaged) flow turbulence can be deemed *approximately* isotropic with slight elevations of turbulence in the axial and radial directions.

Given the approximate correspondence between experimental and simulation circumferential averaged RMS turbulence values, (i.e. the accuracy of the directional content of the simulated turbulence), we proceed to investigate averaged turbulent scalar quantities such as the turbulent kinetic energy $\overline{k'}$, dissipation $\overline{\epsilon'}$, etc.

6.6 Averaged Kinetic Energy $\overline{k'}$

Normalized averaged (mapped) contours of turbulent kinetic energy $\overline{k'}/k_{V_{tip}}$ is shown in Figure 6.6 at the disk-plane (b) and lower blade quarter-depth $z/(H_{BL}/2) = -0.5$ (c) indicating peak turbulence associated with the approximate radial location of the mean flow blade trailing vortex (from the core-line given in Figure 5.18). Specifically, the maximum turbulent kinetic energy is associated with the upper/lower vortex inter-section at the disk-plane where

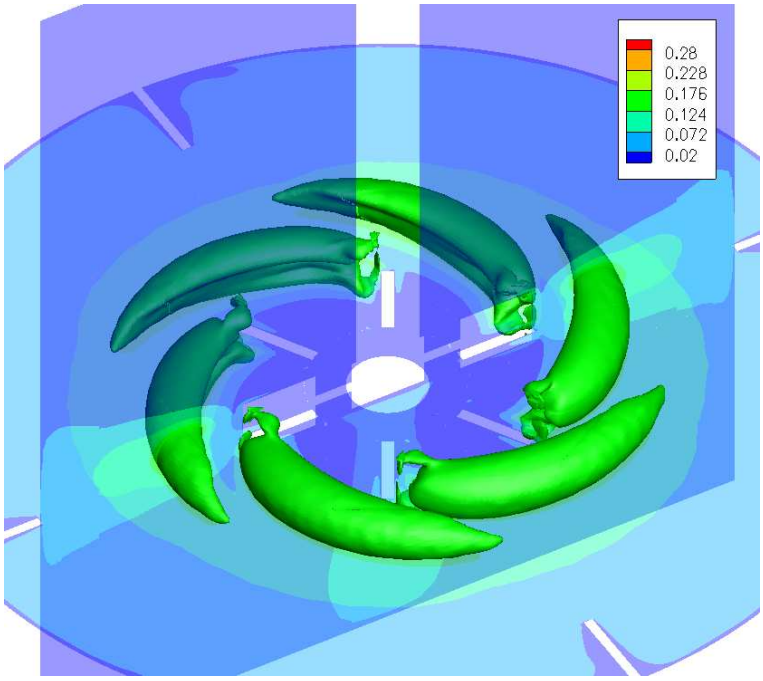

(a) Iso-surface of normalize perturbation $\overline{k'}/ke_{V_{tip}}$ of 0.15.

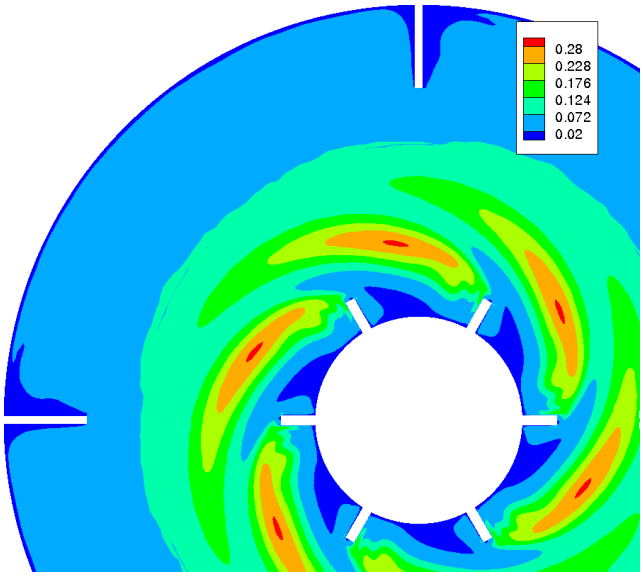

(b) $\overline{k'}/k_{V_{tip}}$ at disk-plane ($z = 0$)

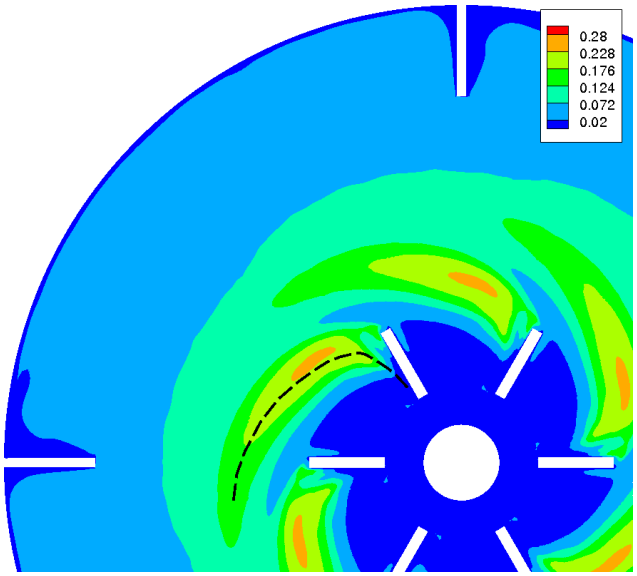

(c) $\overline{k'}/k_{V_{tip}}$ in $x - y$-plane at $(z/(H_{BL}/2) = -0.5)$

Figure 6.6: Normalized mapped averaged perturbation flow Kinetic Energy $\overline{k'}/k_{V_{tip}}$ iso-surface (a) and contours. Blade rotation is clockwise.

$\overline{k'}/k_{V_{tip}} \approx 0.3$[1], while the minimum is associated with the impeller pressure-side (PS) region, the outer tank wall and baffle suction-side (where there exists a mean flow recirculation zone

[1] As discussed in §6.10.4 and 6.10.6, generation of turbulent kinetic energy due to radial variations in the radial mean flow is maximized at the disk-plane between the trailing-edge vortices

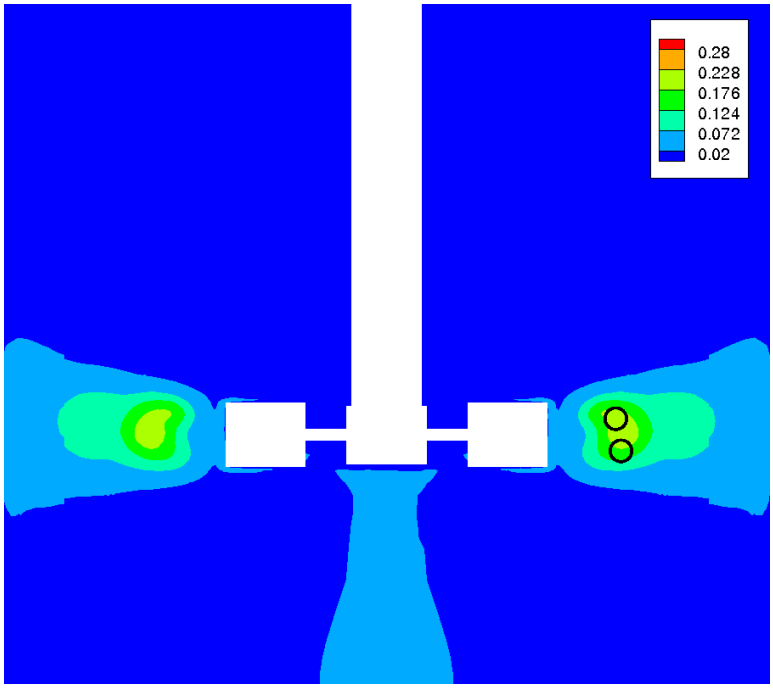

Figure 6.7: Normalized averaged perturbation flow Kinetic Energy $\overline{k'}/k_{V_{tip}}$ at $x-z$-plane ($y=0$).

(see Figure 5.13 (b)). The iso-surface of $\overline{k'}/k_{V_{tip}} = 0.15$ shown in Figure 6.6 (a) indicates a region of high turbulence associated with the break-down of the mean flow trailing vortices (i.e. conversion of mean flow kinetic to turbulent kinetic energy) as well as the near blade upper/lower tips and blade suction-side (SS) mean flow separations (most visible via the area of local elevated turbulence at the blade suction-side (SS) trailing edge as shown in Figure 6.6 (c) and (b)). Finally, it is evident from the same Figure that turbulence decays rapidly as the structures are convected towards the outer tank wall. This results in a decrease of nearly an order of magnitude in $\overline{k'}/k_{V_{tip}}$ from the impeller trailing vortex region to the outer baffles and tank wall. The vortices, as regions of high turbulence (due presumably to high turbulent energy generation as discussed in §6.10.4), can be further illustrated via Figure 6.7 which shows normalized turbulence in the $x-z$-plane indicating an oblong region with maximum turbulence near the disk-plane. Referring to Figure 5.24 (b) and 5.26 (b), one notes that the trailing vortex centers are at an axial

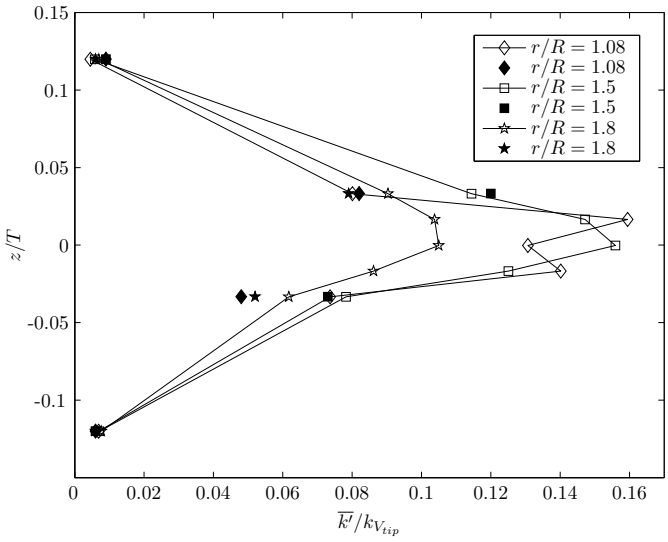

Figure 6.8: Simulation normalized circumferentially averaged turbulent kinetic energy $\overline{k'}/k_{V_{tip}}$ and experimental measurements (solid) of Michelleti [13]

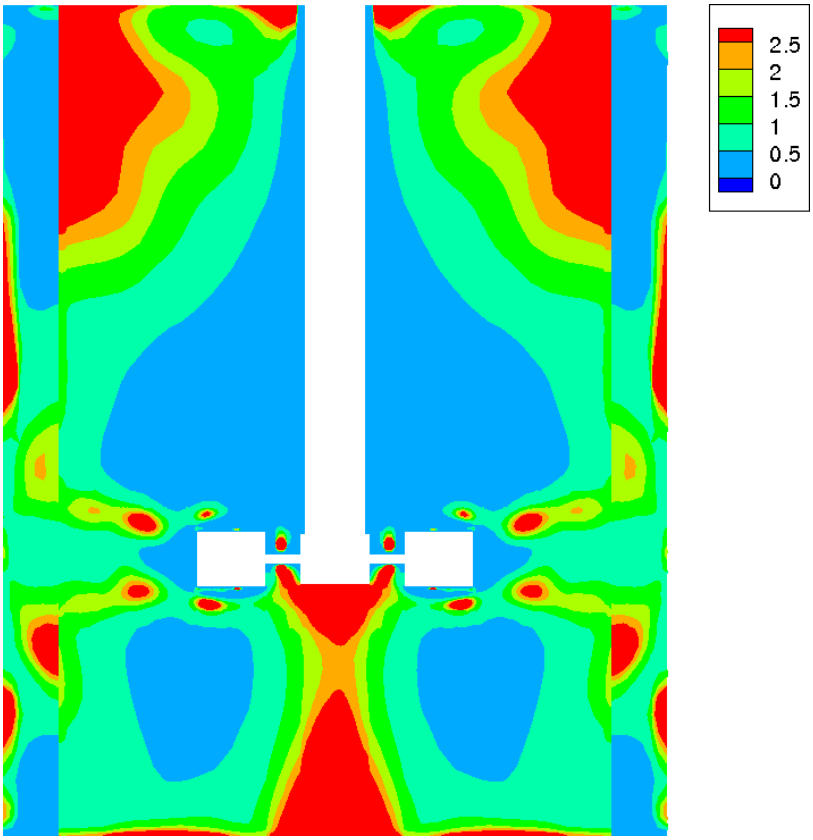

(a) $x-z$-plane at $y=0$

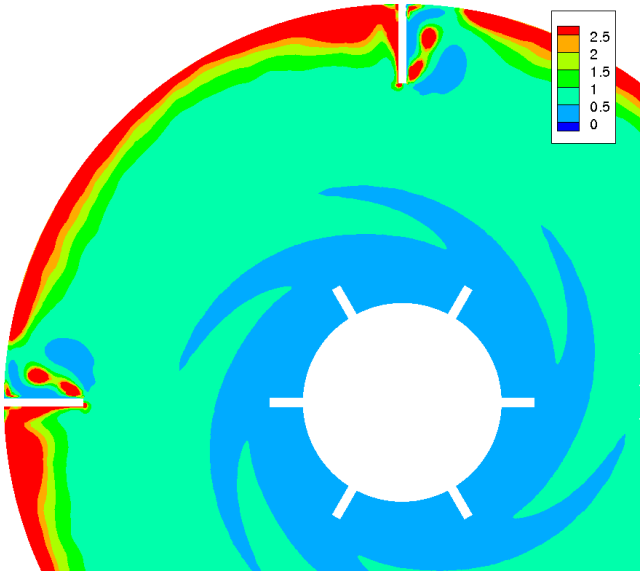

(b) Disk-plane ($z=0$)

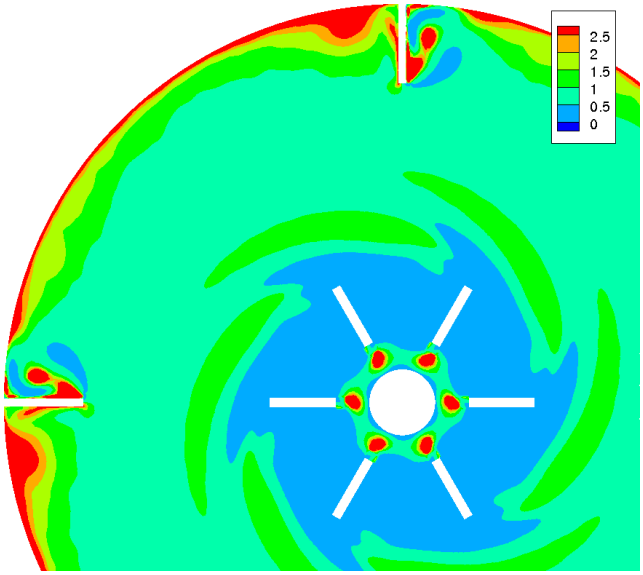

(c) In $x-y$-plane at $(z/(H_{BL}/2)=-0.5)$

Figure 6.9: Local tubulence intensity $\frac{\overline{k'}}{\overline{k}}$ contours. Blade rotation is clockwise in (b) and (c).

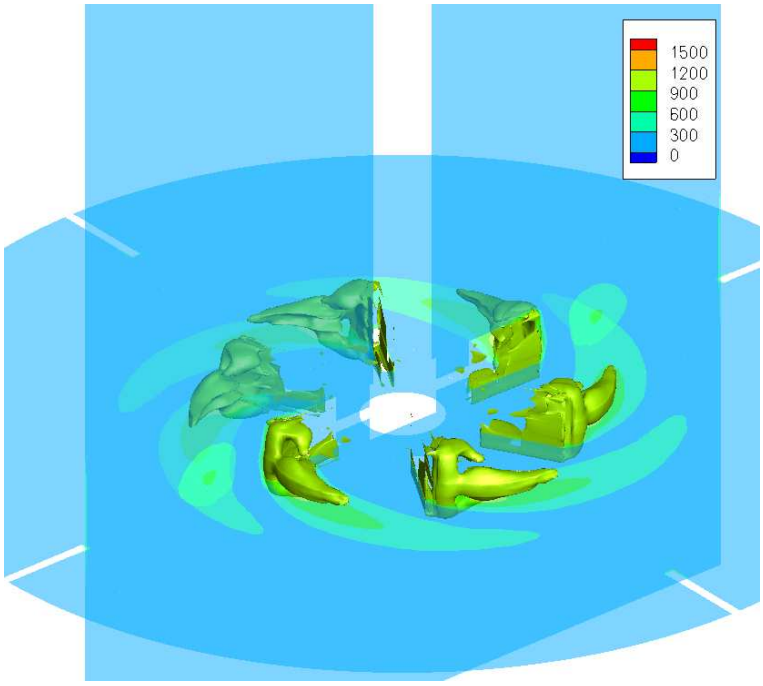

(a) Iso-surface of normalized perturbation dissipation $\overline{\epsilon'}/\epsilon_{V_{tip},D} = 1000$.

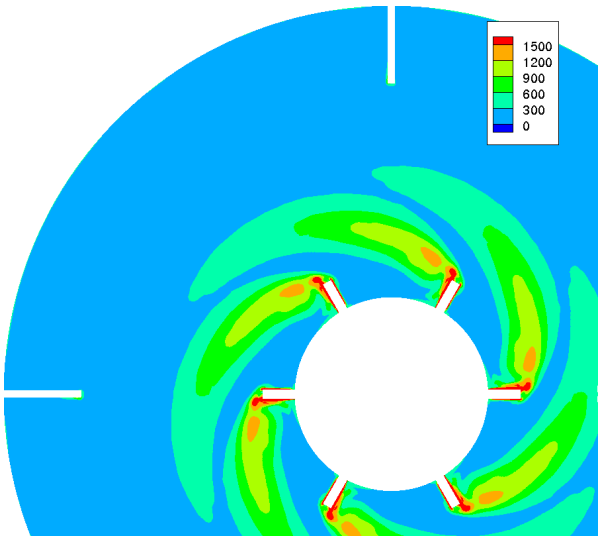

(b) $\overline{\epsilon'}/\epsilon_{V_{tip},D}$ at disk-plane ($z = 0$)

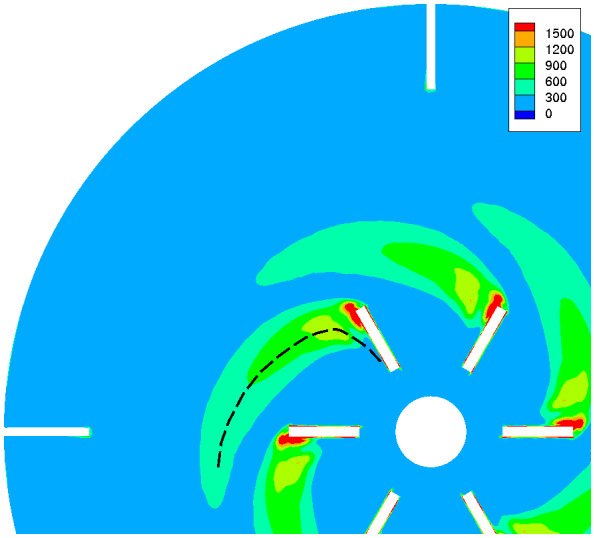

(c) $\overline{\epsilon'}/\epsilon_{V_{tip},D}$ in $x-y$-plane at ($z/(H_{BL}/2) = -0.5$)

Figure 6.10: Normalized averaged perturbation flow dissipation $\overline{\epsilon'}/\epsilon_{V_{tip},D}$ iso-surface (a) and contours. Blade rotation is clockwise.

position $z/(H_{BL}/2) \approx \pm 0.5$ which corresponds to the approximate lower/upper axial limits of the oblong region:

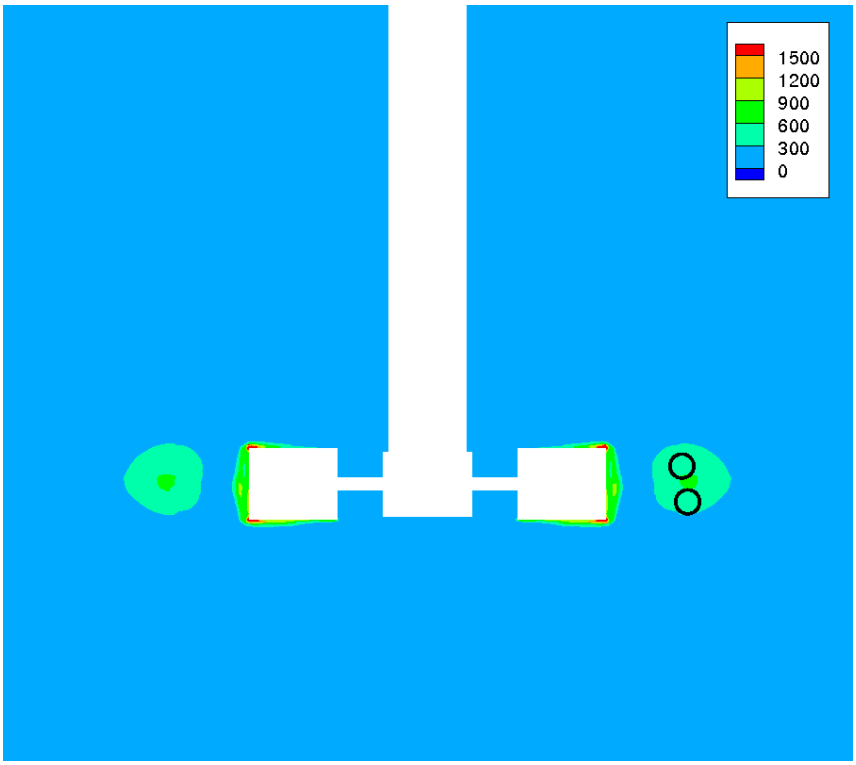

Figure 6.11: Normalized averaged perturbation flow dissipation $\overline{\epsilon'}/\epsilon_{V_{tip},D}$ at $x-z$-plane $(y=0)$.

The approximate vortex location based on pressure-force convergence presented in §5.3.4 are indicated by the 0. Of additional interest is the region of locally elevated turbulence just below the impeller. Inspection of the instantaneous flow field indicates the presence of a macro (large)-scale instability associated with a vortex rotating about the impeller axis of rotation. This vortex originates at the base of the tank and terminates near the axis of rotation at the impeller base. This results in a region of locally high perturbation velocity due to the (presumed) meandering motion of the instability. The remaining regions, including the bulk mean flow recirculation zones above and below the impeller jet (illustrated by the mean flow stream-lines in Figure 5.13), exhibit negligible turbulence compared with the impeller exit stream. Comparison of these results with experimentally determined measurements obtained by Michelleti [13] for an identical geometry at a Reynolds number $Re = 4250$ are shown in Figure 6.8 which gives circumferentially averaged normalized turbulent kinetic energy $\overline{k'}/k_{V_{tip}}$ at various axial and radial locations (excluding the disk-plane). Agreement between experiment and simulation data is quite good with deviation from experimental kinetic energy averaging $\approx 20\%$. In addition, trends in $\overline{k'}/k_{V_{tip}}$ are well resolved including the relatively low strength of turbulence associated with the lower mean flow trailing vortex (recall, the vortices are at an axial position $z/(H_{BL}/2) \approx \pm 0.5$ or $z/T \approx \pm 0.0166$). Again, it should be noted that these experimental values are for an identical tank and impeller geometry at a Reynolds

number $Re = 4250$ (still within the transition region according to Rushton et al [2]). Finally, the experimental measurements of Hall [10] indicate qualitative agreement with the results presented herein, with a global maximum in $\|u'_r\|$ (and thus $\overline{k'}$) at the approximate axial location of the disk-plane near the impeller for $Re \sim 100$ using a similar impeller geometry.

Further investigation of the averaged turbulent motion can be made by examining the *local* turbulence intensity (i.e. the ratio of averaged perturbation-to-mean flow turbulent kinetic energy $\frac{\overline{k'}}{\overline{k}}$) which gives an indication of the relative contribution of turbulent motion to the local fluid motion (i.e. $\vec{U}$). Specifically, Figure 6.9 gives $\frac{\overline{k'}}{\overline{k}}$ contours at the disk-plane $z = 0$, quarter blade-depth $z/(H_{BL}/2) = -0.5$ and $x - z$-plane for $y = 0$ indicating regions of low *local* turbulence intensity within the impeller jet, inter-impeller region, upper and lower tank bulk-flow recirculation zones. With respect to the former, relative turbulence intensity near the impeller is low due to the fact that mean flow velocity magnitude is highest in the impeller exit-stream (at the disk) and inter-impeller region (see Figure 5.31). In the case of the upper and lower tank bulk-flow recirculation zones, normalized turbulence is at a minimum above and below the impeller within the macro-scopic (tank bulk flow) recirculation zones resulting in low turbulence intensity. With respect to the near tank wall region, $\frac{\overline{k'}}{\overline{k}}$ is maximized near the wall due to low mean flow kinetic energy associated with the boundary-layer and impeller mean flow exit stream stagnation-point (radially outwards from impeller disk-plane at outer tank wall), while the baffle suction-side mean flow recirculation zone exhibits vanishing (mean flow) kinetic energy near their cores, resulting in a maximum value for $\frac{\overline{k'}}{\overline{k}}$ near the core. Finally, Figure 6.9 (a) indicates local maximums for turbulence intensity $\frac{\overline{k'}}{\overline{k}}$ on the upper and lower edges of the impeller exit stream and the under-impeller region. The former is due to the low mean flow kinetic energy (relative to the impeller exit jet kinetic energy at the disk-plane (see Figure 5.31 (b))) at the upper and lower trailing vortex outer edge (an artifact for the clockwise and counter-clockwise rotation of the upper and lower mean flow impeller trailing vortex respectively) resulting in local periodic reductions in mean flow radial velocity at the outer impeller jet (which coincides with the trailing vortex outer edge). Finally, in the case of the unsteady, under-impeller macro-instability present in the instantaneous flow, (a source of flow instability within the under-impeller region), the result is a local region of elevated turbulence intensity.

6.7 Averaged Dissipation $\overline{\epsilon'}$

Averaged turbulent dissipation $\overline{\epsilon'}$ was calculated directly from the spatial gradients of the perturbation velocity $\vec{u'}$ according to (2.17). Figure 6.10 gives normalized dissipation (based on perturbation velocity) $\overline{\epsilon'}/\epsilon_{V_{tip},D}$ at the disk-plane $z = 0$ (b) and lower-blade mid-height plane $z/(H_{BL}/2) = -0.5$ (c). Regions of high turbulent dissipation include the turbulent boundary-layer near the blade pressure and, in particular, the blade suction-side (SS) trailing-edge due to turbulence generated by the local mean flow separation (see Figure 6.6 (b) and (c), and 5.29 (d) and (e)). The impeller jet flow at the disk-plane exhibits high turbulent dissipation associated presumably with the region of high turbulent kinetic energy at the local

inter-section of the mean flow trailing vortices. These observations are illustrated by plotting the iso-surface $\overline{\epsilon'}/\epsilon_{V_{tip},D} = 1000$ as shown in Figure 6.10 (a), illustrating the high blade boundary-layer, blade trailing-edge, upper/lower tip separation induced turbulent dissipation, as well as the region of maximum dissipation associated with the impeller exit stream at the disk-plane just down-stream from the impeller.

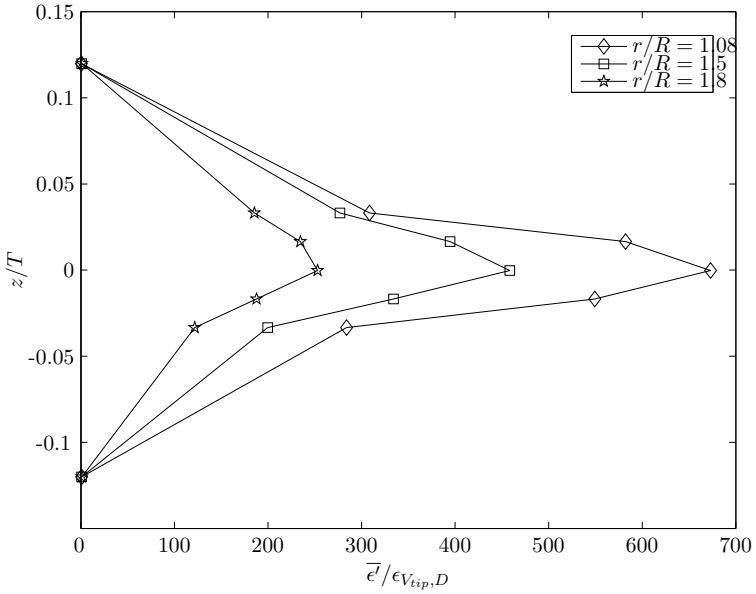

Figure 6.12: Simulation normalized circumferentially averaged tubulent dissipation $\overline{\epsilon'}/\epsilon_{V_{tip},D}$.

Figure 6.11 gives average turbulent dissipation in the $x-z$ ($y=0$) plane (along with the approximate locations of the vortex cores signified by an $\circ$) and indicates high dissipation associated with the blade upper/lower tip and trailing edge separation, as well as high dissipation at the disk-plane for a radial a location between and just down-stream from the trailing vortex cores. Numerical values for circumferential averaged normalized dissipation at various axial and radial locations (near the impeller) are given in Figure 6.12 which, in agreement with the above, indicates maximum turbulent dissipation at the impeller disk-plane near the impeller for all radial locations.[2]

Note that if we use an eddy viscosity concept, we can quantify the turbulent dissipation per unit mass via (2.17) as

$$\overline{\epsilon'} = \nu_{turb}(\frac{\partial \overline{U}_i}{\partial x_j} + \frac{\partial \overline{U}_j}{\partial x_i})\frac{\partial \overline{U}_i}{\partial x_j} = \nu_{turb}\frac{\overline{\epsilon}}{\nu} \Longrightarrow \frac{\overline{\epsilon'}}{\overline{\epsilon}} = \frac{\nu_{turb}}{\nu} \tag{6.1}$$

Thus, the ratio of turbulent-to-mean flow dissipation is equal to the ratio of the turbulent eddy-to-kinematic viscosity. The relative strength of turbulent dissipation, and thus the ratio of eddy-to-kinematic viscosity can be ascertained by plotting the local turbulence intensity $\frac{\overline{\epsilon'}}{\overline{\epsilon}}$. Figure 6.13 (b) and (c) give disk $z=0$ and lower blade quarter-depth $z/(H_{BL}/2) = -0.5$

[2]As in the instantaneous and mean flow case, the normalization dissipation used for the previous is defined as $\epsilon_{V_{tip},D} = \nu V_{tip}^2/D^2$. Thus, for dissipation associated with a velocity scale $u = V_{tip}/520 \sim u_\eta$ and length scale $\ell = D/500 \sim \eta$, $\overline{\epsilon'}/\epsilon_{V_{tip},D}$ takes a value $((V_{tip}/20)/(D/500))^2/(V_{tip}/D)^2) = 625 \sim 1000$. Hence, the normalized turbulent dissipation in regions of high turbulence should take on local values ~ 1000.

local dissipation intensity, indicating a value of eddy viscosity ranging from ~ 1

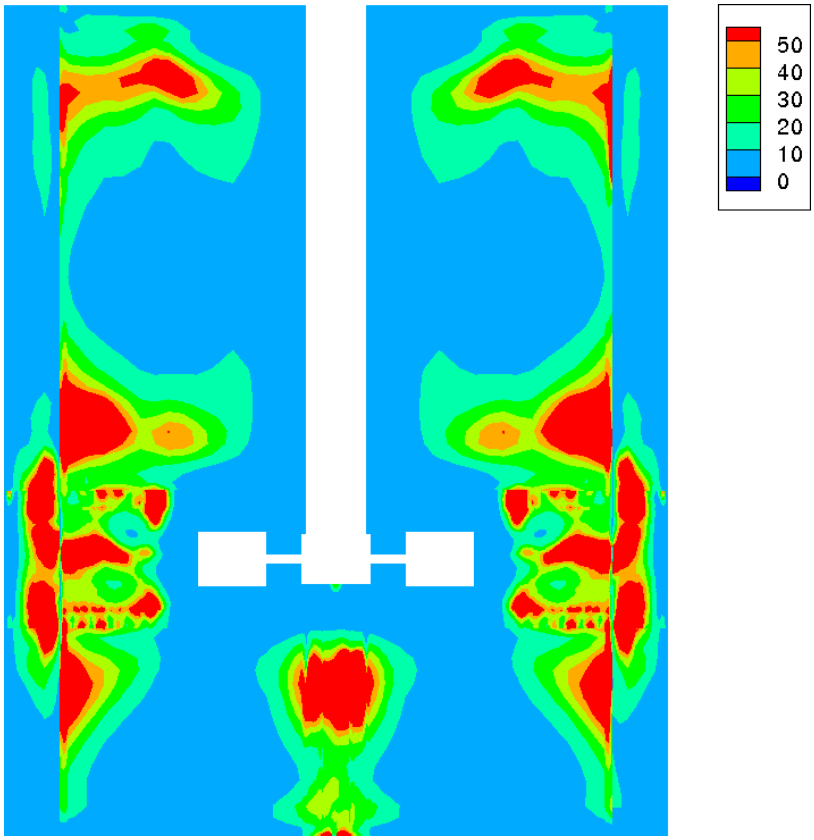

(a) $x-z$-plane at $y=0$

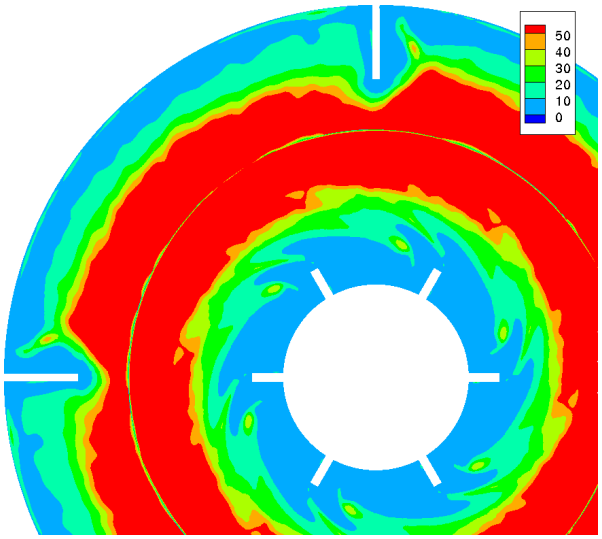

(b) $\frac{\overline{\epsilon'}}{\overline{\epsilon}}$ at disk-plane $(z=0)$

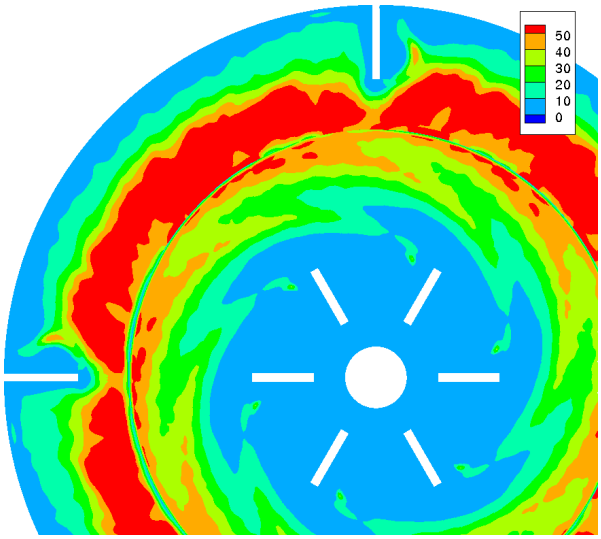

(c) $\frac{\overline{\epsilon'}}{\overline{\epsilon}}$ at $x-y$-plane at $(z/(H_{BL}/2)=-0.5)$

Figure 6.13: Ratio of averaged perturbation-to-mean-flow Dissipation $\frac{\overline{\epsilon'}}{\overline{\epsilon}}$ contours. Blade rotation is clockwise for (b) and (c).

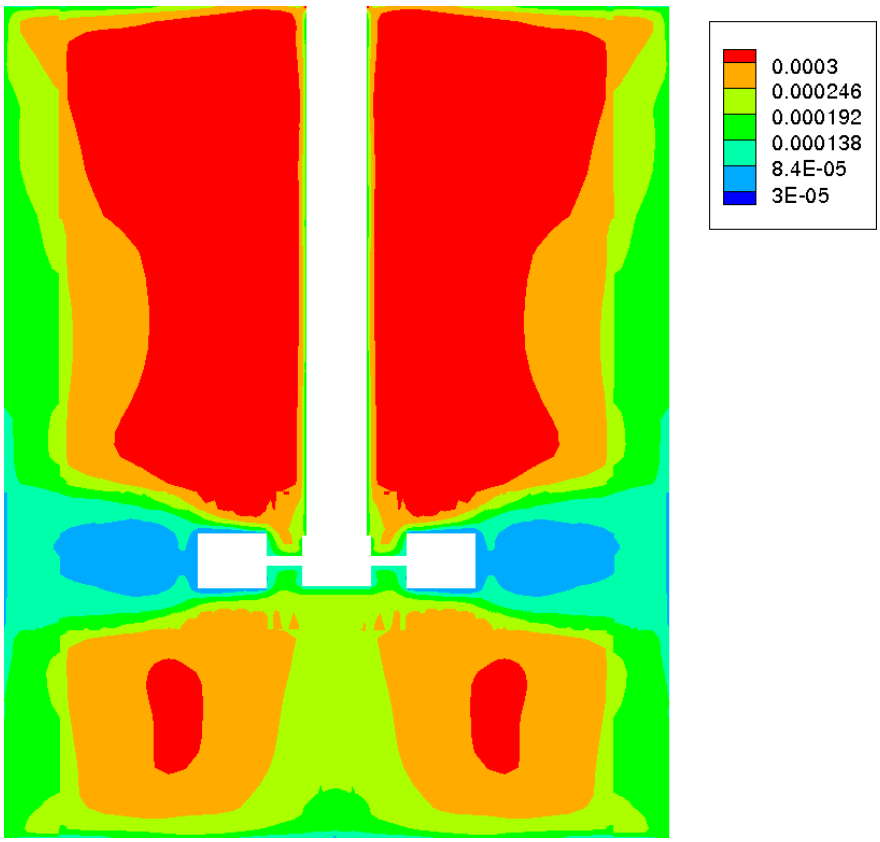

(a) η(m) in $x-z$-plane at $y=0$.

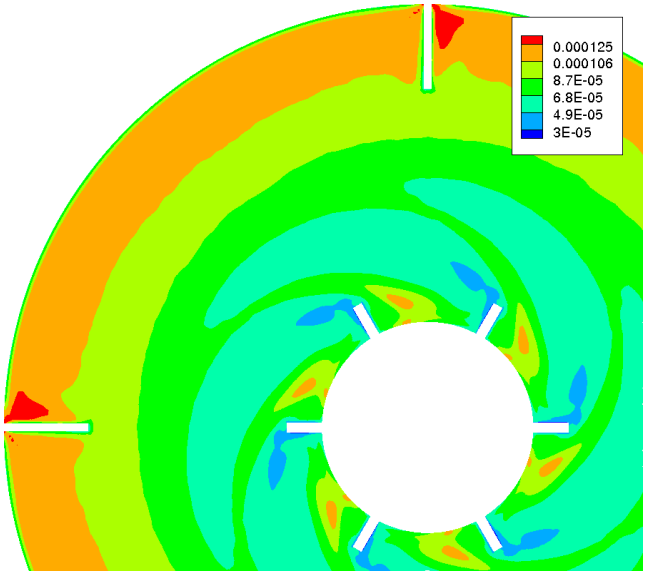

(b) η(m) at disk-plane ($z=0$)

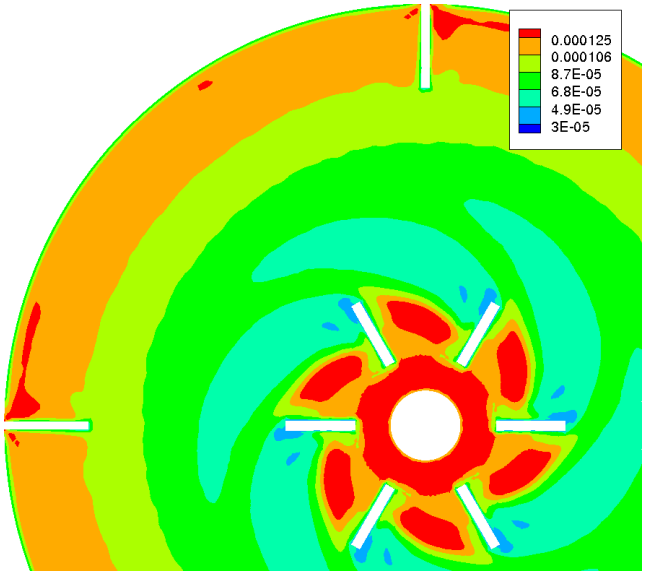

(c) η(m) in $x-y$-plane at $(z/(H_{BL}/2)=-0.5)$

Figure 6.14: Turbulent dissipation length scale η(m) contours based on mapped averaged perturbation flow dissipation $\overline{\epsilon'}$. Blade rotation is clockwise.

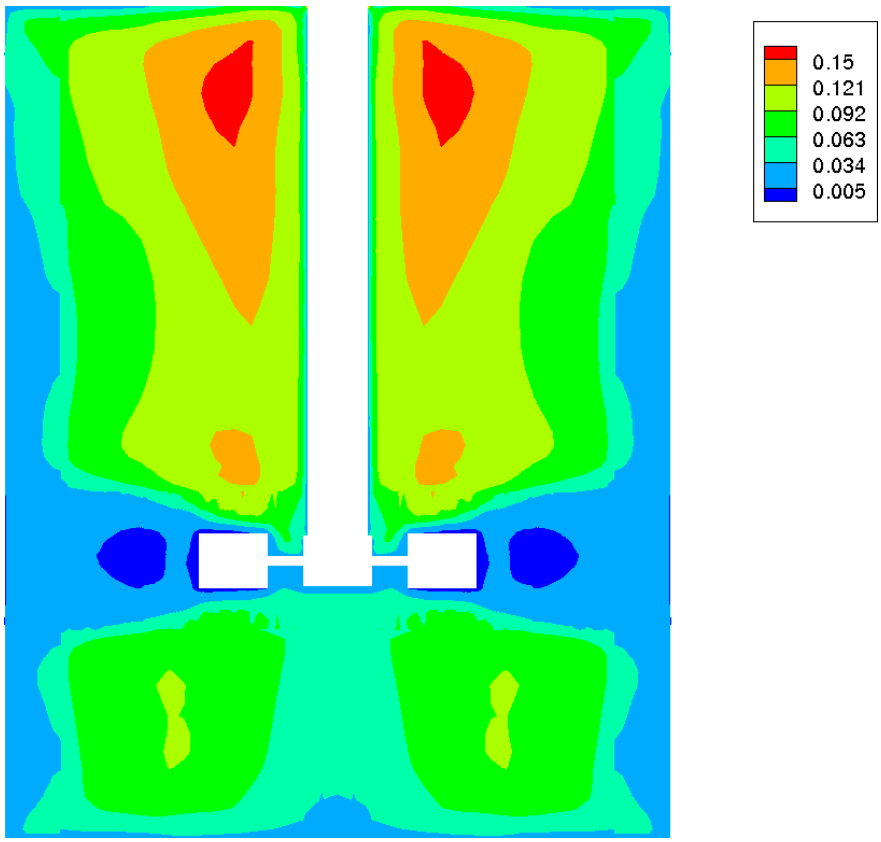

(a) τ_η(sec.) in $x-z$-plane at $y=0$.

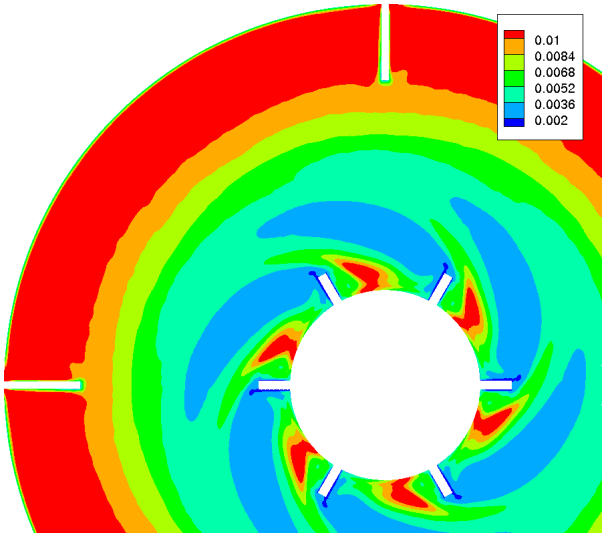

(b) τ_η(sec.) at disk-plane ($z=0$)

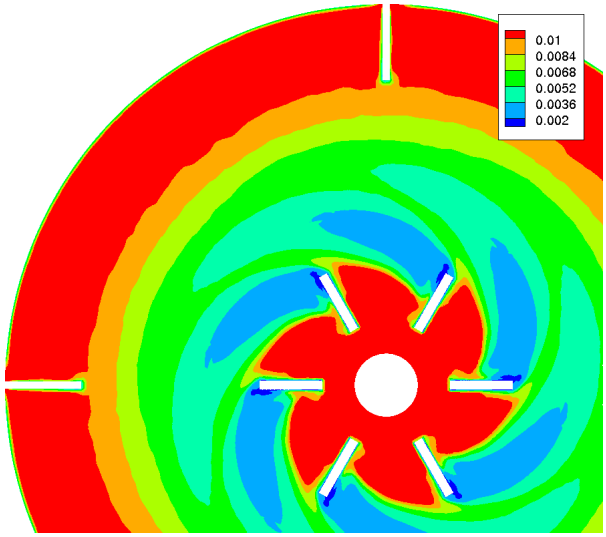

(c) τ_η(sec.) in $x-y$-plane at $(z/(H_{BL}/2)=-0.5)$

Figure 6.15: Turbulent dissipation time scale τ_η(sec.) contours based on mapped averaged perturbation flow dissipation $\overline{\epsilon'}$. Blade rotation is clockwise.

to 10 in the inter-impeller, near impeller jet, near tank wall and bulk recirculation loop regions, to $\sim$ 10 to 100 in the far impeller jet region (due to negligible mean flow viscous dissipation associated with the decaying mean flow trailing vortices (far from the impeller)). The low mean flow dissipation in the under-impeller region coupled with the presence of the under impeller region macro-instabilities results in the relative high turbulent dissipation intensity directly below the impeller hub.

6.7.1 Dissipation Scales

In order to validate the methodology used in formulating the transitional Re high resolution computational grid utilized in the present calculation, it is advantageous to inspect the turbulent dissipation length η and time scale τ_η distribution calculated via the definition (2.29). Figure 6.14 gives contours of the turbulent dissipation length scale η indicating regions of low η near the impeller blade suction-side (SS) and trailing vortex region associated with high local turbulent dissipation (discussed previously with respect to Figures 6.10 and 6.11). Hence, it is in the impeller exit stream/jet and impeller surface turbulent boundary-layers that the smallest dissipative structures reside. Conversely, regions of high η, associated with low local levels of turbulent dissipation and relatively large dissipative structures, are present in the region close to the impeller blade pressure-side (PS) as well as the tank bulk mean flow recirculation loops above and below the impeller jet. Referring to the LES derived (experimentally corrected) dissipative length scale distribution shown in Figure 5.2 (c) and (d), indicate qualitative agreement between LES and the current $\overline{\epsilon'}$-based direct calculation of η. Indeed, as stated in §5.2.2, the estimated circumferential averaged dissipation length scale η via the experiments of Ducci [5] corrected via scaling laws is $\approx 0.06(mm)$ within the impeller exit stream. This result is comparable to the calculations displayed in Figure (6.14 and 6.16). A more precise comparison can be made by plotting the simulation circumferential averaged value for η based on the present direct calculation and rescaled length scale (direct) measurements of Ducci (according to the scaling laws for η via (2.31)) at various radial and axial positions near the impeller. Thus, Figure 6.16 displays radial and axial simulation based and rescaled experimental calculations of η via Ducci eta al (based on direct experimental measurements of turbulent dissipation $\overline{\epsilon'}$), indicating good qualitative agreement in terms of trends. Specifically, the current high resolution simulation exhibits a general mismatch between experimental measurement of the dissipative length scales η on the order of $20 - 40\%$. It should be stated that the results of Ducci et al were for fully turbulent flow ($Re = 32(10^3)$) and that normalized turbulent dissipation and kinetic energy should decrease rapidly as the mixing Re decreases and the flow becomes transitional (this is especially true for regions far from the impeller exit stream). This observation is buttressed by the measurements of Hall [10] who found that local turbulence RMS values within the impeller stream decreased by $\approx 40\%$ with a reduction in Re from ≈ 4000 to ≈ 500. Hence, it is assumed that the rescaled dissipation based on the measurements of Ducci et al correspond to an overestimation of the dissipation found for the much lower Re associated with the transitional flow regime simulated herein. Nevertheless, given that $\eta \sim (\epsilon')^{1/4}$ this implies an underestimation of

local turbulent dissipation no more than $\approx 50\%$ a the disk-plane. This result, applicable for the near impeller region, is comparable to the estimated resolution provided in §5.4.3 of $\approx 60 - 80\%$ based on a comparison of the mean flow vs. averaged instantaneous power number. In addition to turbulent dissipative length scales, turbulent dissipation time scales

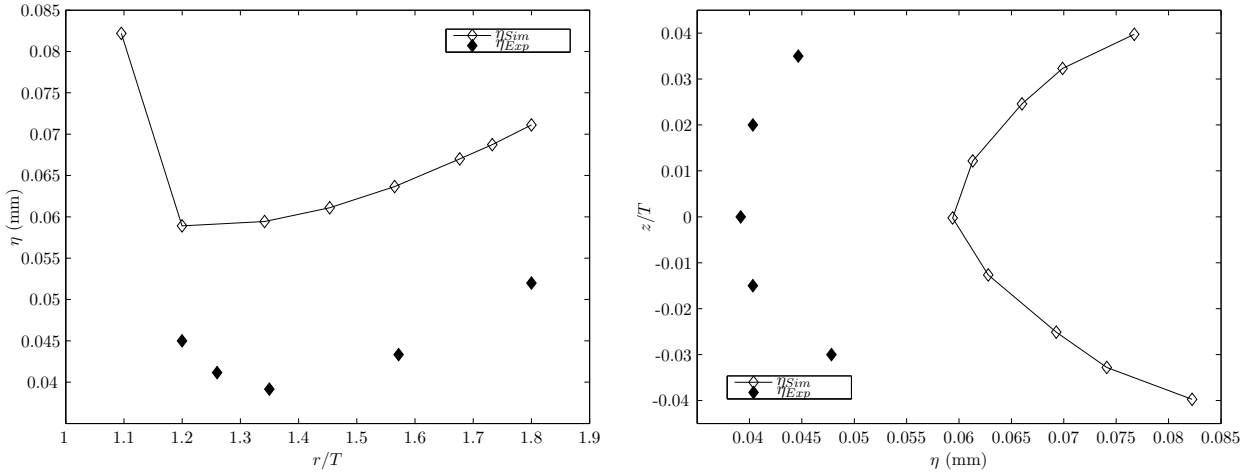

(a) $\overline{\eta}$ vs. r/R at $z/T = 0$ (Disk-plane) (b) $\overline{\eta}$ vs. z/T at $r/R = 1.35$

Figure 6.16: Circumferential averaged η based on turbulent dissipation at various axial and radial locations: Simulation and Experiment [5] (rescaled from high Re measurements using scaling laws (2.31)

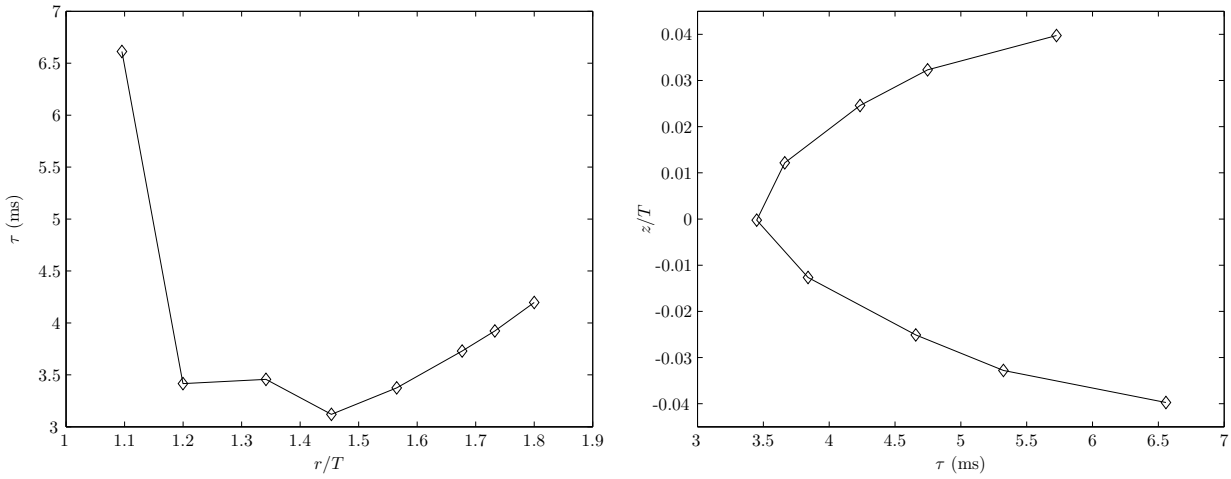

(a) $\overline{\tau_\eta}$ vs. r/R at $z/T = 0$ (Disk-plane) (b) $\overline{\tau_\eta}$ vs. z/T at $r/R = 1.35$

Figure 6.17: Circumferential averaged τ_η based on simulation averaged turbulent dissipation at various axial and radial locations.

τ_η can also be calculated from the definition (2.29) to check the methodology used in setting an appropriate simulation time-step $\Delta t \sim \tau/10$ in the present study. Specifically, Figure 6.15 indicates minimum dissipative time-scales are associated with regions of minimum turbulent length scales η and maximum dissipation (and visa versa).

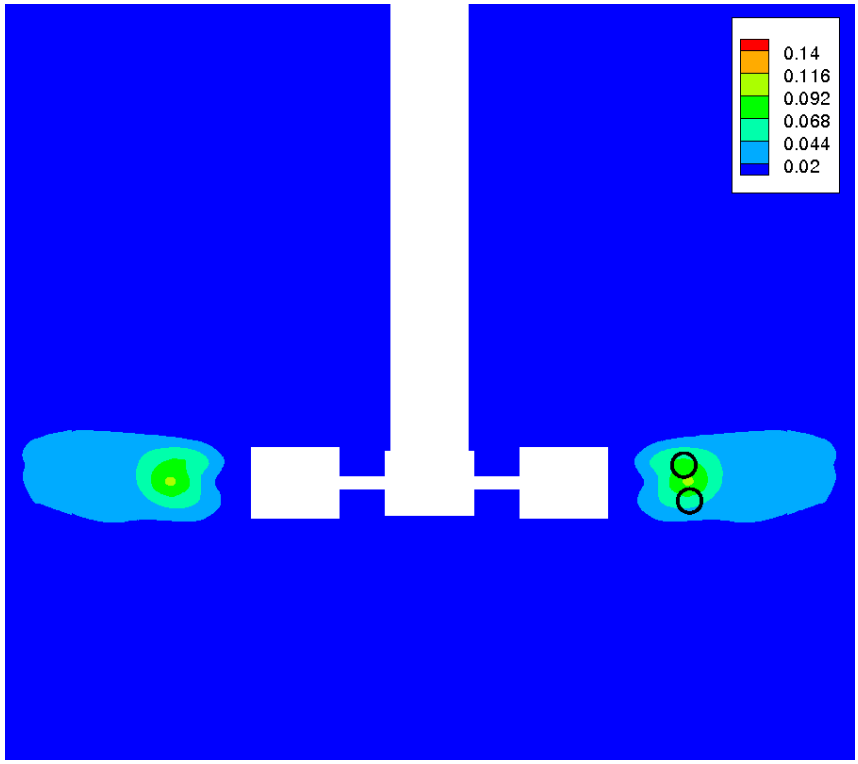

(a) $x-z$-plane at $y=0$

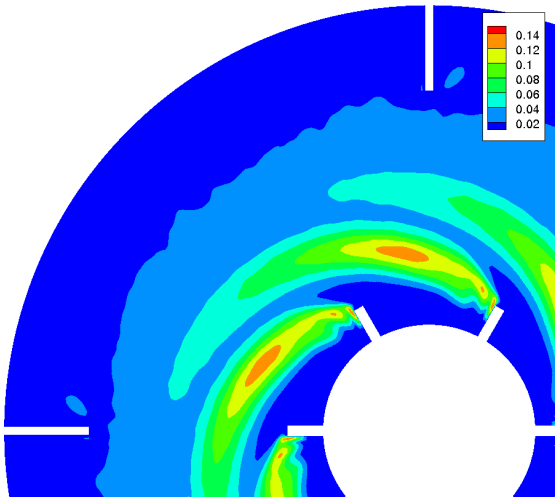

(b) Disk-plane ($z=0$)

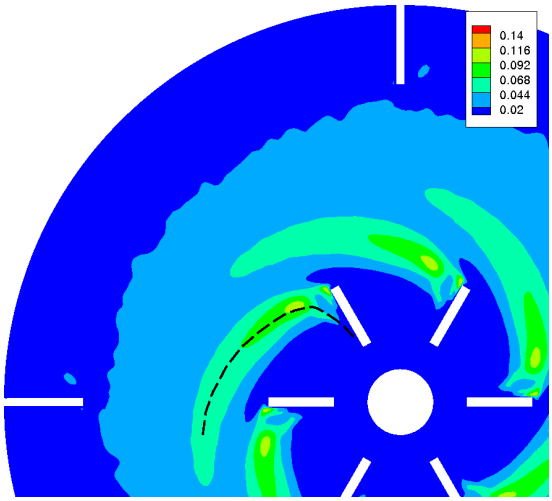

(c) In $x-y$-plane at $(z/(H_{BL}/2)=-0.5)$

Figure 6.18: Normalized Reynolds stress $\overline{u_r' u_r'}/V_{tip}^2$ contours with approximate core locations O (a) and path $- - --$ in (c). Blade rotation is clockwise for (b) and (c).

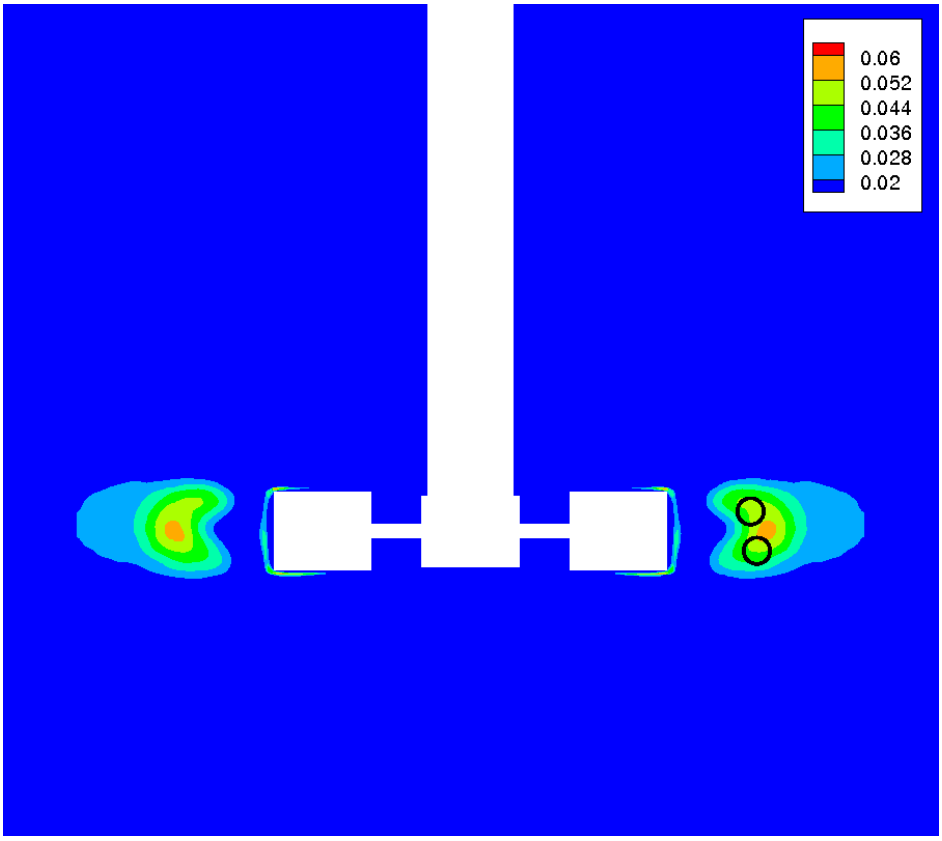

(a) $x-z$-plane at $y=0$

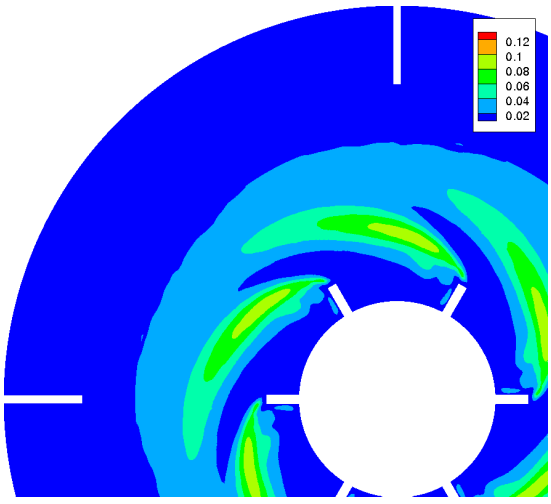

(b) Disk-plane ($z=0$)

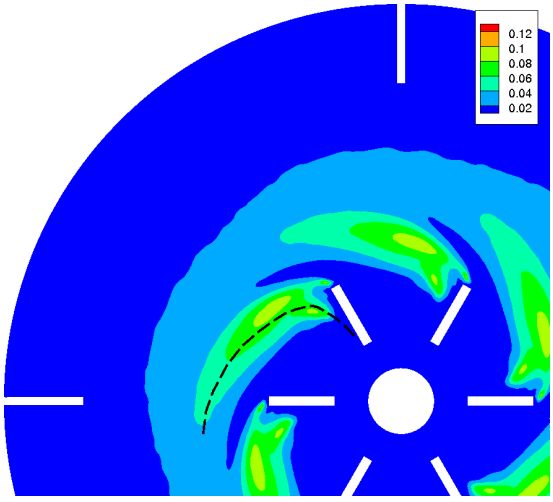

(c) In $x-y$-plane at $(z/(H_{BL}/2)=-0.5)$

Figure 6.19: Normalized Reynolds stress $\overline{u'_\theta u'_\theta}/V_{tip}^2$ contours with approximate core locations O (a) and path $- - --$ in (c). Blade rotation is clockwise for (b) and (c).

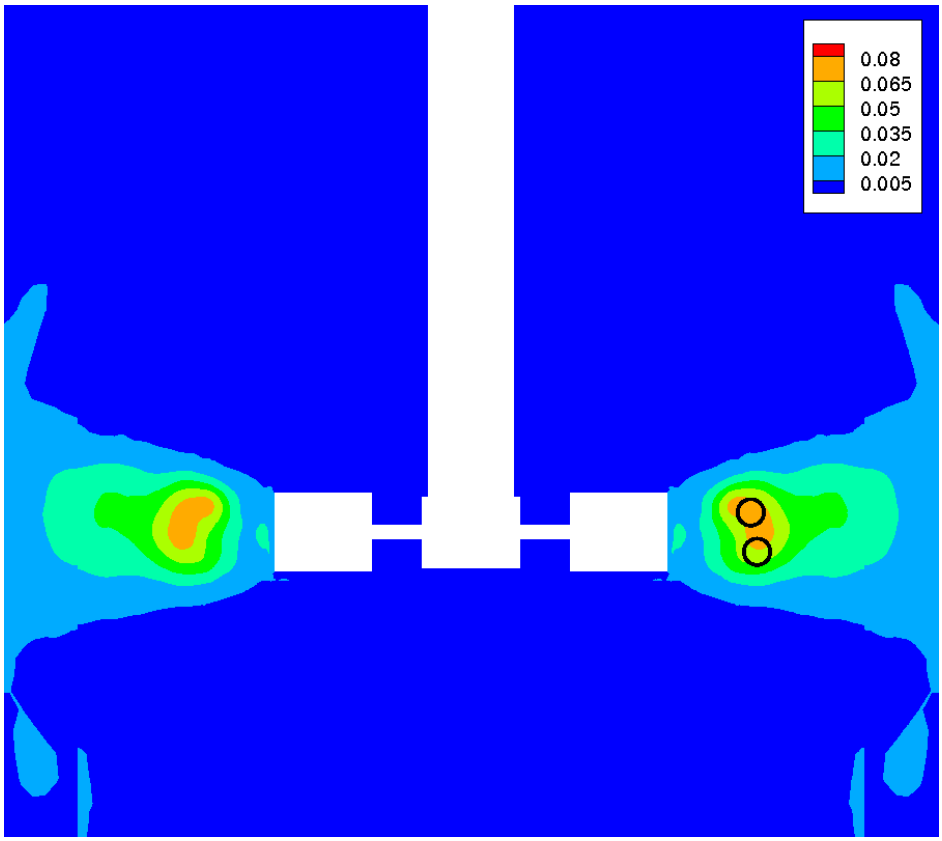

(a) $x-z$-plane at $y=0$

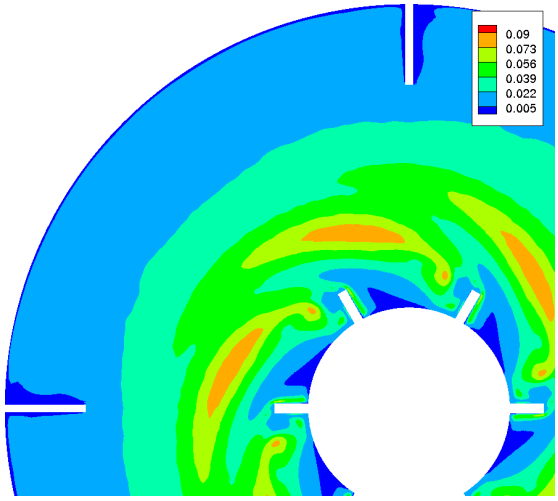

(b) Disk-plane ($z=0$)

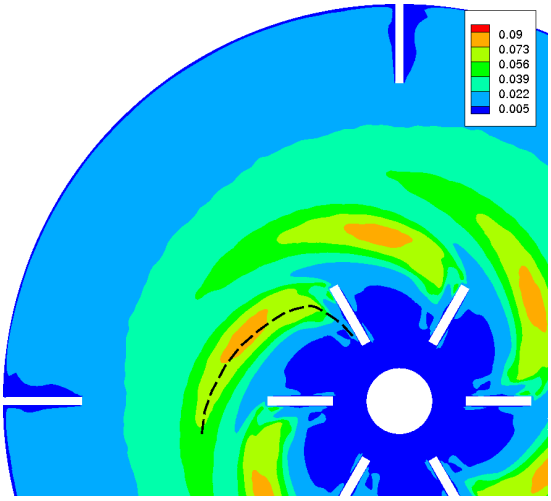

(c) In $x-y$-plane at $(z/(H_{BL}/2)=-0.5)$

Figure 6.20: Normalized Reynolds stress $\overline{u'_z u'_z}/V_{tip}^2$ contours with approximate core locations O (a) and path – – –– in (c). Blade rotation is clockwise for (b) and (c).

Axial and radial circumferentially averaged τ_η is shown in Figure 6.17 and indicates a minimum turbulent time-scale $\tau_\eta \approx 3ms$. This compares well with the simulation time-step chosen $\Delta t = 0.00014(sec) \lesssim 0.0003(sec) = \tau_\eta/10$.

6.8 Reynolds Stress

Further examination of the turbulent motion can be carried out by calculation of the Reynolds stress components $\overline{u_i' u_j'}$. Specifically, the normal Reynolds stress in the radial $\overline{u_r' u_r'}$, circumferential $\overline{u_\theta' u_\theta'}$ and axial direction are shown in Figure 6.18, Figure 6.19 and Figure 6.20 respectively, with associated approximate impeller trailing vortex core locations (based on mean flow pressure force convergence (see §5.3.4)). All three Figures indicate high Reynolds stress in the trailing vortex region of the impeller exit stream, with particular high turbulent stresses at the disk-plane $z = 0$ just down-stream from the radial position of the vortex cores. The tangential Reynolds stress, such as $\overline{u_r' u_\theta'}$ shown in Figure 6.21 indicates, like for the previous normal stresses, a local maximum in magnitude in the region of the impeller trailing vortices at the disk-plane $z = 0$. This is in contrast to tangential Reynolds stresses $\overline{u_\theta' u_z'}$ and $\overline{u_r' u_z'}$ shown in Figure 6.23 and 6.22 which indicate a (global) maximum in magnitude associated with the impeller trailing vortex cores.

6.8.1 Isotropy of Turbulence

Inspection of the normalized Reynolds stresses $\overline{u_i' u_j'}$ as presented in the previous section can be used to ascertain the extent to which the flow turbulence is isotropic. Specifically, we can define the parameter $\beta_{i,j}$ as

$$\beta_{i,j} \equiv \frac{\overline{u_i' u_j'}}{\frac{2}{3}\overline{k'}} = \frac{\overline{u_i' u_j'}}{\frac{1}{3}\overline{u_k' u_k'}} \tag{6.2}$$

where for $i = j$ we have the Reynolds stress $\overline{u_r' u_r'}$, $\overline{u_\theta' u_\theta'}$ and $\overline{u_z' u_z'}$). The limiting behavior of this parameter is as follows (no sum over i or j implied):

$$\beta_{i,i} = \begin{cases} 0, & \overline{u_i' u_i'} = 0 \\ 1, & \overline{u_j' u_j'} = \overline{u_i' u_i'} \text{ for all } j \\ 3, & \overline{u_j' u_j'} = 0 \text{ for } j \neq i \end{cases} \tag{6.3}$$

Thus, for isotropic turbulence $\overline{u_j' u_j'} = \overline{u_i' u_i'}$ for all j, and $\beta_{i,i} = 1$. Figure 6.24 gives the normalized local Reynolds stress parameter $\beta_{r,r}$ indicating regions of minimum (normal radial) Reynolds stress at walls with surface normals parallel to the radial direction $\hat{r}$ (indicative of wall induced damping of turbulent motion normal to the surface). These surfaces include the outer tank walls, impeller shaft, baffle tips and impeller blade trailing edges. Regions of relatively high local normalized Reynolds stress in the radial direction include surfaces whose normal surface vectors are perpendicular to the radial direction unit-vector $\hat{r}$ such as the baffle ((SS) and (PS)) and the impeller suction-side (SS). Remaining regions within the

tank exhibit values of $\beta_{r,r} \approx 1$ indicating approximately isotropic flow in regions such as the impeller exit flow jet, trailing vortices and tank bulk flow recirculation loop regions.

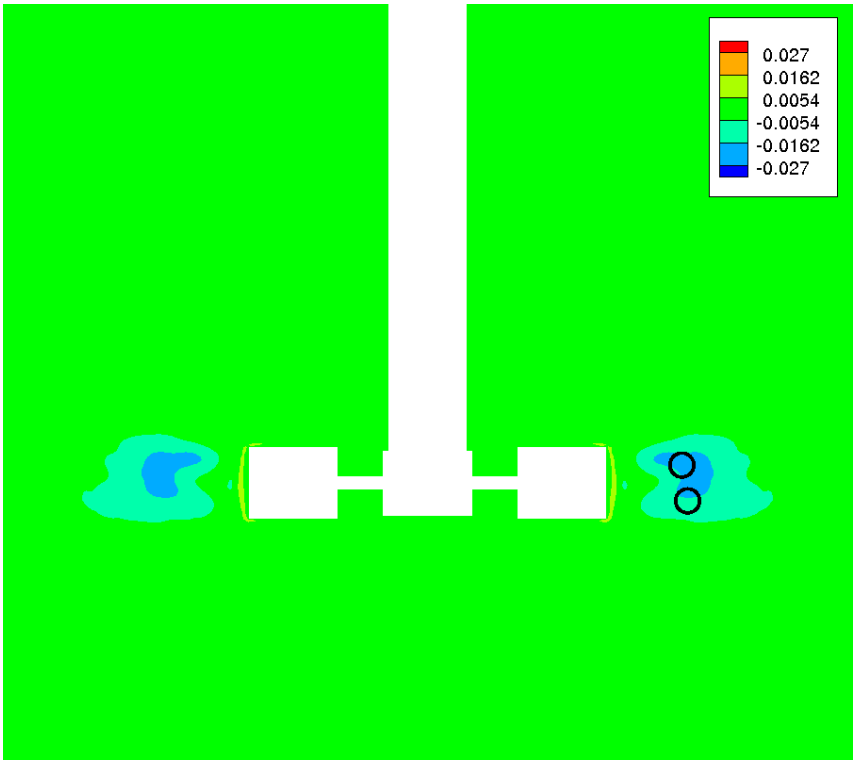

(a) $x-z$-plane at $y=0$

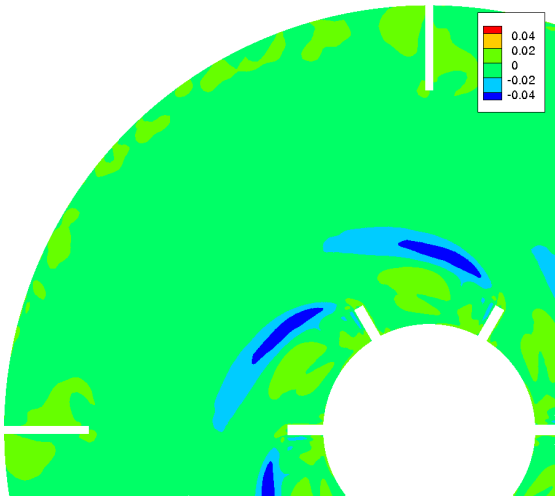

(b) Disk-plane ($z=0$)

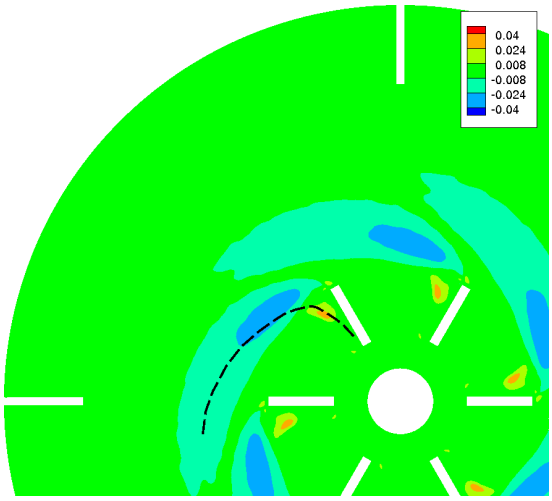

(c) In $x-y$-plane at $(z/(H_{BL}/2) = -0.5)$

Figure 6.21: Normalized Reynolds stress $\overline{u_r' u_\theta'}/V_{tip}^2$ contours with approximate core locations O (a) and path $- - - -$ in (c). Blade rotation is clockwise for (b) and (c).

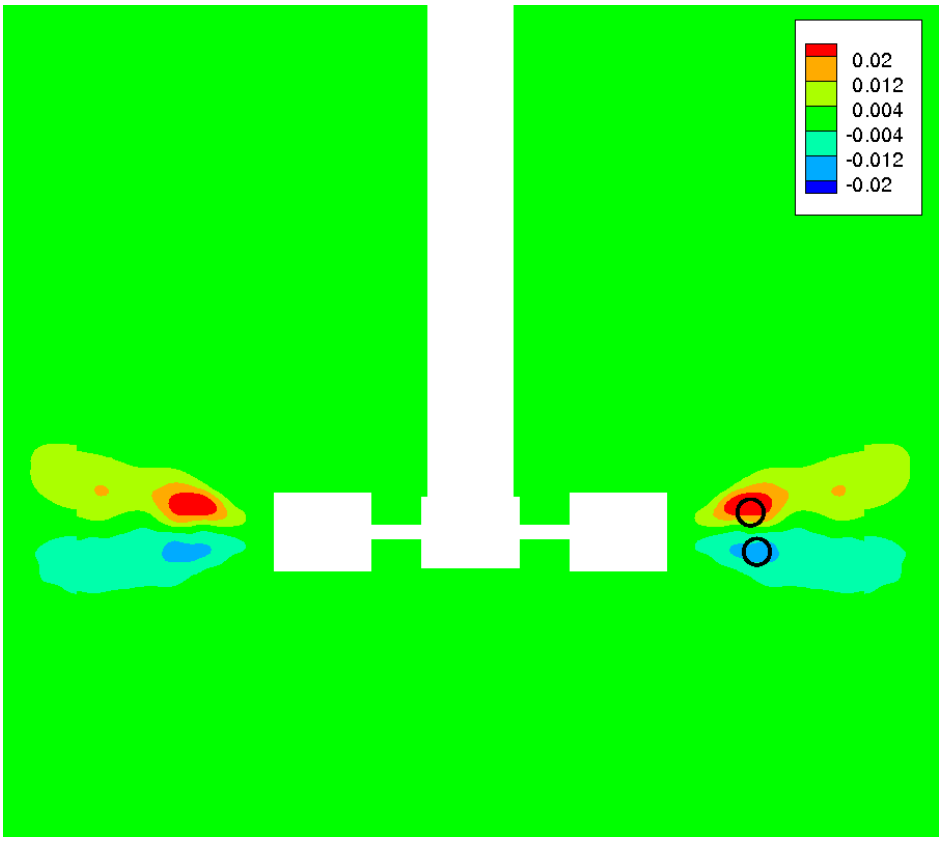

(a) $x-z$-plane at $y=0$

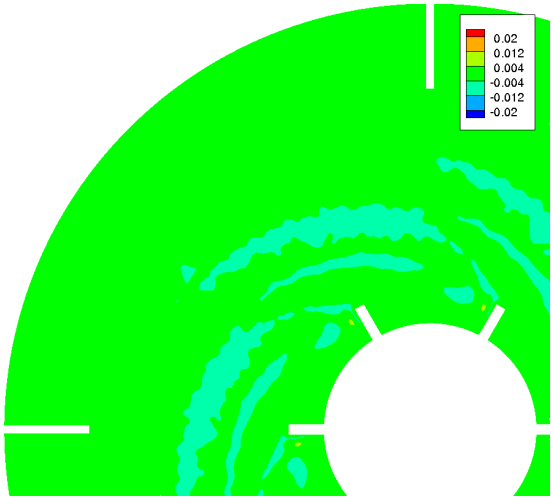

(b) Disk-plane ($z=0$)

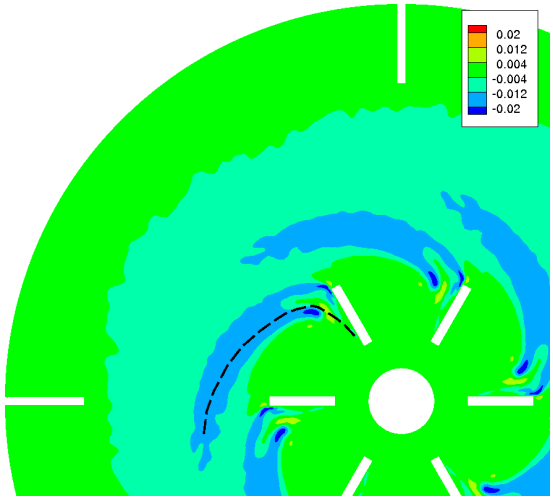

(c) In $x-y$-plane at $(z/(H_{BL}/2)=-0.5)$

Figure 6.22: Normalized Reynolds stress $\overline{u_r' u_z'}/V_{tip}^2$ contours. Blade rotation is clockwise for (b) and (c).

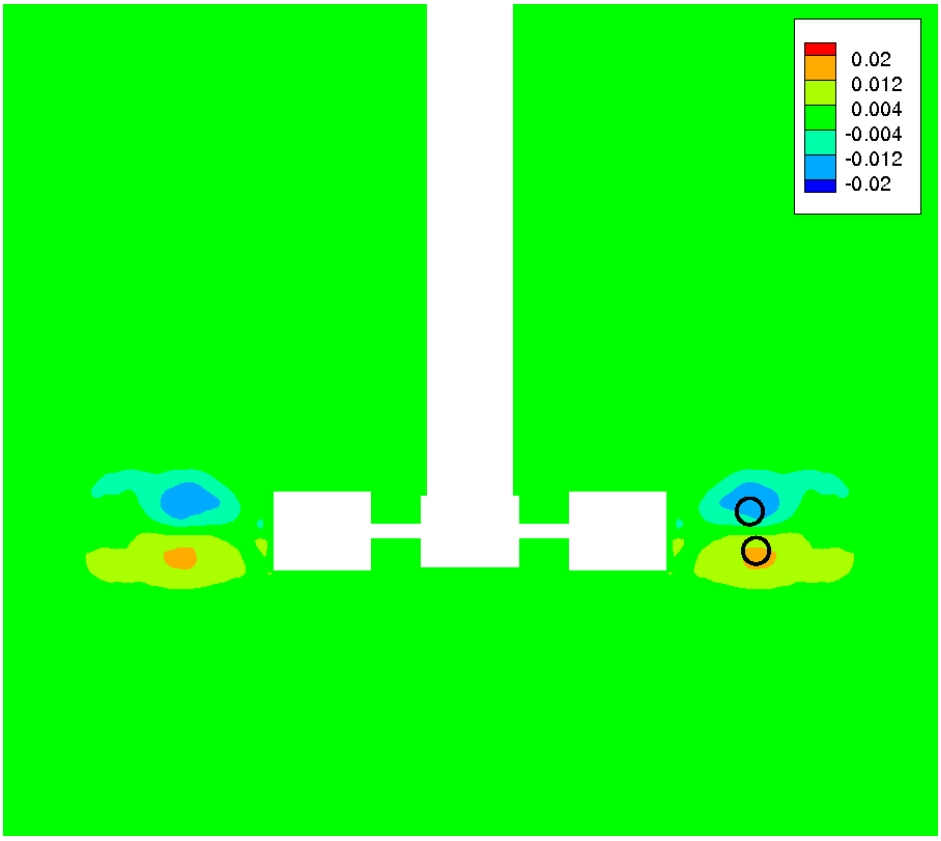

(a) $x-z$-plane at $y=0$

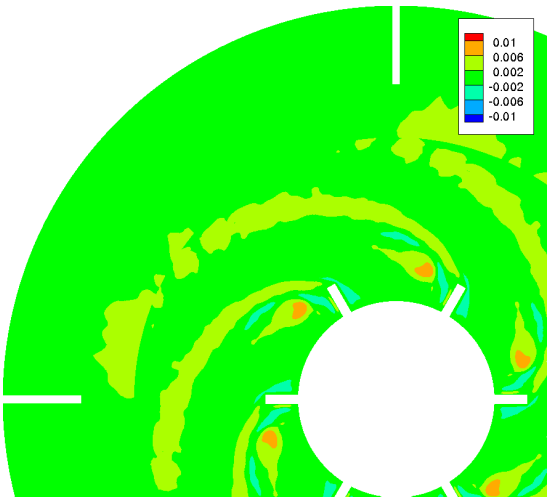

(b) Disk-plane ($z=0$)

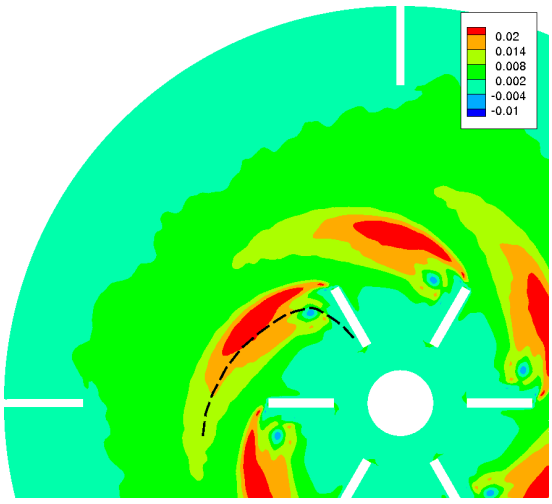

(c) In $x-y$-plane at $(z/(H_{BL}/2)=-0.5)$

Figure 6.23: Normalized Reynolds stress $\overline{u'_\theta u'_z}/V_{tip}^2$ contours with approximate core locations O (a) and path $- - --$ in (c). Blade rotation is clockwise for (b) and (c).

Figure 6.25 gives the normalized local Reynolds normal-stress parameter $\beta_{\theta,\theta}$ indicating regions of minimum Reynolds stress at walls with surface normals parallel to the circumferential direction $\hat{\theta}$ (again, indicative of wall induced damping of turbulent motion normal to the surface). These surfaces include the baffles and the blade pressure (PS) and suction-sides (SS) near the impeller. Regions of relatively high local normalized Reynolds stress in the circumferential direction include the outer tank walls and impeller shaft, the surface normals of which are perpendicular to the circumferential direction unit-vector $\hat{\theta}$. The remaining regions such as the impeller exit flow jet, trailing vortices and tank bulk flow recirculation loop take on values of $\beta_{\theta,\theta} \lessapprox 1$, again indicative of *approximately* isotropic flow turbulence with a slight reduction in the normal Reynolds stress in the θ-direction.

Finally, Figure 6.26 gives the normalized local Reynolds normal-stress parameter $\beta_{z,z}$ indicating regions of minimum Reynolds stress at walls with surface normals parallel to the axial direction $\hat{z}$ (again, due to wall induced damping of turbulent motion normal to the surface). These include the upper/lower tank wall, upper/lower blade edges, disk and under-impeller near surface regions. Regions of relatively high local normalized Reynolds stress in the axial direction include the outer tank walls, the surface normals of which are perpendicular to the axial direction unit-vector $\hat{z}$. As in the previous cases, the remaining regions take of values of $\beta_{z,z} \approx 1$, again indicative of approximately isotropic flow within the impeller exit flow jet, trailing vortices and tank bulk flow recirculation loop region, etc.

It should be noted that the results of Micheletti [13] and Lee and Yianneskis [12] indicate (RMS) turbulence anisotropy on the order 20% corresponding to a value of $0.7 \lessapprox \beta \lessapprox 1.3$ which is in accordance with the results presented previously.

6.9 Flow Kinetic Energy Spectrum

Given the successful prediction of flow (averaged) turbulent kinetic energy $\overline{k'}$, we can proceed onto the statistical decomposition of the instantaneous turbulence by reference back to the averaged turbulent kinetic energy in terms of the energy spectrum function of turbulence $\hat{E}(\|\vec{\kappa}\|)$ as given by (2.35) and repeated here for convenience

$$\overline{k'} = \int_{\|\vec{\kappa}\|=0}^{\infty} \hat{E}(\|\vec{\kappa}\|) d\|\vec{\kappa}\| \tag{6.4}$$

Recalling the definition of $\kappa \equiv 2\pi/\ell$ (where ℓ is the length-scale associated with a given turbulent structure), we found via dimensional analysis, that $\hat{E}(\|\vec{\kappa}\|) \propto \|\vec{\kappa}\|^{-5/3}$ within the equilibrium region while exponential decay is exhibited within the dissipation region (see §2.4.3). In addition, recall that the energy spectrum function $\hat{E}(\|\vec{\kappa}\|)$ represents the kinetic energy per unit wave number and is completely analogous to the Fourier transform of the instantaneous turbulence $\check{E}(\|\vec{\kappa}\|)$ based on spatial or temporal integration. The first calculation method for $\check{E}(\|\vec{\kappa}\|)$ involves direct calculation via the definition

$$\check{E}(\|\vec{\kappa}\|) = \int_{\|r\|=0}^{\infty} k'(r) e^{-\|\vec{\kappa}\cdot\vec{r}\|} d\|r\| \tag{6.5}$$

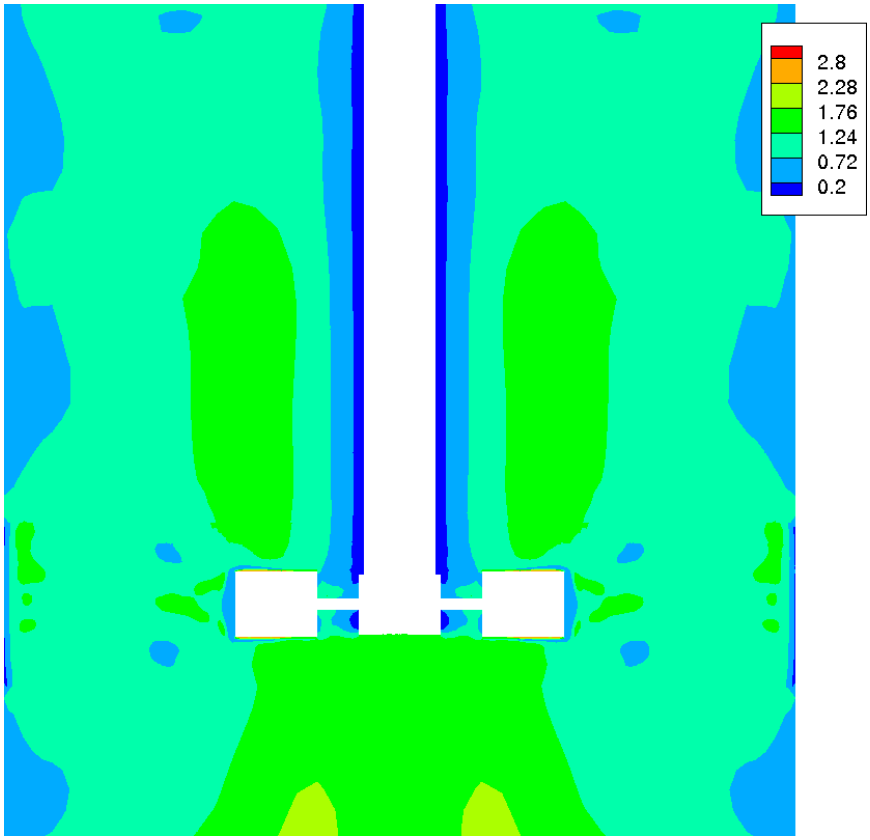

(a) $x-z$-plane at $y=0$

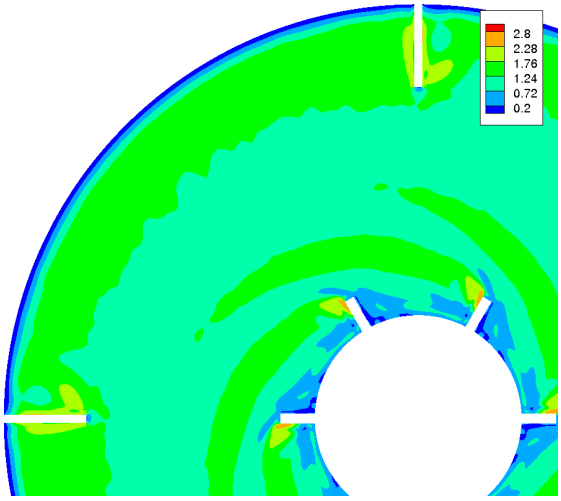

(b) Disk-plane ($z=0$)

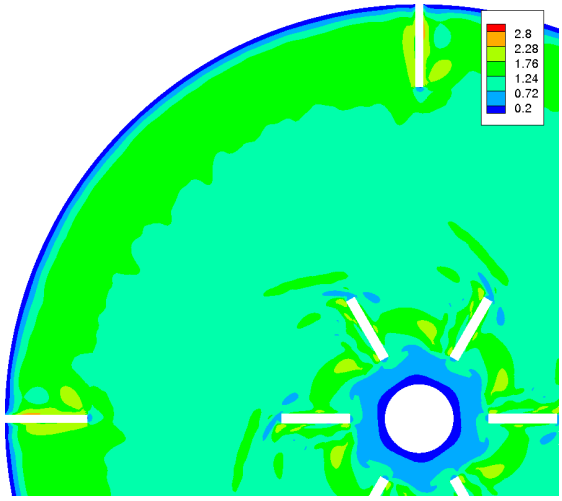

(c) In $x-y$-plane at $(z/(H_{BL}/2)=-0.5)$

Figure 6.24: Reynolds stress intensity parameter $\beta_{r,r}$ contours. Blade rotation is clockwise for (b) and (c).

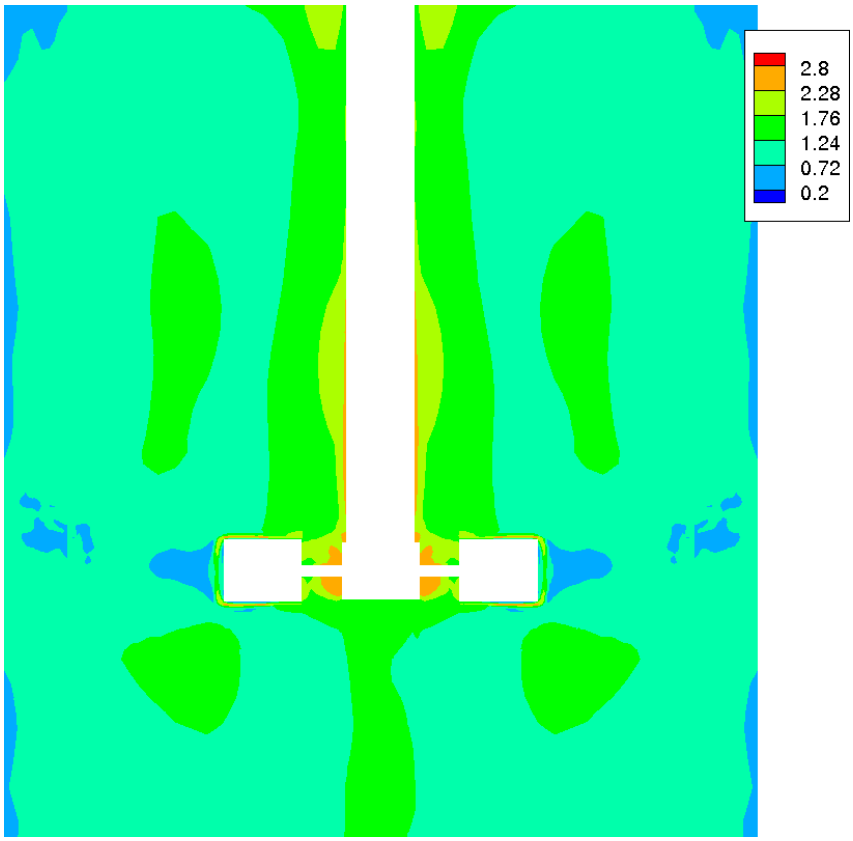

(a) $x-z$-plane at $y=0$

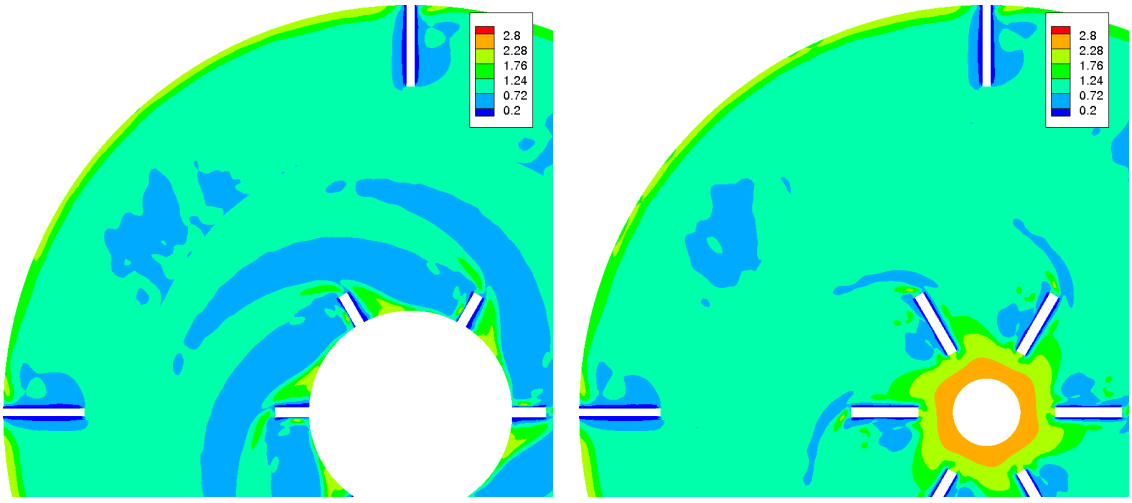

(b) Disk-plane ($z=0$)

(c) In $x-y$-plane at $(z/(H_{BL}/2)=-0.5)$

Figure 6.25: Reynolds stress intensity parameter $\beta_{\theta,\theta}$ contours. Blade rotation is clockwise for (b) and (c).

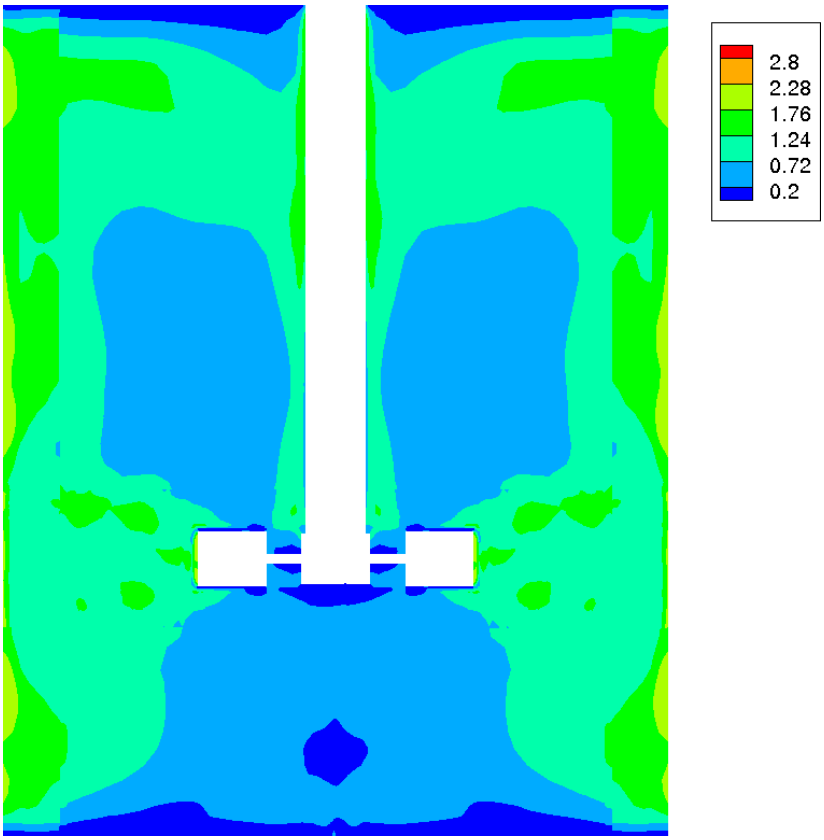

(a) $x-z$-plane at $y=0$

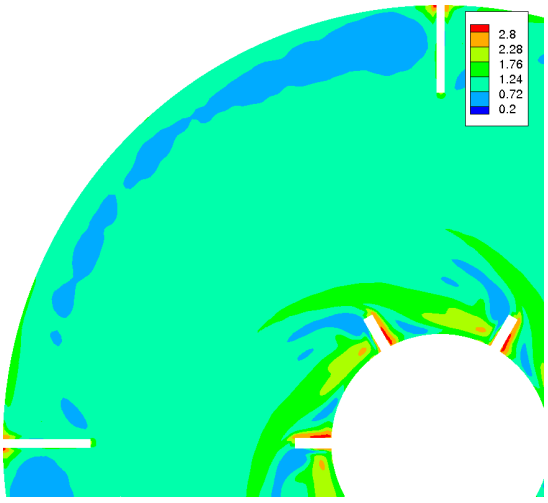

(b) Disk-plane ($z=0$)

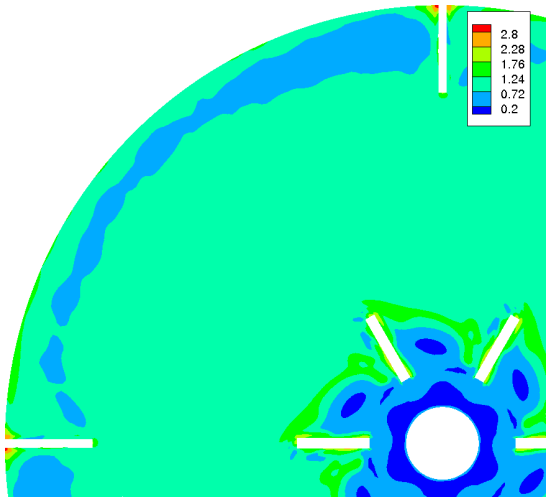

(c) In $x-y$-plane at $(z/(H_{BL}/2)=-0.5)$

Figure 6.26: Reynolds stress intensity parameter $\beta_{z,z}$ contours. Blade rotation is clockwise for (b) and (c).

which represents a *spatial* integration of turbulent kinetic energy $k'(r)$ over all space. The second approach involves temporal integration of $k'(t)$ at a fixed location resulting in

$$\hat{\hat{E}}(\omega) = \int_{t=0}^{\infty} k'(t) e^{-\omega t} dt \tag{6.6}$$

where $\omega \equiv f/(2\pi)$ and f is the frequency associated with a given turbulent structure. In addition, note that $\hat{\hat{E}}(\omega) \sim Energy * time$, hence division by the Kolmogorov time-scale yields $\tilde{E}(\omega) \equiv \hat{\hat{E}}(\omega)/\tau_\eta \sim Energy$.

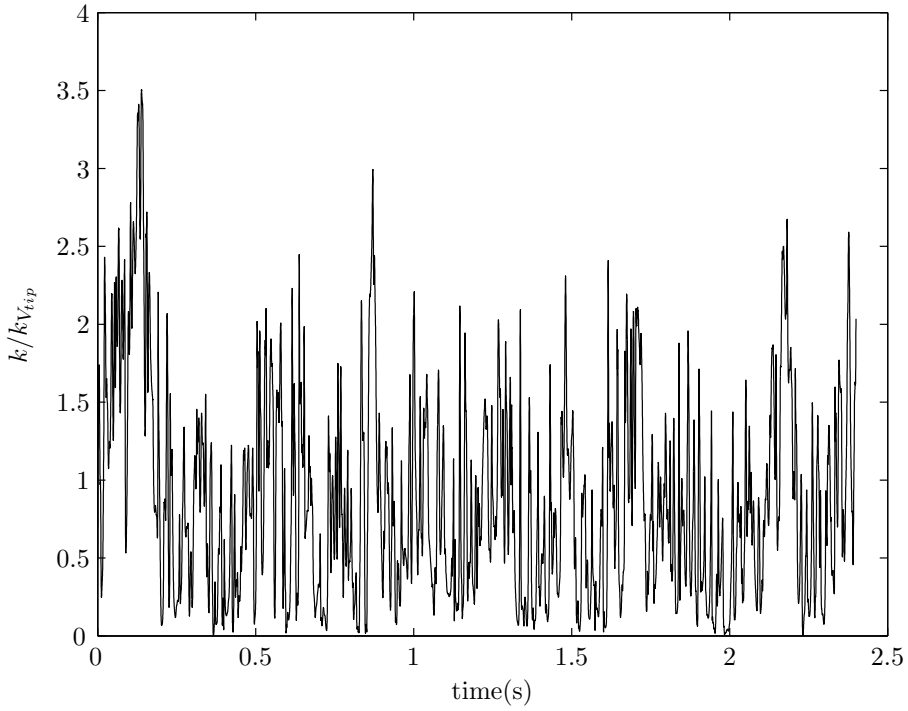

Figure 6.27: Normalized instantaneous flow kinetic energy $k/k_{V_{tip}}$ for revolution 90 (corresponding to time $t = 0(sec.)$) to 100 at a radial location $r/R = 1.26$.

Making the assumption of frozen turbulence (i.e. the Taylor-hypothesis valid for low turbulence intensity $\overline{k'}/\overline{k} \ll 1$), we can relate (turbulent) spatial variations in the flow properties at a given time to observed temporal variation in the (turbulent) flow properties at a given location. Specifically, given a characteristic mean flow or convective velocity U_{conv}, the *spatial* length-scale ℓ of a turbulent structure can be related to the associated observed frequency of the turbulence f and the convective velocity via

$$f = \frac{U_{conv}}{\ell} \Longrightarrow \ell = \frac{U_{conv}}{f} \tag{6.7}$$

Or, noting the definition of κ we have

$$\kappa = 2\pi \frac{1}{\ell} = 2\pi \frac{f}{U_{conv}} \Longrightarrow \kappa\eta = 2\pi\eta \frac{f}{U_{conv}} \tag{6.8}$$

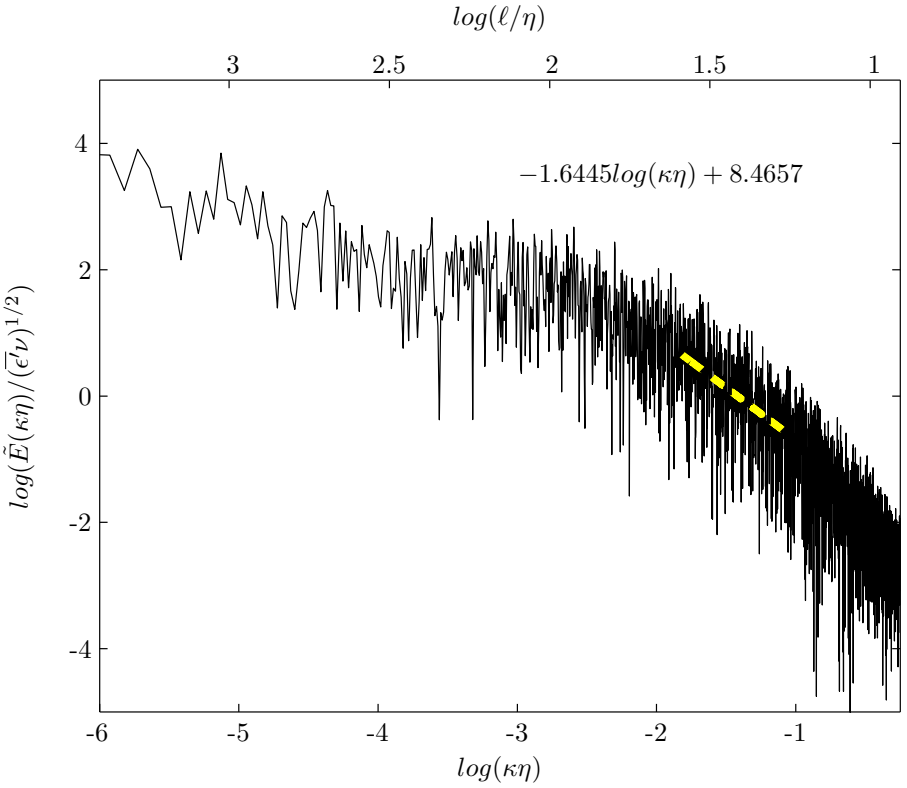

Figure 6.28: Normalized instantaneous flow kinetic energy spectrum $\tilde{E}(\kappa\eta)/(\overline{\epsilon}\nu)^{1/2}$ vs. $\kappa\eta$ for revolution 90 (corresponding to time $t = 0(sec.)$) to 100.

A single-point measurement was thus performed at a mesh location at the disk-plane near the inter-section of the trailing vortex cores ($r/R = 1.26$), (the local maximum of turbulent kinetic energy as indicated in Figure 6.6 (b) and an associated turbulence intensity $\overline{k'}/\overline{k} \lessapprox 0.5 < 1$ as shown in Figure 6.9), over a period of 10 revolutions resulting in the sampling of approximately $17,000$ flow states and their associated instantaneous kinetic energy. The normalized single-point time-series of $k(t)$ at this location is shown in Figure 6.27 as a function of time and indicates the oscillatory nature of the flow as the turbulent structures are convected through the sampling location via the mean flow.[3] A discrete Fourier transform was then performed on this single-point time-series resulting in a spectrum based on a decomposition in the time domain (i.e. $\tilde{E}(f)$). Utilizing the transformation resulting from the assumption of frozen turbulence (6.8), we arrive at $\tilde{E}(\kappa\eta)$ as displayed in Figure 6.28. Specifically, $\tilde{E}(\kappa\eta)$ normalized by the Kolmogorov velocity squared u_η^2 as a function of $\kappa\eta$ are plotted in log scale, indicating three distinct regions: An energy containing region for $-2 \gtrapprox log(\kappa\eta) \gtrapprox -6$. An equilibrium region where $d/dlog(\kappa\eta)(\tilde{E})[log(\kappa\eta)] = -1.64 \approx -5/3$ as indicated by the trend-line $- - -$ for $-1 \gtrapprox log(\kappa\eta) \gtrapprox -2$. And finally, the dissipation region for $log(\kappa\eta) \gtrapprox -1$. Qualitative agreement with a large number of studies presented in Pope [16] is evident, where the onset of the dissipation region occurs for a value $\kappa\eta \approx 0.1$.[4] In addition, the relatively narrow frequency range ($-1 \gtrapprox log(\kappa\eta) \gtrapprox -2$) associated with the

[3]The values for $U_{conv.}/V^{tip} = \|\overline{\vec{V}}\|/V^{tip}$ and $\epsilon/\epsilon_{D,V_{tip}}$ were found to be 0.67 and 973 respectively.
[4]A value of $log(\kappa\eta) = -0.93$ was chosen for the termination of the equilibrium region trend-line

equilibrium region for moderate Re is also demonstrated and is in accordance with lower Re spectra from numerous studies as reproduced by Pope. Finally, it should be stated that for high enough values of frequency, (specifically, $log(\kappa\eta) \gtrsim 0.5$), broad-band noise of amplitude $log(\tilde{E}(\kappa\eta)/u_\eta^2) \approx -4$ is evident, indicating the significant effect of small amplitude numerically induced noise (a noise floor) associated with turbulent length scales $\ell/\eta \lessapprox 2$. This should not be surprising given that the target simulation resolution for turbulent structures was $\ell/\eta \gtrapprox 10$. In addition, the simulation methodology, based on a sliding mesh, exhibits a mesh indexing frequency of approximately $2300Hz$ which corresponds to a value for $\kappa\eta$ of ≈ 3.2 or $log((\kappa\eta)_{index}) \approx 0.5$. Hence, sliding mesh induced periodic property oscillations may also be a contributing cause to the noise floor exhibited for $log(\kappa\eta) \gtrapprox 0.5$.

With respect to physical measurements of flow in Rushton stirred tanks, extraction of the (1-D single-point) energy spectra has been performed by Gunkel et al [9] on a Rushton stirred tank in the fixed (experimental) frame (as opposed to the impeller fixed frame performed herein). They found that near the impeller tip, the energy spectrum was dominated by contributions associated with the frequency of the passing blades and their first harmonic (a side-affect of the tank fixed-frame measurement technique). Further from the blade however, the familiar $-5/3$-power energy spectrum as a function of frequency was evident along with exponential decay associated with the dissipation region. Similar (LDA based) measurements of the energy spectrum were found by Lee et al [12] who employed a band-stop filtering technique to eliminate spurious contribution due to the periodic motion of the passing blades. The result, as in the case of Gunkel et al far from the impeller, is a well defined $-5/3$-power energy spectrum for radial locations far from the impeller $r/R \gtrapprox 1.8$. The measurements of Van't Reit et al [17] also yield a well defined $-5/3$-power energy spectrum only for locations away from the impeller blade tips (but within the impeller discharge stream). Again, this can be attributed (as indeed the Authors do) to the presence of 'pseudo-turbulence' due to the periodic motion of the passing blades. Finally, with respect to computational experiments, Alcamo et al [1] performed an LES-Smagorinsky (impeller fixed frame) simulation on a baffle-less Rushton stirred tank and calculated the energy spectrum as a function of frequency. Their results are in qualitative agreement with the present work with the exception of the high-frequency spectrum which does not exhibit exponential decay associated with the dissipation region. However, this is to be expected given that the LES simulation methodology is capable of resolving motions only within the energy containing and (upper) inertial range of turbulent motion.

These results present herein are therefore consistent with the previous studies mention, but with the advantage of resolving turbulent motion down to (and including) the dissipation range in the *impeller-fixed frame of reference* as a result of employing the sliding-mesh methodology. The result is a full energy spectrum without the spurious contributions from the periodic motion of the blades, nor *ad hoc* data processing required to filter out the periodic motion. However, this advantage is at the cost of possibly introducing high frequency noise associated with the mesh indexing between the impeller and tank-frame computational grids.

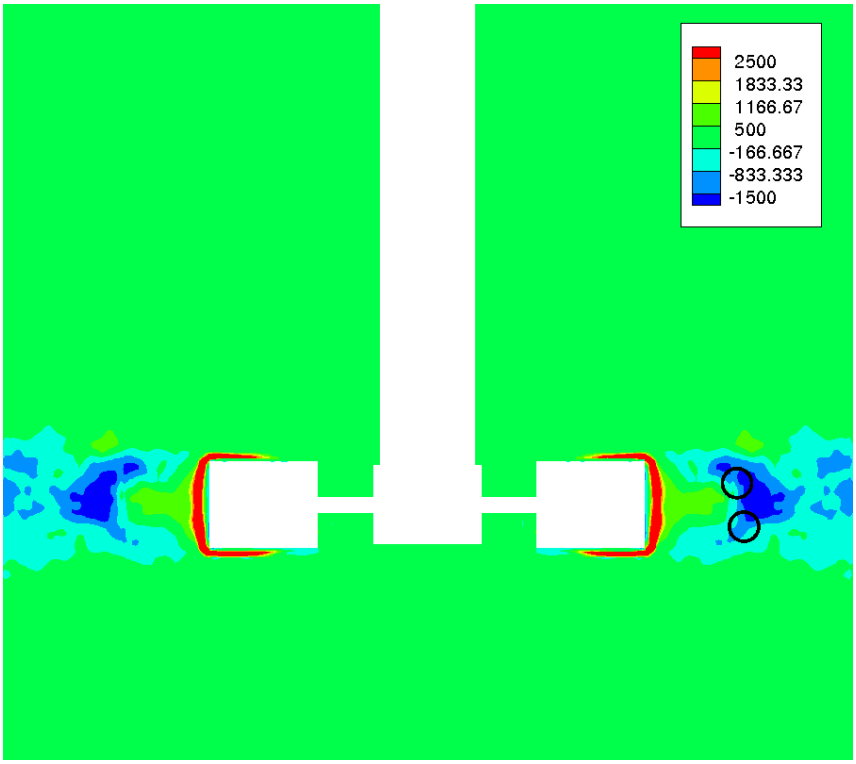

(a) $x-z$-plane at $y=0$

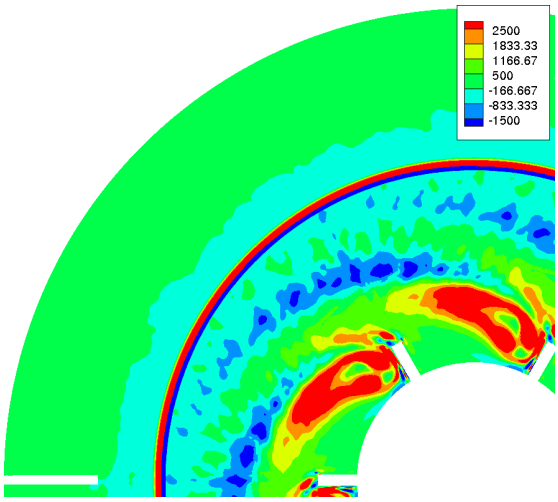

(b) Disk-plane ($z=0$)

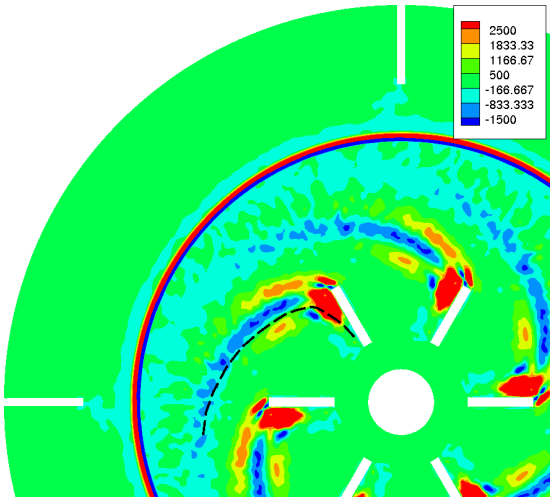

(c) In $x-y$-plane at $(z/(H_{BL}/2)=-0.5)$

Figure 6.29: Normalized mean flow $\overline{k'}$ transport term contours (net *local outflow*). Approximate vortex cores locations are signified by O in (a), and $- - - - - -$ in (c). Blade rotation is clockwise for (b) and (c).

6.10 Transport Equation for $\overline{k'}$

The previous analysis followed by validation from experimental measurements, (specifically those of Micheletti which correspond exactly to the simulation mixing geometry), indicates approximate correspondence between the simulated turbulent and mean flow field performed herein and the actual physical system. Thus, a more detailed analysis of the flow will be performed in an effort to quantify turbulent transport, generation and dissipation processes at the most fundamental level. To this end, the turbulent kinetic energy transport equation will be restated from §2.5 neglecting the contribution due to the periodic motion (which, in §5.5 has been shown to provide a negligible contribution to the kinetic energy of the flow in the impeller and baffle frame), under the assumption of steady-state turbulence

$$\overbrace{\vec{\nabla}\cdot(\overline{\vec{U}}\overline{k'})}^{\text{Conv. } \overline{k'} \text{ Via Mean Flow}} + \overbrace{\vec{\nabla}\cdot(\overline{\vec{u'}k'})}^{\text{Conv. } \overline{k'} \text{ Via Turbulence}} = - \overbrace{\frac{1}{\rho}\vec{\nabla}\cdot(\overline{\vec{u'}P'})}^{\text{Pressure Work/Diff. of } \overline{k'} \text{ via Turb. Motion}} - \overbrace{[\vec{\nabla}\cdot(\overline{\vec{u'}u'_i}\overline{U_i}) - \overline{U_i}\vec{\nabla}\cdot(\overline{\vec{u'}u'_i})]}^{\text{Prod. of } \overline{k'} \text{ Via Mean Flow}} + \overbrace{\nu\vec{\nabla}\cdot\vec{\Psi}}^{\text{Viscous Work/Diff. of } \overline{k'} \text{ Via Turb. Motion}} - \overbrace{\overline{\epsilon'}}^{\text{Viscous Dissipation of } \overline{k'}} \tag{6.9}$$

where the vector quantity $\vec{\Psi}$ is defined via (3.79). Given the present experimental methodology utilizes a finite volume formulation, the above transport equation was integrated over a finite volume (or cell) with volume ΔV yielding a cell averaged transport equation as developed in §3.10 and restated below for constant mesh motion

$$\frac{1}{\Delta V}[\overbrace{\int_{\Delta S}(\overline{\vec{U}^*}\overline{k'})\cdot d\vec{S}}^{\text{Conv. } \overline{k'} \text{ Via Mean Flow}} + \overbrace{\int_{\Delta S}(\overline{\vec{u'}^*k'})\cdot d\vec{S}}^{\text{Conv. } \overline{k'} \text{ Via Turbulence}}] = \frac{1}{\Delta V}[- \overbrace{\frac{1}{\rho}\int_{\Delta S}(\overline{\vec{u'}P'})\cdot d\vec{S}}^{\text{Pressure Work/Diff. of } \overline{k'} \text{ via Turb. Motion}} - \overbrace{[\int_{\Delta S}(\overline{\vec{u'}u'_i}\overline{U_i})\cdot d\vec{S} - \overline{U_i}\int_{\Delta S}(\overline{\vec{u'}u'_i})\cdot d\vec{S}]}^{\text{Prod. of } \overline{k'} \text{ Via Mean Flow}} + \overbrace{\nu\int_{\Delta S}\vec{\Psi}\cdot d\vec{S}}^{\text{Visc. Work/Diff. of } \overline{k'} \text{ Via Turb. Motion}}] - \overbrace{\overline{\epsilon'}}^{\text{Visc. Diss. of } \overline{k'}} \tag{6.10}$$

Finally, it should be noted that all transport terms have dimensions of dissipation and are thus normalized via $\epsilon_{V_{tip},D}$

6.10.1 Mean Flow $\overline{k'}$ Transport

The net convection of turbulent kinetic energy $\overline{k'}$ via the mean flow, as stated previously represents a local kinetic energy sink (net outflow) with an average value over the computational cell of

$$\overbrace{\frac{1}{\Delta V}\int_{\Delta S}(\overline{\vec{U}^*}\overline{k'})\cdot d\vec{S}}^{\text{Conv. } \overline{k'} \text{ Via mean Flow}} \tag{6.11}$$

However, before we proceed let us determine the general behavior of this term. Specifically, given the requirement of continuity as applied to the mean flow, the volume averaged mean flow transport of turbulent kinetic energy (6.11) reduces to

$$\frac{1}{\Delta V}\int_{\Delta S}\overline{\vec{U}^*}(\overline{k'})\cdot d\vec{S} = (\overline{\vec{U}})_{vol.av}\cdot(\vec{\nabla}\overline{k'})_{vol.av} \tag{6.12}$$

Hence, regions of vanishing averaged turbulent kinetic energy gradient, (corresponding to local maximums/minimums in $\overline{k'}$) will tend to correspond to vanishing mean flow transport of turbulent kinetic energy. Thus, insofar as the impeller trailing vortex core line represents an approximate location of maximum turbulent kinetic energy, (for locations projected onto the disk-plane between the upper/lower vortices as shown in Figure 6.6 (b)), we expect that mean flow transport will vanish within the vicinity of and between the vortex cores (near the projected vortex radial location). To this end, Figure 6.29 gives the mean flow induced $\overline{k'}$ transport (sink) at various planes. Specifically, Figure 6.29 (b) gives the mean flow induced transport of $\overline{k'}$ (6.11) at the disk-plane $z = 0$ and indicates an alternating mean flow induced outflow/inflow of $\overline{k'}$ due to the presence of the vortices. This is due to the fact that the vortex core location (approximately indicated by the dashed line), projected onto the disk-plane corresponds to the approximate location of maximum turbulence as indicated in Figure 6.6 (b) and (c). Hence, for radial locations $r \leq R_{core}$ at the disk-plane turbulence is increasing with radius (or $\partial\overline{k'}/\partial r > 0$), yielding net mean flow eflux (outflow) of $\overline{k'}$ from the control volume. Conversely, for radial locations $r \geq R_{core}$ turbulence is decreasing in the radial direction (or $\partial\overline{k'}/\partial r < 0$), again via Figure 6.6 (b) and (c)) resulting in a net inward flux of $\overline{k'}$ into the control volume. Figure 6.29 (c) gives the $\overline{k'}$ mean flow transport sink at the axial location mid-location between the disk and lower impeller tip $z/(H_{BL}/2) = -0.5$ and indicates, as in the previous case of the disk-plane $z = 0$, net local outflow of $\overline{k'}$ for $r \leq R_{core}$, vanishing net convection near the core (corresponding to the local radial location of maximum $\overline{k'}$ associated with the vortex core (see Figure 6.6 (c)) followed by net inflow of $\overline{k'}$ for radial locations $r \geq R_{core}$.

Likewise, Figure 6.29 (a) gives $\overline{k'}$ transport due to the mean flow in the $x - z$-plane and indicate a peak inflow (negative values correspond to a source) at a radial location just downstream (radially outward) from the vortex core (signified by an O in the Figure) at the disk-plane. Note that Figure 6.29 (b) refers to the mean flow $\overline{k'}$ convection sink at the disk-plane, hence insofar as axial velocity is negligible at the disk-plane the primary mode of $\overline{k'}$ transport should be due to radial convection via the radial mean flow velocity component $\overline{U_r}$. Finally, the above observations indicate radially outward convection of turbulent kinetic energy from the impeller vortex region, implying a probable displacement of the location of maximum turbulence outward from a region of presumed peak generation associated with the vortices (as will be discussed in §6.10.4, one of the primary mechanism for turbulence generation within the core region is due to the radial variation in radial mean-velocity). Comparison with the phase averaged results of Ducci indicate similar outward mean flow convection of turbulent kinetic energy into regions downstream from the vortex location within the impeller jet, with a corresponding outflow of turbulent kinetic energy just upstream

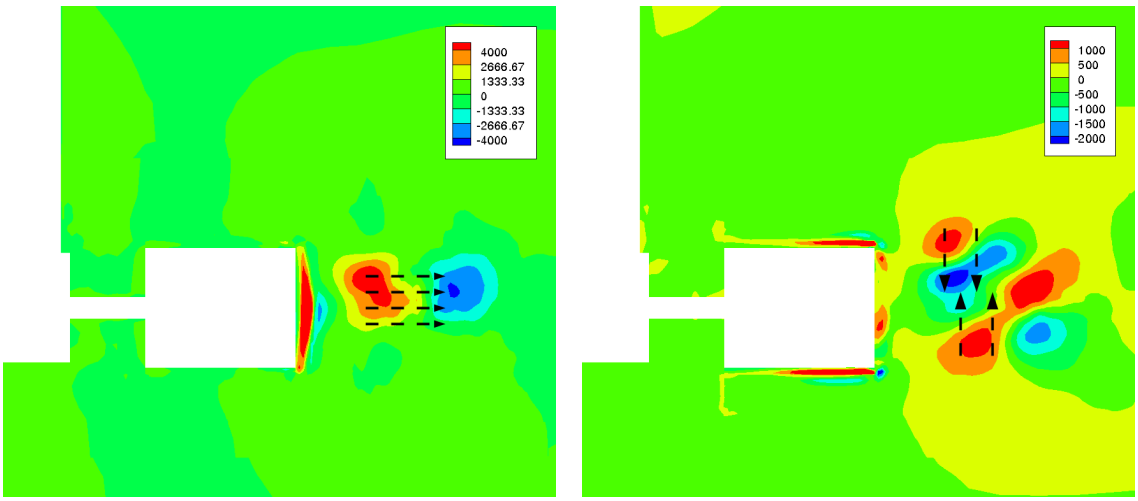

(a) $\frac{\partial(\overline{U_r}\ \overline{k'})}{\partial r}$ (b) $\frac{\partial(\overline{U_z}\ \overline{k'})}{\partial z}$

Figure 6.30: Normalized mean flow $\overline{k'}$ transport eflux (a) radial and (b) axial in the $x-z$-plane ($y = 0$).

from the trailing vortex core radial locations.

Further understanding of the mean flow turbulent kinetic energy transport process can be gleaned by examination of the local mean flow induced $\overline{k'}$ net flux components in the axial and radial directions. Specifically, Figure 6.30 (a) and (b) gives net radial ($\partial(\overline{U_r}\ \overline{k'})/\partial r$) and axial ($\partial(\overline{U_z}\ \overline{k'})/\partial z$) convection of turbulent kinetic energy $\overline{k'}$ due to the mean flow. In the case of radial net convection, we see that the radial flow transports k' from radial locations $r \leq R_{core}$ to locations downstream from the vortex cores, (in the radial direction), or $r \geq R_{core}$. This transport is signified by the flux arrows indicated, where the radial net inflow of $\overline{k'}$ is maximized near the disk-plane (corresponding to the maximum mean flow radial velocity). Net axial eflux of $\overline{k'}$ is shown in Figure 6.30 (b) and indicates relatively small axial mean flow convection of $\overline{k'}$ due to the fact that $\overline{U}_r \gg \overline{U}_z$ near the disk-plane. In addition, very near the impeller trailing edge, axial convection is towards the impeller center/disk-line as indicated by the flux arrows shown. This is due to the convergence of the mean flow towards the impeller disk-plane via entrainment into the jet. Comparison with the results of Ducci indicate qualitative agreement including the relative importance of radial compared to axial mean flow convection of $\overline{k'}$.

6.10.2 Turbulent-Flow $\overline{k'}$ Transport

The net convection of turbulent kinetic energy $\overline{k'}$ via turbulent motion, as stated previously represents a local kinetic energy sink (net outflow) with the average value over the computational cell of

$$\overbrace{\frac{1}{\Delta V}\int_{\Delta V}(\vec{\nabla}\cdot\overline{\vec{u'^{*}}k'})dV}^{Conv.\ \overline{k'}\ Via\ Turbulence} \tag{6.13}$$

Bearing in mind the discussion of turbulent property flux given in §2.5, where in the present context $\phi = \overline{k'}$, the term $\overrightarrow{u'^* k'}$ above can be recast as the convective turbulent flux per unit area $-_{k'}\overline{q}''_{turb.}$. Given large variations in k' compared to $\overline{u'}$, the turbulent transport flux is proportional to $-\nabla\phi$ and hence $\nabla\overline{k'}$. Thus, we have $\overrightarrow{u'k'} \propto \nabla\vec{\overline{k'}}$ and the resulting functionality for (6.13) is of the form

$$\frac{1}{\Delta V}\int_{\Delta V}(-\vec{\nabla}\cdot\nabla\vec{\overline{k'}})dV \tag{6.14}$$

Hence, regions of locally high averaged turbulent kinetic energy $\overline{k'}$ (i.e. a local maximum) yield positive values for (6.14) resulting in local $\overline{k'}$ net eflux and visa versa. The conclusion can be restated more precisely by simply noting that the local convective flux of $\overline{k'}$ due to turbulent motion in the i^{th} direction is $-^{i}_{k'}\overline{q}''_{turb.} = \overline{u'_i k'} \propto \partial\overline{k'}/\partial x_i$ (an eddy viscosity concept where the constant of proportionality would be an eddy viscosity). Hence, the net outflow of turbulence from a differential control volume in the i^{th}-direction is

$$\frac{\partial\overline{u'_i k'}}{\partial x_i} = \frac{\partial^{i}_{k'}\overline{q}''_{turb.}}{\partial x_i} \propto -\frac{\partial^2\overline{k'}}{\partial x_i^2} \tag{6.15}$$

Note that the previous observations provides the motivation for characterizing turbulent convection/transport of $\overline{k'}$ as akin to gradient transport and hence turbulent diffusion of $\overline{k'}$.

With the previous in mind, Figure 6.31 (a) gives the net turbulent convective transport of $\overline{k'}$ for the $x-z$-plane with approximate trailing vortex core locations. Likewise, Figure 6.31 (b) and (c) given turbulent transport of $\overline{k'}$ at the disk-plane $z = 0$ and lower blade quarter-depth $z/(H_{BL}/2) = -0.5$ (approximate planar location of the lower trailing vortex). Both Figures indicate peak $\overline{k'}$ outflow due to turbulent transport in the vicinity of local peak $\overline{k'}$ associated with the region just down-stream of the trailing vortices, and thus correspond to the suggested behavior given in (6.15). This is especially the case at the disk-plane (see Figure 6.6). Additional regions of high turbulent transport are near the impeller surface associated with local turbulence diffusion away from regions of local high turbulence levels present at the top and bottom impeller edge (see Figure 6.7).

Further understanding of the turbulent-flow induced $\overline{k'}$ transport can found by examination of the local $\overline{k'}$ net eflux in the axial and radial directions. Specifically, Figure 6.32 (a) and (b) gives normalized net radial ($\frac{\partial(\overline{u'_r k'})}{\partial r}$) and axial ($\frac{\partial(\overline{u'_z k'})}{\partial z}$) convection of $\overline{k'}$ due to the turbulent convection/diffusion. In the case of radial net convection due to the turbulent motion, we see that the radial transport of $\overline{k'}$ is outward from the radial location $r \approx R_{\overline{k'}_{max}} \gtrapprox R_{core}$ as indicated by the flux arrows (where $R_{\overline{k'}_{max}}$ is the radial location at the disk-plane associated with maximum turbulence just down-stream of the approximate projected radial location of the vortex cores). Thus, the region near the impeller corresponding to a radial location $r \approx R_{\overline{k'}_{max}} \approx 1.5R$ represents a region of high local turbulence and hence local turbulent eflux. This is verified by examination of Figure 6.7 as well as the data plotted in Figure 6.8 which indicates a maximum value for $\overline{k'}$ at the disk-plane for $r \gtrapprox R_{core} \approx 1.5R$. Net axial eflux of $\overline{k'}$ is shown in Figure 6.32 (b) and indicates large outward flux of $\overline{k'}$ away from the trailing vortex region and towards the relatively low turbulence regions above and

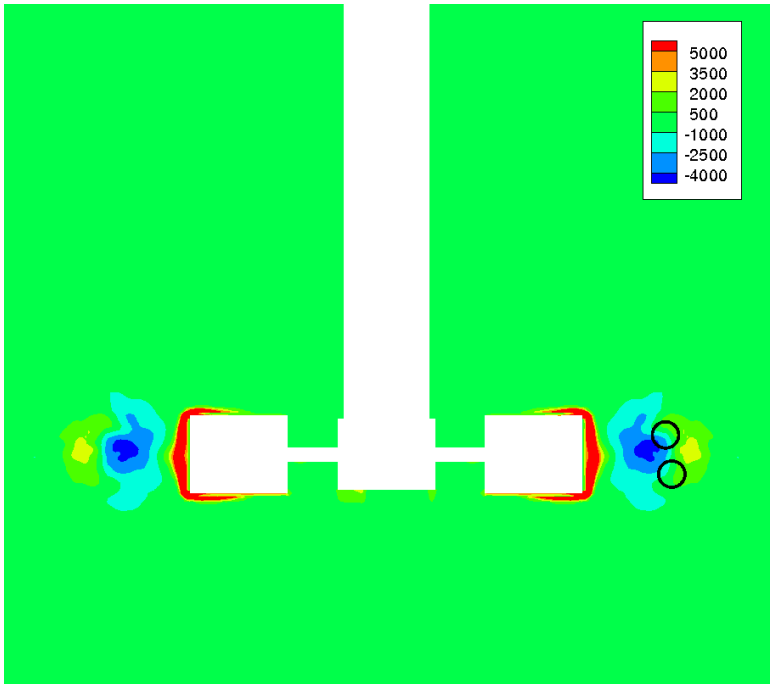

(a) $x-z$-plane at $y=0$

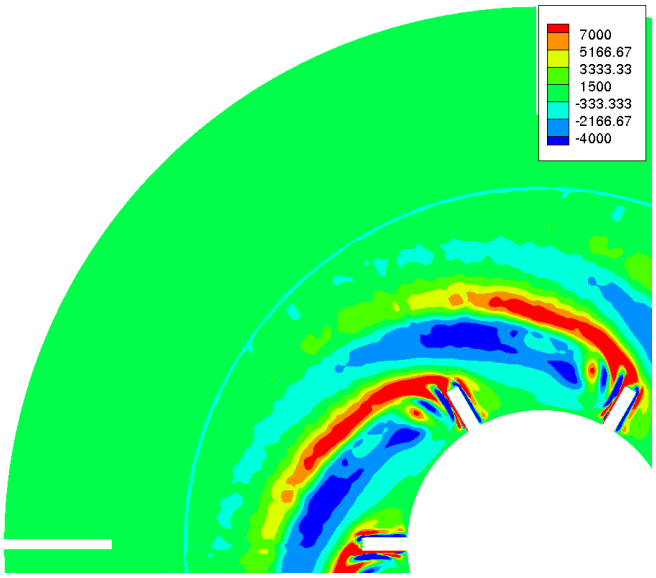

(b) Disk-plane ($z=0$)

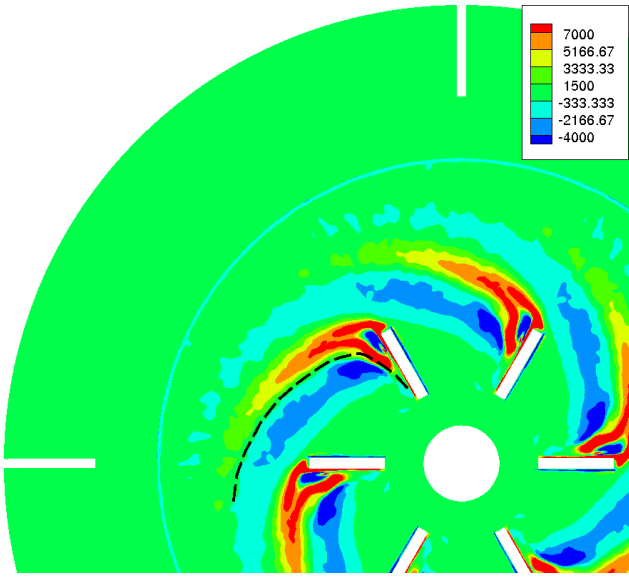

(c) In $x-y$-plane at $(z/(H_{BL}/2)=-0.5)$

Figure 6.31: Normalized turbulent-flow $\overline{k'}$ transport term contours (eflux of $\overline{k'}$). Approximate core locations signified by an O in (a) and core path $- - - - -$ in (c). Blade rotation is clockwise for (b) and (c).

below the impeller jet. As indicated by the Figure, axial turbulent transport of $\overline{k'}$ is more significant than radial transport presumably due to the fact that $\partial^2\overline{k'}/\partial z^2 \gtrapprox \partial^2\overline{k'}/\partial r^2$ within

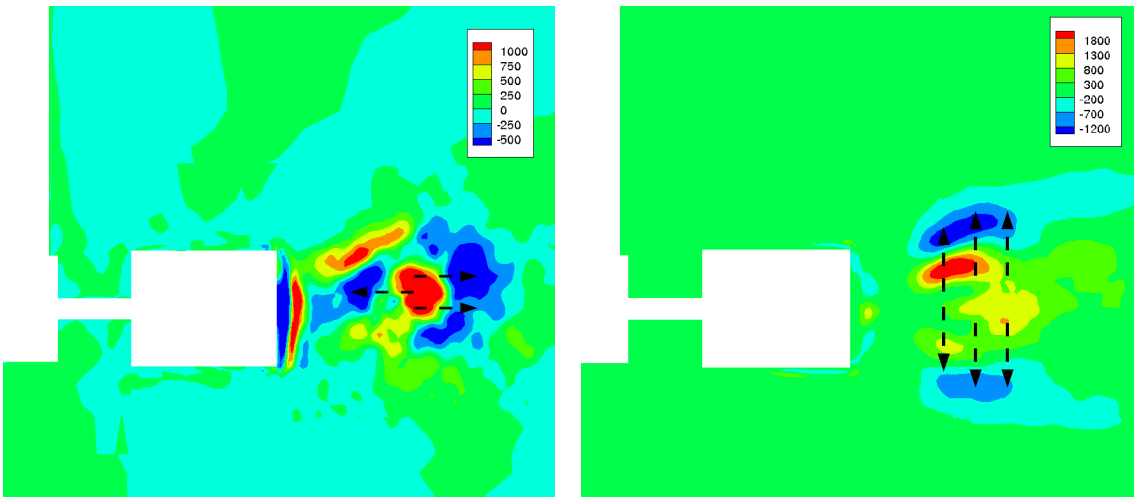

(a) $\frac{\partial(\overline{u_r' k'})}{\partial r}$ (b) $\frac{\partial(\overline{u_z' k'})}{\partial z}$

Figure 6.32: Normalized turbulent-flow $\overline{k'}$ transport (a) radial and (b) axial flux in the $x-z$-plane ($y=0$).

the impeller exit stream (see Figure 6.7). Again, comparison with the results of Ducci indicate qualitative agreement including the relative importance of axial compared to radial convection of $\overline{k'}$.

6.10.3 Turbulent Pressure Work

The net pressure work via the turbulent flow represents a local conversion of turbulent static into turbulent dynamic pressure with an average value over the computational cell

$$\overbrace{-\frac{1}{\Delta V}\frac{1}{\rho}\int_{\Delta V}\vec{\nabla}\cdot(\overline{\vec{u}'P'})dV}^{\textit{Pressure Work/Diff. of } \overline{k'} \textit{ via Turb. Motion}} \tag{6.16}$$

In order to examine the numerical results pertaining to the cell average pressure work we must qualitatively describe the behavior of (6.16), specifically that of the product $\vec{u}'P'$. To this end we note that any local (static) pressure field can be decomposed into the dynamic and total pressure contribution, or $P = P_{tot} - P_{dyn}$. Hence, a finite variation in local pressure ΔP is given by $\Delta(P_{tot} - P_{dyn})$. Assuming no heat or work interactions except pressure work (i.e. no heat transfer and negligible viscous work) then along a stream-line, $\Delta P_{tot} = 0$ and the variation in local pressure ΔP approximately corresponds to the negative variation in local dynamic pressure $-\Delta P_{dyn}$ (which is associated with the variation in local fluid velocity). Next, we note that along a streamline the dynamic pressure is given by $1/2\rho\|\vec{U}\|^2$, hence taking the variation of P_{dyn} gives $\Delta P_{dyn} = \rho[\Delta\|\vec{U}\|]\|\vec{U}\|$, where the local fluid velocity is composed of the mean and perturbation component.

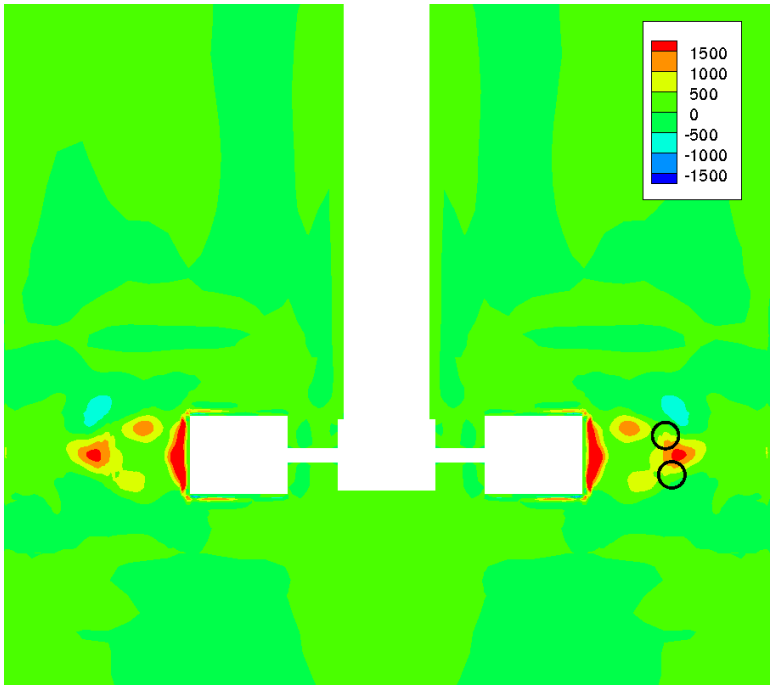

(a) $x-z$-plane at $y=0$

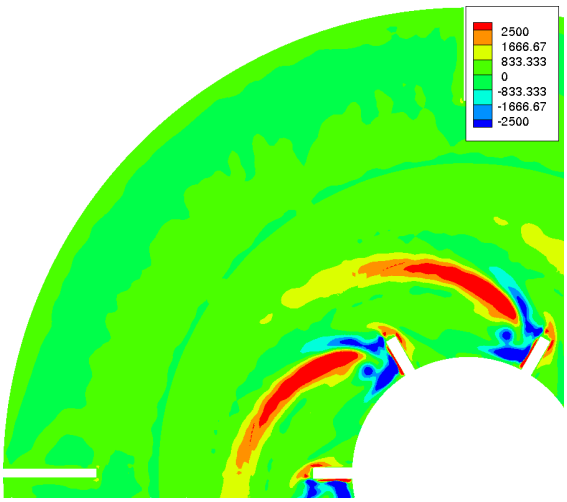

(b) Disk-plane ($z=0$)

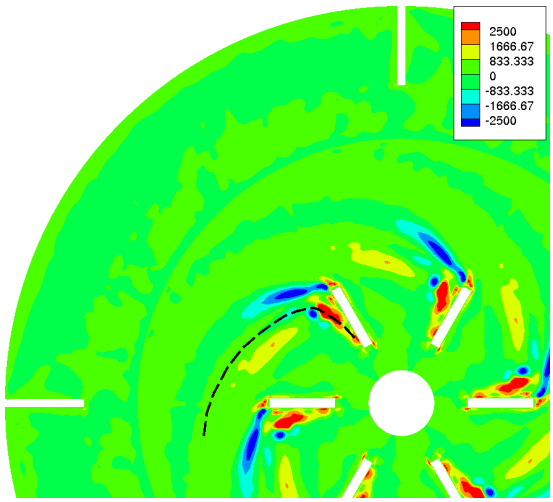

(c) In $x-y$-plane at $(z/(H_{BL}/2)=-0.5)$

Figure 6.33: Normalized turbulent pressure work contours. Blade rotation is clockwise for (b) and (c).

Thus, if we assume that the mean and perturbation flow are comparable in magnitude, but *the variation in the mean flow is much less than the variation in the perturbation velocity* we have $\Delta P_{dyn} = \rho/2\Delta[\|\overrightarrow{\overline{U}} + \vec{u}'\|^2] \approx \rho\|\vec{u}'\|[\|\overrightarrow{\overline{U}} + \vec{u}'\|]$. Or in terms of the local turbulent kinetic energy k' and local flow (instantaneous) kinetic energy (mean plus perturbation), we have $\Delta P_{dyn} \approx \rho\sqrt{k'}[\sqrt{k}]$ and hence associating ΔP with P' gives $P' = -\Delta P_{dyn} \approx -\rho\sqrt{k'}[\sqrt{k}]$ where k is the local instantaneous flow kinetic energy (mean plus perturbation). Hence, the behavior of the turbulent pressure work term (6.16) corresponds to that of the following

$$\frac{1}{\Delta V}\int_{\Delta V} \vec{\nabla}\cdot(\overline{\vec{u}'\sqrt{k'}\sqrt{k}})dV \tag{6.17}$$

Note that the above approximation can take on different limiting values depending on the relative strength of the turbulence intensity $\frac{\overline{k'}}{\overline{k}}$:

$$-\frac{1}{\Delta V}\frac{1}{\rho}\int_{\Delta V} \vec{\nabla}\cdot(\overline{\vec{u}'P'})dV \sim \begin{cases} \frac{1}{\Delta V}\int_{\Delta V} \vec{\nabla}\cdot(\overline{\vec{u}'\sqrt{k'}\sqrt{\overline{k}}})dV & \text{For } \frac{\overline{k'}}{\overline{k}} \ll 1 \\ \frac{1}{\Delta V}\int_{\Delta V} \vec{\nabla}\cdot(\overline{\vec{u}'k'})dV & \text{For } \frac{\overline{k'}}{\overline{k}} \gg 1 \end{cases} \tag{6.18}$$

Thus, in regions on high turbulence intensity $\frac{\overline{k'}}{\overline{k}} \gg 1$, the turbulent pressure-work is analogous to turbulent convection/diffusion with regions of locally high pressure work indicating a local turbulent kinetic energy maximum and visa versa.[5] However, as indicated by (6.17) high mean flow velocities tend to increase the local dynamic pressure variation (for a given velocity perturbation), hence regions of high local mean flow kinetic energy $\overline{k}$ may exhibit elevated turbulent pressure work for a given local turbulence level $\overline{k'}$.

With the previous in mind, Figure 6.33 (a) gives the normalized net turbulent pressure work/diffusion of $\overline{k'}$ for the $x-z$-plane with approximate trailing vortex core locations. Likewise, Figure 6.33 (b) and (c) gives pressure work/diffusion at the disk-plane $z = 0$ and lower blade quarter-depth $z/(H_{BL}/2) = -0.5$ (again, the approximate planar location of the lower trailing vortex is shown). Both Figures indicate a maximum $\overline{k'}$ source due to turbulent pressure work in the vicinity of regions of local peak $\overline{k'}$ associated with the trailing vortices as well as the local $\overline{k'}$ maximum at the impeller disk-plane down-stream from the approximate radial location of the vortex cores. Additional regions of high turbulent pressure work are near the impeller surface associated with the local high turbulence at the top and bottom impeller edge (refer to Figure 6.7).

Further understanding of the turbulent-flow pressure work can found by examination of the local net pressure work components in the axial and radial directions. Specifically, Figure 6.34 (a) and (b) gives normalized net radial ($-1/\rho\frac{\partial(\overline{u_r'P'})}{\partial r}$) and axial ($-1/\rho\frac{\partial(\overline{u_z'P'})}{\partial z}$) turbulent pressure work.

Net normalized axial turbulent pressure work is shown in Figure 6.34 (b) and indicates large conversion of turbulent static pressure into dynamic pressure perturbation, and hence of $\overline{k'}$ in the vortex region near the $\overline{k'}$ maximum at disk-plane in the impeller-stream. As indicated by the Figure, axial pressure work is more important than radial work presumably

[5]It is this limiting behavior as $k'/\overline{k} \to \infty$ which motivates the association of pressure work with a pressure based diffusive mechanism of $\overline{k'}$ utilized in the literature.

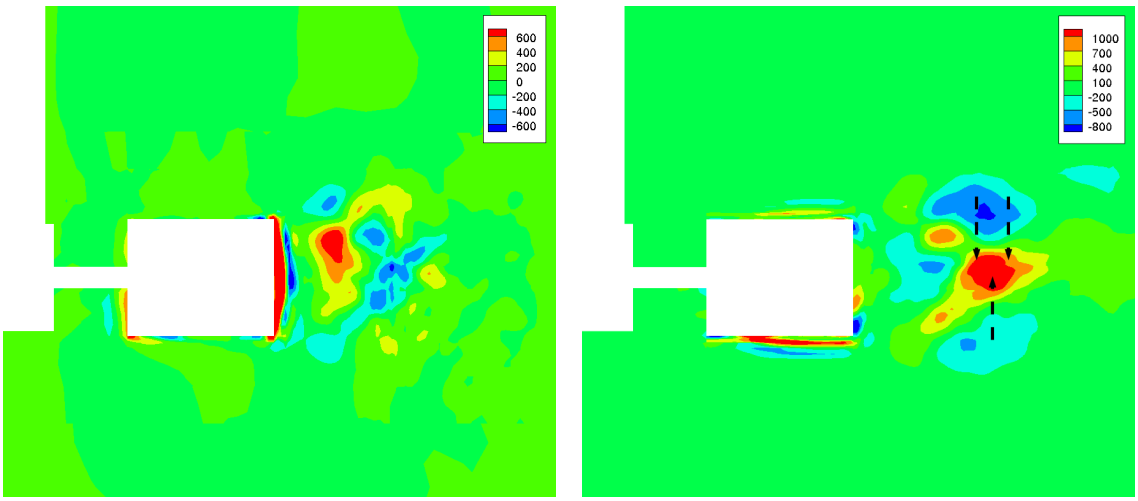

(a) $\frac{-1}{\rho}\frac{\partial \overline{u'_r P'}}{\partial r}$ (b) $\frac{-1}{\rho}\frac{\partial \overline{u'_z P'}}{\partial z}$

Figure 6.34: Normalized turbulent-flow pressure net work in (a) radial and (b) axial directions in the $x-z$-plane ($y=0$).

due to the fact that $\partial^2\overline{k'}/\partial z^2 \gtrapprox \partial^2\overline{k'}/\partial r^2$ within the impeller exit stream. Hence, the above observations generally indicate a reciprocal relationship between turbulent pressure work and turbulent convection/diffusion of $\overline{k'}$: Where net turbulent convection/diffusion of $\overline{k'}$ via turbulent motion is locally outward, turbulent pressure work acts as a local source of $\overline{k'}$ by converting static turbulent pressure fluctuations into turbulent dynamic pressure. This is to be expected given that within the impeller jet $\overline{u'_z} \gg \overline{U_z}$. Hence as indicated via (6.18) the axial turbulent pressure work exhibits the limiting behavior corresponding to a turbulent diffusive mechanism. The pressure work mechanism in operation in the radial direction is less clear given that $\overline{U}_r > \overline{u'}_r$ near the impeller. Comparison of the relative strength of the turbulent convection and pressure work terms also indicates that local turbulent convection is dominant with the magnitude of convection $\approx 100-200\%$ greater than the local pressure work. These general observation are in accordance with the measurements of turbulent boundary-layer and jet flow presented in Pope [16] based on the DNS results of Spalta [20] and Rogers et al [18] both of which indicate a reciprocal relationship between net turbulent pressure work and turbulent convection with the later exceeding the former by $\approx 100-200\%$ in magnitude.

6.10.4 Turbulent Generation of $\overline{k'}$

Flow turbulence generation, as stated previously in §2.5, represents a local conversion of mean flow motion into turbulent velocity perturbations due to a mean flow field gradient in the presence of local turbulent motion. Thus, from (3.87) we have the cell averaged aggregate turbulence generation

$$\overbrace{-\frac{1}{\Delta V}\Big[\int_{\Delta S}(\overline{\vec{u}'u'_i}\overline{U_i})\cdot d\vec{S} - \overline{U_i}\int_{\Delta S}(\overline{\vec{u}'u'_i})\cdot d\vec{S}\Big]}^{Prod.\ of\ \overline{k'}\ Via\ mean\ flow} = -(\overline{u'_i u'_j})\frac{\partial \overline{U}_i}{\partial x_j} \tag{6.19}$$

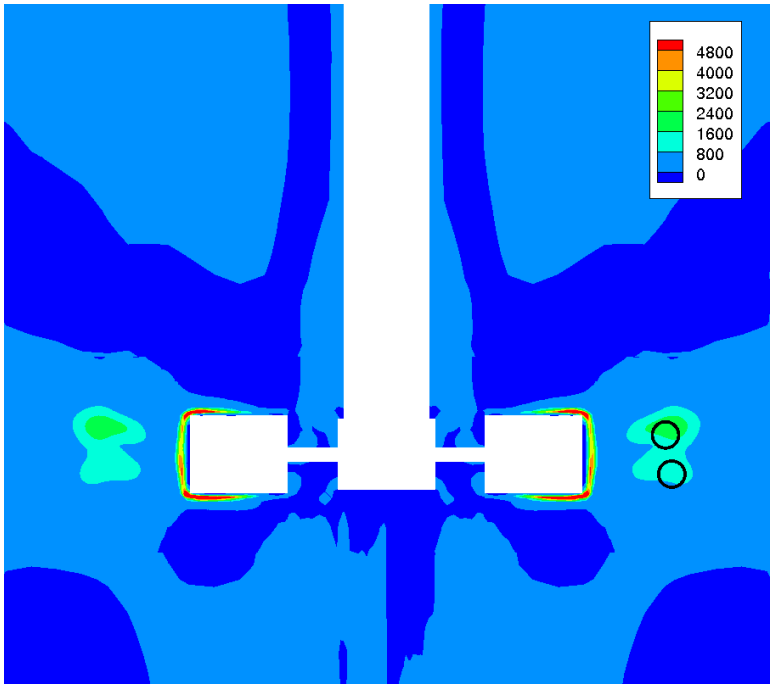

(a) $x-z$-plane at $y=0$

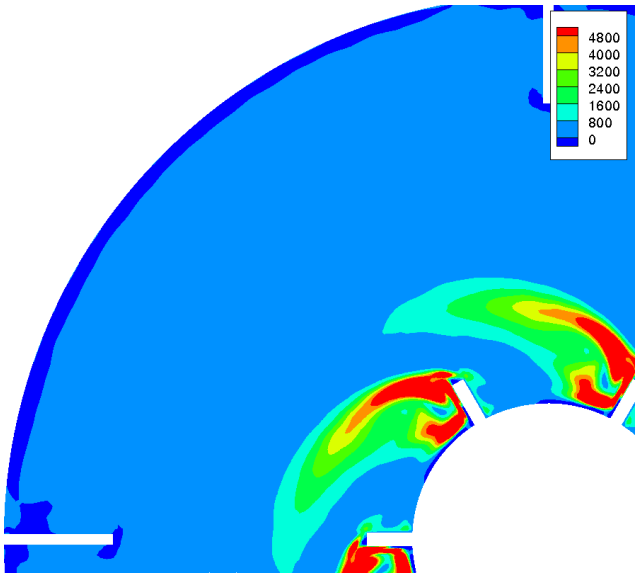

(b) Disk-plane ($z=0$)

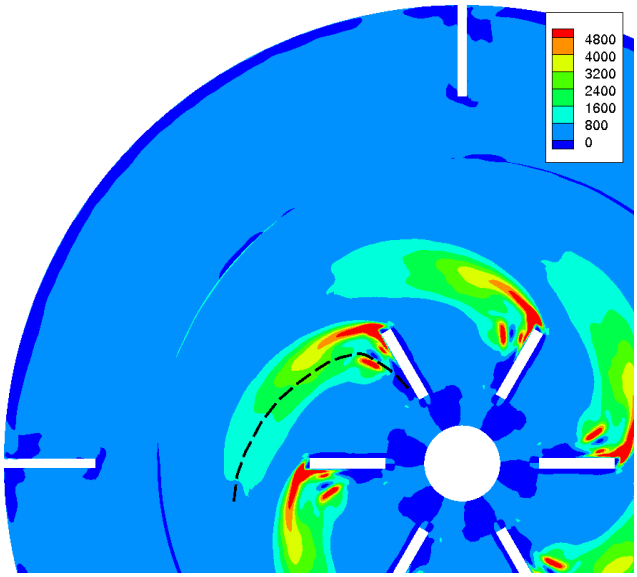

(c) In $x-y$-plane at $(z/(H_{BL}/2)=-0.5)$

Figure 6.35: Normalized $\overline{k'}$ generation contours. Blade rotation is clockwise for (b) and (c).

where the mean flow velocity gradient $\frac{\partial \overline{U}_i}{\partial x_j}$ and Reynolds stresses $\overline{u_i' u_j'}$ are cell centered values. In order to interpret the numerical results pertaining to the above cell average generation, we must again refer to the qualitative description of the behavior of turbulent transport as discussed previously in §2.5. Specifically, we found that the presence of a non-zero mean

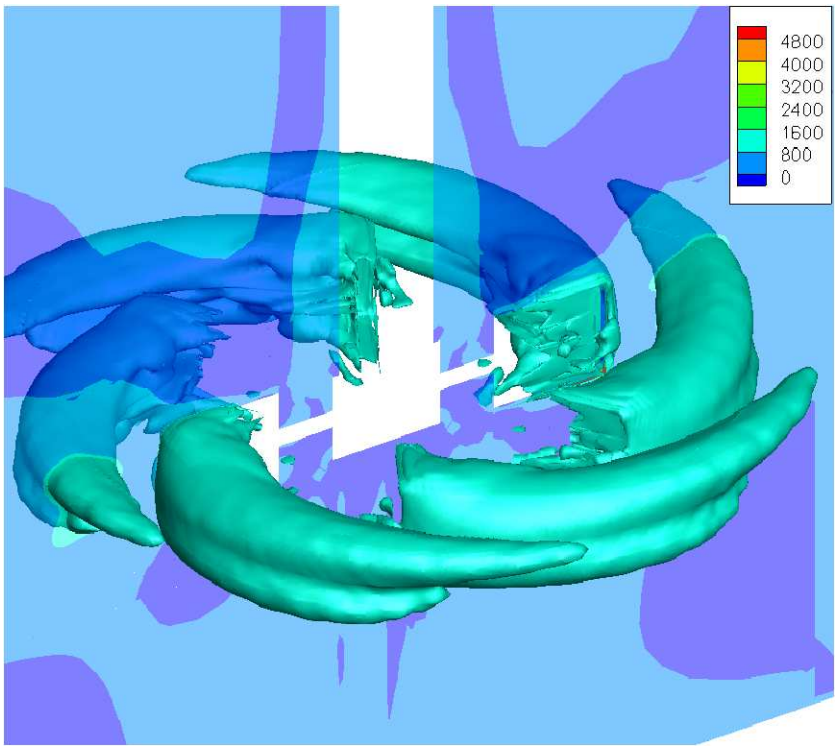

(a) Iso-surface 1000

Figure 6.36: Normalized $\overline{k'}$ generation $-(\overline{u_i' u_j'})\frac{\partial \overline{U}_i}{\partial x_j}$ iso-surface 1000.

property gradient $\partial\overline{\phi}/\partial x_i$ in the direction of x_i induced, within a turbulent flow field, a conversion of the mean property gradient in ϕ into a local perturbation in ϕ (i.e. a source of ϕ'). Hence, via inspection of (6.19), turbulence is generated due to the sum contribution of all the mean flow velocity gradients in the various spatial directions, with large local generation of turbulence corresponding to regions containing high local turbulence *and* mean flow gradients.

With the previous in mind, Figure 6.35 (a) gives the net normalized turbulent generation of $\overline{k'}$ for the $x-z$-plane $y = 0$ with approximate trailing vortex core locations. Likewise, Figure 6.35 (b) and (c) given net generation of $\overline{k'}$ at the disk-plane $z = 0$ and lower blade quarter-depth $z/(H_{BL}/2) = -0.5$. Both Figures (a) and (c) indicate high turbulence generation in the vicinity of regions of local peak $\overline{k'}$ coupled with high mean flow gradients associated with the trailing vortices, as well as the local $\overline{k'}$ maximum at the impeller disk-plane down-stream from the vortex cores. Additional regions of high production of $\overline{k'}$ are near the impeller blade surface associated with the high local turbulence at the top/bottom/trailing impeller edge (see Figure 6.7) as well as the presumed high mean flow velocity gradients associated with the impeller mean flow boundary-layer (and flow separation on the blade suction-side (SS)). A further demonstration of the trailing vortices and impeller boundary-layer separations as significant sources of turbulence is illustrated by the iso-surface of normalized $\overline{k'}_{gen} = 1000$ given in Figure 6.36, which indicates a dual cone-like structure originating at each impeller

blade centered at the approximate location of the trailing vortex cores.

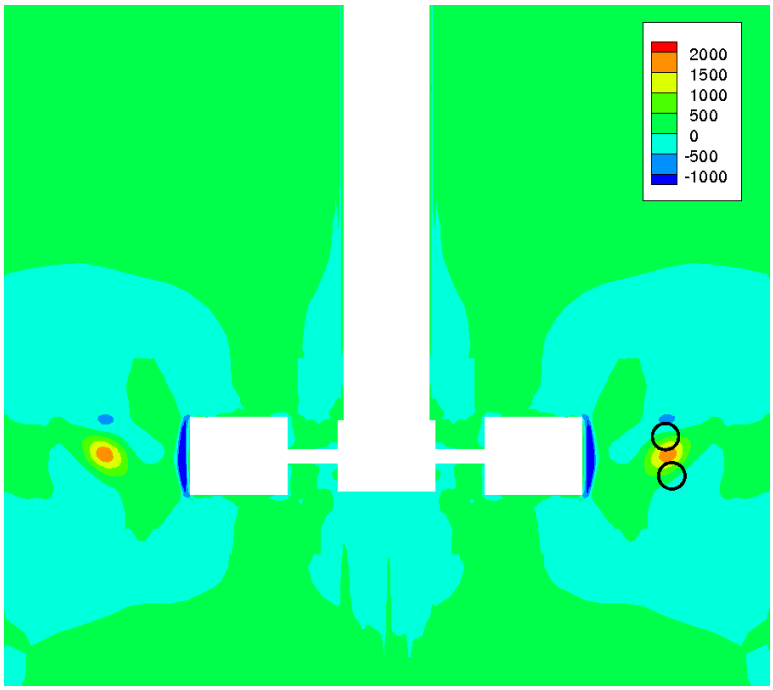

(a) $x-z$-plane at $y=0$

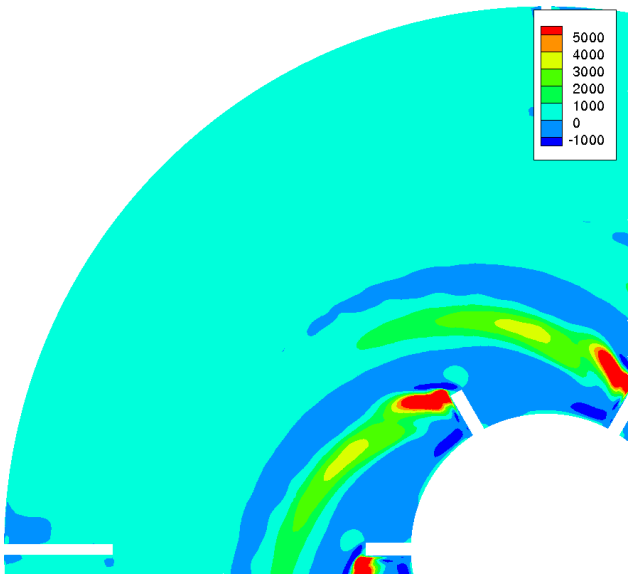

(b) Disk-plane ($z=0$)

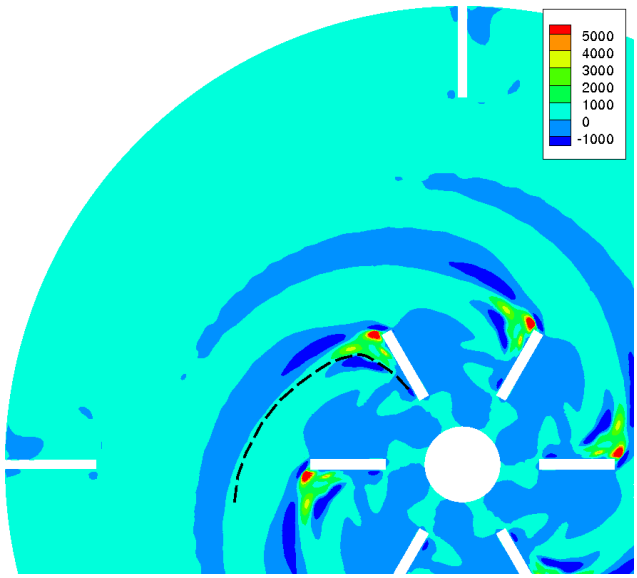

(c) In $x-y$-plane at $(z/(H_{BL}/2)=-0.5)$

Figure 6.37: Normalized $\overline{k'}$ generation term $-\overline{u'_r u'_r}\frac{\partial \overline{U}_r}{\partial r}$ contours. Blade rotation is clockwise for (b) and (c).

Further understanding of the generation of $\overline{k'}$ can found by examination of the local sources due to mean flow gradients in the radial $\hat{r}$, circumferential $\hat{\theta}$ and axial $\hat{z}$ directions.

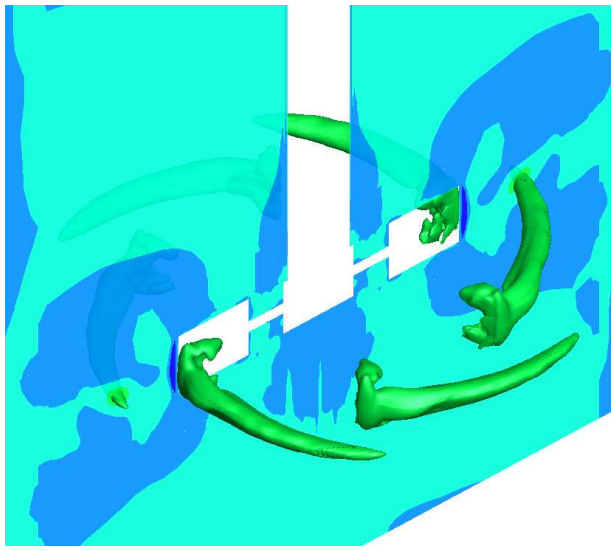

Figure 6.38: Normalized $\overline{k'}$ generation term $-\overline{u'_r u'_r}\frac{\partial \overline{U}_r}{\partial r} = 1500$ iso-surface.

Specifically, Figure 6.37 gives normalized $\overline{k'}$ generation due to mean (radial) flow variations in the radial direction $-\overline{u'_r u'_r}\frac{\partial \overline{U}_r}{\partial r}$. Given the previous discussion, one expects the maximum generation to occur in regions with both high levels of local turbulence as well as radial variations in the radial mean flow velocity component. Referring to Figures 5.16 we see that, at the disk plane, the circumferentially averaged radial mean flow decreases with radial position (i.e. $\partial \overline{U}_r/\partial r < 0$). In addition, Figure 6.18 which gives radial normal Reynolds stress $\overline{u'_r u'_r}$, indicating a peak stress at the disk-plane down-stream of the approximate radial location of the trailing vortex cores. Hence, as expected, Figure 6.37 (a) indicates the region of maximum $\overline{k'}$ production due to radial mean flow variation in the radial direction near the trailing vortex core region as projected onto disk-plane. These observations are strengthened via recourse to the $\overline{k'}$ production iso-surface shown in Figure 6.38, indicating a maximum at the impeller disk-plane between the impeller trailing vortices.

Generation of $\overline{k'}$ due to circumferential variation in circumferential velocity is shown in Figure 6.39 and indicates negligible generation except very near the impeller blade presumably due to blade bottom/top/trailing edge boundary-layer effects.

Next, noting that an *approximate* axial mean flow velocity plane of symmetry exists near the disk-plane we expect that $\partial \overline{U}_z/\partial z \approx 0$ near the disk-plane. However, as indicated by inspection of the mean flow axial velocity component at the disk-plane (see Figure 5.26), we see that the axial velocity exhibits positive or negative values with the passing of each trailing vortex pair (due to the lack of perfect vortex symmetry relative to the disk-plane), thus resulting in small oscillating values of the axial mean velocity axial gradient about zero at the disk-plane. In addition, as shown in Figure 6.20, the Reynolds stress component $\overline{u'_z u'_z}$ is maximized within the vortex core region as well as at the disk-plane slightly downstream of the vortex core locations (corresponding to regions of high $\overline{k'}$). Figure 6.40 gives turbulence generation due to axial variations of axial mean velocity. Specifically, generation as calculated at the disk-plane is given in 6.40 (b) and indicates an oscillating value of generation association

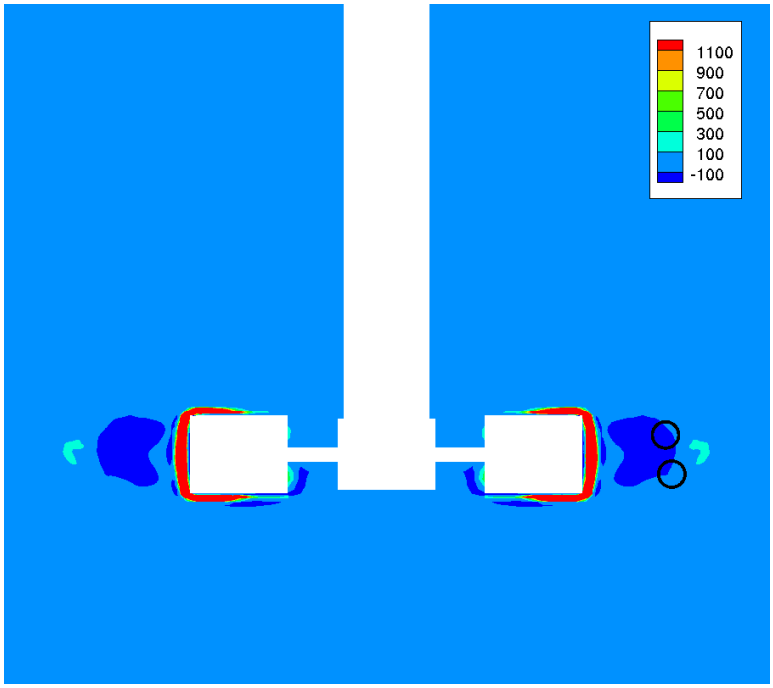

(a) $x-z$-plane at $y=0$

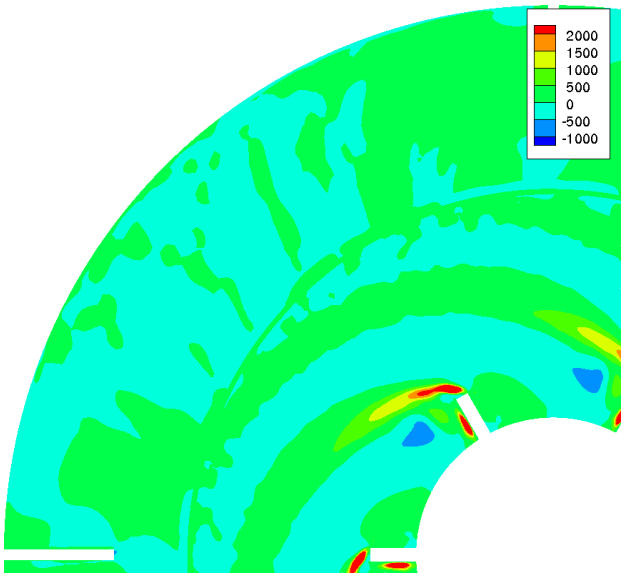

(b) Disk-plane ($z=0$)

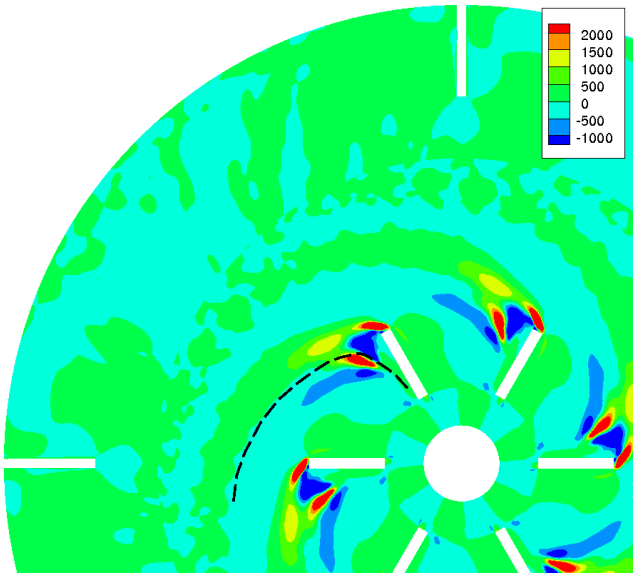

(c) In $x-y$-plane at $(z/(H_{BL}/2)=-0.5)$

Figure 6.39: Normalized $\overline{k'}$ generation term $-\overline{u'_\theta u'_\theta}\frac{\partial \overline{U}_\theta}{\partial \theta}$ contours. Blade rotation is clockwise for (b) and (c).

with the periodic propagation of the trailing vortices and the corresponding region of elevated Reynolds stress $\overline{u'_z u'_z}$ near the disk-plane just downstream from the trailing vortices.

Next, recall the high magnitude of the local $\overline{u'_\theta u'_z}$ component Reynolds stress present at

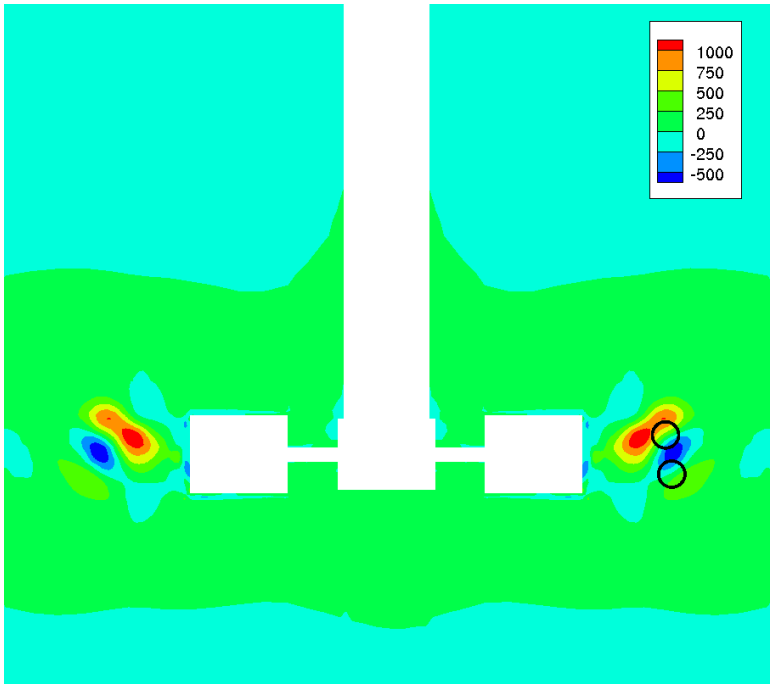

(a) $x-z$-plane at $y=0$

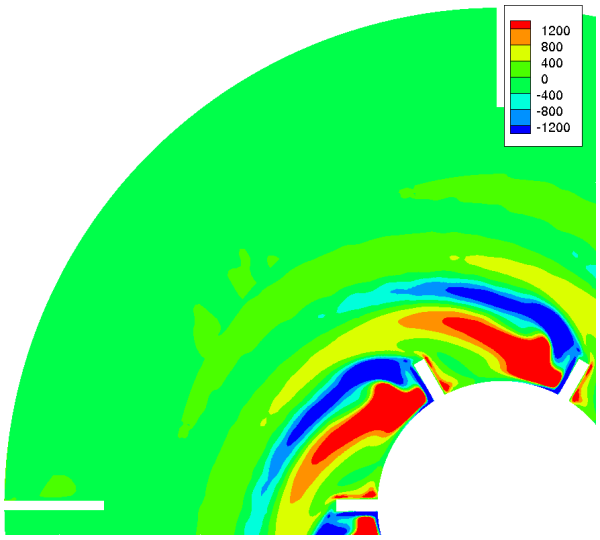

(b) Disk-plane ($z=0$)

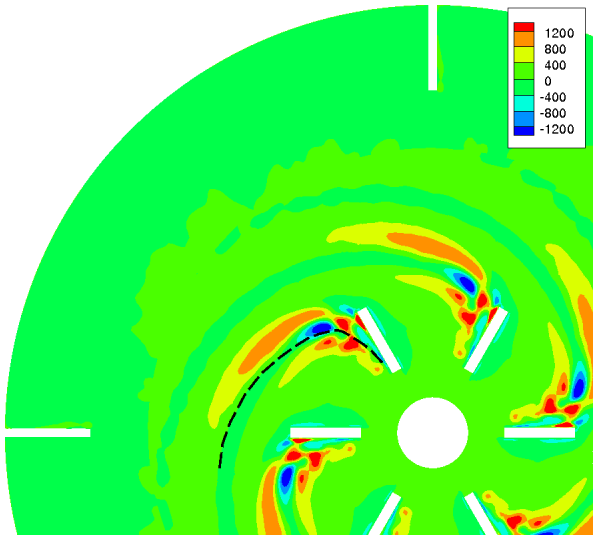

(c) In $x-y$-plane at $(z/(H_{BL}/2)=-0.5)$

Figure 6.40: Normalized $\overline{k'}$ generation term $-\overline{u'_z u'_z}\frac{\partial \overline{U}_z}{\partial z}$ contours. Blade rotation is clockwise for (b) and (c).

the trailing vortex cores (see Figure 6.23) due to high local turbulence. In addition, variation in the mean flow circumferential velocity in the axial direction in the vicinity of the core as shown in Figure 6.43, exhibits an approximately constant increase in magnitude as one moves from above the impeller jet towards the disk. Thus, the resulting generation of $\overline{k'}$ due

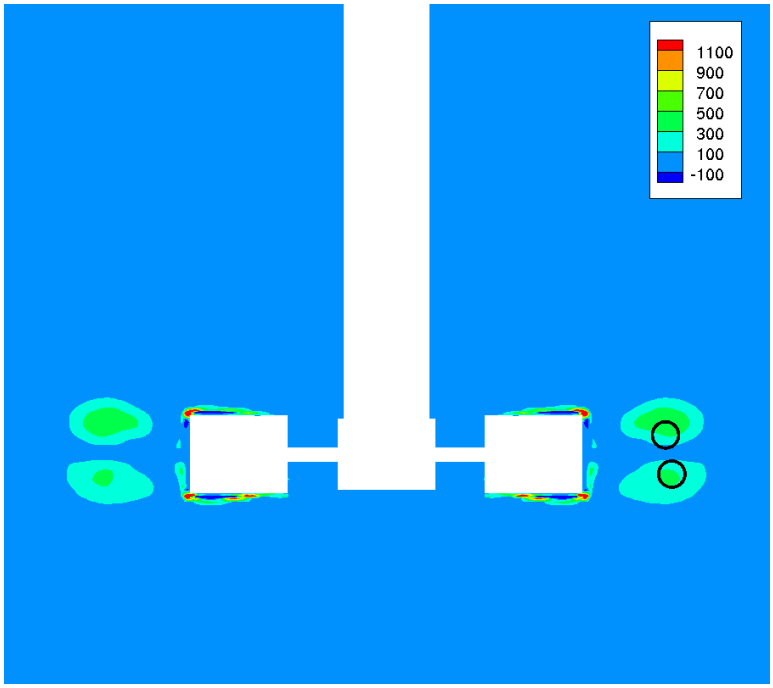

(a) $x-z$-plane at $y=0$

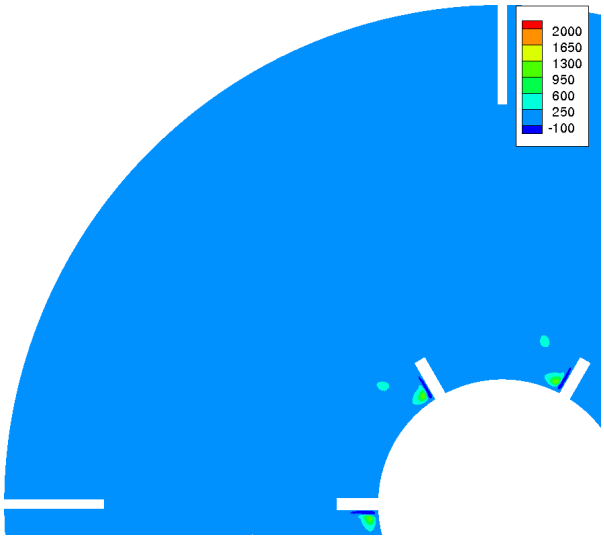

(b) Disk-plane ($z=0$)

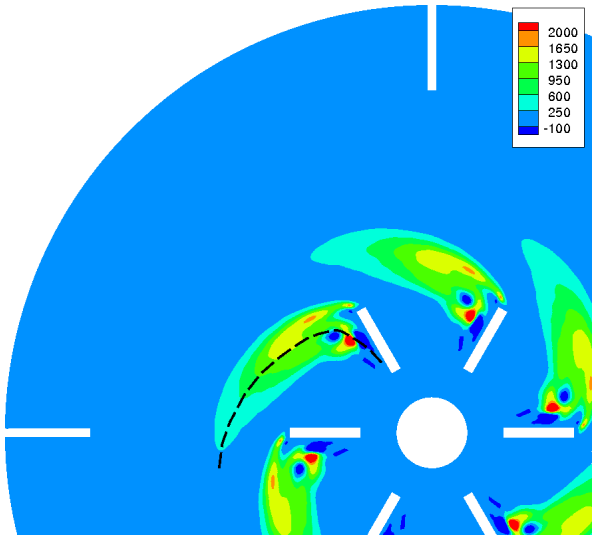

(c) In $x-y$-plane at $(z/(H_{BL}/2)=-0.5)$

Figure 6.41: Normalized $\overline{k'}$ generation term $-\overline{u'_\theta u'_z}\frac{\partial \overline{U}_\theta}{\partial z}$ contours. Blade rotation is clockwise for (b) and (c).

to axial variations in circumferential mean flow velocity $-\overline{u'_\theta u'_z}\frac{\partial \overline{U}_\theta}{\partial z}$ exhibits a local maximum in the trailing vortex region as shown in Figure 6.41 (a) and (c). This association of peak generation with the approximate core location is further illustrated by the iso-surface of this generation term as shown in Figure 6.42 which indicates the cone-like structures in the

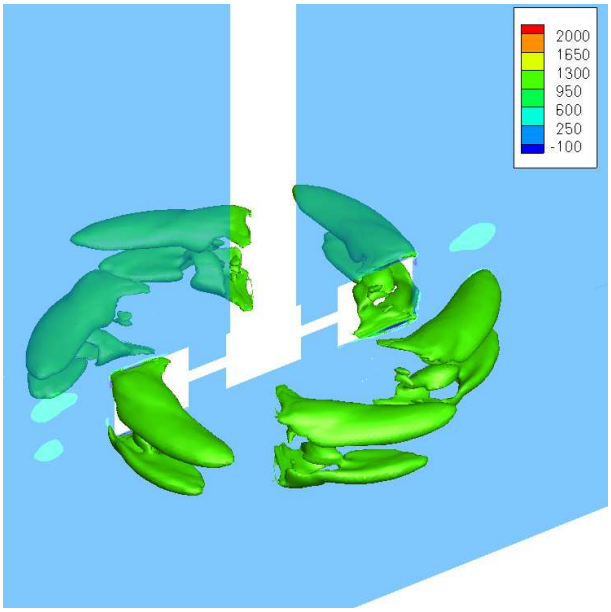

Figure 6.42: Normalized $\overline{k'}$ generation term $-\overline{u'_\theta u'_z}\frac{\partial \overline{U}_\theta}{\partial z} = 1100$ iso-surface.

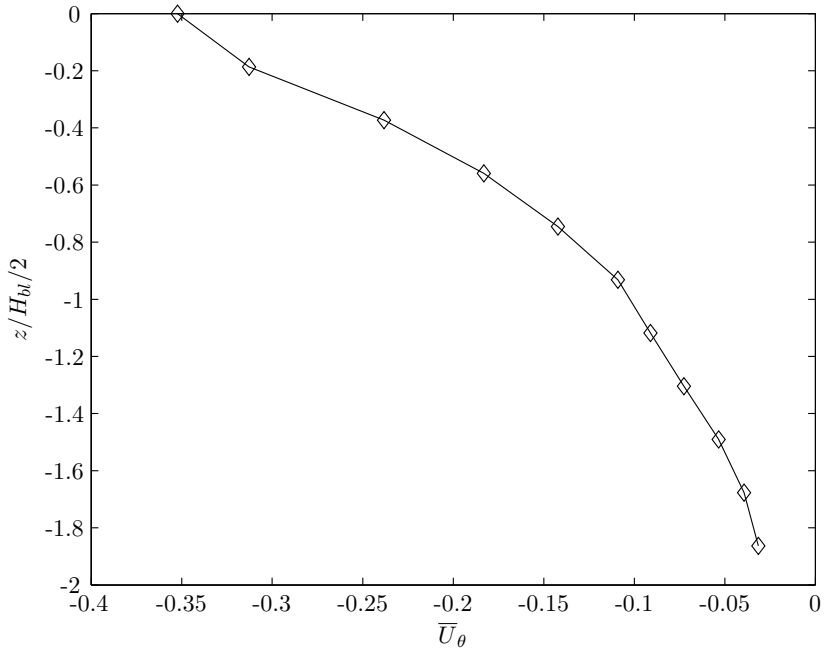

Figure 6.43: $\overline{U}_\theta/V_{tip}$ vs. $z/H_{bl}/2$ in $x-z$-plane at radial location $r/R = 1.5$ (approximate region containing the lower trailing-edge vortex).

vicinity of the vortices. Comparison with Figure 6.37, 6.39 and 6.40 indicates that within the vortex core region, generation of $\overline{k'}$ due to axial variations in the circumferential mean flow velocity is significant. This is in contrast to generation due to circumferential variations in axial mean flow $-\overline{u'_z u'_\theta}\frac{\partial \overline{U}_z}{\partial \theta}$ as shown in Figure 6.44 which is found to be weak (and negative) near the impeller trailing vortices and negligible at the disk-plane. Again, as in the case of generation due to the axial variation in circumferential mean flow, this is due to the fact

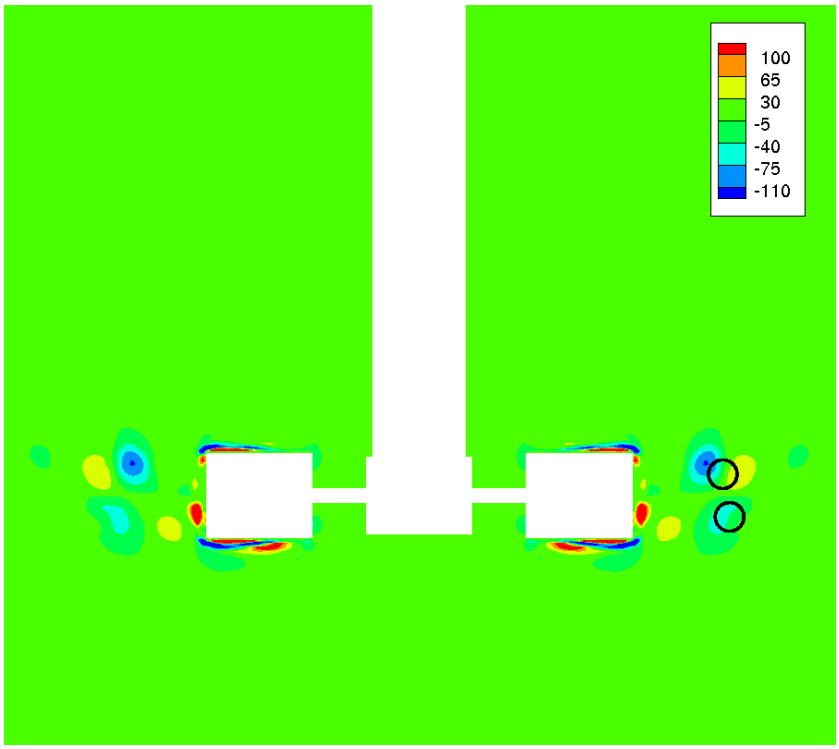

(a) $x-z$-plane at $y=0$

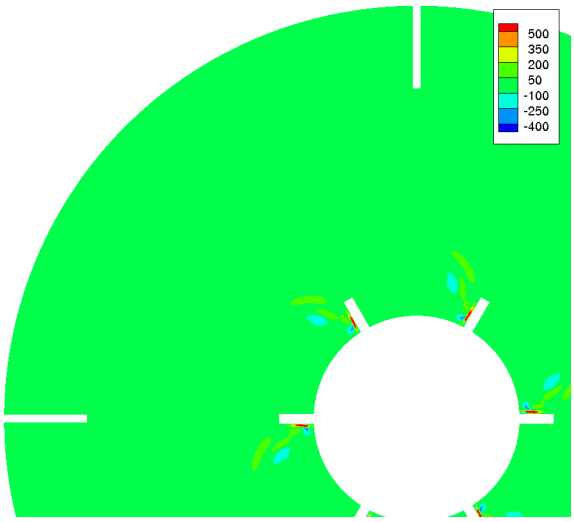

(b) Disk-plane ($z=0$)

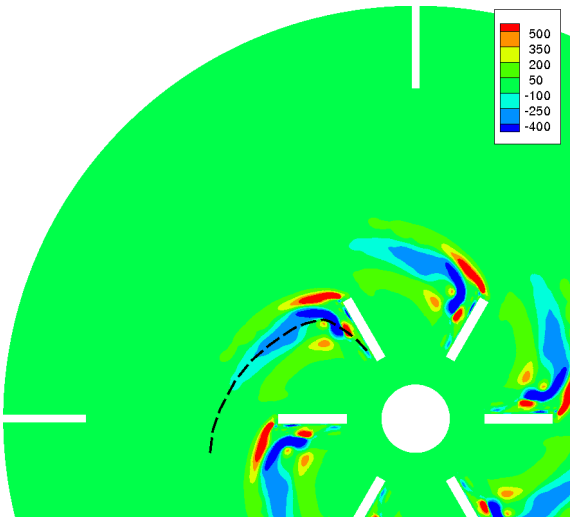

(c) In $x-y$-plane at $(z/(H_{BL}/2)=-0.5)$

Figure 6.44: Normalized $\overline{k'}$ generation term $-\overline{u'_z u'_\theta}\frac{\partial \overline{U}_z}{\partial \theta}$ contours. Blade rotation is clockwise for (b) and (c).

that the tangential Reynolds stress $\overline{u'_\theta u'_z}$ is maximized at the vortices, but vanishes at the disk-plane as shown in Figure 6.23. Comparison with the (relatively) significant generation of $\overline{k'}$ due to $-\overline{u'_\theta u'_z}\frac{\partial \overline{U}_\theta}{\partial z}$ (discussed previously) indicates that $\|\frac{\partial \overline{U}_\theta}{\partial z}\| > \|\frac{\partial \overline{U}_z}{\partial \theta}\|$. Note, that the previous inference is plausible given the gradual propagation (in the radial direction) of the

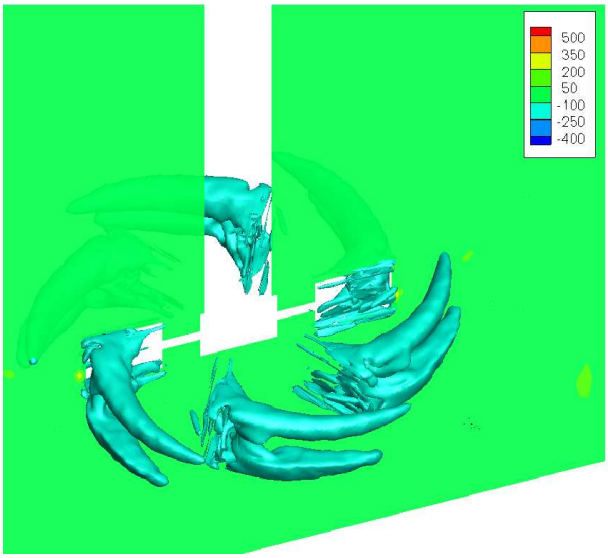

Figure 6.45: Normalized $\overline{k'}$ generation term $-\overline{u'_z u'_\theta}\frac{\partial \overline{U}_z}{\partial \theta} = -100$ iso-surface.

vortex away from the impeller. Hence, one can infer that mean flow property variations in the circumferential direction are small compared with axial variations (i.e. $\|\frac{\partial}{\partial z}\| > \|\frac{\partial}{\partial \theta}\|$). Finally, Figure 6.45 gives the $-\overline{u'_z u'_\theta}\frac{\partial \overline{U}_z}{\partial \theta} = -100$ iso-surface indicating a slight local reduction in overall $\overline{k'}$ generation due to the presence of the vortices.

Generation due to axial variations in radial mean flow velocity $-\overline{u'_r u'_z}\frac{\partial \overline{U}_r}{\partial z}$ has also been found to be significant as shown in Figure 6.46. Specifically, given the high tangential Reynolds stress $\overline{u'_r u'_z}$ in the region of the trailing vortex cores (as shown in Figure 6.22), generation is confined to the region near the trailing vortices and vanishes at the disk-plane. Figure 6.47 gives the $-\overline{u'_r u'_z}\frac{\partial \overline{U}_r}{\partial z} = 700$ iso-surface indicating generation within the cone-like structures due to the presence of the trailing vortices. High generation due to $\frac{\partial \overline{U}_r}{\partial z}$ is in contrast to negligible generation due to radial variations in axial mean flow velocity as shown in Figure 6.48. This implies that $\|\frac{\partial \overline{U}_r}{\partial z}\| > \|\frac{\partial \overline{U}_z}{\partial r}\|$ due (presumably) to the fact that the mean flow radial velocity is high at the disk-plane and decreases rapidly as one moves axially through the vortex core towards the bulk-flow region above the impeller jet.

Finally, Figure 6.49 gives generation due to radial variation of the mean circumferential velocity. To interpret the Figure it is important to first note that the Reynolds stress $\overline{u'_\theta u'_r}$ is negative in the vortex region as shown in Figure 6.21. In addition, given the increase in the mean circumferential velocity with increase in radius (i.e. $\overline{U}_\theta < 0$ near the impeller due to the clockwise rotation of the blades and tends to zero towards the outer wall resulting an increase in velocity (or a decrease in magnitude) with increasing radius), or $\partial \overline{U}_\theta / \partial r > 0$, approximately everywhere within the tank. Hence, this yields positive generation which is maximized near the region of maximum turbulence (and maximum $\|\overline{u'_\theta u'_r}\|$) at the disk-plane ($z = 0$) and the trailing vortices. This observation is re-enforced by inspection of the iso-surface given in Figure 6.50 which indicates a cone-like structure surrounding both trailing vortices and centered at the impeller disk-plane. This in contrast to generation due to circumferential variations in mean radial velocity which, as shown in Figure 6.51, is found to

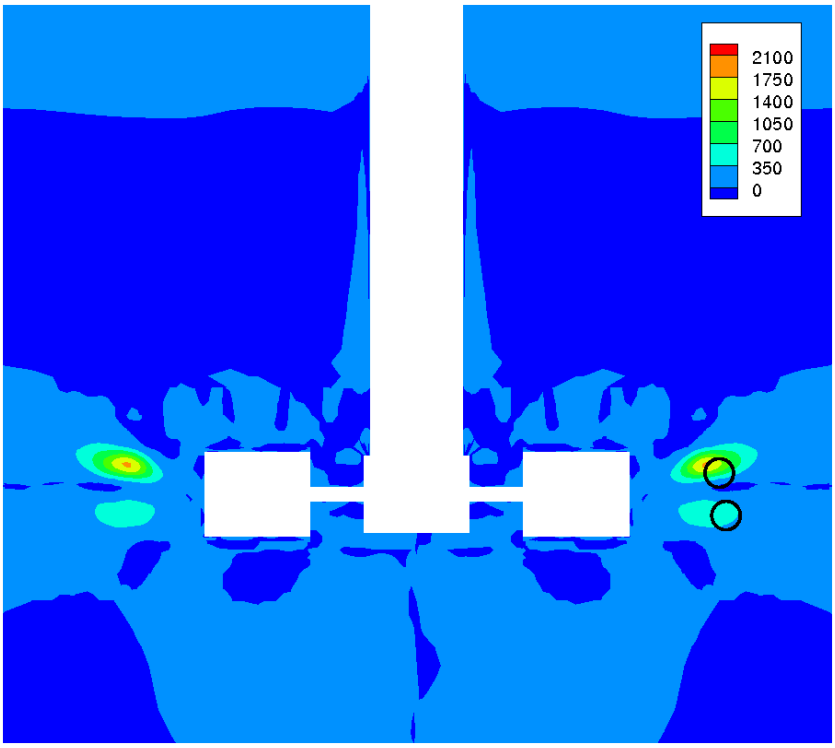

(a) $x-z$-plane at $y=0$

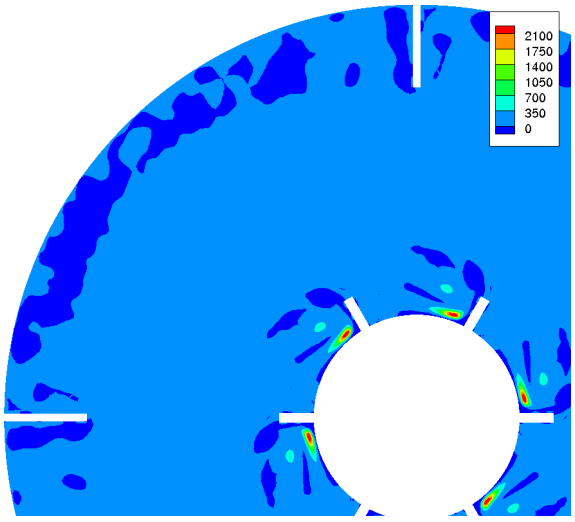

(b) Disk-plane ($z=0$)

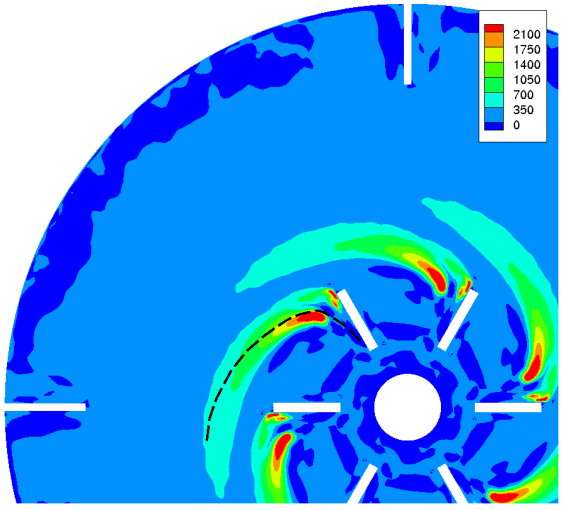

(c) In $x-y$-plane at $(z/(H_{BL}/2)=-0.5)$

Figure 6.46: Normalized $\overline{k'}$ generation term $-\overline{u'_r u'_z}\frac{\partial \overline{U}_r}{\partial z}$ contours. Blade rotation is clockwise for (b) and (c).

be negligible. This is due to the fact that, as for generation due to $\overline{u'_\theta u'_z}$ discussed previously, mean flow property variations in the circumferential direction are small compared with axial (and radial) variations (i.e. $\|\frac{\partial()}{\partial r}\| > \|\frac{\partial()}{\partial \theta}\|$ and since $\|\overline{U}_\theta\| \sim \|\overline{U}_r\|$ then $\|\frac{\partial \overline{U}_\theta}{\partial r}\| > \|\frac{\partial \overline{U}_r}{\partial \theta}\|$).

In conclusion, the primary contributors to turbulence generation in the impeller exit-

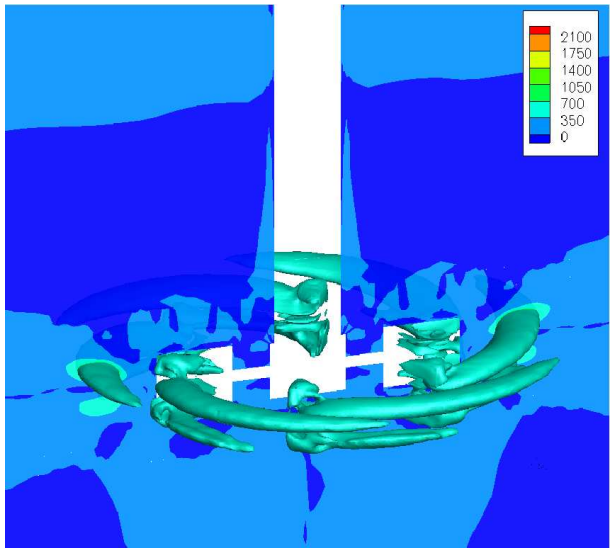

Figure 6.47: Normalized $\overline{k'}$ generation term $-\overline{u'_r u'_z}\frac{\partial \overline{U}_r}{\partial z} = 700$ iso-surface.

stream are the radial variation in radial mean flow velocity $-\overline{u'_r u'_r}\frac{\partial \overline{U}_r}{\partial r}$ (which contributes primarily to generation at the disk-plane as shown in Figure 6.37), the axial variation in circumferential mean flow velocity $-\overline{u'_\theta u'_z}\frac{\partial \overline{U}_\theta}{\partial z}$ and axial variation in radial mean flow velocity $-\overline{u'_r u'_z}\frac{\partial \overline{U}_r}{\partial z}$ (both of which contribute primarily to generation within the vortex core regions as shown in Figure 6.41, 6.42, 6.46 and 6.47).

6.10.5 Turbulent Viscous Work

The viscous work associated with the turbulent velocity fluctuations $\vec{u'}$ represents a local kinetic energy transfer via a viscous work inter-action often termed *viscous diffusion*. The cell averaged value for turbulent viscous net work, or viscous diffusion of $\overline{k'}$ is given by

$$\overbrace{\frac{\nu}{\Delta V}\int_{\Delta V}\vec{\nabla}\cdot\vec{\Psi}dV}^{Visc.\ Work/Diff.\ of\ \overline{k'}\ Via\ Turb.\ Motion} \tag{6.20}$$

where

$$\Psi_i = \sum_{j=1}^{3}\overline{u'_j\left(\frac{\partial u'_i}{\partial x_j}+\frac{\partial u'_j}{\partial x_i}\right)}$$

Under conditions of incompressibility (6.20) reduces to (see Hinze [11])

$$\frac{\nu}{\Delta V}\int_{\Delta V}\vec{\nabla}\cdot\vec{\nabla}\overline{k'}dV \tag{6.21}$$

resulting in a simple gradient transport mechanism for $\overline{k'}$. Hence, we expect regions of locally high average turbulent kinetic energy to yield an outflow of $\overline{k'}$ and visa versa. Thus, the term given by (6.20) represents a $\overline{k'}$ source with positive values at local $\overline{k'}$ minima and visa versa. With this in mind, Figure 6.52 (a) gives the normalized turbulent viscous net work for the

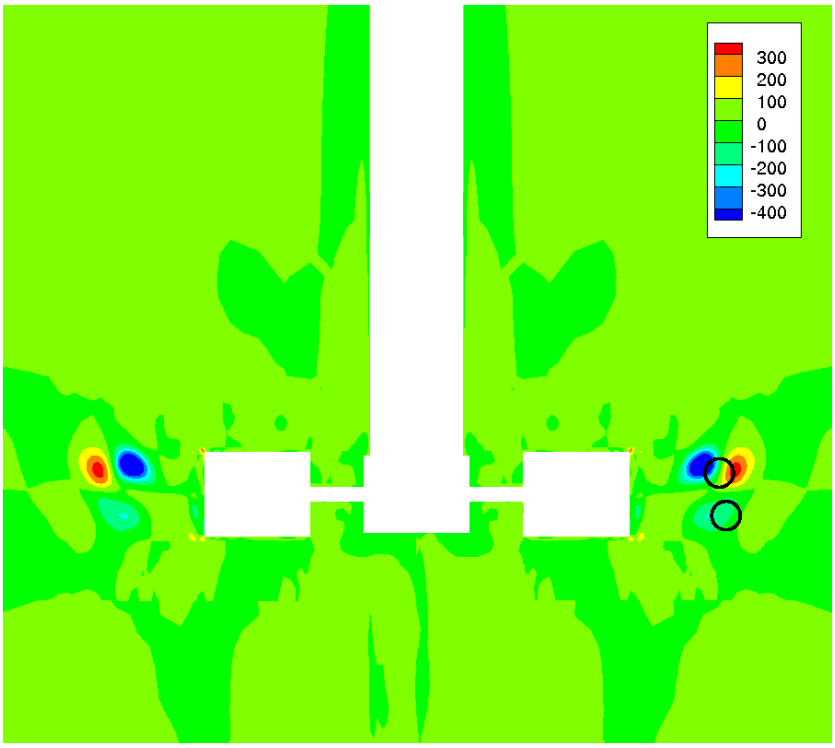

(a) $x-z$-plane at $y=0$

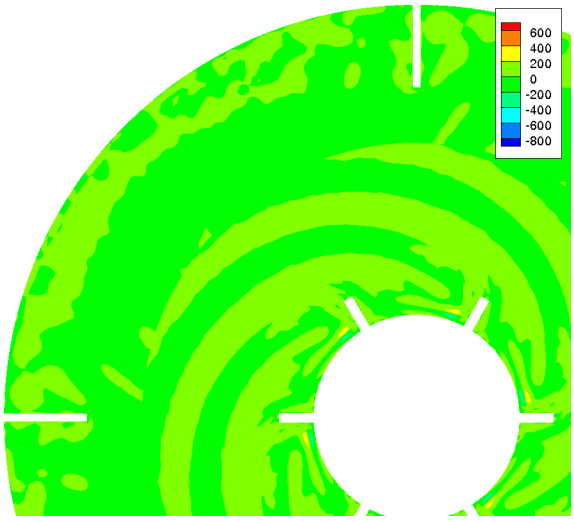

(b) Disk-plane ($z=0$)

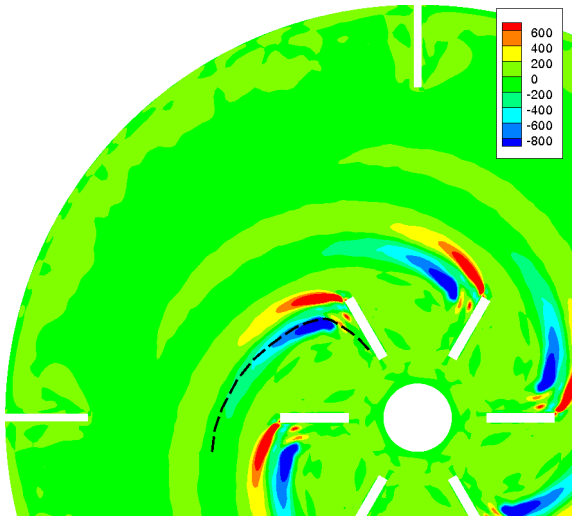

(c) In $x-y$-plane at $(z/(H_{BL}/2)=-0.5)$

Figure 6.48: Normalized $\overline{k'}$ generation term $-\overline{u'_z u'_r}\frac{\partial \overline{U}_z}{\partial r}$ contours. Blade rotation is clockwise for (b) and (c).

$x-z$-plane $y=0$ and approximate trailing vortex core locations.

Likewise, Figure 6.52 (b) and (c) gives the normalized turbulent viscous net work at the disk-plane $z=0$ and lower blade quarter-depth $z/(H_{BL}/2)=-0.5$ (again, the approximate planar location of trailing vortex core). Both Figures indicate peak $\overline{k'}$ outflow via net negative

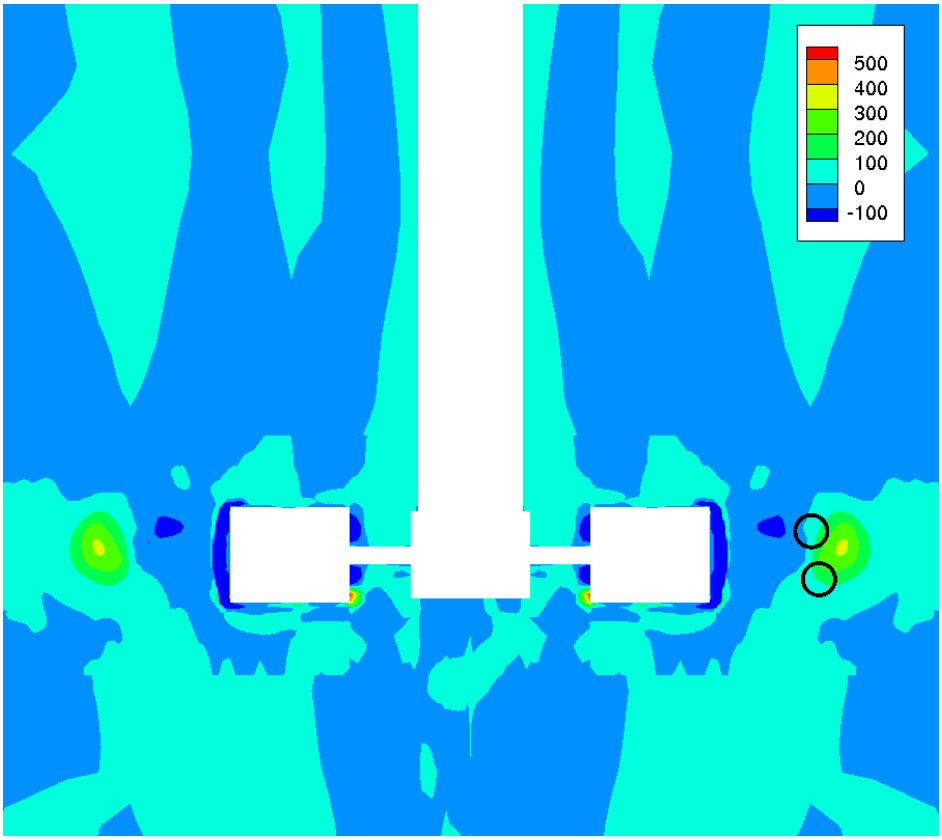

(a) $x-z$-plane at $y=0$

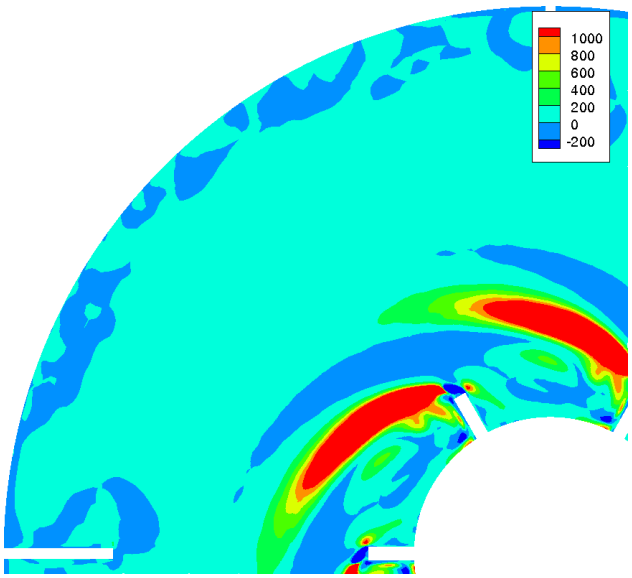

(b) Disk-plane ($z=0$)

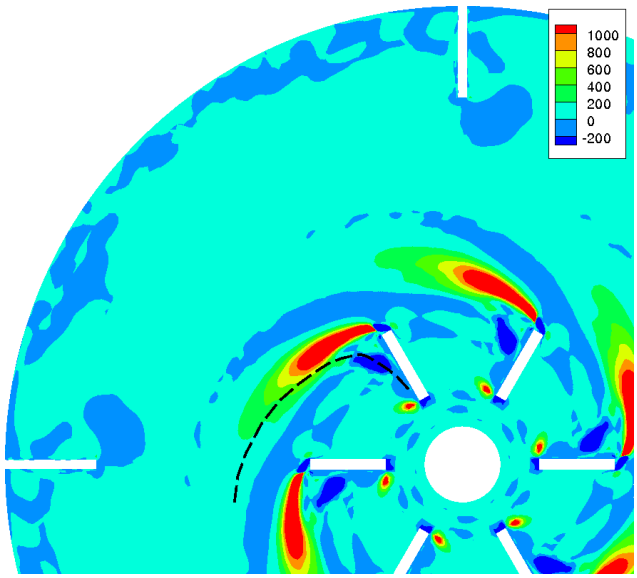

(c) In $x-y$-plane at $(z/(H_{BL}/2)=-0.5)$

Figure 6.49: Normalized $\overline{k'}$ generation term $-\overline{u'_\theta u'_r}\frac{\partial \overline{U}_\theta}{\partial r}$ contours. Blade rotation is clockwise for (b) and (c).

viscous work in the vicinity of regions of local peak $\overline{k'}$, associated with the trailing vortices, as well as at the disk-plane. This is due to the fact that regions of high local turbulence exhibit values for $\vec{\nabla} \cdot \nabla\vec{\overline{k'}} < 0$ and thus result in an outward transfer of $\overline{k'}$ via the (viscous) work inter-action. This can be seen via reference to the trailing vortex core path shown in Figure 6.52 (c) as well as the approximate core locations above and below the disk-plane shown in Figure 6.52 (a). Additional regions of high viscous net work are near the impeller surfaces associated with the high turbulence at the top and bottom impeller edge (see Figure 6.7). The result of this is a transfer of $\overline{k'}$ away from the impeller surface and into the free-steam.

Further insight into the viscous work inter-action can found by examination of the directional components of the local net work in the axial and radial directions. Specifically, Figure 6.53 (a) and (b) gives net radial ($\frac{\partial \Psi_r}{\partial r}$) and axial ($\frac{\partial \Psi_z}{\partial z}$) viscous perturbation flow work (where, for example, $\hat{r}$ is a unit-vector in the r-direction, and thus $\Psi_r = \vec{\Psi} \cdot \hat{r}$). In the case of net radial viscous work due to turbulent motion, we see that the viscous turbulent work results in an outward transfer of $\overline{k'}$ towards the impeller blade and outer tank wall for $r \approx R_{\overline{k'}_{max}}$ at the disk-plane as in indicated by the flux arrows. Hence, the region near the impeller corresponding to a radial location $r \approx R_{\overline{k'}_{max}} \gtrapprox R_{core}$, represents a region of high local turbulence and a local turbulence sink due to negative net viscous work. Net axial viscous work is shown in Figure 6.53 (b) and indicates large transfer of $\overline{k'}$ away from the trailing vortex region and towards the relatively low turbulence regions above and below the impeller jet. In addition to this, (as in the case of turbulent convective transfer), a region

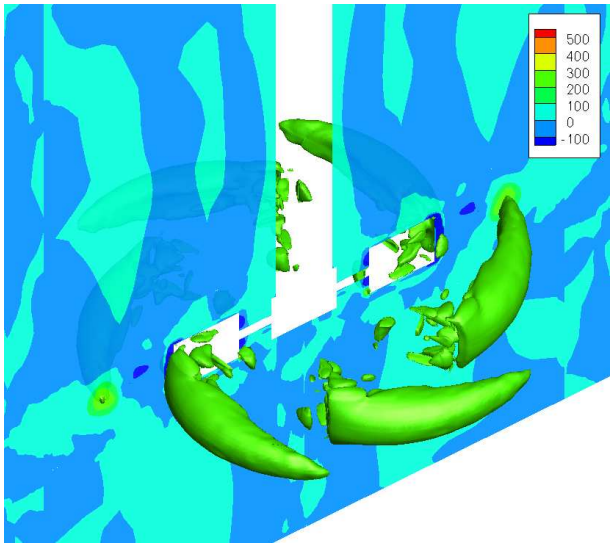

Figure 6.50: Normalized $\overline{k'}$ generation term $-\overline{u'_\theta u'_r}\frac{\partial \overline{U}_\theta}{\partial r} = 300$ iso-surface.

of relatively low local turbulent exists at the disk-plane $z = 0$ (see Figure 6.7) very near the impeller trailing edge, resulting in a small region of inward net viscous axial work/diffusion between and up-stream of the trailing vortices. Comparison with the results of Ducci indicate qualitative agreement between axial and radial net viscous work with the associated outward transfer of $\overline{k'}$ away from the vortex core region towards the free-stream.

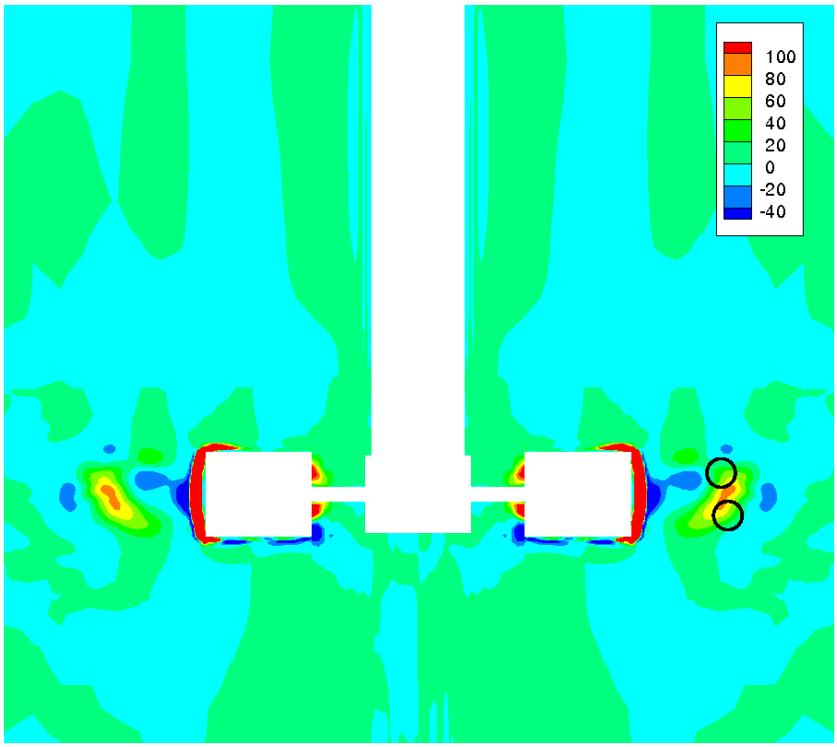

(a) $x-z$-plane at $y=0$

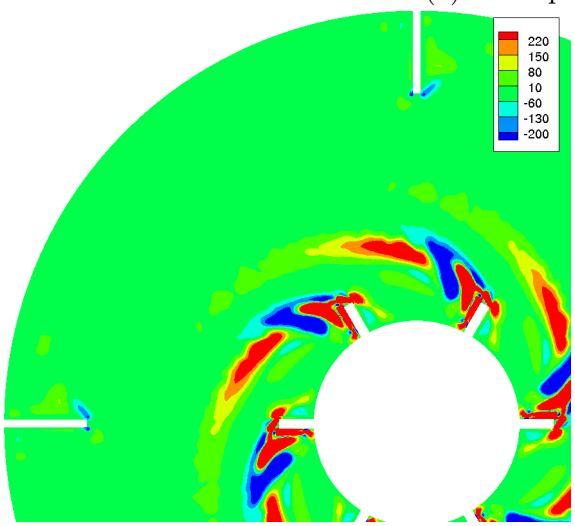

(b) Disk-plane ($z=0$)

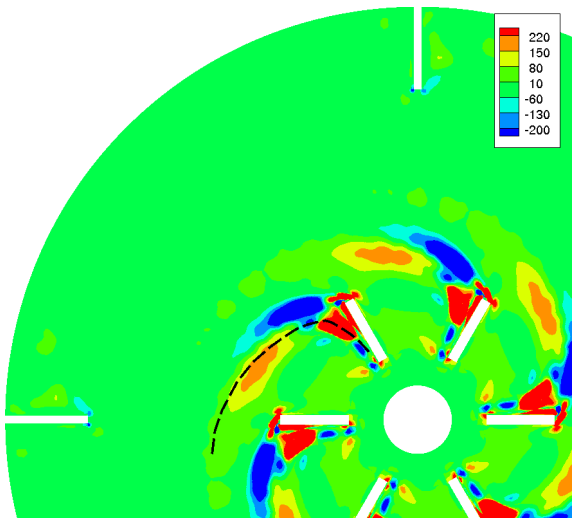

(c) In $x-y$-plane at $(z/(H_{BL}/2)=-0.5)$

Figure 6.51: Normalized $\overline{k'}$ generation term $-\overline{u'_r u'_\theta}\frac{\partial \overline{U}_r}{\partial \theta}$ contours. Blade rotation is clockwise for (b) and (c).

In addition, comparison of the normalized values calculated for the mean flow, turbulent and perturbation pressure work indicated that the net viscous work is approximately two orders of magnitude smaller than the remaining mechanisms of $\overline{k'}$ transport. With the exception of perturbation pressure-work (which was not measured), the measurements of Ducci also indicate a ratio of convection-to-viscous work transport of $\overline{k'}$ to be $\sim 10^2$.

6.10.6 TKE Transport: Assessment

All contributing components of turbulent generation were calculated indicating that the primary mechanisms responsible to turbulence generation were due to the mean flow gradients $\frac{\partial \overline{U}_r}{\partial r}$, $\frac{\partial \overline{U}_r}{\partial z}$ and $\frac{\partial \overline{U}_\theta}{\partial z}$. Specifically, generation due to radial variations in radial mean flow velocity contributed primarily to turbulence within the impeller stream at the approximate disk-plane location between the impeller trailing vortices. On the other hand, axial variations in circumferential and radial mean flow velocity contributed towards turbulence generation almost exclusively within the impeller trailing vortex core region above and below the disk-plane.

In terms of overall contribution, the most significant mechanism responsible for turbulent transport appeared to be, in approximate descending order, the turbulent convection/diffusion, followed by generation, mean flow convection, pressure work, dissipation (see Figure 6.10 and 6.11) and finally, viscous work/diffusion.

Finally, the transport equation given by (6.18) assumes negligible temporal variations in turbulent kinetic energy or $\frac{\partial \overline{k'}}{\partial t} \approx 0$. Assuming correct assessment of the previously discussed turbulent convection, work, generation and dissipation mechanism, the extent to which this assumption is satisfied can be gauged by examining the residual of the terms present previously. Figure 6.54 gives the transport terms sum or net $\overline{k'}$ source due to all transport mechanisms indicating residuals of approximate magnitude to that of the generation term. Given that the transport equation represents an exact conservation relationship for flow turbulence $\overline{k'}$, in the case of steady flow turbulence residuals should be minimal. A number of explanations present themselves such as the presence of perturbation flow unsteadiness within the impeller relative or baffle fixed control volumes. Possible sources of unsteadiness in cell centered turbulent kinetic energy $\overline{k'}$ include statistical sampling over a time period which exhibits globally evolving properties with time (i.e. non-fully developed flow). As indicated by the temporal evolution of the overall tank dissipation via the power number $\mathcal{P}$ in Figure 5.8, clearly the simulation has not achieved a steady-state. On the other hand, the $\overline{k'}$ transport sum does not appear to be biased towards a consistent under or over estimate of the (presumed) negligible temporal term. Another source of possible unsteadiness includes the periodic motion associated with the impeller motion relative to the baffle/tank frame. However, the contribution of the periodic motion to the overall motion within the moving/stationary mesh frame has already been shown in §5.5 to be negligible. An additional source of $\overline{k'}$ transport residuals is lack of convergence in the perturbation statistical quantities used in calculating the transport equation. Higher order perturbation products such as turbulent convection/diffusion (calculated based on a triple product $\vec{u'}(u'_k u'_k)$ (turbulent convection of local turbulent kinetic energy)) is especially susceptible to lack of statistical

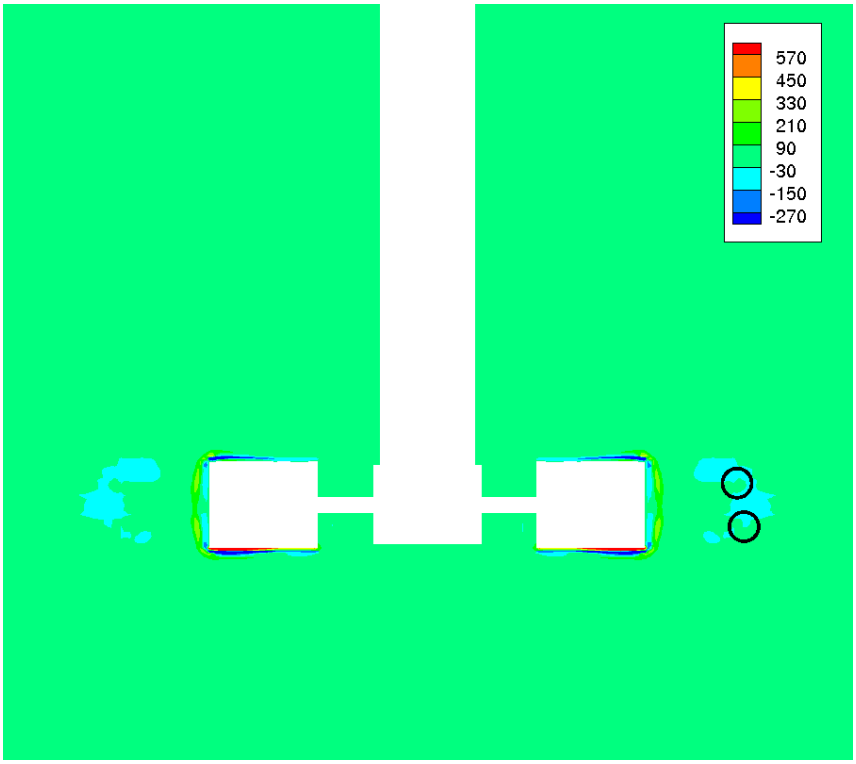

(a) $x-z$-plane at $y=0$

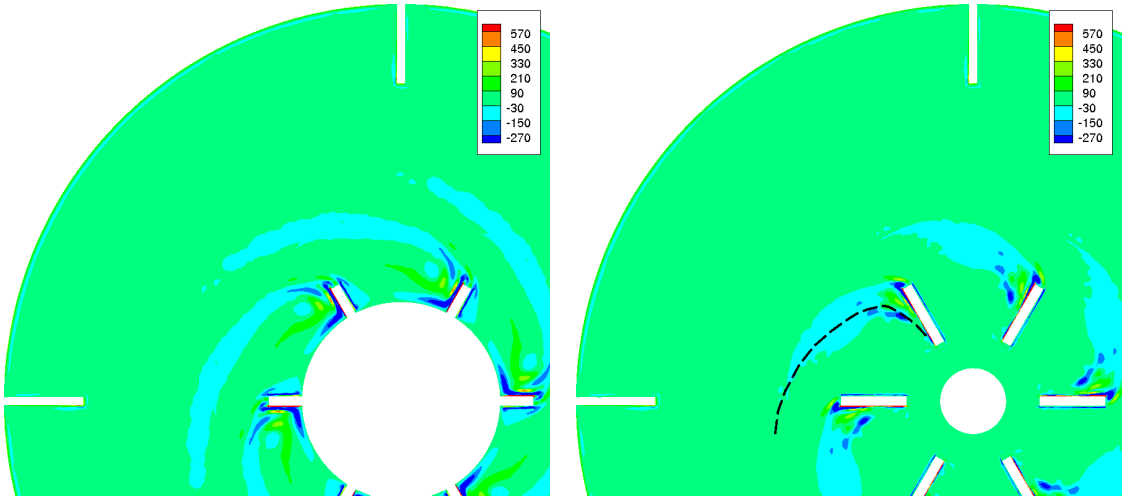

(b) Disk-plane ($z=0$) (c) In $x-y$-plane at $(z/(H_{BL}/2)=-0.5)$

Figure 6.52: Normalized turbulent viscous work/transport of $\overline{k'}$ (source) contours. Blade rotation is clockwise for (b) and (c).

convergence. In addition, the pressure work term, which is a product of a perturbation velocity and pressure is also susceptible to artificial variation in flow field statistics given that $P' \approx -\rho\sqrt{k'}[\sqrt{k}]$. Inspection of the contour plots of all contributing terms indicate that tur-

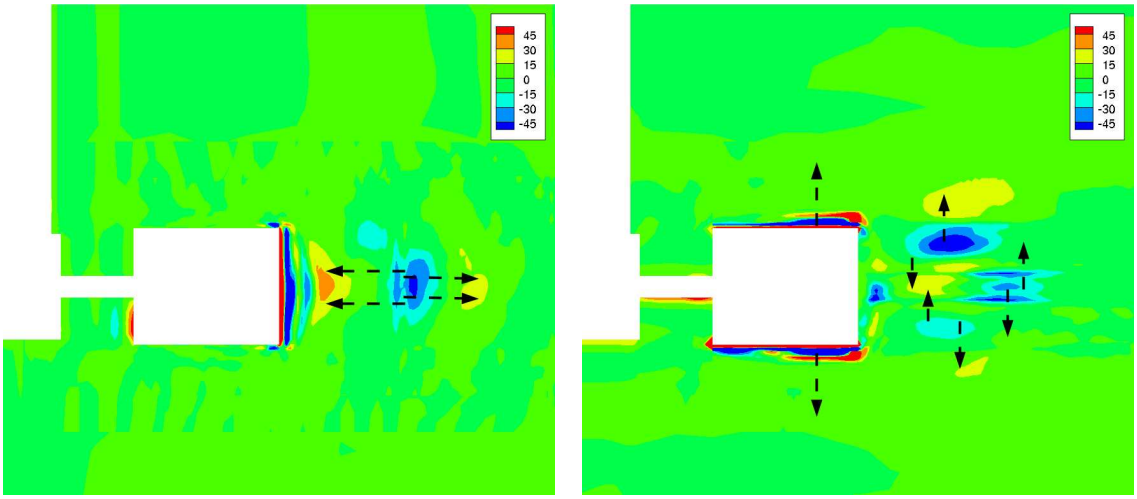

(a) $\nu \frac{\partial \Psi_r}{\partial r}$ (b) $\nu \frac{\partial \Psi_z}{\partial z}$

Figure 6.53: Normalized turbulent viscous work/transport of $\overline{k'}$ (a) radial and (b) axial net flux (source) in the $x-z$-plane ($y=0$).

bulent convection exhibits the largest scatter in local statistics, thus suggesting a deficiency in statistical convergence for this term.

Comparison with the direct simulations results of Spalta [20] for a turbulent boundary-layer flow indicate similar transport equation residuals to the present study. Specifically, Spalta directly calculated all terms of the transport equation, including pressure transport within a turbulent (steady mean flow) wall induced boundary-layer and found that within the viscous sub-layer (where all forms of property convection are negligible), the $\overline{k'}$ transport residual was negligible. However, within the log and outer region (boundary-layer outer edge) the transport residual was of the order of the mean flow convective transport term (approximately half of the magnitude of the turbulent convection term). Additional comparisons with the direct measurement of all but the pressure work transport terms by Ducci [6] indicate comparable residual deviations. Specifically, the residuals measured (less pressure work) were found to be on the order of the turbulent convection/diffusion in magnitude. Given that the present study, as well as the simulation results of Spalta [20], indicate that the contribution from the pressure work is significantly less important that turbulent convective transport, the exclusion of pressure work from the residual calculations of Ducci likely does not account for the bulk of the measure $\overline{k'}$ transport equation residual.

6.11 Implication for Mixing Strategies

The current study, while not simulating the transport of a non-reacting (passive) scalar in a direct manner, can be extended to include the assessment of species transport by implication. Specifically, the momentum and scalar transport mechanisms are identical excluding the effects of pressure (i.e. the pressure force and pressure work term in the momentum and

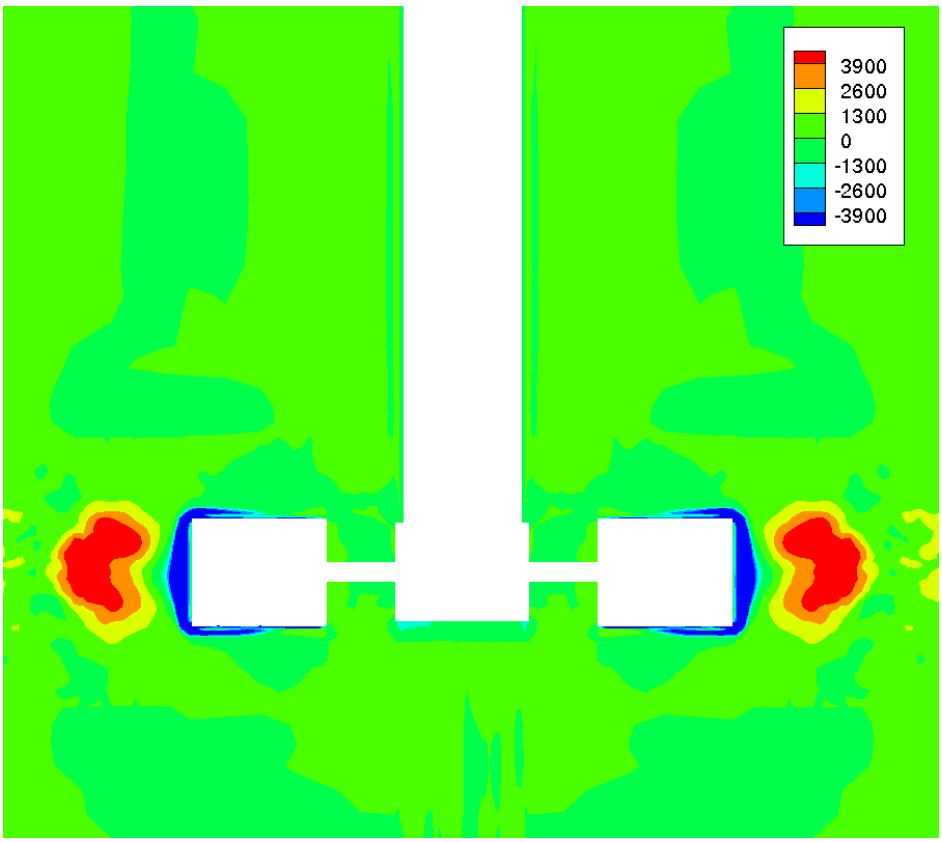

(a) $x-z$-plane at $y=0$

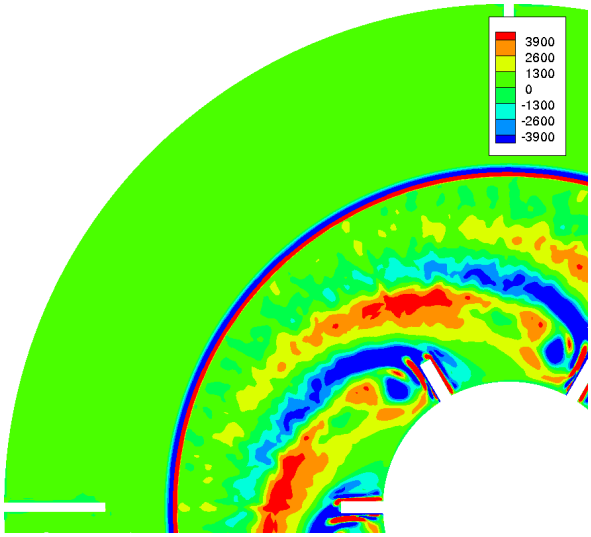

(b) Disk-plane ($z=0$)

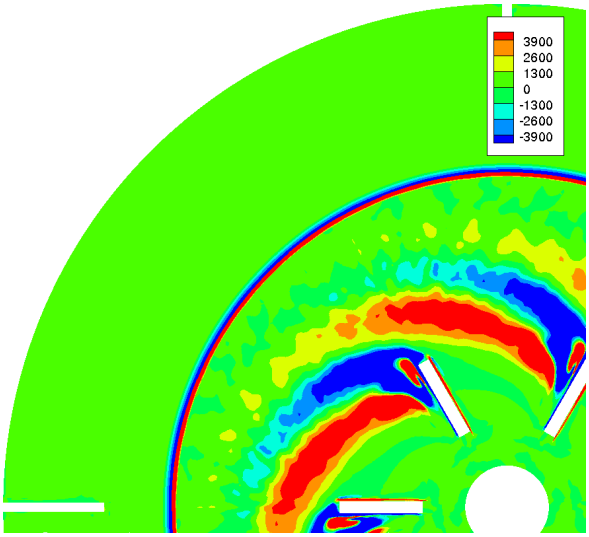

(c) In $x-y$-plane at $(z/(H_{BL}/2)=-0.5)$

Figure 6.54: $\overline{k'}$ normalized sum of terms contours. Blade rotation is clockwise for (b) and (c).

turbulent kinetic energy transport equations). Thus, at a minimum, far from regions of high spatial variation in pressure, (e.g. the very near-impeller region), momentum and scalar transport are physically equivalence so long as momentum and scalar transport (molecular) diffusivity ν and $\mathcal{D}$ are similar (i.e. $\mathcal{S}c \equiv \nu/\mathcal{D} \sim 1$). In addition, given that the pressure work responsible for momentum turbulent transport tends to be minimal and to *partially* counteract the influence of turbulent convective transport, (see assessment of $\overline{k'}$ transport terms given in §6.10.6), one can assume negligible pressure transport of turbulent kinetic energy in general throughout the tank. Making both these assumptions, results is an exact equivalence between average turbulent kinetic energy $\overline{k'}$ and scalar concentration perturbation squared $\overline{C'^2}$ transport as well as momentum and species transport.

Now, given the discussion in §2.2.1, property transport (neglecting pressure effects) is due to convective and molecular transport; the latter taking place over the length scales associated with molecular diffusion which is usually a much smaller scale than that of bulk-flow or convective transport. Hence, on the small scales, where fluid and species filaments are strained and then diffused on the smallest scales, diffusive transport is the most important transport mechanism. And given that turbulent transport augments molecular diffusion (for both momentum and species transport), the effective species diffusivity D_{eff} and, hence for a Schmidt number $\mathcal{S}c \equiv \nu/\mathcal{D} \sim 1$, the local effective viscosity is directly correlated with species transport on the small scales. Thus, at least with respect to mixing on the small scales, regions of high effective species diffusivity D_{eff} and mean species concentration gradients $\nabla\overline{C}$ are highly desirable in terms of enhanced diffusion and therefore species mixing on small scales (associated with *effective* diffusion). Hence, assuming $\nu_{eff} \sim D_{eff}$ and $\nabla\vec{\overline{U_i}} \sim \nabla\vec{\overline{C}}$, regions of high mean flow (momentum) property gradients and effective viscosity also represent regions of high species transport due to effective diffusion (turbulent and molecular) on the small scales.

Based on the above observation, it should be possible to formulate and assess general strategies regarding species injection locations within the tank for the purpose of maximizing the rate of mixing in general, and therefore minimizing mixing time τ_{mix} (see discussion of mixing times given in §2.8.1). Possible strategies include: injection of species into regions of high mean flow dissipation $\overline{\epsilon}$ vs. injection into regions of high turbulence $\overline{k'}$ vs. injection into regions of high $\overline{k'}$ followed by convection into a region of high turbulent dissipation $\overline{\epsilon'}$, etc.. Needless to say, injection of a passive scalar into a region of quiescent flow (e.g. extreme upper/lower tank region where convective transport is minimal), would result in extremely slow overall mixing. Hence convection is also important in minimizing the mixing time τ_{mix}.

From the previous discussion, we can characterize initial species injection locations which should be explicitly avoided, namely those regions in which convection *and* diffusion are minimal. These would include the regions of negligible (compared to the impeller jet region) mean flow velocity far above or below the impeller jet. In addition, these regions are largely devoid of turbulence and hence turbulent, and therefore, effective diffusion (species and momentum) will be minimal. Regions of high convection but minimal diffusion are also to be avoided given that mixing on the small scales would be negligible. Hence, the closed loop

recirculation zones within the bulk of the tank above and below the impeller, both of which represent regions of low mean flow and turbulent dissipation, (and thus mean flow and turbulent species diffusion on the small scales), are to be avoided (see Figure 5.30). In addition, injection of the passive scalars near the outer tank wall is to be avoided given that mean flow dissipation is negligible (again see Figure 5.30) *and* momentum (and therefore species) eddy diffusivity are minimal (see Figure 6.13).

A more interesting choice of injection location includes the region just below the impeller which exhibits the meandering instability (see discussion in §6.6). And although turbulent eddy-diffusivity (and therefore turbulent species eddy-diffusivity) is high in this region, mixing locally is likely to be minimal given negligible mean flow momentum (and presumably species) gradients. However, this is not to say that subsequent convection into the impeller region would not result in decreased mixing times compared with injection into the alternative regions mentioned above.

Remaining regions exhibiting neither negligible turbulent viscosity, mean flow dissipation or negligible convection include the inter-impeller region and impeller jet. In terms of exhibiting both high mean flow convection, mean flow dissipation (i.e. property gradients) as well as high turbulent viscosity (and therefore turbulent species diffusion), the region immediately down-stream of the impeller blade suction-side (i.e. the trailing vortex region) appears highly suitable. Specifically, Figure 6.9 indicates that the turbulent eddy-diffusivity achieves elevated values just down-stream of the impeller for $z/(H_{BL}/2) = -0.5$ with the highest turbulent viscosity being exhibited just down-stream of the blade suction-side (SS). This observation is particularly evident in Figure 6.9 (c). In addition, Figure 5.30 indicates exceptionally high mean flow dissipation (via the mean flow velocity and hence property gradients in general) in the impeller jet region and in particular, just down-stream of the impeller suction-side (SS). It should be noted that the locally high mean flow dissipation is attributable to the presence of the the highly strained mean flow field associated with the impeller (suction-side) trailing vortices. Thus, insofar as species and momentum transport are similar, species injection in the near-impeller region just down-stream of the blade suction-side (SS) would appear the most advantageous towards minimizing species mixing time τ_{mix} within the tank.

To this end, Zhou et al [25] performed CFD simulations of passive scalar transport in a Rushton stirred mixing tank under turbulent conditions ($Re = 50(10^3)$) using a two equation turbulence model ($k - \epsilon$) (with a constant turbulent Schmidt number). It was found that passive scalar injection near the top of the tank resulting in mixing times which exceeded that of injection near the blade (e.g. the the impeller exit stream) by over a factor of two. However, it should be noted that neither the momentum nor mixing solution was validated against experiments.

In addition, as previously discussed in §5.1, Ducci and Yianneskis found that axial vortices (macro-instabilities) associated with the meandering large-scale vortices terminating at the top and bottom of the tank, (identified in the present work and discussed in §6.6), are associated with enhanced mixing. They hypothesized that these axial macro-instabilities feed material into the impeller (and hence the trailing vortex) region, possibly resulting in a signif-

icant increase in mixer effectiveness (i.e. a reduction in mixing time τ_{mix}). Direct injection of a tracer into the axial vortex/macro-instability (with presumed subsequent convective transport into the near-impeller region) was found to result in a statistically significant reduction in mixing time τ_{mix} compared to surface injection without the presence of a vortex (see Ducci et al [7]).

6.12 Concluding Remarks

The detailed turbulent motion within a transitional Rushton turbine stirred vessel at $Re = 3000$ was investigated in detail as an extension of the previous mean flow results examined in the Chapter 5.

The instantaneous turbulent motion was extracted and examined. The resulting perturbation motion exhibited numerous unsteady swirling structures associated with turbulent eddies present in the impeller exit region, emanating from the impeller suction-side. The result is a turbulent wake associated with the trailing edge vortex with corresponding source at the impeller suction-side.

Averaged perturbation properties were calculated and geometric symmetry was utilized to increase the effective number of statistical samples. The resulting statistics included RMS perturbation velocities, Reynolds stress components, perturbation kinetic energy and dissipation. Specifically, average turbulent kinetic energy and dissipation are found to be maximized near the trailing vortex and at the disk-plane between the upper and lower vortices corresponding to the radial location just down-stream (radially outward) of the vortex cores. The Kolmogorov length and time scales were calculated directly from the definition based on turbulent dissipation and found to be minimized in the the impeller exit stream (jet) between trailing vortices at the disk-plane. Comparison with the data of Michelleti for RMS perturbation velocities, turbulent kinetic energy and dissipation were performed with good quantitative agreement with numerical results. In addition, comparison with calculated Kolmogorov length scales and the rescaled dissipation length scales of Ducci were also performed indicating good qualitative agreement.

Calculated Reynolds stress components indicates that the circumferentially averaged flow is approximately isotropic within the impeller stream with an elevation of radial and axial normal Reynolds stress of approximately 20% compared to the circumferential normal stress. These results also compared favorably with data of Michelleti.

The Fourier transform of the instantaneous flow kinetic energy was calculated at a location near the disk-plane maximum for $\overline{k'}$. The result was the expected $-5/3$-slope in the energy spectrum as a function of turbulent wave-number $\kappa\eta$ within the inertial range. In addition, exponential decay was exhibited within the dissipation range as well.

The statistical information provided was used to decompose the turbulent transport equation term-by-term. In the case of mean flow transport of $\overline{k'}$, radial convection is dominant resulting in the net negative convection of $\overline{k'}$ (out of a given volume) for radial locations $r \lessapprox R_{core}$ and net addition for radial locations $r \gtrapprox R_{core}$. The result is a net outward con-

vection of $\overline{k'}$ away from the impeller for location $r \lessapprox R_{core}$ due to the radial mean flow. Axial convection of $\overline{k'}$ due to the mean flow was also important with convection of turbulent kinetic energy towards the impeller disk-plane as a result of the convergence of the mean flow towards the disk-plane from the bulk-region.

Turbulent convection of $\overline{k'}$ was found to correspond to a gradient based diffusive mechanism with the resulting transfer of $\overline{k'}$ away from regions of high turbulence towards those of lower turbulence. The result of this is a net outflow of $\overline{k'}$ away from regions of locally high turbulence such as the impeller disk-plane (down-stream from the impeller). Specifically, the radial turbulent convection of $\overline{k'}$ was, in general, away from the local $\overline{k'}$ maximum at the impeller disk-plane at $r \approx R_{\overline{k'}_{max}} \gtrapprox R_{core}$, while axial convection was away from the disk-plane and local $\overline{k'}$ maximums corresponding to the trailing vortices, towards the free-stream above and below the impeller jet. In addition, it was found that turbulent transport of $\overline{k'}$ was primarily due to axial turbulent convection. These observations were compared with the phase and ensemble averaged measurements of Ducci and found to be in qualitative agreement.

Unlike standard experimental techniques, the present numerical methodology allowed for the calculation of turbulent pressure work directly from the perturbation pressure field. The perturbation pressure work was found to contribute significantly towards the conversion of static to dynamic perturbation pressure near the disk-plane at a position just down-stream from the radial location of the trailing edge vortices and near the location of maximum turbulent kinetic energy ($r \approx R_{\overline{k'}_{max}} \gtrapprox R_{core}$). The total pressure work was found to be primarily due to the net pressure work in the axial direction.

All contributing components of turbulent generation due to mean flow gradients were calculated. The primary mechanisms responsible for turbulence generation correspond to those associated with the mean flow gradients $\frac{\partial \overline{U}_r}{\partial r}$, $\frac{\partial \overline{U}_r}{\partial z}$ and $\frac{\partial \overline{U}_\theta}{\partial z}$. Specifically, generation due to the radial variation in the radial mean flow velocity contributed primarily to turbulence generation within the impeller stream at the approximate disk-plane location between the impeller trailing vortices. Axial variations in circumferential and radial mean flow velocity contributed towards turbulence generation almost exclusively within the impeller trailing vortex core regions above and below the disk-plane.

The viscous work was found to correspond to a gradient transport mechanism with associated $\overline{k'}$ sinks for regions of high $\overline{k'}$ and visa versa. Thus, as in the case of turbulent convection, turbulent kinetic energy was found to be removed from the region of high turbulence $\overline{k'}$ at the disk-plane for radial locations $r \approx R_{core}$ due to net viscous work in the radial direction. Additionally, net viscous work in the axial direction results in $\overline{k'}$ removal from the local region of maximum $\overline{k'}$ at the disk-plane for a radial local $r \gtrapprox R_{core}$ as well the trailing vortex core region away from the impeller jet towards the bulk-flow region. In general, of all contributors to $\overline{k'}$ transport, viscous work is the least important with transport due to viscous effects being approximately two orders of magnitude smaller the turbulent convection. The previous were compared with direct measurements of Ducci for high Reynolds number flow and found to be in qualitative agreement.

Implications for mixing strategies include an explicit avoidance of species injection into

tank regions where property convection *and* (effective) diffusion are minimal. This would include the regions of negligible (compared to the impeller jet region) mean flow velocity far above or below the impeller jet as well as within the closed loop recirculation zones above and below the impeller. In order to minimize mixing time, species injection in the near-impeller region just down-stream of the blade suction-side (SS) would appear the most advantageous. This is due to the presence of large mean-property gradients and effective diffusion associated with the presence of the impeller blade suction-side (SS) trailing vortices as well as high mean flow property convective transport associated with the presence of the high velocity impeller exit flow jet.

References

[1] R. Alcamo, G. Micale, F. Grisafi, A. Brucato, and M. Ciofalo. Large-eddy simulation of turbulent flow in an unbaffled stirred tank driven by a rushton turbine. *Chemical Engineering Science*, 2005.

[2] J. Rushton E. Costich and H. Everett. Power characteristics of mixing impellers: Part ii. *Chemical Engineering Progress:46*, pages 467–476, 1950.

[3] J. Derksen, H. Doelman, and H. Van den Akker. Three-dimension LDA measurements in the impeller region of a turbulently stirred tank. *Experiments in Fluids 27*, 1999.

[4] A. Ducci. *Direct measurement of the viscous dissipation rate of turbulent kinetic energy in a stirred vessel with two-point LDA*. PhD thesis, Department of Mechanical Engineering, King's College London, 2004.

[5] A. Ducci and M. Yianneskis. Direct determination of energy dissipation in stirred vessels with two-point LDA. *AIChe Journal 51*, pages 2133–2149, 2005.

[6] A. Ducci and M. Yianneskis. Turbulent kinetic energy transport processes in the impeller stream of a stirred vessel. *Chemical Engineering Science 61*, pages 2780–90, 2006.

[7] A. Ducci and M. Yianneskis. Vortex tracking and mixing enhancement in stirred processes. *AIChe Journal*, 2007.

[8] R. Escudie, D. Bouyer, and A. Line. Characterization of trailing vortices generated by a Rushton turbine. *AIChE 50*, 2004.

[9] A. Gunkel and M. Weber. Flow phenomena in stirred tanks part i: The impeller stream. *AIChE*, 1975.

[10] J. Hall. *Study of viscous and visco-elastic flows with reference to laminar stirred vessels*. PhD thesis, Department of Mechanical Engineering, King's College London, 2005.

[11] J. Hinze. *Turbulence*. Mc Graw-Hill, 1975.

[12] K. Lee and M. Yianneskis. Turbulence properties of the impeller stream of a Rushton turbine. *AIChE Journal 44*, pages 13–24, 1998.

[13] M. Micheletti. *Study of fluid velocity and mixing characteristics in stirred solid-liquid suspensions*. PhD thesis, Department of Mechanical Engineering, King's College London, 2004.

[14] M. Micheletti, S. Baldi, S. Yeoh, A. Ducci, G. Papadakis, K. Lee, and M. Yianneskis. On spatial and temporal variations and estimates of energy dissipation in stirred reactors. *Chemical Engineering Research and Design 82*, pages 1188–98, 2004.

[15] A. Mujumdar, B. Huang, D. Wold, M. Weer, and W. Douglas. Turbulence parameters in a stirred tank. *Canadian Journal of Chemical Engineering 48*, 1997.

[16] S. Pope. *Turbulent Flows*. Cambridge University Press, 2000.

[17] K. Van't Riet and J. Smith. Real and pseudo-turbulence in the discharge stream from a Rushton turbine. *Chemical Engineering Science*, 1976.

[18] M. Rogers and P. Moser. Direct simulation of a self-similar turbulent mixing layer. *Physics of Fluids*, 1994.

[19] M. Schafer, M. Hofken, and F. Durst. Detailed ldv measurements for visualization of the flow field within a stirred-tank reactor equipped with a Rushton turbine. *IChemE*, 1997.

[20] P. Spalta. Direct simulation of a turbulent boundary-layer up to $re_\theta = 1410$. *Journal of Fluid Mechanics*, 1988.

[21] C. Stoots and R. Calabrese. Mean velocity field relative to a Rushton turbine. *AIChE*, 1995.

[22] H. Wu and J. Patterson. Laser-doppler measurements of turbulent flow parameters in a stirred mixer. *Chemical Engineering Science 44*, pages 2207–, 1989.

[23] M. Yianneskis, Z. Popiolek, and J. Whitelaw. An experimental study of the steady and unsteady flow characteristics of stirred reactors. *Journal of Fluid Mechanics 175*, pages 537–555, 1987.

[24] M. Yianneskis and J. Whitelaw. On the structure of the trailing vortices around Rushton turbine blades. *Trans. IChemE*, 1993.

[25] G. Zhou, L. Shi, and P. Yu. CFD study of mixing process in Rushton turbine stirred tanks. *Third Inter. Conf. on CFD in the Minerals and Process Industries*, 2003.

Chapter 7

Conclusion

7.1 Present Contribution

The objective of this research is to provide a detailed, computationally based analysis of the flow within a Rushton turbine stirred tank.

Laminar Flow

Three different flow patterns have been identified in the literature for laminar mixing in a Rushton stirred vessel: Pumping, stalled and reverse flow. These flow patterns were verified using computational methods and a force decomposition was performed. The resulting decomposition allowed for identification of the dominant forces present within the vessel. Based on the comparison of forces, a corresponding pseudo-analytical solution for the flow was formulated.

Transitional Flow

In the case of transitional flow in a Rushton stirred tank ($Re = 3000$), the source of and physical mechanism responsible for the impeller induced macro-instabilities (i.e. blade trailing vortices) were identified. These vortices were located via the impeller frame mean flow pressure gradient and visualized in the appropriate vortex relative frame (based on a pressure minimum vortex center detection method). In addition, the pressure and viscous forces in the mean flow field were calculated and used to establish causal mechanisms responsible for the vortex formation in detail. As in the case of laminar flow, a comparison of impeller frame mean flow radial forces was made for the purpose of determining the relative strength of radial viscous, pressure and inertial forces near the impeller. The relevant statistics were collected enabling an examination of various turbulence quantities within the vessel. Specifically, an examination of the Reynolds stresses was performed and the extent to which turbulence is isotropic within the vessel was ascertained. An exact calculation of turbulent dissipation was conducted using all required spatial gradients followed by the calculation of the Kolomogorov length and time scales based on the fundamental definition. In addition, local turbulence intensity and turbulent viscosity were calculated and investigated. In order to elucidate the

physical mechanism governing the distribution of turbulence within the vessel, the turbulent kinetic energy transport equation terms were calculated directly from simulation data. These terms are composed of mean flow and turbulent flow convection, pressure work, viscous work, generation and, of course, dissipation. Finally, given the similarity of scalar and momentum transport processes, information gleaned from the investigation of the transport of turbulent kinetic energy was used to elucidate scalar transport processes.

7.2 Main Findings

Laminar Flow

In the case of low Re mixing, three Re were investigated computationally: $Re = 1$, 10 and 28. It was found that as the Re is reduced from 28 to 1, the net pumping capacity of the impeller is reduced. Specifically, for $Re = 28$ the familiar high/medium Re outward pumping action is present, but as the Re is reduced, flow stall is exhibited beginning very near the impeller trailing-edge on the blade suction-side. This stall results in a corresponding reduction of the impeller pumping capacity. For the lowest Re examined ($Re = 1$), pumping all but ceased due to flow reciprocation in the radial direction near the impeller. These numerical simulations results were successfully validated by experimental measurements (not performed in this work). To ascertain the physical mechanism responsible for this change in flow pattern, a force decomposition using the present computationally derived measurements established the progressive strengthening of the pressure and viscous terms compared to inertial forces with reduction in Re (i.e. $Re \rightarrow 1$). Thus, for the lowest Re the flow is characterized by a balance between pressure and viscous forces (in the radial direction), where changes in fluid momentum can be neglected (i.e. for a fluid particle in the the radial direction, $DV_r/Dt \rightarrow 0$. The resulting fluid equation of motion (in the radial direction) becomes linear in velocity with a source term representing the radial pressure force. This equation of motion is amenable to a separable solution for the radial velocity. The periodicity of the radial velocity and pressure force (based on impeller blade angle) was utilized and a sinusoidal pressure force (and radial velocity) variation with impeller angle was assumed. An approximate pressure force magnitude function $f(r)$ was calculated from the computational data (based on a best fit spline at the blade angle of maximum pressure force). Application of no-penetration boundary conditions at the outer tank wall and impeller disk along with an assumed parabolic profile for the axial variation in radial velocity near the impeller (justified by inspection of axial variation in computational radial velocity measurements at low Re) imposed closure on the equation of motion. A simplified analytical model of the radial flow was developed for phase averaged flow in the radial direction $V_r(r, \theta)$ which, depending on the choice of impeller radial flow jet width, is in very good agreement with simulation and experimental measurements: Thus confirming that the driving mechanism for mixing flow(s) at very low Re is a balance between pressure and viscous forces where variation in fluid momentum (i.e. particle following radial acceleration DV_r/Dt) is negligible.

Transitional Flow

A high resolution simulation of transitional flow for a Rushton stirred mixing vessel at a $Re = 3(10^3)$ was performed and mean flow properties were investigated and analyzed. The instantaneous flow solution exhibited flow structures indicative of turbulence over a range of scales as well as the presence of trailing vortices within the impeller stream.

The mean flow field indicates the presence of two, well defined, trailing vortices as well as the familiar dual looped bulk-flow recirculation zones above and below the impeller stream. Comparison with experimentally derived mean flow axial, radial and circumferential velocities indicated quantitative agreement between experimental and simulation results. The fundamental force interactions were also investigated. It was found that the mean flow, except very near the impeller and tank wall surfaces, is pressure driven with an associated balance between pressure and inertial forces. This is in contrast to the case of low and very low Re flows where the inter-action between pressure and viscous forces is dominant. From the calculated pressure force a pressure force convergence based vortex core tracking procedure was used to visualize the trajectory of the trailing vortex. This trajectory is in qualitative agreement with experimental measurements of the vortex core location relative to the blade. The concept of a vortex relative frame was then utilized to distinctly visualize the trailing vortices. The vortices were found to originate due to the movement of fluid from the blade pressure-side, over the blade tip and toward the disk via the blade suction-side (SS) under the influence of the pressure force resulting in flow separation on the blade suction-side.

The instantaneous turbulent motion was extracted and examined. The resulting perturbation motion exhibited numerous unsteady swirling structures associated with turbulent eddies present in the impeller exit region, emanating from the impeller suction-side resulting is a turbulent wake associated with the trailing edge vortices. Averaged perturbation properties were calculated including RMS perturbation velocities, Reynolds stress components, averaged perturbation kinetic energy and dissipation. Specifically, average turbulent kinetic energy and dissipation are found to be maximized near the trailing vortex with a peak value at the disk-plane between the upper and lower vortices corresponding to the approximate radial location just down-stream of the vortex cores. The Kolmogorov length and time scales were calculated directly from the definition based on simulation turbulent dissipation and found to be minimized in the the impeller exit stream between trailing vortices at the disk-plane. Comparison with the experimental data for RMS, turbulent kinetic energy and dissipation were performed with good quantitative agreement with simulation results. In addition, comparison with calculated Kolmogorov length scales and the rescaled (experimentally measured) dissipation length scales indicating good qualitative agreement. Calculated Reynolds stress components also indicate that the flow is approximately isotropic within the impeller stream with an elevation of circumferentially averaged radial and axial normal Reynolds stress of approximately 20% compared to the circumferential normal stress within the jet. These results also compared favorably with experimental data. An estimated $50 - 80\%$ of the turbulent dissipation was resolved compared to the physical system. In addition, sampling of the instantaneous flow field within a region of relatively high turbulence,

(along with the assumption of frozen turbulence), allowed for the calculation of the instantaneous flow kinetic energy spectrum. This spectrum exhibited a distinct energy, equilibrium and dissipation region.

The statistical information provided was used to decompose the turbulent transport equation term-by-term. In the case of mean flow transport of $\overline{k'}$, radial convection is dominant resulting in a net convection of $\overline{k'}$ away from the impeller for location $r \lessapprox R_{core}$. Axial convection of $\overline{k'}$ due to the mean flow was also important and resulted in the convection of turbulent kinetic energy towards the impeller disk-plane (due to the convergence of the mean flow towards the disk-plane from above and below the impeller). In addition, mean-flow transport in the radial direction resulted in convection of turbulence from locations radially inward of the vortex core location to locations radially outward (i.e. down-stream) from the cores. Turbulent convection of $\overline{k'}$ was found to correspond to a gradient based diffusive mechanism with the resulting transfer of $\overline{k'}$ away from regions of high turbulence. Specifically, the radial component of turbulent convection of $\overline{k'}$ was, in general, away from the local $\overline{k'}$ maximum at the impeller disk-plane at $r \approx R_{\overline{k'}_{max}} \gtrapprox R_{core}$ while axial convection was primarily away from the disk-plane and local $\overline{k'}$ maximums corresponding to the trailing vortices towards the free-stream (i.e. regions above and below the impeller exit flow jet). It was found that turbulent transport of $\overline{k'}$ is due primarily to axial convection. The pressure work was found to contribute significantly towards the conversion of static to dynamic perturbation pressure near the disk-plane at a position just down-stream from the radial location of the trailing edge vortices ($r \gtrapprox R_{core}$) due primarily to the net pressure work in the axial direction. The primary mechanisms responsible to turbulence generation are associated with the mean flow gradients $\frac{\partial \overline{U}_r}{\partial r}$, $\frac{\partial \overline{U}_r}{\partial z}$ and $\frac{\partial \overline{U}_\theta}{\partial z}$. Specifically, generation due to radial variations in mean radial flow velocity contributed primarily to turbulence generation within the impeller stream at the approximate disk-plane location between the impeller trailing vortices $r \approx R_{core}$. Finally, axial variations in circumferential and radial mean flow velocity contributed towards turbulence generation almost exclusively within the impeller trailing vortex core region above and below the disk-plane. The viscous work was found to correspond to a gradient transport mechanism with associated $\overline{k'}$ diffusion away from regions of high $\overline{k'}$ and visa versa. As in the case of turbulent convection, $\overline{k'}$ was found to be removed from the local maximum of $\overline{k'}$ at the disk-plane for radial locations $r \approx R_{\overline{k'}_{max}} \gtrapprox R_{core}$ due to net viscous work in the radial direction. Net viscous work in the axial direction results in $\overline{k'}$ removal from the local $\overline{k'}$ maximum at the disk-plane for a radial local $r \approx R_{core}$ as well the trailing vortex core region away from the impeller jet towards the bulk-flow region. In general, of all contributors to $\overline{k'}$ transport, viscous work is the least important with transport due to viscous effects being approximately two orders of magnitude smaller the turbulent convection. With the exception of turbulent pressure work, the previous observations were compared with phase resolved experimental data and found to be in qualitative agreement.

7.2.1 Implications For Mixing Strategies

A qualitative assesment of alternative mixing strategies based on the equivalence of species and momentum transport was performed. This resulted in the following general conclusion: Species deposition or injection points to be avoided reside in tank regions of negligible (compared to the impeller jet region) mean-flow (property) convection, dissipation and effective diffusivity. These regions include tank zones far above or below the impeller jet as well as the closed-loop recirculation zones above and below the impeller.

In contrast, if mixing time is to be minimized, species injection in the near-impeller region just down-stream of the blade suction-side (SS) appeared to be the most advantageous. This conclusion is justified by noting that it is this region of the tank which exhibits the highest mean-property gradients and effective diffusion, both of which are associated with the presence of the impeller blade suction-side (SS) trailing vortices. In addition, the near impeller exit jet region also exhibits significant mean-flow (property) convective transport due to the presence of the high velocity impeller exit flow jet.

These results and subsequent recommendations were found to be consistent with observations from the limited number of studies comparing species deposition at various locations within the vessel which specifically show an minimization of mixing time for species injection or deposition within the impeller exit jet region. However, the previous recommendations made in this work explicitly emphasize the blade trailing edge region as a particularly suitable species deposition location if the goal is the minimization of species mixing time.

7.3 Future Work

The present study used an approximate scalar analysis to determine the requisite cell volume distribution based on a target resolution of, at most, 80% of the turbulent dissipation. Given the nature of the scalar analysis, the resulting estimated cell size distribution is expected to be, at best, accurate to within an order of magnitude. Actual resolution of turbulent dissipation was estimated to be in the range of $60-80\%$. One likely source of deficiency in the estimated resolution is a non-attainment of fully developed flow within the tank (as indicated by the upward trend in integrated power consumption even after 100 revolutions. Thus, future work might involve a more exhaustive study with a much longer total simulation time well in excess of 100 revolutions along with higher spacial and temporal resolution. In addition, a higher order upwinded spatial scheme and a Crank-Nicholson time integration scheme (which conserves flow kinetic energy) could be utilized given sufficiently small time-steps. Also, as indicated by an analysis of the instantaneous energy spectrum, presumed numerically induced noise is significant for length scales $\ell \lesssim \eta$. Implementation of the previous, higher order schemes, along with a reduction in simulation the (residual) tolerance should reduce the noise floor, thus increasing solution accuracy within the dissipation region. Needless to say, all these modifications to the simulation will result in significantly longer simulation times and more extensive use of computing resources.

Further investigation of the source of the apparent large residual in the sum of terms

within the TKE transport equation should also be undertaken. These large residuals do not appear to be confined to the present study, but are found in the case of direct measurements of turbulence in a (physical) mixing vessels as well as simple channel flows.

In addition to the previous, application of the suggested mixing strategies, as outlined in §6.11, should be investigated either experimentally or computationally using a scalar transport model, which assuming a Schmidt number $\mathcal{S}c$ of unity is practicable for the Re investigated in the present study.

Finally, note that although we have dealt with Newtonian fluids at very low Re, the current work can be extended to non-Newtonian fluids as well. In terms of application to industrial processes, mixing of non-Newtonian is highly applicable in the case of paints, petrochemicals, pharmaceuticals and foodstuffs. Hence, investigation of laminar non-Newtonian flows should be undertaken in an effort to predict and understand the onset of localized flow stall and the corresponding breakdown in pumping. In addition, in the case of turbulent flow of non-Newtonian fluids evaluation of the associated turbulent transport processes would yield useful information regarding turbulent and hence, species transport mechanism.

Appendix A

Nomenclature

Symbol	Description
A_P	Present Cell Coefficient
a_f	Neighboring Cell Coefficient
β_{ij}	Turbulence Isotropy Parameter
C	Concentration
C'	Concentration Pertubation
D	Impeller Diameter
Δt	Time-Step
Δx	Computational Cell Displacement
δ	Boundary-Layer Thickness
$\hat{E}()$	Energy Spectra
η	Komogorov Length-Scale
ϵ	Instantenous Dissipation
ϵ'	Perturbation-Flow Instantaneous Dissipation
$\overline{\epsilon'}$	Perturbation-Flow Averaged Dissipation
$\overline{\epsilon}$	Mean-Flow Dissipation
$\vec{F}$	Generic Force
f_r	Radial Velocity Magnitude Function
$\mathcal{F}$	Dimensionless Flow/Flow Number
h	Generic Blade Height
H_{BL}	Impeller Blade Height
κ	Wave Number
k	Instantenous Kinetic Energy
k'	Perturbation-Flow Instantaneous Kinetic Energy
$\overline{k'}$	Perturbation-Flow Averaged Kinetic Energy
$\overline{k}$	Mean-Flow Kinetic Energy
λ	Taylor Length-Scale

Symbol	Description
ℓ	Generic Turbulenc Length-Scale
$\mathcal{L}$	Generic Large-Scale Length-Scale
L_B	Baffle Length
L_{BL}	Impeller Blade Length
μ	Absolute Viscosity
ν	Kinematic Viscosity
N	RPS
$N(r)$	Pressure Force Function
ω	(Impeller) Angular Velocity
$\mathcal{P}$	Dimensionless Dissipation/Power Number
P	Pressure
$\overline{P}$	Mean-Flow Pressure
P'	Perturbation Pressure
PS	Pressure-side
$\overline{P'}$	Averaged Perturbation Pressure
ϕ	Blade/Phase Angle/Generic Intensive Property
Φ	Generic Extensive Property
${}^{i}_{\phi}q''$	Flux of Property ϕ in Direction i
$\dot{Q}$ or Q	Volume Flow Rate
R	Impeller Radius
R_{core}	Trailing Vortex Core Radial Location
R_{sl}	Simulation Sliding Mesh Radius
Re	Reynolds Number
r	Radial Location
ρ	Density
SS	Suction-Side
S_P	Present Cell Source
$\tilde{t}_{mix}$	Dimensionless Mixing Time
t_{mix}	Mixing Time
t_D	Impeller Disk Thickness
t_{BL}	Impeller Blade Thickness
t_B	Tank Baffle Thickness
τ_η	Komogorov Time-Scale
τ_0	Integral Time-Scale
τ_{wall}	Wall Shear Stress
τ_{ij}	Shear Stress Component
T	Tank Diameter

Symbol	Description
θ	Observation Plane/Circumferential Locaiton/Implicit-Explicit Blending Factor
u	Generic Turbulent/Small Scale Velocity
$\vec{u}'$	Perturbation Velocity
$\vec{U}$	Instantaneous Velocity
$\overline{\vec{U}}$ or $\overline{\vec{V}}$	Mean-Flow Velocity
$\tilde{\vec{u}}$	Periodic-Flow Velocity
U^*	Friction Velocity
U^+	
U^∞	Free-stream Velocity
V, U	Generic Velocity
y^+	Normalized Wall Distance
z	Axial Location

Appendix B

Solution to Systems of Equations

We seek the solution to the system as given in (3.76). Or in matrix notation

$$[\mathbf{A}]\vec{\mathbf{\Phi}} = \mathbf{S}\vec{\mathbf{U}} \tag{B.1}$$

Methods for obtaining the solution vector $\vec{\mathbf{\Phi}}$ will be discussed in the following sections and can be generally classified into two broad methods:

- Direct solvers; E.g. Gaussian Elimination, Lower-Upper (LU) decomposition, Lower-Diagonal-Upper decomposition, Block-Tri-Diagonal solvers
- Iterative solvers; Simple iterative schemes (SOR, Gauss-Seidel) , Generalized Newton's method (Newton-Rapson), Incomplete decomposition, Conjugate Gradient solvers.

B.1 Solution to the System:Direct Methods

B.1.1 Row Reduction

The simplest direct method available for the solution to the system given in (B.1), is that of row reduction or Gaussian-Elimination. Specifically, through a series of elementary matrix row operations the system of equations can be reduced to the following equivalent form:

$$\begin{bmatrix} \hat{A_{1,1}} & \hat{A_{1,2}} & \vdots & \vdots & \vdots & \vdots & \vdots & \hat{A_{1,NC}} \\ 0 & \hat{A_{2,2}} & \ddots & \ddots & \vdots & \vdots & \vdots & \vdots \\ \vdots & 0 & \ddots & \ddots & \ddots & \vdots & \vdots & \vdots \\ \vdots & \ddots & 0 & \ddots & \ddots & \ddots & \vdots & \vdots \\ \vdots & \vdots & \ddots & 0 & \ddots & \ddots & \ddots & \vdots \\ \vdots & \vdots & \vdots & \ddots & 0 & \ddots & \ddots & \vdots \\ \vdots & \vdots & \vdots & \vdots & \ddots & 0 & \ddots & \hat{A_{NC-1,NC}} \\ 0 & \vdots & \vdots & \vdots & \vdots & \vdots & 0 & \hat{A_{NC,NC}} \end{bmatrix} \begin{bmatrix} \mathbf{\Phi}_1 \\ \mathbf{\Phi}_2 \\ \vdots \\ \vdots \\ \vdots \\ \vdots \\ \mathbf{\Phi}_{NC-1} \\ \mathbf{\Phi}_{NC} \end{bmatrix} = \begin{bmatrix} {}^*\hat{\mathbf{S}}\mathbf{U}_1 \\ {}^*\hat{\mathbf{S}}\mathbf{U}_2 \\ \vdots \\ \vdots \\ \vdots \\ \vdots \\ {}^*\hat{\mathbf{S}}\mathbf{U}_{NC-1} \\ {}^*\hat{\mathbf{S}}\mathbf{U}_{NC} \end{bmatrix} \tag{B.2}$$

where $[\hat{\mathbf{A}}]$ is an upper triangular matrix (or $[\mathbf{U}]$). The individual components of the solution vector $\mathbf{\Phi}_i$ can now be solved by backward substitution (i.e. from $i = NC \rightarrow 1$). Specifically,

$$\mathbf{\Phi}_i = \frac{\mathbf{S}\hat{\mathbf{U}}_i - \sum_{j=i+1}^{1} \hat{A_{i,j}} \mathbf{\Phi}_j}{\hat{A_{i,i}}}, \quad i = NC \rightarrow 1 \tag{B.3}$$

Unfortunately, this method is restricted to system of limited size given the operational intensity of the algorithm used to generate the upper matrix $[\mathbf{U}] = [\hat{\mathbf{A}}]$.

B.1.2 Lower-Upper Decomposition

A variation on the row reduction technique can be affected by noting that it is possible to decompose a matrix into the product of an upper $[\mathbf{U}]$ and lower $[\mathbf{L}]$ matrix. Thus, the system given by (B.1) becomes

$$[\mathbf{A}] \equiv [\mathbf{L}][\mathbf{U}] \Longrightarrow [\mathbf{L}][\mathbf{U}]\vec{\mathbf{\Phi}} = \mathbf{S}\vec{\mathbf{U}} \tag{B.4}$$

where, if we define $[\mathbf{U}]\vec{\mathbf{\Phi}} = \vec{\mathbf{Y}}$, then the following intermediate system can be solve by forward substitution

$$[\mathbf{L}]\vec{\mathbf{Y}} = \mathbf{S}\vec{\mathbf{U}}, \quad \mathbf{Y}_i = \frac{\mathbf{S}\mathbf{U}_i - \sum_{j=i+1}^{1} L_{i,j}\mathbf{Y}_j}{L_{i,i}}, \quad i = 1 \rightarrow NC \tag{B.5}$$

The remaining system can be solved by backward substitution as in the case of Gaussian-Elimination, i.e.

$$[\mathbf{U}]\vec{\mathbf{\Phi}} = \vec{\mathbf{Y}}, \quad \mathbf{\Phi}_i = \frac{\mathbf{Y}_i - \sum_{j=i+1}^{1} U_{i,j}\mathbf{\Phi}_j}{U_{i,i}}, \quad i = NC \rightarrow 1 \tag{B.6}$$

Techniques such as Crout's Method can be utilized to find $[\mathbf{L}]$ and $[\mathbf{U}]$. Unfortunately, it can be shown that such a decomposition is non-unique.[1] Thus, further constraints must be placed on the decomposition. One such set of constraints is referred to as the Cholesky decomposition whereby one specifies $[\mathbf{U}] = [\mathbf{L}]^T$. Such a decomposition is unique and can provide as a basis for an automated solution technique to a system of equations. Specifically, a technique similar to the Cholesky decomposition will be used within a *global iterative solver* as discussed in §B.3. Again, as in the case of Gaussian elimination, this method is restricted to systems of limited size given the operational intensity of the algorithm.

B.2 Local Iterative Solution Methods

We begin with a description of the most elementary iterative methods by introducing the following notation: The converged or true solution $\vec{\mathbf{\Phi}}_c$ to a system of equations $[\mathbf{A}]\vec{\mathbf{\Phi}} = \mathbf{S}\vec{\mathbf{U}}$ may be solved for iteratively by some iteration process such that in the limit $m \rightarrow \infty$, then

[1] Specifically, Crout's method involves the solving on N^2 equations as a function of N^2 unknowns and N parameters to be chosen.

$\vec{\mathbf{\Phi}}^{m+1}$, $\vec{\mathbf{\Phi}}^{m} \rightarrow \vec{\mathbf{\Phi}}_c$. A large class of solution algorithms for the calculation of $\vec{\mathbf{\Phi}}^{m+1}$ can be expressed as

$$[\mathbf{Z}]\vec{\mathbf{\Phi}}^{m+1} = [\mathbf{Y}]\vec{\mathbf{\Phi}}^{m} + \vec{\mathbf{B}} \tag{B.7}$$

or

$$\vec{\mathbf{\Phi}}^{m+1} = [\mathbf{Z}]^{-1}[\mathbf{Y}]\vec{\mathbf{\Phi}}^{m} + [\mathbf{Z}]^{-1}\vec{\mathbf{B}} \tag{B.8}$$

A successful application of an iterative technique would ensure that the above system (B.7) is 'easily' solved and that the intermediate solution $\vec{\mathbf{\Phi}}^{m+1}$ rapidly converges to the solution $\vec{\mathbf{\Phi}}_c$. To explore several applications of (B.7) four common iterative solution algorithms will be introduced: The Jacobian, Gauss-Seidel, SOR and Newton-Raphson technique. It should be noted that these four solvers are local/Newton like solvers which seek to minimize the solution error on an equation-by-equation basis. This is in contrast to global solver which specifies some 'global residual' functional or solution error and instead seeks to minimize this functional. Indeed the present work utilizes a global solver, but the operation and advantages of this choice will be illustrated by way of an introduction to local solvers in the following section.

B.2.1 Jacobi Method

Recalling the system of equations to be solved, $[\mathbf{A}]\vec{\mathbf{\Phi}} = \mathbf{S}\vec{\mathbf{U}}$, we can rewrite this system via (B.7) as

$$\mathbf{\Phi}_i^{m+1} = (-\sum_{k=1}^{i-1} A_{i,k}\mathbf{\Phi}_i^{m} - \sum_{k=i+1}^{NC} A_{i,k}\mathbf{\Phi}_i^{m} + \mathbf{SU}_i)/A_{i,i} \tag{B.9}$$

Thus, an initial solution $\mathbf{\Phi}^0$ is guessed and the solution is repeatedly updated via (B.9).

B.2.2 Gauss-Seidel Method

From the Jacobi iterative method as given in (B.9) we note that new values of each vector component of $\vec{\mathbf{\Phi}}$ are generated starting at $i = 1$. Thus, for $i = 2$ an updated value for the first component of $\vec{\mathbf{\Phi}}$ (i.e. $\mathbf{\Phi}_1$) would now be available. For solving the third component $\mathbf{\Phi}_3$, updated values of $\mathbf{\Phi}_{i=1,2}$ would be available, etc. Thus, the Jacobian iterative method can be improved using updated values of $\mathbf{\Phi}$ (where available). The result is a slight modification of (B.9) giving

$$\mathbf{\Phi}_i^{m+1} = (-\sum_{k=1}^{i-1} A_{i,k}\mathbf{\Phi}_i^{m+1} - \sum_{k=i+1}^{NC} A_{i,k}\mathbf{\Phi}_i^{m} + \mathbf{SU}_i)/A_{i,i} \tag{B.10}$$

B.2.3 SOR Method

The two previously described solution methods may, under certain conditions, converge to the solution too slowly for use as a *practical* solution algorithm. There are two remedies to this problem: First, a successive *over-relaxation* technique may be used to increase the solution update and hence convergence. Secondly, the system of equations may be *preconditioned* to achieve characteristics which are conducive to faster convergence. The latter will be discussed in §B.3.1 (in the context of the Conjugate Gradient (global) solver), while the former can be introduced via the following: Let $\overline{\mathbf{\Phi}}_i^{m+1}$ be the i-th solution vector component update at iteration $m+1$ according to the Gauss-Seidel method (B.10). However, instead of simply using the updated the solution $\overline{\mathbf{\Phi}}_i^{m+1}$, we instead update via $\mathbf{\Phi}_i^{m+1} = \mathbf{\Phi}_i^m + \omega(\overline{\mathbf{\Phi}}_i^{m+1} - \mathbf{\Phi}_i^m)$ or re-arranging and substituting into (B.10) we get the **S**uccessive **O**ver-**R**elaxation expression for the solution update

$$\begin{aligned} \mathbf{\Phi}_i^{m+1} &= (1-\omega)\mathbf{\Phi}_i^m + \omega\overline{\mathbf{\Phi}}_i^{m+1} = \\ \omega((-\sum_{k=1}^{i-1} A_{i,k}\mathbf{\Phi}_i^{m+1} - \sum_{k=i+1}^{NC} A_{i,k}\mathbf{\Phi}_i^m + \mathbf{SU}_i)/A_{i,i}) &+ (1-\omega)\mathbf{\Phi}_i^m \end{aligned} \tag{B.11}$$

Note that the optimum value for the over-relaxation factor ω is not known *apriori*: A significant disadvantage of this method.

B.2.4 Newton-Raphson

Newton's method for solving single variable equations is well known and described in any elementary Calculus text. However, the technique can also be extended to systems of multivariable equations including our system $[\mathbf{A}]\vec{\mathbf{\Phi}} = \mathbf{S}\vec{\mathbf{U}}$. Specifically, the linear system to be solved can be re-written via

$$\begin{aligned} [\mathbf{A}]\vec{\mathbf{\Phi}} - \mathbf{S}\vec{\mathbf{U}} &= 0 \\ \Downarrow & \\ \mathbf{F}(\vec{\mathbf{\Phi}}) &= 0 \\ \Downarrow & \\ F_1(\vec{\mathbf{\Phi}}) &= 0 \\ F_2(\vec{\mathbf{\Phi}}) &= 0 \\ \vdots & \\ F_{NC}(\vec{\mathbf{\Phi}}) &= 0 \end{aligned} \tag{B.12}$$

where $F()$ is a generalized function or *functional* of the vector $\vec{\mathbf{\Phi}}$. Expanding the i-th functional component near the solution $\vec{\mathbf{\Phi}}_c$ and introducing the *solution error* vector $\vec{\epsilon}$ we have

$$F_i(\vec{\mathbf{\Phi}})\big|_{\vec{\mathbf{\Phi}}^m} = F_i(\vec{\mathbf{\Phi}})\big|_{\vec{\mathbf{\Phi}}_c} + \nabla(\vec{F}_i)\big|_{\vec{\mathbf{\Phi}}^m} \cdot \vec{\epsilon}$$
$$\vec{\epsilon} \equiv -\vec{\mathbf{\Phi}}_c + \vec{\mathbf{\Phi}}^m \Longrightarrow \vec{\mathbf{\Phi}}^{m+1} \approx \vec{\mathbf{\Phi}}_m - \vec{\epsilon} \tag{B.13}$$

where we have assumed that $\vec{\mathbf{\Phi}}_c \approx \vec{\mathbf{\Phi}}^{m+1}$ or at least a better estimate than $\vec{\mathbf{\Phi}}^m$. In matrix form the above can be written as

$$[\mathbf{G}]^m \vec{\epsilon}^m = \vec{\mathbf{F}}^m - \vec{\mathbf{F}}^c = \vec{\mathbf{F}}^m$$
$$\vec{\mathbf{\Phi}}^{m+1} = \vec{\mathbf{\Phi}}^m - \vec{\epsilon}^m$$

$$[\mathbf{G}] \equiv \begin{bmatrix} \frac{\partial F_1}{\partial \mathbf{\Phi}_1} & \frac{\partial F_1}{\partial \mathbf{\Phi}_2} & \cdots & \cdots & \frac{\partial F_1}{\partial \mathbf{\Phi}_{NC}} \\ \frac{\partial F_2}{\partial \mathbf{\Phi}_1} & \frac{\partial F_2}{\partial \mathbf{\Phi}_2} & \cdots & \cdots & \frac{\partial F_2}{\partial \mathbf{\Phi}_{NC}} \\ \vdots & \ddots & \ddots & \ddots & \vdots \\ \vdots & \ddots & \ddots & \ddots & \vdots \\ \frac{\partial F_{NC}}{\partial \mathbf{\Phi}_1} & \frac{\partial F_{NC}}{\partial \mathbf{\Phi}_2} & \cdots & \cdots & \frac{\partial F_{NC}}{\partial \mathbf{\Phi}_{NC}} \end{bmatrix} \tag{B.14}$$

where $[\mathbf{G}]$ is known as the Gaussian of $\mathbf{F}()$. In terms of numerical implementation, the calculation of all partial derivatives can be approximated by explicit finite differences carried out at iteration m, whereupon the Gaussian $[\mathbf{G}]^m$ can be inverted to yield the search vector $\vec{\epsilon}^m$.

Finally, it should be noted that the Newton-Rapson method requires an initial *guess* $\vec{\mathbf{\Phi}}^0$ for a solution $\vec{\mathbf{\Phi}}^m$. However, the method can fail if the initial guess is near a local (as opposed to a global) minimum of $F()$. Thus, the Newton-Rapson method is suitable only for monotonic functionals, or if $\mathbf{F}()$ is not monotonic, the initial guess $\vec{\mathbf{\Phi}}^0$ must be *very near* the correct solution $\vec{\mathbf{\Phi}}_c$. It should also be pointed out that inversion of $[\mathbf{G}]$ may be prohibitively costly for large NC.

B.2.5 Incomplete Decomposition/Factorization

As stated in §B.1.2, if a lower/upper **LU** decomposition is known, a solution to the system can be easily calculated. However, given the computational expense of calculating, for example $[\mathbf{L}]$ in the Cholesky decomposition, an alternative, less computationally intensive decomposition may be used. Specifically, if $[\mathbf{A}]$ is a sparse matrix, then one could calculate the elements of $[\mathbf{L}]$ and $[\mathbf{U}] = [\mathbf{L}]^T$ only for those locations i, j such that $A_{i,j} \neq 0$. The result is a decomposition $[\overline{\mathbf{L}}][\overline{\mathbf{L}}]^T$ which is similar to $[\mathbf{A}]$. This development can be utilized in an iterative solver via the following: Let $[\mathbf{A}] = [\overline{\mathbf{L}}][\overline{\mathbf{L}}]^T - [\mathbf{N}]$ where the over-lined quantities refer to the incomplete Cholesky decomposition (hence the matrix $[\mathbf{N}]$ represents a decomposition error matrix (which is easily calculated)). The system to be solved thus becomes

$$[\mathbf{A}]\vec{\mathbf{\Phi}} = \mathbf{S}\vec{\mathbf{U}} \Longrightarrow [\overline{\mathbf{L}}][\overline{\mathbf{L}}]^T\vec{\mathbf{\Phi}} = -[N]\vec{\mathbf{\Phi}} + \mathbf{S}\vec{\mathbf{U}} \tag{B.15}$$

Note, (B.15) is of the form of (B.7) if the RHS is a function of the m^{th} iteration solution or $\vec{\mathbf{\Phi}}^m$ while the LHS is a function of the $m+1$ solution vector (i.e. $\vec{\mathbf{\Phi}}^{m+1}$) and thus admits an iterative solution procedure. If $[\overline{\mathbf{L}}]^T\vec{\mathbf{\Phi}} = [b]$ and $[\overline{\mathbf{L}}]\vec{b} = \vec{a}$ then (B.15) is equivalent to

$$\vec{a}^{m+1} = -[\mathbf{N}]\vec{\mathbf{\Psi}}^m + \mathbf{S}\vec{\mathbf{U}} \tag{B.16}$$

Thus, $\vec{b}$ and $\vec{\mathbf{\Phi}}$ are easily found via forward and reverse substitution, resulting in a simple algorithm which can be employed for iteratively solving the system within some residual tolerance. Many iterative solvers work upon the previous development, so for purpose of illustration, such an algorithm could be as follows:

Algorithm 2

Set initial solution vector $\vec{\mathbf{\Phi}}^0$
Loop
Calculate $\vec{a}^{m+1} \equiv -[\mathbf{N}]\vec{\mathbf{\Phi}}^m + \mathbf{S}\vec{\mathbf{U}}$
Solve system by forward substitution $= \vec{b}^{m+1} = [\overline{\mathbf{L}}]^{-1}\vec{a}^{m+1}$
Solve system by backward substitution $\vec{\mathbf{\Phi}}^{m+1} = [\overline{\mathbf{L}}]^{T^{-1}}\vec{b}^{m+1}$
Check for convergence to within some residual tolerance $[\mathbf{A}]\vec{\mathbf{\Phi}}^{m+1} - \mathbf{S}\vec{\mathbf{U}} < \epsilon$
Repeat

B.3 A Global Iterative Method

B.3.1 Conjugate Gradient Solver

Approaching the solution to the system from a (global) minimization standpoint one can apply a variational technique for finding the solution $\vec{\mathbf{\Phi}}$. Specifically, the functional

$$L(\vec{\mathbf{\Phi}}^*) = \frac{\vec{\mathbf{\Phi}}^* \cdot ([\mathbf{A}]\vec{\mathbf{\Phi}}^*)}{2} - \vec{\mathbf{\Phi}}^* \cdot \mathbf{S}\vec{\mathbf{U}} \tag{B.17}$$

is minimized as $\vec{\mathbf{\Phi}}^* \rightarrow \vec{\mathbf{\Phi}}_c$. Now, given that one desires $\vec{\mathbf{\Phi}}_c$ we can utilize the above via the following: Let $\vec{\mathbf{\Phi}}^0$ be an initial guess for the solution $\vec{\mathbf{\Phi}}$. In addition, let $\vec{\mathbf{\Pi}}$ be a *search vector*, and α be a *scaling factor* as yet unspecified. Thus, one can express an updated solution $\vec{\mathbf{\Phi}}^1 = \vec{\mathbf{\Phi}}^0 + \alpha^1\vec{\mathbf{\Pi}}^0$. Hence we proceed to determine the scaling factor α^1 which minimizes (B.17) for a given search vector and initial solution guess via

$$\frac{\partial}{\partial\alpha^1}L(\vec{\mathbf{\Phi}}^0 + \alpha^1\vec{\mathbf{\Pi}}^0) =$$
$$\frac{\partial}{\partial\alpha^1}\left(\frac{\vec{\mathbf{\Phi}}^0 \cdot ([\mathbf{A}]\vec{\mathbf{\Phi}}^0) + 2\vec{\mathbf{\Pi}}^0 \cdot \alpha^1([\mathbf{A}]\vec{\mathbf{\Phi}}^0) + (\alpha^1)^2(\vec{\mathbf{\Pi}}^0 \cdot ([\mathbf{A}]\vec{\mathbf{\Pi}}^0)}{2} - (\alpha^1\vec{\mathbf{\Pi}}^0 + \vec{\mathbf{\Phi}}^0) \cdot \mathbf{S}\vec{\mathbf{U}}\right) \tag{B.18}$$

Or, if $[\mathbf{A}]$ is symmetric, positive definite and a residual vector is defined as $\vec{\mathbf{R}}^m \equiv [\mathbf{A}]\vec{\mathbf{\Phi}}^m - \mathbf{S}\vec{\mathbf{U}}$ then

$$\frac{\partial}{\partial\alpha^1}L(\vec{\mathbf{\Phi}}^0 + \alpha^1\vec{\mathbf{\Pi}}^0) = (-\vec{\mathbf{\Pi}}^0 \cdot (\vec{\mathbf{R}}^0) + \alpha^1\vec{\mathbf{\Pi}}^0 \cdot ([\mathbf{A}]\vec{\mathbf{\Pi}}^0)) = 0 \Longrightarrow \alpha^1 = \frac{\vec{\mathbf{\Pi}}^0 \cdot (\vec{\mathbf{R}}^0)}{\vec{\mathbf{\Pi}}^0 \cdot ([\mathbf{A}]\vec{\mathbf{\Pi}}^0)} \tag{B.19}$$

Thus, the update from the initial guess is given by

$$\vec{\mathbf{\Phi}}^1 = \vec{\mathbf{\Phi}}^0 + \alpha^1 \vec{\mathbf{\Pi}}^0 = \vec{\mathbf{\Phi}}^0 + \frac{\vec{\mathbf{\Pi}}^0 \cdot (\vec{\mathbf{R}}^0)}{\vec{\mathbf{\Pi}}^0 \cdot ([\mathbf{A}]\vec{\mathbf{\Pi}}^0)} \vec{\mathbf{\Pi}}^0 \tag{B.20}$$

With the intermediate solution now known, the above procedure could be repeated until convergence. In other words, we have the general expression for the $m+1$ iteration updated solution

$$\vec{\mathbf{\Phi}}^{m+1} = \vec{\mathbf{\Phi}}^m + \alpha^{m+1} \vec{\mathbf{\Pi}}^m = \vec{\mathbf{\Phi}}^m + \frac{\vec{\mathbf{\Pi}}^m \cdot (\vec{\mathbf{R}}^m)}{\vec{\mathbf{\Pi}}^m \cdot ([\mathbf{A}]\vec{\mathbf{\Pi}}^m)} \vec{\mathbf{\Pi}}^m \tag{B.21}$$

Choice of Search Direction $\vec{\mathbf{\Pi}}^2$

The previous procedure produces a scaling factor α as a function of a search vector $\vec{\mathbf{\Pi}}$. Thus, a process must be formulated for choosing $\vec{\mathbf{\Pi}}$ which maximizes the convergence rate. Several possible strategies are open to us: The Method of Steepest Descent where $\vec{\mathbf{\Pi}}^m = -\nabla L(\vec{\mathbf{\Phi}}^m) = -[\mathbf{A}]\vec{\mathbf{\Phi}}^m + \mathbf{S}\vec{\mathbf{U}} = -\vec{\mathbf{R}}^m$. This method, however, suffers from spurious oscillatory behavior and can be slow to converge. Specifically, in the case of finding a solution to a set of *stiff* equations (i.e. rapidly varying residual $\vec{\mathbf{R}}$ with respect to independent variable $\vec{\mathbf{\Phi}}$), such a choice in search direction will result in repeating search directions and thus an oscillatory convergence path. To redress this deficiency one might establish the following search criterion:

- Mimic Greatest Descent Method: $\vec{\mathbf{\Pi}} \sim -\vec{\mathbf{R}}$
- Eliminate spurious oscillation via the constraint (or an equivalent): $\vec{\mathbf{\Pi}}^i \perp \vec{\mathbf{\Pi}}^j$, or $\vec{\mathbf{\Pi}}^i \cdot \vec{\mathbf{\Pi}}^j = 0$ for $i \neq j$

To this end one could envision a procedure whereby a steepest descent search direction is calculated for the $m+1$ step and then the search direction from the previous step m is subtracted off. To make this rigorous, we define the following expression for the $m+1$ search vector in terms of a scaling factor β

$$\vec{\mathbf{\Pi}}^{m+1} = \vec{\mathbf{R}}^m + \beta^{m+1} \vec{\mathbf{\Pi}}^m \tag{B.22}$$

and apply an *equivalent* orthogonality condition $\vec{\mathbf{\Pi}}^{m+1} \cdot [\mathbf{A}]\vec{\mathbf{\Pi}}^m = 0$ which yields the following expression for the scaling factor β:

$$\beta^{m+1} = -\frac{\vec{\mathbf{R}}^m \cdot [\mathbf{A}]\vec{\mathbf{\Pi}}^m}{\vec{\mathbf{\Pi}}^m \cdot [\mathbf{A}]\vec{\mathbf{\Pi}}^m} \tag{B.23}$$

Note that from the conjugacy requirement $\vec{\mathbf{\Pi}}^{m+1} \cdot [\mathbf{A}]\vec{\mathbf{\Pi}}^m = 0$ for all m, it can be shown (by induction) that $\vec{\mathbf{R}}^m \cdot [\mathbf{A}]\vec{\mathbf{\Pi}}^m = \vec{\mathbf{R}}^m \cdot [\mathbf{A}]\vec{\mathbf{R}}^m$ and $\vec{\mathbf{R}}^j \cdot \vec{\mathbf{R}}^i = 0$ for $i \neq j$, $\vec{\mathbf{\Pi}}^j \cdot \vec{\mathbf{R}}^i = 0$ while $\vec{\mathbf{R}}^j \cdot [\mathbf{A}]\vec{\mathbf{\Pi}}^i = 0$ for $i = j, j+1$. This result leads to a simplified equivalent expression for β via (B.23)

[2]Note that the following development paraphrases that given in Hestenes et al [1]

$$\beta^{m+1} = -\frac{\vec{\mathbf{R}}^m \cdot [\mathbf{A}]\vec{\mathbf{R}}^m}{\vec{\mathbf{\Pi}}^m \cdot [\mathbf{A}]\vec{\mathbf{\Pi}}^m} \tag{B.24}$$

Thus, the above results brings us to the Method of Conjugate-Gradients as originated by Hestenes et al [1]. However, before we proceed it is necessary to determine under what circumstances convergence will be hampered or enhanced depending on the coefficient matrix $[\mathbf{A}]$.

Solver Efficiency and Matrix Preconditioning

Given that the converged solution $\vec{\mathbf{\Phi}}_c$ to the system of equations is an unknown, all iterative solvers rely on the calculation of the residual $\sum_j |R_j|$ or equivalently $|\vec{\mathbf{R}}|$ as a criterion for solution convergence. The suitability of this criterion is predicated on the assumption that

$$\frac{\|\vec{\mathbf{R}}\|}{\|\mathbf{S}\vec{\mathbf{U}}\|} = \frac{\|[\mathbf{A}](\vec{\mathbf{\Phi}} - \vec{\mathbf{\Phi}}_c)\|}{\|[\mathbf{A}]\vec{\mathbf{\Phi}}_c\|} \sim \text{solution fractional error} = \frac{\|\vec{\mathbf{\Phi}} - \vec{\mathbf{\Phi}}_c\|}{\|\vec{\mathbf{\Phi}}_c\|} \tag{B.25}$$

In terms of efficiency and accuracy, a steepest descent method essentially relies on the relationship specified in (B.25). However, the above is not true in general, thus a suitable criterion for assessing the validity of (B.25). Specifically, if we define $\Delta()$ as the variation in the quantity $()$, then from (B.1), the definition of the residual, the fact that $\mathbf{S}\vec{\mathbf{U}}$ and $[\mathbf{A}]$ are a given

$$\vec{\mathbf{R}} \equiv [\mathbf{A}]\vec{\mathbf{\Phi}} - \mathbf{S}\vec{\mathbf{U}} \Longrightarrow \Delta\vec{\mathbf{R}} = \Delta[\mathbf{A}]\vec{\mathbf{\Phi}} \Longrightarrow [\mathbf{A}]^{-1}\Delta\vec{\mathbf{R}} = \Delta\vec{\mathbf{\Phi}} \tag{B.26}$$

Taking the absolute value of (B.26) and dividing both sides by $\|\vec{\mathbf{\Phi}}\|$ gives[3]

$$\begin{aligned} \frac{\|\Delta\vec{\mathbf{\Phi}}\|}{\|\vec{\mathbf{\Phi}}\|} = \frac{\|[\mathbf{A}]^{-1}\Delta\vec{\mathbf{R}}\|}{\|\Delta\vec{\mathbf{\Phi}}\|} \le \frac{\|[\mathbf{A}]^{-1}\|\|\Delta\vec{\mathbf{R}}\|}{\|\Delta\vec{\mathbf{\Phi}}\|} \Longrightarrow \\ \frac{\|\Delta\vec{\mathbf{\Phi}}\|}{\|\vec{\mathbf{\Phi}}\|} \le \frac{\|[\mathbf{A}]\|\|[\mathbf{A}]^{-1}\|\|\Delta\vec{\mathbf{R}}\|}{\|[\mathbf{A}]\|\|\Delta\vec{\mathbf{\Phi}}\|} \le \frac{\|[\mathbf{A}]\|\|[\mathbf{A}]^{-1}\|\|\Delta\vec{\mathbf{R}}\|}{\|[\mathbf{A}]\Delta\vec{\mathbf{\Phi}}\|} = \frac{\|[\mathbf{A}]\|\|[\mathbf{A}]^{-1}\|\|\Delta\vec{\mathbf{R}}\|}{\|\mathbf{S}\vec{\mathbf{U}}\|} \end{aligned} \tag{B.27}$$

Or is we define a *condition number* $K()$ via $K([\mathbf{A}]) \equiv \|[\mathbf{A}]\|\|[\mathbf{A}]^{-1}\|$ then (B.27) reduces to the following inequality

$$\frac{\|\Delta\vec{\mathbf{\Phi}}\|}{\|\vec{\mathbf{\Phi}}\|} \le \frac{K([\mathbf{A}])\|\Delta\vec{\mathbf{R}}\|}{\|\mathbf{S}\vec{\mathbf{U}}\|} \tag{B.28}$$

Thus, $K([\mathbf{A}])(\|\Delta\vec{\mathbf{R}}\|)/\|\mathbf{S}\vec{\mathbf{U}}\|$ represents an upper bound on the sensitivity of of the solution to variations in residuals.[4] Specifically, if $K([\mathbf{A}])$ is close to unity then the matrix $[\mathbf{A}]$ is termed

[3] Note the properties of the matrix (P-norm) absolute value operator are: $\|[\mathbf{A}]\vec{x}\| \le \|[\mathbf{A}]\|\|\vec{x}\|$ and $\|[\mathbf{A}][B]\| \le \|[\mathbf{A}]\|\|[B]\|$ where a number of definitions for the operator $\|\dot{|}\|$ can be chosen. Examples include maximum Matrix Eigen-values, maximum absolute matrix element values, etc.

[4] Based on the previously mentioned choices in $\|()\|$ operator definitions, the conditioning number might be calculated via eigenvalues of $[\mathbf{A}]$ (e.g. $K[\mathbf{A}] = \|\lambda_{max}/\lambda_{min}\|$).

well conditioned. It should be stated here that certain *well conditioned matrices* can be used to approximately represent a poorly conditioned matrix. Examples include the incomplete Cholesky decomposition (see §B.2.5) $[\overline{\mathbf{L}}][\overline{\mathbf{L}}]^T \sim [\mathbf{A}]$. In addition, although not shown here, a poorly condition matrix can be improved by pre-multiplication or pre-conditioning $[\mathbf{C}]^{-1}[\mathbf{A}]$ In the case of the Cholesky preconditioner, $[\mathbf{C}] \equiv [\overline{\mathbf{L}}][\overline{\mathbf{L}}]^T$.

A Suitable Algorithm

To produce a suitable solver algorithm we first render well-conditioned the coefficient matrix of the system to be solved: Specifically, our system becomes

$$[\mathbf{C}]^{-1}[\mathbf{A}]\vec{\mathbf{\Phi}} = [\mathbf{C}]^{-1}\mathbf{S}\vec{\mathbf{U}} \Longrightarrow [\mathbf{C}]^{-1}[\mathbf{A}][\mathbf{C}]^{-1}[\mathbf{C}]\vec{\mathbf{\Phi}} = [\mathbf{C}]^{-1}\mathbf{S}\vec{\mathbf{U}} \Longrightarrow [\tilde{\mathbf{A}}]\tilde{\vec{\mathbf{\Phi}}} = \mathbf{S}\tilde{\vec{\mathbf{U}}} \tag{B.29}$$

where $[\tilde{\mathbf{A}}] \equiv [\mathbf{C}]^{-1}[\mathbf{A}][\mathbf{C}]^{-1}$, $\tilde{\vec{\mathbf{\Phi}}} \equiv [\mathbf{C}]\vec{\mathbf{\Phi}}$ and $\mathbf{S}\tilde{\vec{\mathbf{U}}} \equiv [\mathbf{C}]^{-1}\mathbf{S}\vec{\mathbf{U}}$. Thus, we seek the solution $\tilde{\vec{\mathbf{\Phi}}}$ to the conditioned system $[\tilde{\mathbf{A}}]\tilde{\vec{\mathbf{\Phi}}} = \mathbf{S}\tilde{\vec{\mathbf{U}}}$ (needless to say this implies that $[\mathbf{C}]$ should be easily invertible). Applying the ideas given in §B.3.1 we proceed as follows:

Algorithm 3 Preconditioned Conjugate Gradient Algorithm

$m = 0$	
$\tilde{\vec{\mathbf{\Phi}}}^m = \tilde{\vec{\mathbf{\Phi}}}^0$	Guess initial solution for conditioned system (e.g. $\tilde{\vec{\mathbf{\Phi}}} = [\vec{0}]$)
$\tilde{\vec{\mathbf{R}}}^m = -[\tilde{\mathbf{A}}]\tilde{\vec{\mathbf{\Phi}}}^m + \mathbf{S}\tilde{\vec{\mathbf{U}}}$	Calculate residual for the conditioned system.
If $\frac{\tilde{\vec{\mathbf{R}}}^0}{\text{normalization constant}} <$ User Def. Tolerance Return	Check residual tolerance
$\tilde{\vec{\mathbf{\Pi}}}^m = \tilde{\vec{\mathbf{R}}}^m$	Set initial search vector via the Steepest Descent Criterion.
Begin iteration loop:	
$m = m + 1$	
$\epsilon^m = \tilde{\vec{\mathbf{R}}}^m \cdot \tilde{\vec{\mathbf{R}}}^m$	
$\eta^m = \tilde{\vec{\mathbf{\Pi}}}^m \cdot ([\tilde{\mathbf{A}}]\tilde{\vec{\mathbf{\Pi}}}^m)$	
$\alpha^m = \frac{\epsilon^m}{\eta^m}$	Calculate scaling factor using the Steepest Descent (see (B.21).
$\tilde{\vec{\mathbf{R}}}^{m+1} = \tilde{\vec{\mathbf{R}}}^m - \alpha^m[\tilde{\mathbf{A}}]\tilde{\vec{\mathbf{\Pi}}}^m$	Update modified residual vector $\tilde{\vec{\mathbf{R}}}$
$\tilde{\vec{\mathbf{\Phi}}}^{m+1} = \tilde{\vec{\mathbf{\Phi}}}^m + \alpha^m\tilde{\vec{\mathbf{\Phi}}}^m$	Update modified solution vector $\tilde{\vec{\mathbf{\Phi}}}$
If $\frac{\tilde{\vec{\mathbf{R}}}^0}{\text{normalization constant}} <$ User Def. Tolerance:Return	Check residual tolerance
$\tilde{\vec{\mathbf{\Pi}}}^{m+1} = \tilde{\vec{\mathbf{R}}}^{m+1}$	Solve for new search vector $\vec{\mathbf{\Pi}}$.
$\eta^{m+1} = \tilde{\vec{\mathbf{\Pi}}}^{m+1} \cdot ([\tilde{\mathbf{A}}]\tilde{\vec{\mathbf{\Pi}}}^{m+1})$	
$\beta^{m+1} = \frac{\eta^{m+1}}{\eta^m}$	Calc. scaling factor via to conj. req. (see (B.24)).
$\tilde{\vec{\mathbf{\Pi}}}^{m+1} = \tilde{\vec{\mathbf{R}}}^{m+1} + \beta^m\tilde{\vec{\mathbf{\Pi}}}^m$	Update modified search vector $\tilde{\vec{\mathbf{\Pi}}}$
Continue Loop	

Note that the above algorithm is an expression of the transformed or conditioned variables. Making substitutions according their definitions in (B.29) gives the expanded form of the algorithm

Algorithm 4 Preconditioned Conjugate Gradient Algorithm:Expanded

$m = 0$	
$\tilde{\vec{\mathbf{\Phi}}}^m = \tilde{\vec{\mathbf{\Phi}}}^m$	Guess initial solution for conditioned system (e.g. $\tilde{\vec{\mathbf{\Phi}}} = [\vec{0}]$)
$[\mathbf{C}]^{-1}\vec{\mathbf{R}}^m = -[\tilde{\mathbf{A}}]\tilde{\vec{\mathbf{\Phi}}}^m + \mathbf{S}\tilde{\vec{\mathbf{U}}}$	Calculate residual for the conditioned system.
If $\frac{\tilde{\vec{\mathbf{R}}}^0}{\text{normalization constant}} <$ User Def. Tolerance Return	Check residual tolerance
$[\mathbf{C}]\vec{\mathbf{\Pi}}^m = [\mathbf{C}]^{-1}\vec{\mathbf{R}}^m$	Set initial search vector via the Steepest Descent Criterion.
Begin iteration loop:	
$m = m + 1$	
$\epsilon^m = [\mathbf{C}]^{-1}\vec{\mathbf{R}}^m \cdot [\mathbf{C}]^{-1}\vec{\mathbf{R}}^m$	
$\eta^m = [\mathbf{C}]\vec{\mathbf{\Pi}}^m \cdot ([\mathbf{C}]^{-1}[\mathbf{A}][\mathbf{C}]^{-1})([\mathbf{C}]\vec{\mathbf{\Pi}}^m)$	
$\alpha^m = \frac{\epsilon^m}{\eta^m}$	Calculate scaling factor using the Steepest Descent (see (B.21).
$[\mathbf{C}]^{-1}\vec{\mathbf{R}}^{m+1} = [\mathbf{C}]^{-1}\vec{\mathbf{R}}^m - \alpha^m([\mathbf{C}]^{-1}[\mathbf{A}][\mathbf{C}]^{-1})([\mathbf{C}]\vec{\mathbf{\Pi}}^m)$	Update modified residual vector $\vec{\mathbf{R}}$
$[\mathbf{C}]\vec{\mathbf{\Phi}}^{m+1} = [\mathbf{C}]\vec{\mathbf{\Phi}}^m + \alpha^m[\mathbf{C}]\vec{\mathbf{\Phi}}^m$	Update modified solution vector $\vec{\mathbf{\Phi}}$
If $\frac{\vec{\mathbf{R}}^{m+1}}{\text{normalization constant}} <$ User Def. Tolerance: Return	Check residual tolerance
$[\mathbf{C}]\vec{\mathbf{\Pi}}^{m+1} = [\mathbf{C}]^{-1}\vec{\mathbf{R}}^{m+1}$	Solve for new search vector $\vec{\mathbf{\Pi}}$.
$\eta^{m+1} = [\mathbf{C}]\vec{\mathbf{\Pi}}^{m+1} \cdot ([\mathbf{C}]^{-1}[\mathbf{A}][\mathbf{C}]^{-1})([\mathbf{C}]\vec{\mathbf{\Pi}}^{m+1})$	
$\beta^{m+1} = \frac{\eta^{m+1}}{\eta^m}$	Calc. scaling factor via to conj. req. (see (B.24)).
$[\mathbf{C}]\vec{\mathbf{\Pi}}^{m+1} = [\mathbf{C}]^{-1}\vec{\mathbf{R}}^{m+1} + \beta^m([\mathbf{C}]^{-1}\vec{\mathbf{\Pi}}^m)$	Update modified search vector $\vec{\mathbf{\Pi}}$
Continue Loop	

Noting the definition of the identity matrix $[\mathbf{C}]^{-1}[\mathbf{C}] = [I]$, defining the matrix $[M] = [\mathbf{C}]^2$ we get the final form of the Preconditioned Conjugate Gradient algorithm[5]

Algorithm 5 Preconditioned Conjugate Gradient Algorithm:Final Form

$m = 0$	
$\vec{\mathbf{\Phi}}^m = \vec{\mathbf{\Phi}}^0$	Guess initial solution for system (e.g. $\vec{\mathbf{\Phi}} = \vec{0}$)
$\vec{\mathbf{R}}^m = -[\mathbf{A}]\vec{\mathbf{\Phi}}^m + \mathbf{S}\vec{\mathbf{U}}$	Calculate residual system.
If $\frac{\vec{\mathbf{R}}^m}{\text{normalization constant}} <$ User Def. Tolerance Return	Check residual tolerance
$[M]\vec{\mathbf{Z}}^m = \vec{\mathbf{R}}^m$, $\vec{\mathbf{\Pi}}^m = \vec{\mathbf{Z}}^m$	Solve for initial search vector via the Steepest Descent Criterion.
Begin iteration loop:	
$m = m + 1$	
$\epsilon^m = \vec{\mathbf{R}}^m \cdot \vec{\mathbf{Z}}^m$	
$\eta^m = \vec{\mathbf{\Pi}}^m \cdot ([\mathbf{A}]\vec{\mathbf{\Pi}}^m)$	
$\alpha^m = \frac{\epsilon^m}{\eta^m}$	Calculate scaling factor using the Steepest Descent (see (B.21).
$\vec{\mathbf{R}}^{m+1} = \vec{\mathbf{R}}^m - \alpha^m([\mathbf{A}])(\vec{\mathbf{\Pi}}^m)$	Update residual vector $\vec{\mathbf{R}}$
$\vec{\mathbf{\Phi}}^{m+1} = \vec{\mathbf{\Phi}}^m + \alpha^m\vec{\mathbf{\Phi}}^m$	Update solution vector $\vec{\mathbf{\Phi}}$
If $\frac{\vec{\mathbf{R}}^{m+1}}{\text{normalization constant}} <$ User Def. Tolerance: Return	Check residual tolerance
$\vec{\mathbf{Z}}^{m+1} = [M]^{-1}\vec{\mathbf{R}}^{m+1}$	Solve for new auxiliary vector $\vec{\mathbf{Z}}$.
$\epsilon^{m+1} = \vec{\mathbf{R}}^{m+1} \cdot \vec{\mathbf{Z}}^{m+1}$	
$\beta^{m+1} = \frac{\epsilon^{m+1}}{\epsilon^m}$	Calc. scaling factor via to conj. req. (see (B.24)).
$\vec{\mathbf{\Pi}}^{m+1} = \vec{\mathbf{Z}}^{m+1} + \beta^m(\vec{\mathbf{\Pi}}^m)$	Update modified search vector $\vec{\mathbf{\Pi}}$
Continue Loop	

Note that the pre-conditioning in the final algorithm only appears in the calculation of the auxiliary vector $\vec{\mathbf{Z}}$. Finally, if we utilize the Cholesky preconditioning $[\mathbf{C}] \equiv [\overline{\mathbf{L}}][\overline{\mathbf{L}}]^T$, we have $[\mathbf{M}] = [\mathbf{C}]^2 = [[\overline{\mathbf{L}}][\overline{\mathbf{L}}]^T]^2$ the algorithm can be executed.

[5] In other words $[\mathbf{C}]^{-1}\vec{\mathbf{Q}} \cdot [\mathbf{C}]^{-1}\vec{\mathbf{Q}} = \vec{\mathbf{Q}} \cdot \vec{\mathbf{Q}}$ and $[\mathbf{C}]\vec{\mathbf{Q}} \cdot ([\mathbf{C}]^{-1}[\mathbf{A}][\mathbf{C}]^{-1})([\mathbf{C}]\vec{\mathbf{Q}}) = \vec{\mathbf{Q}} \cdot [\mathbf{A}]\vec{\mathbf{Q}})$

References

[1] M. Hestenes and E. Stiefel. Methods of conjugate gradients for solving linear systems. *Journal of Research of the National Bureau of Standards*, 1952.

Appendix C

Discretization Error

In order to successfully resolve spatial and temporal variations in a property $\phi(x,t)$ using numerical methods, it is necessary to know the following:

- Truncation error due to discretization of a given differential equation defining the process: Order of magnitude analysis
- Solution or process resolution: Requires the use of spectral analysis

The first criterion is used to determine the spatial or temporal error associated with approximating continuous derivatives via discretized algebraic expressions. While the second approach involves decomposing the property field (via Fourier analysis) into component spectra, and determining the relative fidelity/accuracy associated with a given discretization scheme.

C.1 Discretization Error:Temporal Term

C.1.1 1^{st}-Order Scheme

To examine the merits of approximating spatial and temporal derivatives according to various discretization schemes, one can examine the following pure $1-D$ convection equation

$$\dot{\phi} + c\frac{\partial \phi}{\partial x} = 0 \tag{C.1}$$

Addressing the temporal term alone, we can determine an exact analytical solution by recourse to a Taylor expansion about time t

$$\phi(t+\Delta t) = \phi(t) + \dot{\phi}\Delta t + \ddot{\phi}\frac{(\Delta t)^2}{2} + \hat{H} \tag{C.2}$$

or solving for $\dot{\phi}$ we have

$$\dot{\phi} = \frac{\phi(t+\Delta t) - \phi(t)}{\Delta t} - \ddot{\phi}\frac{(\Delta t)}{2} - \frac{\hat{H}}{\Delta t} \tag{C.3}$$

where the terms in (C.3) are grouped according to powers of Δt represent the first, second and higher order terms ($\hat{H}$). Specifically, if we assume an approximation for the temporal derivative of the form

$$\hat{\dot{\phi}} \equiv \frac{\phi(t+\Delta t) - \phi(t)}{\Delta t} \tag{C.4}$$

then the truncation error associated with this form of discretization is given by

$$\hat{\dot{\phi}} - \dot{\phi} = \frac{\phi(t+\Delta t) - \phi(t)}{\Delta t} - \frac{\phi(t+\Delta t) - \phi(t)}{\Delta t} - \ddot{\phi}\frac{(\Delta t)}{2} - \frac{\hat{H}}{\Delta t} = -\ddot{\phi}\frac{(\Delta t)}{2} - \frac{\hat{H}}{\Delta t} \tag{C.5}$$

Thus, the choice of temporal discretization as given in (C.4) is 1^{st}*-order accurate* with a truncation error $\tau \sim O(\Delta t)$ corresponding to the leading term on the RHS of (C.5).

C.1.2 2^{nd} Order Scheme: Crank-Nicholson

A reduction in truncation error can be achieved by examining the following approximation for the temporal derivative of ϕ as averaged over the interval $t \to t + \Delta t$:

$$\dot{\phi}\Big|_{t+\Delta t} \approx \frac{\frac{\partial \phi}{\partial t}\Big|_{t+\Delta t} + \frac{\partial \phi}{\partial t}\Big|_{t}}{2} \tag{C.6}$$

Expanding the derivatives $\frac{\partial \phi}{\partial t}\Big|_{t+\Delta t}$ and $\frac{\partial \phi}{\partial t}\Big|_{t}$ via a Taylor expansion gives

$$\frac{\partial \phi}{\partial t}\Big|_{t+\Delta t} = \frac{\phi^{t+\Delta t} - \phi^{t+\Delta t/2}}{\Delta t/2} - \overline{\ddot{\phi}}\Big|_{t+\Delta t}\frac{\Delta t}{2} - \overline{\hat{H}}$$

$$\frac{\partial \phi}{\partial t}\Big|_{t} = \frac{\phi^{t+\Delta t/2} - \phi^{t}}{\Delta t/2} - \hat{\ddot{\phi}}\Big|_{t}\frac{\Delta t}{2} - \hat{\hat{H}} \tag{C.7}$$

where $\hat{\hat{H}}$ and $\overline{\hat{H}}$ are higher order terms. Substitution of (C.7) into (C.6), assuming $\overline{\ddot{\phi}}\Big|_{t+\Delta t} \approx \hat{\ddot{\phi}}\Big|_{t}$ gives

$$\dot{\phi}\Big|_{t+\Delta t/2} \approx \frac{\phi^{t+\Delta t} - \phi^{t}}{\Delta t} - [\overline{\hat{H}} + \hat{\hat{H}}] \tag{C.8}$$

Thus, if we evaluate the model convection equation C.1 at time $t = t + \Delta t/2$ and discretized the temporal term as

$$\hat{\dot{\phi}}\Big|_{t+\Delta t/2} \equiv \frac{\phi^{t+\Delta t} + \phi^{t}}{\Delta t} \tag{C.9}$$

then the truncation error is given by

$$[\overline{\hat{H}} + \hat{\hat{H}}] \sim O((\Delta t)^2) \tag{C.10}$$

Hence, the model equation becomes

$$\dot{\phi}\Big|_{t+\Delta t/2} = -c\frac{\partial \phi}{\partial x}\Big|_{t+\Delta t/2} \tag{C.11}$$

and the previous discretization scheme (C.9), to be henceforth referred to as the Crank-Nicholson scheme, is 2^{nd}-*order accurate* with a truncation error $\tau \sim O((\Delta t)^2)$.

C.1.3 2^{nd} Order Scheme: Implicit Backwards Difference

The Crank-Nicholson scheme described in §C.1.2 is mixed implicit/explicit scheme and therefore suffers from, (in some cases), severe limitations in terms of required time-step to ensure numerical stability. An alternative approximation for the temporal derivative which exhibits improved stability can be developed via a backwards Taylor expansion of $\phi\Big|_t$ about $\phi\Big|_{t+\Delta t}$ (where $\Delta t \rightarrow -\Delta t$)

$$\phi\Big|_t = \phi\Big|_{t+\Delta t} - \dot{\phi}\Big|_{t+\Delta t}\Delta t + \ddot{\phi}\Big|_{t+\Delta t}\frac{(\Delta t)^2}{2} + \hat{H} \tag{C.12}$$

again, where $\hat{H}$ represents the higher order terms. Hence

$$\begin{aligned}
\dot{\phi}\Big|_{t+\Delta t}\Delta t &= \phi\Big|_{t+\Delta t} - \phi\Big|_t + \ddot{\phi}\Big|_{t+\Delta t}\frac{(\Delta t)^2}{2} + \hat{H} \\
&\approx \phi\Big|_{t+\Delta t} - \phi\Big|_t + \frac{\dot{\phi}\Big|_{t+\Delta t} - \dot{\phi}\Big|_t}{\Delta t}\frac{(\Delta t)^2}{2} + \hat{H} \approx \\
\approx \phi\Big|_{t+\Delta t} - \phi\Big|_t &+ \frac{(\phi\Big|_{t+\Delta t} - \phi\Big|_t) - (\phi\Big|_t - \phi\Big|_{t-\Delta t})}{\Delta t}\frac{(\Delta t)^2}{2} + \hat{H}
\end{aligned} \tag{C.13}$$

Or gathering terms

$$\dot{\phi}\Big|_{t+\Delta t} \approx \frac{1}{\Delta t}(\frac{3}{2}\phi\Big|_{t+\Delta t} - 2\phi\Big|_t + \frac{1}{2}\phi\Big|_{t-\Delta t}) + \frac{\hat{H}}{\Delta t} \tag{C.14}$$

The temporal discretization scheme given in (C.14) with truncation error $\frac{\hat{H}}{\Delta t} \sim (\Delta t)^2$ is thus 2^{nd}-order accurate. It is this temporal scheme which is utilized for the high resolution simulations performed in Chapters 5 and 6.

C.2 Discretization Error: Spatial Discretization

In the case of variation in $\phi(t, x)$ with respect to the spatial variable x we have, via a Taylor expansion about x

$$\frac{\partial \phi}{\partial x}\Big|_x = \frac{\phi_{x+\Delta x} - \phi_x}{\Delta x} - \frac{\partial^2 \phi}{\partial x^2}\Big|_x \frac{\Delta x}{2} + \hat{H} \tag{C.15}$$

where the higher order terms are defined by

$$\hat{H} \equiv \frac{\partial^3 \phi}{\partial x^3}\Big|_x \frac{(\Delta x)^2}{6} + H \tag{C.16}$$

Clearly $\hat{H} \sim O((\Delta x)^2)$ and $H \sim O((\Delta x)^3)$ where $\hat{H}$ and H correspond to the 2^{nd}-order and higher terms in (C.15) respectively.

C.2.1 Discretization Error: 2^{nd}-Order Scheme

Using a central difference approximation for all derivatives yields

$$\frac{\partial \phi}{\partial x}\Big|_x \approx \frac{\phi_{x+\Delta x} - \phi_x}{\Delta x} - \frac{\frac{\partial \phi}{\partial x}\Big|_{x+\Delta x/2} - \frac{\partial \phi}{\partial x}\Big|_{x-\Delta x/2}}{\Delta x}\frac{\Delta x}{2} + \hat{H} \approx$$

$$\frac{\phi_{x+\Delta x} - \phi_x}{\Delta x} - \frac{\frac{\phi_{x+\Delta x}-\phi_x}{\Delta x} - \frac{\phi_x - \phi_{x-\Delta x}}{\Delta x}}{\Delta x}\frac{\Delta x}{2} + \hat{H} = \frac{\phi_{x+\Delta x} - \phi_{x-\Delta x}}{2\Delta x} + \hat{H} \tag{C.17}$$

Thus, a discretization of $\partial\phi/\partial x$ according to

$$\hat{\frac{\partial \phi}{\partial x}}\Big|_x \equiv \frac{\phi_{x+\Delta x} - \phi_{x-\Delta x}}{2\Delta x} \tag{C.18}$$

yields a truncation error

$$\hat{\frac{\partial \phi}{\partial x}} - \frac{\partial \phi}{\partial x} = \hat{H} \sim O((\Delta x)^2) \tag{C.19}$$

thus, indicating that the discretization error is, according to (C.19), 2^{nd}-order in Δx.

C.2.2 Discretization Error: Quick Third-Order Scheme

For the purpose of conciseness, the 3^{rd}-order of accuracy for the Quick scheme (introduced in §3.3.3) will not be demonstrated. However, referring to Figure 3.1 the convection equation spatial gradient can be approximated via

$$\frac{\partial \phi}{\partial x}\Big|_x \approx \frac{\phi\Big|_{f_e} - \phi\Big|_{f_w}}{\Delta x} \tag{C.20}$$

Or, if the convection velocity c is negative and we assume uniform grids, then according to (3.42) we have

$$\frac{\partial \phi}{\partial x}\Big|_x \approx \frac{3\phi_{x+\Delta x}^{t+\Delta t} + 3\phi_x^{t+\Delta t} - 7\phi_{x-\Delta x}^{t+\Delta t} + \phi_{x-2\Delta x}^{t+\Delta t}}{8\Delta x} \tag{C.21}$$

A spectral analysis well be carried out in §C.3.1 based on the resulting discretized convection equation for a 1^{st}-order Euler-Implicit scheme

$$\frac{\phi_x^{t+\Delta t} - \phi_x^t}{\Delta t} = -c\frac{3\phi_{x+\Delta x}^{t+\Delta t} + 3\phi_x^{t+\Delta t} - 7\phi_{x-\Delta x}^{t+\Delta t} + \phi_{x-2\Delta x}^{t+\Delta t}}{8\Delta x} \tag{C.22}$$

Although not demonstrated here, the order of the truncation error is $\sim O((\Delta x)^3)$ indicating that the discretization error is 3^{rd}-order in Δx.

C.2.3 Discretization Error: 4^{rth}-Order Scheme

An improved discretization of the spatial derivative can can be found by increasing the interpolation stencil resulting in, for a central difference scheme, a 4^{rth}-order expression for the property gradient

$$\frac{\partial \phi}{\partial x}\Big|_x \approx \frac{-\phi_{x+2\Delta x} + 8\phi_{x+2\Delta x} - 8\phi_{x-\Delta x} + \phi_{x-2\Delta x}}{12\Delta x} \tag{C.23}$$

Although not demonstrated here, the order of the truncation error is $\sim O((\Delta x)^4)$ indicating that the discretization error is 4^{rd}-order in Δx.Finally, a summary of the discretized convection equation and relevant schemes are given in Table C.1.

Table C.1: Summary of Discretization of the $1-D$ Pure Convection Equation

Discretization type	Discretization of convection equation $\dot{\phi} + c\frac{\partial \phi}{\partial x} = 0$
1^{st} order Euler, 2^{nd} order CD	$\frac{\phi_x^{t+\Delta t} - \phi_x^t}{\Delta t} + c\frac{\phi_{x+\Delta x}^{t+\Delta t} - \phi_{x-\Delta x}^{t+\Delta t}}{2\Delta x} = 0$
1^{st} order Euler, 4^{nd} order CD	$\frac{\phi_x^{t+\Delta t} - \phi_x^t}{\Delta t} + c\frac{-\phi_{x+2\Delta x}^{t+\Delta t} + 8\phi_{x+\Delta x}^{t+\Delta t} - 8\phi_{x-\Delta x}^{t+\Delta t} + \phi_{x-2\Delta x}^{t+\Delta t}}{12\Delta x} = 0$
1^{st} order Euler, 3^{rd} order Quick	$\frac{\phi_x^{t+\Delta t} - \phi_x^t}{\Delta t} + c\frac{3\phi_{x+\Delta x}^{t+\Delta t} + 3\phi_x^{t+\Delta t} - 7\phi_{x-\Delta x}^{t+\Delta t} + \phi_{x-2\Delta x}^{t+\Delta t}}{8\Delta x} = 0$
2^{nd} order C-N, 2^{nd} order CD	$\frac{\phi_x^{t+\Delta t} - \phi_x^t}{\Delta t} + c\frac{\phi_{x+\Delta x}^{t+\Delta t} - \phi_{x-\Delta x}^{t+\Delta t} + \phi_{x+\Delta x}^t - \phi_{x-\Delta x}^t}{4\Delta x} = 0$
2^{nd} order C-N, 4^{nd} order CD	$\frac{\phi_x^{t+\Delta t} - \phi_x^t}{\Delta t} + c\frac{-\phi_{x+2\Delta x}^{t+\Delta t} + 8\phi_{x+\Delta x}^{t+\Delta t} - 8\phi_{x-\Delta x}^{t+\Delta t} + \phi_{x-2\Delta x}^{t+\Delta t}}{24\Delta x} + c\frac{-\phi_{x+2\Delta x}^t + 8\phi_{x+\Delta x}^t - 8\phi_{x-\Delta x}^t + \phi_{x-2\Delta x}^t}{24\Delta x} = 0$
2^{st} order backwards implicit, 2^{nd} order CD	$\frac{1.5\phi_x^{t+\Delta t} - 2\phi_x^t + 0.5\phi_x^{t-\Delta t}}{\Delta t} + c\frac{\phi_{x+\Delta x}^{t+\Delta t} - \phi_{x-\Delta x}^{t+\Delta t}}{2\Delta x} = 0$
2^{st} order backwards implicit, 4^{nd} order CD	$\frac{1.5\phi_x^{t+\Delta t} - 2\phi_x^t + 0.5\phi_x^{t-\Delta t}}{\Delta t} + c\frac{-\phi_{x+2\Delta x}^{t+\Delta t} + 8\phi_{x+\Delta x}^{t+\Delta t} - 8\phi_{x-\Delta x}^{t+\Delta t} + \phi_{x-2\Delta x}^{t+\Delta t}}{12\Delta x} = 0$

C.3 Solution Resolution and Error: Spectral Analysis

The preceding analysis described a specific procedure for determining order of magnitude accuracies for several temporal and spatial discretization schemes. However, while informative, such an analysis does little to describe the distortion of a given solution $\phi(x,t)$ via discretization of the governing equation. To proceed further, and in a more *specific* fashion, one can utilize Fourier's' Theorem regarding the decomposition of any given arbitrary function into a series composed of periodic basis functions. Thus, one can decompose the function $\phi(x,t)$

into its Fourier components ${}_j\phi(x,t)$ and ascertain the effect of a given discretization of the governing equation (C.1) on the fidelity/accuracy of ${}_j\phi(x,t)$.

C.3.1 Convection Equation and Discretization Error

Given the previous, we can attempt to express $\phi(x,t)$ in terms of the following product series

$$\phi(x,t) = \sum_{j=1}^{\infty} {}_jA_j\phi(x,t) = \sum_{j=1}^{\infty} {}_jAe^{i({}_j\kappa x - {}_j\omega t)} \tag{C.24}$$

Such a series solution is valid if the individual basis function ${}_j\phi(x,t) = e^{i{}_j\kappa x - {}_j\omega t}$ are a solution to governing differential equation (i.e. the *linear* convection equation (C.1)). Substitution into (C.1) yields

$${}_j\dot{\phi} - c\frac{\partial {}_j\phi}{\partial x} = A_{jj}\phi({}_j\omega - c_j\kappa){}_j\phi = 0 \Rightarrow {}_j\omega = c_j\kappa \tag{C.25}$$

Thus, ${}_j\kappa$ and ${}_j\omega$ are the wave number and angular velocity of the periodic basis function ϕ_j.[1] To proceed with our investigation of the augmentation of a given basis function ${}_j\phi$ via a discretized convection equation, we define the Fourier component complex gain ${}_jG$ according to[2]

$${}_jG \equiv \frac{{}_j\phi_x^{t+\Delta t}}{{}_j\phi_x^t} \tag{C.29}$$

Next, we can write a generalized discretization of the $1-D$ convection equation according to

$$\begin{aligned} &\hat{A}_j\phi_x^{t+\Delta t} + \hat{B}_j\phi_x^t + \hat{C}_j\phi_x^{t-\Delta t} + \\ \frac{c\Delta t}{\Delta x}\Big[&\hat{D}_j\phi_{x+2\Delta x}^{t+\Delta t} + \hat{E}_j\phi_{x+\Delta x}^{t+\Delta t} + \hat{F}_j\phi_x^{t+\Delta t} + \hat{G}_j\phi_{x-\Delta x}^{t+\Delta t} + \hat{H}_j\phi_{x-2\Delta x}^{t+\Delta t} + \\ &\hat{I}_j\phi_{x+2\Delta x}^{t} + \hat{J}_j\phi_{x+\Delta x}^{t} + \hat{K}_j\phi_x^{t} + \hat{L}_j\phi_{x-\Delta x}^{t} + \hat{M}_j\phi_{x-2\Delta x}^{t}\Big] = 0 \end{aligned} \tag{C.30}$$

Dividing (C.30) by ${}_j\phi_x^t$ and noting the results from (C.26) and (C.27) we have, in terms of the complex gain ${}_jG$

[1] Incidentally, a key property of the exponential basis function are the following

$${}_j\phi_x^{t+n\Delta t} = e^{-in{}_j\omega\Delta t}{}_j\phi_x^t,\ {}_j\phi_{x+n\Delta x}^t = e^{-in{}_j\kappa\Delta x}{}_j\phi_x^t \tag{C.26}$$

[2] It should be noted that via the choice of basis functions, the complex gain is invariant with respect to time. In other words,

$$\frac{{}_j\phi_x^{t+2\Delta t}}{{}_j\phi_x^{t+\Delta t}} = \frac{{}_j\phi_x^{t+\Delta t}}{{}_j\phi_x^t}\frac{e^{-{}_j\omega\Delta t}}{e^{-{}_j\omega\Delta t}} = \frac{{}_j\phi_x^{t+\Delta t}}{{}_j\phi_x^t} \equiv {}_jG \tag{C.27}$$

In addition, from the property of the exponent

$$\frac{{}_j\phi^{t-\Delta t}}{{}_j\phi^t} = \frac{1}{{}_jG} \tag{C.28}$$

$$\mathbb{A}_j G^2 + \mathbb{B}_j G + \mathbb{C} = 0 \Rightarrow {}_jG = \frac{-\mathbb{B} \pm \sqrt{\mathbb{B}^2 - 4\mathbb{A}\mathbb{C}}}{2\mathbb{A}} \tag{C.31}$$

where coefficients of the quadratic are given by

$$\mathbb{A} \equiv \hat{A} + \gamma\vec{\alpha}\cdot\vec{\varepsilon},\ \mathbb{B} \equiv \hat{B} + \gamma\vec{\beta}\cdot\vec{\varepsilon},\ \mathbb{C} \equiv \hat{C},$$

$$\vec{\alpha} \equiv \left[\begin{array}{ccccc} \hat{D} & \hat{E} & \hat{F} & \hat{G} & \hat{H} \end{array}\right],\ \vec{\beta} \equiv \left[\begin{array}{ccccc} \hat{I} & \hat{J} & \hat{K} & \hat{L} & \hat{M} \end{array}\right],\ \vec{\varepsilon} \equiv \left[\begin{array}{c} e^{i2_j\kappa\Delta x} \\ e^{i_j\kappa\Delta x} \\ 1 \\ e^{-i_j\kappa\Delta x} \\ e^{-i2_j\kappa\Delta x} \end{array}\right] \tag{C.32}$$

The above expressions can be utilized directly to yield the complex gain for many discretization schemes. For example, a 1^{st}-order Euler implicit scheme using 2^{nd}-order central differences for the spatial gradient results in the following coefficient set

$$\hat{A} = 1,\ \hat{E} = 1/2,\ \hat{B} = -1,\ \hat{G} = -1/2,\ \text{All other coefficients equal to zero} \Rightarrow$$

$$\mathbb{A} = 1 + \frac{\gamma}{2}\left[e^{i_j\kappa\Delta x} - e^{-i_j\kappa\Delta x}\right],\ \mathbb{B} = -1,\ \mathbb{C} = 0 \tag{C.33}$$

and complex gain

$${}_jG = \frac{1 \pm \sqrt{1}}{2(1 + \frac{\gamma}{2}(e^{i_j\kappa\Delta x} - e^{-i_j\kappa\Delta x})} \tag{C.34}$$

where the time-step dependence has been replaced with a dependence on the $CFL \equiv \frac{c\Delta t}{\Delta x}$-number or γ. Taking the non-trivial (i.e. non-zero) solution for the complex gain and noting the definition of *sin* gives

$${}_jG = \frac{1 \pm 1}{2\left(1 + \frac{\gamma}{2}(2isin({}_j\kappa\Delta x))\right)} = \frac{1}{1 + i\gamma sin({}_j\kappa\Delta x)} \tag{C.35}$$

Utilizing (C.32), (C.31) as well as Table C.1 results in complex gains ${}_jG$ for the various discretization schemes for the pure convection equation given in Table C.2.

Table C.2: Gain G for Various Discretization Schemes

Discretization type	Value of non-zero coefficients via (C.30)	${}_jG$
${}^{analytic}{}_j\phi$	NA	$e^{i\gamma_j\kappa\Delta x}$
1^{st} order Euler, 2^{nd} order CD	$\hat{A}=1,\ \hat{B}=-1,\ \hat{E}=1/2,\ \hat{G}=-1/2$	$\frac{1}{1+i\gamma sin({}_j\kappa\Delta x)}$
1^{st} order Euler, 4^{nd} order CD	$\hat{A}=1,\ \hat{B}=-1,\ \hat{D}=-1/12,\ \hat{E}=8/12,\ \hat{G}=-8/12,\ \hat{H}=-1/12$	$\frac{1}{1+i\gamma(-sin(2_j\kappa\Delta x)+8(sin({}_j\kappa\Delta x)))}$
1^{st} order Euler, 3^{rd} order Quick	$\hat{A}=1,\ \hat{B}=-1,\ \hat{E}=3/8,\ \hat{F}=3/8,\ \hat{G}=-7/8,\ \hat{H}=1/8$	$\frac{1}{(1+\gamma(\frac{3}{8}-\frac{1}{2}cos({}_j\kappa\Delta x)+\frac{1}{8}cos(2_j\kappa\Delta x))+i\gamma(\frac{10}{8}sin({}_j\kappa\Delta x)-\frac{1}{8}sin(2_j\kappa\Delta x)))}$
2^{nd} order C-N, 2^{nd} order CD	$\hat{A}=1,\ \hat{B}=-1,\ \hat{E}=\hat{J}=1/4,\ \hat{G}=\hat{L}=-1/4$	$\frac{2-i\gamma sin({}_j\kappa\Delta x)}{2+i\gamma sin({}_j\kappa\Delta x)}$
2^{nd} order C-N, 4^{nd} order CD	$\hat{A}=1,\ \hat{B}=-1,\ \hat{D}=\hat{I}=-1/24,\ \hat{E}=\hat{J}=8/24,\ \hat{G}=\hat{L}=-8/24,\ \hat{H}=\hat{M}=1/24$	$\frac{2-i\gamma(-sin(2_j\kappa\Delta x)+8(sin({}_j\kappa\Delta x)))}{2+i\gamma(-sin(2_j\kappa\Delta x)+8(sin({}_j\kappa\Delta x)))}$
2^{st} order Euler, 2^{nd} order CD	$\hat{A}=1.5,\ \hat{B}=-2,\ \hat{C}=0.5,\ \hat{E}=1/2,\ \hat{G}=-1/2$	$\frac{2\pm\sqrt{1-2i\gamma sin({}_j\kappa\Delta x)}}{3+2i\gamma sin({}_j\kappa\Delta x)}$
2^{st} order Euler, 4^{nd} order CD	$\hat{A}=1.5,\ \hat{B}=-2,\hat{C}=0.5,\ \hat{D}=-1/12,\ \hat{E}=8/12,\ \hat{G}=-8/12,\ \hat{H}=-1/12$	$\frac{2\pm\sqrt{1-2(i\gamma(-\frac{2}{12}sin(2_j\kappa\Delta x)+\frac{16}{12}(sin({}_j\kappa\Delta x))))}}{3+2i\gamma(-sin(\frac{2}{12}{}_j\kappa\Delta x)+\frac{16}{12}(sin({}_j\kappa\Delta x)))}$

C.3.2 Assessment of Gain

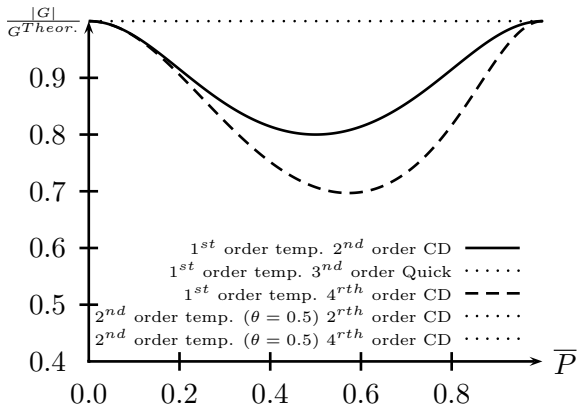

Figure C.1: Normaled gain vs. $\overline{P} \equiv \frac{{}_j\kappa\Delta x}{\pi}$ for CFL (γ) of 0.75

Given that expressions for the complex gain developed in §C.3.1, it would be useful to compare the phase angle as well as magnitude of the discretized gain $|{}_jG|$ with that of the analytic function ${}_j\phi$. Specifically, the magnitude $|{}_jG|$ and phase angle Ψ of the complex gain ${}_jG$ is given by

$$|{}_jG| = \sqrt{{}_jG\,({}_jG^*)},\ {}_j\Psi = tan^{-1}\left(\frac{\mathbf{Im}\,({}_jG)}{\mathbf{Re}\,({}_jG)}\right) \tag{C.36}$$

where ${}_jG^*$ refers to the complex conjugate of ${}_jG$. Clearly the analytical solution via (C.36) has an ab-

solute value for gain $|^{analytical}{}_jG|$ of 1 while the phase angle $^{analytical}{}_j\Psi$ is apparently zero. Utilizing (C.36) as well as the expressions for ${}_jG$ given in Table C.2 the corresponding expressions for $|{}_jG|$ and ${}_j\Psi$ are given in Table C.3.

Table C.3: $|{}_jG|$ and Phase Offset ${}_j\Psi$ for Various Discretization Schemes

Discretization type	$\lvert{}_jG\rvert$	${}_j\Psi$
$^{analytic}{}_j\phi$	${}_jA$	$\gamma_j\kappa\Delta x$
1^{st} order Euler, 2^{nd} order CD	${}_jA\sqrt{\frac{1}{1+(\gamma sin({}_j\kappa\Delta x))^2}}$	$tan^{-1}\left[\frac{-\gamma sin({}_j\kappa\Delta x)}{1}\right]$
1^{st} order Euler, 3^{rd} order Quick	${}_jA$	$tan^{-1}\left[\frac{\gamma(\frac{10}{8}sin({}_j\kappa\Delta x)-\frac{1}{8}sin(2_j\kappa\Delta x)))}{1+\gamma(\frac{3}{8}-\frac{1}{2}cos({}_j\kappa\Delta x)+\frac{1}{8}cos(2_j\kappa\Delta x)}\right]$
1^{st} order Euler, 4^{nd} order CD	${}_jA\sqrt{\frac{1}{1+(\frac{\gamma}{6}(-sin(2_j\kappa\Delta x)+8sin({}_j\kappa\Delta x)))^2}}$	$tan^{-1}\left[\frac{-\gamma(-sin(2_j\kappa\Delta x)+8sin({}_j\kappa\Delta x))}{2}\right]$
2^{nd} order C-N, 2^{nd} order CD	${}_jA$	$tan^{-1}\left[\frac{-4\gamma sin({}_j\kappa\Delta x)}{4-(\gamma sin({}_j\kappa\Delta x))^2}\right]$
2^{nd} order C-N, 4^{nd} order CD	${}_jA$	$tan^{-1}\left[\frac{4\gamma(-sin(2_j\kappa\Delta x)+8sin({}_j\kappa\Delta x))}{4-(-sin(2_j\kappa\Delta x)+8sin({}_j\kappa\Delta x))^2}\right]$

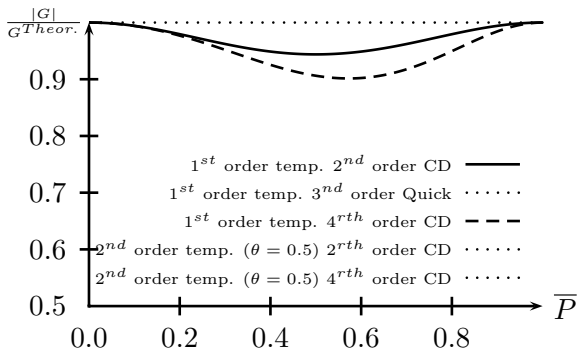

Figure C.2: Normaled gain vs. $\overline{P} \equiv \frac{{}_j\kappa\Delta x}{\pi}$ for CFL (γ) of 0.35

Figures C.2 and C.1 give the ratio of the resolved-to-analytical function gain for 1^{st}-order Euler Implicit and Crank-Nicholson time integration schemes along with 2^{nd} and 4^{rth} (spatial) Order Central Differences as a function of $\overline{P} \equiv {}_j\kappa\Delta x/\pi$ for low and high CFL numbers γ. The Figures illustrate the detrimental effect of increasing the CFL number or cell width (relative to input function wavelength) on gain for the implicit time stepping schemes. This is in contrast to the Crank-Nicholson ($\theta = 0.5$) scheme which accurately resolves the wave gain (or amplitude) regardless of CFL number or cell size relative to wavelength.

C.4 Aliasing Errors

In addition to errors in gain and phase associated with pure convection, discretization of the gradient calculation $\partial/\partial x$ has the effect of augmenting a given wave with wave number κ, thus producing what is referred to as an *aliasing* error (as distinguished from an error in gain). To see this we note that, as in the previous sections, spectral methods can be used

to quantify this error. Specifically, for a given basis function ${}_j\phi = e^{i({}_j\kappa x - {}_j\omega t)}$ we have the 2^{nd}-order CD approximation for $\partial_j\phi/\partial x$ via Table C.2

$$i_j\kappa_j\phi = \frac{\partial_j\phi}{\partial x} \approx \frac{{}_j\phi|_{x+\Delta x} - {}_j\phi|_{x-\Delta x}}{2\Delta x} = e^{i({}_j\kappa x - {}_j\omega t)}\frac{e^{i_j\kappa\Delta x} - e^{-i_j\kappa\Delta x}}{2\Delta x} = i_j\phi\frac{sin({}_j\kappa\Delta x)}{\Delta x} \tag{C.37}$$

or if $\overline{P} \equiv {}_j\kappa\Delta x/\pi$

$$\frac{{}^{2^{nd}ord.CD}{}_j\kappa^{effective}}{{}_j\kappa} = \frac{sin({}_j\kappa\Delta x)}{{}_j\kappa\Delta x} = \frac{sin(\overline{P}\pi)}{\overline{P}\pi} \tag{C.38}$$

A similar procedure applied to the Quick scheme gives

$$i_j\kappa_j\phi = \frac{\partial_j\phi}{\partial x} \approx \frac{3_j\phi|_{x+\Delta x} + 3_j\phi|_x - 7_j\phi|_{x-\Delta x} + {}_j\phi|_{x-2\Delta x}}{8\Delta x} = e^{i({}_j\kappa x - {}_j\omega t)}\frac{3e^{i_j\kappa\Delta x} + 3 + 7e^{i_j\kappa\Delta x} + e^{-i2_j\kappa\Delta x}}{8\Delta x} = i_j\phi\frac{10sin({}_j\kappa\Delta x) - 3i - sin(2_j\kappa\Delta x)}{8\Delta x} \tag{C.39}$$

or

$$\frac{{}^{Quick}{}_j\kappa^{effective}}{{}_j\kappa} = \frac{10sin(\overline{P}\pi) - 3i - sin(2\overline{P}\pi)}{8\overline{P}\pi} \tag{C.40}$$

giving the real part of the complex wave number ratio

$$Real[\frac{{}^{Quick}{}_j\kappa^{effective}}{{}_j\kappa}] = \frac{10sin(\overline{P}\pi) - sin(2\overline{P}\pi)}{8\overline{P}\pi} \tag{C.41}$$

Likewise the 4^{rth}-order CD approximation yields

$$i_j\kappa_j\phi = \frac{\partial_j\phi}{\partial x} \approx \frac{-{}_j\phi|_{x+2\Delta x} + 8_j\phi|_{x+\Delta x} - 8_j\phi|_{x-\Delta x} + {}_j\phi|_{x-2\Delta x}}{2\Delta x} = e^{i({}_j\kappa x - {}_j\omega t)}\frac{-e^{i2_j\kappa\Delta x} + 8e^{i_j\kappa\Delta x} - 8e^{-i_j\kappa\Delta x} + e^{-i2_j\kappa\Delta x}}{2\Delta x} = ie^{i({}_j\kappa x - {}_j\omega t)}\frac{sin({}_j\kappa\Delta x)}{3\Delta x}[4 - cos({}_j\kappa\Delta x)] = i_j\phi[\frac{sin({}_jk\Delta x)}{3\Delta x}[4 - cos({}_jk\Delta x)]] \tag{C.42}$$

or

$$\frac{{}^{4^{rth}ord.CD}{}_jk^{effective}}{{}_jk} = \frac{sin(\overline{P}\pi)}{3\overline{P}\pi}[4 - cos(\overline{P}\pi)] \tag{C.43}$$

Thus, from (C.38), (C.41) and (C.43) we can see that as the cell spacing Δx or the wave

number κ decreases (i.e. $\overline{P}$ decreases), the resolved wave number ${}_jk^{effective} \rightarrow {}_jk$. To illustrate this point ${}_jk^{effective}/{}_jk$ is displayed in Figure C.3 for all spatial discretization schemes and indicates the relative advantage in using either the Quick or 4^{rth}-order CD scheme compared with the 2^{nd}-order CD.

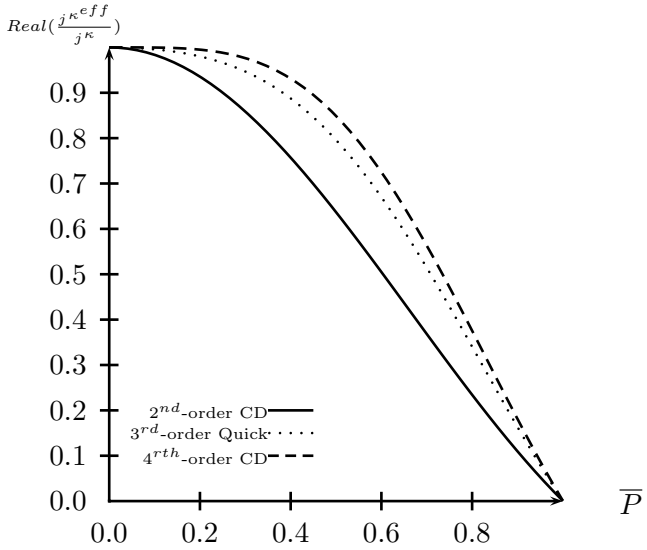

Figure C.3: Normalized effective wave number $\frac{j\kappa^{eff}}{j\kappa}$ vs. $\overline{P} \equiv \frac{j\kappa\Delta x}{\pi}$

Note that the previous analysis can be used to determine a required cell spacing Δx given a target aliasing error for wavelength ℓ. Specifically, from Figure C.2 we see, for example, that to maintain 85% wave number accuracy/fidelity, $\overline{P} \approx 0.45$ for the Quick-scheme. Hence, from the definition of the wave number $\kappa \equiv 2\pi/\ell$ we have the required cell displacement $\Delta x_{reg.} = \overline{P}\pi/\kappa = \overline{P}\ell/2$. If, for example, a wave of length-scale $\ell = 11.2\eta$ is to be resolved, then $\Delta x_{reg.} = 0.45(11.2)/2 = 2.52 \approx 2.45\eta$. It is this target value for cell displacement, ($\Delta x_{reg.} = 2.45\eta$), which is used to formulate the high resolution grid employed during the simulation of transitional mixing (treated in Chapters 5 and 6).

Appendix D

Field Statistics

D.1 Natural Process and Stochastic Variables

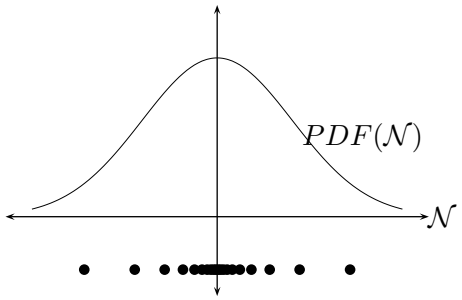

Figure D.1: Data set and corresponding $PDF(V)$

In order to describe natural processes, it is necessary to introduce various statistical quantities. Given a natural property $\mathcal{N}$, which is a function of space $\vec{r}$ and time t, its instantaneous value $\mathcal{N}(\vec{r},t)$ can be described according to the sum of an expectation value $<\mathcal{N}(\vec{r},t)>$ and a fluctuating component $\mathcal{N}'(\vec{r},t)$

$$\mathcal{N}(\vec{r},t) =< \mathcal{N}(\vec{r},t) > +\mathcal{N}'(\vec{r},t) \tag{D.1}$$

If the process variable $\mathcal{N}(\vec{r},t)$ is steady in the mean, then a sampling of values over time, (at a fixed location $\vec{r}$), may yield a frequency function $f(\mathcal{N})$ such as shown in Figure D.1. When the frequency function $f(\mathcal{N})$ is normalized by the total sample size N, we have PDF of the variable $\mathcal{N}$ or

$$PDF(\mathcal{N}) \equiv \frac{f(\mathcal{N})}{N} \tag{D.2}$$

The integral $F(\mathcal{N})$ of the PDF

$$F(V) \equiv \int_{\gamma=-\infty}^{V} PDF(\gamma)d\gamma \tag{D.3}$$

gives the probability (between zero and one) that the process variable $\mathcal{N}(\vec{r},t)$ will take on a value less than or equal to V upon sampling. From this definition it is clearly the case that $F(\infty) = 1$. Introducing an *expectation value operator* $<()>$ we can define the expectation value of any function $G(\mathcal{N}(\vec{r},t))$ via[1]

[1]The *bra-ket* notation is widely used as an *expectation value operator* in Quantum Mechanics.

$$< G(\mathcal{N}(\vec{r},t)) > \equiv \int_{\gamma=-\infty}^{\infty} PDF(\gamma)G(\gamma)d\gamma \tag{D.4}$$

Clearly $< (1) >= 1$ and $< \mathcal{N}(\vec{r},t) >$ represents the expected or mean value of $\mathcal{N}(\vec{r},t)$.

D.1.1 Properties of the Expectation Operator

This work makes use of averaging operations (in time), thus of interest are the relevant properties of the expectation operator $< () >$. For the natural property $\mathcal{N}$ with fluctuating component $\mathcal{N}'(\vec{r},t)$ and expectation value $< (\mathcal{N}(\vec{r})) >= f(\vec{r})$, we have the following properties given in Table D.1

Table D.1: Properties of the (Time Averaging) Expectation Operator $< () >$ on the Natural Function $\mathcal{N}(\vec{r},t)$

Relationship	Via
$< (c) >= c$, $c \neq f(t)$	$< (c) >= c < (1) >= c$
$< (c\mathcal{N}'(\vec{r},t)) >= 0$	$< (c\mathcal{N}'(\vec{r},t)) >= c < (\mathcal{N}'(\vec{r},t) - < (\mathcal{N}'(\vec{r})) >) >= c(< (\mathcal{N}'(\vec{r})) > - < (\mathcal{N}'(\vec{r})) >) = 0$

D.2 Averaging Operations

Given that $\mathcal{N}(\vec{r},t)$ is a spatial and temporally varying stochastic variable, it is useful to specify a filtering or averaging operation on $\mathcal{N}(\vec{r},t)$. The notion of a filtered variable can be approached as follows: We define the infinite integration operator $\backslash\!\backslash () /\!/_m$ as

$$\backslash\!\backslash () /\!/_m \equiv \int_{\tilde{m}=m-\infty}^{m+\infty} ()d\tilde{m} \tag{D.5}$$

where, in relation to the previous section, $\backslash\!\backslash (PDF) /\!/_{\hat{x}} =< (1) >$. If $\mathcal{F}$ is a Box or Gaussian filter $\mathcal{F}$ as shown in Figure D.2, then $\backslash\!\backslash (\mathcal{F}(x)\mathcal{N}(x,t) /\!/_{\hat{x}}$ corresponds to a spatially *filtered* or weighted average of $\mathcal{N}(x,t)$ centered at $\hat{x}$.

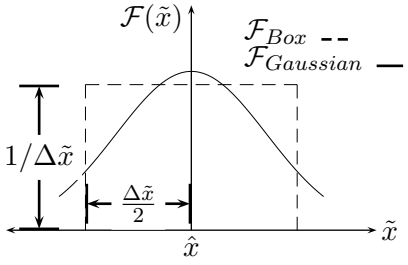

Figure D.2: Box and Gaussian Filter Functions $\mathcal{F}$.

Specifically, the Gaussian Filter yields an average value for $\mathcal{N}$ which is heavily weighted towards property values close to $\hat{x}$. In contrast the box filter is an evenly weighted averaging function over the interval $x = \hat{x} \pm \Delta x/2$. Note that as with the expectation operator we require $\backslash\!\backslash (\mathcal{F}) /\!/_{\hat{x}} = 1$.

D.2.1 Properties of the Averaging Operators

Of specific interest to us is the behavior of the filtered natural/stochastic property, in particular the behavior of the box filtered property $\backslash\!\backslash \mathcal{F}(x,\Delta x)\mathcal{N}(x,t) /\!/_{\hat{x}}$. To illustrate, a

function $\mathcal{N}(x)$ composed of a linear and two sinusoidal components is plotted in Figure D.3 along with the filtered signal $\backslash\!\backslash\mathcal{F}(x,\Delta x)\mathcal{N}(x,t)\,/\!/_{\hat{x}}$ for two different values of the filter width Δx.

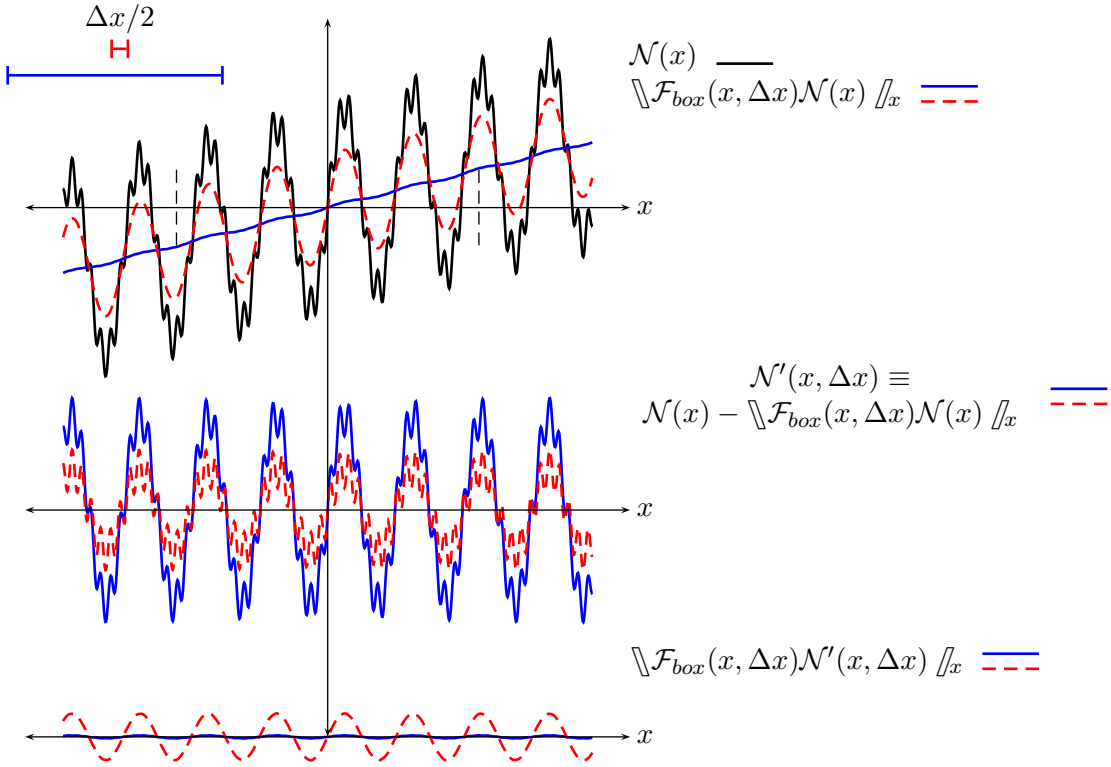

Figure D.3: Stocastic function $N(x)$ with $\backslash\!\backslash\mathcal{F}_{box}(x,\Delta x)\mathcal{N}(x)\,/\!/_x$ superimposed: $\mathcal{N}'(x,\Delta)$: $\backslash\!\backslash\mathcal{F}_{box}(x,\Delta x)\mathcal{N}'(x,\Delta)\,/\!/_x$ where $\mathcal{F}_{box}(x,\Delta x)$ is the box filter/averaging function. Filter half-width $\Delta x/2$ is given in upper-left corner.

The important feature to note from the plot is that the an increase in the filter width Δx produces a smoother averaged value for the filtered variable $\backslash\!\backslash\mathcal{F}_{box}(x,\Delta x)\mathcal{N}(x,t)\,/\!/_x$. In other words, as the filter width is increased, the stochastic component of $\mathcal{N}(x)$ is represented exclusively in the remainder term $\mathcal{N}'(x)$. Thus, for a large filter width, the filtered value of the remainder $\mathcal{N}'(x)$ (i.e. $\backslash\!\backslash\mathcal{F}(x,\Delta)\mathcal{N}'(x)\,/\!/_x$) tends to zero. This can be seen in Figure D.3 which indicates that for a large filter width the filtered remainder $\backslash\!\backslash\mathcal{F}(x,\Delta)\mathcal{N}'(x)\,/\!/_x$ has a negligible magnitude compared to that of the smaller filter width. This fact is of paramount importance when formulating models for turbulent flow: Specifically, in deriving the Reynold's Averaged Navier-Stokes equations (see §2.5) and the Filtered momentum transport equations used in Large Eddy Simulations LES (see §2.6.3).

D.3 Point Statistics

Given that $\mathcal{N}(\vec{r},t)$ is a stochastic variable, a number of descriptive statistics can be calculated based on its fluctuating component $\mathcal{N}'(\vec{r},t) = \mathcal{N}(\vec{r},t) - <\mathcal{N}(\vec{r},t)>$ as shown in Table D.2. Specifically, the single-point auto-correlation $Q_{i,j}(s,\vec{r})$ gives the temporal correlation

between signal measurements at a given location at different times, while the two-point auto-correlation $R_{i,j}(\vec{s},\vec{r})$ gives the temporal correlation between signals measure simultaneously at two different locations.

Table D.2: Random Variable Descriptive Statistics for Fluctuating Vector $\vec{\mathcal{N}}$

Statistic	Definition	Physical Interpretation
Single-Point Auto correlation	$Q_{i,j}(s,\vec{r}) \equiv < \mathcal{N}'_i(\vec{r},t+s)\mathcal{N}'_j(\vec{r},t) >$	Expectation value of the product of present and future disturbance
Normalized Single-Point Auto correlation	${}_{norm}Q_{i,j}(s,\vec{r}) \equiv \frac{Q_{i,j}(s)}{Q_{i,j}(0)}$	Normalized expectation value of the product of present and future disturbance
Two-Point Auto correlation	$R_{i,j}(\vec{s},\vec{r}) \equiv < \mathcal{N}'_i(\vec{r}+\vec{s},t)\mathcal{N}'_j(\vec{r},t) >$	Expectation value of the product of local and spatially remote disturbance
Normalized Two-Point Auto correlation	${}_{norm}R_{i,j}(\vec{s},\vec{r}) \equiv \frac{R_{i,j}(\vec{s})}{R_{i,j}(0)}$	Normalized expectation value of the product of local and spacial remote disturbance

Given that turbulent velocity fluctuations can be expresses in terms of a sum of harmonic basis functions (i.e. a Fourier series (see §2.3.1)) it is natural to decompose turbulent phenomena into Fourier components. Specifically, $R_{i,j}(\vec{s},\vec{r},t)$ can be expressed according to the inverse Fourier Transform

$$R_{i,j}(\vec{s},\vec{r},t) = \int\int\int_{phasespace} e^{i\vec{\kappa}\cdot\vec{r}}\vartheta(\vec{\kappa},\vec{s},t)d\vec{\kappa} \tag{D.6}$$

where the $\vartheta(\vec{\kappa},\vec{s},t)$ is the Fourier Transform of $R_{i,j}(\vec{s},\vec{r},t)$ and $\vec{\kappa}$ is the wave number vector

$$\vartheta_{i,j}(\vec{\kappa},\vec{s},t) = \frac{1}{2\pi}\int\int\int_{physicalspace} e^{-i\vec{\kappa}\cdot\vec{r}}R_{i,j}(\vec{s},\vec{r},t)d\vec{s} \tag{D.7}$$

D.4 Turbulent Kinetic Energy

If the property $\vec{\mathcal{N}}$ is the flow velocity $\vec{V}$, then from (D.6) (letting $\vec{r} \to 0$), the turbulent kinetic energy component per unit mass for wave magnitude $|\vec{\kappa}|$ is given by

$$E(|\vec{\kappa}|,t) = \int\int\int_{phasespace} \frac{1}{2}\vartheta(\vec{\kappa},\vec{0},t)\delta[|\vec{\kappa}| - \vec{\lambda}]d\vec{\lambda} \tag{D.8}$$

Integrating $E(|\vec{\kappa}|,t)$ over all phase space magnitude $|\vec{\kappa}| = 0 \to \infty$ gives the turbulent kinetic energy of the flow

$$\overline{k'} = \int_{\lambda=0}^{\infty} E(|\lambda,t)|d\lambda = \frac{1}{2}R_{i,i}(0,\vec{r},t) = \frac{1}{2} < u'_i u'_i > \tag{D.9}$$

D.5 Iso-tropic Turbulence: Length Scales

In the case of iso-tropic turbulence (as defined in §2.3.2) one can easily define a geometric length scale based on statistical velocity distribution. Specifically, via the two-point velocity correlation $R_{i,i}(\vec{s}, \vec{r}, t)$ we define the integral length-scale

$$L \equiv 2 \int_{|\vec{s}|=0}^{\infty} R_{i,i}(|\hat{\vec{s}}|, \vec{r}, t) d|\vec{s}| \tag{D.10}$$

Appendix E

Fourier Transform

Given the frequency with which Fourier representation and functional decomposition is utilized, a separate treatment will be performed. We begin with a general (qualitative) statement of Fourier's Theorem

Theorem 1 Fourier's Theorem
Any physical function $f(x)$ that varies periodically with wavelength $2\mathcal{L}$ can be expressed as a superposition of harmonic orthogonal basis functions

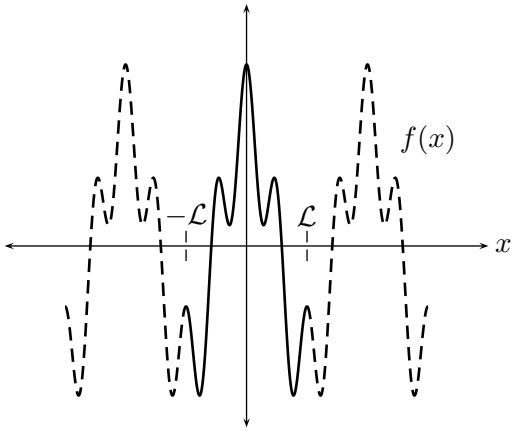

Figure E.1: Periodic function in x

Given a $1-D$ function $f(x)$ which is periodic within the limits $x = \pm\mathcal{L}$ it is possible to decompose $f(x)$ into a 'Fourier Series' of the form

$$f(x) = \sum_{n=1}^{\infty} \hat{f}_\kappa e^{-i\kappa x}, \kappa \equiv \frac{\pi n}{\mathcal{L}}, n = 1, 2, 3, \ldots \tag{E.1}$$

where $\hat{f}_\kappa$ are the Fourier coefficients (whose value is a function of κ). Exploiting the orthogonality of the harmonic function $e^{i\kappa' x}$, the Fourier coefficient (again as a function of κ) can be extracted via

$$\int_{-\mathcal{L}}^{\mathcal{L}} e^{i\kappa' x} f(x) dx = \hat{f}(\kappa') 2\mathcal{L} \Longrightarrow \hat{f}_\kappa = \frac{1}{2\mathcal{L}} \int_{-\mathcal{L}}^{\mathcal{L}} e^{i\kappa x} f(x) dx \tag{E.2}$$

Thus the Fourier transform converts a spatially varying function $f(x)$ into a function $\hat{f}(\kappa)$ which varies in wave space κ.

The above can be generalized to non-periodic functions by taking the limit as $\mathcal{L} \to \infty$. The first consequence is that discrete values for κ, (as shown in (E.1)), now become continuous and range from $-\infty$ to ∞. As a result, $\hat{f}_\kappa$ becomes a continuous function $\hat{f}(\kappa)$ and $f(x)$ can be redefined in terms of an integral referred to as the *inverse Fourier Transform*

$$f(x) = \int_{\kappa=-\infty}^{\infty} \hat{f}(\kappa) e^{-i\kappa x} d\kappa \tag{E.3}$$

Exploiting the orthogonality of the harmonic function $e^{i\kappa' x}$ we have an analogous procedure for the extraction of $\hat{f}(\kappa)$ which can be performed via

$$\int_{x=-\infty}^{\infty} f(x) e^{i\kappa' x} dx = \int_{x=-\infty}^{\infty} [\int_{\kappa=-\infty}^{\infty} \hat{f}(\kappa) e^{-i\kappa x} d\kappa] e^{i\kappa' x} dx = \tag{E.4}$$

$$\int_{\kappa=-\infty}^{\infty} \hat{f}(\kappa) [\int_{x=-\infty}^{\infty} e^{-i\kappa x} e^{i\kappa' x} dx] d\kappa = \int_{\kappa=-\infty}^{\infty} \hat{f}(\kappa) [\delta(\kappa - \kappa')] d\kappa = \hat{f}(\kappa') \tag{E.5}$$

or

$$\hat{f}(\kappa) = \int_{x=-\infty}^{\infty} f(x) e^{i\kappa x} dx \tag{E.6}$$

where we are noting the properties of the Dirac Delta function $\delta()$.